Proceedings of the International
Neural Networks Society 2
Series Editors: Plamen Angelov · Robert Kozma

Lazaros Iliadis
Plamen Parvanov Angelov
Chrisina Jayne
Elias Pimenidis *Editors*

Proceedings of the 21st EANN (Engineering Applications of Neural Networks) 2020 Conference

Proceedings of the EANN 2020

International Neural Network Society

Springer

Proceedings of the International Neural Networks Society

Volume 2

Lazaros Iliadis · Plamen Parvanov Angelov ·
Chrisina Jayne · Elias Pimenidis
Editors

Proceedings of the 21st EANN (Engineering Applications of Neural Networks) 2020 Conference

Proceedings of the EANN 2020

Springer

Editors
Lazaros Iliadis
School of Engineering,
Department of Civil Engineering
Democritus University of Thrace
Xanthi, Greece

Chrisina Jayne
School of Computing
and Digital Technologies
Teesside University
Middlesbrough, UK

Plamen Parvanov Angelov
Lancaster University
Lancaster, UK

Elias Pimenidis
University of the West of England
Bristol, UK

ISSN 2661-8141 ISSN 2661-815X (electronic)
Proceedings of the International Neural Networks Society
ISBN 978-3-030-48790-4 ISBN 978-3-030-48791-1 (eBook)
https://doi.org/10.1007/978-3-030-48791-1

EANN 2020 Preface

Artificial neural networks (ANN) are a typical case of machine learning, which mimics the physical learning process of the human brain. More than 60 years have passed from the introduction of the first perceptron. Since then, numerous types of ANN architectures have been developed. Among them are recurrent ANN, whose nodes' connections are forming a directed graph along a temporal sequence. More recently, generative adversarial neural networks are trying to fuse "imagination" to artificial intelligence (AI) and convolutional neural networks (CNN) are significantly contributing to the enhancement of pattern recognition, machine translation, anomaly detection, and machine vision. Neural networks have a significant contribution in natural language, and they are widely employed for text classification by search engines in the web. In this domain, CNN are successfully applied by the word2vec method, in recommendation systems–sentiment analysis for movies, customer reviews, and so on. Also, they are used in text-to-speech conversion and semantic parsing plus question answering systems.

The engineering applications of neural networks conference aim to bring together scientists from all AI domains and to give them the chance to exchange ideas and to announce their achievements. Since the first conference in 1995, EANN has provided a great discussion forum on engineering applications of all artificial intelligence technologies, focusing on artificial neural networks. More specifically, EANN promotes the use of modeling techniques from all subdomains of AI in diverse application areas, where significant benefits can be derived. The conference is also reporting advances in theoretical AI aspects. Thus, both innovative applications and methods are particularly appreciated. EANN is a mature and well-established international scientific conference held in Europe. Its history is long and very successful, following and spreading the evolution of intelligent systems.

The 21st EANN 2020 was collocated with the 16th EANN 2020 conference.

The first EANN event was organized in Otaniemi, Finland, in 1995. Since then, it has a continuous and dynamic presence as a major global, but mainly European scientific event. More specifically, it has been organized in Finland, UK (England), Sweden, Gibraltar, Poland, Italy, Spain, France, Bulgaria, UK (Scotland), UK

(Bristol), and Greece. It has been technically supported by the International Neural Networks Society (INNS) and more specifically by the EANN Special Interest Group.

This proceedings volume belongs to International Neural Networks (INNS) Springer Series, and it contains the papers that were accepted to be presented orally at the 21st EANN 2020 conference. The diverse nature of papers presented demonstrates the vitality of artificial intelligence algorithms and approaches. It is not only related to neural networks, but it certainly provides a very wide forum for AI applications as well.

The event was held from June 5 to 7, 2020, and it was broadcasted live through web, to all conference participants. There was no potential for physical attendance due to the global problem with CONVI-19 virus.

Regardless of the extremely difficult pandemic conditions, the response of the international scientific community to the EANN 2020 call for papers was more than satisfactory, with 89 papers initially submitted. All papers were peer reviewed by at least two independent academic referees. When needed, a third referee was consulted to resolve any potential conflicts. A total of 47% of the submitted manuscripts (42 papers) have been accepted to be published as full papers (12 pages long) in the Springer proceedings. Due to the high quality of the submissions, the Program Committee has decided that it should accept additionally six more papers to be published as short ones (ten pages long).

Four Keynote speakers gave state-of-the-art lectures (after invitation) in the timely aspects applications of artificial intelligence.

Dr. Pierre Philippe Mathieu

European Space Agency (ESA) Head of the Philab (Φ Lab) Explore Office at the European Space Agency in ESRIN (Frascati, Italy).

Pierre-Philippe is passionate about innovation and our planet: its beauty, fragility and complex dynamics as part of an integrated Earth System. His current role at ESA is to help scientists, innovators and citizens to use high-tech (such as satellite data) to better monitor, understand and preserve our home planet, by making sustainable use of its limited natural resources.

PP's background is in Earth Sciences. He has a degree in engineering and M.Sc from the University of Liege (Belgium), a Ph.D. in climate science from the University of Louvain (Belgium), and a Management degree from the University of Reading Business School (Uk). Over the last 20 years, he has been working in environmental monitoring and modelling, across disciplines from remote sensing, modelling up to weather risk management.

Currently, PP is trying to connect the global picture we get from space with world challenges in daily life, fostering the use of our Earth Observation (EO) missions to support science, innovation and development in partnership with user communities, industry and businesses.

Professor Leontios Hadjileontiadis, Department of Electrical and Computer Engineering, Aristotle University of Thessaloniki, Greece, and Coordinator of i-PROGNOSIS, gave a speech on the subject of "**Smartphone, Parkinson's and Depression: A new AI-based prognostic perspective**".

Professor Hadjileontiadis has been awarded among other awards, as innovative researcher and champion faculty from Microsoft, USA (2012), the Silver Award in Teaching Delivery at the Reimagine Education Awards (2017–2018) and the Healthcare Research Award by the Dubai Healthcare City Authority Excellence Awards (2019). He is a senior member of IEEE.

Professor Nikola Kasabov, FIEEE, FRSNZ, Fellow INNS College of Fellows, DVF RAE, UK, Director, Knowledge Engineering and Discovery Research Institute, Auckland University of Technology, Auckland, New Zealand, Advisory/Visiting Professor SJTU and CASIA China, RGU, UK, gave a speech on the subject of "**Deep Learning, Knowledge Representation and Transfer with Brain-Inspired Spiking Neural Network Architectures**".

Professor Kasabov has received a number of awards, among them: Doctor Honoris Causa from Obuda University, Budapest; INNS Ada Lovelace Meritorious Service Award; NN Best Paper Award for 2016; APNNA "Outstanding Achievements Award"; INNS Gabor Award for "Outstanding contributions to engineering applications of neural networks"; EU Marie Curie Fellowship; Bayer Science Innovation Award; APNNA Excellent Service Award; RSNZ Science and Technology Medal; 2015 AUT Medal; Honorable Member of the Bulgarian and the Greek Societies for Computer Science.

Professor Xiao-Jun Wu Department of Computer Science and Technology, Jiangnan University, China, gave a speech on the subject of "**Image Fusion Based on Deep Learning**".

Professor Xiao-Jun Wu has won the most outstanding postgraduate award by Nanjing University of Science and Technology. He has won different national and international awards, for his research achievements. He was a visiting postdoctoral researcher in the Center for Vision, Speech, and Signal Processing (CVSSP), University of Surrey, UK, from 2003 to 2004.

Tutorials

Prof. John Macintyre

Dean of the Faculty of Applied Sciences, Pro Vice Chancellor at the University of Sunderland, UK. During the 1990s, he established the Center for Adaptive Systems—at the University, which became recognized by the UK government as a center of excellence for applied research in adaptive computing and artificial intelligence. The center undertook many projects working with and for external organizations in industry, science, and academia, and for three years ran the Smart Software for Decision Makers program on behalf of the Department of Trade and Industry.

Professor Macintyre will give a plenary talk on the following subject: "**AI Applications during the COVID-19 Pandemic - A Double Edged Sword?**"

Dr. Kostas Karpouzis

Associate Researcher, Institute of Communication and Computer Systems (ICCS) of the National Technical University of Athens, Greece. Tutorial Subject: "**AI/ML for games for AI/ML**".

Digital games have recently emerged as a very powerful research instrument for a number of reasons: They involve a wide variety of computing disciplines, from databases and networking to hardware and devices, and they are very attractive to users regardless of age or cultural background, making them popular and easy to evaluate with actual players. In the fields of artificial intelligence and machine learning, games are used in a twofold manner: to collect information about the players' individual characteristics (player modeling), expressivity (affective computing), and playing style (adaptivity) and also to develop AI-based player bots to assist and face the human players and as a test bed for contemporary AI algorithms.

This tutorial discusses both approaches that relate AI/ML to games: Starting from a theoretical review of user/player modeling concepts, it discusses how we can collect data from the users during gameplay and use them to adapt the player experience or model the players themselves. Following that, it presents AI/ML algorithms used to train computer-based players and how these can be used in contexts outside gaming. Finally, it introduces player modeling in contexts related to serious gaming, such as health and education.

Intended audience: researchers in the fields of machine learning and human–computer interaction, game developers and designers, health and education practitioners.

The accepted papers of the 21st EANN conference are related to the following thematic topics:

- Classification Machine Learning
- Convolutional Neural Networks in Robotics/Machine Vision
- Deep Learning Applications in Engineering
- Deep Learning LSTM in Environmental Cases
- Deep Learning in Engineering
- Deep Learning/Image Processing
- Deep Learning and Medical Systems
- Fuzzy Logic Modeling
- Unsupervised Machine Learning/Clustering
- Fuzzy Modeling
- Machine Learning and Neuro/Biological Modeling
- Meta-Learning/Nonlinear Modeling
- Algorithmic Foundations of Neural Networks
- Neural Networks in Engineering
- Optimization and Machine Learning
- Hybrid Machine Learning Systems

The authors of submitted papers came from 18 different countries from all over the globe, namely Bulgaria, Czech Republic, Germany, Greece, France, Hong Kong, Hungary, India, Italy, Japan, Norway, Poland, Romania, Russia, Spain, Turkey, UK, and Vietnam.

June 2020 EANN 2020 Chairs

Organization

General Co-chairs

Chrisina Jayne	Teesside University, UK
Vera Kurkova	Czech Academy of Sciences, Czech Republic
Plamen Angelov	Lancaster University, Fellow of the IEEE, of the IET and of the HEA, Vice President of the International Neural Networks Society (INNS) for Conference and Governor of the Systems, Man and Cybernetics Society of the IEEE
John Macintyre	University of Sunderland, UK

Program Co-chairs

Lazaros Iliadis	School of Engineering, Democritus University of Thrace, Greece
Ilias Maglogiannis	University of Piraeus, Greece
Elias Pimenidis	University of the West of England, UK

Honorary Co-chairs

Nikola Kasabov	Auckland University of Technology, New Zealand
Marios Polycarpou	University of Cyprus, Cyprus

Liaison Chair

Ioannis Kompatsiaris	IPTIL Research Institute, Thessaloniki, Greece

Advisory Co-chairs

Andreas Stafylopatis	Technical University of Athens, Greece
Vincenzo Piuri	University of Milan, Italy, IEEE Fellow (2001), IEEE Society/Council Active Memberships/Services: CIS, ComSoc, CS, CSS, EMBS, IMS, PES, PHOS, RAS, SMCS, SPS, BIOMC, SYSC, WIE
Petia Koprinkova	Bulgarian Academy of Sciences, Bulgaria

Workshops Co-chairs

Spyros Sioutas	University of Patras, Greece
Christos Makris	University of Patras, Greece
Phivos Mylonas	Ionio University, Greece
Katia Kermanidis	Ionio University, Greece

Publication and Publicity Co-chairs

Antonis Papaleonidas	Democritus University of Thrace, Greece
Konstantinos Demertzis	Democritus University of Thrace, Greece
George Tsekouras	University of the Aegean, Greece

Special Sessions

Tutorials on Emerging AI Research (Projects and Applications)

Panagiotis Papapetrou	Stockholm University, Sweden
Vangelis Karkaletsis	National Center for Scientific Research, NSCR “Demokritos”, Greece

Steering Committee

Chrisina Jayne	Dean of the School of Computing and Digital Technologies Teesside University, UK
Lazaros Iliadis	School of Engineering, Department of Civil Engineering, Head of the Sector of Mathematics, Programming and GC, Democritus University of Thrace, Greece
Elias Pimenidis	Program Leader Computer Science, Department FET-Computer Science and Creative Technologies, University of the West of England, Bristol, UK

Program Committee

Ioannis Livieris	University of Patras, Greece
Doina Logofătu	Frankfurt University of Applied Sciences, Frankfurt am Main, Germany
Ilias Maglogiannis	University of Piraeus, Greece
Goerge Magoulas	Birkbeck College, University of London, UK
Christos Makris	University of Patras, Greece
Mario Malcangi	University of Milan, Italy
Francesco Marceloni	University of Pisa, Italy
Giovanna Maria Dimitri	University of Cambridge, UK, and University of Siena, Italy
Nikolaos Mitianoudis	Democritus University of Thrace, Greece
Antonio Moran	University of Leon, Spain
Konstantinos Moutselos	University of Piraeus, Greece
Phivos Mylonas	Ionio University, Greece
Stefanos Nikiforos	Ionio University, Greece
Stavros Ntalampiras	University of Milan, Italy
Mihaela Oprea	University Petroleum-Gas of Ploiesti Romania
Ioannis P. Chochliouros	Hellenic Telecommunications Organization, Greece
Basil Papadopoulos	Democritus University of Thrace
Vaios Papaioannou	University of Patras, Greece
Antonis Papaleonidas	Democritus University of Thrace, Greece
Daniel Pérez López	University of Leon, Spain
Isidoros Perikos	University of Patras, Greece
Elias Pimenidis	University of the West of England, Bristol, UK
Panagiotis Pintelas	University of Patras, Greece
Nikolaos Polatidis	University of Brighton, UK
Bernardete Ribeiro	University of Coimbra, Portugal
Leonardo Rundo	University of Cambridge, UK
Alexander Ryjov	Lomonosov Moscow State University, Russia
Simone Scardapane	Sapienza University (Rome), Italy
Evaggelos Spyrou	National Center for Scientific Research—Demokritos, Greece
Antonio Staiano	University of Naples Parthenope, Italy
Andrea Tangherloni	University of Cambridge, UK
Azevedo Tiago	University of Cambridge, UK
Francesco Trovò	Polytecnico di Milano, Italy
Nicolas Tsapatsoulis	Cyprus University of Technology
Petra Vidnerová	The Czech Academy of Sciences, Czech Republic
Paulo Vitor de Campos Souza	CEFET-MG, Brazil
Gerasimos Vonitsanos	University of Patras, Greece

Abstracts of Invited Talks

The Rise of Artificial Intelligence for Earth Observation (AI4EO)

Pierre Philippe Mathieu

European Space Agency (ESA) Head of the Philab (Φ Lab) Explore Office at the European Space Agency in ESRIN (Frascati, Italy)
Pierre.Philippe.Mathieu@esa.int

Abstract. The world of Earth Observation (EO) is rapidly changing as a result of exponential advances in sensor and digital technologies. The speed of change has no historical precedent. Recent decades have witnessed extraordinary developments in ICT, including the Internet, cloud computing and storage, which have all led to radically new ways to collect, distribute and analyse data about our planet. This digital revolution is also accompanied by a sensing revolution that provides an unprecedented amount of data on the state of our planet and its changes.

Europe leads this sensing revolution in space through the Copernicus initiative and the corresponding development of a family of Sentinel missions. This has enabled the global monitoring of our planet across the whole electromagnetic spectrum on an operational and sustained basis. In addition, a new trend, referred to as "New Space", is now rapidly emerging through the increasing commoditization and commercialization of space.

These new global data sets from space lead to a far more comprehensive picture of our planet. This picture is now even more refined via data from billions of smart and inter-connected sensors referred to as the Internet of Things. Such streams of dynamic data on our planet offer new possibilities for scientists to advance our understanding of how the ocean, atmosphere, land and cryosphere operate and interact as part on an integrated Earth System. It also represents new opportunities for entrepreneurs to turn big data into new types of information services.

However, the emergence of big data creates new opportunities but also new challenges for scientists, business, data and software providers to make sense of the vast and diverse amount of data by capitalizing on powerful techniques such as Artificial Intelligence (AI). Until recently AI was mainly a restricted field occupied by experts and scientists, but today it is routinely used in everyday life without us even noticing it, in applications ranging from recommendation engines, language services, face recognition and autonomous vehicles.

The application of AI to EO data is just at its infancy, remaining mainly concentrated on computer vision applications with Very High-Resolution satellite imagery, while there are certainly many areas of Earth Science and big data mining / fusion,

which could increasingly benefit from AI, leading to entire new types of value chain, scientific knowledge and innovative EO services.

This talk will present some of the ESA research / application activities and partnerships in the AI4EO field, inviting you to stimulate new ideas and collaboration to make the most of the big data and AI revolutions.

Smartphone, Parkinson's, and Depression: A New AI-Based Prognostic Perspective

Leontios Hadjileontiadis[1,2]

[1] Department of Electrical and Computer Engineering, Khalifa University of Science and Technology, Technology and Research, Abu Dhabi, United Arab Emirates
[2] Department of Electrical and Computer Engineering, Aristotle University of Thessaloniki, Thessaloniki, Greece
leontios@auth.gr

Abstract. Machine learning (ML) is a branch of artificial intelligence (AI) based on the idea that systems can learn from data, identify patterns, and make decisions with minimal human intervention. While many ML algorithms have been around for a long time, the ability to automatically apply complex mathematical calculations to big data—over and over, faster and faster, deeper and deeper—is a recent development, leading to the realization of the so-called deep learning (DL). The latter has an intuitive capability that is similar to biological brains. It is able to handle the inherent unpredictability and fuzziness of the natural world. In this keynote, the main aspects of ML and DL will be presented, and the focus will be placed in the way they are used to shed light upon the human behavioral modeling. In this vein, AI-based approaches will be presented for identifying fine motor skills deterioration due to early Parkinson's and depression symptoms reflected in the keystroke dynamics, while interacting with a smartphone. These approaches provide a new and unobtrusive way for gathering and analyzing dense sampled big data, contributing to further understanding disease symptoms at a very early stage, guiding personalized and targeted interventions that sustain the patient's quality of life.

Deep Learning, Knowledge Representation, and Transfer with Brain-Inspired Spiking Neural Network Architectures

Nikola Kasabov

Auckland University of Technology, Knowledge Engineering and Discovery Research Institute, Auckland, New Zealand
nkasabov@aut.ac.nz

Abstract. The talk argues and demonstrates that the third generation of artificial neural networks, the spiking neural networks (SNN), can be used to design brain-inspired architectures that are not only capable of deep learning of temporal or spatiotemporal data, but also enabling the extraction of deep knowledge representation from the learned data. Similarly to how the brain learns time space data, these SNN models do not need to be restricted in number of layers, neurons in each layer, etc. When a SNN model is designed to follow a brain template, knowledge transfer between humans and machines in both directions becomes possible through the creation of brain-inspired brain–computer interfaces (BCI). The presented approach is illustrated on an exemplar SNN architecture NeuCube (free software and open source available from www.kedri.aut.ac.nz/neucube) and case studies of brain and environmental data modeling and knowledge representation using incremental and transfer learning algorithms. These include predictive modeling of EEG and fMRI data measuring cognitive processes and response to treatment, AD prediction, BCI for neuro-rehabilitation, human–human and human-VR communication, hyper-scanning, and other.

Image Fusion Based on Deep Learning

Xiao-Jun Wu

Department of Computer Science and Technology, School of IoT Engineering, Jiangnan University, China
wu_xiaojun@jiangnan.edu.cn

Abstract. Deep learning (DL) has found very successful applications in numerous different domains with impressive results. Image fusion (IMF) algorithms based on DL and their applications will be presented thoroughly in this keynote lecture. Initially, a brief introductory overview of both concepts will be given. Then, IMF employing DL will be presented in terms of pixel, feature, and decision level, respectively. Furthermore, a DL-inspired approach called MDLatLRR which is a general approach to image decomposition will be introduced for IMF. A comprehensive analysis of DL models will be offered, and their typical applications will be discussed, including **I**mage **Q**uality **E**nhancement, **F**acial **L**andmark **D**etection, **O**bject **T**racking, Multi-**M**odal **I**mage **F**usion, **V**ideo **S**tyle **T**ransformation, and **D**eep **F**ake of **F**acial **I**mages, respectively.

Contents

Classification/Machine Learning

A Compact Sequence Encoding Scheme for Online Human Activity Recognition in HRI Applications

Georgios Tsatiris[1](✉), Kostas Karpouzis[1], and Stefanos Kollias[1,2]

[1] Artificial Intelligence and Learning Systems Laboratory, School of Electrical and Computer Engineering, National Technical University of Athens, 9 Heroon Politechniou Street, 15780 Athens, Greece
`gtsatiris@image.ntua.gr`, `{kkarpou,stefanos}@cs.ntua.gr`

[2] School of Computer Science, University of Lincoln, Brayford Pool, Lincoln, Lincolnshire, UK

Abstract. Human activity recognition and analysis has always been one of the most active areas of pattern recognition and machine intelligence, with applications in various fields, including but not limited to exertion games, surveillance, sports analytics and healthcare. Especially in Human-Robot Interaction, human activity understanding plays a crucial role as household robotic assistants are a trend of the near future. However, state-of-the-art infrastructures that can support complex machine intelligence tasks are not always available, and may not be for the average consumer, as robotic hardware is expensive. In this paper we propose a novel action sequence encoding scheme which efficiently transforms spatio-temporal action sequences into compact representations, using Mahalanobis distance-based shape features and the Radon transform. This representation can be used as input for a lightweight convolutional neural network. Experiments show that the proposed pipeline, when based on state-of-the-art human pose estimation techniques, can provide a robust end-to-end online action recognition scheme, deployable on hardware lacking extreme computing capabilities.

Keywords: Action recognition · Deep neural networks · Human-Robot Interaction · Radon transform

1 Introduction

Human activity recognition is a very important field of study inside the broad domain of pattern recognition, with many everyday life applications. High level human actions are an important information modality for social interaction and they play a critical role in Human-Robot Interaction (HRI) [12]. Human poses, hand gestures and overall body motion are also important for human-focused HRI, especially in applications with robots interacting with humans daily (e.g. [1,18,20]). Robotic assistants are required to understand and analyse human activity at all levels of interpretation, as well as have the ability to predict intentions and to imitate human actions when forming responses. Social robots and applications aimed at such environments will need to be employed in human-centric contexts, build trust and effectively assist humans beings [6]. In this paper, we focus on online human activity recognition pipelines with the aim to provide solutions on the inherent problems of such endeavours.

1.1 Related Work

Various works on activity analysis and understanding deal with real application scenarios. In the field of preventing unintentional falls in elderly care and assistive environments, the work presented in [29] is one of the most typical attempts for applying convolutional neural networks in a fall detection application. A dataset of daily activities recorded from many people is used as classification is performed on single frames containing human postures. This method performs well on posture classification and can detect falls with a low false alarm rate. In an earlier work [16], an efficient algorithm is proposed to identify temporal patterns in actions. It further utilizes these patterns to construct activity representations for automated recognition.

There is an extensive literature of studies focused on HRI, a comprehensive presentation of which can be found in [12]. In a typical example of such works, authors in [22] propose that state-of-the-art approaches from automatic speech and visual action recognition, fused with multiple modalities, can construct multimodal recognition pipelines focused on assistive robots for elderly environments. An end-to-end approach shown in [3] deals with dynamic gestures using a Dynamic Time Warping approach, based on features extracted from depth data, in a complete HRI scenario.

1.2 Real World Challenges

As stated in [25], applied human activity recognition pipelines are demanding in terms of hardware and general infrastructure. Most action recognition systems, especially smart-home or assistive living applications, depend on network infrastructures for easy data fusion and integration of different sensing modalities. HRI environments are no different, in the sense that they may need computing capabilities similar to common workstations, as well as networking. Especially when dealing with deep learning-based pipelines, we are used to having hardware acceleration (i.e. massive parallel computing, GPU acceleration etc.) at our disposal. This study aims to provide a lightweight pipeline with limited need for high-end infrastructures.

2 Theoretical Primer

In the following section, we attempt a brief documentation of the theoretical background on which the proposed scheme is built upon. This primer emphasizes on the statistical nature of spatio-temporal data, the use of the Radon Transform for feature encoding, as well as the necessary tools to encode the necessary information into a compact pipeline.

2.1 Variance-Based Features

As mentioned in [24], high level human pose and activity descriptors, such as spatio-temporal interest points [14] or human joints, can be treated as probabilistic distributions. Joints detected in a video frame or still image, e.g. using pipelines such as OpenPose [4], can be considered distributed in space, whereas spatio-temporal interest points are distributed both in space and time. Action recognition techniques benefit from accurately modeling these relationships between the salient features describing an action sequence.

Particularly in [24], a method to distinguish between experienced tennis players and amateurs is shown, which employees feature vectors constructed by calculating the per frame variance of interest points. Variance, as the second central moment, is an effective shape descriptor [17]. Interest points and joint locations form a 3D volumes in space and time. In that context, we extend the idea demonstrated in [24], by incorporating the use of Mahalanobis distances.

Mahalanobis Distance. Given a sample vector $\boldsymbol{x}$ from a distribution D with mean $\boldsymbol{\mu}$ and covariance matrix S, the Mahalanobis distance between $\boldsymbol{x}$ and D is given by Eq. 1.

$$mahal(\boldsymbol{x}, \boldsymbol{\mu}, S) = \sqrt{(\boldsymbol{x} - \boldsymbol{\mu})^T S^{-1} (\boldsymbol{x} - \boldsymbol{\mu})} \tag{1}$$

In this work, we are focusing on detected human joints in 3D space, like the ones extracted using depth sensors (e.g. Intel RealSense[1] or Microsoft Azure Kinect[2]) and by pipelines such as the one presented in [19], which extends common 2D heatmap-based pose detection techniques such as [4] without utilizing costly volumetric operations. There is a good indication that skeletal joints can be considered valid spatio-temporal interest points when it comes to human action analysis and, with them being a more refined and targeted source of human posture information, can lead to better results [27].

As the relative position of a joint and the human body is crucial in the definition of human motion, we believe that a compact and robust way to model these individual relations should be central to any action recognition pipeline. The Mahalanobis distance, as an established metric for point-to-distribution distances, is more suitable in this task, instead of more intuitive metrics, such the Euclidean distance between a point and the distribution centroid. Its place in this pipeline will be explained in detail in Subsect. 3.1.

[1] https://www.intelrealsense.com/.
[2] https://azure.microsoft.com/en-us/services/kinect-dk/.

2.2 Use of the Radon Transform

The Radon transform is effectively used as a reconstruction and feature extraction tool for several decades [2]. It has found applications in earlier human activity recognition pipelines based on hand-crafted features [7] and in novel techniques, alongside its generalization, the Trace transform [13], in offline pipelines [9,10]. Another application of the Radon transform in this field leverages the transform's ability to create translation and scale invariant features to use as input for a Recurrent Neural Network (RNN) [26]. However, for reasons which will be demonstrated in the next section, this paper avoids the use of RNN and draws inspiration from such studies as the one in [11], where source images and their Conic Radon transforms are fed into a deep convolutional neural network for fingerprint classification.

Given a 2D function $f(x, y)$ with $x, y \in \mathbb{R}$, its Radon transform R_f is equal to the integral of all values of f under all lines L, defined by parameters $\rho, \theta \in \mathbb{R}$, where ρ is each line's distance from the origin and θ is the angle formed between the line and the horizontal axis:

$$R_f(\rho, \theta) = \int_L f(x, y) dL \tag{2}$$

If we substitute the parametrical ρ, θ line equation in Eq. 2, we have the following:

$$R_f(\rho, \theta) = \int_{-\infty}^{\infty} \int_{-\infty}^{\infty} f(x, y) \delta(x \cos\theta + y \sin\theta - \rho) dx dy \tag{3}$$

where δ the Dirac delta function, ensuring that only the values of f under line ρ, θ will be integrated over.

3 The Proposed Pipeline

At this point, we have documented the theoretical tools to give spatio-temporal prominence to raw joint information using variance-based shape features and, particularly, the Mahalanobis distance. We have also seen how the Radon transform and other relevant transforms can create robust features out of otherwise non-salient 2D and 3D functions. This section will clarify how the aforementioned theoretical tools will be used in a unified and compact pipeline action encoding pipeline.

3.1 Spatio-Temporal Radon Footprints

As we have established, the relationship between the position of one joint and the rest of the body parts of a subject, at a particular point in time, can be encoded by treating the set of joints as a distribution and calculating the Mahalanobis distance (given by Eq. 1) between it and that particular joint. In our context, a point in time is a frame in an action sequence or video. So, if we extend the above claim to all the joints of a subject and across all frames of an action sequence, we can formulate a Mahalanobis matrix M, whose values for joint j and frame f can be calculated using the following equation:

$$M(j,f) = mahal(\boldsymbol{x_f^j}, \boldsymbol{\mu_f}, S_f) \tag{4}$$

where $\boldsymbol{x_f^j}$ is the coordinate vector of joint j in frame f, defined in $\mathbb{R}^2$ or $\mathbb{R}^3$, $\boldsymbol{\mu_f}$ is the mean of all joint coordinate vectors in frame f (essentially the centroid) and S_f is the covariance matrix of the joint distribution at frame f.

In essence, the Mahalanobis matrix formulated in Eq. 4 is a complete 2D representation of the action sequence in space and time. With $J \times t$ resolution, where J is the total number of joints and t is the point in time (number of frames passed) since the beginning of the sequence, each line of the matrix has the Mahalanobis distances of every joint at the corresponding frame.

What this representation lacks, however, is a way to correlate the individual frame information into a compact robust feature which will describe the action sequence from its start up to point t. For this reason, we calculate the Radon transform of the 2D function M by substituting the representation $M(j,f)$ into Eq. 3. This gives as a 2D spatio-temporal feature describing the action sequence up to point t in time. This feature will, for the rest of this paper, be called the Spatio-temporal Radon Footprint of the action up to point t, will be denoted as SRF_t and is calculated as follows:

$$SRF_t(\rho,\theta) = \int_0^{t-1}\int_0^{J-1} M(j,f)\delta(j\cos\theta + f\sin\theta - \rho)\,dj\,df \tag{5}$$

In the above equation, it must hold that $t \geqslant 2$, both for M to be a 2D function of j and f and for the representation to encode a minimum of temporal information. In practice, depending on the action itself, more frames may need to pass before starting to calculate SRFs. Naturally, it should also hold that $F > 2$, which is obvious, both for the aforementioned reason as well as because it is impossible to ascertain the nature of an activity with insufficient joint information.

The process of calculating a SRF at a point in time, from a sequence of frames containing joint information, is depicted in Fig. 1. The frames shown

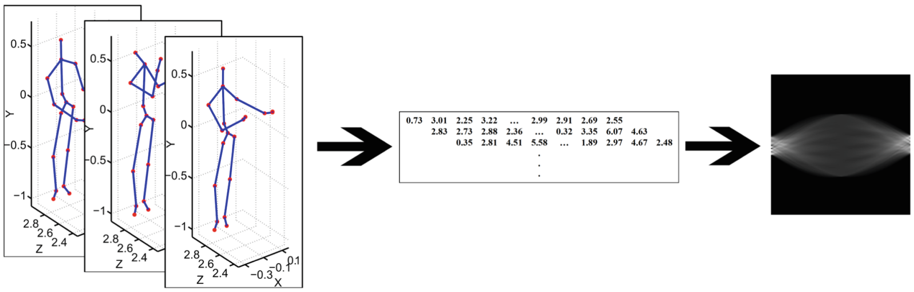

Fig. 1. Calculating SRF_t: the Mahalanobis matrix is calculated from the action sequence at point t and the Radon transform of the matrix gives the final result.

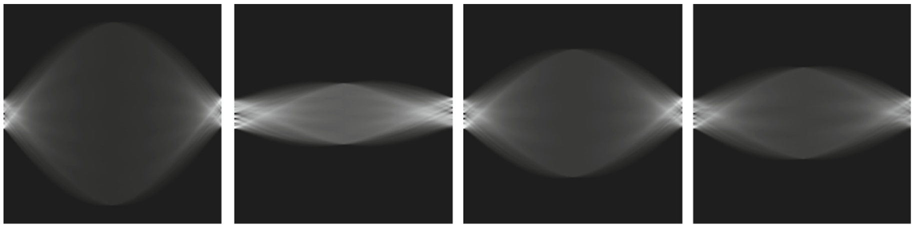

Fig. 2. *SRF* samples from various action sequences of the UTD-MHAD dataset, at varying points in time.

are samples from the UTD-MHAD dataset [5], which will be documented in Subsect. 4.1. Figure 2 shows sample *SRF*s taken from this dataset, from different sequences and at different timestamps.

3.2 A VGG CNN-Based Pipeline

In previous works such as the ones in [10] and [9], the Radon transform and its derivatives were intermediate features, used to produce the final feature vector describing the action sequence, which in turn was used as input for established machine learning techniques, such as SVMs. In this work, however, much like in [11], instead of hand-crafting features based on the transform's result, a convolutional neural network will learn those features directly from the *SRF*s. Particularly, we opted for a VGG-based architecture [23], because of the simplicity, the ease to train and deploy and the ability to adapt to complex pattern recognition problems that this family of convolutional neural networks demonstrates. The network used in our pipeline is shown in Fig. 3.

Preference over RNN-LSTM Architectures. It is customary to use Recurrent Neural Network (RNN, LSTM) architectures for online pattern recognition tasks involving temporal sequences [15], due to their ability to learn and encode temporal information. However, known issues come with the use of such networks, including the need for large training datasets in most cases, the vanishing and exploding gradient problems, as well their high demands in computational resources [8]. By encoding online spatio-temporal information in *SRF*s and using robust object detection architectures, we aim to eliminate the need for such networks and provide an online and compact action recognition pipeline which would not depend on extremely sophisticated hardware.

Per-Frame and Cumulative Classification. Human activity recognition is a temporally sensitive task. Offline techniques need to observe the complete action sequence before performing classification. In an online pipeline aiming towards real-time action recognition, per-frame classification is central. Previous studies, such as the one in [29], perform classification between unintentional falls

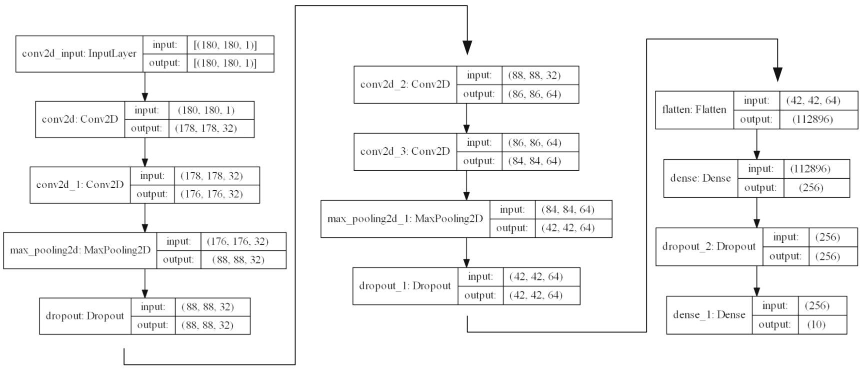
conv2d_input: InputLayer | input: [(180, 180, 1)] | output: [(180, 180, 1)]
conv2d: Conv2D | input: (180, 180, 1) | output: (178, 178, 32)
conv2d_1: Conv2D | input: (178, 178, 32) | output: (176, 176, 32)
max_pooling2d: MaxPooling2D | input: (176, 176, 32) | output: (88, 88, 32)
dropout: Dropout | input: (88, 88, 32) | output: (88, 88, 32)
conv2d_2: Conv2D | input: (88, 88, 32) | output: (86, 86, 64)
conv2d_3: Conv2D | input: (86, 86, 64) | output: (84, 84, 64)
max_pooling2d_1: MaxPooling2D | input: (84, 84, 64) | output: (42, 42, 64)
dropout_1: Dropout | input: (42, 42, 64) | output: (42, 42, 64)
flatten: Flatten | input: (42, 42, 64) | output: (112896)
dense: Dense | input: (112896) | output: (256)
dropout_2: Dropout | input: (256) | output: (256)
dense_1: Dense | input: (256) | output: (10)

Fig. 3. The VGG-based architecture used in our experiments.

and other activities on single postures/frames, rather than complete sequences. The methodology presented in this paper performs online action analysis, while taking into account the history of every previous per-frame classification task.

In a specific frame f of the sequence, the SRF_f is calculated and fed in the aforementioned network. The network then determines the class of the action at that frame. However, the final decision is made by counting the number each action class was deemed the correct class of the sequence, divided by the number of frames which have passed up until the moment of classification. In a sense, for each action class and in every frame, we calculate a confidence that this action belongs to that class. This confidence is updated per-frame, with the ultimate goal of determining the correct class as early in the sequence as possible. This way, we eliminate the possibility of outliers (frames being classified in the wrong class) among a number of correct classifications.

4 Experimental Evaluation

In this section, we will discuss the experimental setup and the data used in the evaluation of the aforementioned methodology. The choice of the validation protocol will also become apparent, as well as the efficiency of the proposed technique.

4.1 Dataset

In our experiments, we used the UTD-MHAD dataset [5]. In particular, we used a more recent subset of this dataset, which contains data captured using the Kinect v2 depth sensor. It includes 10 actions, namely “Right hand high wave”, “Right hand catch”, “Right hand high throw”, “Right hand draw X”, “Right hand draw tick”, “Right hand draw circle”, “Right hand horizontal wave”, “Right hand forward punch”, “Right hand hammer” and “Hand clap (two hands)”. These actions were performed by 6 subjects (3 female and 3 male), each one of whom performed each action 5 times, resulting in a total of 300 action sequences. Figure 4 shows sample data from the dataset.

We opted for this new subset of the UTD-MHAD dataset for two reasons, both of which are sensor related. The Kinect V2 is a relatively state of the art device which can detect joint information for 25 body joints without inducing much noise (Base of the spine, Middle of the spine, Neck, Head, Left shoulder, Left elbow, Left wrist, Left hand, Right shoulder, Right elbow, Right wrist, Right hand, Left hip, Left knee, Left ankle, Left foot, Right hip, Right knee, Right ankle, Right foot, Spine at the shoulder, Tip of the left hand, Left thumb, Tip of the right hand, Right thumb).

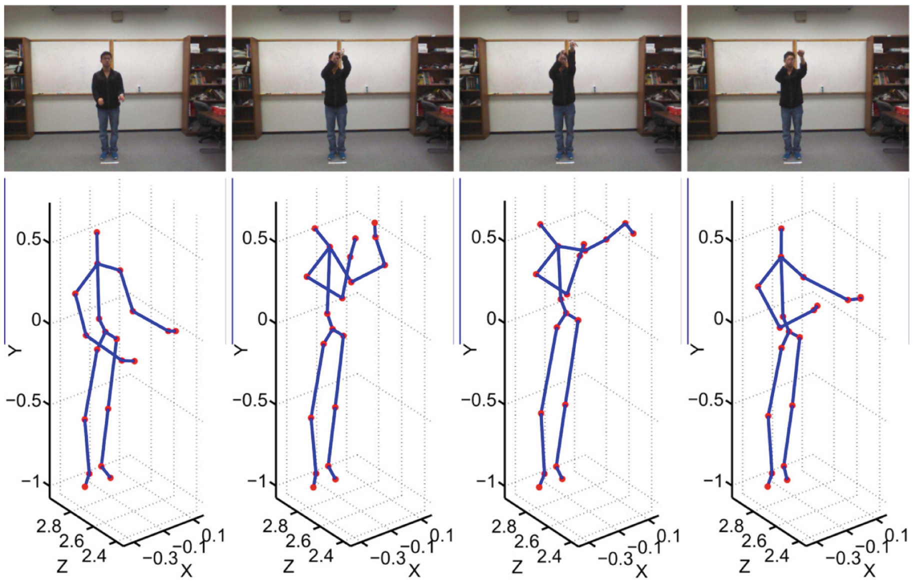

Fig. 4. Samples from the UTD-MHAD dataset.

4.2 Leave-One-Person-Out Cross-Validation

Validating a human activity recognition pipeline entails an inherent complexity which is not found in other classification tasks. In a typical scenario, we would have partitioned the dataset into a training and a testing set. Our dataset, as many other action datasets, is already partitioned by the subjects executing the actions. Simply leaving a person out for validation and training with the rest would not, however, produce reliable results.

Every person performs an action in a unique to every other person's way. For that matter, we perform the Leave-one-person-out cross-validation protocol (LOPO or LOO) across all individuals in our dataset. Essentially, we are training with the actions performed by 5 subjects and test with the actions performed by the one we left out. We repeat this process for all subjects in the dataset. The final reported accuracy would be the mean of the individual accuracies of each training-testing scenario.

4.3 Results

One of the first findings that we should report is that our pipeline achieved high training accuracy across all individual subject training tasks, with the mean training accuracy reaching **99.15%**. The highest achieved training accuracy was as high as **99.25%**, when training with all subjects except for subject #3, which was used for testing.

An expected discrepancy was noticed across the validation tasks. Notably, when testing with subject #6, the pipeline achieved validation accuracy equal to **90.08%**, whereas the worst performance was reported when testing with subject #3 (**66.02%**), on the same task that achieved the highest training accuracy. This hints towards possible issues of overfitting which may need to be dealt with in future works. The mean validation accuracy achieved after performing the complete LOPO protocol across all subjects was equal to **81.06%**. Table 1 shows the confusion matrix of the proposed pipeline after the validation process.

Figure 5 shows a characteristic sample of the evolution of class confidences according to our proposed pipeline. In this figure we observe how action class 4 ("Right hand draw X") emerges as the most possible to be the correct one with the passage of time. More extensive experimentation may lead to more robust findings concerning the similarity and relationship between classes.

Table 1. Confusion matrix of the proposed pipeline.

Truth											
Predicted	a1	a2	a3	a4	a5	a6	a7	a8	a9	a10	Total
a1	**20**	0	0	0	0	0	2	0	1	0	23
a2	0	**10**	1	0	0	0	0	0	0	0	11
a3	0	12	**26**	0	0	0	0	1	0	0	39
a4	0	0	3	**23**	0	6	1	0	0	0	33
a5	0	0	0	5	**30**	0	0	1	0	0	36
a6	4	0	0	2	0	**24**	2	0	0	0	32
a7	0	0	0	0	0	0	**14**	1	0	0	15
a8	0	7	0	0	0	0	6	**27**	0	0	40
a9	6	1	0	0	0	0	5	0	**29**	0	41
a10	0	0	0	0	0	0	0	0	0	**30**	30

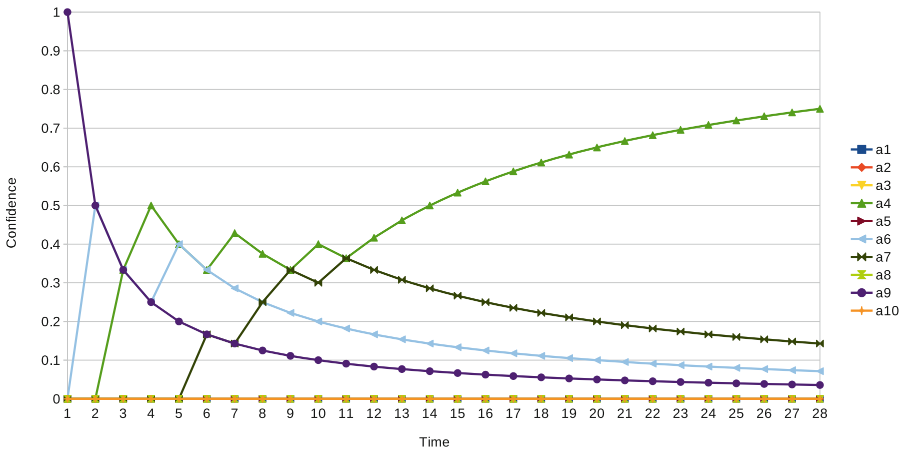

Fig. 5. Evolution of class confidences for action #4, performed by subject #6. After a certain point in time, the correct class (4, Right hand draw X) emerges as the most prevalent class.

5 Conclusion

This paper presented a compact online action recognition methodology, based on a novel sequence encoding scheme and a lightweight convolutional neural network. It is suitable for deployment on hardware with limited capabilities, which can be found even in household robotic systems. Experimentation and cross validation showed this pipeline can be used with state-of-the-art human pose estimation techniques to form efficient end-to-end activity recognition techniques.

Discrepancies in the testing data pointed out that there may be room for improvement, as more novel convolutional neural network architectures emerge. Furthermore, there may be hints of overfitting, as stated in the previous section, which may need to be dealt with.

In our future work, we will include attention models [21,28] in the CNN architecture to further improve the performance of the presented approach. Another direction could also be to focus on decrypting the inherent relationships and similarities between actions as encoded by SRFs, in order to evaluate the proposed scheme's performance as an action analysis and assessment tool.

References

1. Bevacqua, E., Raouzaiou, A., Peters, C., Caridakis, G., Karpouzis, K., Pelachaud, C., Mancini, M.: Multimodal sensing, interpretation and copying of movements by a virtual agent. In: André, E., Dybkjær, L., Minker, W., Neumann, H., Weber, M. (eds.) Perception and Interactive Technologies, pp. 164–174. Springer, Berlin Heidelberg (2006)

2. Beylkin, G.: Discrete radon transform. IEEE Trans. Acoust. Speech Signal Process. **35**(2), 162–172 (1987). https://doi.org/10.1109/TASSP.1987.1165108
3. Canal, G., Escalera, S., Angulo, C.: A real-time human-robot interaction system based on gestures for assistive scenarios. Comput. Vis. Image Underst. **149**, 65–77 (2016). https://doi.org/10.1016/j.cviu.2016.03.004. Special issue on Assistive Computer Vision and Robotics - Assistive Solutions for Mobility, Communication and HMI
4. Cao, Z., Hidalgo, G., Simon, T., Wei, S., Sheikh, Y.: OpenPose: realtime multi-person 2D pose estimation using part affinity fields (2018). CoRR abs/1812.08008. http://arxiv.org/abs/1812.08008
5. Chen, C., Jafari, R., Kehtarnavaz, N.: UTD-MHAD: a multimodal dataset for human action recognition utilizing a depth camera and a wearable inertial sensor. In: 2015 IEEE International Conference on Image Processing (ICIP), pp. 168–172, September 2015. https://doi.org/10.1109/ICIP.2015.7350781
6. Chen, M., Nikolaidis, S., Soh, H., Hsu, D., Srinivasa, S.: Planning with trust for human-robot collaboration. In: Proceedings of the 2018 ACM/IEEE International Conference on Human-Robot Interaction HRI 2018, pp. 307–315. Association for Computing Machinery, New York (2018). https://doi.org/10.1145/3171221.3171264
7. Chen, Y., Wu, Q., He, X.: Human action recognition by radon transform. In: 2008 IEEE International Conference on Data Mining Workshops, pp. 862–868, December 2008. https://doi.org/10.1109/ICDMW.2008.26
8. Gehring, J., Auli, M., Grangier, D., Yarats, D., Dauphin, Y.N.: Convolutional sequence to sequence learning. In: Proceedings of the 34th International Conference on Machine Learning ICML 2017, vol. 70, pp. 1243–1252. JMLR.org (2017)
9. Goudelis, G., Tsatiris, G., Karpouzis, K., Kollias, S.: 3D cylindrical trace transform based feature extraction for effective human action classification. In: 2017 IEEE Conference on Computational Intelligence and Games (CIG), pp. 96–103, August 2017. https://doi.org/10.1109/CIG.2017.8080421
10. Goudelis, G., Karpouzis, K., Kollias, S.: Exploring trace transform for robust human action recognition. Pattern Recogn. **46**(12), 3238–3248 (2013). https://doi.org/10.1016/j.patcog.2013.06.006
11. Hamdi, D.E., Elouedi, I., Fathallah, A., Nguyuen, M.K., Hamouda, A.: Combining fingerprints and their radon transform as input to deep learning for a fingerprint classification task. In: 2018 15th International Conference on Control, Automation, Robotics and Vision (ICARCV), pp. 1448–1453, November 2018. https://doi.org/10.1109/ICARCV.2018.8581072
12. Ji, Y., Yang, Y., Shen, F., Shen, H.T., Li, X.: A survey of human action analysis in HRI applications. IEEE Trans. Circuits Syst. Video Technol., 1 (2019). https://doi.org/10.1109/TCSVT.2019.2912988
13. Kadyrov, A., Petrou, M.: The trace transform and its applications. IEEE Trans. Pattern Anal. Mach. Intell. **23**(8), 811–828 (2001). https://doi.org/10.1109/34.946986
14. Laptev, I.: On space-time interest points. Int. J. Comput. Vis. **64**(2–3), 107–123 (2005)
15. Liu, J., Wang, G., Duan, L., Abdiyeva, K., Kot, A.C.: Skeleton-based human action recognition with global context-aware attention lstm networks. IEEE Trans. Image Process. **27**(4), 1586–1599 (2018). https://doi.org/10.1109/TIP.2017.2785279
16. Liu, Y., Nie, L., Liu, L., Rosenblum, D.S.: From action to activity: sensor-based activity recognition. Neurocomputing **181**, 108–115 (2016). https://doi.org/10.1016/j.neucom.2015.08.096. Big Data Driven Intelligent Transportation Systems

17. Loncaric, S.: A survey of shape analysis techniques. Pattern Recogn. **31**(8), 983–1001 (1998). https://doi.org/10.1016/S0031-2023(97)00122-2
18. Malatesta, L., Murray, J., Raouzaiou, A., Hiolle, A., Cañamero, L., Karpouzis, K.: Emotion modelling and facial affect recognition in human-computer and human-robot interaction. In: Murguía, M.I.C. (ed.) State of the Art in Face Recognition. IntechOpen, Rijeka (2009). https://doi.org/10.5772/6648
19. Nibali, A., He, Z., Morgan, S., Prendergast, L.: 3D human pose estimation with 2D marginal heatmaps. In: 2019 IEEE Winter Conference on Applications of Computer Vision (WACV), pp. 1477–1485, January 2019. https://doi.org/10.1109/WACV.2019.00162
20. Peters, C., Castellano, C., Rehm, M., André, E., Raouzaiou, A., Rapantzikos, K., Karpouzis, K., Volpe, G., Camurri, A., Vasalou, A.: Fundamentals of Agent Perception and Attention Modelling, pp. 293–319. Springer, Berlin, Heidelberg (2011)
21. Rapantzikos, K., Tsapatsoulis, N., Avrithis, Y., Kollias, S.: Bottom-up spatiotemporal visual attention model for video analysis. IET Image Process. **1**(11), 237–248 (2007)
22. Rodomagoulakis, I., Kardaris, N., Pitsikalis, V., Mavroudi, E., Katsamanis, A., Tsiami, A., Maragos, P.: Multimodal human action recognition in assistive human-robot interaction. In: 2016 IEEE International Conference on Acoustics, Speech and Signal Processing (ICASSP), pp. 2702–2706, March 2016. https://doi.org/10.1109/ICASSP.2016.7472168
23. Simonyan, K., Zisserman, A.: Very deep convolutional networks for large-scale image recognition. In: Bengio, Y., LeCun, Y. (eds.) 3rd International Conference on Learning Representations, ICLR 2015, San Diego, CA, USA, 7–9 May 2015, Conference Track Proceedings (2015). http://arxiv.org/abs/1409.1556
24. Tsatiris, G., Karpouzis, K., Kollias, S.: Variance-based shape descriptors for determining the level of expertise of tennis players. In: 2017 9th International Conference on Virtual Worlds and Games for Serious Applications (VS-Games), pp. 169–172, September 2017. https://doi.org/10.1109/VS-GAMES.2017.8056591
25. Tsatiris, G., Karpouzis, K., Kollias, S.: Applications of human action analysis and recognition on wireless network infrastructures: state of the art and real world challenges. In: 2018 Innovations in Intelligent Systems and Applications (INISTA). pp. 1–6, July 2018. https://doi.org/10.1109/INISTA.2018.8466317
26. Uddin, M.Z., Khaksar, W., Torresen, J.: Activity recognition using deep recurrent neural network on translation and scale-invariant features. In: 2018 25th IEEE International Conference on Image Processing (ICIP), pp. 475–479, October 2018. https://doi.org/10.1109/ICIP.2018.8451319
27. Varia, C., Tsatiris, G., Karpouzis, K., Kollias, S.: A refined 3D dataset for the analysis of player actions in exertion games. In: 2018 IEEE Conference on Computational Intelligence and Games (CIG), pp. 1–4, August 2018. https://doi.org/10.1109/CIG.2018.8490458
28. Wang, F., Jiang, M., Qian, C., Yang, S., Li, C., Zhang, H., Wang, X., Tang, X.: Residual attention network for image classification. In: The IEEE Conference on Computer Vision and Pattern Recognition (CVPR), July 2017
29. Yu, M., Gong, L., Kollias, S.: Computer vision based fall detection by a convolutional neural network. In: Proceedings of the 19th ACM International Conference on Multimodal Interaction ICMI 2017, pp. 416–420. Association for Computing Machinery, New York (2017). https://doi.org/10.1145/3136755.3136802

Classification of Coseismic Landslides Using Fuzzy and Machine Learning Techniques

Anastasios Panagiotis Psathas[1(✉)], Antonios Papaleonidas[1], George Papathanassiou[1], Sotiris Valkaniotis[2], and Lazaros Iliadis[1]

[1] Department of Civil Engineering, School of Engineering, Democritus University of Thrace, University Campus, PC 67100 Xanthi, Greece
{anpsatha, papaleon, gpapatha, liliadis}@civil.duth.gr
[2] Koronidos Street 9, 42131 Trikala, Greece

Abstract. Seismically generated landslides represent one of the most damaging hazards associated with earthquakes in countries with high seismicity. The delineation of prone to coseismic landsliding areas is crucial in order to predict the occurrence of earthquake-induced landslides and consequently reduce the relevant risk. The goal of this study is to investigate the correlation of the pattern of coseismic landslides with geological and topographical variables i.e. lithology, slope angle and slope aspect with the volume of landslides based on fuzzy logic and machine learning techniques. For this task, a real dataset of 421 and 767 instances for years 2003 and 2015 respectively from the island of Lefkada was used. A new approach based on *Fuzzy C-Means Algorithm* and *Ensemble Subspace k-Nearest-Neighbors (Ensemble Subspace k-NN)* is proposed. Landslides were classified according to their severity with a success rate of 99.5% and 98.7% for 2003 and 2015 respectively. The performance of the proposed approach was evaluated using "One Versus All" Strategy, calculating Accuracy, Sensitivity, Specificity, Precision and F-1 Score for each cluster.

Keywords: Landslides · Lefkada · Fuzzy C-Means · S-Nome · k-Nearest-Neighbors · Ensemble Subspace k-NN · Clustering · Classification

1 Introduction

It is well known that landslide can be triggered by rainfall, earthquakes, volcanic eruption and man-made activities. Experience has shown that seismically induced landslides represent one of the most damaging hazards associated with earthquakes in countries with high seismicity [1]. According to Jibson et al. [18], the effect of seismically-induced landslides on human lives and facilities may exceed in some cases the damage directly connected to the shaking. The correlation of coseismic landslides with the seismic and morphological parameters has been investigated by several researchers, mainly after the devastating 2008 Wenchuan, China earthquake. The outcome arisen by this correlation is that both the volume and number of landsliding phenomena are relevant to earthquake magnitude. In particular, it was shown that landslide frequencies are higher in areas of highest peak ground acceleration (PGA) and that landslide density decays with the epicentral or fault distance [2, 20, 25, 31].

The delineation of prone to coseismic landsliding areas is crucial in order to predict the occurrence of earthquake-induced landslides and consequently reduce the relevant risk. Nowadays, satellite imagery and GIS technology are considered as basic tools that are used by earth scientist for evaluating the hazard and the risk within an area, initially by the introduction and statistical analyses of geo-environmental and seismologic factors into GIS software [29]. In particular, the characteristics of the landsliding area is statistically related to control factors such as topographic, geologic and seismic parameters e.g. slope angle, slope aspect, curvature, lithology, Peak Ground Acceleration (PGA) and seismic intensity distribution, and distance from the seismic fault or epicenter [27, 39]. These correlations can provide crucial information that can be used for seismic landslide hazard analysis and planning mitigation measures for prone earthquake-induced landslides regions [6, 7, 18, 30].

Frequently, the statistical analysis is based on bivariate and multivariate approaches. The goal of this study is to investigate the correlation of the pattern of coseismic landslides with geological and topographical variables i.e. lithology, slope angle and slope aspect with the volume of landslides based on fuzzy logic and machine learning techniques. In particular, *Fuzzy C-Means Algorithm* [3, 12] was used for data clustering and Ensemble Subspace k-Nearest-Neighbors (Ensemble Subspace k-NN) was used for the classification [10, 15, 37]. Existing bibliography like [23] and [33] does not exploit the combination of the above algorithms.

The motivation for the development of this research was the need for a more flexible model. More specifically, the existing approaches (e.g. the bivariate analysis) are using crisp values for the determination of slope angle or slope aspect classes. Thus, borderline values can be easily misclassified.

2 Area of Research

The geology of the Lefkada island, comprises: (1) a carbonate sequence of the Ionian zone, (2) limestone of Paxos (Apulia) zone restricted in the SW peninsula of the island, (3) few outcrops of ionian flysch (turbidites) and Miocene marls-sandstones mainly in the northern part of the island [9, 34]. The boundary between the two different geological zones – Ionian and Paxos, runs in an approximate NW- SE direction through this region and outcrops onshore south-central Lefkada Island near Hortata village, in the form of a buried thrust fault by scree and late Quaternary deposits [28]. Pleistocene and especially Holocene coastal deposits are extended in the northern edge of Lefkada, where the homonym capital town is founded, in the valley of Vassiliki and in the coast Nydri.

Regarding the seismicity, it is pointed out that the island of Lefkada is considered as one of the most tectonically active areas in Europe being part of the high seismicity Ionian Sea area, and particularly due to the complex crustal deformation resulting from the subduction of the African plate towards NE and the Apulian platform continental collision further to the northwest [14, 16]. The main active tectonic structure, is the 140 km long dextral strike-slip Cephalonia-Lefkada Transform fault (Fig. 1) (CTF;

[24, 36, 38]), which has a GPS slip-rate bracketed between 10 and 25 mm/yr. The steep morphology on the western part of the island, where most of slope failure cases are reported is due to this offshore CTF and its onshore sub-parallel fault; the Athani-Dragano fault [9, 35]. The latter one is a NNE-SSW striking fault forming a narrow elongated continental basin, very well expressed in the region's morphology and marked on satellite images and aerial photos.

There is reliable detailed information for at least 23 events, since 1612 which induced ground failures at the island of Lefkada [26]. A first conclusion arising from the list of historical events is that earthquakes appear in couples (twin or cluster events) with time period of occurrence ranging between 2 months and 5 years e.g. 1612–1613 (16 months); 1625–1630 (5 years); 1722–1723 (10 months); 1767–1769 (2 years); 1783–1783 (2 months, possible aftershock); 1867–1869 (2 years); 1914–1915 (2 months); 1948–1948 (2 months). Thus, it is crucial to determine the location of coseismic landslides since it will be beneficial for reducing the risk and increasing the resilience at the island.

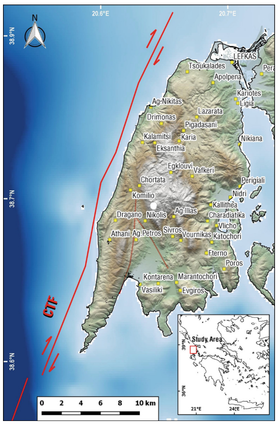

Fig. 1. Map of the island of Lefkada showing the Cephalonia-Lefkada Transform Fault CTF

2.1 Coseismic Landslides at the Island of Lefkada

The most recently occurred and well-studied earthquakes are the ones of 2003 and 2015. The penultimate event triggered extensive slope failures at the western part of the island. The volume of the debris material that moved downwards was larger than the one of the 2015 earthquake. Rock falls were widespread on the whole island and especially in the northwestern and central area, on both natural and cut slopes, as well as, on downstream road embankment slopes. The most characteristic rock falls, with diameters up to 4 m, were observed along the 6 km long road of Tsoukalades-Agios Nikitas, which is within the epicentral area, and are accompanied by gravel, small rock and soil slides [26]. The massive occurrence of these failures is the reason for the closure of the road network at this area of the island for more than 2 years. The reported rock falls followed the trace of a 300 m high morphological scarp, and especially a 10–40 m high artificial slope [26].

Regarding the 2015 earthquake, the dominant geological effects were related to slope failures i.e. rock falls and slides, and shallow and deep-seated landslides on both natural and cut slopes [28]. These failures were documented on the western part of the island, while the most densely concentration of these phenomena was reported on the coastal zone from Porto Katsiki to Egremnoi-Gialos beach and along the 6 km long coastal road of Tsoukalades - Agios Nikitas [28]. Shallow landslides and rock slides were mainly generated in areas where the clastic material covered the bedrock, and particularly in places where the rock mass was heavily jointed. Deep-seated landslides were mainly documented at the area of Egremnoi [29]. At this area, deep-seated landslides were reported, and large amount of debris material moved downslope inducing severe damages to the road network and to residential houses. The debris consists of coarse-grained size material with significant amount of large-diameter gravels and few boulders.

In order to investigate the earthquake-induced landslide density, event-based inventories were developed by taking into account aerial and satellite imagery in Google Earth in order to enrich and update existing landslide datasets, previously compiled for the two earthquakes [27]. In particular, Google Earth imagery of June 12, 2003 and December 19, 2005 was used for mapping 2003 earthquake landslides, and November 15, 2013 and April 15, 2016 for 2015 earthquake, respectively. Landslide activity along the western part of Lefkada is considered as minimal between major earthquakes, as observed on multi-date satellite imagery and confirmed by local residents. Considering this, the short period between each satellite imagery pair (2–3 years) is believed to include only the coseismic landslides, with very few if any at all landslides triggered by other factors. In total, 301 and 596 coseismic landslides were mapped for the 2003 and 2015 earthquakes, respectively. For the extraction of morphological and terrain parameters of the compiled landslide datasets, a detailed digital elevation model (DEM) with spatial resolution of 5 m was used. The 5 m DEM was obtained from Hellenic Cadastre and it was extracted from aerial imagery stereo-pairs, having a vertical accuracy of 4 m [29].

Having completed the polygon-based inventories, a statistical analysis of landslide distribution took place. In total, 596 and 301 landslides were identified covering (planar area) 1.29 km^2 and 1.6 km^2 for the 2015 and 2003 events, respectively. It is pointed out that these planar-oriented areas are obtained as projected measurements. The minimum and maximum landslide area were evaluated as 40.4 m^2 and 42940 m^2 for the 2015 earthquake, while for the penultimate event the relevant values are 129.8 m^2 and 98300 m^2, respectively [29]. The relevant values of minimum and maximum landslide area for the 2015 event, which were evaluated by taking into account the digital elevation model for the delineation of the landslide area, are 1.78 km^2 total area, 51.30 m^2 minimum and 58330 m^2 maximum area, while for the 2003 earthquake the total landsliding area covered 2.28 km^2 with minimum area of 140.9 m^2 and maximum 148469 m^2 [29].

3 Description of Dataset Pre-processing

The initial datasets (*.xlsx files) consist of 6 columns, 4 of which are numeric (Perimeter, Average Slope, Surface, Id) and 2 are nominal (Average Aspect and Geological Form). The 5th column is used only for data processing to determine the distinct incidents. Each vector represents a landslide with a specific Geological Form on the island of Lefkada. As it is already mentioned, 301 and 596 landslides were identified for years 2003 and 2015 respectively. However, numerous landslides are related to more than one types of geological forms. Taking into account this fact, the landsliding areas have been reassigned based on the geological form upon which they were delineated, resulting in 421 and 767 observations for years 2003 and 2015, respectively. The same data pre-processing approach was used for both datasets. However, data handling for each year was applied independently from the other, given that 2003 observations have been mapped on two additional geological forms compared to the case of 2015. Therefore, evaluation of the proposed approach per year has proven its efficiency and consistency. Data processing was performed in three steps. In particular, the first step was applied manually using both *.xlsx files, while second and third steps was achieved by developing code in *Matlab R2019a.*

3.1 Labeling of Nominal Values

Initially, Average Aspect was transformed from nominal to numeric in a scale from one to eight. Geological Form was similarly transformed to a scale from one to twenty for year 2003 and from one to eighteen for year 2015. The transformations can be seen in Tables 1 and 2.

Table 1. Average aspect with the corresponding label for 2003 and 2015.

Average aspect	North	North-East	East	South-East	South	South-West	West	North-West
Average aspect label	1	2	3	4	5	6	7	8

Table 2. Geological form type with the corresponding label for 2003.

Geological form	al	C	Ci	Cs	Csd	E	J1	J1d	Jar	Jc
Geological form label	1	2	3	4	5	6	7	8	9	10
Geological form	Jm	Js	M	Mb	Pc	Qc	Qp	Qt	Tc	Tg
Geological form label	11	12	13	14	15	16	17	18	19	20

Table 3. Geological form type with the corresponding label for 2015.

Geological form	al	C	Ci	Cs	E	J1	J1d	Jar	Jc
Geological form label	1	2	3	4	5	6	7	8	9
Geological form	Jm	Js	M	Mb	Pc	Qc	Qp	Qt	Tg
Geological form label	10	11	12	13	14	15	16	17	18

where al: alluvial; C, Jm, Jc, Jar, J1: limestones of Ionian; Ci, Cs: limestones of Paxos; Csd limestones; E: limestones Eocene; Js: limestone of Paxos; J1d: dolomites; M, Mb: Miocene sandstones; Pc: Pliocene conglomerate; Qc, Qp, Qt: Quaternary sediments; Tc: limestones and dolomites of Triassic; Tg: evaporites.

3.2 Landslides Fuzzy C-Means Clustering

After a statistical pre-processing of data, authors noticed that there were few high values causing a high standard deviation. Therefore, clustering of landslides is deterrent with conventional methods. To overcome this hardship, Fuzzy C-Means Clustering was employed to classify landslides according to their severity. Fuzzy C-Means was used because it offers a very flexible methodology, as each data point can be assigned to more than one clusters with different degrees of membership. This task was performed in order to develop the labeled dataset required for the deployment of the machine-learning model. A subset of available data, perimeter and surface, was used in order to apply the Clustering.

Fuzzy clustering (a well-known soft computing method [4]) is an approach in which each data point can belong to more than one cluster. One of the most widely used fuzzy clustering algorithms is the Fuzzy C-means clustering (FCM) Algorithm. This method, developed by Dunn in 1973 [12] and improved by Bezdek [3], is frequently used in pattern recognition. It is based on minimization of the following objective function:

$$J_m = \sum_{i=1}^{N} \sum_{j=1}^{C} u_{ij}^m \left\| x_i - c_j \right\|^2, \ 1 \le m < \infty \tag{1}$$

Where m is the fuzzifier (the fuzzifier m determines the level of cluster fuzziness), u_{ij} is the degree of membership of x_i in the cluster j, x_i is the ith of d-dimensional measured data, c_j is the d-dimension center of the cluster, and $\|*\|$ is any norm expressing the similarity between any measured data and the center. Fuzzy partitioning is carried out through an iterative optimization of the objective function shown above, with the update of membership u_{ij} and the cluster centers c_j by:

$$u_{ij} = \frac{1}{\sum_{k=1}^{C} \left(\frac{\|x_i - c_j\|}{\|x_i - c_k\|} \right)^{\frac{2}{m-1}}}, \quad c_j = \frac{\sum_{i=1}^{N} u_{ij}^m \cdot x_i}{\sum_{i=1}^{N} u_{ij}^m} \tag{2}$$

This iteration will stop when $\max_{ij}\left\{ \left| u_{ij}^{(k+1)} - u_{ij}^{k} \right| \right\} < \varepsilon$, where ε is a termination criterion between 0 and 1, whereas k are the iteration steps. This procedure converges to a local minimum or a saddle point of J_m.

Parameters used for the FCM algorithm are presented in Table 4 while columns Perimeter and Surface, from source data set, were chosen as input parameters. Exponent (*m fuzzier)* controls the degree of fuzzy overlap between clusters. A large *m* results in smaller membership values, u_{ij}, and hence, fuzzier clusters. In the limit $m = 1$, the memberships, u_{ij}, converge to 0 or 1, which implies a crisp partitioning. maxIterations is the maximum number of optimization iterations and minImprovement is the minimum improvement in the objective function between successive iterations When the objective function improves by a value below this threshold, the optimization stops. A smaller value produces more accurate clustering results, but the clustering can take longer to converge. For parameters' values, the ones most used in the relevant literature were selected [21, 22].

Table 4. Options for FCM algorithm

Exponent (*m fuzzier)*	2
maxIterations	100
minImprovement	0.00001

A script *FCM.m* was developed in Matlab, aiming the transformation of *.xlsx file in Matlab tables. It has already been mentioned that the goal of this step is to create clusters for the severity of lansdlides. The chosen number of clusters is 6 (calculated as the existing combinations of 2 parameters with 3 states each). Clusters with their labels and their names are presented in Table 5. The first part of the name corresponds to Perimeter and the Second to Surface

Table 5. Cluster with the corresponding labels and names

Cluster	Name of cluster
1	Low Low
2	Low Medium
3	Medium Medium
4	Medium High
5	High High
6	Extreme Extreme

The *FCM.m* Script is presented in the form of natural language, in Algorithm 1.

Algorithm 1. *The FCM.m Matlab Script*

```
Script 1: FCM.m
Inputs: 421 incidents of 2003 and 767 incidents of 2015 exported from *.xlsx files.
    Part 1:
        Step 1: Read and convert each *.xlsx file to a Matlab table.
        Step 2: For each Table the column Id Numbers was used to retrieve distinct
                Landslides. 2 new Matlab tables are constructed with the unique values
        Step 3: For each new table Perimeter and Surface column is chosen
    Part 2:
        Step 1: FCM algorithm was applied with options described in Table 4 and
                clusters described in Table 5. Centers of clusters and membership
                degrees of each observation were calculated.
        Step 2: Each instance was classified in the cluster on which the membership
                degree was the highest.
    Part 3:
        Step 1: Clusters pass to the original data
        Step 2: Original data with theirs clusters are plotted in Figures 1a and 1b for
                2003 and 2015 respectively.
```

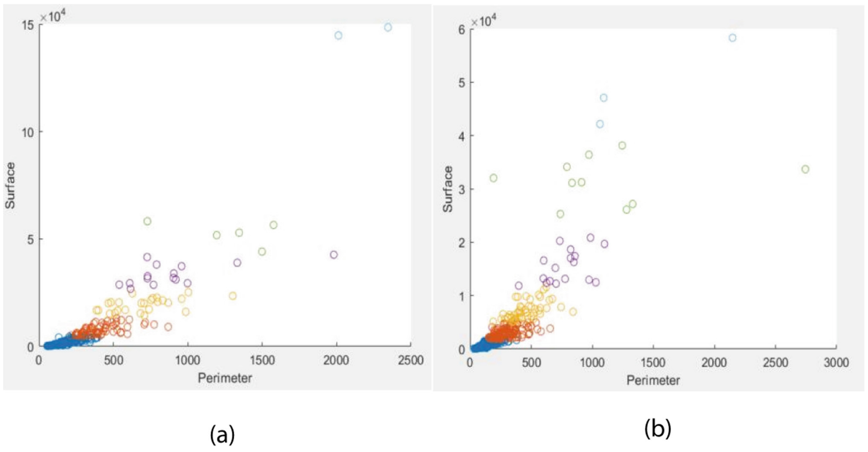

Fig. 2. Clusters for original data for 2003 (1a) and 2015 (1b) respectively.

Total landslides for each cluster for the years 2003 and 2015 are presented in Table 6.

Table 6. Total landslides of each cluster for 2003 and 2015

Clusters	1	2	3	4	5	6	Total instances
2015	448	183	74	35	22	5	767
2003	238	100	44	27	7	5	421

3.3 Fuzzy Clustering with FCM Algorithm and S-Norm

After creating the clusters it was observed that some instances do not belong exclusively to a cluster (e.g. point (1981, $4.2 \cdot 10^4$) presented in Fig. 2a or point (2744, $3.3678 \cdot 10^4$) presented in Fig. 2b), as well as some instances in between 2 clusters with similar membership values for both. Considering the above observation, the re-creation of clusters for all instances is essential. Consequently, we decided that landslides, which have degree of membership, for their dominant class, below a certain threshold will be re-sorted. In order to perform this, it is necessary to use weights on each factor [5, 41].

Equation (3) implements a fuzzy coupling between many fuzzy sets, using a function $f(\mu_i, w_i)$ which assigns the weight w_i to the membership degree μ_i.

$$\mu_{\tilde{S}}(x_i) = Agg\left(f\left(\mu_{\tilde{\mathrm{A}}}(x_i), w_1\right), f\left(\mu_{\tilde{\mathrm{A}}}(x_i), w_2\right), \ldots, f\left(\mu_{\tilde{\mathrm{A}}}(x_i), w_n\right)\right) \tag{3}$$

Where i = 1, 2,…, k and k the number of instances examined and n factors' number [13]. The function f used in the coupling function (Eq. (3)) can be defined as:

$$f(a, w) = a^{\frac{1}{w}} \tag{4}$$

where a is the membership degree and w is the corresponding weight.

For the Aggregation function was used Hamacher aggregation as S-Norm operator [40].

$$\tilde{A} \cap \tilde{B} = \frac{\mu_{\tilde{A}}(x) + \mu_{\tilde{B}}(x) - 2\mu_{\tilde{A}}(x)\mu_{\tilde{B}}(x)}{[1 - \mu_{\tilde{A}}(x) + \mu_{\tilde{B}}(x)]} \tag{5}$$

Another script *S-Norm_Clustering.m* was developed in Matlab. The second script is presented in the form of natural language, in Algorithm 2.

Algorithm 2. *The S-Norm_Clustering.m Matlab Script*

```
Script 2: S-Norm_Clustering.m
Inputs: All membership degrees of each observation for 2003 and 2015.
    Part 1:
        Step 1: Threshold is defined at 0.7
        Step 2: Weights are defined. The highest membership's degree weight is 4, the
                second highest is 2, and for the others 0.
    Part 2:
        Step 1: If a membership degree for a cluster is higher than 0.7 the incident
                belong to this cluster.
        Step 2: Else if the membership degree is under 0.7 the incident belongs to
                a new cluster, for with the membership degree is calculated through
                Eq. (3),(4) and (5).
```

After applied *S-Norm_Clustering.m,* 4 more clusters were created for landslides of 2003 and 5 more for 2015. New clusters were created between the already existing clusters. Therefore, they took their label depending the clusters that are between. For example, cluster between cluster 1 and 2 is labeled as cluster 1.5. Clusters are presented in Fig. 3a, b, and incidents for each cluster in Table 7. It is obvious that new clustering classifies observations more effectively according to severity.

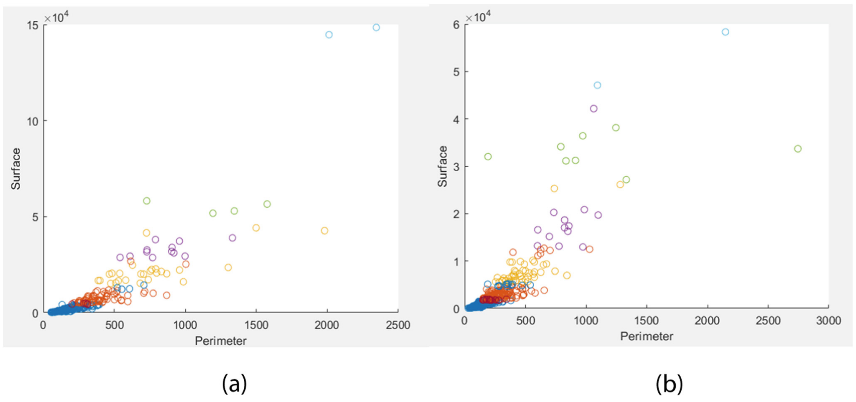

Fig. 3. Clusters for original data for 2003 (2a) and 2015 (2b) respectively after S-Norm

Table 7. Total landslides of each cluster for 2003 and 2015 after S-Norm

Clusters	1	1.5	2	2.5	3	3.5	4	4.5	5	5.5	6	Total instances
2015	417	52	145	27	56	25	18	7	15	2	3	767
2003	222	27	84	9	37	5	22	4	6	0	5	421

4 Classification Methodology

After having clustering done, we used classification algorithms to ascertain coseismic landslides' proper classification. The independent variables used for the classification are Perimeter, Average Slope, Surface, Average Aspect and Geological Form of landslides. Average Slope and Average Aspect were labeled as indicated in Tables 1, 2 and 3. The dependable value is the cluster derived from clustering with S-Norm.

A total of 23 classification algorithms have been employed namely: *Fine Tree, Medium Tree, Coarse Tree, Linear Discriminant, Quadratic Discriminant, Linear SVM, Quadratic SVM, Cubic SVM, Fine Gaussian SVM, Medium Gaussian SVM, Coarse Gaussian SVM, Cosine KNN, Cubic KNN, Weighted KNN, Fine KNN, Medium KNN, Gaussian Naive Bayes, Kernel Naïve Bayes, Boosted Trees, Bagged Trees, Subspace Discriminant, Subspace KNN, RUSBoost Trees.*

However, only the one with the highest values of performance indices will be described herein.

4.1 Ensemble Subspace k-Nearest-Neighbors (Ensemble Subspace k-NN)

Classifying query points based on their distance to specific points (or neighbors) can be a simple but yet effective process. The k-nearest neighbors (k-NN) is a lazy and non-parametric Learning algorithm [8]. It is widely used as a predictive performance benchmark, when we are trying to develop more sophisticated models. Given a set X of n points and a distance function, k-NN search finds the k closest points to a query point or set of them [17]. Dunami [11] first introduced a weighted voting method, called the *distance-weighted (DW) k-nearest neighbor rule* (Wk-NN). According to this approach, the closer neighbors are weighted more heavily than the farther ones, using the DW function. The weight w_i for the *i*-th nearest neighbor of the query x' is defined following function 1:

$$w_i' = \begin{cases} \frac{d(x'x_k^{NN})-d(x'x_i^{NN})}{d(x'x_k^{NN})-d(x'x_1^{NN})} & , \quad if \quad d(x'x_k^{NN}) \neq d(x'x_1^{NN}) \\ 1 & , \quad if \quad d(x'x_k^{NN}) = d(x'x_1^{NN}) \end{cases} \tag{6}$$

Finally, the classification result of the query is determined by the majority weighted voting as in function 2:

$$y' = \arg\max_{y} \sum_{(x_i^{NN}, y_i^{NN}) \in T'} w_i' \times \delta(y = y_i^{NN}). \tag{7}$$

Based on Eq. (7), a neighbor with smaller distance is weighted more heavily than one with greater distance: the nearest neighbor is assigned a weight equal to 1, whereas the furthest one a weight of 0 and the weights of the others are scaled linearly to the interval in between.

Despite its simplicity, k-NN gives competitive results and in some cases even outperforms other complex learning algorithms. However, k-NN is affected by non-informative features in the data, which is something rather common with high dimensional data. Several attempts have been made to improve the performance of nearest neighbors' classifiers by ensemble techniques. Some related work on ensemble of k-NN classifiers can be found in [10, 15, 17].

Subspace ensembles have the advantage of using less memory than ensembles with all predictors, and can handle missing values (NaNs).

The basic random subspace algorithm uses these parameters.

- *m* is the number of dimensions (variables) to sample in each learner.
- *d* is the number of dimensions in the data, which is the number of columns (predictors) in the data matrix X.
- *n* is the number of learners in the ensemble. Set *n* using the NLearn input.

The basic random subspace algorithm performs the following steps:

1. Choose without replacement a random set of *m* predictors from the *d* possible values.
2. Train a weak learner using just the *m* chosen predictors.
3. Repeat steps 1 and 2 until there are *n* weak learners.
4. Predict by taking an average of the score prediction of the weak learners, and classify the category with the highest average score.

4.2 Evaluation of the Activity Model Classifiers

Accuracy is the overall index that has been used in evaluation of the developed Machine Learning models. However, additional indices have been used to estimate the efficiency of the algorithms. Given the fact that we are dealing with a multi-class classification problem, the "One Versus All" Strategy [19, 32] was used. The calculated validation indices that have been considered are presented in the following Table 8.

Table 8. Calculated indices for the evaluation of the multi-class classification approach

Index	Abbreviation	Calculation
Sensitivity (also known as True Positive Rate or Recall)	SNS	SNS = TP/(TP + FN)
Specificity, (also known as True Negative Rate)	SPC	SPC = TN/(TN + FP)
Accuracy	ACC	ACC = (TP + TN)/ (TP + FP + FN + TN)
F1 Score	F1	F1 = 2*TP/(2*TP + FP + FN)
Precision (also known as Positive predictive value	PREC	PREC = TP/(TP + FP)

Precision (PREC) is the measure of the correctly identified positive cases from all the predicted positive cases. Thus, it is useful when the cost of False Positives is high.

On the other hand, ***Sensitivity*** (also known as Recall) is the measure of the correctly identified positive cases from all the actual positive cases. It is important when the cost of False Negatives is high. ***Specificity*** (SPC) is the true negative rate or the proportion of negatives that are correctly identified. ***Accuracy*** (ACC) is the measure of all correctly identified from the predicted cases. It represents the closeness of the measurements to a specific value. The ***F1*** score can be interpreted as the harmonic mean (weighted average) of the Precision and Recall. As it is known from the literature, ***Accuracy*** can be seriously considered when the class distribution is balanced while F1 score is a better metric when there are imbalanced classes as in the above case. Using it as a metric, we are sure that if its value is high, both precision and recall of the classifier indicate good results. In our case the F1 score is the final overall criterion of good performance evaluation.

5 Experimental Results

The experiments were performed with the use of Matlab R2019a software. The options and hyperparameters set for Ensemble Subspace k-NN are presented in Table 9 below:

Table 9. Tuning algorithm's hyperparameters

Algorithm	Hyperparameters	Optimal values-functions
Ensemble subspace k-NN	Maximum number of splits	20
	Number of learners	30
	Learning rate	0.1
	Subspace dimension	3

The Ensemble Subspace k-NN achieved an accuracy equal to 99.5% and 98.7% for 2003 and 2015 respectively. The Confusion Matrix for each year is presented in the following Figs. 4 and 5.

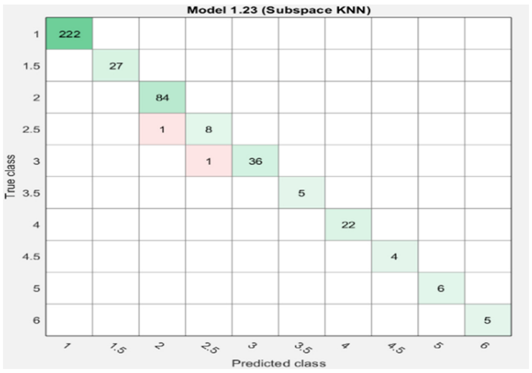

Fig. 4. Confusion matrix of the ensemble subspace k-NN algorithm for 2003

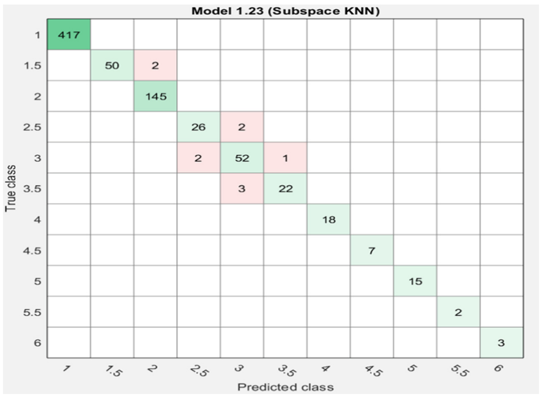

Fig. 5. Confusion matrix of the ensemble subspace k-NN algorithm for 2015

The following two Tables (10, 11), present the values of the performance indices for the above optimal algorithm.

Table 10. Cluster (Cl) classification performance indices for the Ensemble Subspace k-NN Algorithm (2003)

Index	Cl_1	$Cl_{1.5}$	Cl_2	$Cl_{2.5}$	Cl_3	$Cl_{3.5}$	Cl_4	$Cl_{4.5}$	Cl_5	Cl_6
SNS	1	1	1	0.88	0.97	1	1	1	1	0.98
SPC	1	1	0.99	0.99	1	1	1	1	1	0.99
ACC	1	1	0.99	0.99	0.99	1	1	1	1	0.99
PREC	1	1	0.98	0.88	1	1	1	1	1	0.98
F1	1	1	0.99	0.88	0.98	1	1	1	1	0.98

Table 11. Cluster (Cl) classification performance indices for the Ensemble Subspace k-NN Algorithm (2015)

Index	Cl_1	$Cl_{1.5}$	Cl_2	$Cl_{2.5}$	Cl_3	$Cl_{3.5}$	Cl_4	$Cl_{4.5}$	Cl_5	$Cl_{5.5}$	Cl_6
SNS	1	0.96	1	0.93	0.95	0.88	1	1	1	0.97	1
SPC	1	1	0.99	0.99	0.99	0.99	1	1	1	0.99	1
ACC	1	0.99	0.99	0.99	0.98	0.99	1	1	1	0.99	1
PREC	1	1	0.98	0.92	0.91	0.95	1	1	1	0.97	1
F1	1	0.98	0.99	0.92	0.92	0.91	1	1	1	0.97	1

From Tables (10, 11) it is obvious that the values of all indices clearly show a very good performance in both 2003 and 2015's instances.

6 Discussion and Conclusion

Classification of coseismic landslides according to their severity is a really interesting, important and challenging task. In this paper an approach based on *Fuzzy C-Means Algorithm* and *Ensemble Subspace k-Nearest-Neighbors (Ensemble Subspace k-NN) Algorithm* is proposed and tested. The combination of *Fuzzy C-Means* and Hamacher aggregation as S-Norm operator, sorted the data to 10 clusters for year 2003 and 11 clusters for 2015. Thereafter, *Ensemble Subspace k-NN,* using Average Aspect, Average Slope, Geological Form, Perimeter and Surface as independent input variables, managed to achieve high success rates. The overall accuracy is 99.5% and 98.7% for 2003 and 2015 respectively.

The efficiency of the model is also perceivable from Tables 10 and 11, where indices Accuracy, Sensitivity, Specificity, Perception and F1-score range at high levels. However, some ostensibly inaccurate classifications like in $Cl_{2.5}$ of 2003 or $Cl_{3.5}$ of 2015 do not affect the overall performance of the model as all indicators range from 0.88 to 1.

Concluding, the research described herein managed to correctly classify coseismic landslides according to their severity to the island of Lefkada. Future work will focus on the development of hybrid and ensembles' approaches for the forecasting of landslides' severity or even for forecasting the exact area of a landslide.

References

1. Dunn, J.C.: A fuzzy relative of the ISODATA process and its use in detecting compact well-separated clusters (1973)
2. Bezdek, J.C.: Pattern Recognition with Fuzzy Objective Function Algorithms. Springer, New York (2013)
3. Calvo, T., Mayor, G., Mesiar, R. (eds.): Aggregation Operators: New Trends and Applications, vol. 97. Physica, New York (2012)
4. Yager, R.R., Kacprzyk, J.: The Ordered Weighted Averaging Operators. Theory and Applications. Springer, New York (1997)
5. Fan, Z.P., Ma, J., Zhang, Q.: An approach to multiple attribute decision making based on fuzzy preference information on alternatives. Fuzzy Sets Syst. **131**(1), 101–106 (2002)
6. Wei, G., Lu, M.A.O.: Dual hesitant pythagorean fuzzy Hamacher aggregation operators in multiple attribute decision making. Arch. Control Sci. **27**(3), 365–395 (2017)
7. Cover, T., Hart, P.: Nearest neighbor pattern classification. IEEE Trans. Inf. Theory **13**(1), 21–27 (1967)
8. Hechenbichler, K., Schliep, K.: Weighted k-nearest-neighbor techniques and ordinal classification (2004)
9. Dudani, S.A.: The distance-weighted k-nearest neighbor rule. IEEE Trans. Syst. Man Cybern. **8**(4), 311–313 (1978)
10. Grabowski, S.: Voting over multiple k-nn classifiers. In: Modern Problems of Radio Engineering, Telecommunications and Computer Science (IEEE Cat. No. 02EX542), pp. 223–225. IEEE, February 2002

11. Domeniconi, C., Yan, B.: Nearest neighbor ensemble. In: Proceedings of the 17th International Conference on Pattern Recognition, 2004. ICPR 2004, vol. 1, pp. 228–231. IEEE, August 2004
12. Samworth, R.J.: Optimal weighted nearest neighbour classifiers. Ann. Stat. **40**(5), 2733–2763 (2012)
13. Joutsijoki, H., Juhola, M.: Comparing the one-vs-one and one-vs-all methods in benthic macroinvertebrate image classification. In: International Workshop on Machine Learning and Data Mining in Pattern Recognition, pp. 399–413. Springer, Berlin/Heidelberg, August 2011
14. Rifkin, R., Klautau, A.: In defense of one-vs-all classification. J. Mach. Learn. Res. **5**(2), 101–141 (2004)
15. Khalilia, M., Popescu, M.: Fuzzy relational self-organizing maps. In: 2012 IEEE International Conference on Fuzzy Systems, pp. 1–6. IEEE, June 2012
16. Khalilia, M.A., Bezdek, J., Popescu, M., Keller, J.M.: Improvements to the relational fuzzy c-means clustering algorithm. Pattern Recognit. **47**(12), 3920–3930 (2014)
17. Bora, D.J., Gupta, D., Kumar, A.: A comparative study between fuzzy clustering algorithm and hard clustering algorithm. arXiv preprint arXiv:1404.6059 (2014)
18. Robinson, T.R., Rosser, N.J., Densmore, A.L., Williams, J.G., Kincey, M.E., Benjamin, J., Bell, H.J.: Rapid post-earthquake modelling of coseismic landslide magnitude and distribution for emergency response decision support. Nat. Hazards Earth Syst. Sci. Discuss. **17**, 1521–1540 (2017)
19. Kritikos, T., Robinson, T.R., Davies, T.R.: Regional coseismic landslide hazard assessment without historical landslide inventories: a new approach. J. Geophys. Res.: Earth Surf. **120** (4), 711–729 (2015)
20. Ayalew, L., Kasahara, M., Yamagishi, H.: The spatial correlation between earthquakes and landslides in Hokkaido (Japan), a GIS-based analysis of the past and the future. Landslides **8**, 443–448 (2011)
21. Barlow, J., Barisin, I., Rosser, N., Petley, D., Densmore, A., Wrigth, T.: Seismically-induced mass movements and volumetric fluxes resulting from the 2010 Mw = 7.2 earthquake in the Sierra Cucapah, Mexico. Geomorphology **230**, 138–145 (2015)
22. Chang, K.T., Chiang, S.H., Hsu, M.L.: Modeling typhoon- and earthquake induced landslides in a mountainous watershed using logistic regression. Geomorphology **89**(3–4), 335–347 (2006)
23. Collins, B.D., Kayen, R., Tanaka, Y.: Spatial distribution of landslides triggered from the 2007 Niigata Chuetsu-Oki Japan Earthquake. Eng. Geol. **127**, 14–26 (2012)
24. Cushing, M.: Evoluation structurale de la marge nord-ouest hellenique dans l'ile de Lefkada et ses environs (Greece nord-occidentale). Ph.D. Thesis, University de Paris-Sud (XI), Centre d' Orsay, France (1985)
25. Ganas, A., Marinou, A., Anastasiou, D., Paradissis, D., Papazissi, K., Tzavaras, P., Drakatos, G.: GPS-derived estimates of crustal deformation in the central and north Ionian Sea, Greece: 3-yr results from NOANET continuous network data. J. Geod. **6**, 62–71 (2013)
26. Hatzfeld, D., Kassaras, I., Panagiotopoulos, D., Amorese, D., Makropoulos, K., Karakaisis, G., Coutant, O.: Microseismicity and strain pattern in northwestern Greece. Tectonics **14**(4), 773–785 (1995)
27. Jibson, R.W., Harp, E.L., Michael, J.A.: A method for producing digital probabilistic seismic landslide hazard maps. Eng. Geol. **58**, 271–289 (2000)
28. Keefer, D.K.: Landslides caused by earthquakes. Geol. Soc. Am. Bull. **95**(4), 406–421 (1984)
29. Louvari, E., Kiratzi, A.A., Papazachos, B.C.: The CTF and its extension to western Lefkada Island. Tectonophysics **308**, 223–236 (1999)

30. Meunier, P., Hovius, N., Haines, A.J.: Regional patterns of earthquake-triggered landslides and their relation to ground motion. Geophys. Res. Lett. **34**(20), L20408 (2007)
31. Papathanassiou, G., Pavlides, S., Ganas, A.: The 2003 Lefkada earthquake: field observation and preliminary microzonation map based on liquefaction potential index for the town of Lefkada. Eng. Geol. **82**, 12–31 (2005)
32. Papathanassiou, G., Valkaniotis, S., Ganas, A., Pavlides, S.: GIS-based statistical analysis of the spatial distribution of earthquake-induced landslides in the island of Lefkada, Ionian Islands. Greece. Landslides **10**(6), 771–783 (2013)
33. Papathanassiou, G., Valkaniotis, S., Ganas, A., Grendas, N., Kollia, E.: The November 17th, 2015 Lefkada (Greece) strike-slip earthquake: field mapping of generated failures and assessment of macroseismic intensity ESI-07. Eng. Geol. **220**, 13–30 (2017)
34. Papathanassiou G., Valkaniotis S., Ganas, A.: Spatial patterns, controlling factors and characteristics of landslides triggered by strike-slip faulting earthquakes; case study of Lefkada island, Greece. Bull. Eng. Geol. Environ. (Submitted, 2020)
35. Parise, M., Jibson, R.W.: A seismic landslide susceptibility rating of geologic units based on analysis of characteristics of landslides triggered by the 17 January, 1994 Northridge, California earthquake. Eng. Geol. **58**(3–4), 251–270 (2000)
36. Parker, R.N., Densmore, A.L., Rosser, N.J., de Michele, M., Li, Y., Huang, R.Q., Whadcoat, S., Petley, D.N.: Mass wasting triggered by 2008 Wenchuan earthquake is greater than orogenic growth. Nat. Geosci. **4**(7), 449–452 (2011)
37. Rondoyanni-Tsiambaou, Th.: Les seismes et l'environnement géologique de l'île de Lefkade, Grèce: Passe et Futur. In: Marinos, P., et al. (eds.) Engineering Geology and the Environment, Balkema, pp. 1469–1474 (1997)
38. Rondoyianni, Th., Mettos, A., Paschos, P., Georgiou, Ch.: Neotectonic Map of Greece, scale1:100.000, Lefkada Sheet. I.G.M.E., Athens (2007)
39. Sachpazi, M., Hirn, A., Clement, C., Haslinger, F., Laigle Kissling, E., Charvis, P., Hello, Y., Lepine, J.C., Sapin, M., Ansorge, J.: Western Hellenic subduction and Cephalonia transform: local earthquakes and plate transport and strain. Tectonophysics **319**, 301–319 (2000)
40. Scordilis, E.M., Karakaisis, G.F., Karacostas, B.G., Panagiotopoulos, D.G., Comninakis, P. E., Papazachos, B.C.: Evidence from transform faulting in the Ionian Sea: the Cephalonia island earthquake sequence of 1983. PAGEOPH **123**, 387–397 (1985)
41. Tian, Y., Xu, C., Chen, J., Zhou, Q., Shen, L.: Geometrical characteristics of earthquake-induced landslides and correlations with control factors: a case study of the 2013 Minxian, Gansu, China, Mw 5.9 event. Landslides **14**, 1915–1927 (2017)

Evaluating the Transferability of Personalised Exercise Recognition Models

Anjana Wijekoon(✉) and Nirmalie Wiratunga

Robert Gordon University, Aberdeen AB10 7GJ, Scotland, UK
{a.wijekoon,n.wiratunga}@rgu.ac.uk

Abstract. Exercise Recognition (ExR) is relevant in many high impact domains, from healthcare to recreational activities to sports sciences. Like Human Activity Recognition (HAR), ExR faces many challenges when deployed in the real-world. For instance, typical lab performances of Machine Learning (ML) models, are hard to replicate, due to differences in personal nuances, traits and ambulatory rhythms. Thus effective transferability of a trained ExR model, depends on its ability to adapt and personalise to a new user or a user group. This calls for new experimental design strategies that are person-aware, and able to organise train and test data differently from standard ML practice. Specifically, we look at person-agnostic and person-aware methods of train-test data creation, and compare them to identify best practices on a comparative study of personalised ExR model transfer. Our findings show that ExR when compared to results with other HAR tasks, to be a far more challenging personalisation problem and also confirms the utility of metric learning algorithms for personalised model transfer.

Keywords: Exercise Recognition · Transferability · Personalisation · Performance evaluation

1 Introduction

Exercise Recognition (ExR) is an ongoing Machine Learning (ML) research challenge with many practical applications such as self-management of musculoskeletal pain, weight training, orthopaedic rehabilitation and strength and balance improvement of pre-frail adults. Research in ExR falls under Human Activity Recognition (HAR) research, which has broader applications in gait recognition, fall detection and activity recognition for fitness applications, to name a few.

Fitness applications that adopt ExR as an integral component, face many challenges at deployment, compared with other conventional ML or Deep Learning (DL) applications such as image recognition or text classification. For instance

This work is part funded by SELFBACK which has received funding from the European Union's Horizon 2020 research and innovation programme under grant agreement No. 689043.

lack of transferability of learned ML models is one of the main challenges that is present in many forms such as; the transferability to new sensor modalities, to new activities or to new user groups. With new sensor modalities, both heterogeneity of sensor data and differences in sensor configurations must be addressed. Transferability to new activity classes is generally addressed as open-ended HAR, where either a knowledge-intensive method is used with a corpus to learn heuristics that can cover all possible activities classes to be expected in the future [5] or; in contrast a knowledge-light method learns a feature space that is expected to adapt to new activity classes [13]. Lastly, when deploying a generic fitness application, developers are unaware of the target user group. Here transferability to a new user group, must also consider common factors applicable to the group needs.

In this paper, we focus on ExR applications; their transferability to different user groups and importantly how to design comparative studies that are informed by the ownership of data (i.e. data that is generated by a specific person). Naturally, people incorporate many personal nuances when performing exercises and in practice, these personal traits are captured by the sensors. If the ExR algorithm is unaware of the specific person it may find it challenging to map sensor readings to a specific exercise. In this paper we show that adopting the correct evaluation method is crucial to understanding the capabilities of an ExR algorithm amongst a diverse group of users.

We explore person-aware evaluation methods using the HAR personalisation algorithm MN^p [13] that was inspired by Metric-Learning and Meta-Learning ideas in the HAR (physical activity) domain. MN^p achieves personalisation without requiring test user data and learns a feature space that is transferable to a wider range of users. We expect ExR to be a harder personalisation challenge, compared personalisation of HAR models. Lets consider a typical ambulatory physical activity such as walking, where personal gait rhythm easily influences walking cycles but is consistent; contrast that to an exercise, such as a pelvic tilt or a knee roll (see Fig. 4a) where its harder to isolate and capture personal nuances and may vary over the time-period. Our evaluation shows that MN^p can be applied to ExR and is transferable to new users not seen during training.

Rest of the paper is organised as follows. In Sect. 2 we explore related literature in HAR and ExR domains. Next in Sect. 3, we present methods that are explored in this paper; followed by an analysis of results with alternative evaluation strategies in Sect. 4. Finally conclusions and future directions appear in Sect. 5.

2 Related Work

Research in ExR covers a wide variety of application areas such as weight training [6,10], rehabilitation [2] and callisthenics and gym exercises [8,15]. ExR like HAR, is a multi-class classification problem where classes are unique exercises that are captured by a stream of sensor data. Many algorithms have been explored in literature such as k-NN [8,14], Decision Trees and Random Forest [10,15] and CNN and LSTM [2,12].

Personalising such algorithms is intuitively desirable for ExR as personal nuances such as gait, posture and rhythm are known factors that are used by human experts when analysing exercise performance and adherence in the real-world. Although this remains largely unexplored for ExR; there is useful work in HAR, where early research has looked at user-dependent modelling with access to large quantities of labelled end-user data [1,7,9]. Follow on work attempts to reduce this human burden, by adopting semi-supervised learning methods [3,4] that require some model re-training after deployment.

Recent advances in few-shot learning and meta-learning with Matching Networks (MN) [11] and Personalised MN (MN^p) for HAR [13] has addressed the short comings of previous methods by only using few data instances from end-user as well as learning embeddings that are largely transferable to new activities without needing model re-training after deployment. It has also outperformed its non-personalised counterpart in the tasks of pose detection and HAR [13]. Importantly in this paper we investigate, if MN^p is transferable to ExR, which is arguably a more challenging personalised learning problem.

3 Methods

Given sensor data streams recorded while performing exercises, for supervised ExR, data instances are extracted using the sliding window method applied to each of the streams. Typical sensors include inertial sensors, depth cameras and pressure mats. More formally, given a set of data instances, $\mathcal{X}$, ExR involves learning a feature space where the mapping from each instance, x, to an exercise class, y, where y is from the set of exercise classes, $\mathcal{L}$. Accordingly, each sensor-based data instance is a data and class label pair, (x, y), where $y \in \mathcal{L}$.

$$\mathcal{X} = \{(x, y) \mid y \in \mathcal{L}\} \tag{1}$$

In comparison to computer vision or text datasets, each data instance in $\mathcal{X}$ belongs to a person, p. Given the set of data instances obtained from person p is $\mathcal{X}^p$, relationship of $\mathcal{X}^p$ and $\mathcal{X}$ formalised as in Eq. 2. As before all data instances in $\mathcal{X}^p$ will belong to a class in $\mathcal{L}$ except special instances like open-ended HAR where the class set is not fully specified at training time.

$$\mathcal{X} = \{\mathcal{X}^p \mid p \in \mathcal{P}\} \text{ where } \mathcal{X}^p = \{(x, y) \mid y \in \mathcal{L}\} \tag{2}$$

Training and testing methodologies can adopt one of two approaches; *person-agnostic* where an algorithm is trained and tested with the same user group; and *person-aware*, where an algorithm is trained and tested on different user groups. Both maintain disjointed sets of data instances in train and test; but the latter also preserves disjoint persons by preserving the person-to-data relationship during model training and testing.

3.1 Person-Agnostic Evaluation

Person agnostic evaluations can be applied as a repeated hold-out (R-HO) or a cross-fold (CF) validation methodologies. In either case, the person parameter of each data instance is discarded when creating hold-out sets, or folds. This means that a person's data can be split between train and test sets. A percentage, λ, of all data instance in $\mathcal{X}$, is used as the set of test data instances, $\mathcal{X}_{test}$, and the rest as the set of train data instances $\mathcal{X}_{train}$.

$$\begin{aligned} \mathcal{X} &= \{\mathcal{X}_{train}, \mathcal{X}_{test}\} \\ |\mathcal{X}_{train}| \approx (1-\lambda) \times |\mathcal{X}| &\text{ and } |\mathcal{X}_{test}| \approx \lambda \times |\mathcal{X}| \end{aligned} \tag{3}$$

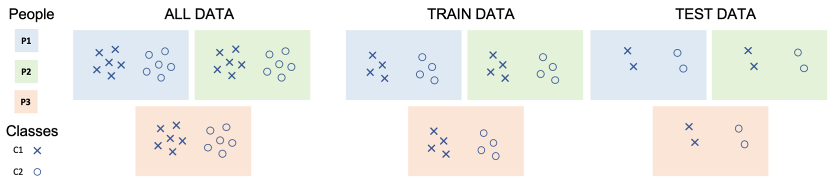

Fig. 1. Person-agnostic train/test split

With R-HO, a λ percentage of the data instances are randomly selected (without replacement) to form the test set and the remainder forming the train set. This is repeated for multiple iterations. With CF, first, the dataset is divided into a number of folds where each fold contains λ percentage of data, and at each iteration, one fold is selected as the test set and the rest of the folds as the training set. Both methods create train and test sets that share the same population $\mathcal{P}$ (see Fig. 1). Unlike with R-HO method, CF guarantees that each data instance appears once in the test set.

A person-agnostic methodology for evaluation, trains and tests on the same population. Accordingly, these methodologies are not designed to evaluate the robustness of an algorithm on a different population following typical deployment. However they provide an "upper-bound" performance of a ML algorithm.

3.2 Person-Aware Evaluation

A Person-aware evaluation can be performed as a repeated Persons-Hold-Out (R-PHO) or a Leave-One-Person-Out (LOPO) methodology. With R-PHO, a percentage, μ, of the user population is selected as the test user set, rest forming the train user set; and this is repeated for multiple iterations. With LOPO methodology, instances from a single user is put aside, to form a singleton test user group, and the rest of the users form the training user group. The train and test set formation with the test user group, $\mathcal{P}_{test}$, and the train user group, $\mathcal{P}_{train}$ can be formalised as follows:

$$\begin{gathered}\mathcal{X} = \{\mathcal{X}_{train}, \mathcal{X}_{test}\} \\ \mathcal{X}_{test} = \{\mathcal{X}^p \mid p \in \mathcal{P}_{test}\} \text{ and } \mathcal{X}_{train} = \{\mathcal{X}^p \mid p \in \mathcal{P}_{train}\} \\ \mathcal{P} = \{\mathcal{P}_{train}, \mathcal{P}_{test}\}\end{gathered} \tag{4}$$

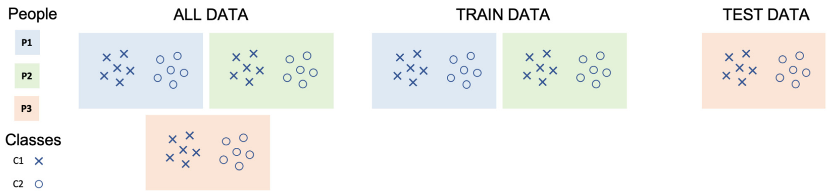

Fig. 2. Person-aware train/test split

LOPO ensures that each user in the population $\mathcal{P}$ is included in the test set in one of the trials (similar to the person-agnostic CF method), but LOPO also ensures disjointedness in selected persons (see Fig. 2). We propose that performance measures obtained with a person-aware methodology should be used as the "lower-bound", likely performance of a ML algorithm after deployment.

3.3 Personalised Matching Networks

The goal of personalisation is to learn a feature space that can dynamically adapt to different test user groups. With reference to Sects. 3.1 and 3.2, the aim here is to find algorithms that outperform the "lower-bound" set by a non-personalised algorithm when evaluated by a person-aware methodology. For this purpose we explore the Personalised Matching Networks (MN^p), which has been successfully used for personalising HAR algorithms.

MN^p is inspired by Metric Learning and Meta-Learning paradigms where the classification task is learning to match a test instance, x, to one instance from a set of representatives. The set of representative instances, S is chosen from the same user (i.e. from. $\mathcal{X}^p$) ensuring all classes are represented. An instance in, S, is a data instance, (x, y), and for each class up to, k, representatives are selected from, $\mathcal{X}^p$, as in Eq. 5.

$$S = \{(x, y) | x \in \mathcal{X}^p, y \in \mathcal{L}\} \text{ where } |S| = k \times |\mathcal{L}| \tag{5}$$

We denote the training data set obtained for person, p's data as $\mathcal{X}^p_{tr}$. An instance in, $\mathcal{X}^p_{tr}$, consists of a query and support set pairs, (q_i, S_i), where, q_i, is a sensor data and class label pair, (x_i, y_i), (similar to a conventional supervised learning training data instance). The complete training data set, $\mathcal{X}_{tr}$, is the collection of all, $\mathcal{X}^p_{tr}$, for the train user group $\mathcal{P}_{tr}$.

$$\mathcal{X}^p_{tr} = \{(q, S) \mid x \in \mathcal{X}^p, y \in \mathcal{L}\} \text{ where } q = (x, y), y \in \mathcal{L}$$
$$\mathcal{X}_{tr} = \{\mathcal{X}^p_{tr} \mid p \in \mathcal{P}_{tr}\} \tag{6}$$

During MN^p training, a parametric model learns a feature space where data instances from different users are successfully transformed and mapped to class labels. Here training can be viewed as a parameterised (Θ) end-to-end learning of a distance/similarity function, using a non-parametric attention-based kernel to compute the objective matching function (see architecture in Fig. 3). At testing, the MN^p algorithm predicts the label $\hat{y}$ for a query instance $\hat{x}$ with respect to its support set $\hat{S}$ from the same user.

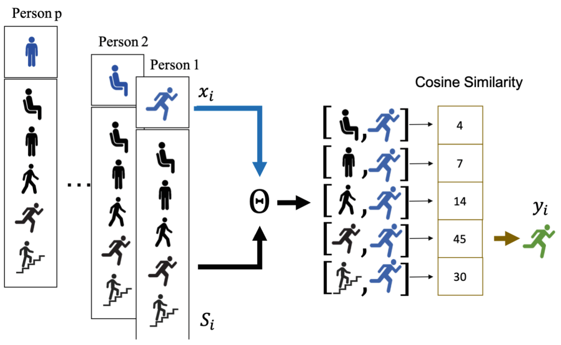

Fig. 3. Training MN^p for HAR; adapted from [13]

4 Evaluation and Results

Aim of the evaluation is two fold; firstly we analyse lower and upper bound performances of ExR algorithms using the 2 alternative methods of evaluation: person-agnostic versus person-aware, secondly we explore the transferability of personalised models for ExR from HAR. All experimental results calculate the mean F1-score and any significance is reported at the 95% level.

4.1 MEx Dataset

MEx is a sensor-rich dataset collected for 7 exercises with four sensors, publicly available at the UCI Machine Learning Repository[1]. Seven exercise classes are included in this data collection; 1-Knee Rolling, 2-Bridging, 3-Pelvic Tilt, 4-Bilateral Clam, 5-Repeated Extension in Lying, 6-Prone Punch and 7-Superman (Fig. 4a). These exercises are frequently used for prevention or self-management of LBP.

There are four sensor modalities; two accelerometers placed on the wrist and the thigh of the person; a pressure mat was where the person lays on to perform

[1] https://archive.ics.uci.edu/ml/datasets/MEx.

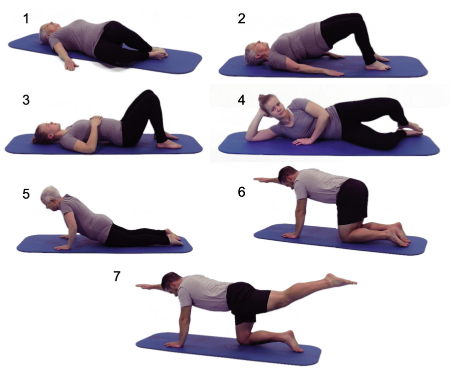

[Exercises]

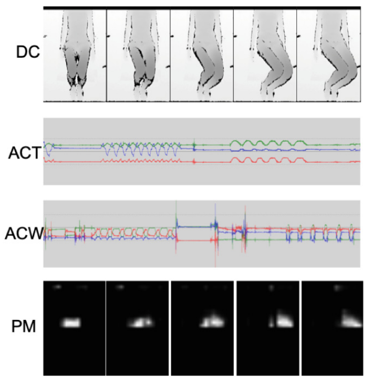

[Raw sensor data]

Fig. 4. MEx dataset

the exercises and a depth camera was placed above the person facing downwords. The tri-axial accelerometers record data at 100 Hz frequency within the range of ±8g. The pressure mat and the depth camera record gray scale frames at 15 Hz frequency and frame sizes are 32×16 and 240×320 respectively. Figure 4b shows a visualisation of each sensor data type.

In this study we focus on ExR with a single modality. Accordingly we create four datasets with the four modalities available on MEx; the thigh accelerometer, the wrist accelerometer, the pressure mat and the depth camera respectively referred to as ACT, ACW, PM and DC in the rest of this paper.

4.2 Pre-processing

The sliding window method is applied on each individual sensor data stream to create data instances; where the window size is 5 s with 3 s overlap. Each resulting window forms a data instance and is labelled with the exercise class. This process yields datasets of 6240 instances ($|\mathcal{X}| = 6240$), with 208 data instance per user in average ($|\mathcal{X}_p| \approx 208$). We apply a set of pre-processing steps for each sensor modality as recommended by the authors of [12]. A reduced frame rate of 1 frame/second is applied for DC and PM data and the DC data frames are compressed from 240×320 to 12×16. The inertial sensor data from ACW and ACT are pre-processed using the Discrete Cosine Transformation (DCT) according to [12].

4.3 Comparison of Person-Agnostic and Person-Aware Settings

In order to demonstrate the effect of different evaluation methods on ExR, we evaluate ExR algorithms using the two person-agnostic evaluation methodologies; R-HO and CF (Sect. 3.1) and the person-aware methodology LOPO. We choose the best performing algorithms for each sensor dataset from [12] for our comparative study. We discard the user parameter on the data instances to obtain the person-agnostic datasets, and use 1/30 as the λ parameter to split a dataset for training and testing or to create folds. Accordingly we repeat the R-HO experiments for 30 iterations and perform 30 CF experiments. These are compared with results from person-aware LOPO from [12].

Table 1. Mean F1-score results: person-agnostic vs. person-aware settings

Methodology		Algorithm	ACT	ACW	DC	PM
Person-agnostic	R-HO	From [12]	0.9807	0.9163	0.9953	0.9905
	CF		0.9798	0.9260	0.9960	0.9880
Person-aware	LOPO	From [12]	0.9015	0.6335	0.8720	0.7408

In Table 1, there is a significant difference between the performance measures obtained with person-agnostic and person-aware methods. Inevitably when there is no person-wise disjoint train and test splits, algorithms have the opportunity to configure its parameters to better fit the expected user population at test time, resulting in significantly improved performance. It is noteworthy that both person-agnostic methods achieve similar mean F1-scores consistently with all four datasets. We highlight that person-aware LOPO performance measures set the "lower-bound" and person-agnostic performance measures set the "upper-bound" for the ExR task with each sensor modality.

4.4 Comparative Study of Non-personalised vs. Personalised Algorithms for ExR

Performance of non-personalised algorithms (from [12]) is compared with the personalised algorithm MN^p (from Sect. 3.3) for ExR. We evaluate with two person-aware evaluation methodologies; R-PHO and LOPO from Sect. 3.2. With R-PHO experiments a test set is formed with randomly selected instances from 1/3 of persons forming the set of test users (μ), and the train instances selected from the other 2/3 of train users. This is repeated for 10 test-train trials. In LOPO experiments, we select the set of data instances from one user as the test set and the rest forming the train set, and this is repeated 30 times but each time with a different test user. While R-PHO helps to evaluate transferability of the algorithms with multiple users at a time, LOPO evaluates the transfer to a single user at a time, both are valid scenarios for ExR and HAR in general. For comparative purposes, we also included results obtained by authors of [13] for general HAR tasks, pose detection tasks and Activities of Daily Living (ADL) classification task.

In Table 2 results are grouped under each task and the difference between the personalised algorithm and the best non-personalised algorithm is presented in the last column. Here the best non-personalised algorithm for the first three tasks is the non-personalised Matching Networks introduced in [11] and for the MEx exercises domain they are the best performing algorithms found by the authors of [12] for each sensor modality. Person-aware evaluation methodologies require a non-parametric statistical significance test as they produce results that are not normally distributed. We use the Wilcoxon signed-rank test for paired samples to evaluate the statistical significance at 95% confidence and highlight the significantly improved performances in bold.

Table 2. Mean F1-score results for the comparison of non-personalised algorithm vs. personalised algorithm for ExR

Problem domain	Evaluation methodology	Dataset	Algorithm		Difference
			Non-personalised	MN^p	
Pose Detection	R-PHO	HDPoseDS$_{17}$	0.7678	**0.9837**	+21.68%
		HDPoseDS$_6$	0.4292	**0.9186**	+48.94%
General HAR	R-PHO	SELFBACK$_{W,T}$	0.7340	**0.9169**	+18.29%
		SELFBACK$_W$	0.6320	**0.8563**	+22.44%
ADL	R-PHO	PAMAP2	0.8715	0.8690	−0.25%
MEx	R-PHO	ACT	0.9064	**0.9424**	+3.60%
		ACW	0.6352	**0.6845**	+4.93%
		DC	0.8741	**0.9186**	+4.45%
		PM	0.6977	**0.8538**	+15.61%
MEx	LOPO	ACT	0.9015	**0.9155**	+1.40%
		ACW	0.6335	**0.6663**	+3.28%
		DC	0.8720	**0.9342**	+6.22%
		PM	0.7408	**0.8205**	+7.97%

The personalised algorithm, MN^p, has significantly outperformed the best non-personalised algorithm on both evaluation methodologies. Overall similar performance measures are observed across both methodologies, with the exception of the PM dataset, where there is a ∼+5% difference when using LOPO compared to R-PHO with the non-personalised algorithm.

We observe that personalisation has the greatest benefit for Pose detection, followed by general HAR tasks which feature both ambulatory and stationary activities; and thereafter on the ExR task. The exception here was ADL tasks, where personalisation neither improved nor degraded performance. Close examination of the activity duration of each domain suggests that pose and ambulatory activities are highly repetitive, or are performed in short repetitive time spans, which minimises the capturing of personal rhythmic nuances. In comparison, a single repetition of an exercise takes a longer time and consists of multiple sub steps making it harder to model due to potential variation opportunities

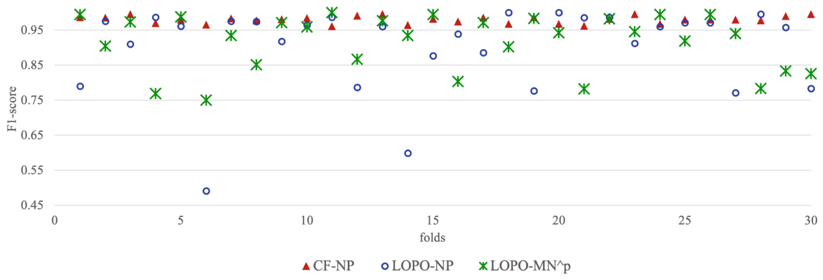

(a) ACT

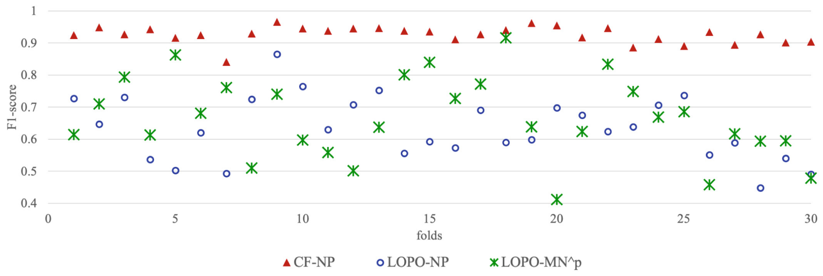

(b) ACW

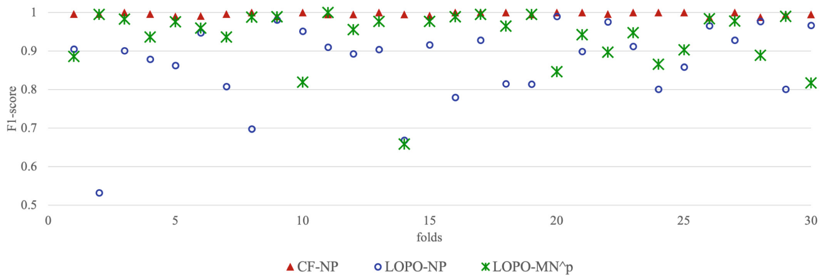

(c) DC

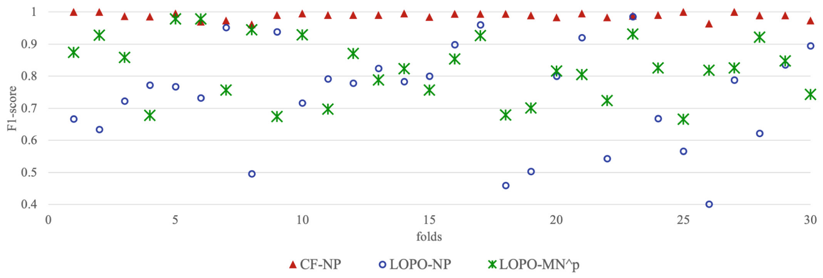

(d) PM

Fig. 5. Distribution of F1-score over the folds

between persons. Essentially MN^p is capable of finding some commonalities between exercise classes, but there is less opportunities than compared with pose or ambulatory movements. In contrast, ADL activities tend to have less clear start and stop demarcations and have even longer spans. They also have the highest possibility of featuring personal traits and nuances. For example, an ADL classes such as ironing or cleaning can be completely different from one user to another. Accordingly, personalised algorithms struggle to find such commonalities between ADL classes; explaining results we had observed here.

4.5 Distribution of Performance Measures

We visualise the distribution of performance measures with different methodologies for datasets ACT, ACW, DC and PM in Figs. 5a to 5d. Each figure shows the distribution of results obtained from three experiments; CF method with the non-personalised algorithm using red triangles, LOPO method with the non-personalised algorithm using blue circles and LOPO method with the MN^p personalised algorithm using green stars.

The CF results on every dataset highlight the upper-bound performance of the ExR task when evaluated under the assumption that the algorithm is trained and tested on the same user distribution. The LOPO results obtained for the non-personalised algorithm sets the lower-bound for the ExR task and highlights how non-personalised algorithms struggle when tested on a person that was not part of the training user group. Personalised algorithm such as MN^p, minimise the gap between the upper-bound and the lower-bound with a majority of users by improving upon the lower-bound. As shown in Table 2, MN^p, is a good choice for personalising across all tasks with significant advantages shown with pose detection and fewest gains with the ExR task.

5 Conclusion

This paper presents a comprehensive study of Exercise Recognition (ExR) model evaluation of adaptability to diverse user groups after deployment. Mainly two approaches are explored; evaluation methods that share the same user set during training and testing (i.e. person-agnostic) and methods that keep disjoint user sets for training and testing (i.e. person-aware). Our evaluation highlight that the prior method sets the upper-bound and the latter sets the lower-bound for the model performance in ExR. We highlight how person-agnostic evaluation results are normally distributed, but person-aware evaluation results are not, thus calling for non-parametric statistical significance testing methods. The paper presents the adaptation of the personalised algorithm, MN^p for ExR, that is capable of learning a feature space that is transferable to unseen users and user groups and show how it outperforms the lower-bound while using the evaluation criteria suitable for model deployment (i.e. person-aware ExR). Improving performance with personalised algorithms in the person-aware setting is a significant step towards deploying user-friendly, unobtrusive ExR algorithms with fitness applications. Finally, we highlight the need to further improve personalised algorithms to better suit the ExR domain.

References

1. Berchtold, M., Budde, M., Gordon, D., Schmidtke, H.R., Beigl, M.: ActiServ: activity recognition service for mobile phones. In: International Symposium on Wearable Computers (ISWC) 2010, pp. 1–8. IEEE (2010)
2. Burns, D.M., Leung, N., Hardisty, M., Whyne, C.M., Henry, P., McLachlin, S.: Shoulder physiotherapy exercise recognition: ML the inertial signals from a smartwatch. Physiol. Measur. **39**(7), 075007 (2018)
3. Longstaff, B., Reddy, S., Estrin, D.: Improving activity classification for health applications on mobile devices using active and semi-supervised learning. In: 2010 4th International Conference on Pervasive Computing Technologies for Healthcare, pp. 1–7. IEEE (2010)
4. Miu, T., Missier, P., Plötz, T.: Bootstrapping personalised human activity recognition models using online active learning. In: 2015 IEEE International Conference on Computer and Information Technology; Ubiquitous Computing and Communications; Dependable, Autonomic and Secure Computing; Pervasive Intelligence and Computing, pp. 1138–1147. IEEE (2015)
5. Ohashi, H., Al-Naser, M., Ahmed, S., Nakamura, K., Sato, T., Dengel, A.: Attributes' importance for zero-shot pose-classification based on wearable sensors. Sensors **18**(8), 2485 (2018)
6. Qi, J., Yang, P., Hanneghan, M., Waraich, A., Tang, S.: A hybrid hierarchical framework for free weight exercise recognition and intensity measurement with accelerometer and ECG data fusion. In: 2018 40th Annual International Conference of the IEEE Engineering in Medicine and Biology Society (EMBC), pp. 3800–3804. IEEE (2018)
7. Sun, X., Kashima, H., Ueda, N.: Large-scale personalized human activity recognition using online multitask learning. IEEE Trans. Knowl. Data Eng. **25**(11), 2551–2563 (2013)
8. Sundholm, M., Cheng, J., Zhou, B., Sethi, A., Lukowicz, P.: Smart-mat: recognizing and counting gym exercises with low-cost resistive pressure sensing matrix. In: Proceedings of the 2014 ACM UbiComp, pp. 373–382. ACM (2014)
9. Tapia, E.M., Intille, S.S., Haskell, W., Larson, K., Wright, J., King, A., Friedman, R.: Real-time recognition of physical activities and their intensities using wireless accelerometers and a heart rate monitor. In: 2007 11th IEEE International Symposium on Wearable Computers, pp. 37–40. IEEE (2007)
10. Velloso, E., Bulling, A., Gellersen, H., Ugulino, W., Fuks, H.: Qualitative activity recognition of weight lifting exercises. In: Proceedings of the 4th Augmented Human International Conference, pp. 116–123. ACM (2013)
11. Vinyals, O., Blundell, C., Lillicrap, T., Wierstra, D., et al.: Matching networks for one shot learning. In: Advances in Neural Information Processing Systems, pp. 3630–3638 (2016)
12. Wijekoon, A., Wiratunga, N., Cooper, K.: MEx: multi-modal exercises dataset for human activity recognition. arXiv preprint arXiv:1908.08992 (2019)
13. Wijekoon, A., Wiratunga, N., Sani, S., Cooper, K.: A knowledge-light approach to personalised and open-ended human activity recognition. Knowl.-Based Syst. **192**, 105651 (2020)

14. Xiao, F., Chen, J., Xie, X.H., Gui, L., Sun, J.L., none Ruchuan, W.N.: SEARE: A system for exercise activity recognition and quality evaluation based on green sensing. IEEE Trans. Emerg. Topics Comput. 1 (2018). https://doi.org/10.1109/TETC.2018.2790080
15. Zhou, B., Sundholm, M., Cheng, J., Cruz, H., Lukowicz, P.: Never skip leg day: a novel wearable approach to monitoring gym leg exercises. In: IEEE International Conference on Pervasive Computing and Communications, pp. 1–9. IEEE (2016)

Convolutional Neural Networks in Robotics/Computer Vision

Deep Learning-Based Computer Vision Application with Multiple Built-In Data Science-Oriented Capabilities

Sorin Liviu Jurj(✉), Flavius Opritoiu, and Mircea Vladutiu

Advanced Computing Systems and Architectures (ACSA) Laboratory, Computers and Information Technology Department, "Politehnica", University of Timisoara, Timisoara, Romania
jurjsorinliviu@yahoo.de,
{flavius.opritoiu,mircea.vladutiu}@cs.upt.ro

Abstract. This paper presents a Data Science-oriented application for image classification tasks that is able to automatically: a) gather images needed for training Deep Learning (DL) models with a built-in search engine crawler; b) remove duplicate images; c) sort images using built-in pre-trained DL models or user's own trained DL model; d) apply data augmentation; e) train a DL classification model; f) evaluate the performance of a DL model and system by using an accuracy calculator as well as the Accuracy Per Consumption (APC), Accuracy Per Energy Cost (APEC), Time to closest APC (TTCAPC) and Time to closest APEC (TTCAPEC) metrics calculators. Experimental results show that the proposed Computer Vision application has several unique features and advantages, proving to be efficient regarding execution time and much easier to use when compared to similar applications.

Keywords: Deep learning · Computer vision · Data collection

1 Introduction

Data is at the core of every DL application. Because the Machine Learning lifecycle consists of four stages such as data management, model learning, model verification and model deployment [1], in order to collect, analyze, interpret and make use of this data, e.g. training accurate models for real-life scenarios, in recent years, new specializations were introduced in Universities around the world such as Machine Learning and Data Science, to name only a few. Additionally, also new career positions were created recently such as Machine Learning Engineer and Data Scientist, being some of the top paid positions in the industry [2].

Regarding Computer Vision applications for image classification tasks, a major bottleneck before training the necessary DL models is considered to be the data collection which consists mainly of data acquisition, data labeling and improvement of the existing data in order to train very accurate DL models [3]. Another bottleneck is that, because the amount of data needed to train a DL model is usually required to be very large in size and because most of this important data is not released to the general public but is instead proprietary, the need of an original dataset for a particular DL project can be very crucial. In general, data can be acquired either by a) buying it from marketplaces or companies such as Quandl [4] and URSA [5]; b) searching it for free on platforms like Kaggle [6]; c) crawling it from internet resources with the help of search engine crawlers [7]; d) paying to a 24 × 7 workforce on Amazon Mechanical Turk [8] like the creators of the ImageNet dataset did to have all of their images labeled [9]; e) creating it manually for free (e.g. when the user takes all the photos and labels them himself), which can be impossible most of the time because of a low-budget, a low-quality camera or time constraints. The importance of image deduplication can be seen in the fields of Computer Vision and DL where a high number of duplicates can create biases in the evaluation of a DL model, such as in the case of CIFAR-10 and CIFAR-100 datasets [10]. It is recommended that before training a DL classification model, one should always check and make sure that there are no duplicate images found in the dataset. Finding duplicate images manually can be very hard for a human user and a time-consuming process, this being the reason why a software solution to execute such a task is crucial. Some of the drawbacks of existent solutions are that they usually require the user to buy the image deduplication software or pay monthly for a cloud solution, they are big in size or are hard to install and use.

Despite all of these options, especially in the case of scraping the images from the internet, once stored they can still be unorganized or of a lower quality than expected, with images needed to be sorted out each in their respective class folder in order for the user (e.g. data scientist) to be able later to analyze and use this data for training a performant DL model. This kind of sorting task can take a tremendous amount of time even for a team, from several days or weeks to even months [11]. Another difficult task is that once the data is cleaned, organized and ready to be trained from scratch or using transfer learning, because of the variety of DL architectures, each with different sizes and training time needed until reaching convergence [12], it can be very difficult to know from the beginning which DL architecture fits the best a given dataset and will, at the end of the training, result in a DL model that has high accuracy. Because energy consumption in DL started to become a very debated aspect in recent months, especially regarding climate change [13–17], the necessity of evaluating the performance of DL models also by their energy consumption and cost is very crucial.

Considering these aspects, our work introduces a DL-based Computer Vision application that has multiple unique built-in Data Science-oriented capabilities which give the user the ability to train a DL image classification model without any programming skills. It also automatically searches for images on the internet, sort these images each in their individual class folder and is able to remove duplicate images as well as to apply data augmentation in a very intuitive and user-friendly way. Additionally, it gives the user an option to evaluate the performance of a DL model and hardware platform not only by considering its accuracy but also its power consumption and cost by using the environmentally-friendly metrics APC, APEC, TTCAPC and TTCAPEC [16].

The paper is organized as follows. In Sect. 2 we present the related work. Section 3 describes the proposed DL-based Computer Vision application. Section 4 presents the experimental setup and results. Finally, Sect. 5 concludes this paper.

2 Related Work

Considering the advancements of DL in recent years, there is a growing interest in computer vision applications in the literature, such as regarding the automatic sorting of images, as shown by the authors in [18]. The authors propose a solution called ImageX for sorting large amounts of unorganized images found in one or multiple folders with the help of a dynamic image graph and which successfully groups together these images based on their visual similarity. They also created many similar applications, e.g. ImageSorter [19], which besides sorting images based on their color similarity, is also able to search, download and sort images from the internet with a built-in Google Image Search option. A drawback of their applications is that the user is able to only visualize similar images, without also having these images automatically cleaned and sorted in their respective class folder with high accuracy. Also, the authors in [20] created an application called Sharkzor that combines user interaction with DL in order to sort large amounts of images that are similar. By comparison, regarding sorting, their solutions only sort images by grouping them based on how similar they are to each other after a human interacted and sorted these images initially, whereas our application sorts them automatically by using in-built pre-trained DL models or gives the user an option to use his own trained DL models. An on-device option that uses DL capabilities and helps users find similar photos (e.g. finding photos that contain certain objects such as flowers, trees, food, to name only a few) is presented also by Apple in their newest version of Photos app [21].

Regarding the detection of duplicate images, this technique has practical applications in many domains such as social media analysis, web-scale retrieval as well as digital image forensics [22, 23], with several works in the literature applying it for the detection of copyright infringements [24] and fraud detection [25]. Recently, a python package that makes use of hashing algorithms and Convolution Neural Networks (CNNs) that finds exact or near-duplicates in an image collection called Image Deduplicator (Imagededup) was released in [26]. In our Computer Vision application, we make use of this package in order to offer a user the option to remove duplicate images from the images dataset (e.g. right before training a DL model).

When training DL models from scratch or by using transfer learning, usually frameworks such as Tensorflow and PyTorch are used [27], either locally (e.g. on a personal laptop or Desktop PC that contains a powerful GPU) or in cloud services such as Cloud AutoML [28, 29], Amazon AWS [30] or Microsoft Azure [31], with the work in [32] even assessing the feasibility and usefulness of automated DL in medical imaging classification, where physicians with no programming experience can still complete such tasks successfully. The problem when training locally is that the user still has to research on his own which size the images should have for a given DL architecture, which DL architecture to choose for his dataset and if it is necessary to apply fine-tuning and image augmentation. Regarding using the cloud services for training a DL model, even though these may solve most of the problems mentioned above, they still have some drawbacks such as that they can be affected by latency, can be difficult to manage (not user-friendly) and most importantly, they can be very expensive when training for several hours (e.g. Cloud AutoML from Google costs around $20 per hour when used for Computer Vision tasks [27]).

Similar work to ours is presented by the authors in [33] where they created the Image ATM (Automated Tagging Machine) tool that automatizes the pipeline of training an image classification model (preprocessing, training with model tweaking, evaluation, and deployment). Regarding preprocessing, the Image ATM tool just resizes the images to fit the model input shape. For training, it uses transfer learning with pre-trained CNNs from Keras by firstly training the last Dense layer followed by the whole network. For evaluation, it calculates the confusion matrix and other metrics. A few disadvantages of Image ATM: the tool is aimed at people with programming knowledge (developers) and is focused mainly on the training function. Also, in order to use the Image ATM tool, the user must take the work of preparing the data in a specific folder structure, e.g. the user must create a .yml file with some of the parameters desired, path to images and destination path. The user must also create a . json file containing the classification of each image. Some advantages of the Image ATM are that the tool offers the possibility for cloud training, has access to more models (although all are trained with the same dataset) and that the evaluation errors can be visualized. When compared to Image ATM, our Computer Vision application has several advantages such as that it is accessible to more kinds of people and offers more functionalities such as image web scraping and sorting, deduplication, calculators for accuracy as well as for the APC, APEC, TTCAPC and TTCAPEC metrics, all in a user-friendly Graphical User Interface (GUI).

3 The Proposed Deep Learning-Based Computer Vision Application

The proposed DL-based Computer Vision application is summarized in Fig. 1 and is built using the Python programming language. It is composed of the most common features needed in the Computer Vision field and facilitate them in the form of a GUI, without requiring the user to have any knowledge about coding or DL in order to be able to fully use it.

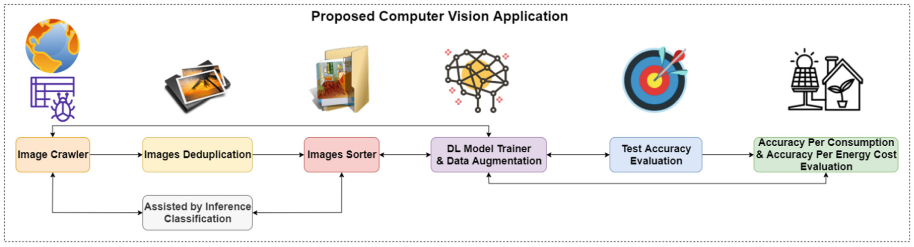
Proposed Computer Vision Application
Image Crawler
Images Deduplication
Images Sorter
DL Model Trainer & Data Augmentation
Test Accuracy Evaluation
Accuracy Per Consumption & Accuracy Per Energy Cost Evaluation
Assisted by Inference Classification

Fig. 1. Summarized view of the proposed Computer Vision application that incorporates features such as an automatic Image Crawler and Image Sorter assisted by inference classification, an Image Deduplicator, a DL Model Trainer with Data Augmentation capabilities as well as calculators regarding Accuracy, APC, APEC, TTCAPC, and TTCAPEC.

Regarding the system, the compilation dependencies and installation requirements of the proposed application are Python 3, Windows 10 (or later version) or Linux (Ubuntu 12 or later version). Regarding the Python libraries, we use PyQt5 for creating the GUI, HDF5 for loading DL model files, Tensorflow for training and inference, OpenCV for image processing, Numpy for data processing, Shutil for copying images in the system, TQDM for showing the terminal progress bar, Imagededup [26] for deduplication of images, Icrawler for crawling the images and fman build system (fbs) for creating installers.

There are certain conventions that are common in all the features of the proposed application:

1. Model files: These are .h5 files that contain the architecture of a Keras model and the weights of its parameters. These are used to load (and save) a previously trained model in order to be able to use it.
2. Model class files: These are extensionless files that contain the labels of each of the classes of a DL model. It contains *n* lines, where *n* is the number of classes in the model, and the line *i* contains the label corresponding to the *ith* element of the output of the DL model.
3. Preprocessing function: In this convention, a preprocessing function is a function that takes as input the path to an image and a shape, loads the image from the input path, converts the image to an array and fits it to the input of the model.

Images folders structures: We use two different folders structures: unclassified structures and classified structures. The unclassified images folders structure is the simplest one, consisting of just one folder containing images, presumably to be classified or deduplicated. The classified images folders structure consists of a folder which in turn contains subfolders. Each subfolder represents a class of images, is named the same as the label for that class, and contains images tagged or classified belonging to that class.

Following, we will present all the built-in features: Automatic web crawler assisted by inference classification, Images deduplication, Images Sorter assisted by inference classification, DL Model Trainer with Data Augmentation capabilities, Accuracy calculator as well as the APC and APEC [16] calculators.

3.1 Image Crawler Assisted by Inference Classification

The purpose of this feature is to collect images related to a keyword (representing a class) from the web and by using a classification algorithm, to make sure that the images are indeed belonging to this class. During the inference process needed for cleaning the images, a preprocessing is happening in the background, which, depending on the pretrained or custom DL model that is chosen, will resize the images, making them have the correct input shape (e.g. $28 \times 28 \times 1$ for MNIST and $224 \times 224 \times 3$ for ImageNet) for the DL model.

A summarized view of the implemented Image Crawler feature can be seen in Fig. 2 and is composed of the following elements: ‘Model’ - a combo box containing all the existent pretrained in-built DL models such as “mnist” or “resnet50” as well as the ‘Custom’ option which gives the user the possibility to load his own previously trained

DL model; Confidence Slider (‘Confidence required’) - a slider to select the minimum accuracy value to be used when classifying the images and which ranges from 0 to 99; Image Class Selector (‘Select a class of images’) - a combo box containing the labels of all the classes from the pretrained built-in selected DL model (e.g. 10 classes for when the “mnist” model is selected and 1000 classes when the “resnet50” model is selected). Additionally, the box contains an autocomplete search function as well; Images Amount (‘Max amount to get’) - a slider to select the number of images that should be crawled from the internet and which ranges from 1 to 999 and ‘Destination Folder’ - a browser to select the path for the final location of the obtained images.

The options under ‘Custom Model Configuration’ only apply when the DL model selected is “Custom” and is not built-in in the proposed Computer Vision application, e.g. when it was trained by the user itself. These options are: ‘Model File’ - a browser to select the .h5 file the user wishes to use for inference and Model Classes - a browser to select the extensionless file containing the name of each output class on which the selected DL model (.h5 file) was trained on. Finally, this feature’s GUI interface has a button (‘Add Images!’) that begins the web crawling process.

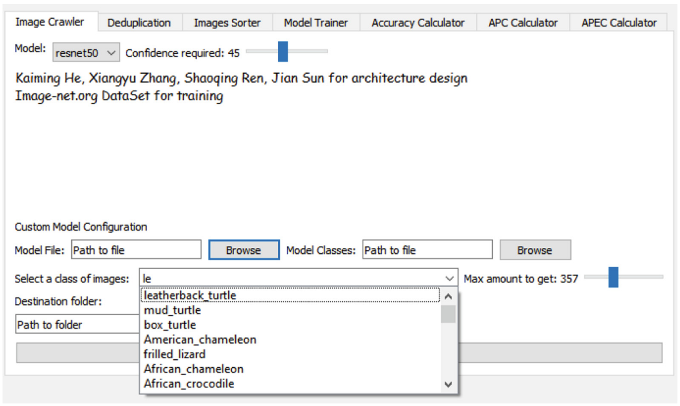

Model: resnet50 Confidence required: 45

Kaiming He, Xiangyu Zhang, Shaoqing Ren, Jian Sun for architecture design
Image-net.org DataSet for training

Custom Model Configuration

Model File: Path to file Model Classes: Path to file

Select a class of images: le Max amount to get: 357

Destination folder:
Path to folder

Fig. 2. Summarized view of the proposed Image Crawler feature assisted by inference classification.

With the help of this feature, images are automatically crawled by the crawler and downloaded to a temporal folder location. After that, each image is classified with the selected DL model, and if the classification coincides with the selected class and the confidence is higher than the selected threshold, the image is moved to the ‘Destination folder’, where each image will be saved in its own class folder.

This feature automatizes the population of image classification datasets by providing a reliable way of confirming that the downloaded images are clean and correctly organized.

3.2 Images Deduplication

The purpose of this feature is to remove duplicate images found in a certain folder. For this, we incorporated the Imagededup techniques found in [26]. A summarized view of the implemented Images Deduplication feature can be seen in Fig. 3 and is composed of the following elements: ‘Images folder’ - a browser to select the location of the folder containing the images that need to be analyzed for duplicate images; ‘Destination folder’ - a browser to select the location of the folder where the deduplicated images will be stored; ‘Duplicates Folder’ - a browser to select the location of the folder where the found duplicate images will be stored.

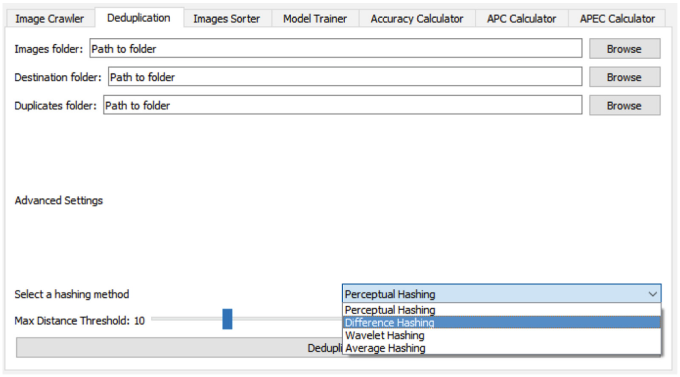

Images folder: Path to folder
Destination folder: Path to folder
Duplicates folder: Path to folder
Select a hashing method: Perceptual Hashing
Max Distance Threshold: 10

Fig. 3. Summarized view of the proposed Image Deduplication feature.

Each duplicate image found will be stored in a subfolder. Regarding advanced settings, it is composed of: Hashing method selector (‘Select a hashing method’) - a combo box containing 4 hashing methods that can be used for deduplication (Perceptual Hashing (default), Difference Hashing, Wavelet Hashing, and Average Hashing) as well as a ‘Max Distance Threshold’ - the maximum distance by which two images will be considered to be the same (default value is 10). Finally, this interface has a button (‘Deduplicate!’) that begins the deduplication process according to the selected parameters.

Following, we will shortly describe the types of hashes we are using in the images deduplication feature: a) **Average Hash:** the Average Hash algorithm first converts the input image to grayscale and then scales it down. In our case, as we want to generate a 64-bit hash, the image is scaled down. Next, the average of all gray values of the image is calculated and then the pixels are examined one by one from left to right. If the gray value is larger than the average, a 1 value is added to the hash, otherwise a 0 value; b) **Difference Hash:** Similar to the Average Hash algorithm, the Difference Hash algorithm initially generates a grayscale image from the input image. Here, from each row, the pixels are examined serially from left to right and compared to their neighbor to the right, resulting in a hash; c) **Perceptual Hash:** After gray scaling, it applies the discrete cosine transform to rows and as well as to columns. Next, we calculate the median of the gray values in this image and generate, analogous to the Median Hash algorithm, a hash value from the image; d) **Wavelet Hash:** Analogous to the Average Hash algorithm, the Wavelet Hash algorithm also generates a gray value image. Next, a two-dimensional wavelet transform is applied to the image. In our case, we use the default wavelet function called the Haar Wavelet. Next, each pixel is compared to the median and the hash is calculated.

Regarding this deduplication feature, first, the hasher generates hashes for each of the images found in the images folder. With these hashes, the distances between hashes (images) are then calculated and if they are lower than the maximum distance threshold (e.g. 10), then they are considered duplicates. Secondly, for each group of duplicates, the first image is selected as "original" and a folder is created in the duplicates folder with the name of the "original" folder. Then all duplicates of this image are stored on that folder.

This feature successfully integrates the image deduplication technique [26] and provides a simple and quick way to utilize it.

3.3 Images Sorter Assisted by Inference Classification

This feature helps a user to sort an unsorted array of images by making use of DL models. A summarized view of the implemented Images Sorter feature assisted by inference classification can be seen in Fig. 4 and is composed of elements similar to the ones presented earlier for the Image Crawler feature, but in this case with the function of selecting the path to the folders from which and where images should be sorted.

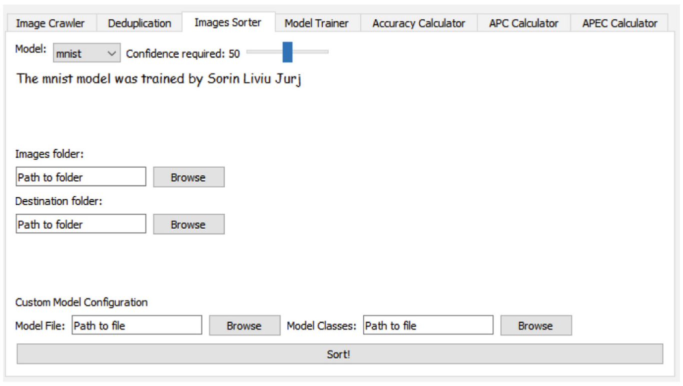

Model: mnist
Confidence required: 50
The mnist model was trained by Sorin Liviu Jurj
Images folder: Path to folder
Destination folder: Path to folder
Custom Model Configuration
Model File: Path to file
Model Classes: Path to file

Fig. 4. Summarized view of the proposed Image Sorter feature assisted by inference classification.

In the destination folder, a new folder is created for each possible class, with the name extracted from the extensionless file that contains all the names of the classes, plus a folder named 'Undetermined'. Then, each image from the 'Images Folder' is automatically preprocessed, feed as input to the selected DL model and saved in the corresponding class folder. The highest value from the output determines the predicted class of the image: if this value is less than the minimum ‘Confidence required’, value, then the image will be copied and placed in the ‘Undetermined’ folder, otherwise, the image will be copied to the folder corresponding to the class of the highest value from the output. We took the decision of copying the files instead of moving them, for data security and backup reasons.

This feature heavily reduces the amount of time required to sort through an unclassified dataset of images by not only doing it automatically but also removing the need to set up coding environments or even write a single line of code.

3.4 Model Trainer with Data Augmentation Capabilities

This feature gives the user a simple GUI to select different parameters in order to train and save a DL image classifier model. A summarized view of the implemented DL Model Trainer feature assisted by inference classification can be seen in Fig. 5 and is composed of the following elements: ‘Model’ – as described earlier for the Image Crawler feature; ‘Sorted images folder’ - a browser to select the folder that contains the classified folder structure with the images to be trained on; ‘Number of training batches’ - an integer input, to specify the number of batches to train and ‘Size of batches’ - an integer input, to specify the number of images per batch. Regarding the custom options, they are the same as mentioned earlier regarding the Image Crawler feature.

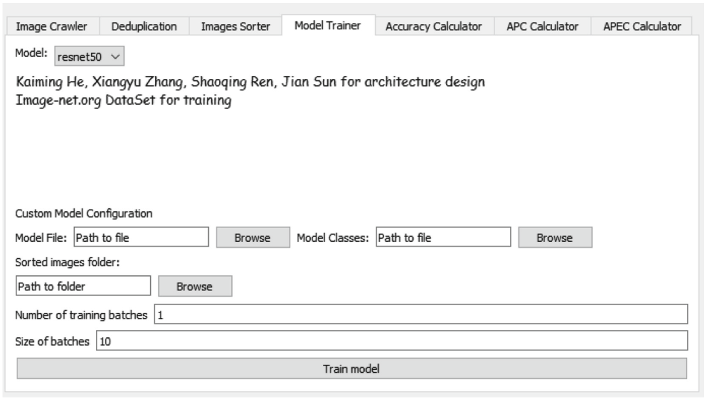

Model: resnet50

Kaiming He, Xiangyu Zhang, Shaoqing Ren, Jian Sun for architecture design
Image-net.org DataSet for training

Custom Model Configuration

Model File: Path to file
Model Classes: Path to file

Sorted images folder: Path to folder

Number of training batches: 1

Size of batches: 10

Fig. 5. Summarized view of the proposed DL Model Trainer feature.

Next, this interface has a button (‘Train model’) that, when clicked on, prompts a new window for the user to be able to visualize in a very user-friendly way all the image transformations that can be applied to the training dataset in a random way during training. More exactly, as can be seen in Fig. 6, the user can input the following parameters for data augmentation: Horizontal Flip - if checked the augmentation will randomly flip or not images horizontally; Vertical Flip - if checked the augmentation will randomly flip or not images horizontally; Max Width Shift - Slider (%), maximum percentage (value between 0 and 100) of the image width that it can be shifted left or right; Max Height Shift - Slider (%), maximum percentage (value between 0 and 100) of the image height that it can be shifted up or down; Max Angle Shift - Slider (degrees °), the maximum amount of degrees (value between 0 and 90) that an image might be rotated and Max Shear Shift - Slider (%), maximum shear value (value between 0 and 100) for image shearing. The data augmentation feature allows the user to visualize the maximum possible changes that can be made to an image in real-time, without the need of guessing the right parameters.

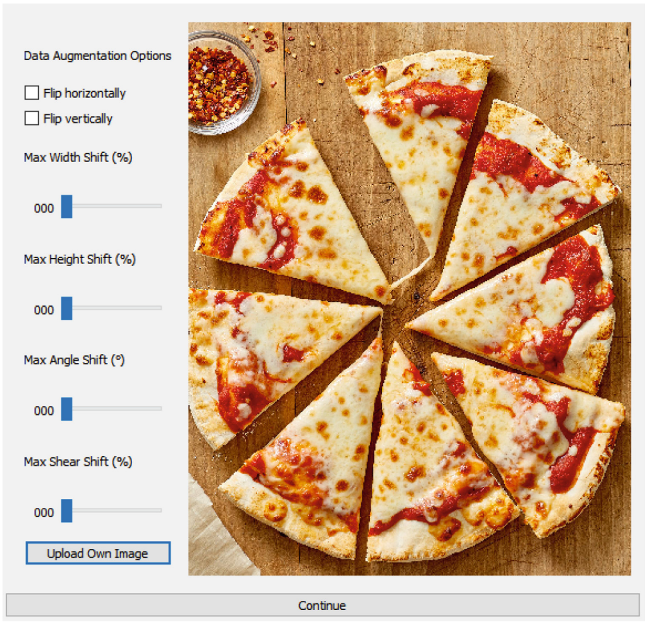
Data Augmentation Options

☐ Flip horizontally

☐ Flip vertically

Max Width Shift (%)
000

Max Height Shift (%)
000

Max Angle Shift (°)
000

Max Shear Shift (%)
000

Fig. 6. Summarized view of the proposed Data Augmentation feature.

Following, a training generator is defined with the selected parameters; The generator randomly takes images from the folder structure and fills batches of the selected size, for the number of batches that are selected. These batches are yielded as they are being generated.

Regarding the training, first, the selected DL model is loaded, its output layer is removed, the previous layers are frozen and a new output layer with the size of the number of classes in the folder structure is added. The model is then compiled with the Adam optimizer and the categorical cross-entropy as the loss function. Finally, the generator is fed to the model to be fitted. Once the training is done, the total training time is shown to the user and a model file (.h5) is created on a prompted input location.

This feature achieves the possibility of training a custom DL model on custom classes just by separating images in different folders. There is no knowledge needed about DL and this feature can later also be easily used by the Image Sorting feature described earlier in order to sort future new unsorted images.

3.5 Accuracy Calculator

This section of the application GUI gives a user the option to compute the accuracy of a DL model on the given dataset in the classified images folder structure. A summarized view of the implemented Accuracy Calculator feature can be seen in Fig. 7 and is composed of the following elements: 'Model' - as described earlier for the Image Crawler feature; 'Test images folder' - a browser to select the folder that contains the classified folder structure to measure the accuracy of a DL classification model; 'Size of batches' - an integer input, to specify the number of images per batch. The custom options are the same as mentioned earlier regarding the Image Crawler feature. Finally, this interface has a button ('Calculate Accuracy') that starts the accuracy evaluation process.

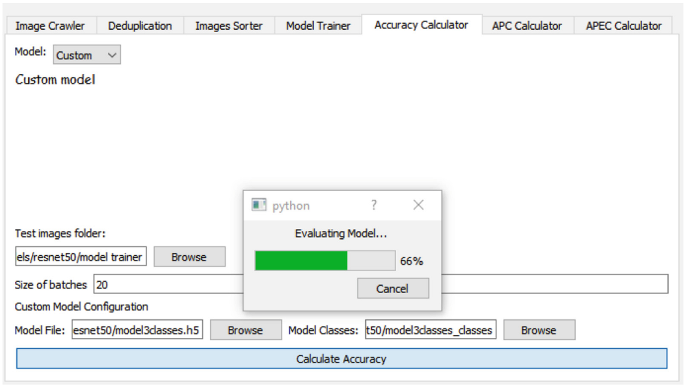

Model: Custom

Custom model

Test images folder: els/resnet50/model trainer

Evaluating Model...

66%

Size of batches 20

Custom Model Configuration

Model File: esnet50/model3classes.h5

Model Classes: t50/model3classes_classes

Fig. 7. Summarized view of the proposed Accuracy Calculator feature.

After loading the DL model and the list of classes, it searches for the classes as subfolders names in the classified images folder structure. Then, for each class (or subfolder) it creates batches of the selected batch size, feeds them to the DL model and counts the number of accurate results as well as the number of images. With these results, it calculates the total accuracy of the DL model and shows it to the user directly in the application GUI. This feature provides a simple and intuitive GUI to measure the accuracy of any DL image classification model.

3.6 Accuracy Per Consumption (APC) Calculator

This GUI feature makes use of our APC metric [16] and which is a function that takes into account not only the accuracy of a system (*acc*) but also the energy consumption of the system (*c*). The APC metric can be seen in Eq. (1) below:

$$APC_{\alpha,\beta}(c, acc) = \frac{acc}{\beta . WC_{\alpha}(c, acc) + 1} \tag{1}$$

where *c* stands from energy consumption of the system and it's measured in Watt/hour (Wh) and *acc* stands for accuracy; α is the parameter for the WC_{α} function, the default value is 0.1; β is a parameter (ranges from 0 to infinity) that controls the influence of the consumption in the final result: higher values will lower more heavily the value of the metric regarding the consumption. The default value is 1.

The application GUI gives a user the option to define the values for α and β as well as to specify and calculate the accuracy and energy consumption of a DL model using the above APC metric equation.

A summarized view of the implemented APC Calculator feature can be seen in Fig. 8 and is composed of the following elements: 'Model test accuracy (%)' - this widget gives a user the option to input the accuracy or use the previously described Accuracy Calculator feature to measure the accuracy of a DL model and 'Energy Consumption (Wh)' - float input to specify the power consumption of a user's DL model.

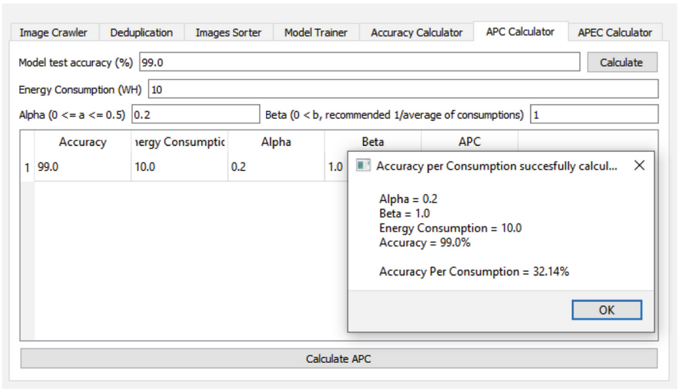

Model test accuracy (%) 99.0

Energy Consumption (WH) 10

Alpha (0 <= a <= 0.5) 0.2 Beta (0 < b, recommended 1/average of consumptions) 1

	Accuracy	ıergy Consumptic	Alpha	Beta	APC
1	99.0	10.0	0.2	1.0	

Accuracy per Consumption succesfully calcul...

Alpha = 0.2
Beta = 1.0
Energy Consumption = 10.0
Accuracy = 99.0%

Accuracy Per Consumption = 32.14%

Fig. 8. Summarized view of the proposed APC Calculator feature.

Regarding the advanced options, it has: Alpha (α) - float input to specify the desired value of α (default 0.2) and Beta (β) - float input to specify the desired value of β (default 1). For simplicity, a table is shown with the following columns: Accuracy, Energy Consumption, Alpha, Beta, and APC. Whenever a value is changed, the table is automatically updated as well. Finally, the application GUI has a button ('Calculate APC') to begin the calculation of the APC metric. The function itself is a Numpy implementation of our previously defined APC metric [16] seen in Eq. (1) and takes as input parameters the values defined in the application GUI.

The implemented feature brings this new APC metric to any user by allowing them to easily calculate the accuracy per consumption and know the performance of their DL model with regards to not only the accuracy but also to the impact it has on the environment (higher energy consumption = higher negative impact on nature). However, the drawback of the current version of this APC calculator feature in the proposed application GUI is that the user has to measure the energy consumption of the system manually. We plan to implement automatic readings of the power consumption in future updates (e.g. by using the Standard Performance Evaluation Corporation (SPEC)

PTDaemon tool [34, 35], which is also planned to be used for power measurements by the MLPerf Benchmark in their upcoming mid-2020 update).

3.7 Accuracy Per Energy Cost (APEC) Calculator

This metric is a function that takes into account not only the accuracy of a system (*acc*) but also the energy cost of the system (*c*). The APEC metric can be seen in Eq. (2) below:

$$APEC_{\alpha,\beta}(c, acc) = \frac{acc}{\beta.WC_{\alpha}(c, acc) + 1} \tag{2}$$

where *c* stands for the energy cost of the system and it's measured in EUR cents per inference and *acc* stands for accuracy.

α is the parameter for the WC_{α} function, the default value is 0.1; β is a parameter (ranges from 0 to infinity) that controls the influence of the cost in the final result: higher values will lower more heavily the value of the metric regarding the cost. The default value is 1.

The APEC feature is presented in Fig. 9 and lets a user define the values for α and β, specify or calculate the accuracy of a DL model, specify the energy consumption and the cost of Wh of the DL as well as calculate the APEC using the formula seen earlier in (2).

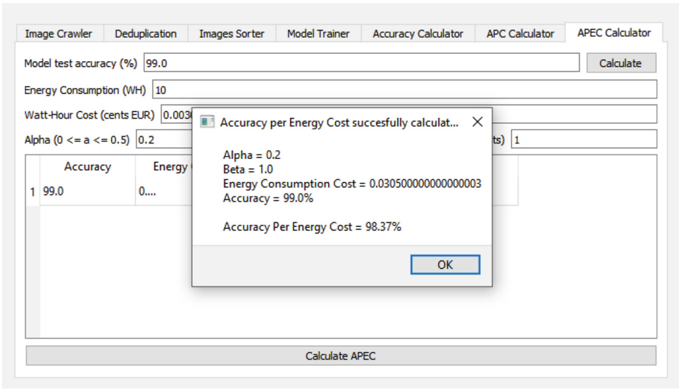

Model test accuracy (%) 99.0
Energy Consumption (WH) 10
Watt-Hour Cost (cents EUR) 0.003
Alpha (0 <= a <= 0.5) 0.2
ts) 1

	Accuracy	Energy
1	99.0	0....

Accuracy per Energy Cost succesfully calculat...

Alpha = 0.2
Beta = 1.0
Energy Consumption Cost = 0.030500000000000003
Accuracy = 99.0%

Accuracy Per Energy Cost = 98.37%

Fig. 9. Summarized view of the proposed APEC Calculator feature.

The APEC feature of the proposed Computer Vision application is composed of the following elements: 'Model test accuracy (%)' – works similar to the APC widget described earlier; 'Energy Consumption (Wh)' - works also similar to the APC widget described earlier and Watt-Hour Cost - float input to specify the cost in EUR cents of a Wh. Regarding the advanced options, we have: Alpha (α) - float input to specify the desired value of α(default 0.2) and Beta β - float input to specify the desired value of β(default 1). A similar table like the one for APC Calculator is shown also here, with the following columns: Accuracy, Energy Cost, Alpha, Beta, and APEC. Whenever a value is changed, the table is automatically updated here as well.

Finally, the application GUI has a button ('Calculate APEC') to begin the calculation of the APEC metric.

The function itself is an implementation on Numpy of our previously defined APEC metric [16] seen in Eq. (2) and takes as input parameters the values defined in the application GUI. The implemented feature brings this new APEC metric to any user by allowing them to easily calculate the accuracy per energy cost and evaluate the performance of their DL model with regards to the impact it has on the environment (higher energy consumption = higher cost = negative impact on nature). However, the drawback of the current version of this APEC calculator feature is that the user has to measure the energy consumption of the system and calculate its Wh cost manually.

3.8 Time to Closest APC (TTCAPC) Calculator

The objective of the TTAPC metric [16] is to combine training time and the APC inference metric in an intuitive way. The TTCAPC feature is presented in Fig. 10 and is composed of the following elements: 'Model test accuracy (%)' and 'Energy Consumption (Wh)', both working similar to the APEC widget described earlier; 'Accuracy Delta' – float input to specify the granularity of the accuracy axis; 'Energy Delta' – float to specify the granularity of the energy axis. Regarding the advanced options, they are the same as the ones presented earlier regarding the APEC feature.

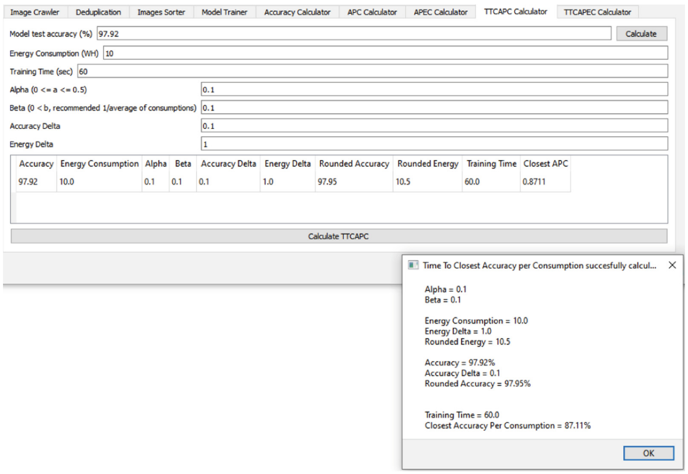

Model test accuracy (%)	97.92
Energy Consumption (WH)	10
Training Time (sec)	60
Alpha (0 <= a <= 0.5)	0.1
Beta (0 < b, recommended 1/average of consumptions)	0.1
Accuracy Delta	0.1
Energy Delta	1

Accuracy	Energy Consumption	Alpha	Beta	Accuracy Delta	Energy Delta	Rounded Accuracy	Rounded Energy	Training Time	Closest APC
97.92	10.0	0.1	0.1	0.1	1.0	97.95	10.5	60.0	0.8711

```
Time To Closest Accuracy per Consumption succesfully calcul...

Alpha = 0.1
Beta = 0.1

Energy Consumption = 10.0
Energy Delta = 1.0
Rounded Energy = 10.5

Accuracy = 97.92%
Accuracy Delta = 0.1
Rounded Accuracy = 97.95%


Training Time = 60.0
Closest Accuracy Per Consumption = 87.11%
```

Fig. 10. Summarized view of the proposed TTCAPC Calculator feature.

A similar table like the one for APEC Calculator is shown also here, with the following columns: Accuracy, Energy Consumption, Alpha, Beta, Accuracy Delta, Energy Delta, Rounded Accuracy, Rounded Energy, Training Time and Closest APC. Whenever a value is changed, the table is automatically updated here as well.

Finally, the application GUI has a button ('Calculate TTCAPC') to begin the calculation of the TTCAPC metric.

3.9 Time to Closest APEC (TTCAPEC) Calculator

The objective of the TTCAPEC metric [16] is to combine training time and the APEC inference metric. The TTCAPEC feature is presented in Fig. 11 and is composed of the same elements like the TTCAPC feature presented earlier and one additional element called ‘Energy Cost (EUR cents per Wh)’ which is similar to the one presented earlier regarding the APEC metric calculator and where the user can specify the cost in EUR cents of a Wh.

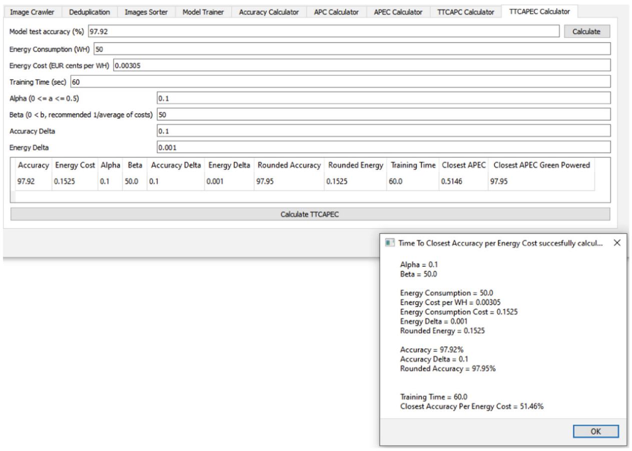

Model test accuracy (%) 97.92
Energy Consumption (WH) 50
Energy Cost (EUR cents per WH) 0.00305
Training Time (sec) 60
Alpha (0 <= a <= 0.5) 0.1
Beta (0 < b, recommended 1/average of costs) 50
Accuracy Delta 0.1
Energy Delta 0.001

Accuracy	Energy Cost	Alpha	Beta	Accuracy Delta	Energy Delta	Rounded Accuracy	Rounded Energy	Training Time	Closest APEC	Closest APEC Green Powered
97.92	0.1525	0.1	50.0	0.1	0.001	97.95	0.1525	60.0	0.5146	97.95

```
Time To Closest Accuracy per Energy Cost succesfully calcul...

Alpha = 0.1
Beta = 50.0

Energy Consumption = 50.0
Energy Cost per WH = 0.00305
Energy Consumption Cost = 0.1525
Energy Delta = 0.001
Rounded Energy = 0.1525

Accuracy = 97.92%
Accuracy Delta = 0.1
Rounded Accuracy = 97.95%


Training Time = 60.0
Closest Accuracy Per Energy Cost = 51.46%
```

Fig. 11. Summarized view of the proposed TTCAPEC Calculator feature.

A similar table like the one for TTCAPC Calculator is shown also here, with the following columns: Accuracy, Energy Cost, Alpha, Beta, Accuracy Delta, Energy Delta, Rounded Accuracy, Rounded Energy, Training Time and Closest APEC. Finally, the application GUI has a button (‘Calculate TTCAPEC’) to begin the calculation of the TTCAPEC metric.

4 Experimental Setup and Results

Following, we will show the experimental results regarding all the implemented features in comparison with existing alternatives found in the literature and industry.

We run our experiments on a Desktop PC with the following configuration: on the hardware side we use an Intel(R) Core(TM) i7-7800X CPU @ 3.50 GHz, 6 Core(s), 12 Logical Processor(s) with 32 GB RAM and an Nvidia GTX 1080 Ti as the GPU; on the software side we use Microsoft Windows 10 Pro as the operating system with CUDA 9.0, CuDNN 7.6.0 and Tensorflow 1.10.0 using the Keras 2.2.4 framework.

4.1 Image Crawler

As can be seen in Table 1, our proposed Image Crawler feature outperforms existent solutions and improves upon them. Even though the crawling took the same amount of time, this is not the case regarding the cleaning part, where, because this feature is not available in any of the existent solutions, this needed to be done manually and took 47 s for a folder containing 97 images as compared to only 10 s for our proposed solution which executed the task automatically.

Table 1. Comparison between existent and the proposed Image Crawling solution.

Features	Existent solutions [7]	Proposed solution
Image crawler	Yes	Yes
Built-in DL models	No	Yes
Custom DL models	No	Yes
Cleans dataset automatically?	No	Yes
Speed Test (sec)		
Crawling 97 images	23	23
Cleaning 97 images	47	10

A comparison between "dirty" images and clean images can be seen in Fig. 12 where, for simplicity, we searched for 97 pictures of "cucumber", which is one class from the total of 1000 classes found in the ImageNet dataset [9].

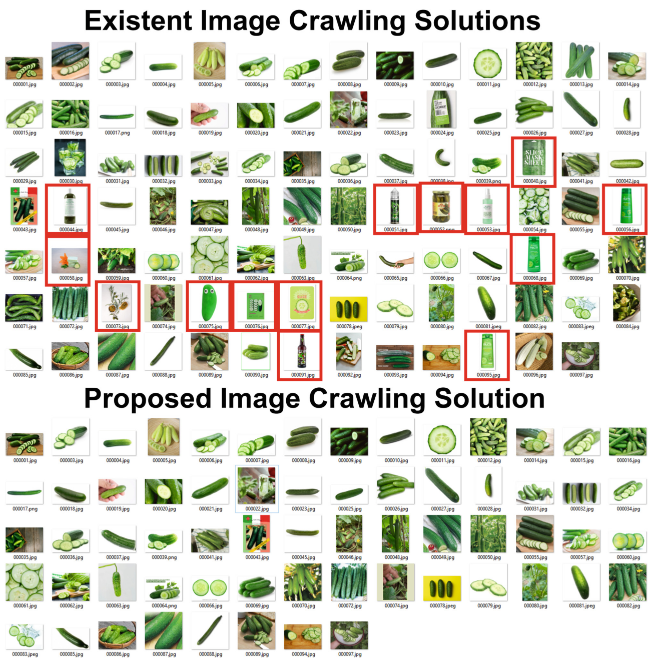
Existent Image Crawling Solutions
Proposed Image Crawling Solution

Fig. 12. Summarized view of existent and the proposed image crawling solution. The pictures marked with a red rectangle are examples of "dirty" images found when crawling with existent solutions. By comparison, the proposed image crawling feature assisted by DL inference contains only clean images.

It can be easily observed how the existent solutions provide images that don't represent an actual cucumber, but products (e.g. shampoos) that are made of it. After automatically cleaning these images with a confidence rate of 50% with the proposed feature, only 64 clean images remained in the folder.

4.2 Deduplication

For the experiments seen in Table 2, we tested the speed time of the proposed built-in image deduplication feature that uses the Imagededup python package [26]. We run these experiments on finding only exact duplicates on the same number of images with a maximum distance threshold of 10 for all four hashing methods.

Table 2. Speed Results for the 4 hashing methods of the proposed Image Deduplication feature.

Nr. of images	Hashing method	Speed time (sec)
1.226	Perceptual Hashing	16
	Difference Hashing	15
	Wavelet Hashing	17
	Average Hashing	16

As can be seen, the average speed is about 16 s for finding duplicates in a folder containing 1.226 images, with Difference Hashing being the fastest hashing method from all four.

4.3 Images Sorter

For our experiments regarding the sorting of images with the proposed images sorter feature, we used both the MNIST as well as the ImageNet pre-trained models with a confidence rate of 50% and presented the results in Table 3.

Table 3. Speed Time for the proposed Images Sorting feature.

DL model	Nr. of classes	Nr. of images	Undetermined images	Speed time (sec)
MNIST	10	70.000	69	307
ImageNet [9]	1000	456.567	135.789	40.817
Custom [37]	34	2.380	34	223

Regarding MNIST experiments, we converted the MNIST dataset consisting of 70.000 images of 28 $\times$ 28 pixels to PNG format by using the script in [36] and mixed all these images in a folder. After that, we run our image sorter feature on them and succeeded to have only 0.09% of undetermined images, with a total speed time of around 6 min. Regarding ImageNet, we used the ImageNet Large Scale Visual Recognition Challenge 2013 (ILSVRC2013) dataset containing 456.567 images belonging to 1000 classes with a confidence rate of 50%. Here we successfully sorted all images in around 11 h and 20 min, more exactly in 40.817 s, with 29.74% (135.789) undetermined images.

Regarding the custom model, we used one of our previously trained DL models (ResNet-50) that can classify 34 animal classes [37] on a number of 2.380 images of 256 $\times$ Ratio pixels (70 images for each of the 34 animal classes) with a confidence rate of 50%. Here we succeeded to have 1.42% undetermined images, with a total speed time of almost 4 min. The percentage of the undetermined images for all cases can be improved by modifying the confidence rate, but it is out of this paper's scope to experiment with different confidence values.

The time that a DL prediction task takes depends on a few variables, mainly the processing power of the machine used to run the model, the framework used to call the inference of the model and the model itself. Since processing power keeps changing and varies greatly over different machines, and all the frameworks are optimized complexity wise and keep evolving, we find that among these three the most important to measure is, therefore, the model itself used in the prediction. Models vary greatly in their architecture, but all DL models can be mostly decomposed as a series of floating points operations (FLOPs). Because, generally, more FLOPs equal more processing needed and therefore more time spent in the whole operation, we measured the time complexity of the built-in ImageNet and MNIST models in FLOPS and presented the results in Table 4.

Table 4. The time complexity of the built-in DL models measured in the number of FLOPS.

DL model	Dataset	MFLOPS	GFLOPS
ResNet-50	ImageNet	3.800	3.8
MNIST	MNIST	9	0.009

4.4 Model Trainer

For the experiments regarding the DL model training feature, because we want to evaluate the application on a real-world problem, we will attempt to show that this feature could be very useful for doctors or medical professionals in the aid of detecting diseases from imaging data (e.g. respiratory diseases detection with x-ray images). In order to prove this, we will attempt to automatically sort between the images of sick patients versus healthy patients regarding, firstly, pneumonia [38], and secondly, COVID-19 [39], all within our application and doing it only with the training feature that the application provides.

For this, first, in order to classify between x-ray images of patients with pneumonia versus x-ray images of healthy patients, we made use of transfer learning and trained a 'resnet50' architecture for around 2 h without data augmentation on pneumonia [38] dataset containing 6.200 train images by selecting 10 as the value for the number of training batches and 10 as the value for the size of batches (amount of images per batch) and achieved 98.54% train accuracy after 10 epochs. Secondly, in order to classify between x-ray images of patients with COVID-19 versus x-ray images of negative patients, we again made use of transfer learning and trained a 'resnet50' architecture for around 1 h without data augmentation on the COVID-19 [39] dataset containing 107 train images by selecting the same values for the number and size of training batches as the pneumonia model mentioned above and achieved 100% train accuracy after 100 epochs.

4.5 Accuracy Calculator

For the experiments regarding the accuracy calculator feature, we used the two custom DL models trained earlier to classify x-ray images of patients with pneumonia versus x-ray images of healthy patients and between x-ray images of patients with COVID-19 versus x-ray images of negative patients, with 20 as the size of batches (20 images per batch).

The evaluation took in both cases around 50 s with a test accuracy of 93.75% regarding the pneumonia model on 620 test images and 91% regarding the COVID-19 model on 11 test images, proving that the proposed Computer Vision application can easily be used by any medical personal with very basic computer knowledge in order to train and test a DL classification model for medical work purposes.

4.6 APC and APEC Calculators

Regarding the experiments with the proposed APC [16] calculator feature, we presented the simulated results for different model test accuracy (%) and energy consumption (Wh) values in Table 5. We run all the experiments with 0.2 as the alpha value and with 1.0 as the beta value.

Table 5. Summarized Results of the proposed APC Calculator feature.

Energy consumption [Wh]	DL model test accuracy [%]	APC [%]
10	99.0	32.14
2	99.0	69.91
1	99.7	82.91
10	99.7	32.96
50	99.7	8.96
10	94.5	27.47
50	50.0	1.61
1	50.0	31.25
10	50.0	7.14
10	40.0	5.12
1	40.0	23.8
1	100	83.33

It is important to mention that our recommendation for a correct comparison between two DL models, is that it is always necessary that they are both tested with the same alpha and beta values. As can be seen in Table 5 where we experimented with random energy consumption and test accuracy values, our APC Calculator feature is evaluating the performance of a DL model by considering not only the accuracy but also the power consumption. Therefore, DL models that consume around 50 Wh (e.g. when running inference on a laptop) instead of 10 Wh (e.g. when running inference on a low-cost embedded platform such as the Nvidia Jetson TX2) [15], are penalized more severely by the APC metric.

Regarding the experiments with the proposed APEC [16] calculator feature, we presented the simulated results for different model test accuracy (%) and energy cost in Table 6. We run all the experiments with 0.2 as the alpha value and with 1.0 as the beta value.

Table 6. Summarized Results of the proposed APEC Calculator feature.

Energy consumption [Wh]	Power cost [cents EUR]	DL model test accuracy [%]	APEC [%]	APEC green energy [%]
10	0.03050	99.0	98.37	99.0
2	0.0061	99.0	98.87	99.0
1	0.00305	99.7	99.63	99.7
10	0.03050	99.7	99.08	99.7
50	0.1525	99.7	96.71	99.7
10	0.03050	94.5	93.8	94.5
50	0.1525	50.0	45.8	50.0
1	0.00305	50.0	49.9	50.0
10	0.03050	50.0	49.1	50.0
10	0.03050	40.0	39.18	40.0
1	0.00305	40.0	39.91	40.0
1	0.00305	100	99.93	100

For simplicity, regarding electricity costs, we took Germany as an example. According to “Strom Report” (based on Eurostat data) [40], German retail consumers paid 0.00305 Euro cents for a Wh of electricity in 2017. We used this value to calculate the cost of energy by plugging it in the equation presented in (2)”, where “*c*” in this case stands for the energy cost. As can be seen, the APEC metric favors lower power consumption and cost, favoring the use of green energy (free and clean energy).

4.7 TTCAPC and TTCAPEC Calculators

Regarding the experiments with the proposed TTCAPC [16] calculator feature, we simulated a custom DL model on two platforms and presented the results in Table 7.

Table 7. TTCAPC with Accuracy delta = 0.1, Energy delta = 1, beta = 0.1, alpha = 0.1.

	Desktop PC	Nvidia Jetson TX2
Accuracy [%]	97.92	
Energy Consumption [Wh]	50	10
Rounded Accuracy [%]	97.95	
Rounded Energy Consumption [Wh]	50.5	10.5
Closest APC [%]	61.28	87.11
Train seconds	60	

As can be seen, even though the accuracy and training time is the same for both platforms, the TTCAPC feature favors the platform which has less power consumption.

Regarding the experiments with the proposed TTCAPEC [16] calculator feature, we simulated with the same DL model values used also in the experiments regarding the TTCAPC calculator earlier and presented the results in Table 8.

Table 8. TTCAPEC with Accuracy delta = 0.1, Energy delta = 1, beta = 0.1, alpha = 0.1.

	Desktop PC	Nvidia Jetson TX2
Accuracy [%]	97.92	
Energy Cost (cents)	0.1525	0.0305
Rounded Energy Cost (cents)	0.1525	0.0305
Rounded Accuracy [%]	97.95	
Closest APEC [%]	51.46	82.96
Closest APEC Green (Solar) Powered [%]	97.95	
Train seconds	60	

As can be also seen in this case, the TTCAPEC feature favors the lower power consumption of a system because it results in a lower cost. Additionally and more importantly, it favors DL-based systems that are powered by green energy, because they have 0 electricity costs and no negative impact on our environment.

5 Conclusions

In this paper, we present a Computer Vision application that succeeds in bringing common DL features needed by a user (e.g. data scientist) when performing image classification related tasks into one easy to use and user-friendly GUI.

From automatically gathering images and classifying them each in their respective class folder in a matter of minutes, to removing duplicates, sorting images, training and evaluating a DL model in a matter of minutes, all these features are integrated in a sensible and intuitive manner that requires no knowledge of programming and DL. Experimental results show that the proposed application has many unique advantages and also outperforms similar existent solutions. Additionally, this is the first Computer

Vision application that incorporates the APC, APEC, TTCAPC and TTCAPEC metrics [16], which can be easily used to calculate and evaluate the performance of DL models and systems based not only on their accuracy but also on their energy consumption and cost, encouraging new generations of researchers to make use only of green energy when powering their DL-based systems [15].

References

1. Ashmore, R., Calinescu, R., Paterson, C.: Assuring the machine learning lifecycle: desiderata, methods, and challenges. arXiv:1905.04223, May 2019
2. Soni, N., et al.: Impact of artificial intelligence on businesses: from research, innovation, market deployment to future shifts in business models. arXiv:1905.02092v1, May 2019
3. Roh, Y., Heo, G., Whang, S.E.: A survey on data collection for machine learning: a big data – AI integration perspective. arXiv:1811.03402v2, August 2019
4. Quandl. https://www.quandl.com/. Accessed 29 Feb 2020
5. URSA. https://www.ursaspace.com/. Accessed 29 Feb 2020
6. Kaggle. https://www.kaggle.com/datasets. Accessed 29 Feb 2020
7. Icrawler. https://pypi.org/project/icrawler/. Accessed 29 Feb 2020
8. Amazon Mechanical Turk. https://www.mturk.com/. Accessed 29 Feb 2020
9. Deng, J., et al.: ImageNet: a large-scale hierarchical image database. In: 2009 IEEE Conference on Computer Vision and Pattern Recognition, Miami, FL, USA (2009)
10. Barz, B., Denzler, J.: Do we train on test data? Purging CIFAR of near-duplicates. arXiv:1902.00423, February 2019
11. Swanson, A., et al.: Snapshot Serengeti, high-frequency annotated camera trap images of 40 mammalian species in an African savanna. Sci Data **2**, 150026 (2015). https://doi.org/10.1038/sdata.2015.26
12. Nakkiran, P., et al.: Deep double descent: where bigger models and more data hurt. arXiv:1912.02292, December 2019
13. Schwartz, R., Dodge, J., Smith, N.A., Etzioni, O.: Green AI. arXiv:1907.10597v3. August 2019
14. Strubell, E., Ganesh, A., McCallum, A.: Energy and policy considerations for deep learning in NLP. arXiv:1906.02243, June 2019
15. Jurj, S.L., Rotar, R., Opritoiu, F., Vladutiu, M.: Efficient Implementation of a Self-Sufficient Solar-Powered Real-Time Deep Learning-Based System, to appear
16. Jurj, S.L., Opritoiu, F., Vladutiu, M.: Environmentally-Friendly Metrics for Evaluating the Performance of Deep Learning Models and Systems, to appear
17. Rolnick, D., et al.: Tackling climate change with machine learning. arXiv:1906.05433v2. November 2019
18. Nico, H., Kai-Uwe, B.: Dynamic construction and manipulation of hierarchical quartic image graphs. In: ICMR 2018 Proceedings of the 2018 ACM on International Conference on Multimedia Retrieval, New York, pp. 513–516 (2018)
19. Image Sorter. https://visual-computing.com/project/imagesorter/. Accessed 29 Feb 2020
20. Pirrung, M., et al.: Sharkzor: interactive deep learning for image triage, sort, and summary. arXiv:1802.05316 (2018)
21. Apple Photos. https://www.apple.com/ios/photos/pdf/Photos_Tech_Brief_Sept_2019.pdf. Accessed 29 Feb 2020
22. Morra, L., Lamberti, F.: Benchmarking unsupervised near-duplicate image detection. arXiv:1907.02821, July 2019

23. Zhou, W., et al.: Recent advance in content-based image retrieval: a literature survey. arXiv:1706.06064v2, September 2017
24. Zhou, Z., et al.: Effective and efficient global context verification for image copy detection. IEEE Trans. Inf. Forens. Secur. **12**(1), 48–63 (2017)
25. Cicconet, M., et al.: Image Forensics: detecting duplication of scientific images with manipulation-invariant image similarity. arXiv:1802.06515v2, August 2018
26. Jain, T., et al.: Image Deduplicator (Imagededup). https://idealo.github.io/imagededup/. Accessed 29 Feb 2020
27. Florencio, F., et al.: Performance analysis of deep learning libraries: TensorFlow and PyTorch. J. Comput. Sci. **15**(6), 785–799 (2019)
28. Cloud AutoML. https://cloud.google.com/automl/. Accessed 29 Feb 2020
29. He, X., et al.: AutoML: A Survey of the State-of-the-Art. arXiv:1908.00709v2, August 2019
30. PyTorch on AWS. https://aws.amazon.com/pytorch/. Accessed 29 Feb 2020
31. Microsoft Azure. https://azure.microsoft.com/. Accessed 29 Feb 2020
32. Faes, L., et al.: Automated deep learning design for medical image classification by health-care professionals with no coding experience: a feasibility study. Lancet Dig. Health **1**(5), e232–e242 (2019)
33. Lennan, C., et al.: Image ATM. https://github.com/idealo/imageatm/. Accessed 29 Feb 2020
34. von Kistowski, J., et al.: Measuring and benchmarking power consumption and energy efficiency. In: Companion of the 2018 ACM/SPEC International Conference on Performance Engineering (ICPE 2018), pp. 57–65. ACM, New York (2018). https://doi.org/10.1145/3185768.3185775
35. Standard Performance Evaluation Corporation (SPEC) Power. https://www.spec.org/power_ssj2008/. Accessed 29 Feb 2020
36. MNIST converted to PNG format. https://github.com/myleott/mnist_png. Accessed 29 Feb 2020
37. Jurj, S.L., Opritoiu, F., Vladutiu, M.: Real-time identification of animals found in domestic areas of Europe. In: Proceedings SPIE 11433, Twelfth International Conference on Machine Vision (ICMV 2019), 1143313, 31 January (2020). https://doi.org/10.1117/12.2556376
38. Chest X-Ray Images (Pneumonia). https://www.kaggle.com/paultimothymooney/chest-xray-pneumonia/. Accessed 01 Apr 2020
39. Cohen, J.P., Morrison, P., Dao, L.: COVID-19 image data collection. arXiv:2003.11597 (2020). https://github.com/ieee8023/covid-chestxray-dataset. Accessed 01 Apr 2020
40. Strom-Report. https://1-stromvergleich.com/electricity-prices-europe/. Accessed 29 Feb 2020

Visual Movement Prediction for Stable Grasp Point Detection

Constanze Schwan(✉) and Wolfram Schenck

Center for Applied Data Science (CfADS), Faculty of Engineering and Mathematics, Bielefeld University of Applied Sciences, Gütersloh, Germany
{constanze.schwan,wolfram.schenck}@fh-bielefeld.de

Abstract. Robotic grasping of unknown objects in cluttered scenes is already well established, mainly based on advances in Deep Learning methods. A major drawback is the need for a big amount of real-world training data. Furthermore these networks are not interpretable in a sense that it is not clear why certain grasp attempts fail. To make the process of robotic grasping traceable and simplify the overall model we suggest to divide the complex task of robotic grasping into three simpler tasks to find stable grasp points. The first task is to find all grasp points where the gripper can be lowered onto the table without colliding with the object. The second task is to determine for the grasp points and gripper parameters from the first step how the object moves while the gripper is closed. Finally in the third step for all grasp points from the second step it is predicted whether the object slips out of the gripper during lifting. By this simplification it is possible to understand for each grasp point why it is stable and - just as important - why others are unstable or not feasible. In this study we focus on the second task, the prediction of the physical interaction between gripper and object while the gripper is closed. We investigate different Convolutional Neural Network (CNN) architectures and identify the architecture(s) that predict the physical interactions in image space best. We perform the experiments for training data generation in the robot and physics simulator V-REP.

Keywords: Robotic grasping · Convolutional Neural Network · Simulation · Physical interaction

1 Introduction

Grasping and manipulating objects are tasks humans carry out effortlessly on an everyday basis. Due to the high object variety and variability of the environment, the same tasks are hard to learn for robots. Two main approaches are distinguished in robot grasping [1]: The first approach determines from the sensory image(s) the optimal grasp pose of the robot arm. A grasp planner determines subsequently the motor commands to drive the robot arm into the optimal grasp configuration. The optimal grasp configuration is determined either analytically with force- and form-closure objectives [9] or is data-driven. In the second approach, the visuomotor controller is directly learned from the sensory image(s). State-of-the-art grasping methods involve deep learning [2–4,6] and focus on training a visuomotor controller. These aforementioned methods have in common that they learn a mapping from image pixels or regions and robot (joint-)parameters to a grasp success probability. An optimization algorithm aids to find the robot parameters that maximize the grasp probability. However it is not possible to evaluate these models such that it is traceable why a certain grasp candidate succeeded or failed. Especially in industrial applications this lack of interpretability prevents the algorithms from being applied. In this study the idea is that vision-based robotic grasping is achieved by finding robot parameters that lead to a collision free path of the robot arm to the object (selected on the image), where closing and lifting the manipulator leads to a stable grasp. We make two contributions: Our first contribution is to divide the complex task of robotic grasping into three simpler tasks that can effectively be learned by simple CNNs. In a first step all grasp points are determined where the gripper can be lowered on the table, while enclosing an object part (Lowering Model). In the second step a Convolutional Neural Network (CNN) is trained that predicts the physical interaction between the gripper and the object visually (Closing Model). Finally a model is learned that predicts the grasp points where the object is liftable (Lifting Model). This model is a simple CNN that classifies the images predicted from the Closing Model into liftable when the object remains between the gripper and not liftable when the object slips out of the gripper during lifting. Our second contribution and focus of this study is the construction of a CNN for learning the Closing Model that predicts the physical interaction between object and gripper in the image domain when the gripper is closed. To the best of our knowledge there are no grasping models where the object movement due to the closing movement of the gripper is directly predicted. There is research on predicting object movements in pushing tasks [5,7] but not in the realm of grasping. In [12,13] the effect of an force acting on an object in an image is predicted in terms of a vector field but without the prediction in the image domain. Oh et al. [10] trained CNNs to predict from an action and frames of an Atari game the next frames driven by the action. We adapt one architecture from [10] and make a thorough parameter analysis to identify the architecture that best suits our data for the Closing Model. To understand the context of the presented Closing Model, the concept of all three models is briefly described as well as the object database and the physics simulation V-REP which is used to generate the training data for each step.

2 Grasp Definition and Object Database

In our study, we use prismatic object shapes which are generated from binary (household) item images, by triangulating the boundaries of the edge filtered images and extruding the resulting faces in 3D. By this simplification the objects

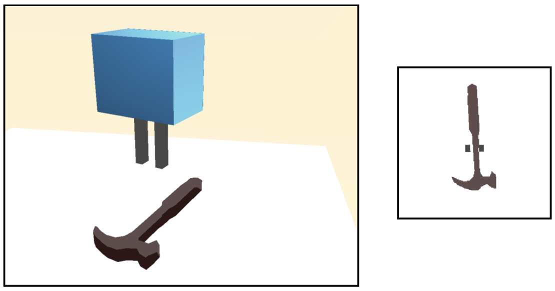

Fig. 1. Left: V-REP simulation of the gripper in pre-grasp position. Right: Image from the orthographic camera between the gripper tips in the pre-grasp position.

considered here all have the same height at each location. To increase the variability of the object shapes, 10 000 objects were created from bitmap images of household items and artificial random polygon shapes in three different sizes. On the left image of Fig. 1 a hammer that was build this way is positioned on a table. The gripper is a parallel-jaw gripper with a maximal opening width of 5 cm. In Fig. 1 the design of the simulation in V-REP [15] is shown. The prismatic objects are placed on a table, one object at a time. Since the objects by design have the same height, we use only four parameters to describe the gripper posture: (x, y, α, s), where x and y are the planar coordinates measured in the world coordinate system, α is the rotation of the gripper around the positive z-axis of the world coordinate system, and s the gripper opening width measured between the inner side of the tips. As input for the Lowering Model, a greyscale snapshot from an orthographic camera that is centred above the table is taken, with a resolution of 512×512 pixels. On this image, pixels are randomly chosen on the object shapes; these pixels are called grasp candidates from now on. The gripper with the maximal opening width of 5 cm spans 51 pixels on this image. The right image of Fig. 1 shows an example of the image obtained by a second orthographic camera which is placed between the gripper tips.

3 Three-Step Model for Stable Grasp Point Detection

The first step of grasp point detection is to determine from all randomly chosen grasp candidates on an orthographic image from the camera centred above the table those where the gripper can be lowered on the table without colliding with the object. For this purpose a two-phase model is applied. In phase I, a forward model (FM) is trained which predicts for an arbitrary gripper configuration tuple $(\alpha_i,\ s_i)$ the image of the gripper tip projections. In phase II Differential Evolution [8] is used as optimization algorithm to predict the gripper tuple $(\alpha_i,$ $s_i)$ that minimizes the intersection between the gripper tip projections and the image patch for a given grasp candidate. The left column of Fig. 2 shows the randomly chosen grasp candidates (red dots) on pliers and a cup shape. The second column of Fig. 2 shows the grasp candidates (green dots) where a gripper

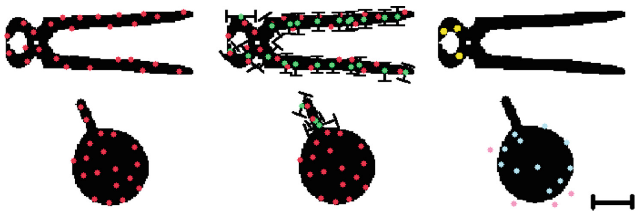

Fig. 2. Examples of the grasp candidates for the orthographic projection of pliers and a cup. Left column: randomly chosen grasp candidates (red dots). Center column: true positive grasp candidates (green dots) where a gripper tuple was found. Right column: false negative grasp candidates (yellow dots) where Differential Evolution was not able to find an existing solution, true negative grasp candidates (blue and pink dots).

tuple $(\alpha_i,\ s_i)$ was found such that the intersection between the object and the gripper tip projections is zero, i.e. the gripper can be lowered without collision. The third column of Fig. 2 shows the grasp candidates where no gripper tuple was found.

The second step (Closing Model) is the prediction of the physical interaction between gripper and object for the true positive grasp candidates from the Lowering Model while closing the gripper. The third step is to predict for the grasp candidates where the object remained between the gripper tips after closing if the object remains between the gripper tips when the manipulator is lifted (Lifting Model). Therefore there are three possible causes why a chosen grasp candidate does not lead to a stable grasp. The first reason is that there is no gripper parameter configuration where the gripper can be lowered onto the table without colliding with the object. This possibly means that the object is too big for the used gripper. The second reason is that for the given grasp candidate the object was pushed out of the gripper during closing due to the local shape of the object. Finally, the last reason for a failed grasp is that the object falls out of the gripper during lifting, because of the distance between the grasp point and the centre of mass of the object. The evaluation of these three steps increases the interpretability of the whole grasping procedure. In the following the Closing Model is presented in-depth together with a thorough analysis of different CNN architectures.

4 The Closing Model

Goal of the Closing Model is to predict the physical interaction between object and gripper in the image domain. More precisely: given the image of the object and gripper before closing, the Closing Model should predict the resulting image after closing the gripper and determine the gripper opening width s. If the resulting s is greater than 0, the object remained between the gripper tips, otherwise the object was pushed out. In the following a thorough analysis of different CNN architectures for the Closing Model is presented. To determine the quality

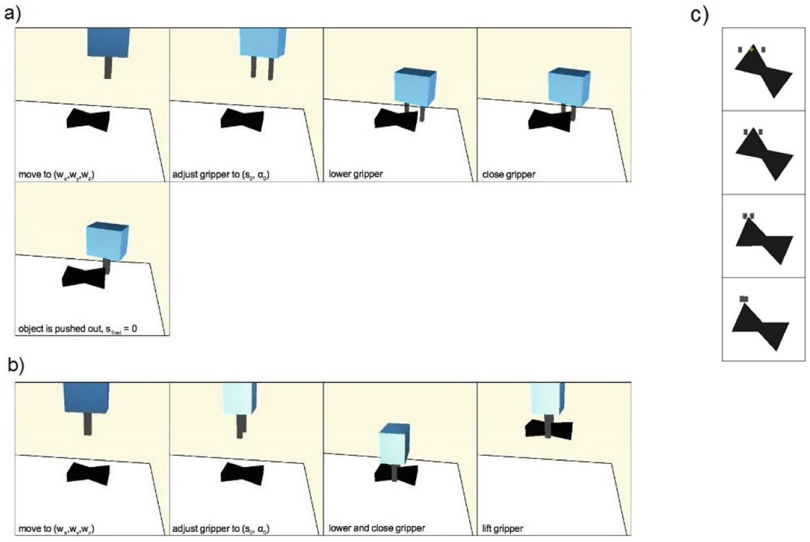

Fig. 3. a) Example of a grasp sequence in V-REP for a negative grasp candidate. b) Example of a grasp sequence in V-REP for a positive grasp candidate. c) Example of an image sequence obtained in simulation.

of the CNNs two measures are evaluated. The Intersection over Union (IOU) measure quantifies the quality of the predicted object and gripper movement. The IOU between two shapes is defined as the fraction of "intersection of the two shapes"/"union of the two shapes". When two shapes are identical in form, position and orientation in an image the IOU value is 1. The confusion matrix for the predicted gripper opening width (classes: "gripper closed" vs. "gripper not closed") is the second measure that is applied for evaluating the networks.

4.1 Training Data Generation for the Closing Model

The resulting true-positive grasp candidates from the Lowering Model are used to create the training data for the Closing Model and Lifting Model. Therefore a grasp trial is initiated for every true-positive grasp candidate and an image sequence recorded during the closing movement of the gripper in the V-REP-simulation. The grasp candidate is transformed to the world coordinate system. The orthographic camera used in this simulation is fixed to the gripper. Therefore the gripper has the 0-orientation in all image sequences. The resolution of the camera is 1024×1024. To reduce the image size, we crop a region of 250×250 pixels and rescale the images to 64×64. When the object is pushed out and the gripper opening width is 0 after the closing movement, the grasp candidate is said to be negative otherwise positive. An example for a negative and positive grasp trial is shown in Fig. 3a) and b). Figure 3c) shows an example of an image sequence obtained by this method. The images are inverted and normalized,

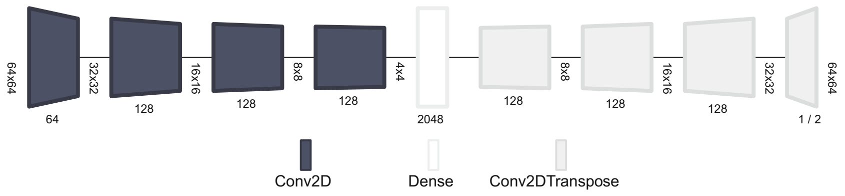

Fig. 4. CNN architecture for 1-channel and 2-channel prediction, adapted from [10]. Net2Vis was used for visualization [11].

such that the pixels of the image that represent the gripper have a value of 0.7, the pixels that represent the object have a value of 1.0 and the background is 0. The different pixel intensities are also used for separating the images into two channels one for the object and one for the gripper as is explained in the following section. All models described in this study are trained with 15 000 positive and 15 000 negative image pairs and evaluated on 2500 positive and 2500 negative image pairs.

4.2 1-Channel Vs. 2-Channel Prediction

The initial design of the CNN architecture presented here is adapted from [10]. In [10] the goal was to predict from an rgb Atari game frame and an action the next frames. The authors no-action feedforward architecture from [10] consisted of four convolutional layers, two dense layers and four deconvolutional layers. In this study this architecture is modified to incorporate only on dense layer as shown in Fig. 4. Since the gripper is closed in an uniform motion and the gripper orientation is the same for each image sequence the gripper parameters are not added as an additional input to the network structure. The kernel-sizes are chosen as (8×8), (6×6), (6×6), (4×4) and in reverse order for the deconvolutional part with a stride of 2 as in [10]. Each convolutional layer is followed by a RELU-layer. Training is done with the Adam-optimizer with the standard values. Goal of this section is to find the optimal architecture for the Closing Model through variation of the number of input and output channels. In the following the 1-channel and 2-channel predictions are compared.

The input of the CNN for the 1-channel prediction is the image of the object and gripper together in 1 channel, the output is a 1-channel image. The training data for the 1-channel network consists of the normalized first and last image of the image sequences obtained from the grasp trials in VREP, where the background is 0, the pixels of gripper tip projection are set to 0.7 and the object pixels to 1.0. The same network is also trained and evaluated with 2-channel images, where the first channel contains the object and the second channel the gripper. Both channels are again greyscale with 0 for the background, 0.7 for the gripper and 1.0 for the object pixels. For computing the IOU value for the 1-channel and 2-channel prediction, the predicted image channels of the network are thresholded such that the background is 0 and the object and gripper pixels 1.

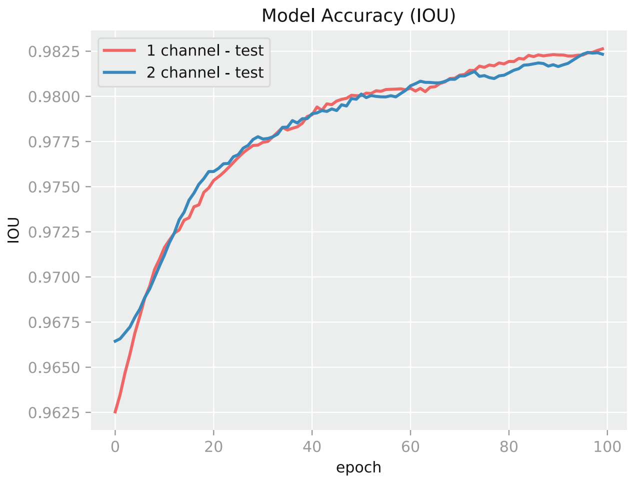

Fig. 5. IOU of the 1-channel prediction and 2-channel prediction on 2500 test data.

The training data are thresholded the same way. Figure 5 shows the improvement of the IOU over 100 epochs for both the 1-channel prediction and 2 channel-prediction. The deviation of both accuracy curves is minimal. Figure 6 shows an example for the 1-channel and 2-channel prediction on unknown objects. The first and second row show the 2-channel and 1-channel prediction respectively. Both models predict that the object is pushed downwards out of the gripper due to the closing movement of the tips. Also the gripper opening width of 0 is predicted correctly by both of the models. The third and fourth row of Fig. 6 illustrate the problem that occurs when using only one channel in contrast to two channels. Separating gripper and object pixels unambiguously is not possible for the 1-channel prediction. In the predicted 2-channel result, the gripper opening width can easily be evaluated by checking for black pixels in the centre region of the gripper channel image. The evaluation with respect to the gripper opening width after closing proves to be difficult for the 1-channel prediction. Since this is a big issue for the evaluation of the model and also for the prediction of the Lifting Model, from now on the 2-channel presentation is chosen.

4.3 CNN-Architectures

Goal of this section is to determine the optimal network architecture through a thorough parameter analysis. The results are compared with respect to two measures. The first measure is the IOU value for determining how well the object and gripper movements are learned. The second measure is the predicted gripper opening width in terms of a confusion matrix: if the gripper was not closed in prediction and physics simulation the result is true positive, if the gripper was closed in prediction and physics simulation the result is true negative. False positive and false negative are analogously defined. This measure determines

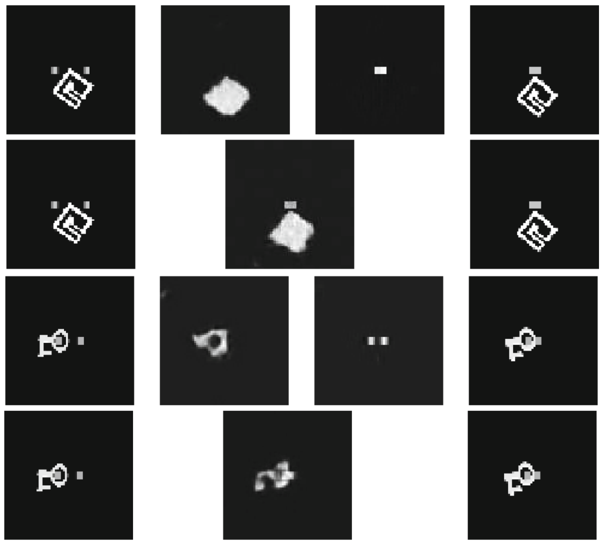

Fig. 6. Examples for 1-/ 2-channel prediction. First column: pre-close image. Second/Third column: prediction results. Fourth column: post-close image (ground truth).

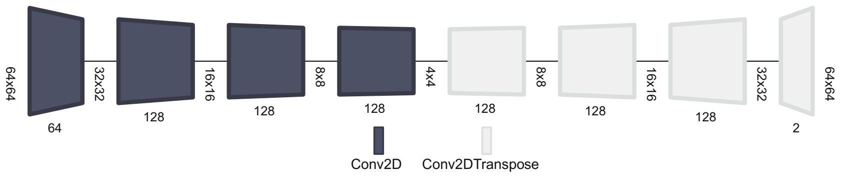

Fig. 7. CNN architectures for evaluating the influence of kernel size and stride. Net2Vis was used for visualization [11].

how good the grasp candidates are classified. However, since the resulting image of the Closing Model is a necessary input for the Lifting Model the IOU values are more important in this analysis. In order to find the optimal architecture, the effect of the kernel size in the convolutional and deconvolutional layers, the stride and the number of filters on the prediction quality for 2 channels is evaluated. Furthermore the number of dense layers that is needed is investigated. The architecture used for the comparisons is the same as in the previous section but without the fully connected layer to additionally investigate if the dense layer is really necessary for successful learning of the Closing Model (see Fig. 7). The kernel sizes for the 4 convolutional layers are varied as I:[(8×8), (6×6), (6×6), (4×4)], II:[(7×7), (5×5), (5×5), (3×3)], III:[(5×5), (4×4), (4×4), (3×3)] and IV:[(3×3), (3×3), (3×3), (3×3)], for the deconvolutional layers in reversed order. The stride is varied in [1,2] and the number of filters is set to I:[64,128,128,128] and II:[32,64,64,64]. Figure 8 shows the IOU-curves obtained

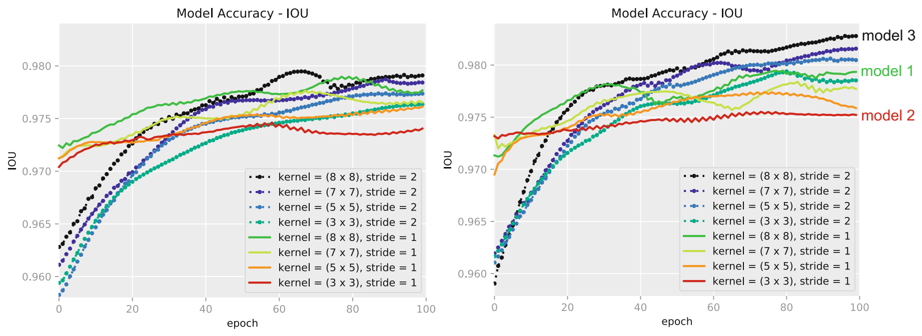

Fig. 8. Left: Model accuracy of 2500 test data for number of filters [32,64,64,64]. Right: Model accuracy of 2500 test data for number of filters [64,128,128,128].

from varying the parameters. The left image shows the model accuracy for the number of filters [32,64,64,64], the right image the model accuracy for the number of filters [64,128,128,128]. As can be seen a bigger number of filters leads to better IOU-values. Increasing the stride from 1 to 2 also increases the IOU-values. Furthermore changing the kernel sizes from bigger (I) to smaller (IV) sizes impair the results. The best IOU-curve is obtained for kernel sizes I:[(8×8), (6×6), (6×6), (4×4)] with stride 2 and filter I:[64,128,128,128]. Table 1 shows the confusion matrix and Matthews correlation coefficient for three selected models for 2500 positive and 2500 negative examples from the test set. Model 1 is the network with filter sizes I, filter I and a stride of 1, model 2 is the network with the filter sizes IV, filter I, stride 1 and model 3 the network with filter sizes I, filter I and stride 2. Matthews correlation coefficient (MCC) suggests that model 2 with the filter sizes 3×3 and stride 1 is the best model. Figure 9 shows an example for the prediction results of the three models line by line. The first column shows the pre-close image, column two and three show the prediction results for the object and gripper channel. The fourth column is the post-close ground truth. The result for model 1 (first row) reproduces a fuzzy image of the object but does not predict any object movement. The predicted gripper image is also not sharp. The predicted gripper opening width is too big compared to the ground truth. Model 2, the second row, produces visually the best result for the object shape. But like model 1 it does not predict the rotation. The gripper tips cannot be clearly seen. Model 3, the last row of Fig. 9, yields a less detailed prediction of the object but it captures the rotation correctly. Furthermore the resulting gripper tip projections and the gripper opening width are well reproduced. The reason for the smaller IOU values of the architectures with smaller filters is that they are not able to capture the movements of the objects when they remain between the gripper tips. But they are able to predict if an object is pushed out or not as the confusion matrix shows. For comparison the confusion matrix and MCC is also determined for the architecture with the fully connected layer (see Table 1 column FC). Even though the MCC is smaller than for the models without a fully connected layer the performance with respect to the IOU-curves is the same

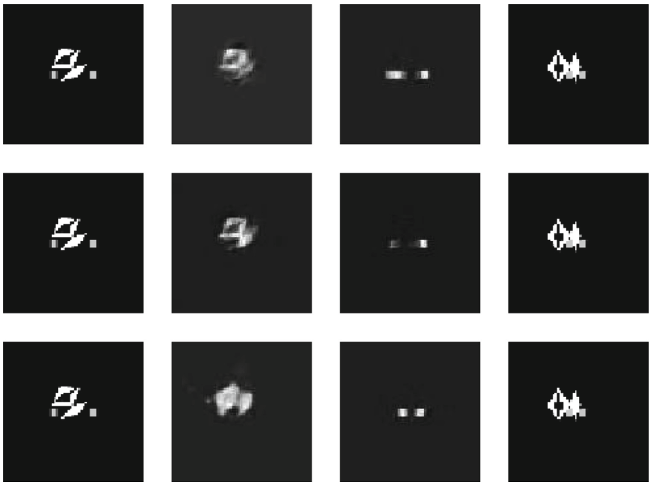

Fig. 9. Example of the influence of kernel size and stride. First column: pre-close image, second column: object channel prediction, third column: gripper channel prediction, fourth column: post-close, ground truth image. First row: result of model 1 (kernel sizes I, filters I, stride 1), second row: result of model 2 (kernel sizes IV, filters I, stride 1), third row: result of model 3 (kernel sizes I, filters I, stride 2).

Table 1. Confusion matrix, Matthews correlation coefficient and IOU after 100 epochs on test data of the described models. For details see text.

Confusion matrix				
	Model 1	Model 2	Model 3	FC
True positive	2394	2435	2375	2334
True negative	2464	2438	2475	2474
False positive	34	60	23	24
False negative	105	64	124	165
MCC	0.9447	0.9504	0.9419	0.9258
IOU	0.979	0.975	0.982	0.982

as for model 3. In summary the optimal architecture in terms of performance and network size is model 3 with kernel sizes $[(8 \times 8), (6 \times 6), (6 \times 6), (4 \times 4)]$ and stride 2. This corresponds also to the model which has the largest receptive field size in the innermost layer. This large receptive fields seems to be necessary to predict the object movement.

4.4 Classification

In order to check if the classification performance of the Closing Model is at a competitive level with classical CNNs used for classification the Closing Model is

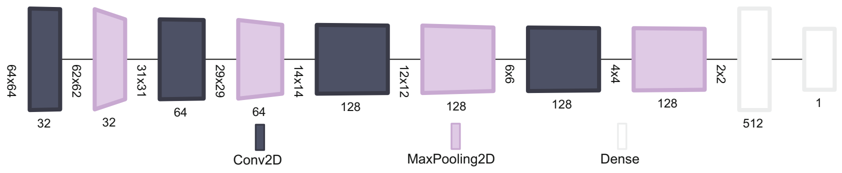

Fig. 10. CNN architecture for classification of pre-grasp images. Net2Vis was used for visualization [11].

also trained as a classification problem. For classification 26 000 pre-close images are separated into two classes. One class contains all images where the gripper can be closed, the other where the gripper cannot be closed. A standard CNN (Fig. 10) is used for classification in order to predict if the object is pushed out of the gripper during closing. The resulting confusion matrix values are true positive = 2428, true negative = 2474, false positive = 72 and false negative = 26. The MCC for the classification network is with a value of 0.9610 only slightly better in the classification task than the previously compared architectures. Therefore it can be concluded that also in this respect the optimal architecture that is chosen for the Closing Model is well appropriate.

5 Conclusion and Future Work

We have proposed to divide the task of robotic grasping into three simpler tasks that allow the interpretation of failed grasp attempts. The models that have to be learned to accomplish these three tasks are the Lowering Model, the Closing Model and the Lifting Model. In this study we have focused on the Closing Model. The task of this model is to predict from a pre-grasp image the object and gripper movement. Therefore image sequences of grasp trials on artificially generated prismatic objects were executed in a simulation. The first and last image of the recorded image sequences were used to train a variety of CNNs to find an optimal architecture. The results show that the movement of the object and gripper can be predicted successfully with high IOU values with a CNN consisting of 4 convolutional and 4 deconvolutional layer with kernel sizes $[(8 \times 8), (6 \times 6), (6 \times 6), (4 \times 4)]$, filter sizes [64,128,128,128] and stride 2. Inserting a dense layer between the convolution and deconvolution part does not increase the model accuracy. The computational complexity of the proposed Closing Model is basically determined by the complexity of the used CNNs. A thorough analysis of the complexity of convolutional layers can be found in [14].

We plan to adapt the three steps and especially the Closing Model to depth images on a real-world setup to extend the physical movement prediction into 3D. Using depth images instead of binary orthographic object images allows the model to be applied to different view angles on an object and loosens the restriction on prismatic objects with a fixed object height. Furthermore we will implement our Closing Model on a real-world robot setup to evaluate the qualitative results of the predicted object movement in the real-world physics for approximately prismatic objects like boxes, pens, pliers and other tools.

Acknowledgements. This work was supported by the EFRE-NRW funding programme “Forschungsinfrastrukturen” (grant no. 34.EFRE-0300119).

References

1. Caldera, S., Rassau, A., Chai, D.: Review of deep learning methods in robotic grasp detection. Multimodal Technol. Inter. **2**(3), 57 (2018)
2. Lenz, I., Lee, H., Saxena, A.: Deep learning for detecting robotic grasps. Int. J. Robot. Res. **34**(4–5), 705–724 (2015)
3. Redmon, J., Angelova, A.: Real-time grasp detection using convolutional neural networks. In: IEEE International Conference on Robotics and Automation (2015)
4. Levine, S., et al.: Learning hand-eye coordination for robotic grasping with deep learning and large-scale data collection. Int. J. Robot. Res. **37**(4–5), 421–436 (2017)
5. Finn, C., Goodfellow, I., Levine, S.: Unsupervised learning for physical interaction through video prediction. In: Proceedings of the 30th International Conference on Neural Information Processing Systems, pp. 64–72 (2016)
6. Morrison, D., Corke, P., Leitner, J.: Closing the loop for robotic grasping: a real-time, generative grasp synthesis approach. CoRR arXiv:1804.05172 (2018)
7. Schenck, W., Hasenbein, H., Möller, R.: Detecting affordances by mental imagery. In: Proceedings of the SAB Workshop on Artificial Mental Imagery, pp. 15–18 (2012)
8. Price, K.V., Storn, R.M., Lampinen, J.A.: Differential Evolution - A Practical Approach to Global Optimization, 2nd edn, p. 110. Springer, Heidelberg (2005)
9. Bicchi, A., Kumar, V.: Robotic grasping and contact: A review. In: IEEE International Conference on Robotics and Automation, vol. 5499, pp. 348–353 (2000)
10. Oh, J., et al.: Action-conditional video prediction using deep networks in Atari games. In: Advances in Neural Information Processing Systems, pp. 2863–2871 (2015)
11. Bäuerle, A., Ropinski, T.: Net2Vis: transforming deep convolutional networks into publication-ready visualizations. CoRR arXiv:1902.04394 (2019)
12. Mottaghi, R., et al.: Newtonian image understanding: unfolding the dynamics of objects in static images. CoRR arXiv:1511.04048 (2015)
13. Mottaghi, R., et al.: “What happens if...” learning to predict the effect of forces in images. CoRR arXiv:1603.05600 (2016)
14. He, K., Sun, J.: Convolutional neural networks at constrained time cost. CoRR arXiv:1412.1710 (2014)
15. Copellia Robotics Homepage. http://www.coppeliarobotics.com. Accessed 26 Feb 2020

Machine Learning in Engineering and Environment

Accomplished Reliability Level for Seismic Structural Damage Prediction Using Artificial Neural Networks

Magdalini Tyrtaiou(✉), Antonios Papaleonidas, Anaxagoras Elenas, and Lazaros Iliadis

Department of Civil Engineering, Institute of Structural Statics and Dynamics, Democritus University of Thrace, 67100 Xanthi, Greece
{mtyrtaio, papaleon, elenas, liliadis}@civil.duth.gr

Abstract. This research aims to determine the optimal Multi-Layer Feed-Forward Artificial Neural Network (MLFF) capable of accurately estimating the level of seismic damage on buildings, by considering a set of Seismic Intensity Parameters (SIP). Twenty SIP (well established and highly correlated to the structural damage) were utilized. Their corresponding values were calculated for a set of seismic signals. Various combinations of at least five seismic features were performed for the development of the input dataset. A vast number of Artificial Neural Networks (ANNs) were developed and tested. Their output was the level of earthquake Damage on a Reinforced Concrete Frame construction (DRCF) as it is expressed by the Park and Ang overall damage index. The potential contribution of nine distinct Machine Learning functions towards the development of the most robust ANN was also investigated. The results confirm that MLFF networks can provide an accurate estimation of the structural damage caused by an earthquake excitation. Hence, they can be considered as a reliable Computational Intelligence approach for the determination of structures' seismic vulnerability.

Keywords: Seismic intensity parameters · Multiple feedforward perceptron artificial neural network · ANN · Park and Ang damage index

1 Introduction

Earthquake structural damage detection is considered one of the core subjects of civil engineering. Numerous methods have been developed and employed for the determination of structures' post-seismic damage status. Several of them are connected with the Seismic Intensity (SIN), which is utilized as a metric of the power and the effect of seismic damage potential. Therefore, in earthquake engineering and engineering seismology, a large number of SIN parameters are considered and interrelated with the structural damage, as it is described by various indices [1–3, 7, 9–12, 24, 34].

In this research, the problem of structural damage state prediction is confronted by the use of Artificial Neural Networks. ANNs have an inherent ability to deploy prediction results for problems where the input data is known. Twenty, well established, seismic intensity parameters are utilized as input to the ANNs, aiming to predict the

DRCF after the application of ninety-two seismic signals. ANNs have the ability to consider any number and combination of seismic parameters for the determination of the optimal correlation between them and the damage state, as it is expressed by the global Park and Ang damage index $DI_{PA,global}$.

This research aims to prove that the accurate estimation of the $DI_{PA,global}$ index, can be accomplished with a high degree of conformity to the actual damage state, by the employment of ANNs that consider related SIP. A large number of ANNs employing various architectures and seven different Transfer functions were developed. Regarding the development of the training set, we have tried all potential combinations of the available input parameters. Thus, the complexity of the experiments was immense.

It has finally been revealed that a large number of ANNs can be considered as reliable models capable of perfectly serving towards the assessment of the seismic vulnerability of constructions. Consequently, we have developed a very promising approach in the area of seismic earthquake engineering.

2 Literature Review - Introduction of the Novel Contribution

Artificial Neural Networks have been utilized in the field of civil engineering, and many researchers [1, 2, 31, 35, 36] have investigated the advantages of using them in the field of structural engineering. They are related to complex algorithms capable of imitating behaviors of biological neural systems. Like human brains, they have the capability to learn applied knowledge from experience in solving new problems under new environments. This task is accomplished through a Supervised Learning process, where a volume of data vectors is used as input in order to obtain the optimal combination of neurons' connection weights. The ultimate target if the estimation of a set of predefined target outputs. Once the network has fit the data, it forms a generalization of the input-output relationship, and it can be used to generate output for input it was not trained on.

There are past publications in the literature that discuss the development of ANN capable of modeling the ability of certain SIP, towards the estimation of the structures' damage potential after an earthquake [1, 2, 19, 23, 31, 35, 36]. In each of them, a limited number of neural networks has been deployed. They have considered all available SIP together, and they were trained with one or two algorithms at a time. Then they were retrained following a specific number of repetitions of the whole process. In the end, the best-retrained network was selected to export the final results. The employment of retrained models has a high probability to cause over-training. This fact means that such models are prone to memorization, and they have extremely limited Generalization ability. Generalization is the ultimate target in the development of reliable computational intelligence models. Moreover, the consideration of all features for the development of the training set does not lead to optimal models. The solution to this problem is Feature Extraction. However, this process requires a big dataset with numerous values if the dependent variable. In this case, this is quite difficult since one has to travel all over the globe where earthquakes incidents occur, and he/she has to be given access to the respective local records. Thus, we have decided to follow the trial and error approach since the availability of modern computational resources makes this process feasible.

3 Established Seismic Intensity Parameters

As aforementioned, many intensity seismic parameters in earthquake engineering literature play a significant role in the assessment of structural damage potential. Twenty of the most recognized seismic parameters in earthquake engineering, which already have been connected with the structural damage [9–11], are selected to be evaluated for a set of examined seismic excitations. These seismic parameters are presented below, in Table 1.

Table 1. Employed seismic intensity parameters

Symbol	Description	Reference
PGA	Peak ground acceleration	[22]
PGV	Peak ground velocity	[22]
PGD	Peak ground displacement	[22]
PGA/PGV	The ratio PGA/PGV	[21]
CP	Central period	[33]
I_{Arias}	Arias intensity	[5]
SMD_{TB}	Strong motion duration of Trifunac-Brady	[30]
$P_{0.90}$	Seismic power	[17]
RMS_a	Root mean square acceleration	[22]
I_{FVF}	Seismic intensity of Fajfar-Vidic-Fischinger	[15]
CAV	Cumulative absolute velocity	[7]
DP_{AS}	Seismic destructiveness potential of Araya-Saragoni	[4]
SD	Spectral displacement	[8]
SV	Spectral velocity	[8]
SA	Spectral acceleration	[8]
E_{inp}	Seismic absolute input energy	[32]
SI_K	Kappos spectrum intensity	[18]
SI_{MR}	Spectrum intensity of Martinez-Rueda	[20]
EPA	Effective peak acceleration	[6]
EPA_{max}	Maximum effective peak acceleration	[6]

4 Park and Ang Structural Damage Index

The damage index (DI) is a quantity that lumps the structural damage status in a single numerical value and can be easily handled. In earthquake engineering, damage indices can quantify the induced damage locally or globally.

Park and Ang damage index ($DI_{PA,global}$) [25, 26] is an index defined as the ratio between the initial and the reduced resistance capacity of a structure during a seismic excitation evaluated by nonlinear dynamic analysis. The classification of the structural damage status, according to $DI_{PA,global}$ values are presented in the table below.

Table 2. Structural damage classification, according to $DI_{PA,global}$.

Structural damage	Structural damage degree			
	Low	Medium	Great	Total
$DI_{PA,global}$	$DI_{PA,global} \leq 0.3$	$0.3 < DI_{PA,global} \leq 0.6$	$0.6 < DI_{PA,global} \leq 0.8$	$DI_{PA,global} > 0.80$

The value of $DI_{PA,global}$ is equal to zero under elastic response, the structural damage located in the "Great" level is non-repairable while $DI_{PA,global} > 0.80$ signifies complete collapse or total damage of the structure.

5 Calculation of Seismic Intensity Parameters and $DI_{PA,Global}$

A total number of ninety accelerograms have been applied to a reinforced concrete (RC) frame structure with a total height of 22 m. The examined structure is designed in agreement with the rules of the recent *Eurocodes* EC2 [13] and EC8 [14], for structural concrete and aseismic structures and shown in Fig. 1. The cross-section of the beams are T-shapes with 30 cm width, 20 cm plate thickness, 60 cm total beam height. The effective plate width is 1.15 m at the end-bays and 1.80 m at the middle-bay. The distance between frames in the three-dimensional structure has been chosen to be 6 m. The building has been considered as an "importance class II", "ductility class Medium", and "subsoil of type B".

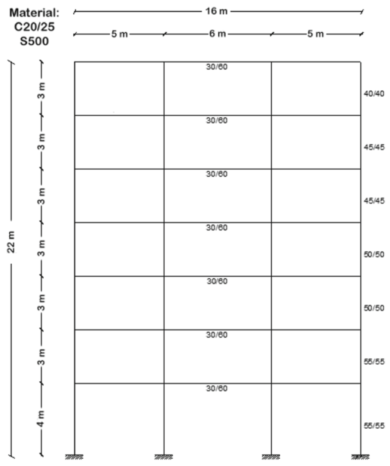

Fig. 1. Reinforced concrete frame.

Additionally, to the dead weight and the seismic loading, snow, wind, and live loads have been taken into account. The fundamental period of the frame is 0.95 s. After the design procedure of the RC frame structure, a nonlinear dynamic analysis has occurred for the evaluation of the structural seismic response for every seismic excitation utilized in the present study. For this purpose, the computer program IDARC version 7 [27] has been used. The hysteretic behavior of beams and columns has been specified at both ends of each member using a three-parameter Park model. This hysteretic model incorporates stiffness degradation, strength deterioration, non-symmetric response, slip-lock, and a trilinear monotonic envelope. The parameter values, which specify the above degrading parameters, have been chosen from experimental results of cyclic force-deformation characteristics of typical components of the studied structure. Thus, the nominal parameter for stiffness degradation and strength deterioration has been chosen. On the other hand, no pinching has been taken into account. Among the several response parameters, the focus is on the overall structural damage index of Park and Ang. From the nonlinear dynamic analysis, the overall damage indices of Park and Ang are derived, as presented in Table 3.

Table 3. The number of excitations employed per $DI_{PA,global}$ range.

$DI_{PA,global}$	Number of accelerograms
0.01–0.1	15
0.1–0.2	18
0.2–0.3	9
0.3–0.4	11
0.4–0.5	2
0.5–0.6	8
0.6–0.7	10
0.7–0.8	6
0.8–0.9	3
>0.9	8

The utilized accelerograms generate a broad spectrum of damage (low, medium, large, and total) for statistical reasons. After the selection of the ninety-two earthquake excitations, all the employed seismic intensity parameters are evaluated for every accelerogram, and their statistical values are presented in Table 4.

Table 4. Statistical values of the seismic intensity parameters.

Seismic parameter	Statistics			
	Min value	Max value	Average	Standard deviation
PGA (m/s^2)	0.304	13.615	4.804	3.343
PGV (m/s)	0.030	1.212	0.386	0.263
PGD (m)	0.003	0.950	0.149	0.146
PGA/PGV($g \cdot s/m$)	0.314	3.248	1.375	0.643
CP (s)	0.052	0.802	0.218	0.110
I_{ARIAS} (m/s)	0.015	28.274	3.728	5.081
SMD_{TB} (s)	2.080	89.100	18.250	18.949
$P_{0.90}$ (m^2/s^4)	0.005	7.442	1.823	2.033
RMS_a (m/s^2)	0.038	1.636	0.569	0.399
I_{FVF} ($m \cdot s^{3/4}$)	0.041	2.428	0.724	0.504
CAV ($g \cdot s$)	0.058	8.469	1.557	1.525
DP_{AS} ($m \cdot s$)	0.000	0.258	0.038	0.050
SD (m)	0.006	0.369	0.092	0.074
SV (m/s)	0.051	2.408	0.660	0.503
SA (m/s^2)	0.058	1.975	0.700	0.469
E_{inp}(m^2/s^2)	0.001	6.175	0.823	1.185
SI_K (m)	0.016	1.024	0.294	0.226
SI_{MR} (m/s)	0.042	1.391	0.493	0.339
EPA (g)	0.018	1.001	0.382	0.247
EPA_{max} (g)	0.030	1.035	0.413	0.264

6 Configuration of ANNs and Datasets

The development of the ANNs based on the universal approximation of MLFF networks requires the determination of the input and the output datasets, the choice of the optimal Learning algorithm, and the determination of the number of hidden layers/neurons. In this research, several Learning Algorithms were employed in order to choose the one that produces the best convergence. Back Propagation (Trainlm) has been proven to be optimal as the optimization algorithm. The obtained data set had been preprocessed in a previous research effort, so no such action was required [9–11].

The available data vectors comprise of twenty seismic intensity parameters that have already been discussed. As mentioned in Chap. 2, due to the nature of the case, it is difficult to obtain a number of $DI_{PA,global}$ data vectors, in order to perform a reliable Principal Component Analysis between those twenty seismic intensity parameters and the overall damage indices $DI_{PA,global}$.

Thus, we have followed a trial and error approach by testing a huge number of potential Input Datasets (IDS) that have emerged by combinations of the available features. Each combination comprised of at least 5 parameters. The maximum number of features was twenty. At the same time, nine different transfer functions were applied for each one of the emerged potential IDS. Every single developed dataset was utilized as Input to a different ANN in order to model the degree of the seismic parameters' influence on the value of the structural damage index. Thus, a total number of the 1,042,380 distinct input tables have been developed and used as input to the ANNs before the determination of the winner (the optimal one).

As the target output parameter of the examined ANNs for the function fitting problem in this study, we used the overall damage indices $DI_{PA,global}$ that derived from nonlinear dynamic analysis after the application of the seismic accelerograms on the structure in study. Therefore, all developed ANNs have one neuron that represents the $DI_{PA,global}$.

All networks that have been developed in this research for the prediction of the $DI_{PA,global}$ had one hidden layer in an effort to keep their architecture as simple as possible. This choice was based on the fact that the single-layered feedforward perceptron networks are able to precisely approach functions f(x): Rm → R1 [19], as well as on the fact that their efficiency has already been proved in numerous relevant investigations [19, 23]. The number of neurons in the hidden layer was also investigated. Several models with 7 to 10 hidden neurons were tried. This range was chosen after several trial and error tests and based on the small number of available vectors (92) in the source training dataset. As a result of that, four additional networks were developed for every produced ANN by the combination of the seismic parameters.

Totally, nine different training algorithms were utilized for every potential dataset, namely [16, 28]: Trainlm (Levenberg-Marquardt BP), Trainbfg (BFGS quasi-Newton BP), Trainrp (Resilient backpropagation), Trainscg (Scaled conjugate gradient BP), Traincgb (Powell-Beale conjugate gradient BP), Traincgf (Fletcher-Powell conjugate gradient BP), Traincgp (Polak-Ribiere conjugate gradient BP), Trainoss (One step secant BP) and Traingdx (Gradient descent with momentum and adaptive linear BP).

Moreover, the Sigmoid, TanH (Tangent Hyperbolic) Transfer function was employed.

7 Experiments - Evaluation and Results

Totally, 37,525,680 ANNs were developed and tested. This procedure was the result of the combination of 5 to 20 seismic parameters and the employment of 7 to 10 hidden neurons and nine training algorithms (one for each network).

For the development of the developed ANNs, MATLAB 2019 a [29] was used. Due to the vast number of different networks and the fact that most of the specific training algorithms are not GPU capable, a private distributed – parallelized environment of 10 virtual instances of Matlab was employed. Each instance had access to eight i9-9900k threads and 12 GB of memory. It was also equipped with two Matlab workers, which means that a total amount of 20 workers were available.

A proper Matlab script was developed, which was able to: a) to develop all ANNs b) to manage the fastest possible training of the total amount of networks based on the distribution and use of the available resources. From the total ninety-two employed seismic excitations, a percentage of 70% comprised the training set. From the rest of the vectors, a percentage of 15% was used as a testing set and 15% as the validation set.

For the comparison of the obtained ANNs, the "R" statistics, the "R^2", and the "Mean Squared Error (MSE)" were employed.

In statistics, R is the "correlation coefficient" between two variables, which reflects the strength and direction of a linear relationship and has a value between –1 (total negative linear correlation and +1 (total positive linear correlation). As R^2 is denoted the "coefficient of determination" with a value that ranges from zero to one and represents the proportion of variance in the dependent variable $DI_{PA,global}$, which may be predicted from the seismic intensity parameters for every investigated ANN. An R^2 value above 0.80 indicates a strong effect of the independent variables on the explanation of $DI_{PA,global}$.

The MSE is an average of the absolute difference between the true values of $DI_{PA,global}$, which considered the calculated ones by nonlinear dynamic analysis and the corresponding ones evaluated by the constructed ANNs.

In Tables (5 and 6), the basic statistics of the R and MSE calculated values are presented respectively for every training algorithm and every investigated number of neurons in the hidden layer of ANNs.

Table 5. Statistics of "R coefficient" values.

R Statistics								
Training algorithm	7 Neurons-hidden layer				8 Neurons-hidden layer			
	Min	Max	Mean	St.dev.	Min	Max	Mean	St.dev.
trainlm	−0.6646	0.9859	0.9271	0.0317	−0.7224	0.9872	0.9268	0.0327
trainbfg	−0.7377	0.9686	0.9073	0.0424	−0.6849	0.9686	0.9072	0.0414
trainrp	−0.6006	0.9647	0.8974	0.0481	−0.7622	0.9731	0.8959	0.0500
trainscg	−0.7175	0.9673	0.9060	0.0458	−0.8070	0.9681	0.9052	0.0451
traincgb	−0.7500	0.9691	0.9115	0.0401	−0.8231	0.9735	0.9110	0.0396
traincgf	−0.6974	0.9677	0.9084	0.0440	−0.6713	0.9690	0.9083	0.0434
traincgp	−0.7708	0.9671	0.9070	0.0437	−0.7407	0.9675	0.9062	0.0431
trainoss	−0.7502	0.9626	0.9025	0.0454	−0.7274	0.9596	0.9022	0.0439
traingdx	−0.9015	0.9569	0.7467	0.3111	−0.9133	0.9563	0.7412	0.3142
	9 Neurons-hidden layer				10 Neurons-hidden layer			
	Min	Max	Mean	St.dev.	Min	Max	Mean	St.dev.
trainlm	−0.6030	0.9883	0.9266	0.0332	−0.6084	0.9866	0.9262	0.0345
trainbfg	−0.6751	0.9669	0.9072	0.0404	−0.5839	0.9665	0.9071	0.0402
trainrp	−0.7957	0.9680	0.8945	0.0519	−0.6713	0.9722	0.8930	0.0539
trainscg	−0.8060	0.9667	0.9044	0.0451	−0.7004	0.9681	0.9036	0.0454
traincgb	−0.6972	0.9702	0.9104	0.0399	−0.6432	0.9746	0.9098	0.0401
traincgf	−0.6994	0.9696	0.9078	0.0429	−0.7446	0.9689	0.9074	0.0434
traincgp	−0.7269	0.9708	0.9053	0.0434	−0.7446	0.9709	0.9045	0.0436
trainoss	−0.7408	0.9633	0.9017	0.0431	−0.7446	0.9636	0.9011	0.0430
traingdx	−0.8928	0.9591	0.7325	0.3211	−0.9106	0.9599	0.7222	0.3287

Table 6. Statistics of MSE values.

MSE Statistics								
Training algorithm	7 Neurons-hidden layer				8 Neurons-hidden layer			
	Min	Max	Mean	St.dev.	Min	Max	Mean	St.dev.
trainlm	0.0026	0.3825	0.0143	0.0073	0.0024	0.2789	0.0144	0.0076
trainbfg	0.0058	0.4192	0.0167	0.0074	0.0057	0.4137	0.0167	0.0074
trainrp	0.0065	0.3490	0.0187	0.0090	0.0049	0.3871	0.0190	0.0096
trainscg	0.0059	0.2861	0.0167	0.0074	0.0057	0.3347	0.0169	0.0076
traincgb	0.0056	0.3650	0.0158	0.0066	0.0049	0.3575	0.0159	0.0068
traincgf	0.0059	0.2805	0.0163	0.0072	0.0056	0.4478	0.0163	0.0073
traincgp	0.0060	0.3707	0.0166	0.0072	0.0059	0.6212	0.0167	0.0073
trainoss	0.0067	0.9041	0.0176	0.0078	0.0073	0.4138	0.0177	0.0078
traingdx	0.0077	0.9163	0.0397	0.0440	0.0079	1.2957	0.0418	0.0476
	9 Neurons-hidden layer				10 Neurons-hidden layer			
	Min	Max	Mean	St.dev.	Min	Max	Mean	St.dev.
trainlm	0.0023	0.4237	0.0145	0.0079	0.0024	0.2804	0.0147	0.0081
trainbfg	0.0060	0.3058	0.0167	0.0073	0.0061	0.4611	0.0168	0.0075
trainrp	0.0058	0.3779	0.0193	0.0102	0.0050	0.5197	0.0197	0.0108
trainscg	0.0061	0.3406	0.0171	0.0077	0.0058	0.3619	0.0172	0.0080
traincgb	0.0054	0.3423	0.0160	0.0069	0.0046	0.4284	0.0161	0.0071
traincgf	0.0056	0.4743	0.0164	0.0074	0.0056	0.6029	0.0165	0.0076
traincgp	0.0053	0.5510	0.0169	0.0075	0.0053	0.6029	0.0171	0.0077
trainoss	0.0066	0.4743	0.0178	0.0078	0.0066	0.4259	0.0179	0.0079
traingdx	0.0075	1.0538	0.0445	0.0520	0.0072	1.1863	0.0478	0.0567

The best results for every performance coefficient in study are described in Table 7 and Table 8. Table 7 presents the quantities (qty.), as a percentage of the results, in regard to the R^2 coefficient with values that range from 0.80 to 1, considering the number of neurons in the hidden layer and the training algorithm. These results are also distributed in three classes.

Table 7. Percentage of ANNs with R^2 values over 0.80.

Classification of R^2 values										
Classes of R^2	Qty. of ANNs	Trainlm	Trainbfg	Trainrp	Trainscg	Traincgb	Traincgf	Traincgp	Trainoss	Traingdx
		7 Neurons-hidden layer								
$R^2 > 0.90$	(%)	11.86	0.14	0.17	0.12	0.30	0.23	0.16	0.03	0.01
$0.85 < R^2 \leq 0.90$	(%)	63.48	46.95	33.18	45.78	54.19	50.36	47.46	38.49	29.21
$0.80 < R^2 \leq 0.85$	(%)	16.90	35.06	39.09	35.50	31.05	32.50	34.32	40.06	21.12
		8 Neurons-hidden layer								
$R^2 > 0.90$	(%)	12.53	0.17	0.22	0.14	0.36	0.29	0.19	0.04	0.02
$0.85 < R^2 \leq 0.90$	(%)	62.35	46.50	32.57	44.29	53.05	49.67	45.95	37.47	28.62
$0.80 < R^2 \leq 0.85$	(%)	16.86	35.08	38.21	35.94	31.42	32.59	34.78	40.29	20.88
		9 Neurons-hidden layer								
$R^2 > 0.90$	(%)	13.14	0.21	0.26	0.16	0.43	0.34	0.22	0.05	0.02
$0.85 < R^2 \leq 0.90$	(%)	61.26	46.01	31.79	42.91	51.88	48.66	44.47	36.50	27.83
$0.80 < R^2 \leq 0.85$	(%)	16.82	35.19	37.57	36.31	31.85	32.91	35.20	40.48	20.50
		10 Neurons-hidden layer								
$R^2 > 0.90$	(%)	13.64	0.26	0.33	0.20	0.50	0.42	0.24	0.07	0.03
$0.85 < R^2 \leq 0.90$	(%)	60.34	45.58	31.20	41.62	50.69	47.83	43.09	35.55	26.87
$0.80 < R^2 \leq 0.85$	(%)	16.75	35.27	36.77	36.69	32.22	33.10	35.66	40.61	20.20

In a correspondent way, the best results for the MSE, which range from 0.05 to 0.02, considering the number of neurons in the hidden layer and the training algorithm, are presented in Table 8.

Investigating the above Tables, the maximum R^2 coefficient, which is 0.9767, and the minimum MSE, which is 0.0023 have been obtained by the ANN, which was trained by the "Trainlm" (Back Propagation) algorithm, with nine neurons in the hidden layer, using the TanH transfer function. It is also obvious that the "Trainlm" algorithm presents the most significant percentage of the highest R^2 values and the lowest MSE values derived from all utilized algorithms.

Table 8. Percentage of ANNs regard to MSE values.

Classification of MSE										
Classes of MSE	Qty. of ANNs	Trainlm	Trainbfg	Trainrp	Trainscg	Traincgb	Traincgf	Traincgp	Trainoss	Traingdx
		7 Neurons-hidden layer								
$MSE < 0.02$	(%)	87.56	82.31	72.55	82.19	86.31	83.89	82.76	78.70	51.90
$0.02 \leq MSE < 0.05$	(%)	11.84	16.96	26.11	17.06	13.16	15.46	16.57	20.42	23.02
$MSE \geq 0.05$	(%)	0.59	0.73	1.33	0.76	0.53	0.65	0.67	0.89	25.08
		8 Neurons-hidden layer								
$MSE < 0.02$	(%)	86.79	81.88	71.18	81.25	85.61	83.45	81.78	77.94	50.99
$0.02 \leq MSE < 0.05$	(%)	12.55	17.42	27.23	18.00	13.85	15.90	17.54	21.20	22.70
$MSE \geq 0.05$	(%)	0.66	0.70	1.58	0.75	0.54	0.66	0.68	0.87	26.31
		9 Neurons-hidden layer								
$MSE < 0.02$	(%)	86.06	81.54	69.82	80.35	84.98	82.85	80.77	77.20	49.76
$0.02 \leq MSE < 0.05$	(%)	13.21	17.77	28.34	18.85	14.44	16.47	18.51	21.92	22.30
$MSE \geq 0.05$	(%)	0.72	0.69	1.83	0.80	0.58	0.68	0.72	0.88	27.95
		10 Neurons-hidden layer								
$MSE < 0.02$	(%)	85.40	81.18	68.54	79.51	84.25	82.30	79.83	76.35	48.38
$0.02 \leq MSE < 0.05$	(%)	13.79	18.12	29.34	19.62	15.14	16.97	19.38	22.75	21.76
$MSE \geq 0.05$	(%)	0.81	0.70	2.12	0.87	0.61	0.73	0.78	0.90	29.86

For the "Trainlm" function the percent of ANN cases with $R^2 > 0.80$ depending on the number of neurons in the hidden layer, ranges from 90.73% to 92.24% while the percentage of ANNs that achieved values of $MSE < 0.05$, ranges from 99.19% to 99.40% of the total number of ANN models that estimate the seismic damage that is expressed by the $DI_{PA.global}$ index (see Table 9). It means that at least 90.73% of the developed ANNs have shown excellent predictive accuracy with $R^2 > 0.80$ και $MSE < 0.05$ simultaneously. At least 85.40% of the ANNs had a performance with $R^2 > 0.80$ and $MSE < 0.02$ simultaneously.

Table 9. Results of ANNs with "Trainlm" algorithm

Number of neurons in the hidden layer	Percentage of evaluated MFPs		
	$R^2 > 0.80$ (%)	$MSE < 0.05$ (%)	$MSE < 0.02$ (%)
7	92.24	99.40	87.56
8	91.74	99.34	86.79
9	91.22	99.27	86.06
10	90.73	99.19	85.40

8 Conclusions and Further Work

This research designates the grade of the ability of Artificial Neural Networks to predict seismic damage from twenty well-established seismic parameters, taking into consideration the already proven in earthquake engineering strong interrelation between the structural damage and the seismic intensity parameters.

The overall damage index of Park and Ang is used to describe the damage of a reinforced concrete frame structure under a number of ninety-two seismic excitations, and the evaluated by nonlinear dynamic analyses indices are utilized as the target values of the examined ANNs. The architecture of the constructed ANNs is the Multiple Feedforward Perceptron (MFP) network with five to twenty seismic parameters as inputs, one hidden layer of seven to ten neurons, trained with nine different backpropagation algorithms. Hence, a number of 37,525,680 ANNs are calculated, and two of their statistical parameters, the “R coefficient” and the “Mean Squared Error (MSE)” of the total data, are investigated.

All the utilized training algorithms led to a significant percentage of ANNs with a high coefficient of determination ($R^2 > 0.80$) and low MSE ($MSE < 0.05$). The most efficient of them turned out to be the “Trainlm” algorithm. In particular, a number of 1,024,380 ANNs configured with the “Trainlm” algorithm conducted to a percentage of over 90.73% of a high explanation of variance of $DI_{PA,global}$ (with $R^2 > 0.80$) with very low MSE ($MSE < 0.05$) simultaneously. It is also observed that the best performance of all the investigated statistical coefficients is displayed among the ANNs with the nine neurons in the hidden layer, which use the “Trainlm” algorithm. In particular, from Table 5, the highest obtained R^2 coefficient presented to be equal to 0.9767 ($R = 0.9883$), while in Table 6, the lowest displayed MSE is equal to 0.0023. Furthermore, according to Table 2, it is obvious that the values of MSE under the value of 0.05 cause no substantial changes to the estimated level of $DI_{PA,global}$, and, thus, to the decisions for the repair interventions.

All the above results confirm that the use of ANNs can be considered a very reliable method for a high accuracy prediction of the post-seismic damage in existing or future structures and a powerful tool for the scientific community in order crucial decisions to be made before and after an earthquake.

In future work, this research could be extended, investigating more seismic intensity parameters with a larger sample of seismic excitations. Following this process, the most efficient parameters and the best combination of them could be obtained and utilized directly for the determination of earthquake vulnerability of the structures.

References

1. Alvanitopoulos, P.F., Andreadis, I., Elenas, A.: A genetic algorithm for the classification of earthquake damages in buildings. In: Proceedings of 5th IFIP Conference on Artificial Intelligence Applications and Innovations, Thessaloniki, pp. 341–346 (2009). https://doi.org/10.1007/978-1-4419-0221-4_40
2. Alvanitopoulos, P.F., Andreadis, I., Elenas, A.: A new algorithm for the classification of earthquake damages in structures. In: Proceedings of the 5th IASTED Conference on Signal Processing, Pattern Recognition and Applications, Innsbruck, pp. 151–156 (2008)
3. Alvanitopoulos, P.F., Andreadis, I., Elenas, A.: Neuro-fuzzy techniques for the classification of earthquake damages in buildings. Measurement **43**(6), 797–809 (2010)
4. Araya, R., Saragoni, G.R.: Earthquake accelerogram destructiveness potential factor. In: Proceedings of the 8th World Conference on Earthquake Engineering, pp. 835–842. EERI, El Cerrito (1984)

5. Arias, A.: A measure of earthquake intensity. In: Hansen, R.J. (ed.) Seismic Design for Nuclear Power Plants, pp. 438–483. MIT Press, Cambridge (1970)
6. ATC 3–06 Publication: Tentative Provisions for the Development of Seismic Regulations for Buildings. US Government Printing Office, Washington, DC (1978)
7. Cabãnas, L., Benito, B., Herráiz, M.: An approach to the measurement of the potential structural damage of earthquake ground motions. Earthq. Eng. Struct. Dyn. **26**(1), 79–92 (1997)
8. Chopra, A.K.: Dynamics of Structures. Prentice-Hall, Englewood Cliffs (1995)
9. Elenas, A., Meskouris, K.: Correlation study between seismic acceleration parameters and damage indices of structures. Eng. Struct. **23**(6), 698–704 (2001)
10. Elenas, A.: Correlation between seismic acceleration parameters and overall structural damage indices of buildings. Soil Dyn. Earthq. Eng. **20**(1), 93–100 (2000)
11. Elenas, A.: Interdependency between seismic acceleration parameters and the behavior of structures. Soil Dyn. Earthq. Eng. **16**(5), 317–322 (1997)
12. Elenas, A.: Seismic-parameter-based statistical procedure for the approximate assessment of structural damage. Math. Probl. Eng. **2014**, 1–22 (2014). Article Id 916820
13. Eurocode 2: Design of Concrete Structures—Part 1: General Rules and Rules for Buildings. European Committee for Standardization, Brussels, Belgium (2000)
14. Eurocode 8: Design of Structures for Earthquake Resistance—Part 1: General Rules, Seismic Actions, and Rules for Buildings. European Committee for Standardization, Brussels, Belgium (2004)
15. Fajfar, P., Vidic, T., Fischinger, M.: A measure of earthquake motion capacity to damage medium-period structures. Soil Dyn. Earthq. Eng. **9**(5), 236–242 (1990)
16. Haykin, S.: Neural Netw, 2nd edn. Prentice Hall, Upper Saddle River (1999)
17. Jennings, P.C.: Engineering seismology. In: Kanamori, H., Boschi, E. (eds.) Earthquakes: Observation, Theory and Interpretation, pp. 138–173. Italian Physical Society, Varenna (1982)
18. Kappos, A.J.: Sensitivity of calculated inelastic seismic response to input motion characteristics. In: Proceedings of the 4th U.S. National Conference on Earthquake Engineering, pp. 25–34. EERI, Oakland (1990)
19. Lautour, O.R., Omenzetter, P.: Prediction of seismic-induced structural damage using artificial neural networks. Eng. Struct. **31**(2), 600–606 (2009)
20. Martinez-Rueda, J.E.: Scaling procedure for natural accelerograms based on a system of spectrum intensity scales. Earthq. Spectra **14**(1), 135–152 (1998)
21. Meskouris, K., Krätzig, W.B., Hanskötter, U.: Nonlinear computer simulations of seismically excited wall-stiffened reinforced concrete buildings. In: Proceedings of the 2nd International Conference on Structural Dynamics (EURODYN'93), Balkema, Lisse, pp. 49–54 (1993)
22. Meskouris, K.: Structural Dynamics: Models, Methods. Examples. Ernst & Sohn, Berlin (2000)
23. Morfidis, K., Kostinakis, K.: Approaches to the rapid seismic damage prediction of r/c buildings using artificial neural networks. Eng. Struct. **165**, 120–141 (2018)
24. Nanos, N., Elenas, A., Ponterosso, P.: Correlation of different strong motion duration parameters and damage indicators of reinforced concrete structures. In: Proceedings of the 14th World Conference on Earthquake Engineering (2008)
25. Park, Y.J., Ang, A.H.-S., Wen, Y.K.: Damage-limiting aseismic design of buildings. Earthq. Spectra **3**(1), 1–26 (1987)
26. Ang, A.H.-S., Park, Y.J., Ang, A.H.-S.: Mechanistic seismic damage model for reinforced concrete. J. Struct. Eng. **111**(4), 722–739 (1985)

27. Reinhorn, A.M., Roh, H., Sivaselvan, M., et al.: IDARC2D version 7.0: a program for the inelastic damage analysis of structures. Technical report MCEER-09-0006, MCEER, State University of New York, Buffalo, NY, USA (2009)
28. Singh, A., Saxena, P., Lalwani, S.: A study of various training algorithms on neural network for angle based triangular problem. Int. J. Comput. Appl. **71**(13), 0975–8887 (2013)
29. The Math Works Inc.: MATLAB and Statistics Toolbox Release 2016b. Natick, Massachusetts, USA (2016)
30. Trifunac, M.D., Brady, A.G.: A study on the duration of strong earthquake ground motion. Bull. Seismol. Soc. Am. **65**(3), 581–626 (1975)
31. Tsou, P., Shen, M.H.: Structural damage detection and identification using neural network. In: Proceedings of the 34thAIAA/ASME/ASCEAHS/ASC, Structural, Structural Dynamics and Materials Conference, AIAA/ASME Adaptive Structural Forum, pt. 5 (1993)
32. Uang, C.M., Bertero, V.V.: Evaluation of seismic energy in structures. Earthq. Eng. Struct. Dynam. **19**(1), 77–90 (1990)
33. Vanmarcke, E.H., Lai, S.S.P.: Strong-motion duration and RMS amplitude of earthquake records. Bull. Seismol. Soc. Am. **70**(4), 1293–1307 (1980)
34. Vui, V.C., Hamid, R.R.: Correlation between seismic parameters of far-fault motions and damage indices of low-rise reinforced concrete frames. Soil Dyn. Earthq. Eng. **66**(11), 102–112 (2014)
35. Wu, X., Ghaboussi, J., Garrett, J.: Use of neural network in detection of structural damage. Comput. Struct. **42**(4), 649–659 (1992)
36. Zhao, J., Ivan, J.N., DeWold, J.T.: Structural damage detection using artificial neural networks. J. Infrastructural Syst. **13**(3), 182–189 (1998)

Efficient Implementation of a Self-sufficient Solar-Powered Real-Time Deep Learning-Based System

Sorin Liviu Jurj(✉), Raul Rotar, Flavius Opritoiu, and Mircea Vladutiu

Advanced Computing Systems and Architectures (ACSA) Laboratory, Computers and Information Technology Department, "Politehnica" University of Timisoara, Timisoara, Romania
jurjsorinliviu@yahoo.de, raul.rotar@student.upt.ro, {flavius.opritoiu,mircea.vladutiu}@cs.upt.ro

Abstract. This paper presents a self-sufficient solar-powered real-time Deep Learning (DL) based system that runs inference 100% on solar energy and which is composed of an Nvidia Jetson TX2 board and a dual-axis solar tracker based on the cast-shadow principle. In order to have a higher energy being generated by the solar tracker as well as a lower energy consumption by the real-time DL-based system, we have: a) updated our solar tracker's panel with a higher number of polycrystalline photovoltaic (PV) cells and connected it to a chain of two inverters, one accumulator and one solar charge controller; b) implemented a motion detection method that triggers the inference process only when there is substantial movement in webcam frame. Experimental results show that our solar tracker generates sufficient and constant solar energy for all the 4 DL models (VGG-19, InceptionV3, ResNet-50 and MobileNetV2) that are running in real-time on the Nvidia Jetson TX2 platform and which requires more than 5 times less energy when compared to a laptop having a Nvidia GTX 1060 GPU, proving that real-time DL-based systems can be powered by solar trackers without the need of traditional power plugs or need to pay for electricity bills.

Keywords: Deep learning · Real-Time · Solar energy

1 Introduction

Recent advancements in the field of Artificial Intelligence (AI), especially DL, are happening especially thanks to the availability of huge amounts of data and powerful hardware. During training and inference of a Deep Neural Network (DNN), usually expensive and power-hungry GPUs are used, resulting in a proportional growth of computational and environmental costs, with some Natural Language Processing (NLP) models even increasing the carbon footprint nearly five times the lifetime emissions of a car [1].

Because climate change is a very relevant problem in our society [2] and considering goal number 7 (affordable and clean energy) and goal number 13 (climate action) of UN's Sustainable Development Goals [3], efforts to develop and use low-power

L. Iliadis et al. (Eds.): EANN 2020, INNS 2, pp. 99–118, 2020.
https://doi.org/10.1007/978-3-030-48791-1_7

embedded devices are made by many companies, an example, in this case, being Nvidia's Jetson TX2 embedded platform [4]. Consequently, in order to reduce the carbon footprint and the electricity bills, efforts towards renewable energy are made [5], with many researchers building solar tracking systems [6, 7] in order to capture sun's energy with maximum efficiency.

Considering that the two domains of AI and renewable energy are of major importance for the development of our society, our work introduces a self-sufficient solar-powered real-time DL-based system that makes use of solar energy from the sun with the help of an updated version of our solar tracker based on the cast-shadow principle [6] and an Nvidia Jetson TX2 board that runs our real-time animal class identification model [8] on videos or using a webcam and also generates additional datasets containing images and textual information about the animals present in front of the frame, in real-time. In order to justify our decision for choosing an embedded platform instead of a laptop, in our experimental results, we present a comparison between the two platforms, mainly in terms of power consumption. Additionally, we also improve the energy efficiency of the proposed real-time DL-based system by implementing a motion detection method based on background subtraction with the help of Python and OpenCV [9].

Concerning the structure of the paper, in Sect. 2, we present an overview of the related work. Section 3 describes the proposed efficient real-time DL-based system. Section 4 presents the experimental setup and results. Finally, Sect. 5 concludes this paper.

2 Related Work

To the best of our knowledge, there is no work in the literature that makes use of a solar tracking device in order to generate solar energy for a real-time DL-based system.

Nevertheless, similar work that evaluates the power efficiency of DL inference for image recognition on embedded GPU systems is presented in [10] where the authors compare different platforms like Nvidia Jetson TX1 and TX2 as well as a Tesla P40 and show that the Nvidia Jetson TX2 board is able to achieve the highest accuracy with the lowest power consumption. The authors in [11] make use of an Nvidia Jetson TX2 to test a fully Convolutional Neural Network (CNN) for detecting traffic lights and employ a power supply unit (12 V) with stabilizer in order to increase the stability of the system, mentioning that the Nvidia Jetson TX2 has a low power consumption of around 10 Watts, which is also confirmed by our experimental results using different CNN architectures. The authors in [12] train and test two CNNs for classifying skin cancer images as Benign or Malignant on the Nvidia Jetson TX2, proving that this embedded platform is capable of handling DL computations even for training CNN models, not only for inference. The authors in [13] propose an object detection implementation using MobileNet as the backbone network on an Nvidia Jetson TX2 board, showing a higher frames-per-second (fps) and reduced model size when compared to other networks. Nvidia Jetson TX2 is used also in [14] where the authors propose a CNN based application that can run onboard a satellite in order to detect and classify boats on the open ocean from satellite imagery. Experimental results show that the Nvidia Jetson TX2 has almost half the power consumption when compared with standard systems designed for a satellite onboard processing. The authors in [15] use Nvidia Jetson TX2 for their proposed methodology regarding a faster and more accurate object detection in unmanned aerial vehicle (UAV) imagery. The work in [16] proposes a vehicle and pedestrian detection system that uses CNNs in order to evaluate traffic violations and which is implemented on an Nvidia Jetson TX2 board. Other related works that use Nvidia Jetson TX2 are regarding real-time ear detection [17], when developing embedded online fish detection and tracking system for ocean observatory network [18], real-time multiple face recognition [19], a streaming cloud platform for real-time video processing [20] and detecting diabetic foot ulcer in real-time [21]. A comparison between different computing platforms is made also by the authors in [22] which show that the Nvidia Jetson TX2 is a reliable and efficient embedded platform for the underwater robotics domain.

Regarding motion detection, the authors in [23] present a comparative analysis of motion-based and feature-based algorithms for object detection and tracking and show that Adaptive Gaussian Mixture Model (AGMM) [24] is faster and more robust to illumination (shadows) than Grimson Gaussian Mixture Models (GGMM) [25] when performing on real-time videos. Also, the authors in [26] present a study on preprocessing methods for tracking objects in soccer videos, showing that background subtraction and edge detection are advantageous for detecting moving objects. OpenCV [9] is also using AGMM together with other several algorithms for background subtraction such as BackgroundSubtractorGMG, BackgroundSubstractorMOG, and BackgroundSubstractor MOG2, which are presented in the works of [27] and [28] but, in comparison with OpenCV [9], the algorithms in OpenCV are more modern, accurate and faster (a reason for this is because they are continuously developed by the OpenCV community).

In this work, we make use of OpenCV in order to implement a motion-based Gaussian algorithm that makes use of pixel's intensity values over a period of time. We decided to implement it in order to trigger the inference process only when there is movement in the frame, thus lowering the energy consumption of the entire real-time DL-based system, as seen in our experimental results presented in Sect. 4.

3 Proposed Solar-Powered Real-Time Deep Learning-Based System

A summarized view of the proposed solar-powered DL-based system can be seen in Fig. 1. It consists of our dual-axis solar tracker based on the cast-shadow principle [6], a solar charge controller, an Ultra Cell accumulator with 12 V 9 Ah acid plumb battery, two DC-to-DC inverters (first DC-to-DC inverter converts 12 V to around 5 V necessary for the solar tracker to become autonomous regarding energy needs and the second DC-to-DC inverter converts 12 V to around 19 V necessary for the Nvidia Jetson TX2 to run only on solar energy) and an Nvidia Jetson TX2 embedded platform that uses and powers an external Logitech C920 HD Pro webcam in order to identify animal classes in real-time [8].

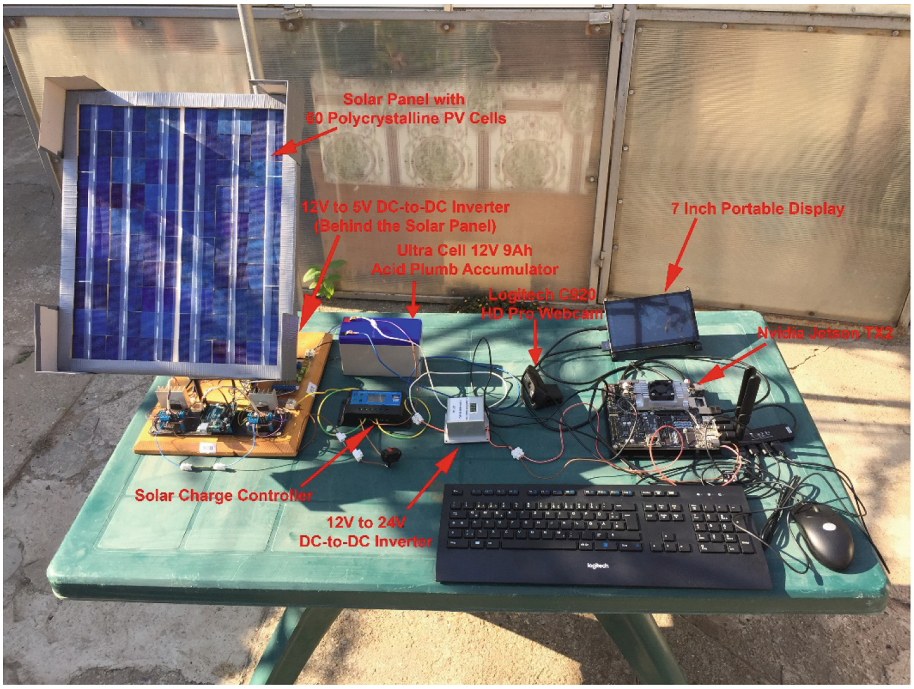

Fig. 1. Summarized view of the proposed solar-powered real-time DL-based system.

3.1 Dual-Axis Solar Tracker Using the Cast-Shadow Principle

Our old dual-axis solar tracker based on the cast-shadow principle [6] used a solar panel with 40 PV monocrystalline cells instead of Light Diode Resistors (LDRs) which are usually found in the literature. Twelve of these PV cells are used to control 4 low-cost circuits, namely 1 $\times$ Optocoupler LTV 847, 1 $\times$ Arduino328 Microcontroller, 2 $\times$ L298N Dual-H Bridge circuits and 2 $\times$ stepper motors which are used for the dual-axis positioning of the solar tracker. Our solar panel makes use of 3 PV cells from each corner to analyze light distribution, 2 bypass diodes (D2) to protect PV cells in case of a sudden increase or decrease in voltage that may occur due to variable light and 2 blocking diodes (D1) to protect solar panel's PV cells from reverse current (i.e. voltage from the load such as the Optocoupler or Arduino UNO).

In order for the real-time DL-based system to run inference completely on solar energy, we considered using an updated version of our earlier proposed dual-axis solar tracker that uses the cast-shadow principle [6] in order to optimize its position for a more efficient solar energy gain, without the need of sensors. The important changes that we made to update our solar tracker in order to use it for the experimental results in this paper are:

1) The effective surface area of the panel used in the above described solar tracker was increased from $L_1 \times l_1 = 36 \times 35 = 1260\ \text{cm}^2$ to an area of $L_2 \times l_2 = 43 \times 36 = 1548\ \text{cm}^2$ to accommodate 60 polycrystalline PV cells.

2) The method used to produce silicon polycrystalline solar cells is easier to implement and less expensive as compared to monocrystalline counterparts, resulting in a more cost-effective investment. Additionally, polycrystalline solar panels tend to be somewhat less tolerant of heat than monocrystalline solar panels [29]. Due to their higher temperature coefficient, the overall heat output will be less significant compared to monocrystalline solar modules. As a consequence, our old monocrystalline PV solar cells were replaced by PV polycrystalline cells that generate a maximum voltage of 0.55 V and a maximum current of 0.60 A per unit, resulting in a total voltage of 17 V and 1.5 A generated by the improved solar panel.

3.2 Deep Learning Models Used for Inference

In order to prove the efficiency of our solar-powered real-time DL-based system, we decided to use our earlier proposed implementation regarding real-time identification of animals found in domestic areas of Europe [8] which can also generate 2 new datasets in real-time, one dataset containing textual information (i.e. animal class name, date and time interval when animal was present in the frame) and one dataset containing images of the animal classes present and identified in videos or in front of a webcam. These newly generated datasets are very useful, as they can provide in-sights about what animal classes are present at a given date and time in a certain area and how they look like.

Our original DL models presented in [8] were trained and tested on a home-made dataset with a total size of 4.06 GB consisting of 90.249 animal images (72.469 images for training, 8.994 images for validation and 8.786 images for testing) belonging to 34 classes on 4 state-of-the-art modified CNN architectures (VGG-19 [30], InceptionV3 [31], ResNet-50 [32] and MobileNetV2 [33]) using Keras with Tensorflow backend, achieving high overall test accuracy (90.56% for the proposed VGG-19 model, 93.41% for the proposed InceptionV3 model, 93.49% for the proposed ResNet-50 model and 94.54% for the proposed MobileNetV2 model).

In order to successfully implement and test our Python implementation on the Nvidia Jetson TX2 board, we needed to make some adjustments and improvements in our initial code from [8] as follows:

1) First, because Keras saves its weights in a hierarchical data format (.hdf5) file which slows the loading of the model on the Nvidia Jetson TX2, we have created an optimized (converted it to a frozen graph base model; here the value of all variables are embedded in the graph itself thus the protocol buffers (.pb) file cannot be retrained) frozen file of our Keras model based on Tensorflow. Keras does not include by itself any means to export a TensorFlow graph as a .pb file, but we could do it using regular Tensorflow utilities.
2) Second, because by default Tensorflow pre-allocates the whole GPU memory [34] (which can cause "out of memory" errors) and because the Nvidia Jetson TX2 GPU doesn't have dedicated RAM and cannot use its full 8 GB processing RAM (the reason for this is because Linux and other processes are using most of the available RAM), we implemented a code to control the GPU memory allocation and to define (choose a GPU memory ratio allocation from 0 to 1) the processing memory

percentage usage of the GPU at running time. By doing this, we can now control how much data we want to transfer to the GPU that processes it and avoid any possible "out of memory" kind of problems which otherwise would appear on the Nvidia Jetson TX2 due to its lack of dedicated GPU memory. We can now choose a ratio from 0 to 1 to decide the GPU usage from low to high by passing the arguments in the command line.

3) Third, we implemented a code for testing a certain number of batch frames in one shot. For this, we make use of a Numpy array. Numpy array is a fast method for data manipulation that saves a matrix of numbers in stacks (e.g. we can observe that when we read a frame in OpenCV it becomes numbers in the Numpy array, meaning that if we have 900 frames, Numpy array size will be 900, 224, 224). Then, we transferred that batch of frames to our model for prediction by changing the number of frames (e.g. we can send 30 frames one time like this: 30, 224, 224, so we have a remaining 870, 224, 224 arrays). We have tested it on the frozen graph. The frames are passed from 1 to 60. Fps batch testing is very useful in our tests because it helps us find the optimal number of fps our model can efficiently run inference on, e.g. when all 900 frames from a 31 s video are predicted in 31 s or less than that, it means that we can run it in real-time (when the identified class name is predicted and shown on the webcam frame without being affected by latency).
4) Forth, because we wanted to increase the security of animals and humans in domestic areas, we also implemented an automated SMS alert system based on Twilio API [35]. This is very helpful, especially in the cases when a wild animal is detected on a private property such as a house or a farming area (e.g. when, because of hunger, a bear is coming near a flock of sheep or a fox is coming near a chicken coop) because it generates and sends an SMS alert to the phone number of the owner, informing him what animal class is detected in real-time trough the webcam and thus helping him to take the necessary actions to maintain security. In order to save the SMS costs and not send an SMS alert every time (e.g. every second) a wild animal is detected in the webcam frame, we wrote a function that sends the SMS only if the wild animal is present in front of the frame for at least 3 s (to make sure that there are no SMS alerts sent by mistake due to some 1 s short animal class misdetections in the webcam frame). Additionally, in case the same wild animal class was detected multiple times in the last 5 min, this SMS alert is sent only one time every 5 min (e.g. if a Bear is detected continuously in the front of the webcam for 10 min, the SMS alert will be sent to owner's phone only two times).

3.3 Motion Detection

Because we wanted to lower the power consumption on both platforms when running the DL models as much as possible, instead of buying a costly motion detection sensor, we implemented a software motion detection method based on the difference between pixel intensity of the frames.

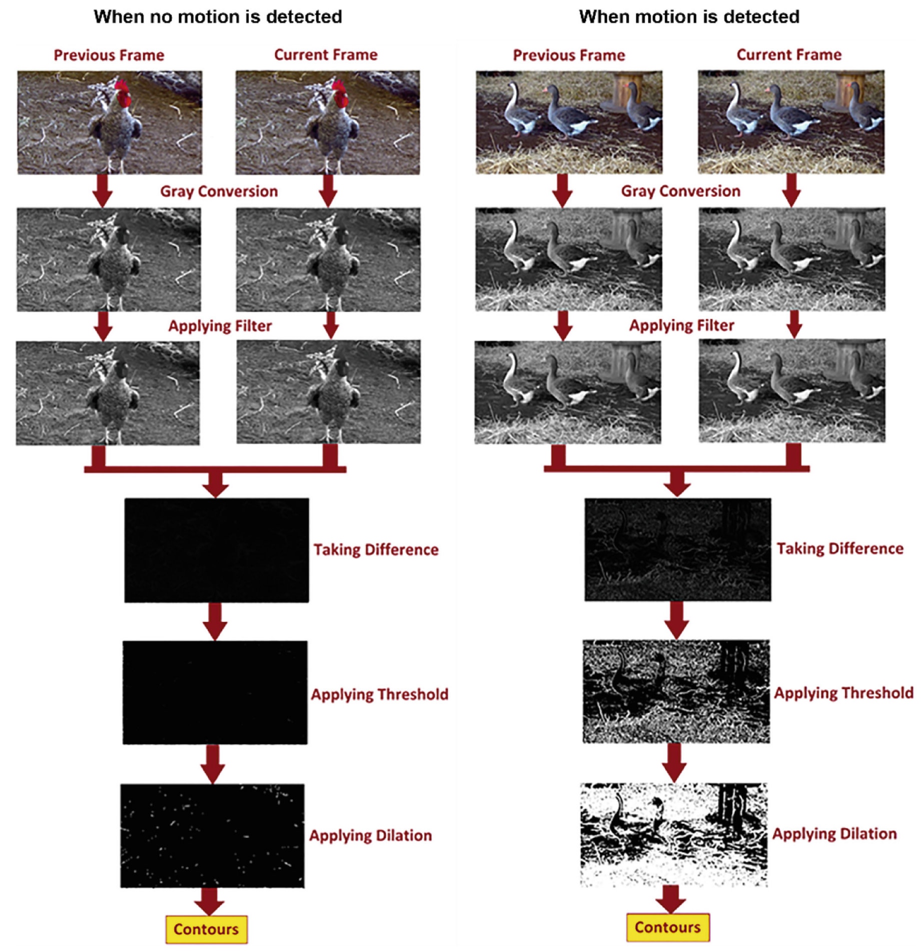

Fig. 2. Summarized view of the proposed motion detection.

For our motion detection method seen in Fig. 2, in order to speed-up the inference processing time of a video or webcam frame, we reduced its size to 224 $\times$ 244 pixels and used several computer vision techniques using OpenCV as follows:

1) We converted the frame color image to grayscale so that we can avoid some effects of illumines. This also results in faster processing.
2) We applied the Gaussian Blur filter to remove any possible noise in the frame image.
3) We computed the absolute difference (subtraction) between the current frame (foreground) and the first frame (modeled background) in order to calculate if their pixel values were close to zero, meaning that motion was not detected, otherwise when pixel values are higher, motion is detected.

4) We applied a frame delta threshold (i.e. with a value of 25), resulting in a black and white image (no other gray light color and mid-value in the image; just black and white).
5) We applied dilation (morphological transformation) to the threshold frame in order to join the broken parts of an object in the image.
6) After that, we applied contour detection on the image and measured the available contour size. If the contour size is smaller then the given threshold, then the pixels in the frame are very similar (as seen on the left side of Fig. 2) and frame image will not be passed to the inference process. If the contour size is higher than the threshold, then it means that the current frame is quite different from the previous frame (as seen on the right side of Fig. 2) and the image will be passed to our model for prediction.

There are some advantages of this vision-based motion approach over motion sensors, e.g. regular motion sensors are having some drawback regarding range and time and require extra acquisition costs whereas this vision-based motion approach checks the difference between previous and present frame in software and if something changed in the image, then it takes it as motion and sends the frame to the inference process. Another advantage is that, even though the program will run all the time having the GPU at running state, the GPU memory transfer will be zero because GPU is not computing anything when there is no significant change in the present frame compared with the previous one; in this way we protect the GPU to heat-up as well.

4 Experimental Setup and Results

We considered implementing the 4 DL model architectures both on an Acer Predator Helios 300 PH317-51-78SZ laptop with an Intel Core i7-7700HQ, 16 GB DDR4 RAM memory and the Nvidia GTX 1060 GPU with 6 GB GDDR5/X frame buffer, 8 Gbps memory speed and 1708 boost clock (MHz) as well as on a Nvidia Jetson TX2 board [4] having the following configuration on the hardware side: CPU: ARM Cortex-A57 (quad-core) @ 2 GHz + Nvidia Denver2 (dual-core) @ 2 GHz, GPU: 256-core Pascal @ 1300 MHz, Memory: 8 GB 128-bit LPDDR4 @ 1866 MHz | 59.7 GB/s, and Storage: 32 GB eMMC 5.1. On the software side, on the Nvidia Jetson TX2 board, we used Nvidia JetPack SDK [36] with Linux Ubuntu18.04 LTS and Tensorflow 1.14.0 (Keras is used from within the tensorflow.keras) for both platforms. For the experimental results using webcam and motion detection, in the case of the laptop, we use its internal webcam, whereas, in the case of the Nvidia Jetson TX2 board, we used an external Logitech C920 HD Pro webcam. It is important to mention that with the help of the command line interface nvpmodel tool, we run all our Nvidia Jetson TX2 tests on the Max-P Core-All mode.

4.1 Nvidia GTX 1060 GPU and Nvidia Jetson TX2 Inference Comparison Regarding Speed Test and Power Consumption

Following, we will show a comparison between the laptop containing the Nvidia GTX 1060 GPU and Nvidia Jetson TX2 regarding inference speed testing and also explain why frames batch testing is important when trying to run a DL model in real-time on both platforms. Finally, we will present a power usage comparison with and without the proposed motion detection on both platforms and motivate our decision for why the Nvidia Jetson TX2 is our platform of choice when designing the solar-powered real-time DL-based system.

The inference speed testing results for the Nvidia GTX 1060 GPU and Nvidia Jetson TX2 are presented in Table 1 where different number of frames were tested on both platforms in order to evaluate the time it takes for each of the 4 DL models to classify a certain number of frames in under a second, both on a video as well as using a webcam.

Table 1. Inference Speed Testing between Nvidia GTX 1060 GPU and Nvidia Jetson TX2 on a video as well as using a webcam for VGG-19 (V), InceptionV3 (I), ResNet-50 (R) and MobileNetV2 (M) model architectures.

Number of frames	Nvidia GTX 1060 GPU inference time (Seconds)				Nvidia Jetson TX2 inference time (Seconds)			
	V	I	R	M	V	I	R	M
1	0.020	0.033	0.027	0.021	0.135	0.114	0.083	0.047
2	0.029	0.030	0.066	0.021	0.223	0.145	0.115	0.062
4	0.054	0.043	0.056	0.044	0.368	0.190	0.187	0.305
8	0.106	0.065	0.080	0.056	0.503	0.289	0.332	0.385
16	0.190	0.106	0.142	0.109	0.682	0.478	0.599	0.525
24	0.304	0.158	0.227	0.177	1.107	0.682	0.898	1.059

Because the results were similar, we presented their average values only once. As can be noticed in Table 1, the inference time of the Nvidia GTX 1060 GPU is always under 1 s for all 4 DL model architectures, even with 24 fps (we also tested the GTX 1060 GPU on up to 60 fps, but it is out of scope to present these results). In comparison, when running the VGG-19 and MobileNetV2 DL models on the Nvidia Jetson TX2 platform with 24 fps, we discovered that the inference time takes more than 1 s, so we decided to run all of our Nvidia Jetson TX2 experiments presented in this paper with 16 fps for all DL architectures.

Regarding frames batch testing, we tested the effect of batch size on computing time by forwarding not just one frame but an n number of frame batches to our model for prediction. The frames batch testing is very important because it helps us choose the fps parameter that finishes the task in the shortest amount of time with the highest number of frames (the higher the number of frames, the better the prediction) and lowest energy consumption without worries of service interruption when deploying later in a real-life scenario. Because of its 6 GB dedicated RAM, we found out that the Nvidia GTX 1060 GPU can make use of 100% GPU memory utilization when running the InceptionV3 and ResNet-50 model architectures but only of 80% GPU memory utilization (a higher value than this resulted in "out of memory" errors) when running the VGG-19 and MobileNetV2 model architectures in real-time. Nevertheless, the laptop containing the Nvidia GTX 1060 GPU can help all DL model architectures run the fastest prediction (when there is no latency between present frame and predicted animal class name on the frame) at different (higher) fps and faster time values (less seconds) as compared with the Nvidia Jetson TX2 which uses more than half of its memory for running the Linux framework, and which is able to run the fps batch testing at only maximum 30% of its memory utilization. The reason for this limitation is because with other ratio values it resulted in "out of memory" related errors.

In order to show the power usage comparison between the two platforms by maintaining a high inference accuracy (more fps = better accuracy), we decided to run all the experimental results presented in this paper with 30 fps and GPU memory ratio = 1 (for the InceptionV3 and ResNet-50) and 0.8 (for the VGG-19 and MobileNetV2) on the laptop containing the Nvidia GTX 1060 GPU and with 16 fps and GPU memory ratio = 0.3 for all 4 DL model architectures on the Nvidia Jetson TX2. Because the final goal is to run the inference in real-time on real-life scenarios, we decided to run the experiments regarding power usage only using the webcam and not also on a video like in the previously described experiments.

We calculated the power consumption for the Nvidia GTX 1060 GPU on our Linux laptop by running the command "sudo powerstat" and for the Nvidia Jetson TX2 board by using a convenient power measurement script [37] and also by using the command e.g. "sudo./tegrastats". We run the experimental results for 5 h (30 samples/values taken every 10 min) for each of the 4 DL models, both with and without motion detection for both platforms and presented the results in Table 2 and Table 3.

Table 2. Power usage comparison on the laptop (GTX 1060 GPU) running the proposed real-time animal class identification implementation during a 5 h test using the webcam without and with motion detection method for VGG-19 (V), InceptionV3 (I), ResNet-50 (R) and MobileNetV2 (M) model architectures. The y-axis represents the Watts value and the x-axis represents the total number of sample values taken every 10 min.

GTX 1060 GPU Idle (Watts)	GTX 1060 GPU without motion detection (Watts)				GTX 1060 GPU with motion detection (Watts)			
V, I, R, M	V	I	R	M	V	I	R	M
15.13	53.04	50.92	53.96	49.77	49.85	50.03	53.9	50.07
15.08	52.78	50.25	54.31	50.83	49.1	52.16	54.35	50.51
15.07	53.79	51.91	54.42	54.15	49.5	52.91	52.1	47.16
14.98	52.68	50.18	53.67	52.61	51.49	53.4	53.24	49.11
14.98	53.07	50.56	54.16	51.43	50.73	53.62	50.04	49.6
14.98	51.95	51.93	55.36	49.48	49.56	52.32	49.44	49.12
14.98	52.64	52.95	54.32	48.19	50.51	54.65	49.6	49.15

(*continued*)

Table 2. (*continued*)

GTX 1060 GPU Idle (Watts)	GTX 1060 GPU without motion detection (Watts)				GTX 1060 GPU with motion detection (Watts)			
V, I, R, M	V	I	R	M	V	I	R	M
14.91	52.3	54.74	53.54	49.57	49.8	55.06	48.89	48.51
14.9	52.76	54.67	53.51	50.21	52.28	54.47	48.18	47.9
14.79	51.98	54.24	53.62	50.52	50.38	53.38	48.58	47.03
14.89	51.89	52.43	53.63	50.03	50.07	53.39	48.41	48.15
15.43	51.76	54.67	53.91	48.75	46.16	52.49	48.14	46.01
15.16	51.53	54.99	53.99	49.34	47.56	51.8	48.56	47.54
15.09	51.98	55.17	53.37	50.31	48.39	52.59	48.12	48.23
14.91	51.91	54.67	53.28	49.53	48.84	51.59	48.61	47.35
14.77	52.04	54.48	54.26	47.62	49.52	54.31	48.2	48.19
14.8	51.87	55.17	53.84	46.91	45.83	54.95	48.26	46.24
14.83	52.09	54.6	52.6	46.77	47.53	54.5	47.32	46.97
15.07	52.02	54.95	52.28	46.46	48.33	54.31	47.01	45.28
21.87	52.18	54.9	53.22	45.72	48.91	53.98	46.92	45.89
18.49	52.19	54.31	51.23	45.23	49.51	54.38	45.07	45.02
22.44	52.31	55.59	53.26	47.62	46.95	53.84	44.75	44.47
23.74	51.97	54.45	53.99	49.43	48.24	52.23	43.26	43.19
24.79	52.5	55.81	53.35	50.23	48.97	53.46	43.47	43.25
21.46	52.36	54.72	53.51	50.32	49.43	53.03	48.91	45.87
21.83	52.48	54.24	52.01	48.26	49.43	52.72	49.14	46.83
17.77	52.4	55.88	52.12	49.52	46.91	53.91	48.64	45.34
15.15	52.21	55.72	51.69	49.77	48.62	54.3	53.9	44.53
14.22	52.22	54.96	51.42	50.83	49.2	53.57	54.35	45.23
14.01	52.05	55.85	51.44	54.15	49.52	53.51	52.1	46.91
Avg. 16.67	**Avg. 52.29**	**Avg. 53.99**	**Avg. 53.30**	**Avg. 49.21**	**Avg. 49.03**	**Avg. 53.36**	**Avg. 48.55**	**Avg. 46.95**
Max. 24.79	**Max. 53.79**	**Max. 55.88**	**Max. 55.36**	**Max. 54.15**	**Max. 52.28**	**Max. 55.06**	**Max. 54.35**	**Max. 50.51**

Without using the proposed motion detection method, the maximum power consumption of the laptop (Nvidia GTX 1060 GPU) was 24.79 W when in idle state, 53.79 W when running the VGG-19 model, 55.88 W when running the InceptionV3 model, 55.36 W when running the ResNet-50 model and 54.15 W when running the MobileNetV2 model. With the proposed motion detection method, the power consumption is lower for both platforms, justifying our decision to implement it. More exactly, the maximum power consumption of the laptop (Nvidia GTX 1060 GPU) when using the proposed motion detection method was 52.58 W when running the VGG-19 model, 55.06 W when running the InceptionV3 model, 54.35 W when running the ResNet-50 model and 50.51 W when running the MobileNetV2 model.

The maximum power consumption of the Nvidia Jetson TX2 without using the proposed motion detection method was 4.11 W when in idle state, 14.77 W when running the VGG-19 model, 12.87 W when running the InceptionV3 model, 11.74 W when running the ResNet-50 model and 10.47 W when running the MobileNetV2 model.

Table 3. Power usage comparison on the Nvidia Jetson TX2 board running the proposed real-time animal class identification implementation during a 5 h test using the webcam without and with motion detection method for VGG-19 (V), InceptionV3 (I), ResNet-50 (R) and MobileNetV2 (M) model architectures. The y-axis represents the Watts value and the x-axis represents the total number of sample values taken every 10 min.

Nvidia Jetson TX2 Idle (Watts)	Nvidia Jetson TX2 without motion detection (Watts)				Nvidia Jetson TX2 with motion detection (Watts)			
V, I, R, M	V	I	R	M	V	I	R	M
2.51	9.99	8.7	9.62	9.61	9.91	8.86	8.9	8.85
2.5	10.87	8.6	9.92	9.33	10.82	9.31	8.93	9.01
2.5	10.14	9.47	10.68	9.61	8.16	10	9.19	9.01
2.49	9.92	8.69	10.49	9.06	7.4	9.2	9.27	9.07
2.48	12.48	9.29	10.36	8.63	12.69	9.71	9.34	6.94
2.47	13.03	10.05	10.07	9.66	12.57	10.35	9.37	8.96
2.48	12.41	10.04	9.9	9.94	12.46	10.07	9.69	9.19
2.47	11.8	11.69	10.88	10.29	12.01	11.53	10.66	9.11
2.47	12.82	11.21	10.52	9.78	12.88	10.7	10.34	9.23
2.45	13.75	10.84	10.99	9.47	13.22	9.82	10.62	9.05
2.47	13.01	11.19	10.98	9.89	13.11	11.11	10.6	9.15
2.56	14.77	12.75	11.28	10.29	12.84	12.03	11.43	9.3
2.52	12.94	12.63	11.51	9.81	12.91	11.65	11.39	8.92
2.5	10.74	11.82	11.74	9.3	9.34	10.3	11.38	9.26
2.47	10.83	12.55	11.56	9.86	10.45	11.66	11.34	9.15
2.45	11.4	11.69	11.1	9.52	12.99	10.88	11.12	9.19
2.46	13.3	12.53	10.94	9.34	12.76	12.16	11.26	9.15
2.46	12.47	12.04	10.91	9.86	11.24	11.27	11.18	9.19
2.5	12.56	11.93	10.84	9.68	12.99	10.81	11.24	9.49
3.63	12.96	12.27	10.66	9.97	12.8	11.27	11.28	9.01
3.07	13.17	12.31	10.55	10.18	12.08	11.2	11.37	9.19
3.72	12.34	12.82	11.11	9.94	10.14	11.56	11.15	9.15
3.94	12.46	12.87	11.54	9.89	12.72	11.3	11.27	9.27
4.11	13.2	12.8	11.72	9.64	12.95	11.86	11.01	9.07
3.56	12.35	11.63	11.73	10.01	12.65	10.78	10.89	9.49
3.62	12.37	11.71	11.26	9.98	12.57	10.62	11.43	9.07
2.95	13.75	12.02	11.55	10.47	12.65	10.99	11.07	9.19
2.51	12.95	12.18	9.62	9.21	12.69	11.1	8.9	9.23

(*continued*)

Table 3. (*continued*)

Nvidia Jetson TX2 Idle (Watts)	Nvidia Jetson TX2 without motion detection (Watts)				Nvidia Jetson TX2 with motion detection (Watts)			
V, I, R, M	V	I	R	M	V	I	R	M
2.36	13.68	12.46	9.92	9.45	13.07	11.68	8.93	9.19
2.33	12.87	11.92	10.68	9.08	12.84	10.52	9.19	7.89
Avg. 2.76	**Avg. 12.37**	**Avg. 11.42**	**Avg. 10.90**	**Avg. 9.69**	**Avg. 11.93**	**Avg. 10.81**	**Avg. 10.61**	**Avg. 9.03**
Max. 4.11	**Max. 14.77**	**Max. 12.87**	**Max. 11.74**	**Max. 10.47**	**Max. 13.22**	**Max. 12.16**	**Max. 11.43**	**Max. 9.49**

The maximum power consumption of the Nvidia Jetson TX2 when using the proposed motion detection method was 13.22 W when running the VGG-19 model, 12.16 W when running the InceptionV3 model, 11.43 W when running the ResNet-50 model and 9.49 W when running the MobileNetV2 model. It is important to mention that in the case of the laptop we used the existent internal webcam, whereas for the Nvidia Jetson TX2 we used the Logitech C920 HD Pro webcam having an input voltage range from +9 V to +15 V DC and which was powered directly from the embedded board itself. Also, it can be observed that for both platforms, the motion detection method reduces the energy consumption by around 5%.

Considering the experimental results from Table 2 and Table 3, which show that the laptop containing the Nvidia GTX 1060 GPU consumes around 5 times more energy than the Nvidia Jetson TX2 and because we wanted to minimize the investment in the improvement of our solar tracker (which otherwise, in the case of laptop would have required a 5× increase in the number of solar cells and solar panel size, as well as updating the entire circuitry), we decided to make the Nvidia Jetson TX2 as the platform of choice for our solar-powered real-time DL-based system.

One of the main reasons for implementing an efficient solar-powered real-time DL-based system is the consideration of recent efforts regarding climate change [1, 3, 38] as well to bring awareness to future researchers about the possibility and necessity to use alternative sources of renewable and green energy such as that from the sun when designing real-time DL-based systems.

4.2 Self-sufficient Solar-Powered Real-Time Deep Learning-Based System

As seen previously in Table 2 and Table 3, the maximum power consumed by the Nvidia Jetson TX2 was that of 14.77 W without using motion detection and 13.22 W when using motion detection for the VGG-19 model architecture during a 5 h test. The architecture that had the lowest power consumption during the 5-h test was the MobileNetV2 model architecture, with 9.69 W when not using motion detection and 9.03 W when using motion detection.

In order to make our Nvidia Jetson TX2 board also autonomous from the energy needs point of view when running inference using the 4 DL model architectures [8] in real-time, instead of using a traditional power plug, we decided to connect it to our previous proposed solar tracking device that uses the cast-shadow principle [6] which we updated and described in Sect. 3.1 of this paper. A diagram block of the summarized solar-powered real-time DL-based system can be seen in Fig. 3. Our improved solar panel comes equipped with 60 polycrystalline cells that are able to provide a maximum output voltage of around 17 V as can be seen in Table 4. The increase from 40 to 60 in the number of PV solar cells is justified by the fact that it reduces the risk of voltage drops below 12 V in order to keep the battery charged continuously even under extreme weather conditions (e.g. cloudy days).

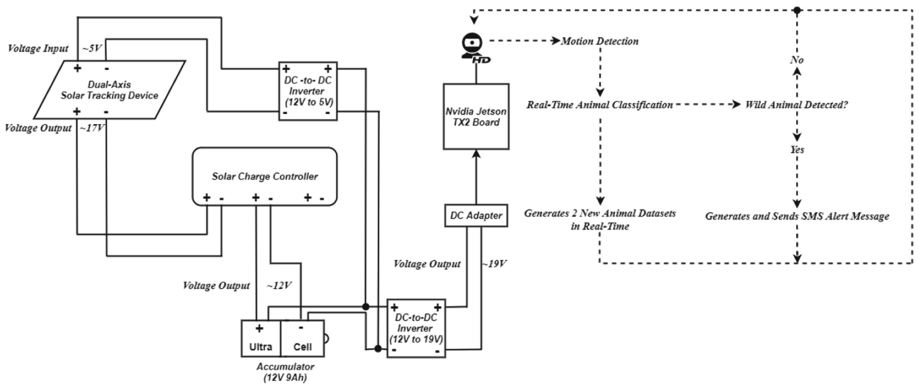
Voltage Input
~5V
Dual-Axis Solar Tracking Device
Voltage Output
~17V
DC -to- DC Inverter (12V to 5V)
Solar Charge Controller
Voltage Output
~12V
Ultra Cell
Accumulator (12V 9Ah)
DC-to-DC Inverter (12V to 19V)
Voltage Output
~19V
DC Adapter
Nvidia Jetson TX2 Board
HD
Motion Detection
Real-Time Animal Classification
Wild Animal Detected?
No
Yes
Generates 2 New Animal Datasets in Real-Time
Generates and Sends SMS Alert Message

Fig. 3. Connection diagram of the proposed autonomous solar-powered real-time DL-based system.

Table 4. Experimental results regarding the energy generated by our solar tracker, the energy stored by the accumulator and the energy requirements of the Nvidia Jetson TX2 when running the VGG-19 (V), InceptionV3 (I), ResNet-50 (R) and MobileNetV2 (M) model architectures in real-time using the external webcam with motion detection during a 5 h test time.

Energy generation of our solar tracker					Energy storage of our solar tracker			
Test time (Hour)	V	I	R	M	V	I	R	M
	Voltage gain [V]				Voltage [V]			
9:00	17.3	16.98	16.67	16.35	12.8	12.74	12.7	12.66
10:00	16.03	16.3	16.59	17.06	12.6	12.66	12.71	12.75
11:00	17.14	17.06	16.99	16.91	12.8	12.8	12.79	12.78
12:00	16.83	16.64	16.46	16.29	12.78	12.76	12.75	12.74
13:00	16.1	16.08	16.07	16.05	12.73	12.76	12.8	12.87
Avg. value	**16.68**	**16.61**	**16.55**	**16.53**	**12.74**	**12.74**	**12.75**	**12.76**

(*continued*)

Table 4. (*continued*)

	Current gain [A]				Charging current [A]			
9:00	1.34	1.36	1.37	1.39	0.84	0.87	0.89	0.92
10:00	1.4	1.22	1.04	0.86	0.94	0.86	0.78	0.65
11:00	0.67	0.67	0.66	0.66	0.9	0.87	0.84	0.82
12:00	0.66	0.64	0.64	0.75	0.92	0.85	0.8	0.79
13:00	0.66	0.65	0.65	0.69	0.88	0.83	0.81	0.8
Avg. value	**0.94**	**0.90**	**0.87**	**0.87**	**0.89**	**0.85**	**0.82**	**0.79**
	Power gain [W]				Power [W]			
9:00	23.18	23.09	22.83	22.72	10.75	11.08	11.30	11.64
10:00	22.44	19.88	17.25	14.67	11.84	10.88	9.91	8.28
11:00	11.48	11.43	11.21	11.16	11.52	11.13	10.74	10.47
12:00	11.10	10.64	10.53	12.21	11.75	10.84	10.2	10.06
13:00	10.62	10.45	10.44	11.07	11.20	10.59	10.36	10.29
Avg. value	**15.76**	**15.09**	**14.45**	**14.36**	**11.41**	**10.90**	**10.50**	**10.14**

Voltage readings for DC-to-DC Inverter (12 V to 19 V)

	Voltage output [V]			
9:00	19.20	19.15	19.16	19.18
10:00	19.17	19.14	19.12	19.10
11:00	19.09	19.10	19.11	19.05
12:00	19.02	19.04	19.05	19.06
13:00	19.03	19.02	19.07	19.00
Avg. value	**19.10**	**19.09**	**19.10**	**19.07**

Energy requirement of the Nvidia Jetson TX2 with external webcam and using motion detection

	Voltage draw [V]			
9:00	19.1	19.1	19.1	19.09
10:00	19.08	19.08	19.08	19.07
11:00	19.07	19.07	19.07	19.06
12:00	19.07	19.08	19.07	19.08
13:00	19.07	19.07	19.06	19.05
Avg. value	**19.07**	**19.07**	**19.07**	**19.07**
	Current draw [A]			
9:00	0.58	0.55	0.51	0.46
10:00	0.52	0.51	0.49	0.46
11:00	0.56	0.62	0.52	0.47
12:00	0.42	0.56	0.53	0.47
13:00	0.66	0.54	0.52	0.47
Avg. value	**0.54**	**0.55**	**0.51**	**0.46**
	Power consumption [W]			
9:00	11.07	10.50	9.74	8.78
10:00	9.92	9.73	9.34	8.77
11:00	10.67	11.82	9.91	8.95
12:00	8	10.68	10.1	8.96
13:00	12.58	10.29	9.91	8.95
Avg. value	**10.44**	**10.60**	**9.8**	**8.88**

The solar charge controller is a robust all-in-one control system that provides three input-output ports: one dedicated to solar modules, one dedicated to feeding the battery from the PV panel with collected voltage, and one output module for connecting a current load. Since our main objective is to store solar energy in the accumulator, we only use two of the available ports.

A few notable features of the solar charge controller are microcontroller unit control, built-in timer, settable voltage and full protection from overvoltage and overcurrent. The Ultra Cell accumulator is a 12 V, 9 Ah acid-plumb battery that is generally used nowadays in UPS systems to provide energy for desktop systems in case of local power outages. Due to its chemical composition and charging current of around 1 A, the charging and discharging time can be analyzed both theoretically as well as in real-time scenarios. The main formula that is generally used in charging time calculus is given by the following equation:

$$T = Ah/A \tag{1}$$

where T represents the charging time, Ah depicts the Ampere hour rating of the battery and A denotes the charging current in Amperes. In our experimental results, first, we calculated the charging current for the 9 Ah battery in theory as well as in practice:

1) As we know, in theory, the charging current should be 10% of the battery's Ah rating. Therefore, charging current for a 9 Ah Battery = 9 Ah × (10/100) = 0.9 A. However, due to some possible current losses that can appear on the battery, instead of exactly 0.9 A, we consider only a value between 0.9 and 1.1 A for the charging purpose. Supposing we take 1 A for charging purposes, so charging current for 9 Ah Battery = 9/1 = 9 h (Hrs), a situation that usually occurs only in theory.
2) As we know, in practice, it has been noted that 40% of losses occur in the case of battery charging. Consequently, the formula will be: 9 × (40/100) = 3.6 resulting in 9 Ah × 40% of losses. Therefore, 9 + 3.6 = 12.6 Ah resulting in 9 Ah + Losses. According to formula (1), we will now substitute the new values and obtain:

$$12.6/1 = 12.6\,\mathrm{h} \tag{2}$$

Therefore, because the accumulator requires 1 A charging current, its 9 Ah capacity takes almost 13 h to fully charge with solar energy from the solar tracker. However, because our solar-powered real-time DL-based system does not drain any solar energy during the night time, this does not influence our experimental outcomes. Consequently, the total discharging time of the accumulator can be determined by applying the following formula:

$$9\mathrm{Ah}/0.6 = 15\,\mathrm{h} \tag{3}$$

Since our accumulator is limited to a 12 V storage capacity, as can be seen in Fig. 3, we used two voltage inverters. The first DC-to-DC inverter was interconnected in parallel so that the battery's output voltage would be increased to around 19 V as can be seen in Table 4, in order to satisfy the Nvidia Jetson TX2 board's (consumer) supply voltage requirements in a real-life scenario. The second DC-to-DC inverter was connected between the energy storage element and the back of our solar panel in order to power the automation equipment (1 × Arduino UNO, 1 × Optocoupler, 2 × L298N, 2 × stepper motors) directly from the accumulator. Due to the implemented mechanical blocking elements, when in idle state, our solar tracking device consumes less energy (0.32 W) with the Arduino UNO and L298N integrated circuits and reaches 2 W power consumption [6] when it updates its position to optimize sun ray exposure (a process which usually takes up to 5 s).

This 2 W power consumption can be successfully covered by the accumulator's solar energy provision, proving that our entire solar-powered real-time DL-based system can run 100% using renewable and green energy from the sun. Finally, we linked the output of the first DC-to-DC inverter to the input of the Nvidia Jetson TX2 board with the help of a dedicated DC adapter, as seen in Fig. 3 as well.

The experimental cases were carried out with our previously described setup over a 5 h time span for each of our previously trained architectures (VGG-19, InceptionV3, ResNet-50, and MobileNetV2) [8] during 4 days test time. Our results show that the output voltage and current values of our solar panel are always maintained at an optimum level despite changing weather conditions (e.g. partial clouds in the afternoon).

Also, regarding the energy requirement of the Nvidia Jetson TX2 with the external webcam using the implemented motion detection method during a 5 h test, we present the results in Table 4. These results prove that a real-time DL-based system can easily take advantage of renewable and green energy sources such as solar energy from a solar tracking device in order to become self-sustaining from the energy needs point of view. More exactly, we can observe that the improved solar tracker generates in average around 15 Wh, the accumulator stores around 11 Wh and the Nvidia Jetson TX2 board consumes not more than around 10 Wh when running all 4 DL models with the motion detection method in real-time.

The experimental cases were considered relevant for our work due to the fact that the DL-based system can run autonomously using free energy from the portable solar tracker, thus eliminating the need of connecting it to an AC network. In order to check the working conditions and take full control of the Nvidia Jetson TX2 board when connected to our solar tracker, we made use of a 7 inch portable monitor that was connected with the help of a HDMI as well as a micro-to-USB cable to the Nvidia Jetson TX2 board, as can be seen on the right side of Fig. 1.

5 Conclusions and Future Work

This paper presents, to the best of our knowledge, the first solar-powered real-time DL-based system in the literature that is self-sustaining from the energy point of view, can run inference using 100% solar energy and which is composed of a dual-axis solar tracking device based on cast-shadow principle [6] and a low-power embedded platform called Nvidia Jetson TX2. In order to justify the choice of this platform, experimental results, especially regarding the energy consumption while running 4 DL model architectures (VGG-19, InceptionV3, ResNet-50 and MobileNetV2) in real-time [8] are made also on a laptop containing the Nvidia GTX 1060 (6 GB) GPU. Additionally, in order to reduce the power consumption of the entire solar-powered real-time DL-based system, we also implemented a motion detection method that triggers the inference process only when there is movement in the frame. Details about the construction of the entire solar-powered real-time DL-based system as well as calculations regarding the time needed for the accumulator to be charged with solar energy as well as discharged by the Nvidia Jetson TX2 when running the 4 DL models are also taken into consideration. Experimental results show that the Nvidia Jetson TX2 platform is a very good choice when designing an efficient solar-powered real-time DL-based system, consuming only around 10 Wh of power as compared to around 50 Wh consumed by a laptop.

As future work, we plan to run similar experiments also on other low-power platforms such as the Nvidia Jetson Nano Developer Kit, Google Coral, Raspberry Pi 4 Model B (4 GB) and also on FPGAs, in order to show that real-time DL-based systems can run inference 100% on solar energy using even less energy than we demonstrated, to the best of our knowledge, for the first time in literature, in this paper. Additionally to inference, we also want to train a few other state-of-the-art DL model architectures using 100% solar energy from our solar tracker on the above-mentioned platforms, with the intent to encourage new researchers to investigate the combination of green energy and AI, eventually proposing new green energy-based DL metrics. We believe that a "green" approach can lead researchers to a better understanding of how to evaluate the performance of DL-based systems and will also result in a more friendly and respectful attitude towards nature and life on this planet.

References

1. Strubell, E., Ganesh, A., McCallum, A.: Energy and policy considerations for deep learning in NLP. arXiv:1906.02243 (2019)
2. Schmidt, V., Luccioni, A., Mukkavilli, S.K., Balasooriya, N., Sankaran, K., Chayes, J., Bengio, Y.: Visualizing the consequences of climate change using cycle-consistent adversarial networks. arXiv:1905.03709 (2019)
3. UN Sustainable Development Goals. https://www.un.org/sustainabledevelopment/sustainable-development-goals/. Accessed 01 Dec 2019
4. Nvidia Jetson TX2. https://www.nvidia.com/en-us/autonomous-machines/embedded-systems/jetson-tx2/. Accessed 01 Dec 2019
5. Yan, J., Yang, Y., Elia Campana, P., He, J.: City-level analysis of subsidy-free solar photovoltaic electricity price, profits and grid parity in China. Nat. Energy **4**, 709–717 (2019)
6. Rotar, R., Jurj, S.L., Opritoiu, F., Vladutiu, M.: Position optimization method for a solar tracking device using the cast-shadow principle. In: IEEE 24th International Symposium for Design and Technology in Electronic Packaging (SIITME), Iasi, Romania, pp. 61–70. IEEE (2018)

7. Carballo, J.A., Bonilla, J., Berenguel, M., Fernandez-Reche, J., García, G.: New approach for solar tracking systems based on computer vision, low cost hardware and deep learning. arXiv:1809.07048v1 (2018)
8. Jurj, S.L., Opritoiu, F., Vladutiu, M.: Real-time identification of animals found in domestic areas of Europe. In: Proceedings of the SPIE 11433, Twelfth International Conference on Machine Vision (ICMV 2019), 1143313, 31 January 2020. https://doi.org/10.1117/12.2556376
9. Bradski, G.: The openCV library. Dr. Dobb's J. Softw. Tools **120**, 122–125 (2000)
10. Rungsuptaweekoon, K., Visoottiviseth, V., Takano, R.: Evaluating the power efficiency of deep learning inference on embedded GPU systems. In: 2nd International Conference on Information Technology (INCIT), Nakhonpathom, Thailand, pp. 1–5. IEEE (2017)
11. Yudin, D., Slavioglo, D.: Usage of fully convolutional network with clustering for traffic light detection. In: 7th Mediterranean Conference on Embedded Computing (MECO), Budva, Montenegro, pp. 1–6. IEEE (2018)
12. Shihadeh, J., Ansari, A., Ozunfunmi, T.: Deep learning based image classification for remote medical diagnosis. In: IEEE Global Humanitarian Technology Conference (GHTC), San Jose, CA, USA, pp. 1–8. IEEE (2018)
13. Yin, X., Chen, L., Zhang, X., Gao, Z.: Object detection implementation and optimization on embedded GPU system. In: IEEE International Symposium on Broadband Multimedia Systems and Broadcasting (BMSB), Valencia, Spain, pp. 1–5. IEEE (2018)
14. Arechiga, A.P., Michaels, A.J., Black, J.T.: Onboard image processing for small satellites. In: NAECON 2018 - IEEE National Aerospace and Electronics Conference, Dayton, OH, USA, pp. 234–240. IEEE (2018)
15. Vandersteegen, M., Van Beeck, K., Goedemé, T.: Super accurate low latency object detection on a surveillance UAV. arXiv:1904.02024v1 (2019)
16. Špaňhel, J., Sochor, J., Makarov, A.: Detection of traffic violations of road users based on convolutional neural networks. In: 14th Symposium on Neural Networks and Applications (NEUREL), Belgrade, Serbia, pp. 1–6. IEEE (2018)
17. Yuan, L., Lu, F.: Real-time ear detection based on embedded systems. In: International Conference on Machine Learning and Cybernetics (ICMLC), Chengdu, China, pp. 115–120. IEEE (2018)
18. Liu, S., Li, X., Gao, M., Cai, Y., Nian, R., Li, P., Yan, T., Lendasse, A.: Embedded online fish detection and tracking system via YOLOv3 and parallel correlation filter. In: OCEANS 2018 MTS/IEEE Charleston, Charleston, SC, USA, pp. 1–6. IEEE (2018)
19. Saypadith, S., Aramvith, S.: Real-time multiple face recognition using deep learning on embedded GPU system. In: Asia-Pacific Signal and Information Processing Association Annual Summit and Conference (APSIPA ASC), Honolulu, HI, USA, pp. 1318–1324. IEEE (2018)
20. Zhang, W., Sun, H., Zhao, D., Xu, L., Liu, X., Zhou, J., Ning, H., Guo, Y., Yang, S.: A streaming cloud platform for real-time video processing on embedded devices. IEEE Trans. Cloud Comput. **13**, 1 (2019)
21. Goyal, M., Reeves, N.D., Rajbhandari, S., Yap, M.H.: Robust methods for real-time diabetic foot ulcer detection and localization on mobile devices. IEEE J. Biomed. Health Inf. **23**, 1730–1741 (2019)
22. Modasshir, M., Li, A.Q., Rekleitis, I.: Deep neural networks: a comparison on different computing platforms. In: 15th Conference on Computer and Robot Vision (CRV), Toronto, ON, Canada, pp. 383–389. IEEE (2018)
23. Vaidya, B., Paunwala, C.: Comparative analysis of motion based and feature based algorithms for object detection and tracking. In: International Conference on Soft Computing and its Engineering Applications (icSoftComp), Changa, India. pp. 1–7. IEEE (2017)

24. Zivkovic, Z.: Improved adaptive Gaussian mixture model for background subtraction. In: Proceedings of the 17th International Conference on Pattern Recognition (ICPR), Cambridge, UK, pp. 28–31. IEEE (2004)
25. Stauffer, C., Grimson, W.E.L.: Adaptive background mixture models for real-time tracking. In: Proceedings 1999 IEEE Computer Society Conference on Computer Vision and Pattern Recognition (Cat. No PR00149), Fort Collins, CO, USA, pp. 246–252. IEEE (1999)
26. Moon, S., Lee, J., Nam, D., Yoo, W., Kim, W.: A comparative study on preprocessing methods for object tracking in sports events. In: 20th International Conference on Advanced Communication Technology (ICACT), Chuncheon-si Gangwon-do, Korea (South), pp. 460–462. IEEE (2018)
27. Godbehere, A.B., Matsukawa, A., Goldberg, K.: Visual tracking of human visitors under variable-lighting conditions for a responsive audio art installation. In: 2012 American Control Conference (ACC), Montreal, QC, Canada, pp. 4305–4312. IEEE (2012)
28. Kaewtrakulpong, P., Bowden, R.: An improved adaptive background mixture model for realtime tracking with shadow detection. In: Remagnino, P., Jones, G.A., Paragios, N., Regazzoni, C.S. (eds.) Video-Based Surveillance Systems, pp. 135–144. Springer, Boston (2002)
29. Berthod, C., Kristensen, S.T., Strandberg, R., Odden, J.O., Nie, S., Hameiri, Z., Sætre, T.O.: Temperature sensitivity of multicrystalline silicon solar cells. IEEE J. Photovolt. **9**, 957–964 (2019)
30. Simonyan, K., Zisserman, A.: Very deep convolutional networks for large-scale image recognition. arXiv:1409.1556v6 (2015)
31. Szegedy, C., Liu, W., Jia, Y., Sermanet, P., Reed, S., Anguelov, D., Erhan, D., Vanhoucke, V., Rabinovich, A.: Going deeper with convolutions. arXiv:1409.4842v1 (2014)
32. He, K., et al.: Deep residual learning for image recognition. arXiv preprint arXiv:1512.03385 . (2015)
33. Sandler, M., Howard, A., Zhu, M., Zhmoginov, A., Chen, L.C.: MobileNetV2: inverted residuals and linear bottlenecks. arXiv:1801.04381v4 (2019)
34. TensorflowProtobuf. https://github.com/tensorflow/tensorflow/blob/master/tensorflow/core/protobuf/config.proto/. Accessed 01 Dec 2019
35. Twilio Programmable SMS. https://www.twilio.com/docs/sms/send-messages. Accessed 01 Dec 2019
36. JetPack. https://developer.nvidia.com/embedded/jetpack/. Accessed 01 Dec 2019
37. Convenient Power Measurement Script on the Jetson TX2/Tegra X2. https://embeddeddl.wordpress.com/2018/04/25/convenient-power-measurements-on-the-jetson-tx2-tegra-x2-board/. Accessed 01 Dec 2019
38. Schwartz, R., Dodge, J., Smith, N.A., Etzioni, O.: Green AI. arXiv:1907.10597v3 (2019)

Leveraging Radar Features to Improve Point Clouds Segmentation with Neural Networks

Alessandro Cennamo[1,2](✉), Florian Kaestner[1], and Anton Kummert[2]

[1] Aptiv Services Deutschland GmbH, 42199 Wuppertal, Germany
{alessandro.cennamo,florian.kaestner}@aptiv.com
[2] University of Wuppertal (BUW), 42199 Wuppertal, Germany
kummert@uni-wuppertal.de

Abstract. Radar sensors, unlike lidars or cameras, can measure objects' instantaneous velocity and composition. However, the ability to process and retrieve spatial information from radar point clouds has not yet been fully established. In this work, we propose a key technique for improving the performance of standard machine learning point-wise processing methods on radar point clouds. We show that a network can learn to extract object-related signatures for every point using automotive radar measurements. In addition, we propose RadarPCNN, a novel architecture for performing semantic segmentation, specifically designed for radar point clouds. RadarPCNN uses PointNet++, aided with mean shift as feature extractor module and an attention mechanism to fuse information from different neighborhood levels. We show that our model outperforms state-of-the-art solutions on our dataset.

Keywords: Radar point clouds · Neural network · Segmentation

1 Introduction

During the last years, vehicles have been equipped with sensors such as camera, radar and lidar to achieve autonomous driving capabilities [3]. While cameras produce data in the form of images – that are efficiently consumed by Convolutional Neural Networks (CNNs) [17,18] –, radars and lidars data are often processed as point clouds (PCs): 3D points representing reflections of the surrounding objects. However, CNNs do not scale well to such unstructured data-format [21], therefore new Machine Learning (ML) techniques have been devised.

The most simple method consists of structuring the data – by voxel/pixel encoding of the input PC –, thus enabling the application of 3D CNNs [4,22]. Similarly, multi-view representation techniques take several snapshots of the input and process each image with a different CNN: the features computed for every view are then fused to perform 3D shape recognition or semantic segmentation [7,20]. Despite such approaches have achieved dominating performance

L. Iliadis et al. (Eds.): EANN 2020, INNS 2, pp. 119–131, 2020.
https://doi.org/10.1007/978-3-030-48791-1_8

on a variety of tasks, they either significantly increase the input size, thus raising the computational demands, or exhibit loss of input information. In order to overcome these limitations, other approaches use order-invariant networks to consume raw PCs. Although this constraint hardens the task of extracting information of spatial correlation between points, several researchers have succeeded in the design of architectures capable to achieve state-of-the-art performance [11,14,15]. These approaches possess the advantage of maintaining low computational/memory demands while retaining all the input information.

Over the last decades, radar has been extensively used in the automotive industry [1,5], yet object recognition/classification in urban scenes remains an open challenge. Unfortunately, though extremely low-cost, automotive radars are different than other sensors. For instance, radar PCs are the result of a thresholding process and come with much lower density than lidar PCs. Hence any grid-based approach would result in either sparse cells and/or resolution degradation [8]. On the other hand, radars can capture intrinsic object-related properties. Therefore, we think that the ability of point-wise processing methods to exploit all the information present in the input plays a major role when consuming radar PCs.

We believe that addressing/exploiting intrinsic characteristics of this specific sensor is of paramount importance to efficiently process radar data. In this work, we propose to build informative point signatures by leveraging radar object features. We use a shared fully connected (FC) network to design a pre-processing module that can compute new per-point features, facilitating the final segmentation task. The output of this module can then be used as an input to any existent point-wise approach. We show that the proposed pre-processing module improves the semantic segmentation performance of PointNet++ [16] on our radar dataset. In addition, we develop RadarPCNN, a novel architecture for performing semantic segmentation on raw PCs, specifically designed for radar. We use the pre-processing module proposed in this work and the mean shift clustering algorithm [9] to improve usage of spatial relationship in such sparse data. We also use an attention mechanism to let the network learn the features of major interest. Our scheme uses PointNet++ [14] as a feature extractor module to directly consume point clouds. Finally, we show that RadarPCNN is able to achieve state-of-the-art semantic segmentation performance on radar data, outperforming PointNet++.

2 Related Works

Recently, point clouds have played a paramount role in a broad variety of applications by enabling detailed understanding of complex 3D structures/objects. Formally, a point cloud is defined as an unordered collection of $N \in \mathbb{N}$ individual points $x_i \in \mathbb{R}^m$, $i = 1, \ldots, N$ whose elements are the 2D/3D spatial coordinates. In addition, each point could possess supplementary features like color (RGBD sensor) or reflection intensity (lidar). The semantic segmentation task on such inputs consists in the estimation of a function $f : \mathbb{R}^{N\times m} \rightarrow \mathbb{R}^{N\times d}$

such that every point gets a score of the probability to belong to every one of d semantic classes. In this work we focus on point-wise processing – rather than grid-based – methods, because of their ability to exploit all the information in the input.

2.1 Deep Learning on Point Clouds

Despite DL has proven to be an effective tool for extracting information from low level data, the unordered nature of PCs precludes the direct application of standard techniques like CNNs, Recurrent Neural Networks (RNNs) or FC nets.

PointNet [15] represents a milestone for point-wise processing approaches. The authors focused on the development of a network which is invariant to point-order. They achieved this by the joint deployment of two elements: shared FC networks – to compute point-related features – and max-pooling – for global features aggregation. Furthermore, they devised T-Net – a transformation network resembling PointNet – to achieve invariance under different viewpoints. In spite of the network's good performance on a broad variety of tasks, it fails to capture the local structure induced by the input space geometry.

The authors of PointNet observed that a key factor for the success of CNNs has been their ability to hierarchically abstract local low-level structures into high-level descriptive patterns. Based on this observation, Qi et al. devised PointNet++ [14], a hierarchical architecture capable of extracting geometric information from overlapping sub-regions of the input. The network follows an encoder-decoder structure: set-abstraction (SA) layers abstract groups of points into local region descriptors, while feature-propagation (FP) layers serve to propagate high-level features back into low-level points. Skip connections are used to enrich single-point signatures and PointNet is selected as the local feature extractor module in SA layers. PointNet++ is currently considered the benchmark for point-wise processing architectures.

Further, Li et al. noticed that, provided some ordering, classical convolution could be directly applied to point clouds. Therefore, they proposed to weight and permute the input by means of a learned $\mathcal{X}$ matrix to achieve order equivariance. The resulting $\mathcal{X}$-Conv layer performs a $\mathcal{X}$-transformation on local neighborhood of points and then applies standard convolution. Finally, the authors developed PointCNN [11], a hierarchical encoder-decoder network using $\mathcal{X}$-Conv as feature extractor module. The work shows that the architecture achieves state-of-the-art results on a broad variety of tasks, thus proving the effectiveness of the $\mathcal{X}$-transformation.

2.2 Deep Learning on Radar Point Clouds

Radar has the advantage of being more reliable under various weather conditions, e.g. rain/fog. This aspect, along with the ability to measure instantaneous velocity, makes them particularly well-suited for automotive applications.

The lack of pubic radar datasets hardens the development of new ML techniques, therefore, during the last years, researchers resorted to conventional methods (described in the previous section) to process private radar data. Schumann et al. addressed the classification problem of radar reflections between 6 classes: car, pedestrian, pedestrian group, bike, truck and static targets [16]. They equipped two vehicles with several sensors and collected training and test data. Then, they trained a PointNet++ [14] to perform semantic segmentation. The authors proved that point-wise techniques designed to process dense PCs can effectively process radar data. In addition, they showed how the network can benefit from the introduction of radar-specific features (such as Doppler and RCS) as supplementary dimensions. Feng et al. wanted to classify radar reflections as vehicle or guardrail [8]. They resorted again to the PointNet++ architecture, with few minor tweaks: hand-crafted statistics of the area around the representative points (such as density, points number and covariance) were collected and appended to the neighborhood tensors. The authors showed how these features contribute to enhance the network performance.

A different approach consists of clustering together points and then deploy a ML technique to classify the whole cluster. In this direction, Wöhler et al. used DBSCAN [6] to group together reflections belonging to the same object [19]. Lately, they calculated clusters statistics from radar measurements – i.e. x, y, Doppler and RCS – and performed multi-class classification using a long-short term memory (LSTM) network [10]. The authors proved that the LSTM classifier outperforms the random forest algorithm [2]. Moreover, they ranked the cluster features according to their importance for the classification task and showed that spatial and Doppler-related features dominate the ranking.

3 Our Method

Unlike lidar, radar reflections contain valuable information about the object generating them. Classical radar processing methods generally exploit this property in a two-stage process: first, reflections from the same object are clustered together, then, they manually extract statistics from radar measurements to build cluster signatures [13]. Unfortunately, these approaches strongly rely on clustering algorithms to group measurements of the same instance. However, each single reflection contains object-related information.

Considering a ML framework, we believe that a network can learn to encode radar features into point-signatures useful for further point-wise processing. In this way we overcome the limitations of clustering algorithms. Herein, we propose to use a data-learned pre-processing module for generating new PC features, uniquely based on single-reflection measurements. Specifically, we deploy a shared FC network to produce a deeper version of the input: for each point, our module derives new features by combining together x, y, Doppler and RCS. Therefore, the new input will have the same spatial point locations, but features abstracting the radar perception of the object. In this way, we assume that the network would learn to cast the input into a representation that facilitates the classification task, by providing better separations between reflections from objects with different radar properties. Finally, due to the simplicity of the process, we think that our approach can be easily extended to any other architecture consuming raw PCs.

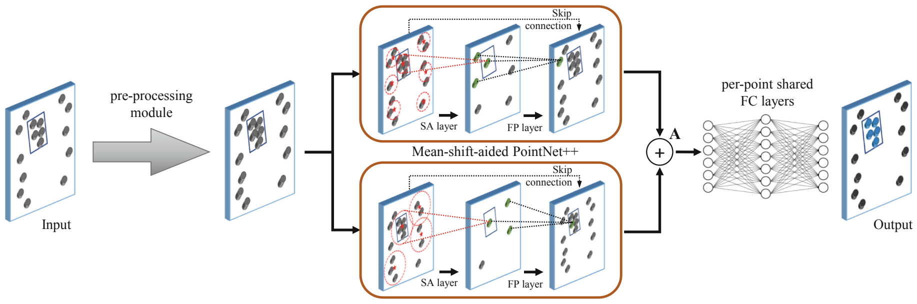

Fig. 1. RadarPCNN architecture. Our pre-processing module computes (32) new features for each reflection. Two single-layer PointNet++ extract per-point neighborhood-dependent features. FPS is substituted by mean shift to select the representative points (red stars). Per-point features are finally fused using an attention mechanism and processed with two shared fully-connected layers to produce the class scores.

PointNet++ [14] is a benchmarking architecture in the point-wise processing field. It is notoriously good at fusing information of point proximity to build useful object-part signatures. However, radar is extremely poor at providing this information. Therefore, despite this architecture has proven to perform well on radar PCs [8,16], we think that it does not represent the optimal solution for consuming such particular data. We believe that tailoring the network to operate at object level and improving the usage of spatial relationship would result in a more efficient processing. To this end, we develop RadarPCNN, a point-wise processing technique for performing semantic segmentation on radar PCs.

Figure 1 shows the architecture. Our network uses the proposed pre-processing module to build a deeper input for the remaining part. Here, meaningful classification features must be computed for every point. We decide to use PointNet++ as feature extractor module because of its ability to abstract information from local neighborhoods. However, we alter the architecture by replacing the farthest point sampling (FPS) method with mean shift (MS), to enhance usage of the scarce spatial proximity information. Specifically, we sum up Gaussian kernels (with given bandwidth) centered at each point location and use local maxima of the resulting distribution as representative points in the SA layer. Notice how we do not rely on mean shift at the grouping stage, but only to sample more meaningful representative points. In this way, MS helps the network to optimize the sampling process, obeying to the high-level input shape. Furthermore, we decide to discard the hierarchical PointNet++ structure in favor of several independent object-focused ones. More precisely, in this work we use two single-layer PointNet++. One seeking for small objects such as pedestrians, using dense representative points (MS with bandwidth 2.0) and neighborhood areas below 2 m. The other focuses on larger targets like cars/trucks, using representative points with bandwidth 8.0 and neighborhood areas from 4 to 8 m.

The two mini-PointNet++ output the input point locations, with different neighborhoods-dependent features. Since every point has two feature vectors,

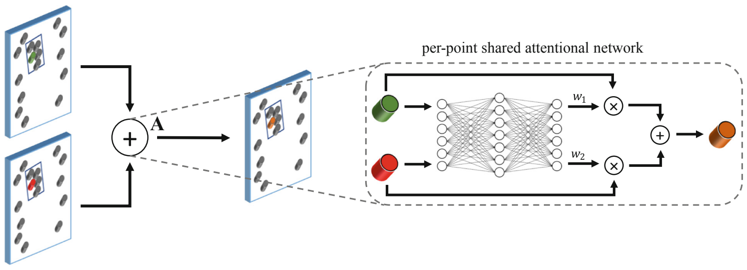

Fig. 2. Attention mechanism. For each point, the features produced by the top and bottom branches (see Fig. 1) are used as input of a FC regression network. The output of the network is used to perform a weighted combination of the input features.

similarly to [20], we let the network decide the best way to combine them. In particular, we design the attention mechanism showed in Fig. 2. Given a point location, the features computed from top (green point) and bottom (red point) PointNet++ are used as input to a shared FC network which regresses two scalars (w_1 and w_2). These scalars are then used to perform a weighted combination of the two vectors and build the classification features (orange point). In this way the network would learn to weight the features vectors based on its importance to the final task. Finally, the classification features are processed with a shared FC network to produce the output semantic segmentation score.

As every layer entails a differentiable operation, the whole network can be trained in an end-to-end fashion, using the output segmentation loss.

4 Experiments

In this section, we provide the results achieved on a 2-semantic-classes segmentation task: moving pedestrian and moving vehicle. We report precision, recall and F_1 score on the two positive classes along with the macro-average version of them (where each class contributes equally). We also show confusion matrices of the three total classes (pedestrian, vehicle, other).

4.1 Dataset

We conduct experiments on our dataset, composed of real-world radar reflections in urban scenes under different weather conditions. The data were collected by a fleet of vehicles equipped with six 77 GHz radars (sides, front and back corners), recording targets up to ± 90 m, with a field-of-view of $\pm 75°$. In total, our dataset counts 84 video sequences and more than 40 million points annotated accordingly to two classes: pedestrian and vehicle. Any other point is labeled as other/clutter. In this work, we focus on moving objects because automotive radars provide low information about stationary ones: indeed, they share the same Doppler of other still instances (e.g. buildings), therefore only RCS can be used for classification purposes. A crucial decision in our evaluation is the definition of a moving object. We consider a pedestrian/vehicle to be moving if its ground-truth velocity is above 0.5/2.5 m/s. It is worth noting that high threshold values would make the problem trivial, while low ones might confuse the network. However, we find out that these parameters mostly impact the numerical results: the network would still be able to classify points slightly below the thresholds as moving. Therefore, we force reflections below these values to be transparent during training and evaluation. Yet, points from parked vehicles (which do not move at all) are present in the other/clutter class. Table 1 contains the points distribution in the dataset configuration described. We create the train/test sets to contain the same distribution of rainy/cloudy/clear scenes.

4.2 Settings

Each video sequence in our dataset is divided into frames containing a few hundreds of points. Similarly to [16], we aggregate reflections from adjacent frames (200 ms) and compensate the point locations to the ego-vehicle position at the last frame. Moreover, we fix the input size to 1200 points and use the ego-compensated Doppler feature to sample with importance. In more detail, if the input has more than 1200 points, we give higher sampling probability to reflections with large absolute Doppler value. If it has less than 1200 points, we duplicate reflections in the same fashion. Bearing in mind that Doppler is only a radial velocity measure, in this way we decrease the probability of discarding moving objects reflections or duplicating static ones, thus increasing the positive class populations. Furthermore, since our radar sensors have a low elevation resolution, we decide to discard this information and use the Doppler value as z-coordinate. RCS is used as points feature. Regarding the representative points, we set a fixed number of 500/150 positions for the top/bottom branch of Fig. 1. Therefore, if MS outputs more than the necessary number of points, we perform FPS among them. If less, we fill the gaps by FPS from the input locations.

During training, we use focal loss [12] to deal with the extreme class imbalance. Moreover, we decide to address two binary tasks (pedestrian vs non-pedestrian, vehicle vs non-vehicle) and exclude the negative class to avoid biasing the network too much. Sigmoid is used as the output activation function. The final prediction would be the class achieving the highest score. If none of the positive classes scores exceed the threshold of 0.5 the negative class is predicted. Finally, we split the train-set into sub-sets and perform five-fold cross validation to tune the hyper-parameters. The pedestrian/vehicle loss weighting factor (α in [12]) is set to 0.9/0.85 for all the networks to enable fair comparison. For evaluation, we train the models for 20 epochs on the whole train-set. Then, we select the best performing configuration and test it 10 times to average random effects. Mean values are reported, while standard deviations (<0.1%) are omitted.

Table 1. Data distribution. Percentages and total number of points are reported.

Set	Moving pedestrian	Moving vehicle	Other & clutter
Train	2.26% (721 865)	6.12% (1 955 937)	91.62% (29 282 877)
Test	1.40% (142 647)	5.63% (574 321)	92.98% (9 493 667)

4.3 Results

One could think that detecting moving objects with radar is a trivial task. To prove that it is not the case, we train a random forest model [2] to perform semantic segmentation on our dataset. Random forests use an ensemble of decision-trees to infer the classification output. Decision-trees, in turn, make predictions by comparing the input's features with a set of learned thresholds. Table 2 shows that this advanced thresholding algorithm achieves much poorer performance than our model, hence proving the non-triviality of the problem.

We decide to conduct experiments with PointNet++ as, to the best of our knowledge, it represents the best architecture tested on radar PCs. In particular, we slightly modify the implementation of [16] to account for the lower number of input-points/output-classes of our framework: both the number of samples in each SA layer and the number of nodes in the output FC network have been halved. However, we notice that the model have a much higher capacity than ours. We therefore design a shallow version of PointNet++ to enable fair comparison: the number of SA/FP layers has been reduced to two and set similarly to our architecture. Finally, we equip this shallow version of PointNet++ with the proposed pre-processing module to investigate its impact on the performance.

Table 2 contains the results. Despite the higher number of parameters/FLOPs, PointNet++ exhibits considerably poorer performance than RadarPCNN. As expected, the shallow PointNet++ experiences slight performance degradation. Interestingly, however, when equipped with our pre-processing module, it can achieve comparable results with RadarPCNN. This shows that our module can be successfully used on other point-wise processing architecture, helping the network to craft meaningful features for radar reflections. Moreover, it suggests that the proposed layer plays a major role

Table 2. Semantic segmentation results on our dataset (%).

Method	Moving pedestrian			Moving vehicle			Average			Param.	FLOPs
	Prec.	Recall	F_1	Prec.	Recall	F_1	Prec.	Recall	F_1		
Random forest	16.92	70.43	27.29	54.49	84.09	66.13	35.71	77.26	46.71	–	–
PointNet++ [16]	46.10	75.77	57.33	72.77	82.89	77.50	59.44	79.33	67.41	418.6K	1.55G
PointNet++ (shallow)	43.82	75.31	55.40	71.18	84.01	77.06	57.50	79.66	66.23	191.2K	**0.95G**
PointNet++ (sh. + our mod.)	47.70	**76.77**	58.84	73.16	**93.24**	81.99	60.43	**85.01**	70.42	198.8K	1.02G
RadarPCNN (ours)	**48.64**	75.82	**59.27**	**75.78**	91.44	**82.88**	**62.21**	83.63	**71.07**	**175.3K**	1.02G

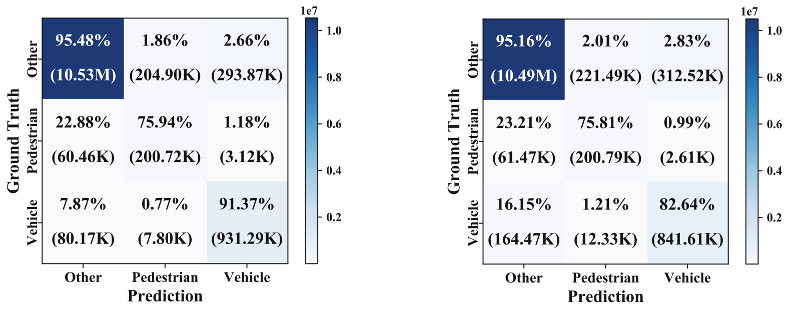

Fig. 3. Confusion matrices of RadarPCNN (left) and PointNet++ [16] (right). The color-map shows the points count: the darker the color, the higher the points number.

in the enhanced performance of our method w.r.t. PointNet++ [16]. Finally, it is worth noting that the improved shallow Pointnet++ still cannot outperform RadarPCNN, despite having nearly 15% more parameters. This suggests that our architecture has a better number-of-parameters/performance trade-off, resulting in a more efficient processing.

Figure 3 shows the confusion matrices of RadarPCNN (left) and PointNet++ [16] (right). It confirms the observation drawn from Table 2. Moreover, it is interesting to see how most of the errors come from negative predictions of positive class samples: only less than 2% of them are, indeed, mistakenly predicted as the wrong positive class. This effect is strongly due to the class imbalance in our dataset, which unfortunately makes the network marginally biased towards the negative class, despite all the precautions taken during training.

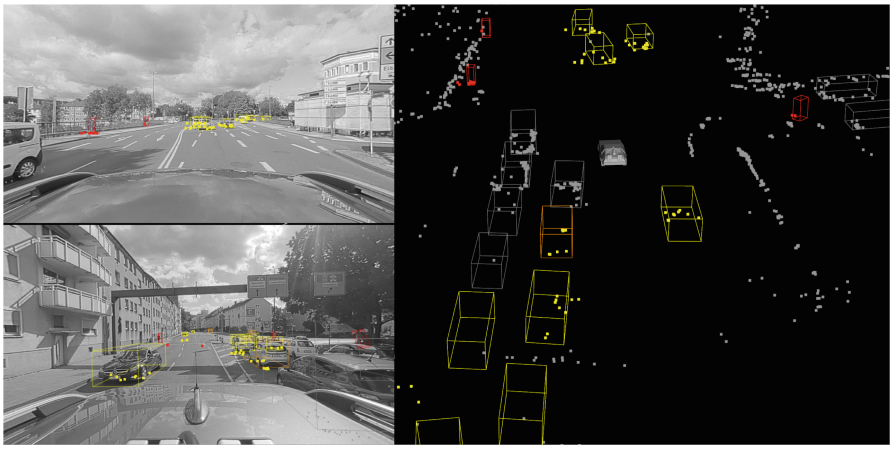

Fig. 4. RadarPCNN predictions. Yellow/red points are moving vehicle/pedestrian predictions. Ground truth BBs follow the same color-map. Gray BBs belong to stationary vehicles, while orange BBs marks vehicles with absolute speed between 1 and 2.5 m/s. Left. Front/rear camera view. Right. 3D visualization. Best viewed in color.

Figure 4 shows RadarPCNN predictions on a test frame. It can correctly classify moving vehicle/pedestrian as well as distinguish between moving and stationary vehicles. Moreover, it is worth noting how the network learns to predict moving objects independently from the threshold set during training. The orange bounding-box (BB) marks a slowly moving vehicle (see Fig. 4 caption): RadarPCNN can classify reflections from this object as belonging to a moving vehicle, even though during training these points were not assigned to that specific class. Finally, we find that sometimes the network mistakenly classifies reflections from bushes as pedestrian: we attribute this effect to the strong similarity between these two instances from the radar perspective.

4.4 Ablation Studies

Fusion Method. In this section we compare our attention mechanism with two fusion techniques: addition and concatenation. Table 3 shows that our attention mechanism represents the best solution, achieving the best F_1 scores with a reasonable number of parameters. The concatenation approach achieves comparable performance with ours, but involves ∼30K more parameters. Finally, notice how all the tested methods are well-suited for fusing multiple vectors.

Mean Shift vs FPS. Herein, we assess the impact of mean shift compared with the traditional farthest point sampling method. Figure 5 plots RadarPCNN F_1 scores while changing the number of representative points in the top/bottom branches of Fig. 1. We compute MS with different bandwidth values to account for the different number of representative points. Regarding FPS, we sample the necessary number of points directly from the input. We notice that, in the best configuration (leftmost), MS brings minor improvements over FPS. This is not a surprise: indeed, as the number of representative points increases, MS and FPS will tend to be similar, achieving the very same output when we sample all the input points (MS with infinitesimal bandwidth). Interestingly, however, as the number of representative points decreases, the impact of MS increases. This suggests that, focusing on high density locations, MS optimizes the usage of spatial relationship in such sparse data. Conversely, as the number of sampled points decreases, FPS cannot significantly cover the whole input space, thus failing to generate representative points for object of interest. The different behavior of the vehicle and pedestrian classes further confirms our observations. Since pedestrians have smaller sizes than vehicles, they produce lesser radar reflections. Therefore, a decrement in the number of representative points, dramatically decreases their likelihood of being sampled by FPS. Finally, it is worth stressing that the number of representative points strongly affects the amount of FLOPs demanded by the network. Since MS proved much more robust than FPS, it represents a promising solution for trading-off performance with computation, a very crucial resource in embedded, real-time systems.

Table 3. RadarPCNN performance using different fusion methods (%).

Method	Moving pedestrian			Moving vehicle			Average			Param.
	Prec.	Recall	F_1	Prec.	Recall	F_1	Prec.	Recall	F_1	
Conc	48.27	**76.50**	**59.19**	74.98	91.78	82.54	61.63	**84.14**	70.87	206.9K
Add	47.11	75.87	58.88	74.07	**92.13**	82.12	61.09	84.00	70.50	**174.1K**
Att (ours)	**48.64**	75.82	**59.27**	**75.78**	91.44	**82.88**	**62.21**	83.63	**71.07**	175.3K

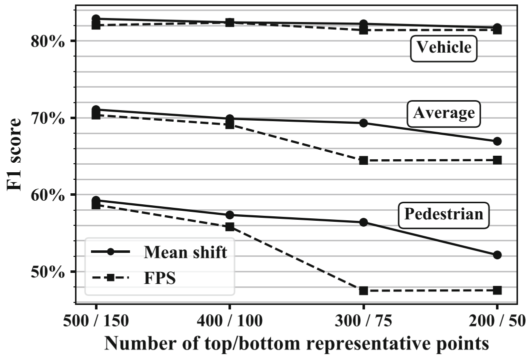

Fig. 5. MS vs FPS under various configuration of the number of representative points.

5 Conclusions

Despite PointNet++ being a milestone in raw PCs processing, radar data requires further tweaks in order to be efficiently processed. In this work, we show that the performance of PointNet++ – and presumably other methods – on radar PCs can be drastically improved by using radar information to learn new point features. In addition, we show that it is possible to further improve semantic segmentation performance by taking into account the intrinsic properties of radar while designing the architecture. Indeed, RadarPCNN is capable to achieve state-of-the-art results, using less memory than previous ML approaches.

About promising future directions, it would be interesting to see how the preprocessing module proposed in this work would suit other point-wise processing architectures. Finally, we notice from visualization analyses that most of the errors performed by our architecture are present only for few frames, therefore we believe that the network performance can be further improved by the use of temporal information. To this end, we strongly believe that MS could represent a key element for the deployment of RNNs in point-wise techniques for radar.

References

1. Alessandretti, G., et al.: Vehicle and guard rail detection using radar and vision data fusion. IEEE Trans. Intell. Transp. Syst. **8**(1), 95–105 (2007). https://doi.org/10.1109/TITS.2006.888597

2. Breiman, L.: Random forests. Mach. Learn **45**(1), 5–32 (2001). https://doi.org/10.1023/A:1010933404324
3. Caesar, H., et al.: nuScenes: a multimodal dataset for autonomous driving. CoRR **abs/1903.11027** (2019)
4. Engelcke, M., et al.: Vote3Deep: fast object detection in 3D point clouds using efficient convolutional neural networks. In: IEEE International Conference on Robotics and Automation, ICRA, pp. 1355–1361 (2017). https://doi.org/10.1109/ICRA.2017.7989161
5. Eriksson, L.H., As, B..: Automotive radar for adaptive cruise control and collision warning/avoidance. In: Radar 1997 (Conf. Publ. No. 449), pp. 16–20 (1997). https://doi.org/10.1049/cp:19971623
6. Ester, M., et al.: A density-based algorithm for discovering clusters in large spatial databases with noise. In: Proceedings of the Second International Conference on Knowledge Discovery and Data Mining (KDD-1996), pp. 226–231 (1996)
7. Feng, Y., et al.: GVCNN: group-view convolutional neural networks for 3D shape recognition. In: IEEE Conference on Computer Vision and Pattern Recognition, CVPR, pp. 264–272 (2018). https://doi.org/10.1109/CVPR.2018.00035
8. Feng, Z., et al.: Point cloud segmentation with a high-resolution automotive radar. In: 10th GMM-Symposium on Automotive meets Electronics, AmE 2019, pp. 1–5 (2019)
9. Fukunaga, K., Hostetler, L.D.: The estimation of the gradient of a density function, with applications in pattern recognition. IEEE Trans. Inf. Theory **21**(1), 32–40 (1975). https://doi.org/10.1109/TIT.1975.1055330
10. Hochreiter, S., Schmidhuber, J.: Long short-term memory. Neural Comput. **9**(8), 1735–1780 (1997). https://doi.org/10.1162/neco.1997.9.8.1735
11. Li, Y., et al.: PointCNN: convolution on x-transformed points. In: Advances in Neural Information Processing Systems 31: Annual Conference on Neural Information Processing Systems, NeurIPS, pp. 828–838 (2018)
12. Lin, T., et al.: Focal loss for dense object detection. In: IEEE International Conference on Computer Vision, ICCV, pp. 2999–3007 (2017). https://doi.org/10.1109/ICCV.2017.324
13. Prophet, R., et al.: Pedestrian classification for 79 GHz automotive radar systems. In: IEEE Intelligent Vehicles Symposium IV, pp. 1265–1270 (2018). https://doi.org/10.1109/IVS.2018.8500554
14. Qi, C.R., et al.: PointNet++: deep hierarchical feature learning on point sets in a metric space. In: Advances in Neural Information Processing Systems 30: Annual Conference on Neural Information Processing Systems, pp. 5099–5108 (2017)
15. Qi, C.R., et al.: PointNet: deep learning on point sets for 3D classification and segmentation. In: IEEE Conference on Computer Vision and Pattern Recognition, CVPR, pp. 77–85 (2017). https://doi.org/10.1109/CVPR.2017.16
16. Schumann, O., et al.: Semantic segmentation on radar point clouds. In: 21st International Conference on Information Fusion, FUSION, pp. 2179–2186 (2018). https://doi.org/10.23919/ICIF.2018.8455344
17. Shelhamer, E., et al.: Fully convolutional networks for semantic segmentation. CoRR **abs/1605.06211** (2016)
18. Sultana, F., et al.: Advancements in image classification using convolutional neural network. CoRR **abs/1905.03288** (2019)
19. Wöhler, C., et al.: Comparison of random forest and long short-term memory network performances in classification tasks using radar. In: Sensor Data Fusion: Trends, Solutions, Applications, SDF, pp. 1–6 (2017). https://doi.org/10.1109/SDF.2017.8126350

20. Yang, B., et al.: Attentional aggregation of deep feature sets for multi-view 3D reconstruction. CoRR **abs/1808.00758** (2018)
21. Zaheer, M., et al.: Deep sets. In: Advances in Neural Information Processing Systems 30: Annual Conference on Neural Information Processing Systems, pp. 3391–3401 (2017)
22. Zhou, Y., Tuzel, O.: VoxelNet: end-to-end learning for point cloud based 3D object detection. In: IEEE Conference on Computer Vision and Pattern Recognition, CVPR, pp. 4490–4499 (2018). https://doi.org/10.1109/CVPR.2018.00472

LSTM Neural Network for Fine-Granularity Estimation on Baseline Load of Fast Demand Response

Shun Matsukawa[1(✉)], Keita Suzuki[1], Chuzo Ninagawa[1], Junji Morikawa[2], and Seiji Kondo[2]

[1] Smart Grid Power Control Engineering Joint Laboratory, Gifu University, Gifu, Japan
s_matsu@gifu-u.ac.jp
[2] Mitsubishi Heavy Industries Thermal Systems, Ltd., Kiyosu, Japan

Abstract. In the future power system called Smart Grid, power generators using renewable energies will be widely introduced to the power grid and required to balance supply and demand on the grid quickly. Therefore, fast automated demand response (FastADR) that contributes to balance the power grid from demand side through electrical facilities like building air conditioner are focused recently. When electric grid operator will pay incentive to aggregators of the demand side, it is important to estimate accurate baseline load. However, the FastADR must returns quick response by unit of seconds or minute (fine-granularity), therefore it is difficult to estimate baseline load accurately using conventional method. In this research, the baseline load estimation model for air-con time-series data is constructed using long short-term memory (LSTM) neural network, and compared with multilayer perceptron (MLP) neural network model for baseline load estimation. The training and evaluating time-series data is generated by air-con simulator (AE) carried out on the virtual building. In the estimation results using data that were simulated for a month, the average estimation error of the LSTM model is 2.7% and of the MLP model is 5.3%. Therefore, the LSTM model is more effective for baseline estimation than the MLP model. However, data in various situations are required.

Keywords: Smart Grid · FastADR · Baseline estimation · Neural networks · LSTM

1 Introduction

In the future power system, called Smart Grid, photovoltaics and other power generators using renewable energies will be widely introduced to the power grid. These generators may face difficult supply and demand balancing on the grid because these renewable supplies are depending on the environmental condition such as weather [1]. To solve this problem, it is effective to control electrical load quickly from demand side, that is, so-called demand response (DR). The quick and automatic responses of the demand side, discharge from storage batteries or power limitation of electrical facilities for example, help the grid effectively. The system for it is called fast automated demand response (FastADR) [2].

As regards target electrical facilities for FastADR, building air-conditioners (ACs) are to be promising. The power consumption of ACs accounts for about 40% of the building power consumption, and more, it can be controlled flexible [3]. These large capacity and control flexibility are advantages for the target of the FastADR. When the electrical demand is high, an aggregator receives an order of power suppression from the electric grid operator. The aggregator sends power consumption limitation commands to the ACs, and ACs suppress the power consumptions. The suppressed powers will be aggregated from many ACs in many buildings. The electric grid operator will pay incentive to the aggregator.

Here, the price of the incentive depends on the amount of the power suppressed during the DR period. Therefore, estimating the power consumption when the DR is not occurred is required. This amount of the power consumption is called baseline load. Conventional DR is a slow demand response that responds through over 30 min, and is kept for a long period of time. Therefore, a baseline load estimation method that averages past data, such as the XofY method [4], has been applied.

However, the FastADR is required to response quickly through unit of seconds or minute [5]. Therefore it is not appropriate to estimate baseline load using conventional method. The AC operation data acquired during FastADR has 2 features, 1) the data highly depends on short-term (fine-granularity) time-series, 2) only a few valuable data can be acquired from ACs on actual building. Considering these features, the regression method [4, 6] is the most appropriate for AC's baseline estimation in FastADR between some method studied previously [7].

In previous studies, the multilayer perceptron (MLP) model is adopted to estimate electrical load of many facilities [8]. Time-series data is required to input into the model parallelly. On the other hand, the long short-term memory (LSTM) neural networks [9, 10] is used as models represented AC protecting operation [11, 12]. However, the baseline estimation research work using LSTM is not very targeted.

In this research, baseline estimation model using LSTM neural networks is constructed. The model is trained and evaluated with AE [13], an air-con simulation model. In comparison, a MLP model is constructed, trained and evaluated simultaneously.

2 Simulation Environments

2.1 Baseline Load of AC Operation on FastADR

In this research, the FastADR occurs in 4 time periods, from 9:00 to 10:00, from 11:00 to 12:00, from 14:00 to 15:00 and from 16:00 to 17:00. Power limitation command is send to AC for every 10 min. The limitation command is determined by Real-Time Pricing (RTP) optimizing algorithm [12, 15].

Figure 1 shows the concept of the FastADR operation. Bold black line indicates the power limitation command and circle marker indicates the power consumption P [kW] in a minute. The baseline load [kWh] is indicated by gray area, it is integral value between dotted line (Ps when the FastADR does not occurred) and x axis line ($P = 0.0$). The dotted line does not be estimated in this research because the baseline load is estimated directly. Since the power limitation command determines the upper limit of the power consumption, power consumption does not always follow the power limitation command.

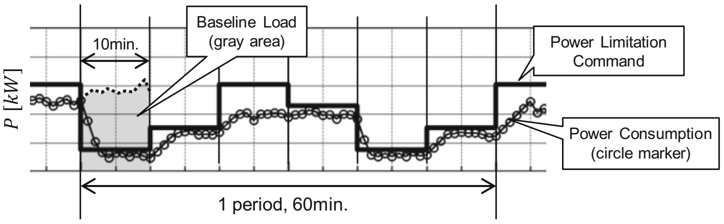

Fig. 1. Concept diagram of the power limitation command and baseline load

2.2 Construction of Virtual Building

The construction of a virtual building using in this research is shown in Fig. 2. The building has 10 floors, and all floors are separated into 2 areas, called blocks. Each block is installed 6 numbers of indoor units, and these indoor units are controlled by 20 outdoor units. Total cooling area is 6000 [m^2], separated into 20 blocks, installed 120 indoor units. This building does not exist, but assumed general office building.

The outdoor units in blocks are grouped in 3 types of rated power. The rated power of type 1 is 45 [kWh], and type 2 is 32 [kWh]. These are determined from actual units installed in office room on actual building. And the rated power of type 3 is 68 [kWh], this unit is installed in rooms that is required high air-con load like server room or ceiling floor. The AE is simulated these units by changing its parameter, therefore the power consumption and room temperature are follow to common dynamic characteristics.

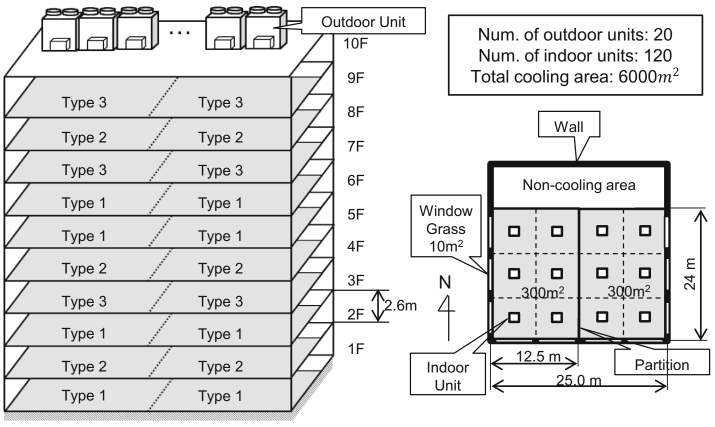

Fig. 2. Construction of the virtual building

2.3 Construction of Air-Con Simulation Model

In AE, the power consumption and room temperature is simulated according to the following formula based on the recurrence formula developed in the previous study [13]:

$$p(t+\Delta t) = p(t) + D(t)\Delta t \tag{1}$$

$$T_{Ai}(t+\Delta t) = T_{Ai}(t) + \frac{1}{C_{Hi}}(Q_{Li}(t) - Q_{ACi}(\mathrm{t}))\Delta t \tag{2}$$

Here, $P(t)$ indicates power consumption [kW] for each discrete time t [sec], and $D(t)$ indicates power change rate [kW/s]. Δt indicates a time step and 10 [sec] is assigned to it in this research. T_{Ai} indicates room temperature measured by inner unit i, C_{Hi} is heat capacity of inner unit i, $Q_{Li}(t)$ and $Q_{ACi}(\mathrm{t})$ are inner heat load and air-con cooling capacity of inner unit i, respectively. $D(t)$ is described as following formula:

$$D(t) = S_{OV}^{PL} D_{DWN} + \left(1 - S_{OV}^{PL}\right)\left\{S_{OV}^{P^*} D_{DWN} + \left(1 - S_{OV}^{P^*}\right) S_{FR}^{PL} S_{FR}^{P^*} D_{UP}\right\} \tag{3}$$

$\mathrm{D_{UP}}$ is the power rise rate [kW/s], and $\mathrm{D_{DWN}}$ is the power fall rate [kW/s]. S_{OV}^{PL} and S_{FR}^{PL} represent the current power consumption tracking state (0 or 1) with respect to the power limitation command value $\mathrm{P_L}$ [kW], and $S_{OV}^{P^*}$ and $S_{FR}^{P^*}$ are the target power indicates the tracking state (0 or 1) for $P^*(t)$ [kW]. $P^*(t)$ is determined from multiple linear regression model [7] with outdoor temperature and thermo-on capacity (total cooling capacity of operating indoor unit) as input variables. Since it is difficult to construct the fine vibration of P model analytically, a stochastic model is constructed from the acquired data.

Figure 3 indicates power consumption acquired from actual building on a day in August, 2018 (Fig. 3 top) and simulated power consumption on same day (Fig. 3 bottom). Some parameters like inner head load cannot acquire accurately, therefore it is impossible simulate actual consumption completely from the outset. However, AE simulates power consumption and room temperature sequentially, then the time dependency of the simulated data is plausible.

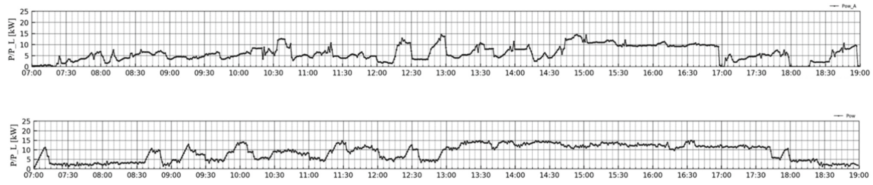

Fig. 3. Acquired power consumption (top) and simulated power consumption (bottom). The data were acquired from 7:00 to 19:00. Data is plotted on 1 min interval.

3 Long Short-Term Memory Model for Baseline Estimation

The LSTM neural network [9, 10] is a kind of recurrent neural network (RNN) used in computational neuroscience and machine learning applications widely. In LSTM, nodes in the hidden layer are replaced with complicated units called memory units, so it is possible to overcome the vanishing gradient problem and hold long time-series input data information compared with the normal RNN.

The memory unit has input/forget/output gates and a memory cell in addition to a normal input receiving node. By forgetting unnecessary information with a forget gate while recursively referring to the memory cell holding its own state, it can be expected to keep long-term characteristics of time-series into the unit. The three gates and the input receiving node are represented following formula:

$$g(\boldsymbol{x}) = f\left(\sum\nolimits_i \boldsymbol{u}_{in}\boldsymbol{x}_i(t) + \boldsymbol{u}_{re}\boldsymbol{z}_i(t-1)\right) \tag{4}$$

Here, u_{in} is the weight of an input variable x_i, and u_{re} is the weight of output value from the memory cell z_i. f indicates an activation function.

The LSTM model constructed in this research is shown in Fig. 4. The minimum unit of time is 5 min, called frame m. The representation value of a frame is an average value during 5 min. Moreover, q indicates the 10 min separation. A time point when estimate baseline is represented as (q, m), it means the last minute of the last frame m of the separation q. Dimension of input vector $\boldsymbol{x}(q, m)$ is 10, and dimension of output vector $\boldsymbol{y}(q+1)$ is 2.

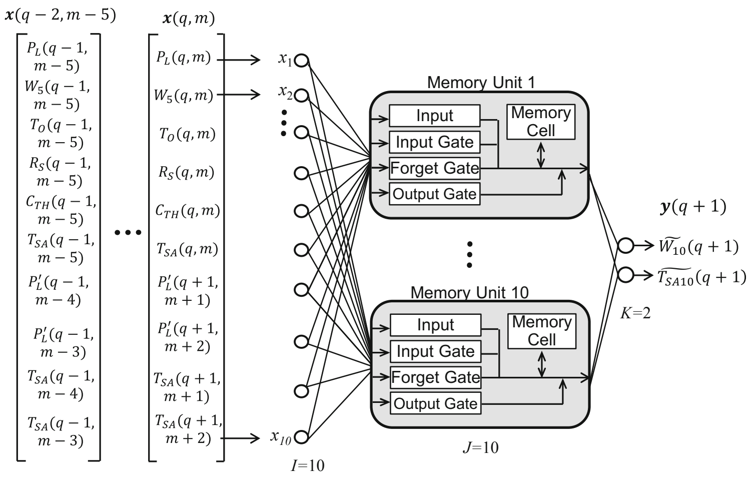

Fig. 4. LSTM model for baseline estimation

In this research, a input time-series is consisted from 6 frames data. The length of the time-series is determined from covariance of the input variables. The covariance between power consumption at time t [min.] and room temperature is maximized at $t = -15$ and others are $t = 0$, then we determined the time-series length to 30 min, in other words, 6 frames. Then a time-series contains $\boldsymbol{x}(q-2, m-5)$ to $\boldsymbol{x}(q, m)$.

The following variables were used for $\boldsymbol{x}(q, m)$; $P_L(q, m)$ is the "acquired" power limitation command [kW], $W_5(q, m)$ is the "acquired" amount of power consumption for frame m [kWh]. $T_O(q, m)$ is the outdoor temperature [°C], and $R_S(q, m)$ is the solar radiation [kWh]. T_O and R_S are acquired at Nagoya, Japan by Japan Meteorological Agency. $T_{SA}(q, m)$ is the average difference between set temperature T_{Si} and room temperature T_{Ai} of indoor unit i. $P'_L(q+1, m+1)$ and $P'_L(q+1, m+2)$ are power limitation command [kW] of "next" 10 min. While baseline estimation, these variables will be assigned a "limitation released" value. $T_{SA}(q+1, m+1)$ and $T_{SA}(q+1, m+2)$ are the "acquired" temperature difference of next 10 min. These variables have highly relation to power consumption [7].

The model outputs the power consumption and average difference between set room temperature and observed room temperature for next 2 frames.

The size of the hidden layer is 10. In our previous studies, this size effects to learning time but not accuracy, then it was determined empirically considering learning rate and learning epoch. Activation function of the hidden layer is sigmoid, and optimization algorithm is Adam [14].

4 Examination and Results

4.1 Data Processing and Model Training

The LSTM models are trained for each block. To train the LSTM models, it is necessary to observe the data simultaneously that FastADR was occurred data and was not occurred. However, these data can be acquired in an either-or situation. Therefore, in this research, the LSTM models were trained using the data simulated by the AE. The data simulated by the AE is slightly different for each block of the same type because the AE operates stochastically.

The AE simulated 5 patterns of the FastADR occurrence, 1) not occurred, 2) occurred in period 1, 3) occurred in period 1 and 2, 4) occurred in period 1-3 and 5) occurred in all periods. 17 days in August were assumed as the simulation situation. Training data was constructed based on the pattern 5. The training answer of the power consumption during 10 min W_{10} for each period was merged from each pattern data. For example, a $W_{10}(q, m)$ during a period was calculated from pattern 1 data, and it was used as one element of the $\boldsymbol{y}(q+1)$ in pattern 5. This preprocess is possible because of simulation.

After that, these frame data were scaled by max/min constant value respectively. The data per a day were acquired every minute for 10 h, therefore frame data $\{\boldsymbol{x}(1, 1), \ldots., \boldsymbol{x}(q, m), \ldots., \boldsymbol{x}(59, 119)\}$ were acquired per a day in a block.

Training time-series is constructed from them. The n-th training time-series X_n is represented as below:

$$\boldsymbol{X}_n = \{\boldsymbol{x}(\left\lfloor \frac{n}{10} \right\rfloor, n - m + 6) \mid m = 0, \ldots, 6\} \tag{5}$$

The X_n is a time-series obtained by shifting X_{n-1} forward by a frame.

All weights of the LSTM models were initialized randomly by uniform distribution between 0.0 and 0.001. The gradients of the weights were calculated by Back Propagation Through Time (BPTT) method [16] and new weights were calculated from these gradients. The training data batch size is 1 (same as online learning). The learning rate was optimized by the Adam algorithm. In this research, the training was repeated for 100 epochs.

For comparing, the MLP models were trained simultaneously. The structure of the MLP model was same as the LSTM model without inputting time-series parallelly into MLP model.

4.2 Evaluation on Performance of the Model

The models were evaluated using 2 days in August, 2018 that were not used to train. One day is the hottest day in the month, and another is the generally day in the month.

The estimation errors were defined as relative rate of difference between total estimated baseline load and total actual baseline load during FastADR periods. Represent the k-th estimated baseline load for $\boldsymbol{X}_k$ at period Pr on block b as $\widetilde{\mathrm{W}_{10}}_k^{\mathrm{Pr,b}}$. The index k is assigned from 1 to 12, it means the frame number during a period. The total estimated baseline load at period Pr is represented as follows:

$$\widetilde{\mathrm{W}_{60}}^{\mathrm{Pr}} = \sum\nolimits_b^{20} \sum\nolimits_k^{12} \widetilde{\mathrm{W}_{10}}_k^{\mathrm{Pr,b}} \tag{6}$$

The total actual baseline load $\mathrm{W}_{60}{}^{\mathrm{Pr}}$ is calculated in the same way. The estimation error at period Pr is represented as:

$$\varepsilon^{Pr} = \frac{\left(\widetilde{\mathrm{W}_{60}}^{\mathrm{Pr}} - \mathrm{W}_{60}{}^{\mathrm{Pr}}\right)}{\mathrm{W}_{60}{}^{\mathrm{Pr}}} \times 100[\%] \tag{7}$$

ε^{Pr} indicates the errors in a period on the entire building. The aggregator will estimate the baseline load for each entire building, therefore evaluating ε^{Pr} is considered appropriate in practice.

Estimation results are shown in Fig. 5. Black bar indicates the $\mathrm{W}_{60}{}^{\mathrm{Pr}}$, gray bar indicates the $\widetilde{\mathrm{W}_{60}}^{\mathrm{Pr}}$ estimated by the LSTM model, dotted bar indicates the $\widetilde{\mathrm{W}_{60}}^{\mathrm{Pr}}$ estimated by the MLP model. Bar with horizontal line indicates the observed power consumption, $\mathrm{W}_{60}{}^{\mathrm{Pr}'}$. ε^{Pr} is shown as difference between the black bar and the gray bar compared to the black bars and dotted bars.

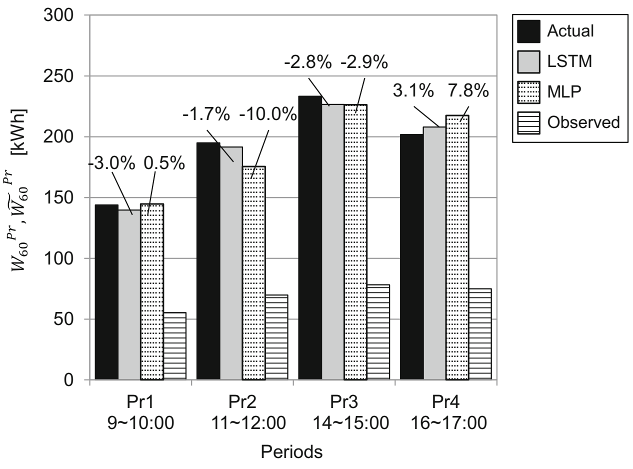

Fig. 5. Comparison of the estimation results

Calculated errors of the LSTM model are, $\varepsilon^1 = -3.0[\%]$, $\varepsilon^2 = -1.7[\%]$, $\varepsilon^3 = -2.8[\%]$ and $\varepsilon^4 = 3.1[\%]$. Calculated errors of the MLP model are, $\varepsilon^1 = -0.5[\%]$, $\varepsilon^2 = -10.0[\%]$, $\varepsilon^3 = -2.9[\%]$ and $\varepsilon^4 = 7.8[\%]$. The estimation results of the LSTM model are better than the MLP model except for period 1. In particular, the error is smaller than 8.3% in period 2.

Comparing the average $\varepsilon^{avg} = \frac{1}{4}\sum_{Pr=1}^{4} |\varepsilon^{Pr}|$ between the LSTM and the MLP model, the ε^{avg} of LSTM model is 2.7[%], and the ε^{avg} of the MLP model is 5.3[%]. Therefore, it can be said the LSTM model is more effective than the MLP model for the baseline load estimation.

4.3 Study on a Few Training Data

To train the LSTM model, large amount of data (over 1000 time-series) is used in general [9]. In this research, the models were trained using data acquired in a month similarly. However, in application, there may be cases where only a small number of data can be acquired in a few days. It is necessary to examine how many and various data are required to train the LSTM model effectively.

In this study, three kinds of data sets are used. First is a data set acquired in one day, 120 time-series, from august, 2018 (set A). Second is a data set acquired in one week (5 days), 600 time-series, from august, 2018 (set B). Third, sampled 10% from data acquired in a month, 273 time-series (set C). The set A and B reproduce the situation where the number of obtainable data is small. The set C reproduces the situation where the wide variety of the few data can be acquired. The estimation results are evaluated using data that were not used to train. Kullback–Leibler divergence (KLD) [17] between the all-time actual baseline load and the all-time estimated baseline load is calculated.

Figure 6 shows the results. Sparse dotted bar indicates the KLD of the MLP model, and dense dotted bar indicates the KLD of the LSTM model. Vertical axis indicates the KLD, the lower value is similar (good) and upper value is dissimilar (poor). In this result, the MLP model is less affected by data set, but the LSTM model is affected. The MLP model is better than the LSTM model on the set A, but in the set C, that result has been reversed. It is considered that the LSTM model learns data trends through a variety of training data rather than the number of data.

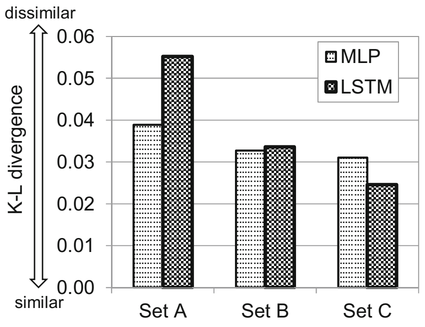

Fig. 6. Comparison between MLP model and LSTM model trained using 3 data sets

5 Conclusion

It is required to estimate baseline load in short-term (fine-granularity) time-series for FastADR in the future Smart Grid. In this research, a LSTM model was constructed to estimate baseline load under the assumed FastADR situation. The FastADR was assumed to last 1 h and send a power limitation command every 10 min.

The LSTM model was trained using time-series generated by an air-con simulator, AE. The virtual building for the AE simulation is constructed from 20 blocks on 10 floors and set upped 6 air-con inner units controlled by 1 outdoor unit for each block. AE simulated each outdoor unit on different situation. The power limitation commands were sent 4 times for a day, and the simulator generates data for a month. The estimation errors were calculated for each power limitation.

Comparison with the MLP model inputted time-series data parallelly, the average estimation error of the LSTM model is 2.7% and of the MLP model is 5.3%. Therefore, the LSTM model is more effective for baseline estimation than the MLP model. However, when trained the models using few data, the estimation error of the LSTM model was increased compared with the MLP models. On the other hand, when trained using the data set that contains various but small amounts of data, the result has been reversed. Therefore, it is more important for the LSTM model to training using various data than the amount of the data.

References

1. California ISO: What the duck curve tells us about managing a green grid. https://www.caiso.com/Documents/FlexibleResourcesHelpRenewables_FastFacts.pdf. Accessed 28 Feb 2020
2. Nakamura, T., Morikawa, J., Ninagawa, C.: Prediction model on room temperature side effect due to FastADR aggregation for a cluster of building air-conditioning facilities. Electr. Eng. Jpn. **199**(3), 17–25 (2017)
3. Ma, O., Alkadi, N., Cappers, P., Denholm, P., Dudley, J., Goli, S., Hummon, M., Kiliccote, S., MacDonald, J., Matson, N., Olsen, D., Rose, C., Sohn, M.D., Starke, M., Kirby, B., O'Malley, M.: Demand response for ancillary services. IEEE Trans. Smart Grid **4**(4), 1988–1995 (2013)
4. Wijaya, T.K., Vasirani, M., Aberer, K.: When bias matters: an economic assessment of demand response baseline for residential customers. IEEE Trans. Smart Grid **5**(4), 1755–1763 (2014)
5. PJM: PJM Empirical Analysis of Demand Response Baseline Methods Results. https://www.pjm.com/-/media/markets-ops/demand-response/pjm-empirical-analysis-of-dr-baseline-methods-results.ashx?la=en. Accessed 28 Feb 2020
6. Wang, F., Li, K., Liu, C., Mi, Z., Shafie-Khah, M., Catalão, J.P.S.: Synchronous pattern matching principle-based residential demand response baseline estimation: mechanism analysis and approach description. IEEE Trans. Smart Grid **9**(6), 6972–6985 (2018)
7. Matsukawa, S., Ninagawa, C., Morikawa, J., Inaba, T., Kondo, S.: Stable segment method for multiple linear regression on baseline estimation for smart grid fast automated demand response. In: Proceedings of 9th IEEE PES ISGT Asia 2019, pp. 2571–2576. IEEE, Chengdu (2019)
8. Debnath, K.B., Mourshed, M.: Forecasting methods in energy planning models. Renew. Sustain. Energy Rev. **88**, 297–325 (2018)
9. Hochreiter, S., Schmidhuber, J.: Long short-term memory. Neural Comput. **9**(8), 1735–1780 (1997)
10. Gers, F.A., Schmidhuber, J., Cummins, F.: Learning to forget: continual prediction with LSTM. Neural Comput. **12**(10), 2451–2471 (2000)
11. Matsukawa, S., Ninagawa, C., Morikawa, J., Inaba, T., Kondo, S.: LSTM prediction on sudden occurrence of maintenance operation of air-conditioners in real-time pricing adaptive control. In: ICANN 2019. Lecture Notes in Computer Science, vol. 11730, pp. 426–435 (2019)
12. Matsukawa, S., Takehara, M., Otsu, H., Morikawa, J., Inaba, T., Kondo, S., Ninagawa, C.: Prediction model on disturbance of maintenance operation during real-time pricing adaptive control for building air-conditioners. IEEJ Trans. Electr. Electron. Eng. **14**, 1219–1225 (2019)
13. Aoki, Y., Ninagawa, C., Morikawa, J., Kasai, T., Kondo, S.: A building multi-type air-conditioner emulator for development of machine learning algorithm on electric energy services. In: The papers of Technical Meeting on Smart Facilities. IEE Japan, Tokyo, pp. 61–66 (2019). (in Japanese)
14. Kingma, D.P., Ba, J.L.: Adam: a method for stochastic optimization. In: 3rd International Conference for Learning Representations, San Diego. arXiv:1412.6980 (2017)
15. Morikawa, J., Yamaguchi, T., Ninagawa, C.: Smart grid real-time pricing optimization management on power consumption of building multi-type air-conditioners. IEEJ Trans. Electr. Electron. Eng. **11**, 823–825 (2016)

16. Ismail, S., Ahmad, A.M.B.: Recurrent neural network with backpropagation through time algorithm for arabic recognition. In: Proceedings of 18th European Simulation Multiconference, Magdeburg. SCS Publishing House (2004)
17. Kullback, S., Leibler, R.A.: On information and sufficiency. Ann. Math. Stat. **22**(1), 79–86 (1951)

Predicting Permeability Based on Core Analysis

Harry Kontopoulos[1(✉)], Hatem Ahriz[1], Eyad Elyan[1], and Richard Arnold[2]

[1] School of Computer Science and Digital Media, The Robert Gordon University, Garthdee Rd., Aberdeen AB10 7QB, UK
h.kontopoulos1@rgu.ac.uk

[2] Corex (UK) Ltd., Units B1 - B3, Airport Industrial Park, Howe Moss Drive, Dyce, Aberdeen AB21 0GL, UK

Abstract. Knowledge of permeability, a measure of the ability of rocks to allow fluids to flow through them, is essential for building accurate models of oil and gas reservoirs. Permeability is best measured in the laboratory using special core analysis (SCAL), but this is expensive and time-consuming. This is the first major work on predicting permeability in the in the UK Continental Shelf (UKCS) based only on routine core analysis (RCA) data and a machine-learning approach. We present a comparative analysis of the various machine learning algorithms and validate the results, using permeability measured on 273 core samples from 104 wells. Results suggest that machine learning can predict permeability with relatively high accuracy. This opens new research directions in particular in the oil and gas sector.

Keywords: Machine learning · Support vector regression · Core analysis · Permeability prediction

1 Introduction

A range of different data is generated during the life-cycle of oil and gas fields, from exploration to abandonment. This data include regional geology, seismic reports, sedimentological models, drilling data, fluid and rock properties [16]. Geologists, reservoir engineers and other scientists combine this data and use their expertise to construct models of the reservoir, evaluate the volume of available hydrocarbons and engineer the most efficient and profitable way to extract them from the reservoir [18]. The most direct type of geological data about the formation come from core analysis, the laboratory examination of well core samples extracted during the drilling. It is the only time scientists can see and physically examine material from within the reservoir.

This work is part of a Knowledge Transfer Partnership (KTP) programme, funded by Corex UK Ltd. and Innovate UK.

Core analysis is usually divided into two stages. The first stage is called Routine Core Analysis (RCA) and the second stage is called Special Core Analysis (SCAL) [16]. RCA usually includes tests such as fluid saturations, porosity and permeability measurements. Those measurements are taken on plugs or core samples. A SCAL programme might include the measurement of relative permeabilities, capillary pressures and wettability among others. Furthermore, the effect of coring and other fluids on the SCAL parameters could be used to evaluate the damage they cause to the formation [23].

Core analysis data are usually expensive and time consuming (several weeks) to obtain [27]. However, they are deemed to be the most accurate source of information for reservoir characterisation and a thoroughly designed core analysis programme can result in a more productive reservoir later in their lifetime [18].

2 Related Work

Machine learning techniques have been used in the past in the context of core analysis mainly to extrapolate rarely available core analysis data to other more available types of data such as well log data [27]. Examples include prediction of permeability of gas reservoirs using well logs and core data [9,22], identifying drilling sweet-spots for gas hydrate reservoirs without pre-existing well logs [10,15], rock texture image classification using support vector machines [21], predicting permeability during acidizing [11] and predicting the optimal rate of penetration during drilling [12]. The work closest to ours is the study by Erofeev et al. [5] on the Chayandinskoye oil and gas condensate field in Russia. However, that study was limited to a single field and used desalination instead of drilling mud application during core analysis.

In contrast, this work relies on high quality data of actual permeability measurements obtained in the laboratory from a substantial number of core samples across a large number of wells across multiple fields of the UKCS and the north sea. Oil and Gas operators value the core analysis derived data as indispensable. However, budget constraints often limit the number of tests included in core analysis projects. A reliable and effective predictive method could be used alongside traditional routine core analysis techniques to fill the gap. The aim is to be able to provide the next best estimate when there is not enough funding for extensive laboratory measurements. As a proof of concept, the permeability is predicted after drilling mud application has been performed to the samples.

3 Methods

3.1 Dataset

The private dataset used here is part of the historical archive of Corex UK Ltd. It covers a significant part of the offshore area of the UK Continental Shelf (UKCS) and the north sea.

Table 1. Table showing the variables used, their corresponded type in R and their units

Feature	Type	Units
Top depth	Numeric	m
Pore volume	Numeric	cc
Porosity	Numeric	rate
Grain density	Numeric	gcc
Gas permeability	Numeric	mD
Initial permeability	Numeric	mD
Final permeability	Numeric	mD
Brine concentration	Numeric	ppm
Mud weight	Numeric	ppg
Mud type	Character	NA
Reservoir temperature	Numeric	C
Pore pressure	Numeric	atm
Overburden pressure	Numeric	psi

After data cleaning and preparation, the final dataset contained 273 observations and 13 features (Table 1). The number of samples might look small but core analysis is a laborious process with relatively small pace of generating data. The features include the pore volume, porosity, grain density, the top depth of the core, gas permeability, initial permeability, final permeability (output), brine concentration, mud weight, mud type, reservoir temperature, pore pressure, overburden pressure. Mud type is a categorical feature and it is encoded into three dummy variables, with LTOBM (Low Toxicity OBM) the reference level.

Initial permeability is the permeability measurement before drilling mud application while final permeability is the permeability measured after drilling mud application. Drilling mud application for the context of this research means the laboratory simulation of the drilling procedure in the field using a specific drilling mud system. Drilling mud systems are expected to interact with the rock formation and potentially reduce its permeability (Fig. 1). When centering or scaling of the input data is performed it is explicitly mentioned at the relevant model subsection otherwise the original values were used.

3.2 Prediction Models

A range of well established machine and statistical learning algorithms were applied to the given dataset. The main research question was whether the final permeability, after drilling mud application, can be predicted using the results of routine core analysis (RCA) tests as input. Therefore, the final permeability

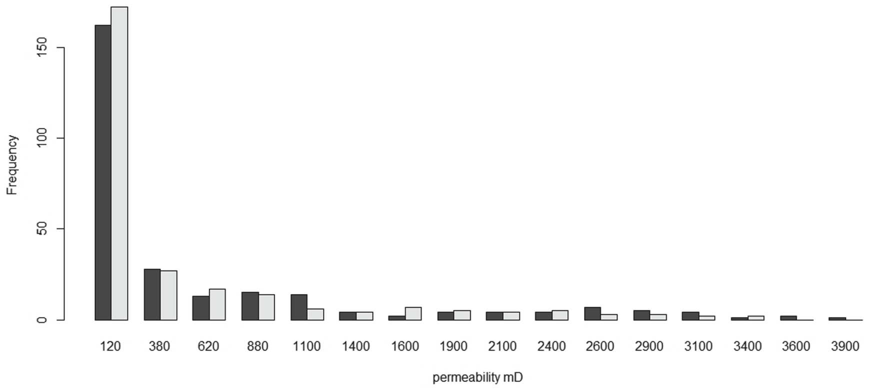

Fig. 1. The distribution of permeabilities before (dark grey) and after drilling mud application (light grey).

was selected as the output of the models. All the variables in Table 1 were used as input parameters.

Least Squares Linear Regression. The starting point of this research was to try and fit a linear model, represented by the formula:

$$Y = \beta_0 + \beta_1 X_1 + ... + \beta_p X_p + \epsilon \tag{1}$$

Least squares estimates the coefficients that minimise the following:

$$RSS = \sum_{i=1}^{n} \left(y_i - \beta_0 - \sum_{j=1}^{p} \beta j x_{ij} \right)^2 \tag{2}$$

The linear model was fitted using the **lm()** function from the R stats package [19]. The QR decomposition of the input matrix is used to estimate the coefficients [6].

Ridge Regression. Ridge regression adds a penalty to the loss function of least squares (Eq. 2). The penalty has the form $\lambda \sum_{j=1}^{p} \beta_j^2$ [13]. The penalty is controlled by the hyper-parameter λ, which is usually selected with grid search and cross validation. Ridge was fitted using the glmnet package in R [7].

Lasso Regression. This model is similar to Ridge except it applies an ℓ_1 penalty to minimise the RSS subject to the constraint $\lambda \sum_{j=1}^{p} |\beta j|$ [24]. Lasso tries to address some of the problems arising in Ridge regression. The ℓ_2 penalty used in Ridge minimises the coefficients towards zero but it does not turn any of them to exactly zero. Lasso instead can set a coefficient to zero and effectively perform feature selection. Lasso was fitted using the glmnet package in R [7].

Partial Least Squares (PLS). PLS identifies a set of components $Z_1, ...Z_M$ that are a linear combination of the original features [25]. The new components are fitted so they explain most of the variance in the predictors [14]. The idea behind this approach is that there are latent variables affecting the output that are not necessarily measured or captured in the dataset [26].

Support Vector Regression (SVR). Support Vector Regression estimates the weights of a hyperplane such that the RSS of the support vectors is minimised [4]. The support vectors are the only part of the dataset that participate in the estimation of the hyperplane equation and the minimization of the loss function. The input space was transformed into a higher dimension feature space using the radial basis function [3]. The SVR model was fitted using the e1071 R package [17]. The variables were scaled for zero mean and unit variance. The cost and gamma hyper-parameters were estimated by 10-fold cross validation, using the tune.svm() function.

Artificial Neural Networks (ANNs). A multi-layer perceptron [20] was used consisting of a feed-forward neural network with 13 neurons at the input layer, two hidden layers with five and three neurons respectively and an output layer with a single neuron for the final permeability. The model was trained using resilient back-propagation (RPROP) with weight backtracking [20] and the neuralnet R package [8]. The input was scaled with mean 0 and unit variance. The learning rate was set to 100 and the maximum number of allowed steps to 1e+05. The sum of square errors was the loss function.

Decision Trees and Random Forests. Regression Trees [1] predict the value of a continuous variable by dividing the input space into j distinct and not overlapping areas. For every new observation that falls into this area the average of the values of the training observations is returned. The regression tree was fitted with the tree package in R [2]. Random Forests build a number of trees in a bootstrapped version of the training samples. In each split step it only considers a random sample of m predictors from the total available ones. This number is typically $\sqrt{p}$, where p is the total number of features [14]. It then uses averaging across the trained trees to produce a final prediction.

4 Results and Discussion

A summary of the results for predicting the final permeability, after drilling mud application, using the various algorithms is presented in (Table 2). The dataset was divided into a training set (67%) and a test set (33%). The R^2, given by $1 - \frac{RSS}{TSS}$ with $TSS = \sum_i^n (y_i - \bar{y})$, on the training set and the MSE, given by $\frac{1}{n} \sum_i^n (\hat{y}_i - \bar{y})$, on the test set will be used to evaluate the models on the training and test set respectively.

Table 2. Table showing the R^2 on the training set and the MSE on the test set.

Algorithm name	R^2	MSE
Least Squares	0.916	50,020.24
Linear Lasso	0.725	50,927.96
Linear Ridge	0.881	51,251.47
PLS	0.894	50,150.91
SVR	0.900	44,135
ANN	0.997	323,477.3
Decision Tree	0.937	108,424.7
Random Forest	0.925	57,202.81

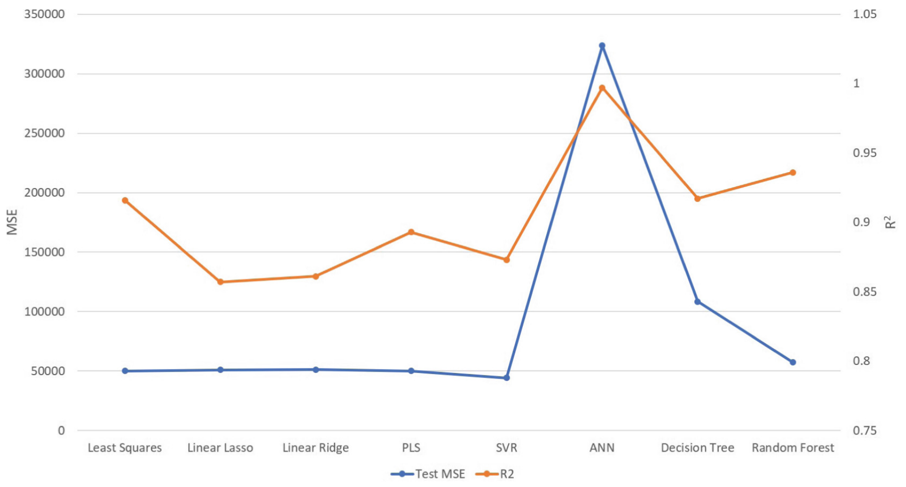

Fig. 2. Compare the models using R^2 on the training set (orange) and MSE on the test set (blue).

R^2 scores show that many algorithms fit the training data well. SVR, Least Squares and PLS having the lowest MSE (Fig. 2) on the test set. PLS and Lasso can give us great insight on the predictors affecting the response variable. According to the Least Squares model initial permeability, gas permeability and pore volume are the most significant features. (Fig. 3).

Lasso produced a sparse model only assigning the pore volume, initial permeability and mud type (WBM) non zero coefficients. PLS also produced a sparse model. The first six components are linear combinations of the top depth, gas permeability, initial permeability, brine concentration, pore pressure and overburden pressure.

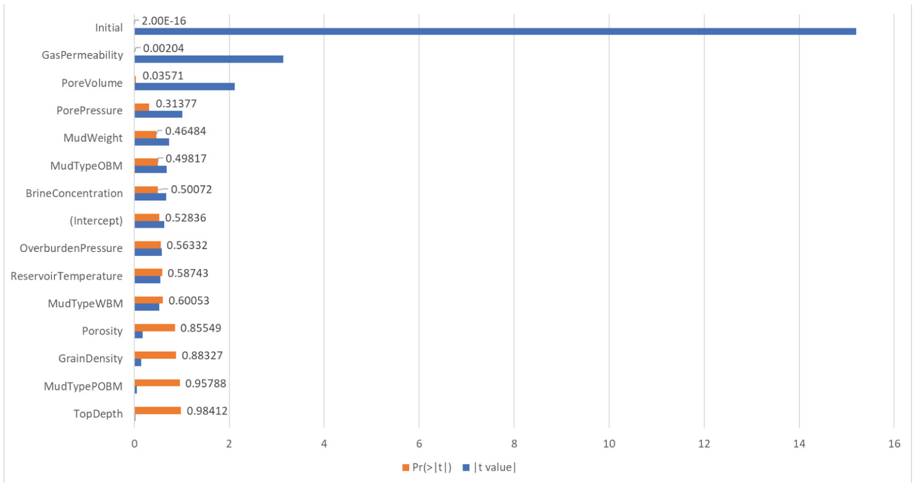

Fig. 3. The t value and the associated p value of the features for the least squares model.

Linear Regression Least Squares. The linear regression model has a R^2 on the training set of 0.916 and test set MSE 50020.24 (Fig. 4). R^2 suggests that the model fits the data relatively well but the MSE on the test set indicates that the predictive power requires further improvement.

Linear Lasso. The best lambda for the Lasso model was estimated by 10-fold cross validation at 12.429. The non zero coefficients for the best λ are pore volume, gas permeability, initial permeability, and mud type (WBM). Lasso has a test MSE of 50927.96 (Fig. 5). The model does not fit the training data as well as the Least Squares but it still manages to generalise well on the test set according to the MSE figure.

Linear Ridge. Ridge regression λ parameter was estimated similarly to Lasso using 10-fold cross validation. The value that resulted in the lowest cross validation error was 89.749. Ridge regression performance on the training dataset was estimated by means of R^2 at 0.881 (Fig. 5).

Partial Least Squares. PLS fit the data on par with the regularised linear models and SVR. R^2 is estimated at 0.894 (Fig. 6) on the training set and the MSE at 50150.91 on the test set. The number of components of the final model was estimated by 10-fold cross validation. The number of components with the lowest CV error was 5 components and it was the one used to generate the model PLS R^2 and MSE values.

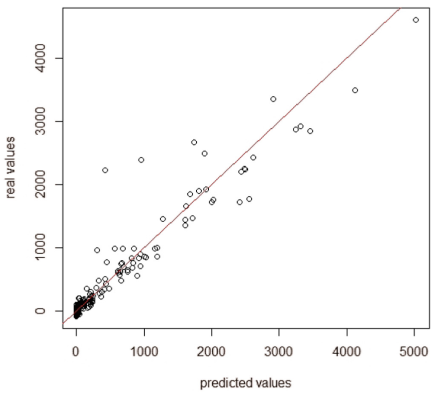

Fig. 4. The real against the predicted permeability values on the training set by Least Squares Regression.

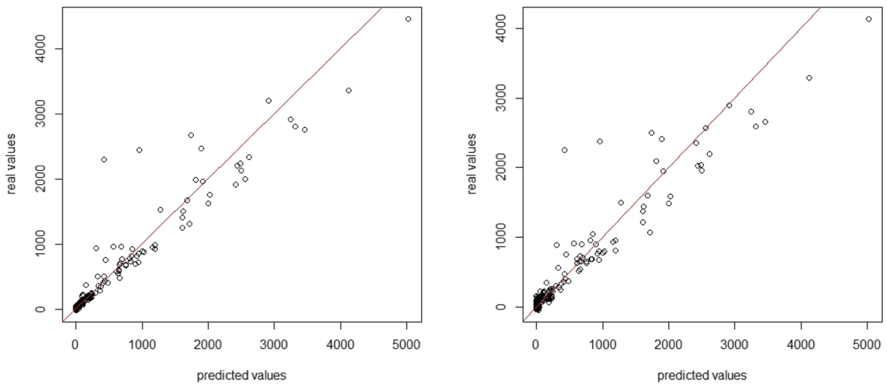

Fig. 5. The real against the predicted permeability values on the training set for the Lasso (left) and the Ridge model (right).

Support Vector Regression. SVR gave the most promising results so far. The SVR hyper-parameters were estimated by grid search at $\gamma = 0.01$ and cost $= 10$. The model fit the training data with a R^2 value of 0.9. Its MSE on the test set was estimated at 44135 (Fig. 6). SVR performs much better than Least Squares in the test set.

Artificial Neural Network. The Artificial Neural Network was the model that followed the closest the training data with an R^2 value of 0.997. However, it performed very poorly on the test set with an MSE of 323477.3 (Fig. 7). The high R^2 indicates that the model over-fits the training data while the very high test set MSE suggests that it fails to predict the permeability on unseen core samples.

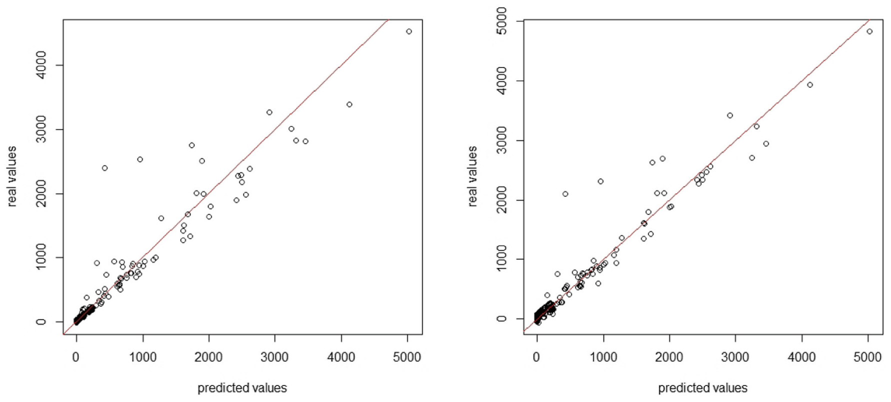

Fig. 6. The real against the predicted permeability values on the training set for the PLS (left) and the SVR model (right).

Decision Tree. The Decision tree model appeared to slightly over-fit the training data. Its R^2 was estimated at 0.937 and generalised poorly with MSE on test set at 57202.81. The decision tree model performs better on the test set than the neural network but not as good as the SVR model.

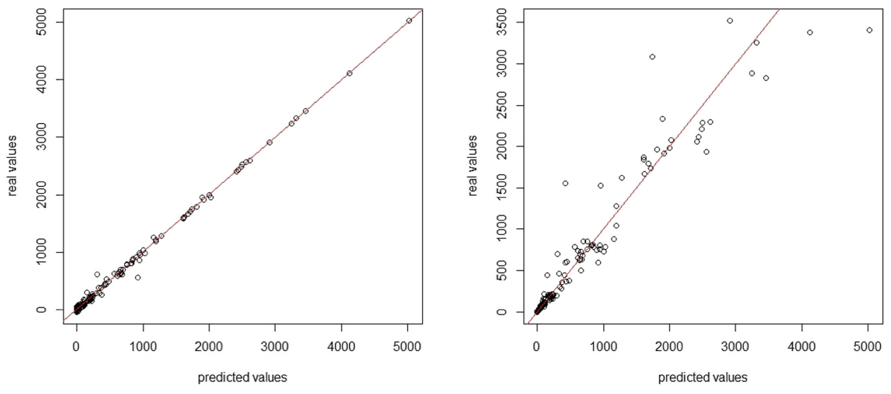

Fig. 7. The real against the predicted permeability values on the training set for the ANN (left) and the Random Forest model (right).

Random Forest. The mtry hyperparameter, that controls the number of variables randomly sampled as candidates at each split, was estimated at 11 using 10-fold cross validation, repeated three times. The R^2 value on the training set was 0.925. The Random Forest model was an improvement compare to the decision tree model and generalised relatively well on the test set with an MSE of 57202.81 (Fig. 7), albeit not as good as SVR.

5 Conclusion

This work showed that machine learning can be used alongside routine core analysis to predict final permeability, with SVR, Least Squares and PLS being the best models. Traditionally oil and gas companies only contract a small number of representative samples to be tested in the laboratory, due to financial constraints. Learning models based on historical data together with laboratory measurements of the limited number of financially approved measurements can alternatively provide a prediction for the rest of the available samples. This could be a new source of revenue for core analysis laboratories and a new service that can provide valuable information to operators to better manage their reservoirs. Future work might include more input features e.g. stratigraphic data that will improve the algorithm's performance in unseen cases or predict different types of output that can be of value for the oil and gas sector.

References

1. Breiman, L., Friedman, J., Stone, C.J., Olshen, R.A.: Classification and Regression Trees. Taylor & Francis, Monterey (1984)
2. Brian Ripley: tree: Classification and Regression Trees (2019). https://CRAN.R-project.org/package=tree. r package version 1.0-40
3. Burges, C.J.: A tutorial on support vector machines for pattern recognition. Data Min. Knowl. Disc. **2**(2), 121–167 (1998). https://doi.org/10.1023/A:1009715923555
4. Drucker, H., Burges, C.J.C., Kaufman, L., Smola, A.J., Vapnik, V.: Support vector regression machines. In: Mozer, M.C., Jordan, M.I., Petsche, T. (eds.) Advances in Neural Information Processing Systems, vol. 9, pp. 155–161. MIT Press (1997). http://papers.nips.cc/paper/1238-support-vector-regression-machines.pdf
5. Erofeev, A., Orlov, D., Ryzhov, A., Koroteev, D.: Prediction of porosity and permeability alteration based on machine learning algorithms. Transp. Porous Media **128**(2), 677–700 (2019). https://doi.org/10.1007/s11242-019-01265-3
6. Francis, J.G.F.: Comput. J., 265–271 (1961). https://academic.oup.com/comjnl/article/4/3/265/380632
7. Friedman, J.H., Hastie, T., Tibshirani, R.: Regularization paths for generalized linear models via coordinate descent. J. Stat. Softw. **33**(1), 1–22 (2010). https://www.jstatsoft.org/index.php/jss/article/view/v033i01
8. Fritsch, S., Guenther, F., Wright, M.N.: neuralnet: Training of neural networks (2019). https://CRAN.R-project.org/package=neuralnet
9. Gholami, R., Shahraki, A.R., Jamali Paghaleh, M.: Prediction of hydrocarbon reservoirs permeability using support vector machine (2012). https://www.hindawi.com/journals/mpe/2012/670723/
10. Gholami, R., Moradzadeh, A., Maleki, S., Amiri, S., Hanachi, J.: Applications of artificial intelligence methods in prediction of permeability in hydrocarbon reservoirs. J. Petrol. Sci. Eng. **122**(C), 643–656 (2014). https://doi.org/10.1016/j.petrol.2014.09.007
11. Gümrah, F., Sarkar, S., Tasti, Y.A., Erbas, D.: Genetic algorithm for predicting permeability during production enhancement by acidizing. Energy Sources **23**(3), 245–256 (2001). https://doi.org/10.1080/00908310151133942

12. Hegde, C., Gray, K.E.: Use of machine learning and data analytics to increase drilling efficiency for nearby wells. J. Nat. Gas Sci. Eng. **40**, 327–335 (2017). https://doi.org/10.1016/j.jngse.2017.02.019
13. Hoerl, A.E., Kennard, R.W.: Ridge regression: biased estimation for nonorthogonal problems. Technometrics **42**(1), 80–86 (2000). http://www.tandfonline.com/doi/abs/10.1080/00401706.2000.10485983
14. James, G., Witten, D., Hastie, T., Tibshirani, R.: An Introduction to Statistical Learning: with Applications in R. Springer Texts in Statistics. Springer-Verlag, New York (2013). https://doi.org/10.1007/978-1-4614-7138-7. https://www.springer.com/gp/book/9781461471370
15. Lee, J., Byun, J., Kim, B., Yoo, D.G.: Delineation of gas hydrate reservoirs in the Ulleung Basin using unsupervised multi-attribute clustering without well log data. J. Nat. Gas Sci. Eng. **46**, 326–337 (2017). https://doi.org/10.1016/j.jngse.2017.08.007. http://www.sciencedirect.com/science/article/pii/S1875510017303104
16. McPhee, C., Reed, J., Zubizarreta, I.: Core Analysis: A Best Practice Guide. Developments in Petroleum Science, vol. 64. Elsevier, Amsterdam (2015)
17. Meyer, D., Dimitriadou, E., Hornik, K., Weingessel, A., Leisch, F.: e1071: Misc Functions of the Department of Statistics, Probability Theory Group (Formerly: E1071), TU Wien (2019). https://CRAN.R-project.org/package=e1071. r package version 1.7-3
18. Ottesen, B., Hjelmeland, O.: The Value Added from Proper Core Analysis, p. 12 (2008)
19. R Core Team: R: A language and environment for statistical computing (ISBN 3-900051-07-0). R Foundation for Statistical Computing (2019). https://www.R-project.org/
20. Riedmiller, M.: Advanced supervised learning in multi-layer perceptrons-from backpropagation to adaptive learning algorithms. Comput. Stan. Interfaces **16**(3), 265–278 (1994). https://doi.org/10.1016/0920-5489(94)90017-5. https://linkinghub.elsevier.com/retrieve/pii/0920548994900175
21. Shang, C., Barnes, D.: Support vector machine-based classification of rock texture images aided by efficient feature selection. In: The 2012 International Joint Conference on Neural Networks (IJCNN), pp. 1–8, June 2012. https://doi.org/10.1109/IJCNN.2012.6252634
22. Singh, S.: Permeability Prediction Using Artificial Neural Network (ANN): A Case Study of Uinta Basin. Society of Petroleum Engineers (2005). https://doi.org/10.2118/99286-STU. https://www-onepetro-org.ezproxy.rgu.ac.uk/conference-paper/SPE-99286-STU
23. Stiles, J.J., Hutfilz, J.: The use of routine and special core analysis in characterizing Brent Group reservoirs, U.K. North Sea. J. Petrol. Technol. (U.S.) **44**(6) (1992). https://doi.org/10.2118/18386-PA
24. Tibshirani, R.: Regression shrinkage and selection via the Lasso. J. Roy. Stat. Soc. B **58**, 267–288 (1994)
25. Wold, H.: 11 - Path Models with Latent Variables: The NIPALS Approach**NIPALS = Nonlinear Iterative PArtial Least Squares. In: Blalock, H.M., Aganbegian, A., Borodkin, F.M., Boudon, R., Capecchi, V. (eds.) Quantitative Sociology: International Perspectives on Mathematical and Statistical Modeling, pp. 307–357. Academic Press, January 1975. https://doi.org/10.1016/B978-0-12-103950-9.50017-4. http://www.sciencedirect.com/science/article/pii/B9780121039509500174

26. Wold, S.: Personal memories of the early PLS development. Chemometrics and Intelligent Laboratory Systems **58**(2), 83–84 (2001). https://doi.org/10.1016/S0169-7439(01)00152-6. http://www.sciencedirect.com/science/article/pii/S0169S0169743901001526
27. Wong, K.W., Fung, C.C., Ong, Y.S., Gedeon, T.D.: Reservoir characterization using support vector machines. In: International Conference on Computational Intelligence for Modelling, Control and Automation and International Conference on Intelligent Agents, Web Technologies and Internet Commerce (CIMCA-IAWTIC 2006), vol. 2, pp. 354–359, November 2005. https://doi.org/10.1109/CIMCA.2005.1631494

Probabilistic Estimation of Evaporated Water in Cooling Towers Using a Generative Adversarial Network

Serafín Alonso(✉), Antonio Morán, Daniel Pérez, Miguel A. Prada, Juan J. Fuertes, and Manuel Domínguez

Grupo de investigación en Supervisión, Control y Automatización de Procesos Industriales (SUPPRESS), Esc. de Ing. Industrial e Informática, Universidad de León, Campus de Vegazana s/n, 24007 León, Spain
{saloc,a.moran,dperl,ma.prada,jjfuem,manuel.dominguez}@unileon.es
http://suppress.unileon.es

Abstract. Water is a critical resource for life on the earth but it is becoming increasingly scarce. Therefore, water use should be sustainable and properly managed. The problem of water scarcity is still more stressed in cities, where buildings consume more and more water, especially commercial and institutional ones. In those buildings, HVAC (*Heating, Ventilating and Air Conditioning*) systems make an intensive use of water, especially the water-based cooling systems such as cooling towers, where a large amount of water is evaporated. In this paper, a method is proposed in order to estimate the evaporated water in cooling towers, considering the variations of environmental and operating conditions. We propose the use of a generative model which is able to generalize the estimation of the evaporated water, even in situations not included in the training data. A generative adversarial network (GAN) is used for training a deep learning-based generative model. The proposed method is tested using real data from a cooling tower located at the Hospital of León. Results show the probability distribution within which the estimation of evaporated water can be found, given the environmental and operating conditions.

Keywords: HVAC systems · Cooling tower · Evaporated water · Probabilistic estimation · Generative adversarial network

1 Introduction

Water is an increasingly scarce resource on the earth due to population growth, water contamination and droughts provoked by climate changes [18]. All of the above entails the depletion of aquifers and changes of groundwater recharge [14]. Water is a critical resource for life, so it should not be wasted and water supplies should attract sufficient attention. However, groundwater is unmonitored and mismanaged in many places in the world [5]. Due to its global importance, the use of water should be sustainable and properly managed.

L. Iliadis et al. (Eds.): EANN 2020, INNS 2, pp. 155–166, 2020.
https://doi.org/10.1007/978-3-030-48791-1_11

In cities, proliferation of urbanization areas, deficient maintenance of water infrastructures and poor waste management stress the problem of water scarcity [13]. The public water supply represents 21% in European Union [1], including buildings which account for the major use, in particular commercial and institutional ones [19,21]. One of the facilities which make an intensive use of water (around 48%) in those buildings are HVAC (*Heating, Ventilating and Air Conditioning*) systems [3,21], specially the water-based cooling systems such as cooling towers [9]. These systems can benefit from water efficiency measures, saving water and energy [4,9]. Some reports state that up to 30% of the volume of water consumed in buildings could be saved [1]. Therefore, sustainable water management should be adopted in order to reduce water use in buildings and protect the global water resources [19].

In large buildings, water for cooling towers accounts for almost all of the HVAC system's water consumption [21]. Moreover, the performance of the cooling towers depends mainly on ambient conditions, given a fixed quantity of heat to reject. Thus, the use of water for cooling towers should be analyzed in detail, previously to establish management strategies and plan its operation.

In the literature, authors focus on the use of differential equations solved with numerical methods for predicting the water loss in cooling towers [17]. In this case, many simulations with different data are required in order to cover all scenarios. However, artificial intelligence techniques are rarely applied for that purpose. On the other hand, artificial neural networks are used for predicting the performance of cooling towers, under a range of operating and ambient conditions [6,10]. However, traditional neural networks are not able to generate a trustworthy output if the surrounding conditions are not considered in the training data. The operating and environmental conditions in a cooling tower could vary, so the method should be able to generate a likely output, given the new conditions. Generative Adversarial Networks (GAN) [7] can engender a likely output, just from noise. In the literature, GANs have been mainly used for image processing and computer vision [15,20]. Apart from that, GANs have been applied recently for time series prediction, for instance, forecasting sensory data [12], predicting stock market [23] and generating melodies from lyrics [22]. Other applications of GANs include natural language, speech, voice and data augmentation [8].

In this paper, a method is proposed in order to estimate the evaporated water in cooling towers, considering the variations of environmental and operating conditions. Our method is able to provide a probabilistic distribution of the evaporated water, considering new and varying conditions. It relies on a generative model based on real past data. On the contrary, the state-of-the-art methods predict the water loss, given known conditions. These models are based on mathematical equations or artificial neural networks. The main contributions of this paper are:

– The development of a methodology to implement a virtual sensor able to estimate the evaporated water in cooling towers in different scenarios.

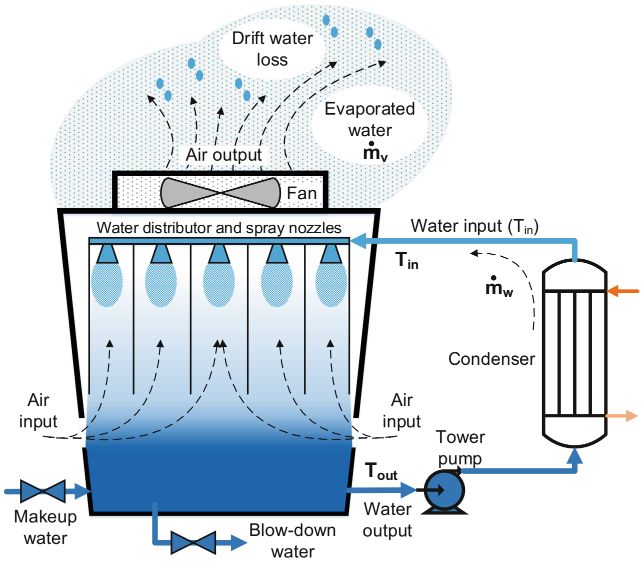

Fig. 1. Cooling tower scheme.

- The application of a generative model in a different research field, far away from well-known image generation.
- The test of the method using real data from a cooling tower located in a hospital building.

This paper is organized as follows: Sect. 2 defines the problem. In Sect. 3, the proposed methodology is presented. Here, the generative model is explained in detail. Section 4 describes the real cooling tower and the dataset used in the experiment. In Sect. 5, the experiment and results are presented and discussed. Finally, conclusions and future work are drawn in Sect. 6.

2 Problem Definition

A cooling tower is a system used to cool water by exchanging heat with the atmosphere, i.e. a water-air heat exchanger (see Fig. 1). The hot water (input) is passed through some nozzles located on the top which spray the water to increase contact surface with the air in order to improve the evaporation. Small droplets of water fall down on the fill in the tower. A fan usually induces an air draft in the opposite direction to falling droplets [11]. The water changes its phase from liquid to vapor, transferring the latent heat to the air. The air carries the heat from evaporating water in the cooling tower to the atmosphere. Therefore, atmospheric conditions influence directly on the evaporation process.

Cooling towers are commonly used by equipment in industries and buildings in order to dissipate heat. For example, water-cooled chillers make use of cooling towers to condense the refrigeration gas [10].

Their great water consumption is mainly due to the loss of water which is evaporated [10]. Moreover, some droplets of water are carried out through the air draft (drift), despite of using a maze of baffles. Furthermore, the water is drained regularly (blow-down) in order to adjust the concentration of the total dissolved solids (TDS) in the water. Summarizing, the water loss in a cooling tower is mainly due to the evaporation (E), drift (D) and blow-down (B), i.e., $Loss = E + D + B$. Lost water must be replaced with water from supply what has an important environmental impact and economic cost. Lost water due to drift (D) and blow-down (B) processes is usually insignificant with regard to the evaporation (E), so water loss could be calculated as $Loss = E$, assuming that the total loss is due to the water loss through evaporation. The evaporated water flow $\dot{m}_v$ could be calculated from measuring water flow $\dot{m}_w$, water input temperature (warm) T_{in} and water output temperature (cold) T_{out} in the cooling tower, according to the Eq. 1.

$$\dot{m}_v = \frac{\dot{m}_w * c_w * (T_{in} - T_{out})}{H_v} \tag{1}$$

c_w is the specific heat of water and H_v is the latent heat of vaporization necessary for water changes from liquid to vapor. Thus, a flow meter connected in the input of the cooling tower could provide the lost water.

On the other hand, several factors influence on the evaporation process and define the performance of the cooling tower, so they should be considered. For example, the air flow (natural or forced by the fan), the input and output water temperatures and the environmental conditions (outdoor temperature and humidity) determine the operation of the cooling tower. Moreover, these factors could vary slightly, modifying the surrounding conditions which affect the evaporation and consequently, the operation and performance of the cooling tower.

Therefore, the estimation of the evaporated water in a cooling tower, considering the environmental and operating conditions, could be useful to plan the operation of a cooling tower and save water and improve its performance. Note that, that estimation is affected by the environmental and operating conditions and therefore the quantity of evaporated water may be estimated with a certain confidence interval since those conditions could change. For that task, a method to implement a virtual sensor could be developed so that it is able to estimate the probability distribution of the evaporated water in a cooling tower, given the surrounding conditions.

3 Methodology

In this paper, we propose the development of a methodology to implement a virtual sensor able to estimate the probability distribution of the evaporated water in a cooling tower, given any potential environmental and operating conditions. Once the virtual sensor is built, it should be able to estimate the evaporated water even under abnormal conditions (not only normal ones). For example, the outdoor temperature could increase above normal values during a heat wave or

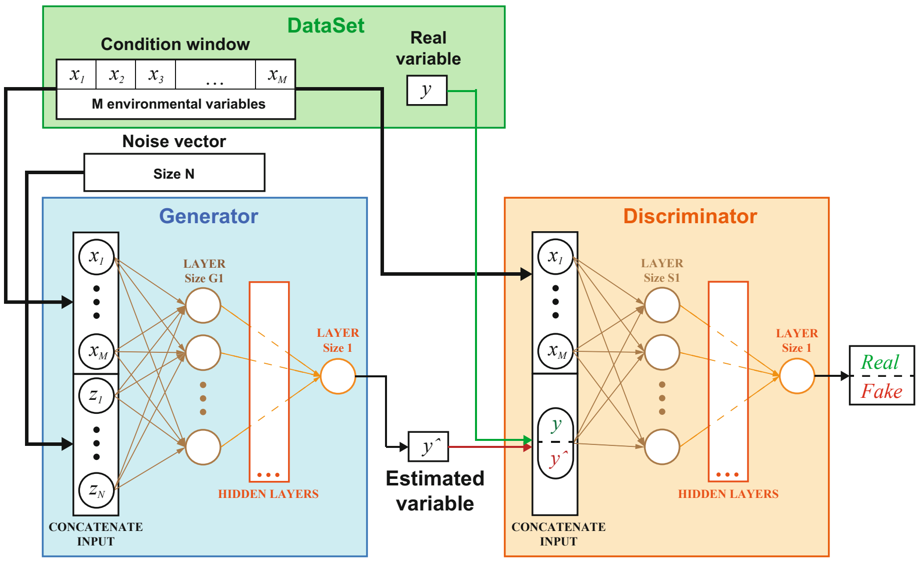

Fig. 2. Proposed methodology based on cGAN.

the relative humidity could increase because of fog banks, affecting the evaporation process in a cooling tower. These abnormal situations should be considered by the method in order to estimate a range within which the evaporated water value is very likely to be found.

In order to tackle that problem, we propose the use of a generative model which is able to generalize the estimation of the evaporated water, even in situations not included in training data. A generative adversarial network (GAN) is used for training a deep learning-based generative model. GAN is a framework for building generative models via an adversarial process, which uses two models simultaneously: a generator model that captures the data distribution and a discriminator model that estimates the probability that a sample is from the training data rather than the generator [7]. The generator is in charge of providing new plausible data that are similar to real data. The function of the discriminator is to classify data as either real (from the input dataset) or fake (from the generator). To sump up, the generator tries to fool the discriminator by generating real-looking data.

In our case, the evaporated water (estimation) is influenced by the environmental and operating conditions, so the generative model is conditioned on some auxiliary variables (outdoor temperature, humidity and air flow). Thus, an extension of GAN, called conditioned generative adversarial network (cGAN) [16], is required. A model based on cGAN is able to consider contextual information with slight variations.

Therefore, the evaporated water $\hat{y}$ could be estimated using a cGAN, from environmental and operating variables $\mathbf{x}$ and the potential fluctuations $\mathbf{z}$ (see Eq. 2)

$$\hat{y} = f(\mathbf{x}, \mathbf{z}), \tag{2}$$

where the environmental and operating variables are $\mathbf{x} = [x_1, x_2, \ldots, x_m]$ and the noise representing the potential fluctuations are $\mathbf{z} = [z_1, z_2, \ldots, z_n]$.

Figure 2 summarizes the proposed methodology. It is based on a cGAN which comprises a generator and a discriminator models. The generator model is fed with the environmental and operating variables $\mathbf{x}$ and the noise $\mathbf{z}$, which are concatenated. The generator is a deep model with several hidden layers, being its output the estimation. The discriminator uses as input the environmental and operating variables $\mathbf{x}$ and they are concatenated with either the real y or the estimated $\hat{y}$ values of the evaporation. The discriminator is also a deep model with several hidden layers, being its output the class (real of fake) which they belong to.

First of all, the discriminator is trained with the conditional variables $\mathbf{x}$ and the real data of evaporated water y assuming that the output class is always real, updating the discriminator model. Then, the combined model, i.e. both the generator and the discriminator are trained with the conditional variables $\mathbf{x}$, the noise $\mathbf{z}$ and the estimated data of evaporated water $\hat{y}$ assuming that the output class is always fake, updating only the generator model.

4 Real System and Dataset

Data from a mechanical draft cooling tower located at the Hospital of León are used in the experiment. That cooling tower by Baltimore Aircoil, model S-3654-NM (see Fig. 3), cools water from a chiller by Trane, model CVGF650 (cooling capacity of 650 tons). An axial fan, driven by a three-phase induction motor (18.5 KW) and managed by a variable speed drive (Moeller DF6-340-22K), forces the air through the cooling tower. Two pumps NK 150-315/307/BAQE by Grundfos driven by three-phase induction motors (30 KW) are used, one to propel water to the cooling tower and the other to maintain a water flow through the condenser. Moreover, the temperatures of input and output water are measured using sensors by Johnson Controls, model TS-9101-8224. It also incorporates three resistors of 5 KW to avoid water freezing.

BMS (*Building Management System*) acquires and stores data from the operation of the cooling tower (input and output water temperatures and fan speed) and also from the ambient (dry-bulb temperature and relative humidity). The water flow through the condenser ($\dot{m}_w$) has been measured by an ultrasonic portable meter (Fluxus F601 by Flexim), due to the lack of permanent flow meter in the chiller. Note that, the water flow is required to calculate the evaporated water $\dot{m}_v$ using Eq. 1. Table 1 lists the variables involved in the experiment.

According to Eq. 2, the estimation of evaporated water $\hat{\dot{m}}_v$ is

$$\hat{\dot{m}}_v = f\big([Ta, Hr, Dt, Fs], \mathbf{z}\big) \tag{3}$$

Fig. 3. Photo of cooling tower at the Hospital of León.

Table 1. Variables used in the experiment.

Symbol	Variable name	Unit
Ta	Dry-bulb temperature	°C
Hr	Relative humidity	%
Dt	Input-Output water temperature difference ($T_{in} - T_{out}$)	°C
Fs	Fan speed	%
$\dot{m}_v$	Evaporated water flow	m^3/h

where the conditional variables are $\mathbf{x} = [Ta, Hr, Dt, Fs]$, and noisy variables introduced to the model are $\mathbf{z}$. The noisy variables are generated using a normal distribution centered at 0 and within 1 standard deviation.

Data from these variables are collected for 40 days. The sampling rate is 1 min, but then data are resampled, averaging values each hour. Therefore, the total number of samples is 960. The evaporated water flow $\dot{m}_v$ is computed from measured water flow $\dot{m}_w$, specific heat c_w, difference of input and output water temperatures $(T_{in} - T_{out})$ and latent heat of vaporization H_v.

Data are scaled in range [−1, 1] and split into training and test datasets. 75% of total samples are used for training (30 days) and the remaining for testing (10 days).

5 Experiment and Results

Figure 4 shows the architecture of the cGAN developed to estimate the evaporated water. Several configurations were tested but a simple network with only

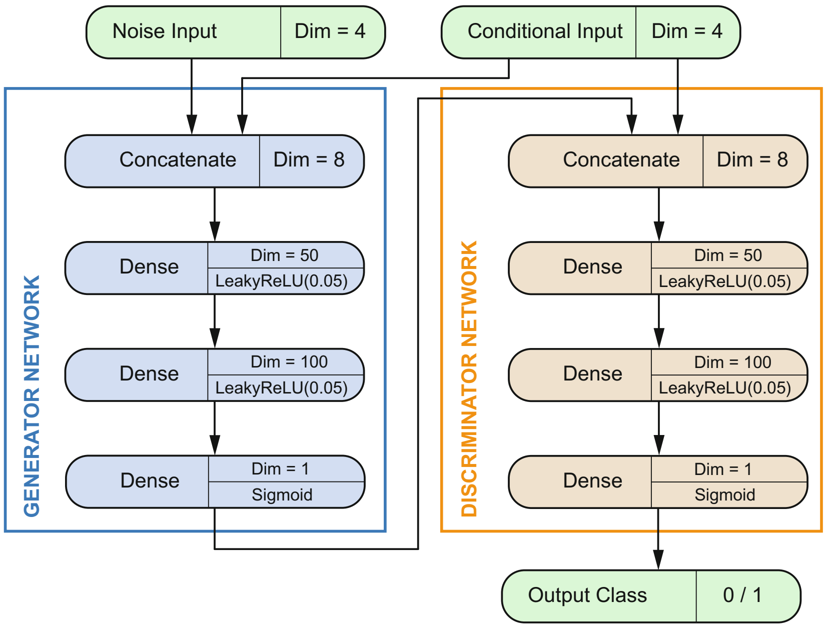

Fig. 4. Architecture of cGAN model implemented.

dense layers for both generator and discriminator is used since it gave the most accurate results. The dense layers are trained using a *LeakyRelu* activation since this function introduces non-linearity in the model without the *Dying ReLU problem* where some neurons remain inactive. The last layer of each network, since they are composed of only one neuron, uses a sigmoid function since the output of the generator is a regressor, and the output of the discriminator is a classification.

The input of the model are two concatenated vectors since we are working with a conditional GAN. One vector is composed of the variables related to the cooling tower which define the working state $\mathbf{x}$ and a noise vector $\mathbf{z}$ that is used to create the generative model. The size of the noise vector is tunable and is another parameter of the model. In our case, the size of the noise is set to 4 (equal to variables) since it provides the best results.

The MAPE index (see Eq. 4) is used as metrics to evaluate the model since the values are easily understood by any engineer providing a direct measurement of the accuracy of the evaporated water and delimits the error in the cooling production estimation [2].

$$MAPE = \frac{100\%}{n} \sum_{i=1}^{n} \left| \frac{y_i - \hat{y}_i}{y_i} \right| \tag{4}$$

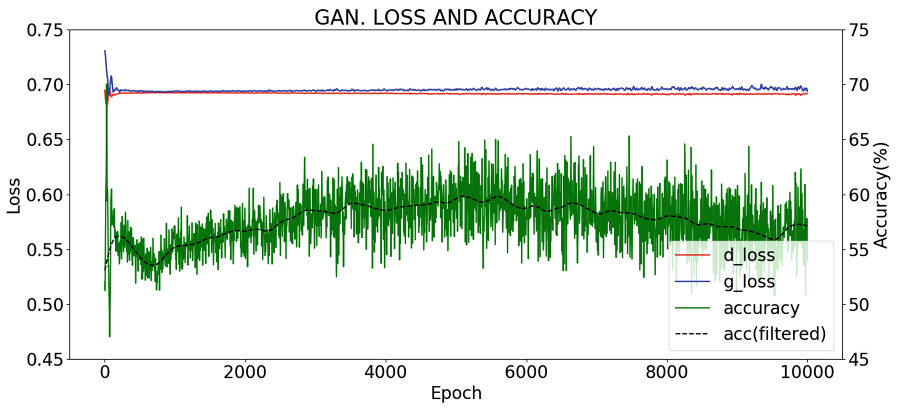

Fig. 5. Loss and accuracy for both generator and discriminator.

Since the cGAN provides a probabilistic estimation of the calculated variable, to test the performance of the algorithm, once the model is trained, several values of the evaporated water are calculated for the same timestep. The mean value is calculated for this probability distribution and this mean is used as value in the MAPE index. So the model is tuned to minimize the error of the mean value of the calculated variable, the accuracy of the distribution is not taken into account.

The model is trained using the training dataset (75% of total). Cross validation is applied for selecting the parameters which provide the lowest MAPE value. Figure 5 shows the loss results for both the generator and the discriminator and the accuracy of the model. The accuracy variability denotes that there is no convergence error so the model is not always generating false data. Since the accuracy fluctuates, the filtered value is shown. The maximum accuracy is achieved around 5000 epochs. Also, since the loss of both networks are not zero and the values are stable through the epochs, the model does not collapse.

Once the model is trained, the evaporated water of the test dataset (remaining 25% of total) is calculated. Since we want to obtain a distribution, each sample is calculated several times changing the noise values which are generated randomly. In order to obtain a detailed distribution, 5000 values are calculated for each sample. Figure 6 shows the results of applying the resulting cGAN model to the test dataset. The MAPE error for this dataset is 1.54%. Figure 6a shows the results of the mean estimated value of water evaporation (blue points) and the real one (cyan stars) and the areas are the results of the confidence interval for the distribution of each sample.

Figure 6b shows in detail the probability distribution for three different working points of the cooling tower that are considered as representative. The left one corresponds to a high cooling demand. This distribution has a high variance so the results are less accurate, also it shows a bit of asymmetry. The right one corresponds to a low cooling demand where the tower is more stable so the

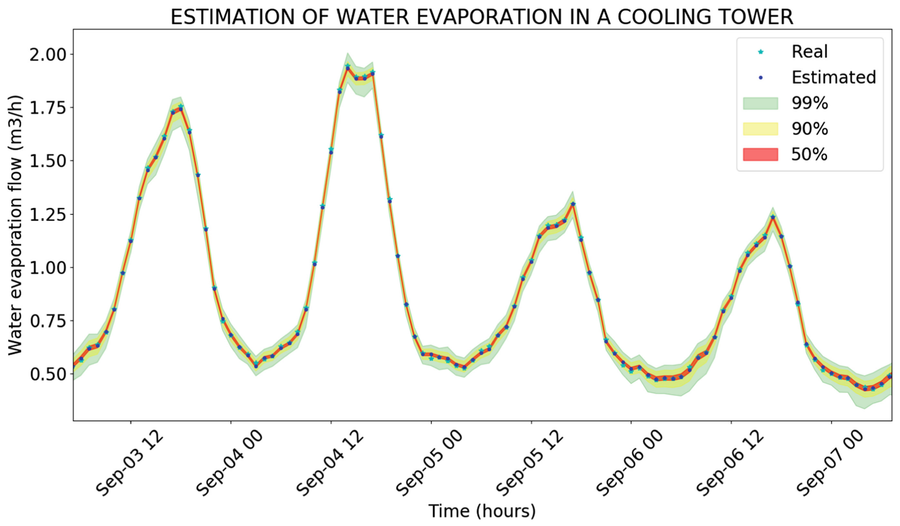

(a) Estimation of evaporated water and the confidence interval for the test dataset.

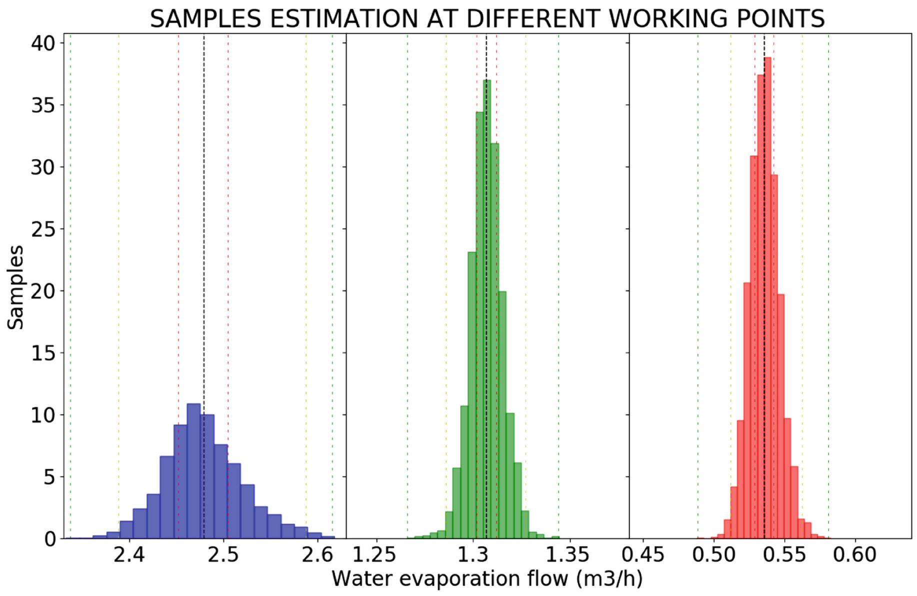

(b) Histograms of evaporated water in different working points of the cooling tower.

Fig. 6. Estimation of evaporated water.

variance is less and the forecasting is more accurate. Lastly, the central one is a transient point between two states and it also has a low variance.

6 Conclusions

This paper proposes the use of a Generative Adversarial Network (GAN) to estimate a variable that is not measured directly so it can be seen as a virtual sensor. Since the evaporated water is highly dependable of varying environmental variables, it is difficult to estimate the real value so the use of this kind of neural networks let us estimate a probabilistic distribution of the real value.

GAN, which has been widely use in image generation so far, has proven to estimate analog values taking into account external variables that provide a working condition and noise that alter the working point introducing several disturbances. The output of the model provides a probabilistic estimation of the value of the evaporated water so instead of using a unique value we can use the confidence interval to estimate the extreme values that the evaporation can have.

Although the cGAN model provides good results, only the static information has been considered, the actual sample of evaporated water is estimated using only the actual values of the conditional variables. As future work, it should be used past information of the variables with temporal layers such as LSTM to improve the results. Moreover, the proposed methodology should be compared with other probabilistic methods.

References

1. BIO Intelligence Service: Water performance of buildings. Tech. rep. Final report prepared for European Commission, DG Environment (2012)
2. Bowerman, B., O'Connell, R., Koehler, A.: Forecasting, Time Series, and Regression: An Applied Approach. Duxbury Advanced Series in Statistics and Decision Sciences. Thomson Brooks/Cole, Belmont (2005)
3. Dziegielewski, B., Kiefer, J.C., Opitz, E.M., Porter, G.A., Lantz, G.L.: Commercial and Institutional End Uses of Water. American Water Works Association Research Foundation (2000)
4. Eades, W.G.: Energy and water recovery using air-handling unit condensate from laboratory HVAC systems. Sustain. Cities Soc. **42**, 162–175 (2018). https://doi.org/10.1016/j.scs.2018.07.006
5. Famiglietti, J.S.: The global groundwater crisis. Nat. Clim. Change **4**(11), 945–948 (2014). https://doi.org/10.1038/nclimate2425
6. Gao, M., Sun, F.Z., Zhou, S.J., Shi, Y.T., Zhao, Y.B., Wang, N.H.: Performance prediction of wet cooling tower using artificial neural network under cross-wind conditions. Int. J. Therm. Sci. **48**(3), 583–589 (2009). https://doi.org/10.1016/j.ijthermalsci.2008.03.012
7. Goodfellow, I., Pouget-Abadie, J., Mirza, M., Xu, B., Warde-Farley, D., Ozair, S., Courville, A., Bengio, Y.: Generative adversarial nets. In: Ghahramani, Z., Welling, M., Cortes, C., Lawrence, N.D., Weinberger, K.Q. (eds.) Advances in Neural Information Processing Systems, vol. 27, pp. 2672–2680. Curran Associates, Inc. (2014)

8. Gui, J., Sun, Z., Wen, Y., Tao, D., Ye, J.: A review on generative adversarial networks: Algorithms, theory, and applications. CoRR abs/2001.06937 (2020). https://arxiv.org/abs/2001.06937
9. Hawit, O., Jaffe, T.: Water-energy nexus: heat rejection systems. ASHRAE J. **59**(9), 28–39 (2017)
10. Hosoz, M., Ertunc, H., Bulgurcu, H.: Performance prediction of a cooling tower using artificial neural network. Energy Convers. Manage. **48**(4), 1349–1359 (2007). https://doi.org/10.1016/j.enconman.2006.06.024
11. Jin, G.Y., Cai, W.J., Lu, L., Lee, E.L., Chiang, A.: A simplified modeling of mechanical cooling tower for control and optimization of HVAC systems. Energy Convers. Manage. **48**(2), 355–365 (2007). https://doi.org/10.1016/j.enconman.2006.07.010
12. Koochali, A., Schichtel, P., Ahmed, S., Dengel, A.: Probabilistic forecasting of sensory data with generative adversarial networks - ForGAN. CoRR abs/1903.12549 (2019). http://arxiv.org/abs/1903.12549
13. Koop, S.H.A., van Leeuwen, C.J.: The challenges of water, waste and climate change in cities. Environ. Dev. Sustain. **19**, 385–418 (2017). https://doi.org/10.1007/s10668-016-9760-4
14. Kundzewicz, Z.W., Döll, P.: Will groundwater ease freshwater stress under climate change? Hydrol. Sci. J. **54**(4), 665–675 (2009). https://doi.org/10.1623/hysj.54.4.665
15. Ledig, C., Theis, L., Huszar, F., Caballero, J., Aitken, A.P., Tejani, A., Totz, J., Wang, Z., Shi, W.: Photo-realistic single image super-resolution using a generative adversarial network. CoRR abs/1609.04802 (2016). http://arxiv.org/abs/1609.04802
16. Mirza, M., Osindero, S.: Conditional generative adversarial nets. CoRR abs/1411.1784 (2014). http://arxiv.org/abs/1411.1784
17. Qureshi, B.A., Zubair, S.M.: A unified approach to predict evaporation losses in evaporative heat exchangers. Int. J. Refrig. **34**(8), 1866–1876 (2011). https://doi.org/10.1016/j.ijrefrig.2011.06.008
18. Richey, A.S., Thomas, B.F., Lo, M.H., Reager, J.T., Famiglietti, J.S., Voss, K., Swenson, S., Rodell, M.: Quantifying renewable groundwater stress with GRACE. Water Resour. Res. **51**(7), 5217–5238 (2015). https://doi.org/10.1002/2015WR017349
19. Stec, A.: Sustainable Water Management in Buildings, Water Science and Technology Library, vol. 90. Springer International Publishing, Cham (2020). https://doi.org/10.1007/978-3-030-35959-1
20. Tran, L., Yin, X., Liu, X.: Disentangled representation learning GAN for pose-invariant face recognition. In: 2017 IEEE Conference on Computer Vision and Pattern Recognition (CVPR). pp. 1283–1292, July 2017. https://doi.org/10.1109/CVPR.2017.141
21. Weimar, D., Browning, A.: Reducing water costs in building HVAC systems. Facilities Engineering Journal **37**(3), 24–26 (2010)
22. Yu, Y.B., Canales, S.: Conditional LSTM-GAN for melody generation from lyrics. ArXiv abs/1908.05551 (2019)
23. Zhang, K., Zhong, G., Dong, J., Wang, S., Wang, Y.: Stock market prediction based on generative adversarial network. Procedia Comput. Sci. **147**, 400–406 (2019). https://doi.org/10.1016/j.procs.2019.01.256

Reconstructing Environmental Variables with Missing Field Data via End-to-End Machine Learning

Matteo Sangiorgio[1], Stefano Barindelli[2](✉), Valerio Guglieri[2], Giovanna Venuti[2], and Giorgio Guariso[1]

[1] Department of Electronics, Information, and Bioengineering, Politecnico di Milano, Milan, Italy
[2] Department of Civil and Environmental Engineering, Politecnico di Milano, Milan, Italy
stefano.barindelli@polimi.it

Abstract. Real-world time series often present missing values due to sensor malfunctions or human errors. Traditionally, missing values are simply omitted or reconstructed through imputation or interpolation methods. Omitting missing values may cause temporal discontinuity. Reconstruction methods, on the other hand, alter in some way the original time series. In this paper, we consider an application in the field of meteorological variables that exploits end-to-end machine learning. The idea is to entrust the task of dealing with missing values to a suitably trained recurrent neural network that completely by-passes the phase of reconstruction of missing values. A difficult case of reproduction of a rainfall field from five rain gauges in Northern Italy is used as an example, and the results are compared to those computed by more traditional methods. The proposed methodology is general-purpose and can be easily applied to every kind of spatial time series prediction problem, quite common in many environmental studies.

Keywords: Time series · Rainfall field · Data augmentation · Artificial neural networks · LSTM cell

1 Introduction

A frequent issue encountered while working on environmental problems, such as weather forecasting or air pollution, that exploit data recorded with ground sensors, is the presence of missing values. This may be due to human errors, but more frequently depends on the failure of the sensors or the transmission network, particularly in severe weather conditions. The most common methods to deal with missing values are imputation or interpolation [1–3]. Since both operations present critical aspects, the approach investigated in this work aims at training a Long Short-Term Memory (LSTM) Neural Network (NN) bypassing this step.

The presence of missing data can be tackled with a variety of methods, depending on the dimension of the dataset, the choice of the prediction task, and the nature of data themselves. A classical approach is to fill the gaps with the mean of the data (mean imputation) or with the closest known value (i.e., nearest-neighbour substitution). More sophisticated techniques fit a function to the known data and then evaluate it in the unknown spots to fill the gaps. The fitted function is usually a polynomial or, in case of spline interpolation, a combination of polynomials. Other techniques to perform this task investigate the statistical behavior of the dataset: one of them is the kriging method, which relies on the computation of the empirical variogram of the considered data [4, 5].

When the problem deals with both spatial and temporal distribution of different variables, the number of interpolation possibilities increases, as spatial cross-correlations and temporal autocorrelation can be taken into account. Another approach that considers both time and space relations is using an (often very complex) physically-based model which assimilates the current available data [6–9]. However, real-time assimilation is mostly computationally prohibitive and requires data about other variables that may also be missing.

Regardless of the algorithm being used to obtain the cleansed input data, this procedure introduces a reconstruction error that will propagate in the subsequent phases necessary to compute the desired output.

In this paper, we propose an end-to-end machine learning approach [10, 11] able to autonomously deal with missing input values, completely bypassing the phase of reconstruction. Our idea consists of training a Recurrent Neural Network (RNN), specifically an LSTM net, using the raw dataset with missing data, letting the RNN itself compensate for the lack of information by exploiting the spatial and temporal correlations in the dataset.

The dataset considered in this contribution consists of five time-series of rain rate, collected by a network of gauges located in Northern Italy. Artificial failures are introduced in the data series to test the capacity of an LSTM architecture to overcome the problem of missing input values. The ability to compute a nonlinear analytical function of the measurement values is used as a performance indicator.

2 Materials and Methods

2.1 The Measurement Network

The study area (Fig. 1) is located in the North of Italy and is delimited by the watersheds of the Olona, Lambro, and Seveso rivers, covering a surface of about 1400 km^2. This is an almost completely flat area, except for the northern boundary where the Alpine mountain chain begins. The region is well known to be subject to very intense and localized convective storms [12–15] that lead to severe damages, especially in Milan municipality.

The input dataset consists of 4 complete years (2015 to 2018) of rainfall values collected by five rain gauges, namely s_1, s_2, s_3, s_4, and s_5, with a temporal resolution of

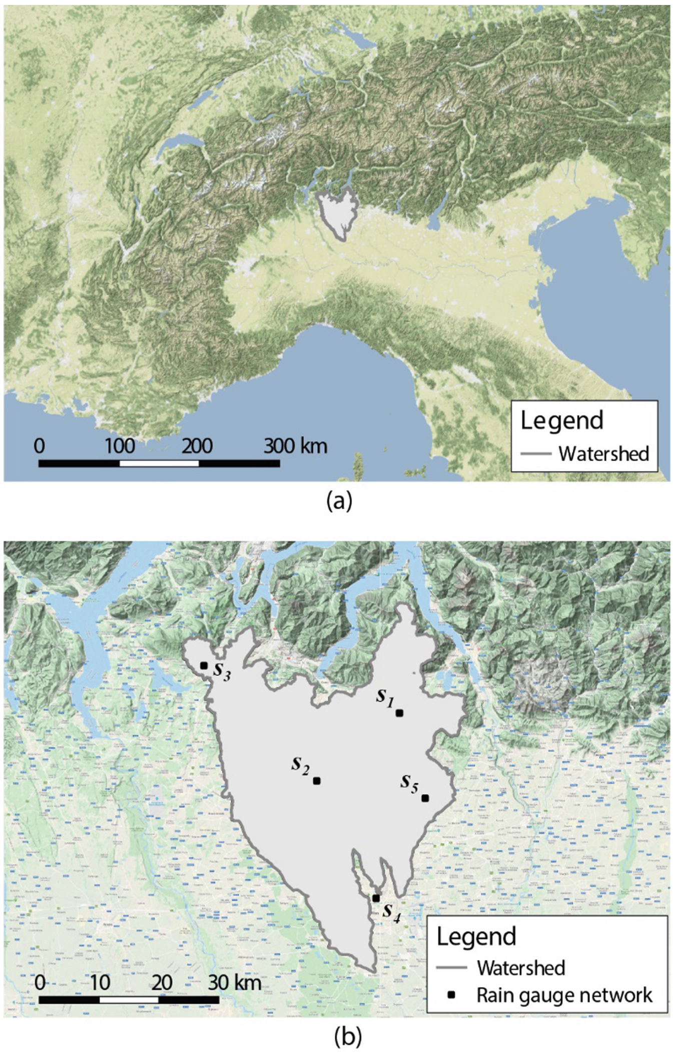

Fig. 1. Panel (a) shows a geographical overview of the study area. Panel (b) shows the position of the considered rain gauge network in the Seveso, Olona and Lambro hydrological basins

5 min (Fig. 2). These rain gauges belong to the network managed by ARPA Lombardia, the environmental protection agency of the Lombardy region.

Pearson's and Spearman's correlation coefficients have been computed to quantify the spatial correlation and the results are reported in Table 1 and Table 2. These values have been calculated for every couple of rain gauges only when they were recording at

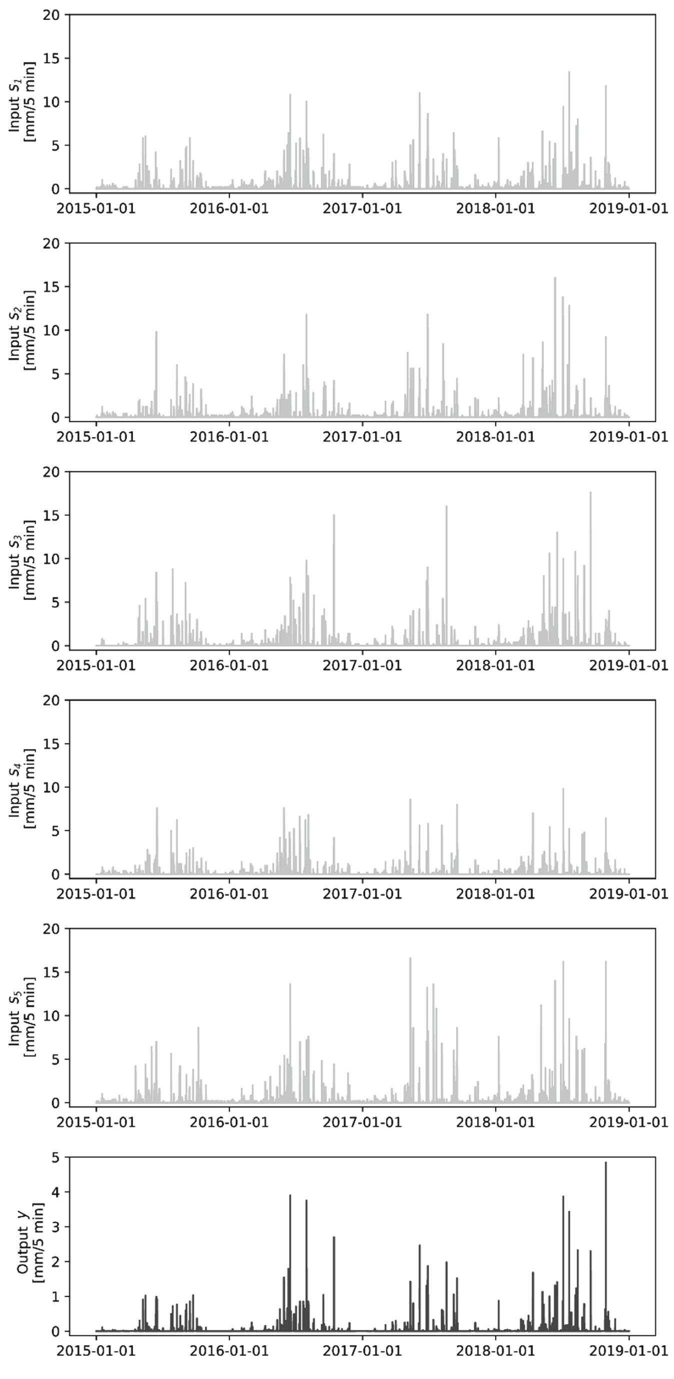

Fig. 2. Temporal series of the five inputs (light grey), i.e., the rainfall rate measured by s_1, s_2, s_3, s_4, s_5 rain gauges, and the corresponding output y (dark grey), computed as a non linear function of the inputs.

the same time an amount of rain different from zero. In this way, we investigate the correlation only during rain periods.

The spatial correlation between the measurement stations is not high, despite the relatively small dimension of the basin. This makes the reconstruction of the rainfall field particularly difficult.

Table 1. Pearson's correlation coefficients.

Stations	s_1	s_2	s_3	s_4	s_5
s_1	–	0.25	0.14	0.21	0.36
s_2	0.25	–	0.25	0.31	0.24
s_3	0.14	0.25	–	0.13	0.12
s_4	0.21	0.31	0.13	–	0.23
s_5	0.36	0.24	0.12	0.23	–

Table 2. Spearman's correlation coefficients.

Stations	s_1	s_2	s_3	s_4	s_5
s_1	–	0.30	0.20	0.30	0.37
s_2	0.30	–	0.26	0.34	0.30
s_3	0.20	0.26	–	0.23	0.20
s_4	0.30	0.34	0.23	–	0.34
s_5	0.37	0.30	0.20	0.34	–

For each time step, the five values recorded by the rain gauges are combined into a nonlinear analytical function to obtain the correspondent output:

$$s_{tot}(t) = (p_1 \cdot s_1(t) + p_2 \cdot s_2(t) + p_3 \cdot s_3(t) + p_4 \cdot s_4(t) + p_5 \cdot s_5(t)) / \sum_i p_i \qquad (1)$$

$$y(t) = f(s_{tot}(t)) \cdot s_{tot}(t) = \left(1 - e^{-s_{tot}(t)}\right) \cdot s_{tot}(t) \qquad (2)$$

where $s_{tot}(t)$ is a normalized weighted linear combination of the inputs; $s_1(t)$, $s_2(t)$, $s_3(t)$, $s_4(t)$, $s_5(t)$ are the rainfall rates at each rain gauge measured at each time step (5 min); $y(t)$ is the output of the nonlinear function considered (bottom panel of Fig. 2). The weights and the function have been chosen in order to simulate the computation of the effective runoff in the catchment. This is usually computed using, as weights p_i, the areas of the Thiessen polygons represented by each sensor, or some spatial interpolation method. The exponential factor $f(s_{tot}(t))$ represents the effect of soil saturation for which runoff is small when the total precipitation is limited and becomes almost equal to the total rainfall when it is abundant. The full dynamic of the soil water content is not taken into account by this formulation.

Note that the definition of a known analytical function, instead of using the actual runoff of the river system, is necessary to detect the NN performances in solving the missing value issue alone. When using real runoff data, the overall performance of the

NN would be due both to the ability to interpret missing data and to replicate the actual rainfall-runoff process. For the same reason, using other, more complex, analytical formulations of the target set *y*, does not change the general conclusions we reach.

The characteristic of this dataset is the absence of missing data along the considered time horizon: this allows the computation of the output at each time step.

2.2 Machine Learning Training Dataset

Since rain gauges require careful maintenance, it is not always possible to avoid the onset of technical problems, external damages, or failures that compromise the continuity of the collected temporal series. The characterization of the missing data is performed investigating the time to failure (TTF) and the time to restore (TTR) of the entire regional rain gauge dataset managed by ARPA Lombardia, consisting of the data collected by 19 sensors for about 20 years (they were activated at different dates). The TTF is defined as the length of the time interval between two consecutive failures, i.e., the period of correct functioning of the sensor. On the other hand, the TTR is defined as the length of the time interval required to fix a malfunctioning sensor, i.e., the period in which the instrument collects no data. For both TTF and TTR histograms, an exponential distribution [16] has been fitted with $\text{mean}_{\text{TTF}} = 442.00$ and $\text{mean}_{\text{TTR}} = 10.79$ time steps, respectively. These two values also represent the exponential rate of the distributions. Thus their values strongly affect the shape of such distributions: the lower the mean value, the more the probability density function is stretched to the left. This is due to the presence of many short duration values and fewer long duration values. By sampling these two estimated distributions iteratively, it is possible to generate any number of synthetic time series of missing data within the complete input dataset of the five rain gauges. Missing values of these synthetic time series are filled with a marker constituted by an out-of-range value: in this case, -1. The obtained input sequences with out-of-range values are used to train an LSTM model together with the known output of the complete time series.

It must be noted that, despite the training set being constituted by more than a million values for each sensor, the number of rainfall episodes is much more limited: recorded values differ from zero only 3% of the time. Failures are distributed on the time series according to actual statistics, and thus cases, when a simulated failure occurs during a rainfall event, are also rare.

2.3 The Training Procedure

The proposed procedure, hereafter called end-to-end machine learning, differs from the traditional pipeline: the data filling step, with its related critical aspects, is avoided, and the LSTM model directly manages missing values (Fig. 3). Note that Fig. 3 describes the use of the model in inference mode, i.e., it shows the forward pass only, without representing the backward pass.

Starting from the four years without missing values, we generated an arbitrary number (5 in this case) of repetitions of the entire dataset with missing values extracted from the distribution of TTF and TTR. All the repetitions of 2015 (a year with low precipitation) and 2018 (with high rainfall) composed the training set. The validation

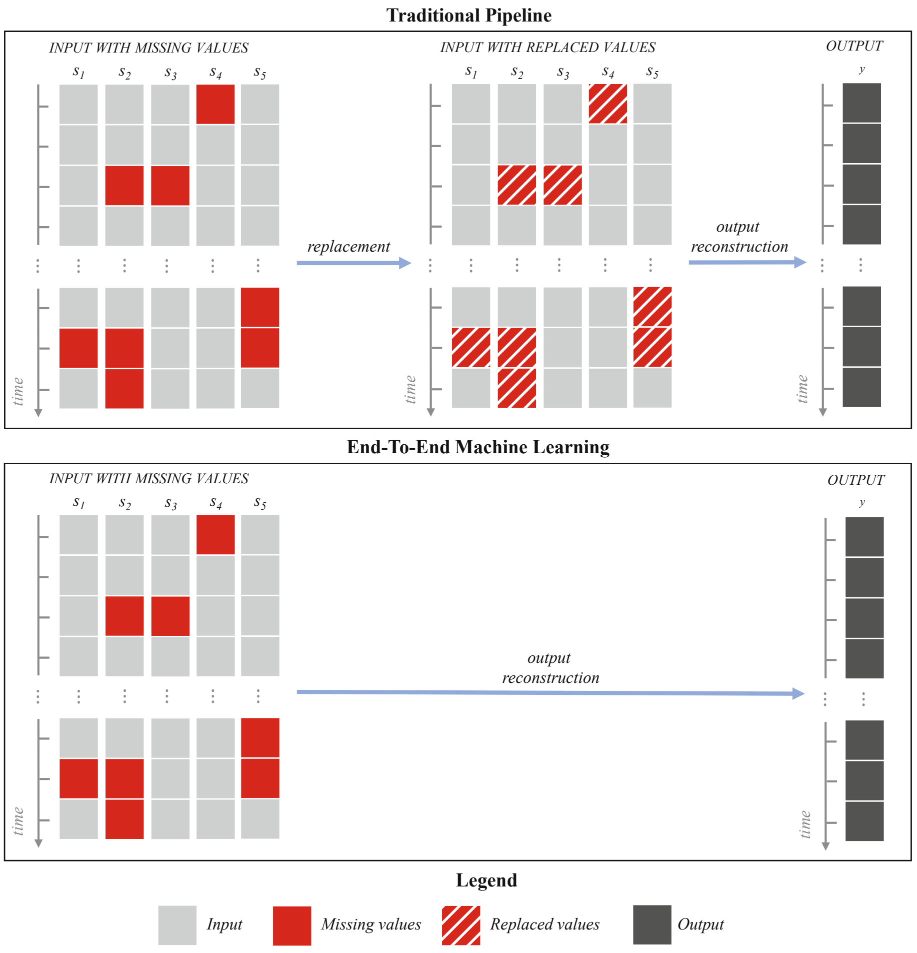

Fig. 3. Comparison between the Traditional Pipeline for managing missing data and the End-to-End Machine Learning used in this work.

set, used to determine the NN architecture and hyperparameters, is made by the five synthetic repetitions of the year 2016. Finally, the repetitions of the year 2017 have not been involved in the NN identification and are used to evaluate the network performances fairly. Performance metrics are thus computed as averages of five synthetic repetitions.

The neural structure adopted in this work is an LSTM net. Each LSTM cell has three gates (input, output, and forget gate), a cell state, and a hidden state [17, 18]. The hidden and cell states are responsible for keeping track of the relevant information provided by the input. The input and forget gates define how much a new input and the current state respectively affect the new state of the cell. The output gate determines how much the current state affects the output. The best combination of the hyperparameters has been selected using a traditional grid search approach. We evaluated the following values: 1 or 2 hidden layers; 5 or 10 neurons; learning rates of 10^{-1}, 10^{-2}, 10^{-3}; decay rates of 10^{-3}, 10^{-4}; batch sizes of 256, 512, or 1024 samples. We repeated the training three times for each combination of the hyperparameters to avoid particularly unfortunate cases. After the tuning process, the number of LSTM neurons was set to 10 (organized in a single hidden layer), the learning rate to 10^{-2}, the decay rate to $10^{-3,}$ and the batch size to 512.

3 Results

Several indicators have been computed to evaluate the performances of the proposed approach. First, as shown in Table 3, the Mean Squared Error (MSE) and coefficient of determination (R^2) have been computed over the training, validation, and test datasets. These values are compared in Table 3 with those obtained by an analytical benchmark: when a rain gauge is not working, its weight is set to zero, and the weights of the working sensors are increased accordingly. Once s_{tot} has been obtained, we apply the real nonlinear function to compute the output. Note that the proposed analytical benchmark is somehow unfair because we assume to know exactly the shape of the nonlinearity, which is generally unknown. Despite that, the NN clearly dominates this benchmark, with a 22% improvement of R^2 in the test set.

Figure 4 presents the traditional scatterplots showing the NN performance in reconstructing the output when the dataset is complete, i.e., no missing values, and incomplete, as in one of the synthetic sequences generated. Besides the generally good agreement between the actual output and the computed one, it is interesting to note that

Table 3. Performance comparison between the end-to-end approach and the analytical benchmark. The metrics are computed on the samples with at least one missing input and an actual output greater than 0.

Set	Metric	End-to-end machine learning	Analytical benchmark
Training	MSE	$0.83 \cdot 10^{-3}$	$1.52 \cdot 10^{-3}$
Training	R^2	0.94	0.89
Validation	MSE	$1.14 \cdot 10^{-3}$	$2.10 \cdot 10^{-3}$
Validation	R^2	0.91	0.84
Test	MSE	$1.86 \cdot 10^{-3}$	$4.81 \cdot 10^{-3}$
Test	R^2	0.86	0.64

the NN misses some episodes for which it definitely underestimated the output values. There are points in training, validation, and test datasets where the modeled output is very low, while the correct value should have been much higher. They represent the cases when the missing values were exactly related to the rain gauge where the peak precipitation was taking place.

One such episode is illustrated in column (a) of Fig. 5 (note that the input hyetographs go to −1 when the value is missing). The values recorded at s_4 are high and missing for the whole episode. Since the blackout started when it was not raining, nothing can be gained from the time profile. The rainfall episode partly interested also

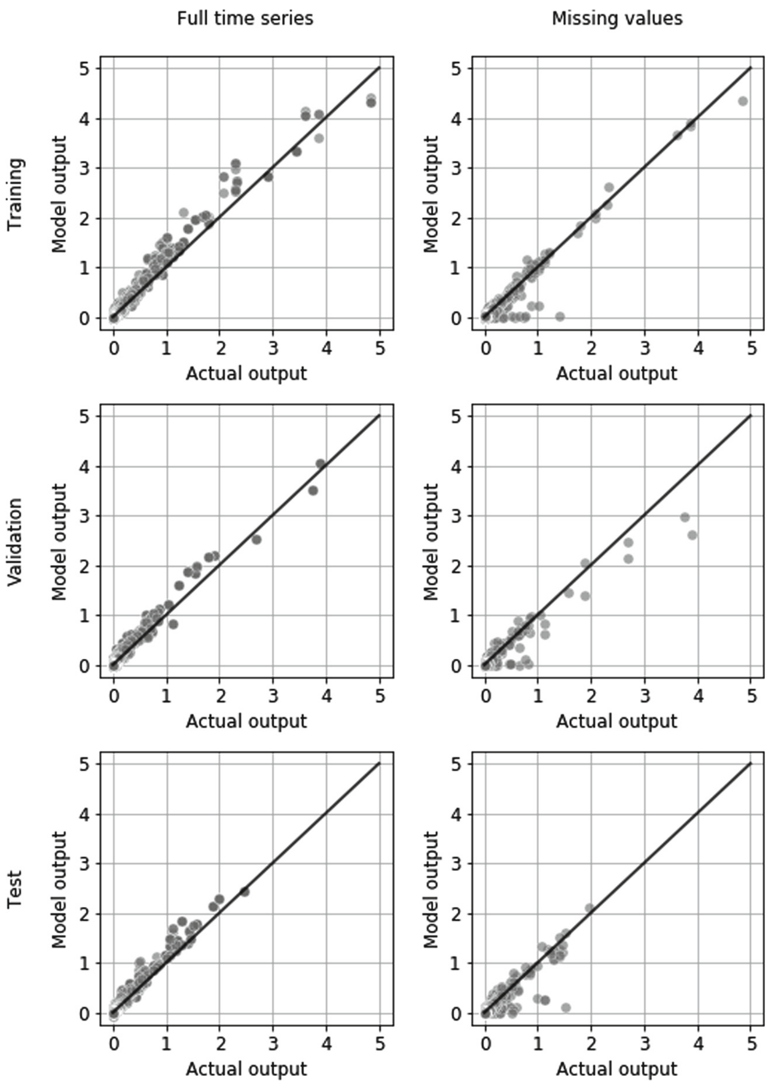

Fig. 4. Scatterplots showing the LSTM performances in the output reconstruction with a complete input dataset (left column) and with a dataset with missing values (right column). Performances are computed over train, validation, and test sets.

station 5, which however has a limited area and thus the output, particularly the second peak, is substantially missed. Things are different for the second episode in column (b). Again, station 4 is out-of-service, but the rainfall episode is more relevant on the other stations, and thus, peak values are almost perfectly fitted.

The NN performance in Fig. 5 (b), demonstrates that the information provided by the out-of-service station is not necessary to predict the output in the considered episode correctly. Despite that, the analytical benchmark strongly overestimates the peaks.

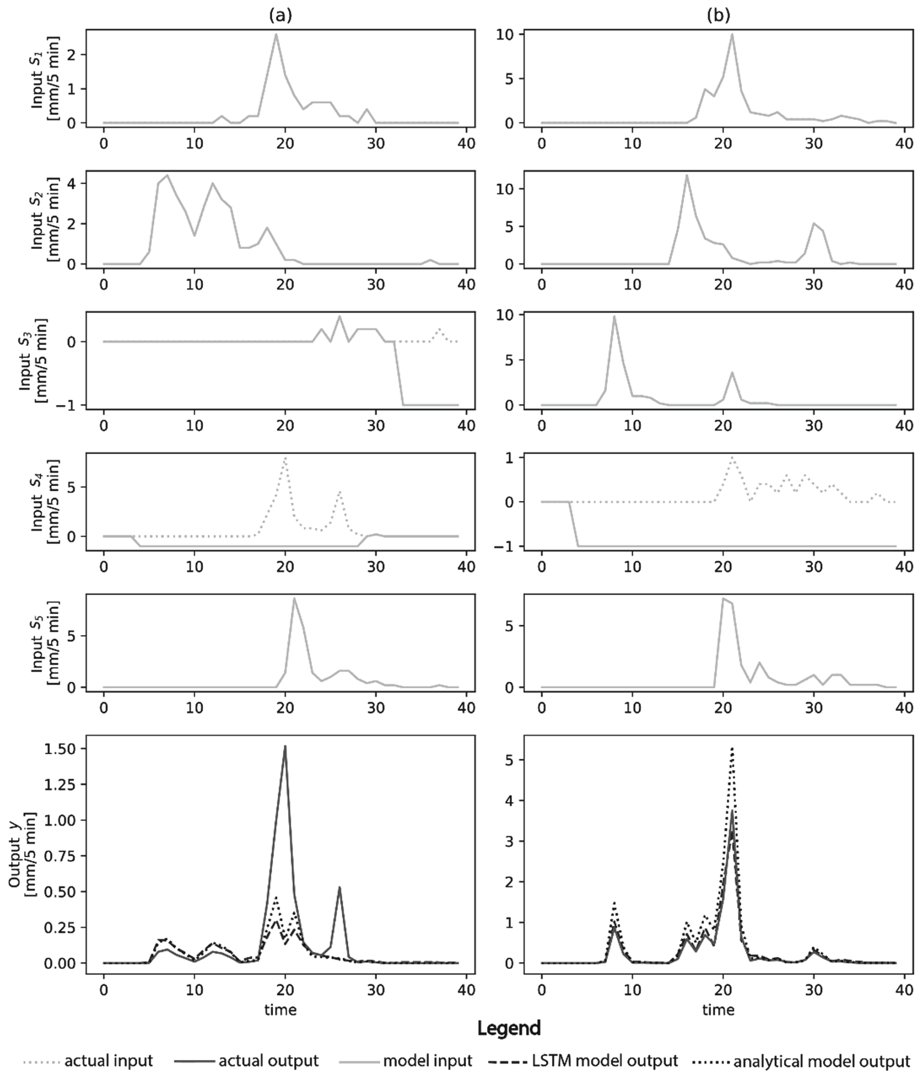

Fig. 5. Two rain episodes, (a) and (b), showing the 5 input hyetographs and the actual output compared with the LSTM model and the analytical model output.

4 Conclusion

The problem of missing data in a spatial time series set of environmental variables is addressed in this study using an LSTM neural network that directly operates between input (the time series with missing values) and output (the computed environmental variable). This means the NN operates end-to-end. The proposed approach completely by-pass the traditional phase of replacing the missing values with some external operation (some statistics, replacement with other sensor's values, omission) that, in one way or the other, alters the original information content. The NN must be suitably trained to learn how to deal with missing values, and, to do so, it is necessary to start from a complete dataset on which "artificial" failures are produced with the same statistical distribution of the real downtimes. Once this is accomplished, the NN is ready to enter operation and can immediately compute a real-time output, that inherently considers both time (on the same sensor) and space (between sensors) relations. This makes the approach much quicker than other methods, such as model assimilation that requires much more runtime power, and more precise than classical interpolation or imputation methods that simplify the time and/or space dependencies.

The proposed approach has been tested on a quite difficult case study of rainfall field reconstruction in Northern Italy, where episodes are rare, intense, and concentrated. This means that both temporal and spatial correlations are low, and when some critical sensors are not working, an accurate reconstruction of the rain field is definitely impossible. Nevertheless, even in this challenging case, the end-to-end neural approach outperforms the analytical benchmark competitor.

In this work, the gauge malfunctioning refers to a complete breakdown of a sensor, as in the actual dataset. In general, other situations may occur, leading to corrupted values (e.g., outliers). The proposed end-to-end approach can be specifically trained to compensate also for these faulty values.

When dealing with a more complex task, such as the forecasting of the actual runoff in the example considered here, the NN architecture may need to be enriched, but the results shown above suggest that the traditional "art" of filling field data gaps may progressively become obsolete.

Acknowledgements. We would like to thank ARPA Lombardia for providing the rainfall dataset. Valerio Guglieri is supported by Fondazione Cariplo (2017-0725), project: Lombardy-based Advanced Meteorological Predictions and Observations (LAMPO). The authors would like to thank all the administrative, management and scientific partners of the project.

References

1. Radi, N.F.A., Zakaria, R., Azman, M.A.Z.: Estimation of missing rainfall data using spatial interpolation and imputation methods. In: AIP Conference Proceedings, vol. 1643, no. 1, pp. 42–48. American Institute of Physics (2015)
2. Dhevi, A.S.: Imputing missing values using inverse distance weighted interpolation for time series data. In: 2014 Sixth International Conference on Advanced Computing (ICoAC), pp. 255–259. IEEE (2014)

3. Teegavarapu, R.S.: Missing precipitation data estimation using optimal proximity metric-based imputation, nearest-neighbour classification and cluster-based interpolation methods. Hydrol. Sci. J. **59**(11), 2009–2026 (2014)
4. Cressie, N.: The origins of kriging. Math. Geol. **22**(3), 239–252 (1990)
5. Stein, M.L.: Interpolation of Spatial Data: Some Theory for Kriging. Springer Science & Business Media, New York (2012)
6. Liu, Y., Weerts, A., Clark, M., Hendricks Franssen, H.J., Kumar, S., Moradkhani, H., Seo, D.J., Schwanenberg, D., Smith, P., Van Dijk, A.I.J.M., Van Velzen, N.: Advancing data assimilation in operational hydrologic forecasting: progresses, challenges, and emerging opportunities. Hydrol. Earth Syst. Sci. **16**, 3863–3887 (2012)
7. Weerts, A.H., Seo, D.J., Werner, M., Schaake, J.: Operational hydrologic ensemble forecasting. In: Applied Uncertainty Analysis for Flood Risk Management, pp. 387–406 (2014)
8. Pezij, M., Augustijn, D.C., Hendriks, D.M., Hulscher, S.J.: The role of evidence-based information in regional operational water management in the Netherlands. Environ. Sci. Policy **93**, 75–82 (2019)
9. Lagasio, M., Parodi, A., Pulvirenti, L., Meroni, A.N., Boni, G., Pierdicca, N., Marzano, F.S., Luini, L., Venuti, G., Realini, E., Gatti, A., Tagliaferro, G., Barindelli, S., Monti Guarnieri, A., Goga, K., Terzo, O., Rucci, A., Passera, E., Kranzlmueller, D., Rommen, B.: A synergistic use of a high-resolution numerical weather prediction model and high-resolution earth observation products to improve precipitation forecast. Remote Sensing **11**, 2387 (2019)
10. Xingjian, S.H.I., Chen, Z., Wang, H., Yeung, D.Y., Wong, W.K., Woo, W.C.: Convolutional LSTM network: a machine learning approach for precipitation nowcasting. In: Advances in Neural Information Processing Systems, pp. 802–810 (2015)
11. Ng, A.: Machine learning yearning, p. 96 (2017). http://www.mlyearning.org/
12. Sangiorgio, M., Barindelli, S.: Spatio-temporal analysis of intense convective storms tracks in a densely urbanized Italian basin. ISPRS Int. J. Geo-Inf. **9**, 183 (2020)
13. Sangiorgio, M., Barindelli, S., Biondi, R., Solazzo, E., Realini, E., Venuti, G., Guariso, G.: Improved extreme rainfall events forecasting using neural networks and water vapor measures. In: Proceedings of the 6th International Conference on Time Series and Forecasting (ITISE), Granada, Spain, vol. 2, pp. 820–826 (2019)
14. Sangiorgio, M., Barindelli, S., Biondi, R., Solazzo, E., Realini, E., Venuti, G., Guariso, G.: A comparative study on machine learning techniques for intense convective rainfall events forecasting. In: Advances in Time Series and Forecasting (Contributions to Statistics) stage of publication (under review)
15. Foresti, L., Sideris, I.V., Panziera, L., Beusch, L., Nerini, D., Germann, U.: Nowcasting orographic precipitation growth and decay using machine learning algorithms on a 10-year radar archive in the Swiss Alps. In: EGU General Assembly Conference Abstracts, vol. 20, p. 6361 (2018)
16. Meeker, W.Q., Escobar, L.A.: Statistical Methods for Reliability Data. Wiley, New York (2014)
17. Hochreiter, S., Schmidhuber, J.: Long short-term memory. Neural Comput. **9**(8), 1735–1780 (1997)
18. Goodfellow, I., Bengio, Y., Courville, A.: Deep learning. MIT Press, Cambridge (2016)

Semantic Segmentation Based on Convolution Neural Network for Steel Strip Position Estimation

Aline de Faria Lemos(✉) and Bálazs Vince Nagy

Department of Mechatronics, Optics and Mechanical Engineering Informatics, Budapest University of Technology and Economics, Budapest, Hungary
{alinefaria,nagyb}@mogi.bme.hu

Abstract. In this paper, a method to access the location of a steel strip in the rolling process was developed. The method consists of a hybrid system composed of a CNN-based semantic segmentation followed by morphological operation and outlier removal. The proposed method was capable of estimating the position of the strip with high precision and low computational burden, making it suitable for the application. The implementation of automatic estimation for the steel strip positioning, replacing the current human operation, can yield substantial costs saving. Future work will be carried out for the and integration of automatic control in the process.

Keywords: Steckell mill · Semantic segmentation · Convolution neural network · Hot strips

1 Introduction

Steel strips are manufactured from slabs, which undergo several times between a pair of work rolls until the obtention of the intended thickness reduction [15, 16, 31, 32]. During the rolling process in Steckell mill lines, the strips are moved in the rolling direction by the roller table. However, the strips could also be driven perpendicularly to this direction by the rolling procedure, which causes a misalignment of the strip. Consequently, the unaligned strips are prone to collide with the mill structure. As the 20 *ton* strips are rolled at 10 m/s, the collisions are an impairment for the production lines, causing material losses and severe damage to the mill structure and equipment. Annually, the material loss due to collisions and equipment failure expenses are about one million euros [9].

Most of the Steckell lines apply a semi-manual procedure to correct the aforementioned strips unalignment. In this procedure, a human operator has access to real-time process images acquired from analog cameras settled over the mill

Supported by Budapest University of Technology and Economics.

structure. From the content of the images, the operator evaluates the strip position and judges whether it displays misalignment. Based on this information the operator will attempt to manually correct the strip position through an encoder, which creates a gap difference between the extremities of the work rolls pair and steers the strip on the direction of the major gap. The alignment correction procedure is susceptible to failure due to the high longitudinal speed of the strips, which requires a reaction time that might exceed the human capability. Besides, a manual encoder is not a precise tool and can lead to inadequate control [7,9].

Automate the alignment of the strips in a Steckell mill line could reduce the damage to the plant, maintenance costs, and prevent material losses [9]. The start point through the automated process is to determine the strip position, which could be accessed by detecting the strip portion on process images. Nowadays, semantic segmentation based on the convolution neural network is largely used in object detection and classification. However, from the best of the authors' knowledge, there is no work on the available literature that employes such an approach to strip detection in a rolling mill process. On the other hand, there are a considerable number of studies that apply convolution neural networks in metalworking. Some examples are the detection of defects in metal casting [3,8], recognition of slab identification numbers [17], mechanical properties predicting [30], bearing fault diagnosis [12,14,24,28,33], steel defect identification [20,26], and crystallographic defects in structural alloys [23]. This work presents a method that employs the process images to estimate the strip position. The system extracts the strip portion of the image via semantic segmentation based on convolution neural network (CNN) and infers the strip position in relation to the image bottom edge.

2 Methodology

This work presents a method that employs supervised learning to estimate the position of steel strips in a Steckell Mill line. The method consists of a system that applies semantic segmentation based on a convolution neural network to extract the strip portion from process digital images and estimate its position in relation to the image bottom edge. The flowchart presented in Fig. 1 illustrates a summary of the system steps for obtaining the position of the strips.

The dataset is composed of 704×480 px RGB images, which were acquired by an analog camera installed over the mill structure with a frame rate of 30 fps. The acquired images are selected by the algorithm according to the activation command signal of the descaler and the strip tracking signal. During the descaler period, the images will present excessive noise content, due to the dense steam on the region between strip and camera. Also, the images acquired in the instants that the strip is not positioned under the camera are not relevant to the analysis. Therefore, in both circumstances, the acquired images will not be processed for position estimation.

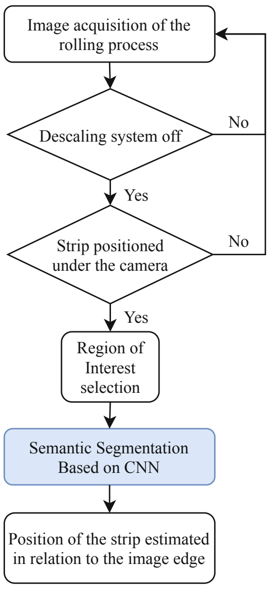
Image acquisition of the rolling process
Descaling system off
No
Yes
Strip positioned under the camera
No
Yes
Region of Interest selection
Semantic Segmentation Based on CNN
Position of the strip estimated in relation to the image edge

Fig. 1. System flow chart.

2.1 Regions of Interest and Labeling

The images contain a portion of the strip, horizontally aligned to the image bottom edge, and parts of the mill structure, which are irrelevant to the task in hand. Thus, a selection of a region of interest that lowers the number of mill components present on the image reduced its complexity. The elected region of interest (ROI) is highlighted in Fig. 2 over an example of the process images used as the system input.

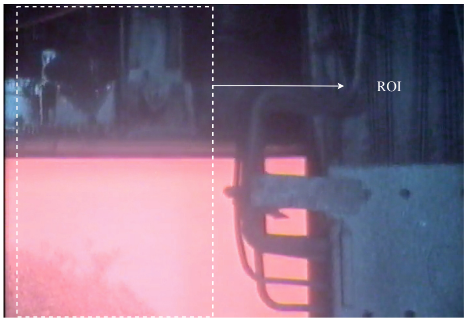

Fig. 2. Elected region of interest (ROI) over an example of the process images used as the system input.

The ground truth labeling of the strips was created by manual annotation, in which pixels belonging to the strip portion were assigned with intensity 1 and to the background with intensity 2. The selected dataset comprises 1390 images, which were split into training and test datasets on the proportion of 1112 to 278 images, respectively.

The images were acquired in a complex environment. The strip incandescence, resulting from the strip high temperature, reflects over the mill structures present in the surroundings of the strip. These structures mirror the strip color and could be easily mistaken as a strip portion. Examples of these reflections are indicated in Figs. 3-1*b*, -2*a*, -2*b*, and -2*c* by white arrows. Another complication is the presence of remaining elements from the descaler process. These elements are usually water over the strip and steam content on the strip location and surroundings. The water creates unpredictable patterns over the strip, as can be perceived in Figs. 3-1*b*, -1*c*, -2*b*, and -2*c*. On the other hand, the steam content blurry the acquired images. Figures 3-1*a*, -1*c*, and -2*a* show some of these blurring particularities. Considering these occasions, the labeling process was handled carefully to avoid misclassifications. In cases that portions of the strip were covered by steam, the labeling considers that the strip location is parallel to the image bottom.

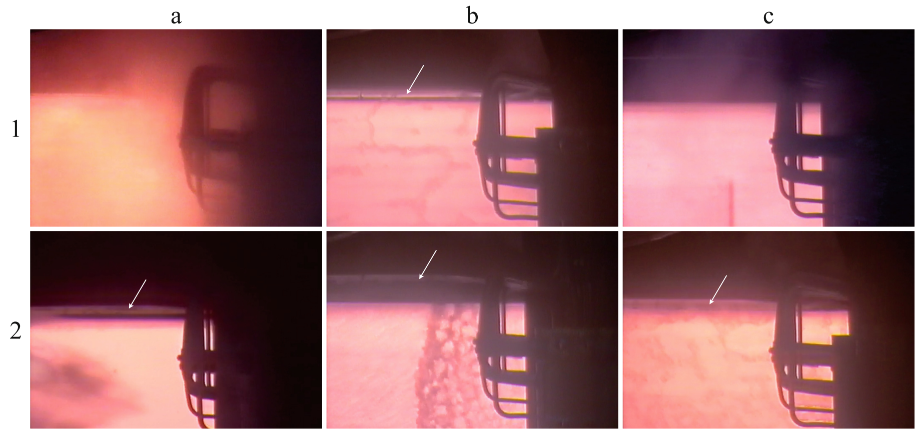

Fig. 3. Example of images acquired in a complex environment. The white arrows indicate the reflection of the strip incandescence over the mill structure. Images 1*a*, 1*c*, and 2*a* are blurred due to the steam content. Remaining water from the descaler process creates unpredictable patterns over the strip, which can be perceived in images 1*b*, 1*c*, 2*b*, and 2*c*.

2.2 Semantic Segmentation CNN Architecture

Semantic segmentation is a pixel-wise classification, which gathers pixels belonging to the same category [19,23,25]. This kind of network is widely used in autonomous driving [4,6,10,27], medical applications [1,21,22,34], object detection [11,29], automatic localization of defects in steel [8,23] to name a few. The architecture of a semantic segmentation network usually consists of an encoder-decoder task [2,13,18]. In the present work, the first part is composed of one or more convolution and max pooling operations, that extract high-level features by mapping the input to a lower dimension representation [18]. In contrast, the decoder architecture, commonly composed of transposed convolutions and up-pooling layers, expands the high-level features to recover the feature map size compatible with the input layer size [23], followed by another convolution layer and a softmax layer, enabling pixel-level classification.

In this study, 3 architecture configurations were investigated. They differ among each other by the number of encoder/decoder, varying between 1, 2, or 3 pairs. Figure 4 illustrates the largest network in terms of the number of layers (three encoders and three decoders). The influence of the number of filters in each operation was also ascertained, the number of filters could hold values from the set {2, 4, 8, 16, 32, 64}. Hence, eighteen architectures were explored altogether. Moreover, the Rectified Linear Unit (ReLU) activation function was applied after the convolution layers. As optimization parameters were selected Adam optimizer with a learning rate of 0.001.

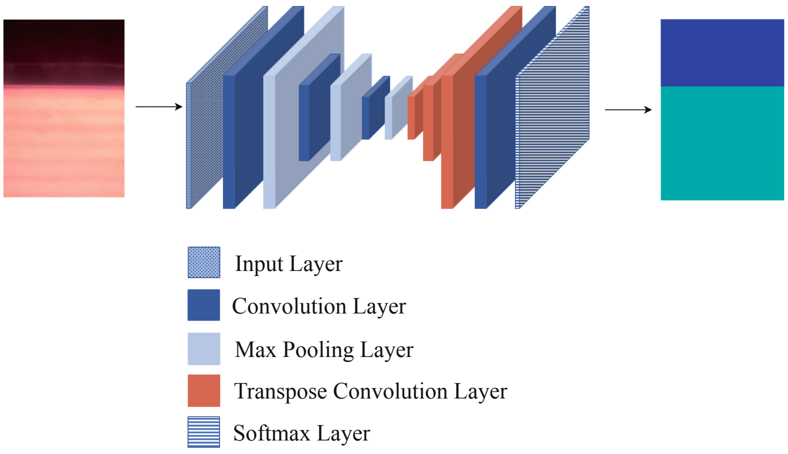

Fig. 4. Schematic illustration of one of the semantic segmentation architectures designed for strip detection.

2.3 Position Estimation

Morphological operations and outliers exclusion were employed to refine the semantic segmentation predictions. The strip portions predicted by CNN were extracted into a binary image, from which the largest connected component was kept and the smaller components were deleted. Afterward, a flood-fill was applied to fill possible holes in the strip area. Out of the resulting binary image, the strip position was estimated from the pixel locations of the top edge. As some of the predictions could present an irregular edge, an outlier removal with a threshold between 40 and 60% was applied and the position was calculated from the average of the remaining values.

2.4 Representation of the Strip Position in Physical Units

The frame size for the sampled pictures is 704 × 480 px. When the strip is not located under the camera it is possible to identify the presence of two rolls of the roller table arranged vertically in the image. The diameter of the rollers is equal to 400 mm and they comprehend 140 px of the image. Therefore, the images resolution is equal to 2.9 mm/px and the total area of the sampled images is 2011 × 1371 mm. From this information, the strip position could be estimated in millimeters.

2.5 Performance Evaluation

The proposed method is evaluated by comparing the estimated strip position to the expected values, calculated from the ground truth, by the Mean Absolute Error (MAE) and the Standard Deviation (STD). The execution time was also analyzed in order to access if the solution is fit for a real-time application. Additionally, the evaluation of each architecture was performed on the test set by common metrics used to evaluate the convolution neural network, which are pixel accuracy (Eq. 1), precision (Eq. 2), recall (Eq. 3), Jaccard index (Eq. 4), F1 score (Eq. 5), and specificity (Eq. 6) determined from the values of true positive (TP), true negative (TN), false positive (FP) and false negative (FN) results [5,19,23].

- Pixel accuracy

$$Pixel\ accuracy = \frac{TP + TN}{TP + FP + TN + FN} \tag{1}$$

- Precision

$$Precision = \frac{TP}{TP + FP} \tag{2}$$

- Recall

$$Recall = \frac{TP}{TP + FN} \tag{3}$$

- Jaccard index or Intersection-over-Union (IoU)

$$IoU = \frac{TP}{TP + FP + FN} \tag{4}$$

- F1 score (F1)

$$F1 = \frac{2 \times (Recall \times Precision)}{Recall + Precision} \tag{5}$$

- Specificity or true negative rate (TNR)

$$Specificity = \frac{TN}{TN + FP} \tag{6}$$

3 Results and Discussion

The present work aims to effectively localize steel strips in a Steckell mill line. This section presents the results achieved by the proposed methodology. All results and discussion are referring to the test set and were obtained with an Intel Core i7-8750H CPU, 2.20 GHz, processor and installed memory (RAM) of 16.0 Gb. The results of the semantic segmentation step from each network can be observed in Table 1. Concerning pixel accuracy, precision, recall, IoU, F1 score, and specificity, the models present similar performance with a maximum divergence between the best and worse results of $[0.2, 0.3, 0.2, 0.4, 0.2, 0.5]$, respectively. Considering the execution time, the results confirm the intuition that the lesser the numbers of layers and filters, the higher the processing frame rate.

Table 1. Semantic segmentation performance evaluation and position estimation metrics.

Model ID	Architecture	Number of filters	Pixel accuracy [%]	Precision [%]	Recall [%]	IoU [%]	F1 [%]	TNR [%]	Frame rate [fps]	MAE [mm]	STD [mm]
1	1	2	99.5	99.4	99.7	99.1	99.6	99.0	53.7	5.0	5.2
2		4	99.5	99.4	99.8	99.2	99.6	99.0	51.1	4.3	4.8
3		8	99.6	99.6	99.8	99.4	99.7	99.3	40.8	3.4	4.0
4		16	99.6	99.5	99.9	99.3	99.7	99.1	26.1	3.7	4.3
5		32	99.6	99.6	99.8	99.4	99.7	99.3	7.8	3.7	4.1
6		64	99.6	99.5	99.8	99.3	99.7	99.2	1.6	3.6	4.2
7	2	2	99.4	99.3	99.8	99.1	99.6	98.8	42.5	4.8	4.9
8		4	99.6	99.5	99.8	99.3	99.7	99.1	52.5	3.8	4.7
9		8	99.6	99.5	99.8	99.4	99.7	99.2	40.0	3.7	3.8
10		16	99.5	99.4	99.9	99.3	99.6	98.9	24.5	4.3	4.4
11		32	99.6	99.5	99.9	99.3	99.7	99.1	6.1	3.7	3.9
12		64	99.6	99.5	99.9	99.4	99.7	99.1	1.6	3.4	3.9
13	3	2	99.5	99.4	99.8	99.2	99.6	99.0	41.2	5.2	4.6
14		4	99.6	99.6	99.8	99.4	99.7	99.3	47.1	3.7	4.2
15		8	99.6	99.5	99.9	99.4	99.7	99.1	38.5	3.9	3.6
16		16	99.6	99.4	99.9	99.4	99.7	99.0	23.9	4.2	3.4
17		32	99.6	99.5	99.9	99.4	99.7	99.2	5.4	3.8	3.3
18		64	99.7	99.6	99.9	99.5	99.7	99.3	1.6	3.4	3.3

However, the segmentation process is only an intermediate step of the process. The actual output of the system is the strip position estimation and the system performance regarding this value is evaluated from the Mean Absolute Error and the Standard Deviation metrics, which are also presented in Table 1. Even though all the models presented satisfactory results, under 5.2 mm, a sensible differentiation can be drawn among the results.

The model configuration with architecture 1 (one encoder and one decoder set) and 8 convolution filters in each layer (Model ID 3) was elected the best model by the authors. This model achieved the best combination of Mean Absolute Error and frame rate, 3.4(±4.0) mm, and 40.8 fps, respectively. Even though another two models (Model ID 12 and 18) achieved a comparable degree of precision, their frame rate is lesser than 30 fps (frame rate of the video-camera), which is non-desirable for a real-time application.

Moreover, Fig. 5 shows the evolution of the estimated and expected position through time for model 3. The graphical representation reiterates the numerical results showing that the proposed methodology can estimate successfully the strip position.

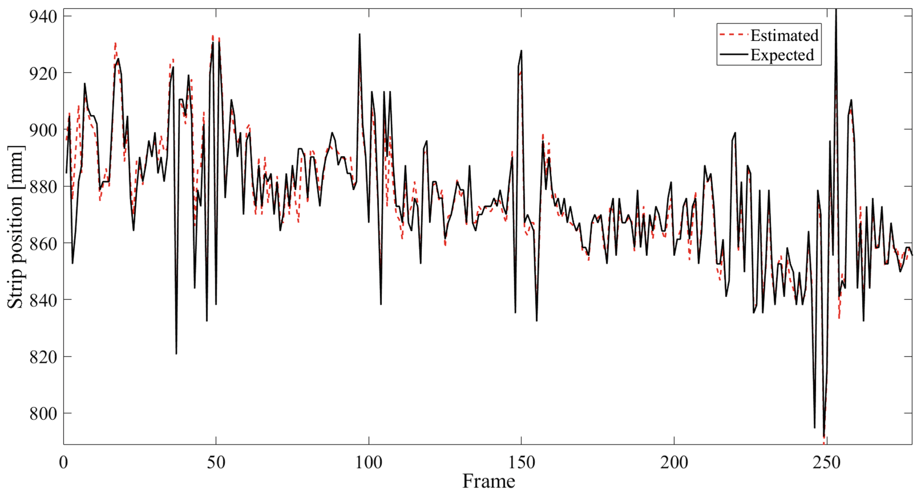

Fig. 5. Estimated strip position in relation to the expected values of model ID 3.

Lastly, Fig. 6 exemplifies the whole process, showing six samples. For each pair, it can be observed the input on the left and the output on the right. The output image consists of the image overlaid by the segmentation classification in pink and a black line showing the estimated position given by the morphological operations and outliers exclusion. It is worth mentioning the robustness of the system, correctly placing the black line even when the segmentation step provides insufficient results. The proposed methodology can estimate the strip position even in a complex environment, such as the steam presence (pairs 1*c* and 2*b*), mill structures reflecting the strip incandescence (pairs 1*b* and 2*a*) and water presence over the strip (pairs 1*a*, 1*b* and 2*c*).

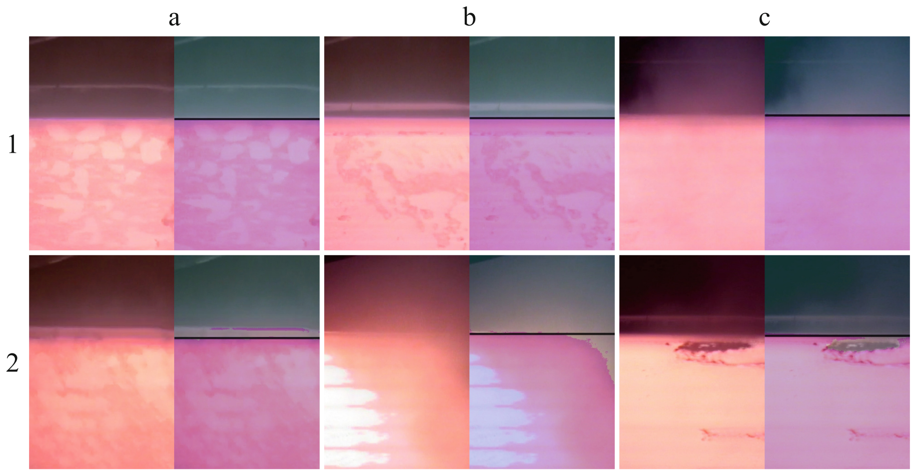

Fig. 6. Pairs of regions of interest containing the acquired image, on the left, and the semantic segmentation prediction, on the right. The black line over the labeled image indicates the position of the strip estimated by the system.

4 Conclusion

In this paper, a method to access the location of a steel strip in the rolling process was developed. The method consists of a hybrid system composed of a CNN-based semantic segmentation followed by morphological operation and outlier removal. The proposed method was capable of estimating the position of the strip with high precision and low computational burden, making it suitable for the application. The implementation of automatic estimation and control for the steel strip positioning, replacing the current human operation, can yield substantial costs saving. Future work will be carried out for the and integration of automatic control in the process.

Acknowledgment. The research reported in this paper was supported by the Higher Education Excellence Program of the Ministry of Human Capacities in the frame of Artificial Intelligence research area of Budapest University of Technology and Economics (BME FIKP-MI/FM); by the National Research, Development and Innovation Fund (TUDFO/51757/2019-ITM, Thematic Excellence Program); by the János Bolyai Scholarship of the Hungarian Academy of Sciences to BVN; and by the Stipendium Hungaricum Scholarship Programme.

References

1. Almotairi, S., Kareem, G., Aouf, M., Almutairi, B., Salem, M.A.M.: Liver tumor segmentation in CT scans using modified segnet. Sensors **20**(5), 1516 (2020)
2. Badrinarayanan, V., Kendall, A., Cipolla, R.: SegNet: a deep convolutional encoder-decoder architecture for image segmentation. IEEE Trans. Pattern Anal. Mach. Intell. **39**(12), 2481–2495 (2017)

3. Chen, F.C., Jahanshahi, M.R.: NB-CNN: deep learning-based crack detection using convolutional neural network and naïve bayes data fusion. IEEE Trans. Industr. Electron. **65**(5), 4392–4400 (2017)
4. Cordts, M., Omran, M., Ramos, S., Rehfeld, T., Enzweiler, M., Benenson, R., Franke, U., Roth, S., Schiele, B.: The cityscapes dataset for semantic urban scene understanding. In: Proceedings of the IEEE Conference on Computer Vision and Pattern Recognition, pp. 3213–3223 (2016)
5. DeCost, B.L., Lei, B., Francis, T., Holm, E.A.: High throughput quantitative metallography for complex microstructures using deep learning: a case study in ultrahigh carbon steel. Microsc. Microanal. **25**(1), 21–29 (2019)
6. Ess, A., Müller, T., Grabner, H., Van Gool, L.J.: Segmentation-based urban traffic scene understanding. In: BMVC, vol. 1, p. 2. Citeseer (2009)
7. de Faria Lemos, A., da Silva, L.A.R., Furtado, E.C., de Paula, H.: Positioning error estimation of steel strips in steckel rolling process using digital image processing. In: 2017 IEEE Industry Applications Society Annual Meeting, pp. 1–8. IEEE (2017)
8. Ferguson, M., Ak, R., Lee, Y.T.T., Law, K.H.: Automatic localization of casting defects with convolutional neural networks. In: 2017 IEEE International Conference on Big Data (Big Data), pp. 1726–1735. IEEE (2017)
9. Ferreira, A.B.S.: Adaptive fuzzy logic steering controller for a Steckel mill. Ph.D. thesis, University of Johannesburg (2005)
10. Geiger, A., Lenz, P., Urtasun, R.: Are we ready for autonomous driving? the kitti vision benchmark suite. In: 2012 IEEE Conference on Computer Vision and Pattern Recognition, pp. 3354–3361. IEEE (2012)
11. Girshick, R., Donahue, J., Darrell, T., Malik, J.: Rich feature hierarchies for accurate object detection and semantic segmentation. In: Proceedings of the IEEE Conference on Computer Vision and Pattern Recognition, pp. 580–587 (2014)
12. Hoang, D.T., Kang, H.J.: Rolling element bearing fault diagnosis using convolutional neural network and vibration image. Cogn. Syst. Res. **53**, 42–50 (2019)
13. Hong, S., Oh, J., Lee, H., Han, B.: Learning transferrable knowledge for semantic segmentation with deep convolutional neural network. In: Proceedings of the IEEE Conference on Computer Vision and Pattern Recognition, pp. 3204–3212 (2016)
14. Janssens, O., Slavkovikj, V., Vervisch, B., Stockman, K., Loccufier, M., Verstockt, S., Van de Walle, R., Van Hoecke, S.: Convolutional neural network based fault detection for rotating machinery. J. Sound Vib. **377**, 331–345 (2016)
15. Konovalov, Y.V., Khokhlov, A.: Benefits of steckel mills in rolling. Steel Transl. **43**(4), 206–211 (2013)
16. Kwon, W., Kim, S., Won, S.: Active disturbance rejection control for strip steering control in hot strip finishing mill. IFAC-PapersOnLine **48**(17), 42–47 (2015)
17. Lee, S.J., Yun, J.P., Koo, G., Kim, S.W.: End-to-end recognition of slab identification numbers using a deep convolutional neural network. Knowl.-Based Syst. **132**, 1–10 (2017)
18. Lin, G., Milan, A., Shen, C., Reid, I.: RefineNet: Multi-path refinement networks for high-resolution semantic segmentation. In: Proceedings of the IEEE Conference on Computer Vision and Pattern Recognition, pp. 1925–1934 (2017)
19. Long, J., Shelhamer, E., Darrell, T.: Fully convolutional networks for semantic segmentation. In: Proceedings of the IEEE Conference on Computer Vision and Pattern Recognition, pp. 3431–3440 (2015)
20. Masci, J., Meier, U., Ciresan, D., Schmidhuber, J., Fricout, G.: Steel defect classification with max-pooling convolutional neural networks. In: The 2012 International Joint Conference on Neural Networks (IJCNN), pp. 1–6. IEEE (2012)

21. Pham, D.L., Xu, C., Prince, J.L.: Current methods in medical image segmentation. Annu. Rev. Biomed. Eng. **2**(1), 315–337 (2000)
22. Rashed, E.A., Gomez-Tames, J., Hirata, A.: End-to-end semantic segmentation of personalized deep brain structures for non-invasive brain stimulation. Neural Netw. **125**, 233–245 (2020)
23. Roberts, G., Haile, S.Y., Sainju, R., Edwards, D.J., Hutchinson, B., Zhu, Y.: Deep learning for semantic segmentation of defects in advanced stem images of steels. Sci. Rep. **9**(1), 1–12 (2019)
24. Sadoughi, M., Hu, C.: Physics-based convolutional neural network for fault diagnosis of rolling element bearings. IEEE Sens. J. **19**(11), 4181–4192 (2019)
25. Sevak, J.S., Kapadia, A.D., Chavda, J.B., Shah, A., Rahevar, M.: Survey on semantic image segmentation techniques. In: 2017 International Conference on Intelligent Sustainable Systems (ICISS), pp. 306–313. IEEE (2017)
26. Soukup, D., Huber-Mörk, R.: Convolutional neural networks for steel surface defect detection from photometric stereo images. In: International Symposium on Visual Computing, pp. 668–677. Springer (2014)
27. Treml, M., Arjona-Medina, J., Unterthiner, T., Durgesh, R., Friedmann, F., Schuberth, P., Mayr, A., Heusel, M., Hofmarcher, M., Widrich, M., et al.: Speeding up semantic segmentation for autonomous driving. In: MLITS, NIPS Workshop, vol. 2, p. 7 (2016)
28. Wei, Y., Chang-Qing, S., Xiao-Jie, G., Zhong-Kui, Z.: Bearing fault diagnosis using convolution neural network and support vector regression. In: DEStech Transactions on Engineering and Technology Research (ICMECA) (2017)
29. Xie, C., Wang, J., Zhang, Z., Zhou, Y., Xie, L., Yuille, A.: Adversarial examples for semantic segmentation and object detection. In: Proceedings of the IEEE International Conference on Computer Vision, pp. 1369–1378 (2017)
30. Xu, Z.W., Liu, X.M., Zhang, K.: Mechanical properties prediction for hot rolled alloy steel using convolutional neural network. IEEE Access **7**, 47068–47078 (2019)
31. Yang, S.S., He, Y.H., Wang, Z.L., Zhao, W.S.: A method of steel strip image segmentation based on local gray information. In: 2008 IEEE International Conference on Industrial Technology, pp. 1–4. IEEE (2008)
32. Youkachen, S., Ruchanurucks, M., Phatrapomnant, T., Kaneko, H.: Defect segmentation of hot-rolled steel strip surface by using convolutional auto-encoder and conventional image processing. In: 2019 10th International Conference of Information and Communication Technology for Embedded Systems (IC-ICTES), pp. 1–5. IEEE (2019)
33. Zhang, W., Li, C., Peng, G., Chen, Y., Zhang, Z.: A deep convolutional neural network with new training methods for bearing fault diagnosis under noisy environment and different working load. Mech. Syst. Signal Process. **100**, 439–453 (2018)
34. Zhang, Z., Wu, C., Coleman, S., Kerr, D.: DENSE-inception U-net for medical image segmentation. Comput. Methods Programs Biomed. **192**, 105395 (2020)

Towards a Digital Twin with Generative Adversarial Network Modelling of Machining Vibration

Evgeny Zotov(✉), Ashutosh Tiwari, and Visakan Kadirkamanathan

Department of Automatic Control and Systems Engineering, University of Sheffield, Sheffield, UK
{ezotov1,a.tiwari,visakan}@sheffield.ac.uk

Abstract. Transition towards Industry 4.0 relies heavily on manufacturing digitalisation. Digital twin plays a significant role among the pool of relevant technologies as a powerful tool that is expected provide digital access to detailed real-time monitoring of the physical processes and enable significant optimisation due to utilisation of big data acquired from them. Over the past years a significant number of works produced conceptual frameworks of digital twins and discussed their requirements and benefits. The research literature demonstrates application examples and proofs of concepts, although the content is less rich. This paper presents a generative model based on generative adversarial networks (GAN) for machining vibration data, discusses its performance and analyses the drawbacks. The proposed model includes process parameter inputs used to condition the features of generated signals. The control over the generator and a neural network architecture utilising techniques from style-transfer research provide the means to analyse the signal building blocks learned by the model and explore their relationship. The quality of the learned process representation is demonstrated using a dataset obtained from a machining time-domain simulation. The novel results constitute a critical component of a machining digital twin and open new research directions towards development of comprehensive manufacturing digital twins.

Keywords: Generative adversarial network · Digital twin · Machining

1 Introduction

The 4th industrial revolution, i.e. the strategic vision of transition to Industry 4.0, draws a path to a totally customisable production with viable single-item batch production, just-in-time execution and high resource-efficiency. Advances along this path are believed to be feasible as a result of pervasive digitalisation throughout the industry, spanning from the shop-floor to the whole supply chain and to the users of the end-products [7]. Total factory digitalisation is being made possible by the technologies emerging from the research fields of big data, cyber-physical systems (CPS) and industrial internet of things (IIoT). Digital twin is a precise representation of a physical object or process in the digital realm. Development of digital twins is an important step of the digitalisation process, as the unification of digital and physical data within a single virtual object enables significant efficiency improvements across multiple stages of the object's life cycle [17].

Expert-based analytics models tend to achieve high accuracy rates, but have several drawbacks that can become blocking factors for implementation of a digital twin. On one hand, in an interconnected CPS environment interactions between the components introduce very high complexity of the modelled phenomena. On the other hand, the incremental character of module development and the fluid module composition cause an almost constant stream of changes in the system [12]. Data-driven modelling addresses these issues by making use of big data produced by the various manufacturer's CPS and automating the modelling process, thus aligning the digital twin state with the evolutionary changes in the modelled systems.

Development of efficient and flexible generative data-driven models of physical manufacturing processes is an important step towards CPS digitalisation in general, and particularly to wide adoption of digital twins throughout the industry. Artificial neural networks (ANN) have shown increasingly impressive state-of-art results on many data-driven problems during the past decades. Generative adversarial network (GAN) is a type of ANN architecture based on a minimax game between two ANN: the generator that learns to produce artificial data samples and the discriminator that learns to identify fake data samples [5]. Recently GANs found various uses, most notable in generation of realistic images of human faces [10].

GAN is a suitable candidate for digital twin development due to its efficiency at inference time and the generative nature of the model, in addition to the flexibility of a data-driven method. This paper proposes a GAN-based digital twin model that captures the conditional distribution of a signal, conditioned on the controlled parameters of the underlying process. Vibration is selected as the analysed signal type based on the low expected cost of its acquisition and potential usefulness in analysis of the process.

2 Methodology

2.1 Dataset: Machining Tool Vibration

The proposed model is tested on a simulated dataset representing the displacement (vibration) of a cutting tool along the x direction originating from the interactions between the tool and a workpiece. The operation considered is a linear non-slotting milling cut performed with a straight-teeth cutting tool on a metal workpiece. The dataset is produced using a physics-based time domain simulation model described in [15]. The model tracks the position of each cutting tooth and the workpiece geometry produced by previous cuts and derives the tool displacement from the forces produced by the interaction of the cutting teeth and the workpiece at each simulation time step. The simulation parameters used are detailed in Table 1. The parameter values are constant throughout each cutting operation, and the parameters varied across the samples in the produced dataset are chip width and spindle speed in ranges from 4e-3 to 5e-3 and 3000 to 4000 respectively. The generated signals represent the displacement of the cutting tool during the third revolution of the cutting tool, sampled at a rate proportional to the spindle speed so that all signals are of the same length.

Table 1. Milling time domain simulation parameters

Parameter	Value
Feed rate f	10.2
Spindle speed ω	3000 to 4000
Number of teeth N_t	3
Chip width b	4e-3 to 5e-3
Steps per revolution	256
Start angle of cut ϕ_s	126.9
Exit angle of cut ϕ_e	180
Process dependent coefficient K_s	2250e6
Force angle β	75
x Direction dynamics parameter k_x	9e6
x Direction dynamics parameter ζ_x	0.02
y Direction dynamics parameter k_y	1e7
y Direction dynamics parameter ζ_y	0.01
Number of revolutions (data recorded for third revolution only)	3

2.2 Model Architecture

The proposed digital twin is based on the generative adversarial network (GAN) model conceived in 2014 [5]. The authors combined two neural networks within a zero-sum game. One network, the discriminator is rewarded for high accuracy of classification of data samples as either real or fake. The other network, the generator, is rewarded for generation of fake samples that are classified by the discriminator as real. Therefore, the generator approximates the true data distribution through the training process. The approach was extended in multiple directions, including but not limited to research on various neural network architectures for the generator and the discriminator (e.g., Deep Convolutional GAN [13], BigGAN [2], StackGAN [19], WaveGAN [4], SeqGAN [18], Bayesian GAN [14]) reviews of the GAN training approaches and the networks' loss functions (notably, the application of Earth Mover distance as the loss metric in Wasserstein GAN [1], its extension with gradient penalty in WGAN-GP [6] and progressive GAN growing [9]),experiments with conditioning the GAN by additional inputs or outputs, as proposed in Conditional GAN [11], InfoGAN [3] and ss-InfoGAN [16].

The developed neural network architecture is inspired by StyleGAN [10], an image generation model based on two-dimensional deep convolutional discriminator and generator networks. Elements of the StyleGAN are repurposed for the 1D case of a time domain signal, excluding the noise inputs, as the variation of outputs of the target model is deterministic with respect to the input process parameters. The architecture is enhanced with the substitution of the random input latent vector for continuous labels C: the machining process parameters, chip width and spindle speed. The process parameters are used as inputs to the generator and as outputs of the discriminator, i.e. the discriminator learns to not only identify synthetic data samples, but also to estimate the labels associated with a given time-series. The architecture includes a non-linear mapping network M that projects latent inputs into disentangled latent space, approximated by a multi-layer feedforward neural network. The styles $S = M(C)$ produced from the input labels C by the mapping network subsequently control the modulation of outputs of the convolutional layers within the synthesis network F of the generator (see Fig. 1).

The GAN loss function is based on Wasserstein GAN with gradient penalty (WGAN-GP) [6]. WGAN-GP losses for the generator and the discriminator are

$$\begin{aligned} L_G^{wgan\text{-}gp} &= -\mathop{\mathbb{E}}_{\tilde{x}\sim\mathbb{P}_g}[D(\tilde{x})], \\ L_D^{wgan\text{-}gp} &= \mathop{\mathbb{E}}_{\tilde{x}\sim\mathbb{P}_g}[D(\tilde{x})] - \mathop{\mathbb{E}}_{x\sim\mathbb{P}_r}[D(x)] + \lambda_{gp}L^{gp} \end{aligned} \tag{1}$$

respectively, where

$$L^{gp} = \mathop{\mathbb{E}}_{\tilde{x}\sim\mathbb{P}_{\tilde{x}}}[(||\nabla_{\tilde{x}}D(\tilde{x})||_2 - 1)^2] \tag{2}$$

is the gradient penalty and λ_{gp} is its scaling hyperparameter. The loss functions are adjusted to accommodate the inclusion of machining process parameters in the networks architecture by addition of terms that penalise inaccurate label predictions. This is similar to the approach followed by the authors of InfoGAN [3], with the following difference. The accuracy of label predictions for training data L_D^{info} impacts only the discriminator, while the accuracy of the predictions for fake data samples L_G^{info} is taken into account only by the generator. The loss terms are

$$\begin{aligned} L_G^{info} &= \sqrt{\frac{\sum_{j=1}^{n}(c_{f,j} - c_{t,j})^2}{n}}, \\ L_D^{info} &= \sqrt{\frac{\sum_{j=1}^{n}(c_{r,j} - c_{t,j})^2}{n}}, \end{aligned} \tag{3}$$

where $c_{f,j}$ is a value of parameter j predicted by the discriminator based on a fake signal, $c_{r,j}$ is a value predicted from a real signal, and $c_{t,j}$ are the true parameter values. On one hand, the generator is thus incentivised to encode the

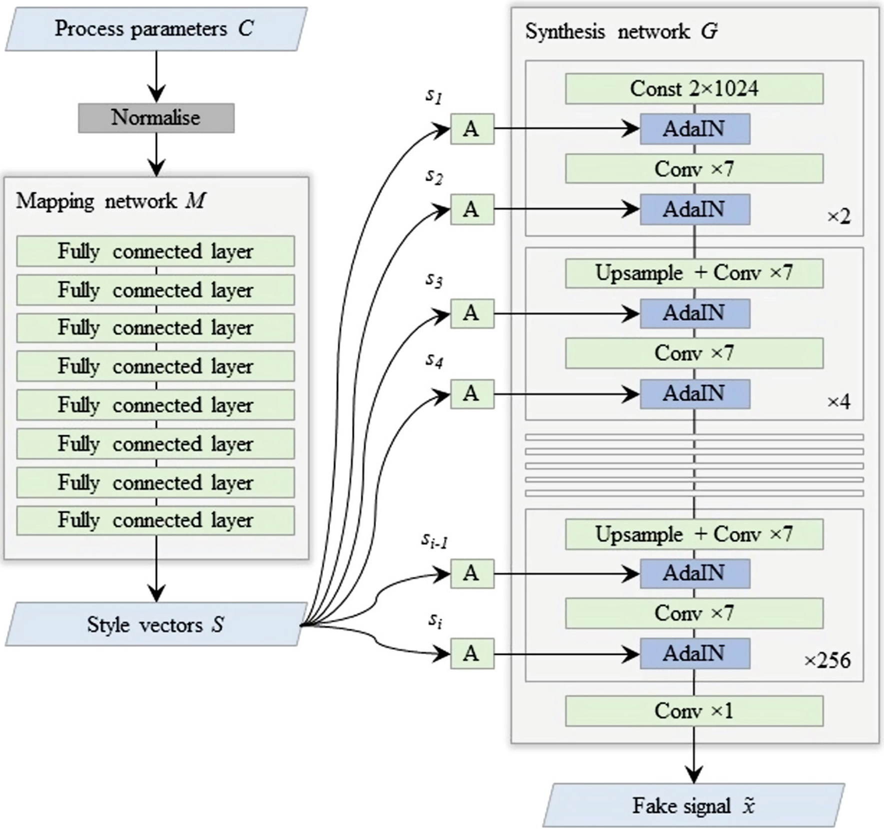

Fig. 1. Architecture of the generator F. "A" denotes learned affine transformations of style components s_i; "AdaIN" - adaptive instance normalisation [8], outputs of which are modulated by the transformed style components.

label information in an identifiable way within the synthesised samples. On the other hand, the discriminator learns the relationship between labels and samples only on the real data, thus preserving the non-cooperative nature of the minimax game between the generator and the discriminator. The total loss functions for the generator L_G and the discriminator L_D are therefore:

$$\begin{aligned} L_G &= L_G^{wgan\text{-}gp} + \lambda_{info} L_G^{info}, \\ L_D &= L_D^{wgan\text{-}gp} + \lambda_{info} L_D^{info}, \end{aligned} \tag{4}$$

where λ_{info} is the scaling factor for the label prediction accuracy error loss.

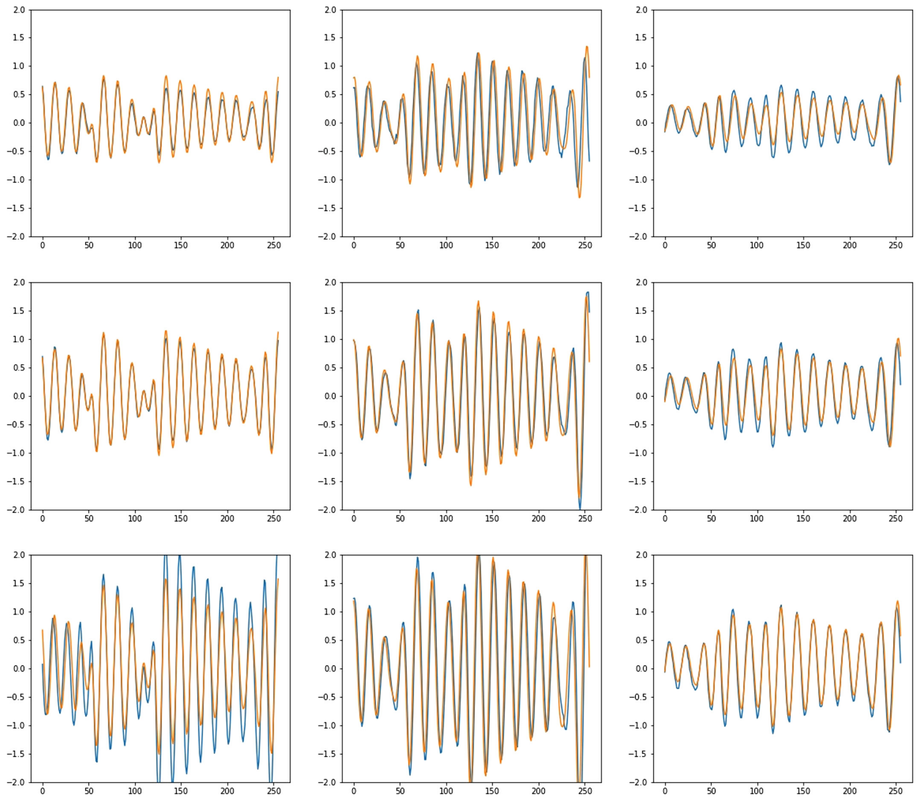

Fig. 2. Comparison of generated time-series samples (blue) and validation data samples (yellow). X axis represents time steps, Y axis - displacement magnitude in log scale.

3 Experimental Results

The paper shows that the generator successfully learns to capture the relationship between the process parameters and the time domain signal and performs well both on training and validation data. Figure 2 depicts several samples of generated time-series against the signals from training data produced using the same process parameters.

3.1 Visualisation of Generator Performance

The generative performance of the neural network is investigated via analysis of metrics mapped across machining process parameter values, chip width and spindle speed. This is visualised by calculating the inspected metric for a range of process parameter pairs and plotting the values on a two-dimensional figure with spindle speed varied across the X axis and chip width across the Y axis. The training data exhibits high variability, especially across the spindle speed parameter values, visible on the plot of standard deviations of the training data signals (Fig. 3). Figure 4 depicts the root mean square error (RMSE) of the generated time-series (i.e. the error between synthetics signals and dataset signals) on training and on validation data. RMSE distributions are nearly identical, i.e. the generator performs equivalently during both training and validation.

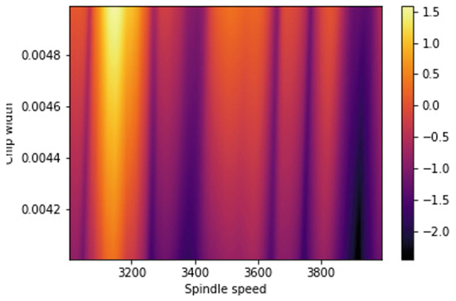

Fig. 3. Standard deviation of training data samples (log scale).

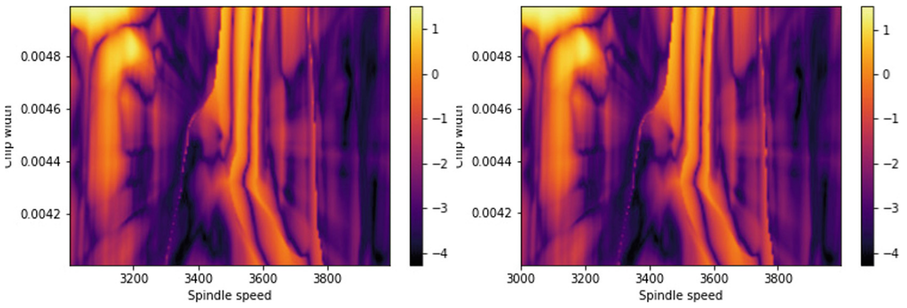

Fig. 4. RMSE values in log scale for generated time-series across various process parameter values for training data (left) and validation data (right). Equivalence of accuracy on both indicates low over-fitting.

In contrast to the high accuracy of the generator in the areas of the parameter space characterised by low dispersion in the training data, the generative performance is suboptimal in some regions of high training data variance. Closer inspection of a region between 3500 and 3600 spindle speed reveals that the generator experiences local mode collapse (for an example refer to Fig. 5). The troughs visible on the RMSE map in this region represent a parameter space where the generator successfully learnt the modes of the target signal, while the three peaks between and to the sides along the X axis from these narrow bands of high accuracy are indicative of the dropped modes. An inspection of the dynamics of change of the training data signals compared to the change of the synthesised signals reveals that whereas the training data signals change shape

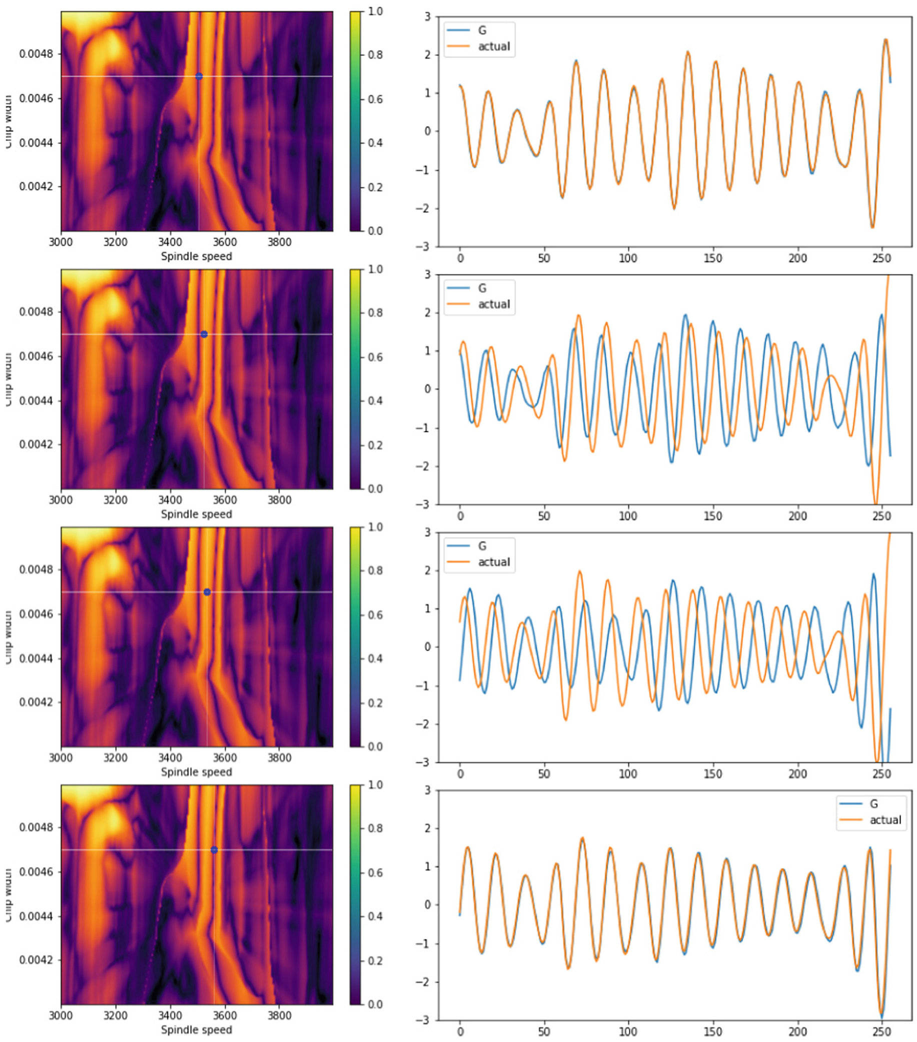

Fig. 5. Example of a path in labels space where the transition between the signal modes is smooth in the training data, but abrupt in the signals produced by the generator. The blue dot on the RMSE maps (left) indicates the parameter values used to compare the two signals (right), real signal in yellow and generated signal in blue. The differences between the fake signals along the labels transition paths shown on the two top figures and the two bottom figures are much lower than for the real signal. The opposite is true for the transition captured by the two middle figures.

linearly with the change in spindle speed, the generated signals remain constant for most of the inspected parameter space and sharply switch to the next mode near the peak on the RMSE map.

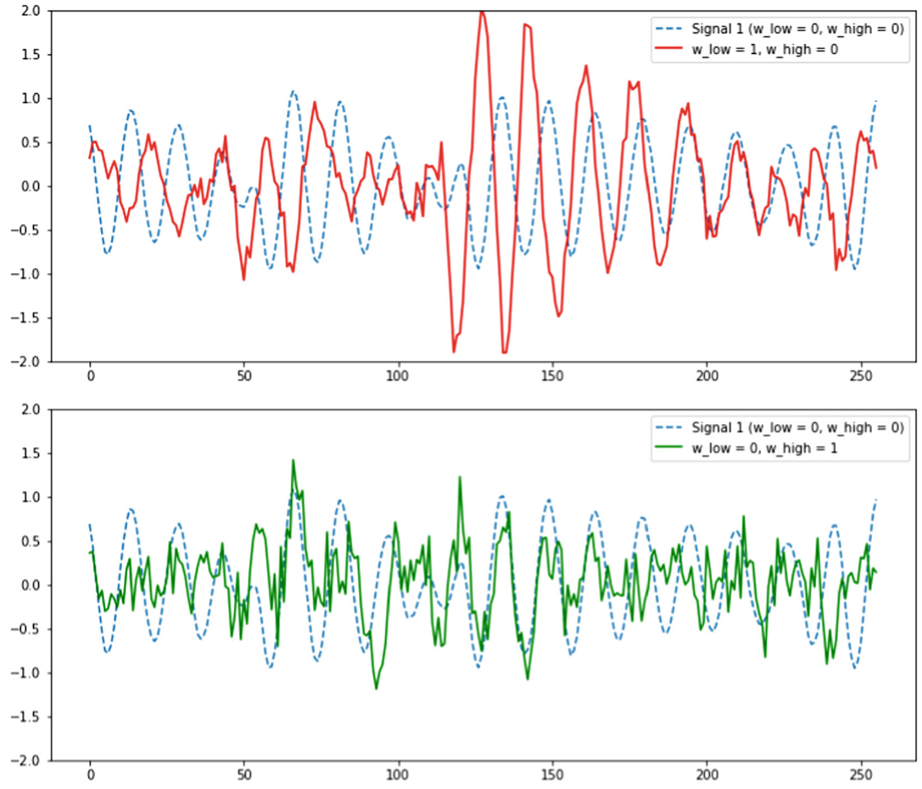

Fig. 6. Interpolated signal $\tilde{x}_3$ comparison with a source signals $\tilde{x}_1$ (top two figures) and $\tilde{x}_2$ (bottom two figures). The blue dashed line on the first figure represents the initial signal $\tilde{x}_1$. Red line, an interpolated signal based on $s_{1..5}$ from signal 2 style set S_2 and $s_{6..16}$ from S_1, is significantly different from $\tilde{x}_1$ in its phase and modes. Green line, an interpolated signal for $w_{1..5} = 0, w_{6..16} = 1$, differs from the source in its local high-frequency features.

3.2 Interpolation Analysis

The style-based neural network architecture enables inspection of the influence of the disentangled input parameter vectors s_i at the different layers i of the synthesis network $G(S)$ within GAN, where $S = \{s_i\} = M(C)$ is a set of style vectors produced by the mapping network of the generator $M()$ from the input label vectors C. This is performed by analysing the changes in the generated signals arising from alteration of the disentangled inputs. For two different sets of styles $S_1 = \{s_{1,i}\}$ and $S_2 = \{s_{2,i}\}$ and the respective generated signals $\tilde{x}_1 = G(S_1)$ and $\tilde{x}_2 = G(S_2)$, an interpolated styles set S_3 is produced as a set of affine combinations of elements of S_1 and S_2: $S_3 = \{s_{3,i}\} = \{s_{1,i} * w_i + s_{2,i} * (1 - w_i)\}$. Thus, at each style level i the style component of S_3 is the weighted sum of the components of S_1 and S_2 at this level, with the weight $w_i = 0$ indicating that only the component of the first style set is used and $w_i = 1$ implying that only the second style is applied at this level. The interpolated signal is acquired from the interpolated style set by feeding the styles into the synthesis network, $\tilde{x}_3 = G(S_3)$.

The variation of the generated signals produced as a result of gradual changes to one or several style components reveals the features that the style components at the respective levels control. By performing a linear interpolation between $s_{1,i}$ and $s_{2,i}$ for each $i = k$ while keeping $s_{3,i} = s_{1,i}$ for each $i \neq k$, we observe that the generator model style layers can be classified into two groups: low-level styles s_1 to s_5 and high-level styles s_6 to s_{16}. The low-level styles significantly affect the low-frequency features of the output signal like its phase and general shape. The high-level styles impact the high-frequency detail of the generated output. Figure 6 visualises the end points of this interpolation: an initial signal $\tilde{x}_1$, its interpolation towards $\tilde{x}_2$ in low-level styles only and in high-level styles only.

4 Conclusion

To the best of authors' knowledge this work is the first attempt to develop a generative model of a machining process using GANs. The neural network architecture at the base of the proposed model is computationally cheap at inference time. This and the generative nature of GAN enable the development of a machining digital twin component that digitally recreates the underlying physical process in real-time. The architecture described in the paper allows a significant degree of control over the generator via input process parameters, thus enhancing the flexibility of the model and opening the potential for exploratory analysis of the modelled process. The shown success of GAN in recreating the machining vibration is an important step towards widespread implementation of data-driven simulation models in Industry 4.0, which could find important applications in monitoring and predictive analytics within manufacturing.

The analysis of the interaction between the inputs and the per-layer style components within the trained GAN model shows the distinct parts of the model that separately control the high- and the low-level features of the generated signal. The accuracy of developed model is analysed, revealing certain conditions under which the generator fails to learn the correct signal mode distribution. Investigation of the conditions under which the proposed model performance is suboptimal would be the likely next research steps. The conditions of suboptimal model behaviour can be investigated via analysis of the activations output by the convolutional layers of the generator. Furthermore, the convolutional kernels learned by the neural network could be analysed to identify possible similarities with filter models used in expert-based signal processing. Both the activations and the kernels could be analysed relationship with the style modulation components could be additionally explored via the interpolation analysis described in the paper.

As a real world implementation would likely be limited in terms of available data, an investigation of the model's capability with sparse data or unobservable factors is an important step in its verification. Categorisation of the continuous labels used to condition the model could make the dataset more closely represent data likely to be encountered on a shop-floor. Other next steps in this research direction would include evaluation of alternative neural network architectures and validation of the proposed model on real manufacturing data, as well as broadening the scope of the digital twin with inclusion of multiple data sources and modelled processes.

Acknowledgments. Professor Ashutosh Tiwari acknowledges the support of the Royal Academy of Engineering under the Research Chairs and Senior Research Fellowships scheme (RCSRF1718\5\41).

References

1. Arjovsky, M., Chintala, S., Bottou, L.: Wasserstein GAN (2017). http://arxiv.org/abs/1701.07875
2. Brock, A., Donahue, J., Simonyan, K.: Large scale GAN training for high fidelity natural image synthesis (2018). http://arxiv.org/abs/1809.11096
3. Chen, X., Duan, Y., Houthooft, R., Schulman, J., Sutskever, I., Abbeel, P.: InfoGAN: interpretable representation learning by information maximizing generative adversarial nets (2016). http://arxiv.org/abs/1606.03657
4. Donahue, C., McAuley, J., Puckette, M.: Adversarial audio synthesis (2018). http://arxiv.org/abs/1802.04208
5. Goodfellow, I.J., Pouget-Abadie, J., Mirza, M., Xu, B., Warde-Farley, D., Ozair, S., Courville, A., Bengio, Y.: Generative adversarial networks (2014). http://arxiv.org/abs/1406.2661
6. Gulrajani, I., Ahmed, F., Arjovsky, M., Dumoulin, V., Courville, A.: Improved training of Wasserstein GANs (2017). http://arxiv.org/abs/1704.00028
7. Henning, K., Wolfgang, W., Johannes, H.: Recommendations for implementing the strategic initiative INDUSTRIE 4.0. Technical Report, April (2013)
8. Huang, X., Belongie, S.: Arbitrary style transfer in real-time with adaptive instance normalization (2017). http://arxiv.org/abs/1703.06868
9. Karras, T., Aila, T., Laine, S., Lehtinen, J.: Progressive growing of GANs for improved quality, stability, and variation (2017). http://arxiv.org/abs/1710.10196
10. Karras, T., Laine, S., Aila, T.: A style-based generator architecture for generative adversarial networks (2018). http://arxiv.org/abs/1812.04948
11. Mirza, M., Osindero, S.: Conditional generative adversarial nets (2014). http://arxiv.org/abs/1411.1784
12. Niggemann, O., Biswas, G., Kinnebrew, J.S., Khorasgani, H., Volgmann, S., Bunte, A.: Data-driven monitoring of cyber-physical systems leveraging on big data and the internet-of-things for diagnosis and control. CEUR Workshop Proc. **1507**, 185–192 (2015)
13. Radford, A., Metz, L., Chintala, S.: Unsupervised representation learning with deep convolutional generative adversarial networks (2015). http://arxiv.org/abs/1511.06434
14. Saatchi, Y., Wilson, A.G.: Bayesian GAN (2017). http://arxiv.org/abs/1705.09558
15. Schmitz, T.L., Smith, K.S.: Machining Dynamics. Springer, Cham (2019). https://doi.org/10.1007/978-3-319-93707-6

16. Spurr, A., Aksan, E., Hilliges, O.: Guiding InfoGAN with semi-supervision. In: Ceci, M., Hollmén, J., Todorovski, L., Vens, C., Džeroski, S. (eds.) Machine Learning and Knowledge Discovery in Databases, Lecture Notes in Computer Science, pp. 119–134. Springer, Cham (2017)
17. Tao, F., Cheng, J., Qi, Q., Zhang, M., Zhang, H., Sui, F.: Digital twin-driven product design, manufacturing and service with big data. Int. J. Adv. Manuf. Technol. **94**(9–12), 3563–3576 (2018)
18. Yu, L., Zhang, W., Wang, J., Yu, Y.: SeqGAN: sequence generative adversarial nets with policy gradient (2016). https://doi.org/10.1001/jamainternmed.2016.8245
19. Zhang, H., Xu, T., Li, H.: StackGAN: text to photo-realistic image synthesis with stacked generative adversarial networks. In: 2017 IEEE International Conference on Computer Vision (ICCV), vol. 2017-Octob, pp. 5908–5916. IEEE (2017)

λ-DNNs and Their Implementation in Aerodynamic and Conjugate Heat Transfer Optimization

Marina Kontou(✉), Dimitrios Kapsoulis, Ioannis Baklagis, and Kyriakos Giannakoglou

Parallel CFD & Optimization Unit, School of Mechanical Engineering, National Technical University of Athens, Athens, Greece
kgianna@mail.ntua.gr

Abstract. A fully-connected Deep Neural Network (DNN) architecture, to be referred to as λ-DNN, used to predict 2D/3D scalar fields is presented. In aerodynamics, the λ-DNN is firstly trained on fields computed using a Computational Fluid Dynamics (CFD) software. Then, it can be incorporated into engineering processes in various ways. One possibility is to use them in optimization problems solved by stochastic population-based methods, in which the λ-DNN may act as the surrogate evaluation model, replacing calls to the CFD tool. Another possibility is in multi-disciplinary problems, to replicate the numerical solver for any of the disciplines. This small list of possible usages is not exhaustive and, of course, different usages can be combined. The input to each DNN contains information to identify the geometrical shape and case-related data, nodal coordinates and, in multi-disciplinary problems, interfacing data connecting solvers for different disciplines on adjacent domains. In this paper, the λ-DNN is firstly used in the aerodynamic shape optimization of a wing using evolutionary algorithms, in which it replicates the CFD solver. Then, it is used in a conjugate heat transfer problem dealing with a solid domain in contact with a flow within a duct. In this problem, the λ-DNN acts as a surrogate to the solver of the heat conduction equation on the solid domain, by interfacing with a CFD solver of the fluid domain.

Keywords: Deep Neural Networks · Flow prediction · Computational Fluid Dynamics · Conjugate heat transfer · Evolutionary optimization of aerodynamic shapes · Multi-disciplinary optimization

1 Introduction

In shape optimization, in one or more disciplines, a number of different designs must be evaluated in order to reach optimal solutions. This number increases when a stochastic optimization method is used so as to avoid being trapped into a local minimum. In multi-disciplinary optimization, such as a Conjugate

Heat Transfer (CHT) one, the analysis of any configuration requires the iterative solution of the flow equations over the fluid domain and the heat conduction PDE over the adjacent solid domain; during the iterative solution, the two domain solvers communicate at their interface by exchanging heat flux and temperature distributions. The repetitive calls to the two solvers make the cost of a CHT analysis high enough. As industrial requirements become more demanding, not only the number of evaluations needed to reach the optimal solution but, also, the cost per evaluation must be kept as low as possible. This is the main purpose of this paper and the main reason for developing the proposed λ-DNN.

Deep Neural Networks (DNNs) [6] are known to effectively replicate complex tasks by recognizing their core features. As such, in view of the previous discussion, DNNs should learn how to predict the outcome of simulation codes solving PDEs modeling physical phenomena or only the integral quantities needed to evaluate the quality of a configuration, as it may suffice in most optimization problems. In a CHT or any other multi-disciplinary problem, a good idea is to make them replicate the solver corresponding, for instance, to one of the involved disciplines. This might be good enough to shorten the wall clock time of such a simulation. For instance, in an optimization loop, the expected gain from such an algorithm must be evaluated by considering the cost for performing runs to collect the necessary training patterns and that for training the DNN together with the expected reduction in the cost of the optimization loop involving DNNs. This paper demonstrates the efficiency of the proposed optimization techniques based on the newly developed DNNs.

The proposed DNN, which will be referred to as the λ-DNN, Fig. 1, is a Fully-Connected Neural Network (FCNN), compact and with a relatively small number of trainable parameters. This is described in detail in Sect. 2.1.

It is not the first time DNNs are used for predicting flow fields. Convolutional Neural Networks (CNNs), which consist of convolutional layers with local connections between neurons of successive layers, have been used to predict aerodynamic flow fields in unseen flow conditions and geometries, [4]. U-Networks have been used for the prediction of incompressible laminar flows, [5]. They consist of an encoder which compresses the information with successive convolutional layers and a decoder which decompresses it with deconvolution layers and yields the output. In [9], a hybrid DNN, formed by CNN, convolutional Long Short Term Memory network (ConvLSTM) and decoding-CNN (D-CNN), is used for the prediction of unsteady flows.

In this paper, the λ-DNN architecture is applied in the aerodynamic shape optimization of a wing and that of a fluid and a solid domain in a CHT problem, using evolutionary algorithms occasionally assisted by on-line trained metamodels (Radial Basis Function, RBF) networks. The λ-DNN is capable of predicting physical quantities (flow fields in CFD, temperature distributions in CHT) on any type of computational grids (structured or unstructured), since grid connectivity is not required. The λ-DNN requires a small number of training fields and has a low computational cost (compared to [4,5]), ensuring acceptable accuracy.

2 Methods and Tools

2.1 The Proposed λ-DNN

A DNN consists of many layers of neurons, with weights and biases being the network parameters to be computed during the training phase. During this phase, a cost function expressed as the root-mean-squared (RMS) of the differences between the network outputs and the known/archived responses is minimized. To this end, the back-propagation algorithm, [15], using closed-form expressions for the derivatives of the cost function with respect to the network parameters, is used.

The λ-DNN is exclusively formed by fully-connected layers. For better data handling, its architecture consists of two separated branches (Fig. 1), one for each type of input. Each branch first passes through fully-connected layers and then connects to the main branch which further processes signals through its own fully-connected layers and concludes to the network output(s). In the cases presented below, there are two different kinds of inputs, one refers to the mesh (nodal coordinates) and the other to parameterization or physical quantities. The different branches allow separate processing of input data of different nature. This leads to extraction of different features for each branch, before merging them to produce the final output.

The Rectified Linear Unit (ReLU) activation function [8] is used in all but the last layer which uses the sigmoid function, for the one-discipline case, and the Hyberbolic Tangent function (tanh) for the two-discipline one. The pre- and post-processing of the set of training patterns and all DNN phases (construction, training and testing) have been implemented in Python 3.6 [14] linked with TensorFlow [1] and run on both GPUs and CPUs.

The λ-DNN is applied according to two different modes. The first is based on a node-to-node logic, meaning that the network predicts only one output, namely the flow variable at each grid node, while the second processes the whole grid at once and the output of a λ-DNN run is a whole field. The difference between the two modes lies on whether grid connectivity is taken into account; the former is independent of the grid connectivity while the latter is not.

2.2 Computational Tools for Aerodynamic and CHT Analyses

For the numerical solution of CHT problems, [2,12], coupled and decoupled solution schemes are in use. In the coupled approach, PDEs on different domains are simultaneously solved while, in the decoupled approach, each discipline is solved separately and provides boundary conditions for the others by exchanging information along their interface. In either approach, proper solvers' interfacing guarantees heat flux conservation and equal temperatures over the fluid-solid interface. Herein, the decoupled approach is used. The procedure is computationally expensive as it requires many iterative cycles (CHT cycles), with calls to the CFD solver (for the fluid domain) and the Heat Conduction one (for the solid domain). Each domain is solved separately and the interaction of the

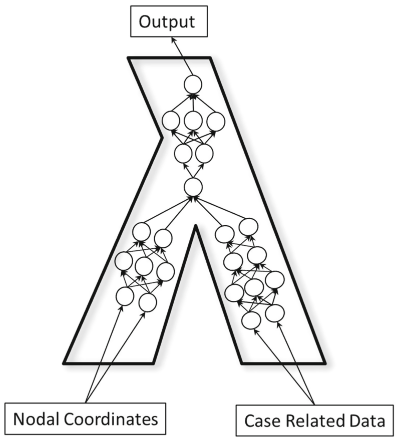

Fig. 1. The proposed λ-DNN architecture. The DNN is named after its shape that looks like the Greek letter λ. For visualization reasons, each circle/layer comprises a number of neurons/layers. The number of inputs/outputs and that of fully-connected layers vary among the cases.

solvers is taking place at their interface, so a DNN trained on the contribution of the one solver to the interface can be very helpful. By doing so, the cost of one solver will be significantly reduced, together with the overall cost of the CHT evaluation. More details about this implementation and the offered gains will be provided in Sect. 4, where the corresponding case is described.

Regarding the analysis of fluid flows, an in-house Reynolds-Averaged Navier-Stokes equations' solver, [3,10], coupled with a Heat Conduction equations' solver is used. The governing equations are discretized using the finite volume technique. The CFD code solves incompressible and compressible flows; herein, all cases are studied with the compressible variant. Fluid and solid domain solvers fully exploit the CUDA programming environment and run on a GPU cluster. CFD/CHT evaluations and DNN training were performed on NVIDIA K20 or K40 GPUs.

2.3 EA-Based Optimization, Without or with Metamodels

For the EA-based optimizations presented in Sects. 3 and 4, the optimization platform EASY, [7], developed by the Parallel CFD & Optimization Unit of the National Technical University of Athens is used. Real encoding of the design variables, with 5% mutation probability and simulated binary crossover with 90% probability are used. To reduce the cost of the EA-based optimization, EASY optionally employs on-line trained metamodels (RBF networks) and this is performed in a rather unique way compared to other similar tools. The role of the metamodel(s) is to replace calls to the problem-specific method (PSM; herein, either a CFD or a CHT solver) by approximating the objective function(s) value(s) at negligible cost, after training them on data collected for individuals already evaluated on the PSM. The distinguishing feature of the Metamodel-Assisted EA (MAEA) implemented in EASY is that the RBF networks' training occurs during the evolution (this is what "on-line" stands for). The use of metamodels starts after the first T^{MM} individuals have been evaluated on the PSM and recorded in the MAEA database (DB). In all subsequent generations, a different RBF network per individual is trained on a few selected neighboring DB entries. Using these RBF networks, all population members are pre-evaluated and only the most promising among them (λ_e; a small user-defined value per generation) are re-evaluated on the PSM, [11] and recorded in the DB.

This is contrasted to the most widely used EAs supported by off-line trained metamodels, which usually rely on a single metamodel, valid over the whole search space. This metamodel is trained with evaluated individuals resulting from a Design of Experiments (DoE) technique, [13]. In such an algorithm, the EA–based search relies exclusively upon the previously (off-line) trained metamodel. The "optimal" solution(s) is/are re-evaluated on the PSM and the process goes on by re-training the metamodel on the updated DB and performing a new EA-based search until a termination criterion be met.

In this paper, in the sake of pluralism, both on- and off-line metamodels are used within EASY. The λ-DNN is used as off-line metamodel, replacing the CFD tool. The λ-DNN is updated if, upon convergence of the EA-based search using the same λ-DNN, the re-evaluation of the "optimal" solution (quotes denote the outcome of an optimization in which the evaluation tool is a surrogate model) on the CFD asks for better accuracy. In the CHT problem, the evaluation s/w combines an accurate tool (CFD solver) for the fluid domain and the λ-DNN for the solid domain. This optimization also uses on-line trained metamodels (a MAEA with RBF networks, implemented as described above).

3 Case I: Aerodynamic Shape Optimization

The first application is concerned with the use of the λ-DNN in the prediction and the aerodynamic shape optimization of a transonic wing. The geometry of [16] is the reference wing. The flow is inviscid with free-stream Mach number and flow angles equal to $M_\infty = 0.8395$, $a_{\infty,pitch} = 3.06^o$ and $a_{\infty,yaw} = 0^o$. The wing shape is encapsulated within a $6 \times 3 \times 3$ volumetric NURBS (trivariate Non-Uniform Rational B-Splines) control grid. A knot vector and a degree per parametric direction are needed to complete the parameterization. The morphing used in this case is graphically presented (as a 2D example, though) in Case II. 12, out of the 54 control points (CPS), are allowed to move in the chordwise and the normal-to-the-planform directions within ±20% of their reference coordinate values, resulting to $12 \times 2 = 24$ design variables in total. In this case, the parameterization is used not only for generating training patterns but, also, as an input to the DNN to identify different wing shapes. An unstructured 3D CFD grid of ∼1.33 $\times 10^6$ nodes generated around the reference geometry and adapted to all changed shapes is used. A single run of the CFD software takes ∼2min on a K20 GPU.

Both a λ-DNN and an FCNN are used. The first branch of the λ-DNN consists of four fully-connected layers with $128, 256, 256, 128$ neurons each; the second branch consists of three fully-connected layers with $128, 256, 128$ neurons each. After their merging, another three fully-connected layers with $128, 256, 128$ neurons each lead to the final output. For comparison reasons the number of neurons and layers in the λ-DNN and the FCNN are kept the same. The FCNN consists of seven layers with $256, 512, 512, 256, 256, 512, 256$ neurons, respectively. The 200 wings are used for training the λ-DNN and the FCNN by randomly changing the position of the pre-defined CPs of the morphing box. In this case, a node-to-node procedure is followed.

The networks are trained on the $M \simeq 27000$ surface nodes of each CFD grid, thus the total number of training patterns is 200×27000. The input data to the networks are the 24 coordinates of the free-to-move control points along with the (x, y, z) coordinates of any surface node, i.e. 27 inputs in total, and the output is a single pressure value at this surface node. The first branch of the λ-DNN processes the coordinates of the control points, while the second one the (x, y, z) coordinates.

In this case, the training cost is $\sim$1.2 h for both networks. Before proceeding with the shape optimization, the prediction quality of the DNNs on two new wings generated by displacing the control points within the aforementioned bounds, and not seen by the DNNs before, is checked. Predictions of pressure (p_{DNN}) using the trained DNNs are compared with CFD evaluations (p_{CFD}) using the Mean Absolute Percentage Error $(MAPE_p)$ indicator per wing, given by:

$$MAPE_p = \frac{1}{M} \sum_{i=1}^{M} \left| \frac{p_{i,CFD} - p_{i,DNN}}{p_{i,CFD}} \right| \tag{1}$$

The average $MAPE_p$ computed on the two new wings is equal to 0.81% for the λ-DNN and 3.83% for the FCNN; and this demonstrates the superiority of the proposed network type.

Then, two EA-based shape optimizations, for maximum wing lift (L), are performed. During the first one, the λ-DNN assists the EAs to reduce the total number of calls to the expensive CFD s/w, by acting as an off-line trained surrogate (Run_1). The λ-DNN predicts the pressure field on the surface of each new wing presented to it which, through integration, computes the lift force. A CFD run on the "optimal" solution is performed only at the end of the EA-based cycle. The second one is a MAEA (with on-line trained RBF networks, $T^{MM} = 40$ and $\lambda_e = 3$) optimization relying upon the CFD code instead of the λ-DNN (Run_2). A comparison between Run_1 and Run_2 is made. Both are configured with 10 parents and 20 offspring, i.e. they are (10,20) EAs or MAEAs. This is a well performing set-up of the optimization method in this case which was kept the same in both cases, in the sake of fair comparison.

For either run, a total budget of 250 CFD evaluations ("time-units") is a priori defined. For Run_1, this budget corresponds to: 200 time-units to form the DB, 33 to train the network and only 17 for running the optimization, spent, in particular, for the necessary CFD re-evaluations. Run_1 resulted to a wing geometry having a lift that is by 2.9% higher than the solution of Run_2. We conclude that the usage of the λ-DNN improves the efficiency of the EA-based search even more than the (already very fast) MAEA. In Fig. 2, the convergence histories of the two optimizations are illustrated. To quantify the gain with respect to the original shape, L is always dimensionalized by the reference wing L value.

In Fig. 3, the pressure field for the optimal geometry is shown for the solutions of Run_1 and Run_2. For the former, two pressure fields are presented, that evaluated by the CFD and that predicted by the λ-DNN. The pressure fields differ between Run_1 and Run_2, since the two optimizations resulted in different wing shapes. For the optimized wing of Run_1, the pressure prediction of the λ-DNN (Fig. 3, right) is so close to the CFD solution (Fig. 3, middle), and this demonstrates the reliability of the proposed network.

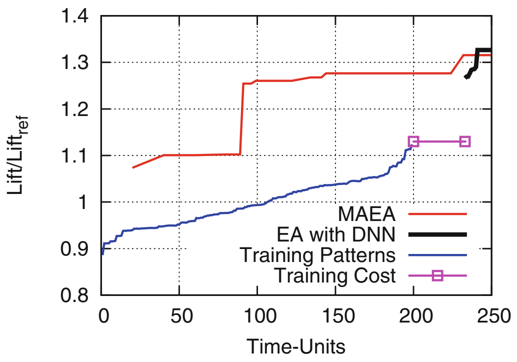

Fig. 2. Case I: Convergence History of the EA relying on the λ-DNN (Run_1) and the MAEA (based on on-line trained RBF networks) (Run_2). The blue line corresponds to the 200 training patterns plotted in ascending order, the pink line represents the training cost, while the black line represents the EA relying on the λ-DNN; all three of them stand for Run_1.

4 Case II: CHT Shape Optimization

Here, the λ-DNN is used in the CHT optimization of a fluid duct adjacent to a solid domain, to replace the heat conduction equation solver on the solid domain. The same CFD code for the fluid domain (this time solving the Reynolds-Averaged Navier-Stokes equations with the Spalart-Allmaras turbulence model, [17]) is used. In the absence of the λ-DNN, the CFD code interacts with a solver for the conduction equation over the solid domain. The same morphing technique (adapted to 2D cases) is used. The high temperature solid domain is cooled by fluid of lower temperature (T) flowing within the S-bend duct. The two domains are solved in a decoupled manner, by interchanging the computed heat flux (from the fluid to the solid) and temperature (in the opposite direction) distributions over the fluid-solid interface (FSI).

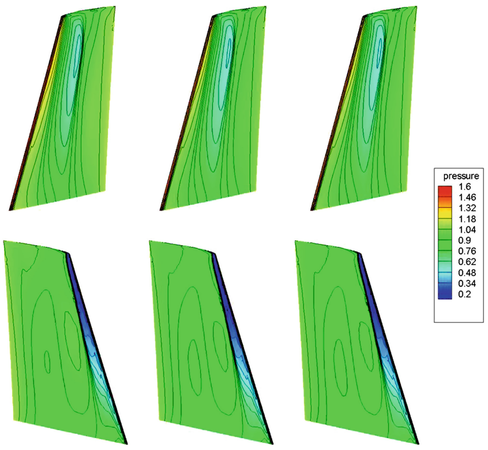

Fig. 3. Case I: Pressure Fields on the surface of the transonic wing. Left: Optimized solution of Run_2. Middle: Optimized solution of Run_1, evaluated by CFD. Right: Optimized solution of Run_1, re-evaluated by the λ-DNN.

For the fluid domain, the flow has inlet total pressure $p_{t,inlet} = 105\,\text{kPa}$, inlet total temperature $T_{t,inlet} = 300\,\text{K}$, outlet static pressure $p_{outlet} = 100\,\text{kPa}$. For the solid domain, a constant temperature of $T = 500\,\text{K}$ is imposed along its bottom boundary, while the rest non-FSI nodes are considered adiabatic. The geometry is parameterized using a 8×6 volumetric NURBS control grid, Fig. 4. 24 CPs are allowed to move within ±10% of their reference coordinate values in either direction, resulting to $24 \times 2 = 48$ design variables in the optimization problem. In this 2D case, the parameterization is common for both the fluid and the solid domain but it is not used as input (information) to the DNN. A mono-block structured grid of ∼330000 nodes is used to discretize both domains, where $M = 240000$ of them correspond to the solid domain. A single run of the CHT solver takes ∼20min on a K40 GPU.

The database for training the λ-DNN is built by evaluating 180 geometries by randomly moving the CPs. As in the previous case, a λ-DNN and an FCNN are used. The two branches of the λ-DNN consist of one layer each with 512 neurons. The two branches merge to a single layer of 20 neurons that leads to the final output. The network architecture is selected after a trial-and-error procedure. The FCNN consists of two layers with 1024 and 512 neurons each.

The input data are the (x, y) coordinates and the heat fluxes at the 600 FSI nodes, i.e. 1800 inputs in total. At the λ-DNN, the first branch processes the (x, y) coordinates, while the other the heat fluxes. The output is the temperature (T) field on the entire solid domain; grid connectivity and number of nodes remain the same for all the geometries. It is important to notice that, in contrast to the previous case where a node-to-node procedure was followed, here, the nodal T values over the entire solid domain are simultaneously predicted. Two new geometries, not seen by the DNNs before, are used to validate the λ-DNN and the FCNN. In this case the average values $MAPE_T$ 0.3% for the λ-DNN and 0.8% for the FCNN are computed. The λ-DNN has better prediction accuracy and, thus, this is used during the optimization.

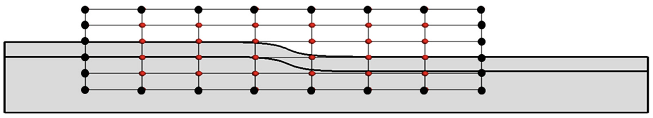

Fig. 4. Case II: Control Points of the volumetric NURBS, morphing box, parameterizing the S-bend duct (upper) and a small part of the solid domain (lower). Black points are kept fixed, whereas red ones are allowed to vary in either direction, morphing the enclosed parts of the fluid and solid domains.

Three MAEA-based optimizations are performed with 10 parents and 20 offspring, supported by on-line trained RBF networks with $T^{MM}=40$ and $\lambda_e=3$.

The first two optimizations aim at minimizing the mass-averaged total pressure losses between the inlet (I) and the outlet (O) of the S-bend duct, i.e. they are dealing with an objective defined only in the fluid domain,

$$F_1 = \frac{\int_{S_I} p_t \rho v_n dS + \int_{S_O} p_t \rho v_n dS}{\int_{S_I} \rho v_n dS} \tag{2}$$

ρ, v_n stand for the density and the normal (directed outwards) to the boundary velocity component.

The first optimization (Run_1) uses the λ-DNN as surrogate to the solid domain solver, while the second one (Run_2) is based exclusively on the solution of the governing PDEs. A total budget of 250 CHT evaluations ("time-units"; one time-unit is the cost per evaluation in Run_2) is decided for both of them. For Run_1, this budget corresponds to 30 time-units to form the database, 24 for training the network and 196 for the optimization, since an evaluation on the (CFD and λ-DNN) tool costs about 0.76 time-units. Then, Run_2 is performed. Figure 5 presents the convergence histories of the MAEAs and the resulting optimal geometry; a reduction in $F_1 \sim 8.6\%$, compared to the initial/reference geometry, is obtained in both Run_1 and Run_2. F_1 is normalized by the value of the same quantity in the reference geometry. The optimal solution of Run_1 is re-evaluated on the exact CHT solver; the λ-DNN error is less than 0.008% verifying the network accuracy.

Then, a two-objective optimization, by adding a second target defined over the solid domain, is performed. The second objective function is the percentage of the area of the solid domain over which T exceeds a threshold value, scaled by the excess temperature, namely

$$F_2 = \frac{1}{\Omega_s} \int_{\Omega_S} (T - T_{thres}) d\Omega \tag{3}$$

F_2 should be minimized. The $T = 500\,\mathrm{K}$ value along the bottom boundary of the solid domain is the highest temperature over the domain. The value of the $T_{thres} = 450\,\mathrm{K}$ is defined in order to minimize the area of the domain which exceeds this threshold value. In whatever follows, F_1 and F_2 are presented in a non-dimensional form; they are both divided by the corresponding values of the reference solution (the one presented in Fig. 4).

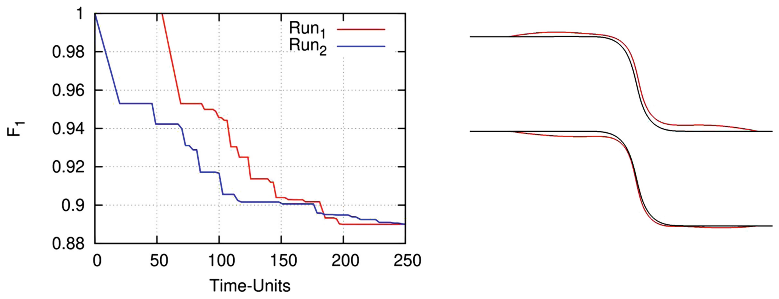

Fig. 5. Case II: Left: Convergence histories of the MAEA-based optimizations for Run_1 (Fluid-(λ-DNN)) and Run_2 (Fluid-Solid). Right: The initial (black) and the optimal (red) geometries (x and y axes not in scale).

The new optimization (Run_3) uses the λ-DNN as the surrogate to the solid domain solver. The total budget is still 250 CHT evaluations distributed as for Run_1. In Fig. 6, the front of non-dominated solutions resulted from Run_3 is presented. The members of the front are re-evaluated with the exact CHT solver to verify the network accuracy. The re-evaluated members remain non-dominated and the errors in F_1 and F_2 are ∼0.008% and ∼0.09%, respectively.

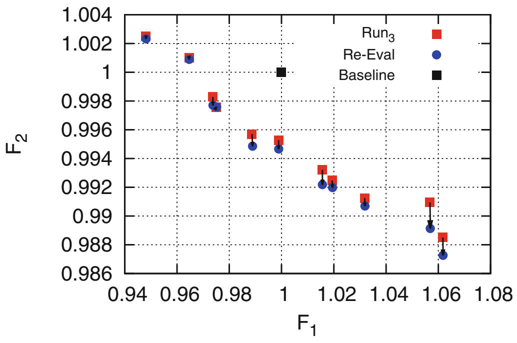

Fig. 6. Case II: Front of non-dominated solutions computed from Run_3 (red squares), plotted along with the baseline geometry (black square). The front members are re-evaluated on the exact CHT solver resulting to a new non-dominated front (blue circles). The computed "optimal" members on the front remain non-dominated after the re-evaluation using the computational mechanics s/w.

The T field from Run_3 and its re-evaluation as well as the prediction error are shown for the member of the front with $F_1 = 0.975$ and $F_2 = 0.997$ in Figs. 7 and 8, respectively. As shown in Figs. 6, 7 and 8, the accuracy of the λ-DNN is high enough to sufficiently replicate the heat conduction equation solver on the solid domain during an optimization and reduce its overall cost.

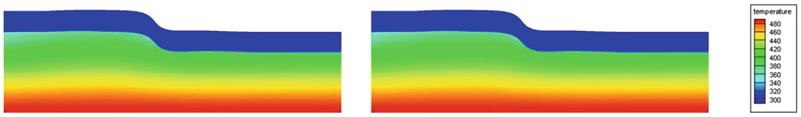

Fig. 7. Case II: Temperature field as resulted from Run_3 (left) and re-evaluated with the exact CHT solver (right) for the member of the front with $F_1 = 0.975$ and $F_2 = 0.997$ (x and y axes not in scale).

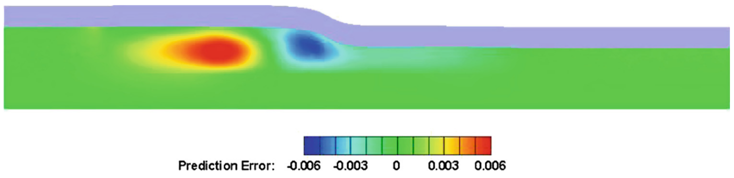

Fig. 8. Case II: Prediction error of the solid domain temperature field for the member of the front with $F_1 = 0.975$ and $F_2 = 0.997$.

5 Conclusions

This paper presented a new DNN architecture, called λ-DNN, which can be used in single- and multi-disciplinary optimization. The λ-DNN is used to predict CFD and CHT results in the form of entire flow fields or temperature distributions, so as to replace expensive runs of CFD/CHT solvers in design/optimization processes. The proposed method has been demonstrated in a 3D one-discipline and a 2D two-discipline case. The DNN yields very good predictions of fields. Inputs are presented to two different branches for better and separate processing of the given input data and, then, these two branches meet at a single one that gives the required output. The λ-DNN manages to reduce the training cost and number of patterns required. The high prediction accuracy of the proposed λ-DNN was demonstrated in a wing flow problem and a solid domain adjacent to a S-bend duct as a surrogate to the heat conduction solver. Regarding the one-discipline case optimization, the trained λ-DNN is used as metamodel during an EA-based optimization and improves the search performance with results comparable with those provided by the MAEA. Regarding the two-discipline case, the λ-DNN is used instead of the Heat Conduction solver during a MAEA optimization. Therefore, the proposed λ-DNN is shown to be capable of replacing the CFD and CHT solvers in expensive (analysis and optimization) processes. Future work includes the use of the λ-DNN in 3D real-world one- and two- discipline applications, such as aeroelastic shape optimization.

Acknowledgments. This work has been supported by the Greek Research and Technology Network (GRNET) High Performance Computing Services, through the TurboNN and CGT-DNN projects.

References

1. Abadi, M., Agarwal, A., Barham, P.: TensorFlow: Large-scale machine learning on heterogeneous systems (2015). http://tensorflow.org/, software available from tensorflow.org
2. Andrei, L., Andreini, A., Facchini, B., Winchler, L.: A decoupled CHT procedure: application and validation on a gas turbine vane with different cooling configurations. In: 68th Conference of the Italian Thermal Machines Engineering Association (2013)
3. Asouti, V., Trompoukis, X., Kampolis, I., Giannakoglou, K.: Unsteady CFD computations using vertex-centered finite volumes for unstructured grids on graphics processing units. Int. J. Numer. Methods Fluids **67**(2), 232–246 (2011)
4. Bhatnagar, S., Afshar, Y., Pan, S., Duraisamy, K., Kaushik, S.: Prediction of aerodynamic flow fields using convolutioanl neural networks. Comput. Mech. **64**, 525–545 (2019)
5. Chen, J., Viquerat, J., Hachem, E.: U-net architectures for fast prediction of incompressible laminar flows (2019)
6. Deng, L., Yu, D.: Deep learning: methods and applications. Found. Trends Signal Process. **7**(3–4), 1–199 (2014)
7. Giannakoglou, K.: The EASY (Evolutionary Algorithms SYstem) software (2008). http://velos0.ltt.mech.ntua.gr/EASY
8. Goodfellow, I., Bengio, Y., Courville, A.: Deep Learning. The MIT Press, Cambridge (2016)
9. Han, R., Wang, Y., Zhang, Y., Chen, G.: A new prediction method of unsteady wake flow by the hybrid deep neural network (2019)
10. Kampolis, I., Trompoukis, X., Asouti, V., Giannakoglou, K.: CFD-based analysis and two-level aerodynamic optimization on graphics processing units. Comput. Methods Appl. Mech. Eng. **199**(9–12), 712–722 (2010)
11. Karakasis, M., Giotis, A., Giannakoglou, K.: Inexact information aided, low-cost, distributed genetic algorithms for aerodynamic shape optimization. Int. J. Numer. Methods Fluids **43**(10–11), 1149–1166 (2003)
12. Moretti, R., Errera, M.P., Couaillier, V., Feyel, F.: Stability, convergence and optimization of interface treatments in weak and strong thermal fluid-structure interaction. Int. J. Therm. Sci. **126**, 23–37 (2017)
13. Myers, R., Montgomery, D.: Response Surface Methodology Process and Product Optimization Using Designed Experiments, 2nd edn. Wiley, New York (2002)
14. Rossum, G.: Python tutorial. Technical Report CS-R9526 (1995)
15. Rumelhart, D., Hinton, G., Williams, R.: Learning representations by back-propagating errors. Nature **323**(6088), 533–536 (1986)

16. Schmitt, V., Charpin, F.: Pressure distributions on the ONERA M6 wing at transonic mach numbers, experimental data base for computer program assessment. Technical report, AGARD 138 (1979)
17. Spalart, P., Allmaras, S.: A one-equation turbulence model for aerodynamic flows. La Rech. Aerosp. **1**, 5–21 (1994)

Symbols in Engineering Drawings (SiED): An Imbalanced Dataset Benchmarked by Convolutional Neural Networks

Eyad Elyan(✉), Carlos Francisco Moreno-García, and Pamela Johnston

The Robert Gordon University, Garthdee Road, Aberdeen, UK
{e.elyan,c.moreno-garcia,p.johnston2}@rgu.ac.uk

Abstract. Engineering drawings are common across different domains such as Oil & Gas, construction, mechanical and other domains. Automatic processing and analysis of these drawings is a challenging task. This is partly due to the complexity of these documents and also due to the lack of dataset availability in the public domain that can help push the research in this area. In this paper, we present a multiclass imbalanced dataset for the research community made of 2432 instances of engineering symbols. These symbols were extracted from a collection of complex engineering drawings known as Piping and Instrumentation Diagram (P&ID). By providing such dataset to the research community, we anticipate that this will help attract more attention to an important, yet overlooked industrial problem, and will also advance the research in such important and timely topics. We discuss the datasets characteristics in details, and we also show how Convolutional Neural Networks (CNNs) perform on such extremely imbalanced datasets. Finally, conclusions and future directions are discussed.

Keywords: CNN · Multiclass · Classification · Imbalanced dataset · Engineering drawings · P&ID

1 Introduction

Engineering drawings are known to be one of the most complex types of documents to process and analyse. They are widely used in different industries such as construction and city planning (i.e. floor plan diagrams [2]), Oil & Gas (i.e. P&IDs [9]), Mechanical Engineering [33], AutoCAD Drawing Exchange Format (DXF) [13] and others. Interpreting these drawings requires highly skilled people, and in some cases long hours of work. Processing and analysing these drawings is becoming increasingly important. This is partly due to the urgent need to improve business practices such as inventory, asset management, risk analysis, safety checks and other types of applications, and also due to the recent advancements in the domain of machine vision and image understanding. Deep Learning

L. Iliadis et al. (Eds.): EANN 2020, INNS 2, pp. 215–224, 2020.
https://doi.org/10.1007/978-3-030-48791-1_16

(DL) [15], in particular, had significantly improved the performance by orders of magnitude in many domains such as the Gaming and AI [17], Natural Language Processing [36], Health [12], Cyber Security [28], and others.

The concept of Convolutional Neural Networks (CNNs) [16] has made significant progress in recent years in many image-related tasks. It has been successfully applied to several fields such as hand-written digit recognition [22], image classification [20,30], face recognition & biometrics [27], amongst others. Before CNNs, improvements in image classification, segmentation, and object detection were marginal and incremental. CNNs revolutionised this field. For example, Deep Face [31], which is a face recognition system that was first proposed by Facebook in 2014, achieved an accuracy of 97.35%, beating the then state-of-the-art, by 27%.

Despite extensive progress in the field of image processing and analysis, very little progress has been made in the area of analysing complex engineering drawings, and extracting information from these diagrams is still considered a challenging problem [5]. Consider for example the case of the Piping and Instrumentation Diagram (P&ID), which is a schematic engineering drawing, commonly used in the Oil and Gas industry [9,24]. This type of diagram, as can be seen in Fig. 1, is made of symbols, connectivity information (lines, dashed lines, combinations of lines), text, and other graphical elements.

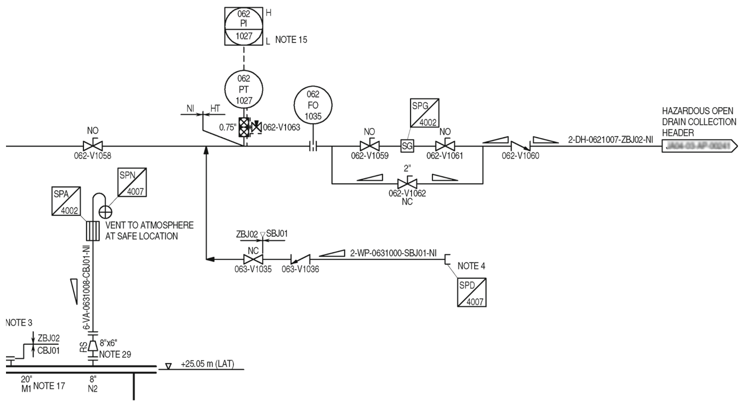

Fig. 1. A typical example of elements within a P&ID diagram

Identification of the symbols within this kind of diagram would appear to be an ideal problem which could be easily solved by convolutional neural networks. However, a recent review on the subject [7] showed that publicly available datasets are not common in this area, with research commonly applied to small, proprietary datasets. To take full advantage of the recent advances in machine vision, and to facilitate reproducible experiments, a sizeable, labelled dataset in the public domain is required.

Several factors make processing and analysing engineering drawings a challenging tasks. First, the quality of the images/scanned documents is sometimes of a standard which requires the application of various image-enhancements methods. Second, the nature of these diagrams, where various types of elements might be overlapping (i.e. a text overlaid on a symbol), in addition to possible data annotations and other graphic elements makes accurate localisation of individual elements more challenging. It is difficult to isolate one particular symbol from its neighbours. Another inherent problem is the imbalanced distribution of various symbols within these drawings. Handling all related challenges is beyond the scope of this paper. The reader is referred to [24] for more detailed description about the inherent characteristics and challenges of these types of drawings.

In this paper, we present a new multiclass dataset of symbols extracted from engineering drawings to the research community. Realistically reflecting the problem, this dataset is subject to some class-imbalance. The remaining parts of this paper are organised as follows: In Sect. 2 we discuss relevant literature to the digitisation of engineering drawings and class imbalance. In Sect. 3 we present our methods which includes detailed discussion of the dataset, and our approach for classifying engineering symbols. Benchmarking experiments and results are presented in Sect. 4, and finally, conclusions and future directions are discussed in Sect. 5.

2 Related Work

Attempts to process and analyse symbolic drawings date back to at least the early 90's. These include: analysis of musical notes [6]; processing mechanical drawings [19]; and optical character recognition (OCR)[21,23,26]. In recent years, digitising engineering drawings has become increasingly important as they are widely used in different domains [2,9,13,33], however, literature is still limited. To the best of our knowledge, there is no large, publicly available dataset to facilitate the advantages of modern, data-hungry CNNs. A recent review [7] detailed the whole process of digitisation and contextualisation of the three main shapes contained in engineering drawings (i.e. text, lines and symbols). The authors identified that, typically, symbols are located within the drawing either in a *specific* or a *holistic* way. In *specific* localisation, the system has a predefined symbol description/template, and an algorithm recursively looks for such symbol. In contrast, *holistic* methods require differentiation of the three shapes to then be able to split the drawing into layers. One of the most widely-used frameworks in this regard is text-graphics separation [32], which is a family of algorithms which distinguish text from lines and symbols based on properties such as height-to-width radio, stroke, amongst others. CNNs could be applied to both of these, given sufficient labelled data.

One type of engineering drawings, namely P&IDs, has attracted more research attention in recent years. Typical examples, presented in [9,18,25], aimed at detecting and recognising symbols within these diagrams. It can be argued however, that most of the existing literature followed a traditional image processing approach [14], which requires feature extraction [8], feature representation [37], and classification to determine the class of objects (i.e. symbols, digits, ...) [1].

Most recently in [9], authors presented a first step towards creating a symbol repository for engineering drawings. A total of 1187 symbols split into 37 different classes was compiled. The repository was then processed by means of class decomposition [10,11], resulting in a total of 57 sub-classes. Classification accuracy was calculated using three different classification frameworks: Random Forests (RF), Support Vector Machine (SVM) and a CNN. Class decomposition demonstrated a slight improvement in classification results for SVM and CNN, with a more considerable improvement in RF.

Overall, there is a growing interest in the research community in digitising and analysing engineering drawings. Yet, the lack of public domain datasets is considered as one of the main challenges to push the research boundaries in this area. In addition to this, the class-imbalance problem could also be considered as another challenge, in particular when certain types of symbols either dominate, or rarely appear in the dataset. Class-imbalance is common across different domains, and not only limited to engineering drawings [34,35]. Handling this problem is often done by means of data resampling, where majority classes are undersampled to reduce their dominance, or minority classes are oversampled [35]. In addition to this, Generative Adversarial Neural Networks [15] were successfully applied recently to augment an imbalanced dataset and improve learning algorithm performance [3,4].

3 Methodology

This section presents our novel dataset of Symbols in Engineering Drawings (SiED). First we give a brief description of how this dataset was constructed. This is followed by a detailed description of dataset and class distribution. Finally, a brief discussion related to the classification method used to benchmark this dataset is presented.

3.1 Data Extraction

A collection of P&ID sheets was provided by an industrial partner. Following the work in [25], a thresholding method was first applied to reduce noise. Areas of interest were then identified interactively to discard boundaries, text and annotation outside the border of each drawing. A traditional machine-vision approach was then used to extract a set of symbols. A set of heuristic-based methods were developed and applied sequentially to localise symbols within each P&ID drawing. Figure 2 shows a random selection of typical symbols that appear in P&IDs.

The methods proved to be stable enough to provide a list of extracted and well-defined symbols. However, a key limitation of such heuristic-based methods is that they require extensive feature engineering and require fine-tuning and customisation to generalise to unseen symbols or different types of diagrams [7].

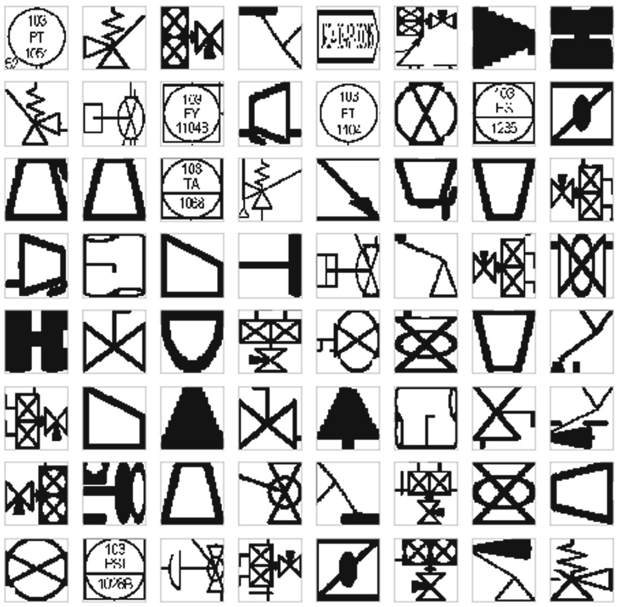

Fig. 2. A random selection of typical symbols that appear in P&IDs

3.2 Dataset

Using the method presented above, a series of P&IDs have been processed and analysed. This resulted in a collection of symbols that represent different types of equipment within the drawings. In total, a dataset of 2432 instances representing 39 different type of symbols were compiled. All symbols have been scaled to a standard size of 100×100 pixels. The dataset provides rich source of information to evaluate various supervised machine learning algorithms. However, and as can be seen in Fig. 3, the dataset is hugely imbalanced. Some symbols, such as sensors, dominate the dataset, while others appear only once or are vastly underrepresented.

The imbalance between symbols is huge in some cases. For example symbols of type *sensor* appears 392 times in the dataset, while symbols such as *Barred Tee* and *Ultrasonic Flow Meter* appear only once. Similarly, *Reducer* appears in the dataset 285 times, while *Control Valve Angle Choke* only once.

Interestingly, eight types of symbols populate more than 64% of the dataset. These are: Sensor, Reducer, Arrowhead, Valve Ball, DB&BBV, Valve Check, Continuity Label and DB&BPV. At the same time, 18 symbols populate together less than 6% of the whole dataset. These are: Valve Slab Gate, Control Valve Globe, Flange + Triangle, Control, Exit to Atmosphere, Rupture Disc, ESDV Valve Slab Gate, Box, ESDV Valve Butterfly, Temporary Strainer, Control Valve, Valve Gate Through Conduit, Deluge, Vessel, Line Blindspacer, Control Valve Angle Choke, Barred Tee and Ultrasonic Flow Meter. In other words, the dataset is hugely imbalanced.

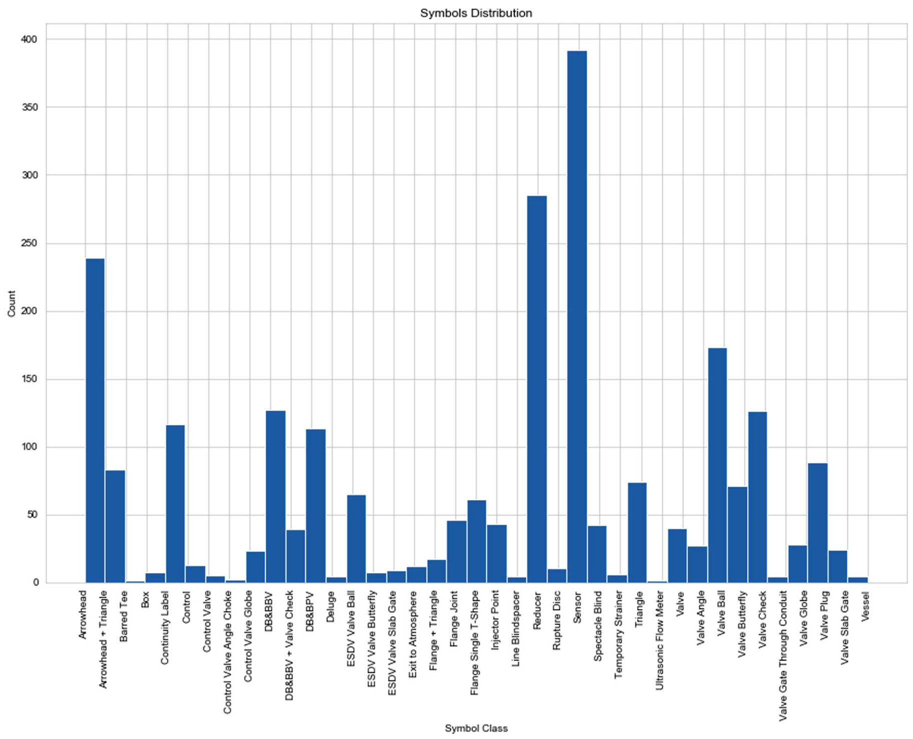

Fig. 3. Class distribution in the dataset

3.3 Classification Method

To provide base-line results on this imbalanced dataset of symbols, we use CNNs. CNNs [16] have made significant progress in recent years in many image-related tasks and in particular in image classification [20,30].

The network architecture used in this paper consists of an input layer of 100×100 of the raw pixel values of the symbol and 32 filters (3×3). Then a 2×2 max pooling layer. Then, two convolutional layers followed by a 2×2 max pooling layer. This structure is then repeated twice with two convolutional layers, with 64 filters of size (3×3) followed by a max pooling layer. Finally, a fully-connected layer composed of two hidden layers and an output layer of 39 (number of classes) units with softmax activation function. All convolutional layers in the network used *ReLU* activations. Dropout [29] was used in the in the fully connected layer with rates 0.1.

4 Experiments and Results

A series of experiments were carried out to establish the validity and stability of the proposed CNN architecture.

Table 1. Performance across different symbols in the dataset

Symbol	Precision	Recall	F1-score	Symbol	Precision	Recall	F1-score
Control Valve	0.00	0.00	0.00	Control	1.00	1.00	1.00
Flange + Triangle	0.00	0.00	0.00	DB& BBV	1.00	1.00	1.00
Line Blindspacer	0.00	0.00	0.00	DB& BBV + Valve Check	1.00	0.90	0.95
Valve Gate Through Conduit	0.00	0.00	0.00	DB& BPV	1.00	0.95	0.98
Rupture Disc	0.33	1.00	0.50	Deluge	1.00	1.00	1.00
Valve Angle	0.33	1.00	0.50	ESDV Valve Ball	1.00	0.92	0.96
Valve Slab Gate	0.50	1.00	0.67	ESDV Valve Slab Gate	1.00	0.50	0.67
Valve Globe	0.57	1.00	0.73	Exit to Atmosphere	1.00	1.00	1.00
ESDV Valve Butterfly	0.67	1.00	0.80	Flange Single T-Shape	1.00	0.93	0.96
Control Valve Globe	0.80	0.57	0.67	Injector Point	1.00	0.62	0.77
Valve	0.80	1.00	0.89	Reducer	1.00	1.00	1.00
Flange Joint	0.85	1.00	0.92	Sensor	1.00	0.98	0.99
Arrowhead + Triangle	0.90	1.00	0.95	Spectacle Blind	1.00	1.00	1.00
Triangle	0.94	0.84	0.89	Valve Ball	1.00	0.97	0.99
Arrowhead	1.00	0.96	0.98	Valve Butterfly	1.00	1.00	1.00
Box	1.00	1.00	1.00	Valve Check	1.00	0.93	0.96
Continuity Label	1.00	1.00	1.00	Valve Plug	1.00	0.89	0.94

4.1 Set up

The dataset was split into disjoint training, validation and testing sets. First, the dataset was split into training and testing sets where 80% of the data was used for training and the remaining 20% for testing. The training set was then split into training and validation sets with ratios of 90% and 10% of the remaining training set respectively. The CNN model was trained with a batch size of 64 for 25 epochs. These parameters were set empirically.

4.2 Results and Discussion

On the training set, an accuracy of 99.8%, with only 2 symbols incorrectly classified was recorded. On the test set, results were slightly lower, with accuracy of 95.3%. In other words 23 symbols were incorrectly identified. Table 1 provides more details about performance across the different symbols and using three different metrics: Precision, Recall, and F1-Score.

A closer look at the results, shows as expected that some of the minority class instances went completely undetected. For example, for the control valve symbols which has only five instances in the whole dataset, the corresponding F1-score is zero. Such score can also be seen in Table 1 for the symbols the *'Flange + Triangle'* (17 instances in the whole dataset), the *'Line Blindspacer'* (4 instances only), *'Valve Gate Through Conduit'* with only 4 instances in the whole dataset. Conversely, well represented symbols in the dataset were correctly classified with relatively high precision and recall. For example, the *'Reducer'* F1-score is 1. Notice that 285 instances of reducers are present in the dataset. A similar performance can be observed for other majority class instances such as *'Sensor'* (392 instances), *'Valve Ball'* (173 instances in the dataset), and others.

These results are consistent with the literature and showed clearly that the learning algorithm tend to be biased toward majority class-instances. Despite this, it can be said that CNN performed extremely well on the testing set with an overall accuracy reaching 95.3%, and an average precision, recall, and F1-score of 0.785, 0.822, and 0.784 respectively across all symbols in the dataset.

5 Conclusions

In this paper, we presented a new multiclass imbalanced dataset for the research community. The dataset represents a collection of symbols extracted from P&IDs. Despite the importance of processing and analysing engineering drawings, no such dataset exists in the public domain. We anticipate that donating this dataset to the research community will help researchers in the domain of machine learning and in particular imbalanced-class classification, and also research in the machine vision domain who are interested in processing and analysing engineering drawings. Future work will focus on handling this multi-class imbalanced problem, where advanced methods such as GANs and other data augmentation techniques might be utilised to improve the learning performance.

References

1. Ablameyko, S.V., Uchida, S.: Recognition of engineering drawing entities: review of approaches. Int. J. Image Graph. **07**(04), 709–733 (2007)
2. Ahmed, S., Liwicki, M., Weber, M., Dengel, A.: Automatic room detection and room labeling from architectural floor plans. In: 2012 10th IAPR International Workshop on Document Analysis Systems, pp. 339–343, March 2012

3. Ali-Gombe, A., Elyan, E., Jayne, C.: Multiple fake classes GAN for data augmentation in face image dataset. In: 2019 International Joint Conference on Neural Networks (IJCNN), pp. 1–8, July 2019
4. Ali-Gombe, A., Elyan, E.: Mfc-gan: class-imbalanced dataset classification using multiple fake class generative adversarial network. Neurocomputing **361**, 212–221 (2019)
5. Arroyo, E., Fay, A., Chioua, M., Hoernicke, M.: Integrating plant and process information as a basis for automated plant diagnosis tasks. In: Proceedings of the 2014 IEEE Emerging Technology and Factory Automation (ETFA), pp. 1–8, September 2014
6. Blostein, D.: General Diagram-Recognition Methodologies. In: Proceedings of the 1st International Conference on Graphics Recognition (GREC 1995), pp. 200–212 (1995)
7. Moreno-García, C.F., Elyan, E., Jayne, C.: New trends on digitisation of complex engineering drawings. Neural Computing and Applications, June 2018
8. Chhabra, A.K.: Graphics Recognition Algorithms and Systems. In: Proceedings of the 2nd International Conference on Graphics Recognition (GREC 1997), pp. 244–252 (1997)
9. Elyan, E., Moreno-Garcia, C.F., Jayne, C.: Symbols classification in engineering drawings. In: 2018 International Joint Conference on Neural Networks (IJCNN), pp. 1–8, July 2018
10. Eyad Elyan and Mohamed Medhat Gaber: A fine-grained random forests using class decomposition: an application to medical diagnosis. Neural Comput. Appl. **27**(8), 2279–2288 (2016)
11. Eyad Elyan and Mohamed Medhat Gaber: A genetic algorithm approach to optimising random forests applied to class engineered data. Inf. Sci. **384**, 220–234 (2017)
12. Esteva, A., Robicquet, A., Ramsundar, B., Kuleshov, V., DePristo, M., Chou, K., Cui, C., Corrado, G., Thrun, S., Dean, J.: A guide to deep learning in healthcare. Nat. Med. **25**(1), 24–29 (2019)
13. Goh, K.N., Mohd. Shukri, S.R., Manao, R.B.H.: Automatic assessment for engineering drawing. In: Zaman, H.B., Robinson, P., Olivier, P., Shih, T.K., Velastin, S. (eds.) Advances in Visual Informatics, pp. 497–507. Springer, Cham (2013)
14. Gonzalez, R.C., Woods, R.E.: Digital Image Processing. Prentice Hall, Upper Saddle River (2008)
15. Goodfellow, I., Bengio, Y., Courville, A.: Deep Learning. MIT Press, 2016. http://www.deeplearningbook.org
16. Jiuxiang, G., Wang, Z., Kuen, J., Ma, L., Shahroudy, A., Shuai, B., Liu, T., Wang, X., Wang, G., Cai, J., Chen, T.: Recent advances in convolutional neural networks. Pattern Recogn. **77**, 354–377 (2018)
17. Holcomb, S.D., Porter, W.K., Ault, S.V., Mao, G., Wang, J.: Overview on deepmind and its alphago zero AI. In: Proceedings of the 2018 International Conference on Big Data and Education, ICBDE 2018, pp. 67–71. ACM, New York (2018)
18. Howie, C., Kunz, J., Binford, T., Chen, T., Law, K.H.: Computer interpretation of process and instrumentation drawings. Adv. Eng. Softw. **29**(7), 563–570 (1998)
19. Kanungo, T., Haralick, R.M., Dori, D.: Understanding engineering drawings: a survey. In: Proceedings of the 1st International Conference on Graphics Recognition (GREC 1995), pp. 119–130 (1995)
20. Krizhevsky, A., Sutskever, I., Hinton, G.E.: Imagenet classification with deep convolutional neural networks. Commun. ACM **60**(6), 84–90 (2017)

21. Kulkarni, C.R., Barbadekar, A.B.: Text detection and recognition: a review. Int. Res. J. Eng. Technol. (IRJET) **4**(6), 179–185 (2017)
22. Lecun, Y., Bottou, L., Bengio, Y., Haffner, P.: Gradient-based learning applied to document recognition. Proc. IEEE **86**(11), 2278–2324 (1998)
23. Lu, Y.: Machine printed character segmentation - an overview. Pattern Recogn. **28**(1), 67–80 (1995)
24. Moreno-Garcia, C.F., Elyan, E.: Digitisation of assets from the oil gas industry: challenges and opportunities. In: 2019 International Conference on Document Analysis and Recognition Workshops (ICDARW), vol. 7, pp. 2–5, September 2019
25. Moreno-García, C.F., Elyan, E., Jayne, C.: Heuristics-based detection to improve text / graphics segmentation in complex engineering drawings. Eng. Appl. Neural Netw., volume CCIS **744**, 87–98 (2017)
26. Mori, S., Suen, C.Y., Yamamoto, K.: Historical review of ocr research and development. Proc. IEEE **80**(7), 1029–1058 (1992)
27. Park, U., Jain, A.K.: Face matching and retrieval using soft biometrics. IEEE Trans. Inf. Forens. Secur. **5**(3), 406–415 (2010)
28. Shone, N., Ngoc, T.N., Phai, V.D., Shi, Q.: A deep learning approach to network intrusion detection. IEEE Trans. Emerg. Topics Comput. Intell. **2**(1), 41–50 (2018)
29. Srivastava, N., Hinton, G., Krizhevsky, A., Sutskever, I., Salakhutdinov, R.: Dropout: a simple way to prevent neural networks from overfitting. J. Mach. Learn. Res. **15**, 1929–1958 (2014)
30. Szegedy, C., Liu, W., Jia, Y., Sermanet, P., Reed, S., Anguelov, D., Erhan, D., Vanhoucke, V., Rabinovich, A.: Going deeper with convolutions. In: 2015 IEEE Conference on Computer Vision and Pattern Recognition (CVPR), pp. 1–9, June 2015
31. Taigman, Y., Yang, M., Ranzato, M., Wolf, L.: Deepface: closing the gap to human-level performance in face verification. In: 2014 IEEE Conference on Computer Vision and Pattern Recognition, pp. 1701–1708, June 2014
32. Tombre, K., Tabbone, S., Lamiroy, B., Dosch, P.: Text/Graphics separation revisited. Document Anal. Syst. **2423**, 200–211 (2002)
33. Vaxiviere, P., Tombre, K.: Celesstin: CAD conversion of mechanical drawings. Computer **25**(7), 46–54 (1992)
34. Vuttipittayamongkol, P., Elyan, E.: Neighbourhood-based undersampling approach for handling imbalanced and overlapped data. Inf. Sci. **509**, 47–70 (2020)
35. Vuttipittayamongkol, P., Elyan, E., Petrovski, A., Jayne, C.: Overlap-based undersampling for improving imbalanced data classification. In: Yin, H., Camacho, D., Novais, P., Tallon-Ballesteros, A. (eds.) Intelligent Data Engineering and Automated Learning, pp. 689–697. Springer, Cham (2018)
36. Yang, Z., Yang, D., Dyer, C., He, X., Smola, A., Hovy, E.: Hierarchical attention networks for document classification. In: Proceedings of the 2016 Conference of the North American Chapter of the Association for Computational Linguistics: Human Language Technologies, pp. 1480–1489. Association for Computational Linguistics, San Diego, June 2016
37. Zhang, D., Lu, G.: Review of shape representation and description techniques. Pattern Recogn. **37**(1), 1–19 (2004)

Deep Learning/Image Processing-Classification

A Novel Spatial-Spectral Framework for the Classification of Hyperspectral Satellite Imagery

Shriya T. P. Gupta(✉) and Sanjay K. Sahay

Department of Computer Science and Information Systems,
BITS Pilani Goa Campus, Goa, India
shriyatp99@gmail.com, ssahay@goa.bits-pilani.ac.in

Abstract. Hyperspectral satellite imagery is now widely being used for accurate disaster prediction and terrain feature classification. However, in such classification tasks, most of the present approaches use only the spectral information contained in the images. Therefore, in this paper, we present a novel framework that takes into account both the spectral and spatial information contained in the data for land cover classification. For this purpose, we use the Gaussian Maximum Likelihood (GML) and Convolutional Neural Network (CNN) methods for the pixel-wise spectral classification and then, using segmentation maps generated by the Watershed algorithm, we incorporate the spatial contextual information into our model with a modified majority vote technique. The experimental analyses on two benchmark datasets demonstrate that our proposed methodology performs better than the earlier approaches by achieving an accuracy of 99.52% and 98.31% on the Pavia University and the Indian Pines datasets respectively. Additionally, our GML based approach, a non-deep learning algorithm, shows comparable performance to the state-of-the-art deep learning techniques, which indicates the importance of the proposed approach for performing a computationally efficient classification of hyperspectral imagery.

Keywords: Neural networks · Hyperspectral imaging · Machine learning · Land cover classification · Spatial segmentation

1 Introduction

Hyperspectral satellite imaging collects high resolution images within contiguous spectral bands across a wide range of the electromagnetic spectrum. Its primary aim is to obtain the spectrum of each pixel in the image of a scene, with the goal of identifying materials or discovering objects. In general, hyperspectral satellite images are captured through an imaging spectrometer in narrow bands of 10–20 nm with up to thousands of bands. On the contrary, multispectral images have 3–10 bands and are captured using a remote sensing radiometer. Such remotely

L. Iliadis et al. (Eds.): EANN 2020, INNS 2, pp. 227–239, 2020.
https://doi.org/10.1007/978-3-030-48791-1_17

sensed satellite images, either air-borne or space-borne, cover large areas of the earth's surface with rich spectral information and hence can be used for the robust classification of land cover with a good accuracy.

Recently, machine learning and deep learning techniques have shown promising results for various classification problems in the fields of natural language processing, computer vision, speech recognition, etc. [1]. Thus, we investigate both, GML, a machine learning technique as well as CNN, a popular deep learning approach. In conventional pixel-wise classification techniques, the algorithms independently process each and every pixel without using the neighboring spatial information. However, to minimize the uncertainty in the data, one can exploit the spatially adjacent pixels, which have more or less similar spectral features. Therefore, in this paper, we develop a novel spatial-spectral algorithm for the robust classification of land cover. Experimental results show that our model is suitable for the classification of images with large spatial structures especially when the spectral responses of different classes are dissimilar. Hence, our proposed approach works well for the task of hyperspectral image classification and it can also be adapted to other domains that are similar to terrain feature classification.

The rest of this paper is organized as follows: Sect. 2 covers the related work and in Sect. 3, we give a brief outline of the classification and segmentation methods. Section 4 describes the datasets used and the detail of our approach is given in Sect. 5. In Sect. 6, we discuss our experimental results and finally, Sect. 7 contains the conclusion and future directions.

2 Related Work

Spectral imaging techniques are now widely being used for solving land cover classification problems. In this context, Ahmad et al. [2] have shown that if there exists a distinct separation between the classes in the decision space, as seen in the case of land cover classification tasks, the use of a GML classifier provides a good accuracy. Further, Ablin et al. [3] reported that classifying an unknown pixel can be done efficiently by the maximum likelihood classifier, as it quantitatively evaluates both the variance and co-variance of the spectral response pattern for each class.

In 2018, Khan et al. [4] discussed in detail the recent research in classification techniques used for hyperspectral satellite imagery. In their paper, they state that most of the current research efforts and studies follow the standard pattern recognition paradigm, which is based on the construction of complex handcrafted features. In contrast to the approaches discussed by Khan et al. [4], LeCun et al. [5] proposed the deep learning based classification methods which use hierarchically constructed high-level features in an automated way. In the context of deep learning based satellite image classification, Makantasis et al. [6] used a combination of CNN for feature extraction along with a multi layer perceptron for classification and achieved an accuracy of up to 98.88% on the Indian Pines dataset. Similarly, Audebert et al. [7] used 3D CNNs for the classification of Indian Pines and Pavia University datasets, and obtained accuracies of 96.87% and 96.71% respectively. An alternate approach of using Recurrent Neural Networks (RNN) was proposed by Ma et al. [8]. Their RNN based model achieved an accuracy of 96.20% on the Pavia University dataset which indicates the superiority of CNNs over RNNs for image classification tasks.

Later, many authors combined the aforementioned pixel-wise classification algorithms with different segmentation approaches to enhance the efficiency of the spectral classification. For instance, Tarabalka et al. [9] studied the use of Watershed segmentation methodologies for spatial-spectral classification of hyperspectral images. They also described the various plausible approaches to combine it with a pixel-wise classifier, viz. they used a SVM classifier with Watershed segmentation and reported an accuracy of 90.64% on the Indian Pines image and 95.21% on the University of Pavia dataset. Furthermore, some authors have explored the use of Markov Random Fields (MRF) to incorporate the spatial information contained in the data. For example, Qing et al. [10] used an MRF-based loopy belief propagation technique and obtained an accuracy of 98.5% on the Indian Pines dataset.

Hence, we consider these approaches as the baselines for our work and in our proposed model, we further improve the classification accuracy as well as the computational efficiency using both, GML, a machine learning technique as well as CNN, a deep learning approach for pixel wise classification. To the best of our knowledge, land cover classification has rarely been done by using the watershed segmentation algorithm with the above-mentioned spectral classifiers.

3 Preliminaries

In this section, we briefly explain the GML and CNN models used for the pixel-wise classification as well as the Watershed algorithm used to generate the segmentation maps.

3.1 Gaussian Maximum Likelihood

The Gaussian Maximum Likelihood classifier is a supervised classification method derived from the Naive-Bayes theorem. It classifies each unidentified pixel θ by using the probability density functions to compute the likelihood of a given pixel belonging to a particular category C. The GML algorithm evaluates the probability values for each class as follows:

$$P(C|\theta) = P(C)\frac{P(\theta|C)}{P(\theta)} \tag{1}$$

Here, the pixel is assigned to the most likely class based on the highest probability value or it is labelled as 'unknown' if the probability values are below an analytically defined threshold. As the GML is a pixel by pixel classification method, it does not take into account the contextual information about neighboring classes while labeling a pixel. Also, it is assumed that the distribution of the cloud of points forming a particular class is Gaussian. Here, the mean vector and the co-variance matrix can be used to entirely describe the distribution of the response pattern for each category.

3.2 Convolutional Neural Network

A Convolutional Neural Network is comparatively more accurate than a traditional machine learning algorithm mainly because a CNN learns the filters automatically while the features of a traditional algorithm are hand-engineered. Here, we briefly describe the working of a CNN with hyperspectral image data as the input and the detailed description of its usage in our model is presented in Sect. 5. Since a hyperspectral image is composed of L spectral layers, the input image can be represented as X $= [x_1, x_2, ..., x_L]$ where x_i is a matrix of pixels corresponding to the layer i. The first convolutional layer consists of n_1 filters of kernel size $f_1 \times f_1$ and it is employed to extract the features of the input image as follows:

$$F_1(X) = \theta_1(u_1) \tag{2}$$

where θ_1 denotes the activation function of the entire layer. Here $u_1 = \sum_{l=1}^{L} x_l * w_l + b_1$, where w_l represents the weights of the filter acting on the input hyperspectral data, $*$ represents the convolution operation, and b_1 is an n_1-dimensional vector which represents the bias of the entire layer. Also, each element of this vector is associated with every filter and the output is composed of n_1 feature maps corresponding to the n_1 filters.

3.3 Watershed Transformation

The Watershed transformation is a powerful mathematical technique for geomorphological image segmentation. It considers a 2D one-band image as a topographic structure wherein the value of a pixel stands for its elevation. In order to associate each basin with a minima, the Watershed lines divide the entire image into catchment basins. This segmentation method requires the user to define seeds, which are pixels belonging unambiguously to a region. The Watershed transformation is usually applied to the gradient function of the image. The gradient defines the transitions between regions, so that it has high values on the borders between objects and minima in the homogeneous regions. If the crest lines in the gradient image correspond to the edges of image objects, then the Watershed transformation successfully partitions the entire image into meaningful regions. Hence, it is very well suited for hyperspectral satellite image segmentation where the main aim is to segment the imagery into distinct geographical regions.

4 Datasets and Pre-processing

In this section we describe the two publicly available benchmark datasets (Indian Pines [11] and Pavia University [12]) and the preprocessing that has been used for our experimental analysis.

4.1 Indian Pines

The Indian Pines dataset consists of 145×145 pixels and 224 spectral reflectance bands and was gathered by the 220-band Airborne Visible / Infrared Imaging Spectrometer (AVIRIS) sensor over the Indian Pines test site in North-western Indiana. The ground truth corresponding to this dataset is designated into sixteen classes which is not entirely mutually exclusive and consists of two-thirds agriculture and one-third forest or other natural perennial vegetation. Along with this, there are two dual lane highways, a rail line, low density housing, and some smaller roads.

4.2 Pavia University

The Pavia University dataset was acquired by the 103-band Reflective Optics System Imaging Spectrometer (ROSIS) sensor during a flight campaign over Pavia, northern Italy with dimensions of 610×610 pixels and 103 spectral bands. However, some of the samples contain no information. Hence, they are discarded in our experimental analysis and are depicted using broad black strips. The geometric resolution of this image is 1.3 m and the corresponding ground truth differentiates among all the nine classes.

4.3 Pre-processing

For the empirical analysis, the preprocessing steps of the Indian Pines and the Pavia dataset are same for both the approaches (GML and CNN). First, we over sample the weak classes in order to make the hyperspectral images more balanced. The pixel values are then standardized by subtracting the mean and scaling them to unit variance. Next, we apply Principal Component Analysis (PCA) to the input data in order to transform the original high-dimensional data into a low-dimensional space by extracting the key features and then padding it with zeros. Then, we save the preprocessed data for the experimental analysis.

5 Methodology

This section describes our approach in detail which includes the pixel-wise classification techniques, the segmentation method, and the modified majority vote algorithm.

5.1 Spatial-Spectral Classifier

An overall architecture of the CNN used in our work is shown in Fig. 1. It comprises of two 2D convolutional layers with the first layer having C_1 filters of size $f_1 = 3$, second layer having $C_2 = 3 \times C_1$ filters of size $f_2 = 3$, and followed by a flatten layer. Here, the parameter C_1 corresponds to the number of principle components that preserve at least 99.9% of the initial information

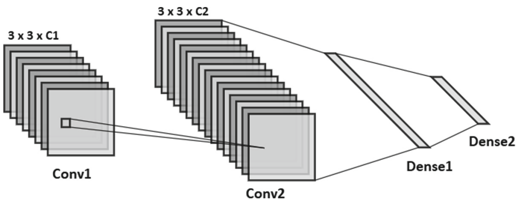

Fig. 1. An overall architecture of the CNN

contained in the original datasets after applying PCA. The size of the filter is determined empirically which dictates the number of neighbors of each pixel that has been taken into consideration during the classification. The convolution layer is composed of a set of separate filters and each filter is independently convolved with the image to obtain the corresponding feature maps as described in Sect. 3.2. In contrast to the conventional CNNs, we do not use a max pooling layer after the convolution layer, since there is no need to account for the translation and scale invariance. Next, we use two regular densely connected neural network layers in our model. The first dense layer has 120 units with a dropout of 0.5 and the second layer is the last layer of the network. It has as many units as the number of classes and in this layer, we use a softmax algorithm to produce the final outputs.

The second pixel-wise classification scheme that we used is the GML algorithm as outlined in Sect. 3.1, and in our analysis, the GML classification technique differs significantly from the CNN method. The GML algorithm performs the classification in a pixel by pixel fashion which preserves their individual values. On the contrary, the convolution operation in the CNN technique averages out individual values using adjacent pixels that lie within the dimensions of an applied filter.

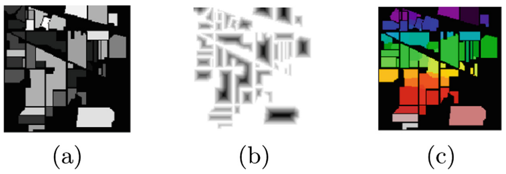

Fig. 2. (a) Overlaps (b) Distances and the (c) Separated objects for Indian Pines data

Next, we generate a segmentation map of the image using the Watershed algorithm as detailed in Sect. 3.3. In our model, local maxima of the distance map to the background are used as seeds. These maxima are chosen as markers in order to segment the entire image into regions and the flooding of catchment basins from such markers separates the areas along a Watershed line. The segmentation maps obtained using the Watershed algorithm are shown in Fig. 2

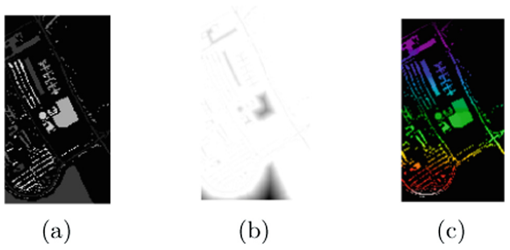
Fig. 3. (a) Overlaps (b) Distances and the (c) Separated objects for the Pavia dataset

and Fig. 3 for the Indian Pines and the Pavia University datasets respectively. For images where the pixels are not uniformly distributed across the classes, the Watershed algorithm typically produces over segmented maps, and so in our case, the image is over segmented. However, the problem is alleviated when we combine the segmentation map with the pixel-wise classification results.

Algorithm 1: Our majority vote approach.

```
1: uni_labels = unique values (labels in segmentation map)
2: final_map = 0
3: for i in uni_labels do
4:     arr ← []
5:     height ← height of segmentation map
6:     width ← width of segmentation map
7:     for j = 0 to j = height do
8:         for k = 0 to k = width do
9:             find all pixels in the segmentation map having label i
10:            append their pixel-wise classification labels to arr
11:        end for
12:    end for
13:    max_freq_label ← most frequent label in arr
14:    for j = 0 to j = height do
15:        for k = 0 to k = width do
16:            find all pixels in the segmentation map having label i
17:            assign max_freq_label as the label for these pixels in the final_map
18:        end for
19:    end for
20: end for
21: return final_map
```

Finally, we combined the outputs of the pixel-wise classification algorithms with the segmentation maps using a modified majority vote technique (Algorithm 1), wherein for each region of the segmentation map, all the pixels are assigned to the most frequent class. However, in our proposed approach, the majority vote is performed with an adaptive neighborhood instead of a fixed neighborhood and for every pixel, the region it belongs to is defined by the segmentation map. Then, we use this region as its neighborhood for the vote on the spectral classification.

6 Experimental Results

First, we test our proposed models, GML with Watershed (GML-W) and CNN with Watershed (CNN-W), on the Indian Pines and the Pavia University datasets. Then, we compare the performance of our hybrid models with the traditional GML and CNN algorithms on the same datasets. For this purpose, we split the datasets in the ratio of 3:1 for the training and testing data respectively.

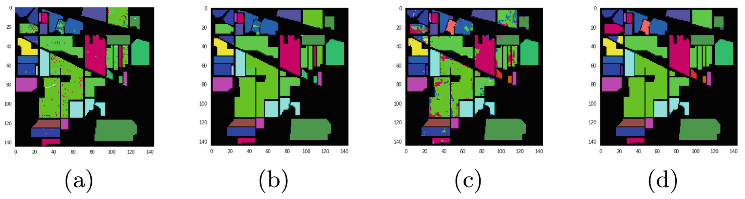

Fig. 4. Results of (a) GML (b) GML-W (c) CNN and (d) CNN-W on Indian Pines data

The results obtained by the traditional GML and the proposed GML-W algorithms are shown in Fig. 4(a) and Fig. 4(b) respectively. For the Indian Pines dataset, the GML gives an accuracy of 97.46% and the GML-W provides an accuracy of 98.31%. Next, we experimented with the CNN classifier and the obtained results are shown in Fig. 4(c) and Fig. 4(d). In terms of accuracies, the CNN and CNN-W models give results of 87.08% and 97.7% respectively. As is evident from the results, the use of the spatial-spectral classifier led to a significant improvement with an increase of 10.6% in the overall accuracy. Additionally, from a visual observation, the classification maps obtained by the spatial-spectral classification are seen to be much less noisy than the ones obtained by the pixel-wise classification.

The detailed results obtained for each category, viz. GML, CNN, GML-W, and CNN-W on the Indian Pines dataset is shown in Table 1. From the results, it is evident that incorporating the spatial information with the traditional pixel-wise classification algorithm improves the accuracies considerably. This is due to the fact that most of the classes in the image represent large crop fields, and the segmentation step makes these regions of fields homogeneous, thereby improving the classification results. The accuracies of almost all classes are significantly improved, except for some small classes like Oats and Stone-Steel Towers which are incorrectly assimilated into neighboring regions. However, the GML algorithm fails to correctly identify the regions of Corn-notill, Hay-windrowed, and Soybean-notill as the number of pixels in the training set is almost a hundred

Table 1. Accuracies (%) for Indian Pines dataset

Category	GML	GML-W	CNN	CNN-W
Alfalfa	100.0	100.0	100.0	100.0
Corn-notill	0.00	100.0	80.11	0.00
Corn-mintill	94.74	82.35	89.90	100.0
Corn	97.83	88.19	96.61	93.37
Grass-pasture	100	100.0	95.04	100.0
Grass-trees	99.79	96.89	98.90	96.89
Grass-pasture-mowed	99.72	100.0	100.0	100.0
Hay-windrowed	0.00	100.0	100.0	0.00
Oats	100.0	100.0	100.0	100.0
Soybean-notill	0.00	100.0	88.06	0.00
Soybean-mintill	99.48	99.48	72.14	99.48
Soybean-clean	90.59	98.20	87.83	98.28
Wheat	99.32	100.0	100.0	100.0
Woods	100.0	100.0	98.41	100.0
Buildings-Grass-Trees	99.60	99.20	93.81	99.84
Stone-Steel-Towers	98.96	87.56	100.0	87.04
Average accuracy	93.80	96.99	80.10	91.76
Overall accuracy	97.46	98.31	87.08	97.7

times lesser than other regions, which leads to the misclassification of the pixels into neighboring categories.

A similar analysis of the Pavia University dataset has been done by splitting the data in the ratio of 3:1 for training and testing. First, using the GML classifier, we were able to obtain an accuracy of 99.03% which was later on improved to 99.52% using our proposed hybrid classifier and the results are shown in Fig. 5(a) and Fig. 5(b), respectively. Next, we carried out the pixel-wise classification using a deep learning based CNN model and obtained an accuracy of 97.39%. We further improved the performance by $\sim$ 2% using our proposed approach which led to an overall accuracy of 99.44%. Figure 5(c) and Fig. 5(d)

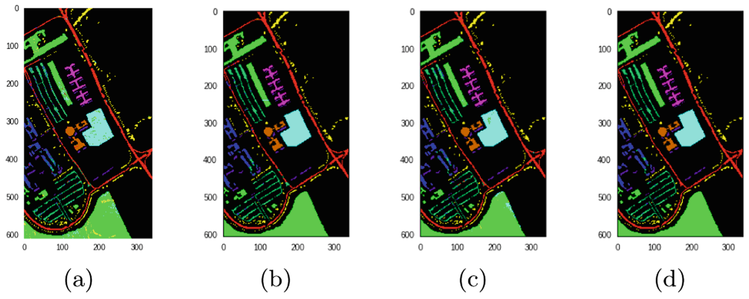

Fig. 5. Results of (a) GML (b) GML-W (c) CNN and (d) CNN-W on the Pavia dataset

represent the results obtained before and after combining with the Watershed transformation respectively.

Table 2. Accuracies (%) for the Pavia university dataset

Category	GML	GML-W	CNN	CNN-W
Asphalt	100.0	100.0	98.13	100.0
Meadows	95.02	98.02	98.62	97.49
Gravel	94.98	96.02	89.33	96.02
Trees	92.42	96.56	99.73	91.47
Painted metal sheets	99.18	99.18	100.0	99.18
Bare soil	100.0	100.0	98.96	100.0
Bitumen	94.96	100.0	99.39	100.0
Self-blocking bricks	96.76	100.0	93.81	100.0
Shadows	92.85	99.10	100.0	98.66
Average accuracy	96.24	98.76	97.55	98.09
Overall accuracy	99.03	99.52	97.39	99.44

Furthermore, we did a detailed analysis of our models for the Pavia University dataset and the category wise results for the nine classes are summarized in Table 2. From the analysis, we observed that the spatial-spectral algorithm using GML gives the best overall accuracy (99.52%). The variations in the accuracies for different regions depends largely on the area of that particular region. For instance, a comparatively bigger structure belonging to the painted metal sheets class in the center of the image is mostly represented by one region, which leads to a significant improvement on combining it with the segmentation map. On the contrary, regions like the asphalt and bitumen are spread across a large number of regions.

Table 3. Comparison of the overall accuracies of our methods

Classifiers	Indian Pines	Pavia Scene
GML	97.46%	99.03%
GML-W	98.31%	99.52%
CNN	87.08%	97.39%
CNN-W	97.7%	99.44%

A summary of the overall results obtained on the two datasets are given in Table 3. Our experimental results show that the GML based approach outperforms the CNN based approach for both the datasets. This is because the

GML performs the classification on a pixel by pixel basis and hence it precisely assigns most of the pixels to their correct classes. However, the CNN technique averages out individual pixel values during the convolution step and so it classifies many of the pixels into neighboring regions which leads to lower accuracies. Our technique also proved to be better than the traditional classifiers of GML and CNN, which gave accuracies of 99.03% and 97.39% respectively. As for the Indian Pines dataset, our proposed approach led to a significant improvement of 10.6% over the traditional CNN based classification approach. In addition to this, our method performed considerably better than the conventional GML classifier with an overall accuracy of 98.31% on the Indian Pines dataset.

Table 4. Comparison with existing deep learning based methods

Classifiers	Indian Pines	Pavia Scene
3D CNN [13]	99.07%	99.39%
CNN-MRF [14]	99.27%	99.55%
Ours (GML-W)	98.31%	99.52%

In order to have a more detailed analysis, we compare our approach to the existing deep learning based methods in Table 4. As seen from the empirical results on the Pavia university scene, our GML based spatial-spectral methodology, without any kind of deep learning aspects has an accuracy of 99.52%, which is better than the performance of 99.39% achieved by the 3D CNN based spectral classification technique proposed by Li et al. [13]. Our method's performance is also comparable to the state-of-the-art deep learning based technique of CNN-MRF given by Cao et al. [14] that has an accuracy of 99.55%, even though our approach does not require any sort of expensive training or learning procedures. However, our method achieves an accuracy of 98.31% on the Indian Pines dataset which is lesser than the accuracy of 99.27% given by the existing deep learning method because our approach is more suitable for images where the distribution of pixels amongst the different classes is comparatively uniform.

7 Conclusion

In this paper, we present a novel spatial-spectral methodology for the classification of land cover using hyperspectral satellite image data. The proposed approach combines the results of a pixel-wise spectral classification and segmentation maps of the Watershed algorithm, by performing a majority vote on the initial classification output using adaptive neighborhoods defined by the segmentation map. We investigated GML, a machine learning technique as well as CNN, a popular deep learning approach for the pixel-wise image classification, and found that by incorporating the spatial information with the spectral data, the overall classification map contains more homogeneous regions, as compared to only pixel-wise classification of the hyperspectral images. The empirical analyses indicate that our approach performs better than the results discussed in Sect. 2 for the spatial-spectral classification of hyperspectral images, with an overall accuracy of 99.52% on the Pavia University dataset and up to 98.31% on the Indian Pines dataset. Experimental results also demonstrate that our proposed GML based framework - without any kind of expensive training or learning procedures, achieves comparable performance to the state-of-the-art deep learning based methods and is hence a computationally efficient alternative for the classification of hyperspectral image data.

In order to further improve the overall classification, different feature extraction methods need to be investigated so as to find the most effective features for segmentation. Also, our proposed approaches should be verified on multispectral satellite image data to analyze their robustness and in this direction, work is in progress.

References

1. Shrestha, A., Mahmood, A.: Review of deep learning algorithms and architectures. IEEE Access **7**, 53040–53065 (2019)
2. Ahmad, A., Quegan, S.: Analysis of maximum likelihood classification on multispectral data. Appl. Math. Sci. **6**(129), 6425–6436 (2012)
3. Ablin, R., Sulochana, C.H.: A survey of hyperspectral image classification in remote sensing. Int. J. Adv. Res. Comput. Commun. Eng. **2**(8), 2986–3000 (2013)
4. Khan, M.J., Khan, H.S., Yousaf, A., Khurshid, K., Abbas, A.: Modern trends in hyperspectral image analysis: a review. IEEE Access **6**, 14118–14129 (2018)
5. LeCun, Y., Bengio, Y., Hinton, G.: Deep learning. Nature **521**(7553), 436 (2015)
6. Makantasis, K., Karantzalos, K., Doulamis, A., Doulamis, N.: Deep supervised learning for hyperspectral data classification through convolutional neural networks. In: 2015 IEEE International Geoscience and Remote Sensing Symposium (IGARSS), pp. 4959–4962. IEEE (2015)
7. Audebert, N., Le Saux, B., Lefèvre, S.: Deep learning for classification of hyperspectral data: a comparative review. IEEE Geosci. Remote Sens. Mag. **7**(2), 159–173 (2019)
8. Ma, A., Filippi, A.M., Wang, Z., Yin, Z.: Hyperspectral image classification using similarity measurements-based deep recurrent neural networks. Remote Sens. **11**(2), 194 (2019)
9. Tarabalka, Y., Benediktsson, J.A., Chanussot, J.: Spectral-spatial classification of hyperspectral imagery based on partitional clustering techniques. IEEE Trans. Geosci. Remote Sens. **47**(8), 2973–2987 (2009)
10. Qing, C., Ruan, J., Xu, X., Ren, J., Zabalza, J.: Spatial-spectral classification of hyperspectral images: a deep learning framework with markov random fields based modelling. IET Image Process. **13**(2), 235–245 (2018)
11. Landgrebe, D., Biehl, K.: Aviris nw indiana's indian pines data set (1992). https://engineering.purdue.edu/~biehl/MultiSpec/hyperspectral.html
12. Gamba, P.: Pavia university scene (2001). http://www.ehu.eus/ccwintco/index.php/

13. Li, Y., Zhang, H., Shen, Q.: Spectral-spatial classification of hyperspectral imagery with 3D convolutional neural network. Remote Sens. **9**(1), 67 (2017)
14. Cao, X., Zhou, F., Xu, L., Meng, D., Xu, Z., Paisley, J.: Hyperspectral image classification with markov random fields and a convolutional neural network. IEEE Trans. Image Process. **27**(5), 2354–2367 (2018)

Detection of Shocking Images as One-Class Classification Using Convolutional and Siamese Neural Networks

Pavel Gulyaev(✉) and Andrey Filchenkov

ITMO University, Kronverkskiy Pr. 49, 197101 St. Petersburg, Russia
paw.gulyaev@yandex.ru, afilchenkov@corp.ifmo.ru

Abstract. Not safe for work content automatic detection is a serious challenge for social media due to overwhelming growth of uploaded images, gifs and videos. This paper focuses on shocking images automatic detection by convolutional neural networks. It was considered that the correct recognition of the shocking class is more important than the non-shocking one. Binary classification by a convolutional network that training during operation has been used as a baseline solution. However, this solution has two drawbacks: the network highlights incorrect features of non-shocking images (infinite class) and tends to forget rare subclasses of shocking images, which is unacceptable. To eliminate the first drawback, we approach this problem as a one-class classification with having in mind that a "non-shocking" image can be defined only via contradiction with a shocking one. This method is based on using sparse autoencoders build on top of a pretrained convolutional neural network and is not trained during operation. To eliminate the second drawback, we memorized vectors of images that were incorrectly classified during operation. A trained siamese network during the prediction is used to search for similar images in the database. In the case of an incorrect prediction by the combined model, vectors of images are added to the database and the siamese network is trained on them. This method allows you to minimize the number of errors in rare subclasses identified only during the operation phase of the model.

Keywords: Image recognition · One-class classification · Siamese network

1 Introduction

The amount of information uploaded by users to social media instantly grows, and this information flow becomes more and more difficult to control in terms of preventing uploading of socially unacceptable content, which may be not safe for work (NSFW) or even not safe for life (NSFL).

NSFW content contains nudity, intense sexuality, profanity, violence/gore or other disturbing subject matter, which usually are seen inappropriate if accesses in a public or formal environment including a workplace or school.

Not safe for life content is a subclass of NSFW-content refers to subject matter that might not be in the interest of a person to view regardless of location and potential coviewers for being horrifying, disgusting, offensive, or even mentally disturbing to the viewer.

Many works are devoted to detecting possible negative effect of NSFW content present and availability for a wide audience [1, 3, 4, 9].

Existing works on the shock image detection, which will be discussed in detail in Sect. 3, has two main drawbacks. The first problem encountered by the developers of the shock image recognition system is the lack of a specific definition of shock-content. To overcome this drawback, we decided to narrow the concept of shock content to images of real cruelty over people, blood, mutilations, etc.

The second problem is related to solving shocking content detection as a binary classification task. These days, social networks and search engines prefer to block shock-content on user complaints and train a binary classification model using these complaints, which is later used for blocking similar images. This approach has the following weaknesses:

A model needs many diverse non-shocking content and a large number of complaints to learn, requiring thus a large number of users getting acquainted with shocking materials before reporting.

A model shows unpredictable behavior for objects that are different from those in the training sample. It can support its decision based on features of non-shocking content, which is incorrect, because 1) the number of classes of non-shocking images is infinite, and 2) the presence of features of a non-shocking image should not reduce the significance of the features of the shocking image (for example, the presence of a nice cat in an image should not prevent the system from detecting a severely torn mouse in the same photo).

The network quickly forgets or does not learn at all rare subclasses of shocking images, such as, for instance, brain worms.

To overcome these limitations, we will reduce the problem to the one-class classification task. A one-class classification, unlike a binary one, occurs in the conditions of impossibility to collect a sufficiently large number of objects of one of the classes, or the impossibility of unambiguous representation of one of the classes [6].

In this task, shocking images are contrasted with all other existing images, because it is impossible to correctly define the class of “non-shocking images”.

This helps to eliminate the listed weakness of binary classification:

1. There is no need for many non-shocking images.
2. A model learns only features of shocking content. If an image is dissimilar to any of the shocking images in the training sample, it is classified as non-shocking.
3. The amount of data for training is smaller, therefore the relative number of representatives of rare subclasses is larger, hence the model is easier to learn from them.

When developing a one-class classifier of shock images, we took into account the heterogeneity and a large number of subclasses of this class of images.

The rest of the paper has the following structure. In Sect. 2, we review and discuss related papers. We present the methods and technique we use in Sect. 3. Empirical study of their performance is presented in Sect. 4 and discussed in Sect. 5. Section 6 concludes.

2 Related Work

In one of the first papers on the recognition of cruelty in images [13], the images used as training data were collected by sending relevant queries to Google. Despite the good results presented in the article (90.1 ± 1.5% accuracy), such inaccurate data collecting led to the results presented in Fig. 1. In addition, the approach used by the authors (bag of words using various selected features) did not consider the relationship of different parts of an image, which is critically important in cruelty recognition.

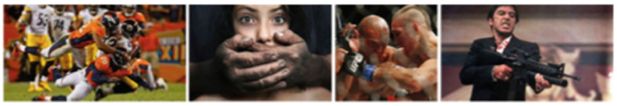

Fig. 1. Images classified by the system [13] as cruel.

In another paper [8], the authors recognized images from horror movies using the concept of image context, which was an important innovation. However, the context and the "awfulness"' of an image were determined solely using color features, which was inefficient for recognizing shock images.

Finally, in the work using pretrained convolutional networks [14], the problem of accounting for the interaction of different image segments was solved, but it had drawbacks: the use of binary classification and careless (semi-automatic) data collection. Binary classification leads to the uncertainty of the network, as already discussed in the introduction.

3 Learning Methods

3.1 One-Class Classification

Convolutional Autoencoders. Autoencoders perform a data-specific lossy coding learned automatically from training data [2]. One-class classification is performed by a convolutional autoencoder (CAE) learned using images of a given class (shock-content), which would receive a smaller error for recovering images of this class in comparison with error of restoring any other random images submitted to the input. Setting the boundary of the recovery error will result into a classifier, which will detect shocking image in case of a smaller recovery error and a non-shocking image otherwise.

Ordinary and Sparse Autoencoders. We trained both types of autoencoders [2, 10] to encode the values of the last layer of a pretrained convolutional neural network (CNN). In this case, the last layer was trained from scratch and was added on top of the layers of pretrained networks. First, we used an idea similar to the one from the CAE approach: the recovery error for the learning class is significantly less than the recovery error for the remaining values.

However, using only recovery error is just a single feature, so we decided to add values of autoencoder internal representation vector as new features, increasing thus their number from 1 to 2001.

One-class support vector machine (OCSVM). OCSVM is another approach we can use on top of a CNN. We use a one-class support vector machine [11] on the values of the last layer vectors of the CNNs pretrained on ImageNet images. There was no significant difference in the quality of the CNNs performance.

We found out when learning these networks that replacement of a loss function softmax to hinge loss function gives a significant increase in quality for OCSVM. This can be explained by the fact that the estimates given by the softmax function are non-normalized logarithmic probabilities of the class, which can easily be transformed into class probabilities. When training a network, changing the evaluation of one class affects the ratings of all other classes. In this work, we try to isolate the characteristics of a certain class, estimating random images should not affect the estimates of shocking images. To do this, we replace the used loss function: from binary cross-entropy to hinge and change the activation function of last layer from softmax to tanh (because binary hinge loss function should be used with labels in interval $\{-1, +1\}$).

3.2 Siamese Network

Siamese network is a class of neural network architectures that contain two or more subnetworks (CNN) that share all their parameters and weights [7]. They are used in tasks that involve finding similarity or a relationship between two comparable objects. A set of pairs of such objects labelled with values of their proximity are used as training data. The architecture of Siamese networks used in this work is shown in the Fig. 2.

It consists of three components:

1. *Feature extraction* is pretrained CNNs that do not update their parameters during training. In this paper, we use Inception3 [12] (Inc3), ResNet50 [5] (RN50) and ResNet50 + fused [15] (RN50f) CNNs as feature extraction components.
2. *Distance* is a measure of vectors dissimilarity. In this paper, we use the cosine distance, the Manhattan distance and the Euclidean distance.
3. *Classifier* is a classifier that determines the similarity $(0; 1)$ of input objects on an integrated vector. In this paper, this role is performed by SVM, Random Forest, XGBoost and Feedforward Neural Network (FNN).

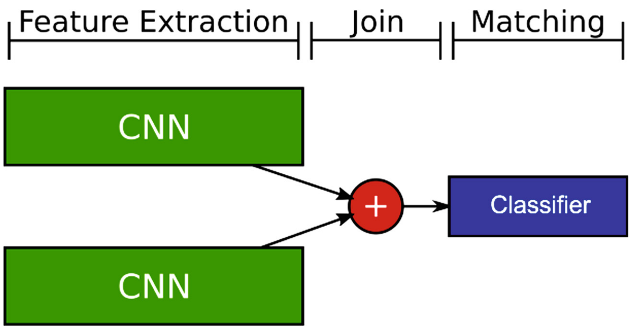

Fig. 2. General architecture for all siamese networks used in this work.

In this work, siamese network learns to determine how similar the pairs of images are to each other and helps to consider the presence of very rare subclasses of shocking images. During the exploitation of the system, after the classification by the one-class classifier, an image is checked for similarity to a limited number of images poorly recognized by the network and the one-class classifier. If the image is similar to one of the representatives of the rare subclasses, then the final answer is the class to which the subclass belongs, otherwise—the prediction of the one-class classifier. In case of detection of incorrect classification by a one-class classifier and the absence of similar images in the base of rare subclasses, a new subclass is created and additional training of the siamese network starts: similar images are generated by data augmentation methods, and not similar images are taken randomly from opposite class; new image proximity pairs and sampled old pairs become a learning sample. Since the siamese network is designed to solve one-shot learning problems, two images of the same subclass are enough for it to remember a new subclass.

4 Empirical Study

4.1 Dataset

The problem of the methods described in the Introduction is an inaccurate semiautomatic data collection. Often on pages with materials about accidents, as well as in the search for relevant requests, in addition to images of the deaths and injuries themselves, there are photos of rescuers, landscape, etc. which is not a shock-content. These images were selected manually.

The collection of data took into account the presence of contextual shock (for example, worms inside a human body or python, which completely swallowed a person). We manually collected:

1. 2500 shocking images;
2. 5150 non-shocking images (random pictures from the Internet);
3. 115 “border”‘ shocking images divided into 14 subclasses that were incorrectly classified by the model [14];

4. 50 “border”‘ non-shocking images divided into 5 subclasses that were incorrectly classified by the model [14].

The breakdown into the training, validation and test sets was stratified: the image of each class and each boundary subclass was represented proportionally in three sets. For the validation set, 20% of all images were used. For test, 20% of the remaining sample was used. Thus, the ratio of classes was used: 64%:16%:20% (train:test:validation). For the training of a pre-trained convolutional network and siamese networks, images of all classes are used. To train auto-encoders and a one class SVM, only shocking and “border”‘ shocking images are used. To test all models, both shocking and non-shocking images are used.

We compare the models with respect to their accuracy, precision and recall in classifying shocking and non-shocking images. Additionally, we compare recall and precision measures for “border” shock and non-shock images separately.

4.2 Baseline Model

As a baseline solution, we used the binary classification with modern convolutional networks ImageNet v3, ResNet50 and the implementation of ResNet50 with Fused-layers. We used threshold movement to increase the recall of recognizing shock images and see how other metrics change. The probabilities of the classes were weighed in accordance with the cost matrix of the classes. The cost of misclassification of shocking images as non-shocking consistently increased until the overall quality of the model did not start to fall precipitously, or metrics ceased to change. The results of the work are presented in Table 1.

Table 1. Results of the basic models.

CNN	Accuracy	Shock Precision	Shock Recall	Border Precision	Border Recall	Precision	Recall
Inception3	0.936	0.882	0.906	0.792	0.790	0.942	0.937
ResNet50	0.949	0.927	0.915	0.792	0.801	0.949	0.949
ResNet50 Fused	**0.957**	**0.946**	0.918	**0.807**	**0.813**	**0.956**	**0.956**
Inception3 with moving threshold	0.861	0.709	0.962	0.740	0.433	0.891	0.861
ResNet50 with moving threshold	0.883	0.736	0.993	0.788	0.432	0.912	0.883
ResNet50 Fused with moving threshold	0.898	0.763	**0.988**	0.802	0.504	0.919	0.897

4.3 Results of One-Class Classification

Convolutional Autoencoders. Several CAEs with different sizes and activation functions were built and trained:

1. Six-layer CAE with ReLu at the inner layers and at the output.
2. Six-layer CAE with tanh at the inner layers and at the output.
3. Six-layer CAE with tanh at the inner layers and ReLu at the output.
4. Eight-layer CAE with tanh at the inner layers and ReLu at the output.
5. A thirty-two-layer CAE using VGG-16 as an encoder.
6. A thirty-two-layer CAE using pre-engineered VGG-16 as an encoder.

The best recovery error was shown by the eight-layer autoencoder, but the recovery threshold could not be found: recovery errors for both classes are uniformly distributed across the sample. As a result, the model gives 0.528 accuracy on the validation set, with precision equals to 0.598 and recall equals to 0.525, which is which is very close to random selection. There are some factors that should be taken into consideration in the analysis of reasons for failure, including short network training time and too broad definition of a class of shocking images for such small sample. This conclusion is because when CAE work with the subclass "cut hands" (a small sample of 150 images containing cut hands), the six-layer CAE showed a 0.86 accuracy on validation after the threshold was selected with F1-score. Photos of the cut hands are very similar to each other and can clearly be combined into one subclass of images. An example of the work is shown in Fig. 3, the recovery errors of different classes differ by an order of magnitude.

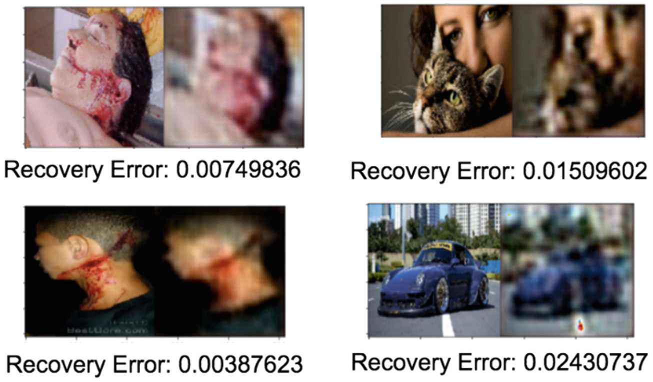
Recovery Error: 0.00749836
Recovery Error: 0.01509602
Recovery Error: 0.00387623
Recovery Error: 0.02430737

Fig. 3. Original image and image recovered by an eight-layer convolutional autoencoder.

OCSVM. The models were trained only on shocking images without considering the boundary shock, because this increases the efficiency of the model. The model is primitive enough and cannot handle with boundary images well enough.

The main parameters for tuning were the type of kernel (linear, rbf, polynomial) and ν that sets an upper bound on the fraction of outliers (training examples regarded out-of-class) and sets a lower bound on the number of training examples used as support vectors. Results are shown in Table 2.

Table 2. OCSVM-model classification results.

Pretrained CNN/loss	Accuracy	Shock Precision	Shock Recall	Border Precision	Border Recall	Precision	Recall
Inceptionv3 cross-entropy	0.846	0.683	0.944	0.632	0.365	0.880	0.846
Inceptionv3 hinge	0.908	0.787	**0.979**	0.732	0.614	0.923	0.908
ResNet50 cross-entropy	0.852	0.696	0.945	0.637	0.370	0.883	0.885
ResNet50 hinge	0.917	0.825	0.941	**0.745**	**0.628**	0.923	0.917
ResNet50 Fused cross-entropy	0.862	0.715	0.956	0.645	0.377	0.891	0.861
ResNet50 Fused hinge	**0.924**	**0.843**	0.953	0.744	0.625	**0.932**	**0.921**

Autoencoders. Stacked autoencoder can store a large amount of information in its internal representation and improve the basic solution with respect to all metrics, as it presented in Table 3.

Table 3. Autoencoder-model classification results.

Autoencoder	Accuracy	Shock Precision	Shock Recall	Border Precision	Border Recall	Precision	Recall
SAE	0.920	0.821	**0.962**	0.826	0.650	0.929	0.920
SAE + internal representation	**0.973**	**0.973**	0.942	**0.885**	**0.887**	**0.974**	**0.973**
AE	0.896	0.772	**0.962**	0.797	0.521	0.912	0.896
AE + internal representation	0.927	0.968	0.8	0.661	0.702	0.930	0.927

As it can be seen, SAE using internal representation showed the best performance.

4.4 Siamese Networks

Siamese Network Training. As a result of all experiments, feed-forward network proved to be the best classifier, so the Table shows only the results of the work of the best models using other classifiers (for comparison). As it can be seen from Table 4, siamese network that has Resnet50Fused as the feature extractor, the Euclidean distance, and feedforward neural network as classifier was the best.

Table 4. Comparison of siamese networks.

Feature extractor	Distance	Classifier	Accuracy	Precision	Recall
ResNet50	Euclidean	SVM	0.801	0.807	0.807
ResNet50	Euclidean	RF	0.792	0.794	0.793
ResNet50	Manhattan	XGBoost	0.898	0.902	0.908
Inception v3	Manhattan	FNN	0.900	0.904	0.906
ResNet50	Manhattan	FNN	0.905	0.909	0.909
ResNet50 Fused	Manhattan	FNN	0.909	0.911	0.912
Inception v3	Euclidean	FNN	0.912	0.919	0.920
ResNet50	Euclidean	FNN	0.918	0.923	0.924
ResNet50 Fused	Euclidean	FNN	**0.924**	**0.929**	**0.931**
Inception v3	Cosine	FNN	0.878	0.881	0.885
ResNet50	Cosine	FNN	0.881	0.884	0.897
ResNet50 Fused	Cosine	FNN	0.885	0.892	0.895

After finding the best siamese network, we combined it with the best one-class classifier. Results are presented in Table 5.

Table 5. The results of the best reviewed models.

Model	Accuracy	Shock Precision	Shock Recall	Border Precision	Border Recall	Precision	Recall
Baseline	0.957	0.946	0.918	0.807	0.813	0.956	0.956
SAE + internal representation	0.973	0.973	0.942	0.885	0.887	0.974	0.973
SAE + internal representation + siamese neural network	**0.985**	**0.979**	**0.977**	**0.940**	**0.939**	**0.986**	**0.986**

As it can be seen, the proposed solution significantly outperforms the baseline, and usage of siamese networks help to achieve the highest result.

5 Discussion

The empirical study presented in Sect. 5 reveals that the best result is a model that uses a CNN resnet50 fused as feature extractor for autoencoder and siamese network, SVM trained on stacked autoencoder internal representation and recovery error as one-class classifier and siamese network with the Euclidean distance and feed-forward neural network as classifier. It is quite obvious that simpler models such as the normal autoencoder or one-class SVM showed the worst results, because they could not allocate sufficient information for good classification. The reason for the unsuccessful application of the convolutional auto-encoder is most likely that it was not pretrained but was trained from scratch on a small diverse set of data. The resulting pipeline is presented on Fig. 4.

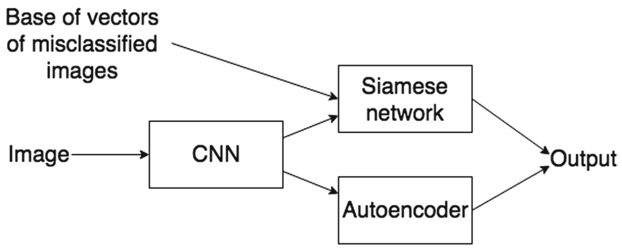

Fig. 4. Architecture of the best solution.

6 Conclusion

In this paper, we suggest a new method for shocking image detection. It includes using one-class classifiers for learning representation solely of shocking images, and siamese network for handling with different and rare subclasses of shocking images.

For method evaluation, we use manually collected dataset that contains 2500 shocking images, 5150 random non-shocking images, as well as 115 “border” shocking images divided into 14 subclasses and 50 “border” non-shocking images divided into 5 subclasses, which were tricky for the best-known model.

We used several methods of one-class classification, namely CAE, AE and SAE with pretrained CNN, OCSVM with pretrained CNN. Due to the class of shock images contains a lot of very dissimilar subclasses, it was necessary to get the maximum amount of information about the data during the training, which was performed with the help of information stored in the internal representation of the sparse autoencoder.

As a result, SAE recovery error combined with vector of inner representation of images showed the best result.

The achieved results are improved by using siamese networks, which remember images-representatives of especially rare subclasses. We tested several siamese network architectures resulting in the best model being the siamese network with ResNet50 + Fused network for extracting image feature vectors, Euclidean distance for combining feature vectors and FNN as a classifier.

In the future, we are going to more intently consider the possibilities of using the siamese network as an assistant to the main classifier. We plan to investigate whether the use of the Siamese network will reduce the number of errors of the classifier training in the process of operation (algorithm of online machine learning).

Acknowledgments. This work was financially supported by the Government of the Russian Federation (Grant 08-08). The authors would like to thank Aleksey Artamonov for his constructive comments and suggestions.

References

1. Anderson, C.A., Berkowitz, L., Donnerstein, E., Huesmann, L.R., Johnson, J., Linz, D.: The influence of media violence on youth. Psychol. Sci. Public Interest **4**, 81–110 (2003)
2. Bourlard, H., Kamp, Y.: Auto-association by multilayer perceptrons and singular value decomposition. Biol. Cybern. **59**(4–5), 291–294 (1988)
3. Bushman, B.J., Huesmann, L.R.: Short-term and long-term effects of violent media on aggression in children and adults. Arch. Pediatr. Adolesc. Med. **160**, 348–352 (2006)
4. Dubberley, S., Griffin, E., Bal, H.M.: Making secondary trauma a primary issue: a study of eyewitness media and vicarious trauma on the digital frontline (2015). http://eyewitnessmediahub.com/uploads/browser/files/Trauma%20Report.pdf. Accessed 15 Jan 2020
5. He, K., Zhang, X., Ren, S., Sun, J.: Deep residual learning for image recognition. In: Proceedings of the IEEE Conference on Computer Vision and Pattern Recognition, pp. 770–778 (2016)
6. Khan, S.S., Madden, M.G.: A survey of recent trends in one class classification. In: Irish Conference on Artificial Intelligence and Cognitive Science, pp. 188–197. Springer, Heidelberg (2009)
7. Koch, G., Zemel, R., Salakhutdinov, R.: Siamese neural networks for one-shot image recognition. In ICML Deep Learning Workshop, vol. 2 (2015)
8. Li, B., Xiong, W., Wu, O., Hu, W., Maybank, S., Yan, S.: Horror image recognition based on context-aware multi-instance learning. IEEE Trans. Image Process. **24**(12), 5193–5205 (2015)
9. Luxton, D.D., June, J.D., Fairall, J.M.: Social media and suicide: a public health perspective. Am. J. Public Health **102**(S2), S195–S200 (2012)
10. Poultney, C., Chopra, S., Cun, Y.L.: Efficient learning of sparse representations with an energy-based model. In: Advances in neural information processing systems, pp. 1137–1144 (2007)
11. Schlkopf, B., Williamson, R.C., Smola, A.J., Shawe-Taylor, J., Platt, J.C.: Support vector method for novelty detection. In: Advances in Neural Information Processing Systems, pp. 582–588 (2000)
12. Szegedy, C., Vanhoucke, V., Ioffe, S., Shlens, J., Wojna, Z.: Rethinking the Inception architecture for computer vision. In: Proceedings of the IEEE Conference on Computer Vision and Pattern Recognition, pp. 2818–2826 (2016)
13. Wang, D., Zhang, Z., Wang, W., Wang, L., Tan, T.: Baseline results for violence detection in still images. In: IEEE Ninth International Conference on Advanced Video and Signal-Based Surveillance, pp. 54–57 (2012)
14. Zampoglou, M., Papadopoulos, S., Kompatsiaris, Y., Spangenberg, J. A WebBased Service for Disturbing Image Detection. In: *International Conference on Multimedia Modeling*, pp. 438–441, Springer, Cham (2017)
15. Zheng, L., Zhao, Y., Wang, S., Wang, J., Tian, Q.: Good practice in CNN feature transfer (2016). arXiv preprint arXiv:1604.00133

Factors Affecting Accuracy of Convolutional Neural Network Using VGG-16

Jyoti Rawat(✉), Doina Logofătu(✉), and Sruthi Chiramel(✉)

Department of Computer Science and Engineering,
Frankfurt University of Applied Sciences, 60318 Frankfurt a.M., Germany
{rawat,chiramel}@stud.fra-uas.de, logofatu@fb2.fra-uas.de

Abstract. In this paper, performance evaluation of image data-set using 2-layer Convolutional Neural Network Architecture and transfer learning method, is studied on Fashion MNIST dataset. Fashion MNIST is a dataset of images consisting 70000 28×28 gray-scale images, associated with label of 10 classes. The area of research of this paper in transfer learning is limited to pre-trained neural network VGG-16. The accuracy and respective losses are evaluated using the two mentioned methods. The work under this paper is inspired by widely famous Image-net Large Scale Visual Recognition Challenge, although due to constraint on time, resources, a smaller data set i.e. Fashion MNIST is taken for the study. The work is dependent on Keras Functional API and Tensor Flow. With the accuracy 88.24% and loss 29.02 as per CNN model, the model can be utilised by online clothing stores to classify their articles under right category.

Keywords: Deep learning · ConvNet · Learning rate · Image classification · VGGNet · Dense layer · Neural Networks · Machine Learning · Algorithm Optimisaton · Transfer learning

1 Introduction

Image classification is one of the core task in Computer Vision which has always enjoyed limelight. We have taken into account 70000 Grayscale images of size 28×28. Images are treated as a 2-D matrix by Convolutional Neural Network(CNN). Depending on pixel i.e. intensity of color at a particular point, a numeric integer on the scale of 0–255 is assigned. The numeric values in pixel are uniformly changed from zero (black pixels) to 255 (white pixels). The grid of matrix changes with factors like light, occlusion, viewpoint, deformation etc. but somehow overall grid represents the same picture. Hence, a model should be robust enough to overcome such limitations. A CNN uses multiple linear classifiers within it to classify images on their respective class labels. Class label is assigned to the image on the basis of maximum probability attained.

The approach used in Neural Networks is called parametric approach as it is driven by the parameters obtained on different layers during the course of training. In real time, almost all small and big firms are extensively using Image Classifiers, made up of different learning algorithms.

As training of a CNN with large datasets can exhaust a significant amount of time, concept of transfer learning can be used as a saviour. It is defined as a situation where what has been learned in one setting is exploited to improve generalization in another setting [18]. It enables CNN to utilise its learning (features, weights) and generalize it on another similar problems. The smaller datasets give a better result on a pre-trained neural network. VGG-16 is a CNN proposed by Simonyan and Zisserman from the University of Oxford in the paper "Very Deep Convolutional Networks for Large Scale Image Recognition". The model was fed on ImageNet, which is a dataset of over 14 million images belonging to 1000 classes. It achieved an accuracy of 92.7%, which was among top-5 test accuracy. VGG-16 was trained on NVIDA Titan Black GPU's for couple of weeks.

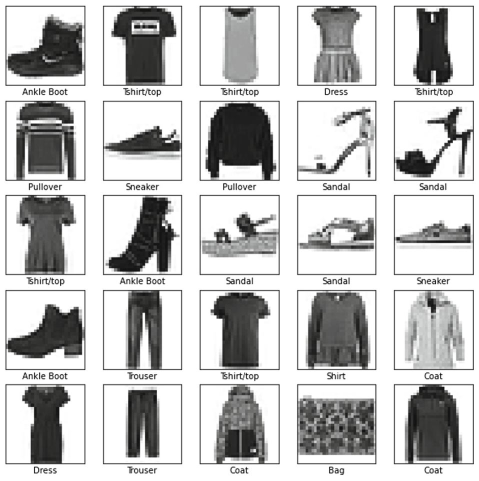

Fig. 1. MNIST dataset

2 Problem Description

Image Classification is a well known supervised learning problem, which defines a set of target classes and train a model to recognize them using training data. Training data comprises of images and labels associated with them. A model is required to learn features of training images and provides a good accuracy on test data. In a parametric approach, a test image (28×28 here) is converted into $28 \times 28 \times 1$ (1 as the images are gray-scale, in case of coloured images 3 is used to represent each of RGB channel) matrix, which is a representation of array consisting 784 elements. The array is convoluted with predefined weights generating scores i.e. probabilities for each class label. Class label with highest probability is assigned as the "correct" label of image. The more accuracy we get, better is the model. Figure 2 shows an image from data set, the label of the image is Sneaker in parenthesis. After passing the image from a classifier model the prediction should also be maximum for 'Sneaker class'. In the figure, 100% shows the probability obtained by the 'Class Sneaker' which is represented by a full length green bar. The aim of Image Classification problem is to classify images to their 'correct classes'. One of the approach to solve such problems is neural networks, where model gains features and information from training data and based on its knowledge, classifies the new data.

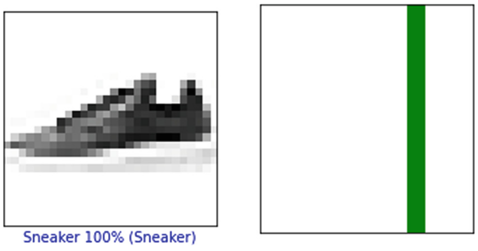

Fig. 2. Graphic representation of the problem

A neural network is made of neurons arranged in layers. Input (Image matrices: X) are fed to each and every neuron and convoluted with weights (w) of the next layer results in activation functions (a). Mathematically,

$$a_1^{(2)} = g(\Theta_{10}^{(1)} x_0 + \Theta_{11}^{(1)} x_1 + \Theta_{12}^{(1)} x_2 + \Theta_{13}^{(1)} x_3)$$
$$a_2^{(2)} = g(\Theta_{20}^{(1)} x_0 + \Theta_{21}^{(1)} x_1 + \Theta_{22}^{(1)} x_2 + \Theta_{23}^{(1)} x_3)$$
$$a_3^{(2)} = g(\Theta_{30}^{(1)} x_0 + \Theta_{31}^{(1)} x_1 + \Theta_{32}^{(1)} x_2 + \Theta_{33}^{(1)} x_3)$$
$$output = h_\Theta(x) = a_1^3 = g(\Theta_{10}^{(2)} x_0 + \Theta_{11}^{(2)} x_1 + \Theta_{12}^{(2)} x_2 + \Theta_{13}^{(2)} x_3)$$

$a_i{}^{(j)}$ = activation unit i in layer j
$\Theta^{(j)}$ = matrix of weights controlling function mapping from layer j to j+1
$g(\Theta)$ = Sigmoid function

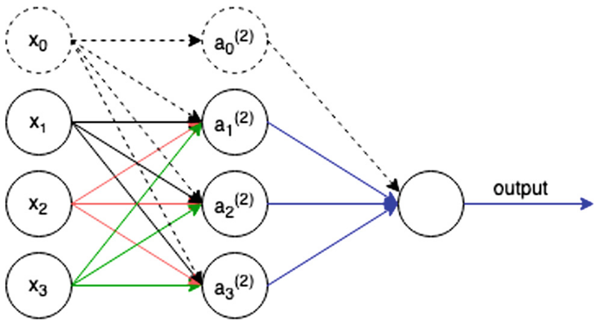

Fig. 3. Neural network

3 Related Research

Deep learning techniques are famous among the fashion related business on their e-commerce websites such as apparel search, apparel recognition, apparel classification and automatic product recommendation. Apparel classification is a complex task due to various apparel properties, and categorisation in the depth of categorisation. CNNs are a popular choice of researchers in this area. There are various models based on neural network are published with trustworthy results [11].

3.1 ALEXNet(2012)

The paper, titled "ImageNet Classification with Deep Convolutional Networks", has been referenced a total of 6,184 times and is widely regarded as one of the most core source of publications in the field. It contains eight learned layers—five convolutional and three fully-connected. It used Relu non Linear function, as deep convolutional network with ReLu function trains several times faster than their tanh units. The model was trained on two GTX 580 GPU connected in parallel. The two-GPU net takes slightly less time to train than the one-GPU net. The output of the last fully-connected layer is fed to a 1000-way softmax which produces a distribution over the 1000 class labels. The first convolutional layer filters the $224 \times 224 \times 3$ input image with 96 kernels of size $11 \times 11 \times 3$ with a stride of 4 pixels. It achieves top-1 and top-5test set error rates of 37.5% and 17.0%. In 2012, the improvised version attained top-1 and top-5 error rates on this dataset are 67.4% and 40.9%, with an additional, sixth convolutional layer over the last pooling layer [8].

3.2 ZF Net(2013)

In the paper titled "Visualizing and Understanding Convolutional Neural Networks", Zeiler and Fergus begin by discussing the idea due to the accessibility of large training sets and increased computational power with the usage of GPUs, the topic came into limelight. It requires a careful initialization and does not give any information about the unit's in-variances. A large set of N labeled images x,y, where label y_i is a discrete variable indicating the true class. A cross-entropy loss function, suitable for image classification, is used to compare $\hat{y}$ and y_i. The parameters of the network (filters in the convolutional layers, weight matrices in the fully connected layers and biases) are trained by back-propagating the derivative of the loss with respect to the parameters throughout the network, and updating the parameters via stochastic gradient descent. The visualization technique used was a multi-layered De-convolutional Network (de-convnet), as proposed by (Zeiler et al. [9]), to project the feature activations back to the input pixel space. It used an architecture of 8 layer convnet model.

3.3 VGGNet(2014)

The use of only 3×3 sized filters is quite different from AlexNet's 11×11 filters in the first layer and ZF Net's 7×7 filters. The combination of two 3×3 convolution layers has an effective receptive field of 5×5. This in turn simulates a larger filter while keeping the benefits of smaller filter sizes. One of the benefits is a decrease in the number of parameters. Also we can use two ReLU layers instead of one with the combination of two 3×3. 3 convolutional layers back to back have an effective receptive field of 7×7. As input volumes at each layer decreases in terms of spatial (result of the convolution and pool layers), the depth of the volumes increase due to the increased number of filters as network goes to interiors. However, the number of filters doubles after each maxpool layer. This adds up the idea of shrinking spatial dimensions, but growing depth.

4 Implementation Details

We evaluate the performance of Fashion MNIST on a 2 layer CNN trained from scratch and on a model which uses pre-trained weights of VGG-16.

Figure 4 depicts handling of data during the course of work.

- Understand dataset
- Pre-process Data
- Visualize Data
- Build a Model
- Train and Test Data

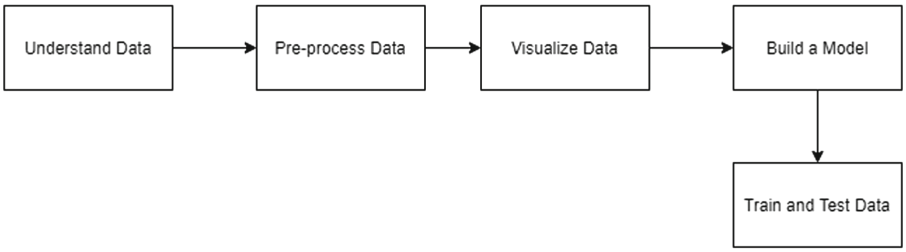

Fig. 4. Data processing flow

4.1 Understand and Pre-process Data

Fashion MNIST consists of 70000 28*28 grayscale images. Out of which 60000 images are in training set along with their class labels. Rest of 10000 images are in test data set. Data set is directly accessed from Keras library of python. There are ten class labels: Tshirt/top, Trouser, Pullover, Dress, Coat, Sandal, Shirt, Sneaker, Bag, Ankle Boot. Data has been shuffled 5 times to include randomness in the values. The large scale image has been pre-processed first before undergoing through convolution. The images are flattened to 1- D array and the pixel values ranging from 0–255 are normalised between 0,1.

4.2 Model Building

A model is the sequence of the layers, which generates predictions by finding patterns in the data. The model used here comprises of input layer, that converts 2D array of 28*28 into 1D array to get computed in further layers, dense layer which is a fully connected node (i.e. each input neuron is connected to each output neuron) and output layer that has 10 outputs as data set has 10 class labels. The non linear function used is ReLu in the hidden layer and softmax in the output layer. Softmax function will predict the labels in the form of probabilities. ADAM optimiser is used to combat with loss function of data-sets and optimisation of the model. This 2-layer neural network model uses back-propagation technique to find the best suitable weights for the datasets.

The model provides the accuracy of 87.8% with loss of 0.27. Predictions can be viewed in the Fig. 5, where green bar shows the right predictions and red bar shows the wrong predictions. In the pictures with multiple bars, the bar with highest probability is considered as the right label. The other bars with less probabilities show that the test image might be similar to the templates of those other probabilities. The graphs shown in Fig. 6 and Fig. 7 shows that accuracy is increasing from 82% to 87% on test images as epochs are increasing and in the same way losses occurred are decreasing from 0.50 to 0.24 with number of epochs.

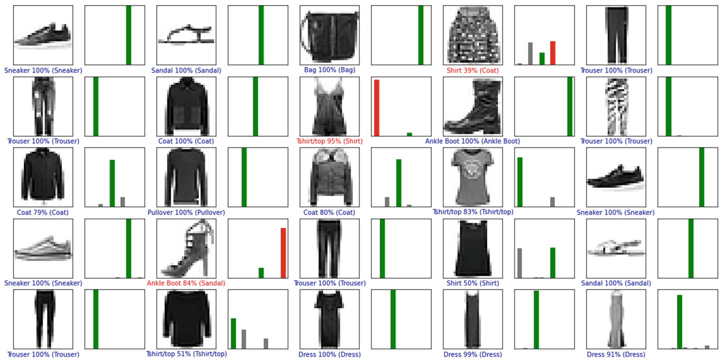

Fig. 5. Prediction on test images

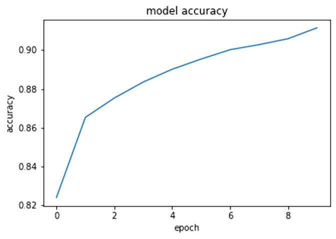

Fig. 6. Accuracy graph

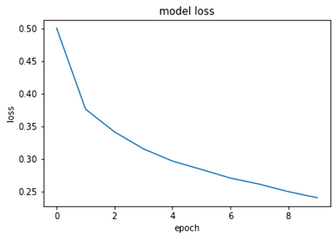

Fig. 7. Loss graph

4.3 Transfer Learning Using VGG-16

The Neural Information Processing Systems (NIPS) 1995 workshop Learning to Learn: Knowledge Consolidation and Transfer in Inductive Systems is believed to have provided the initial motivation for research in this field. Transfer Learning is different from traditional learning as traditional learning is isolated and occurs purely based on specific tasks, datasets and training separate isolated models on them, on the contrary, transfer learning can leverage (features, weights etc.) from previously trained models for training newer models. As mentioned there are various transfer learning models available. VGG-16, is considered as it has 92.7% accuracy top-5 test accuracy in ImageNet, which is a dataset of over 14 million images belonging to 1000 classes [7].

```
Model: "sequential_1"
_________________________________________________________________
Layer (type)                 Output Shape              Param #
=================================================================
block1_conv1 (Conv2D)        (None, 224, 224, 64)      1792
_________________________________________________________________
block1_conv2 (Conv2D)        (None, 224, 224, 64)      36928
_________________________________________________________________
block1_pool (MaxPooling2D)   (None, 112, 112, 64)      0
_________________________________________________________________
block2_conv1 (Conv2D)        (None, 112, 112, 128)     73856
_________________________________________________________________
block2_conv2 (Conv2D)        (None, 112, 112, 128)     147584
_________________________________________________________________
block2_pool (MaxPooling2D)   (None, 56, 56, 128)       0
_________________________________________________________________
block3_conv1 (Conv2D)        (None, 56, 56, 256)       295168
_________________________________________________________________
block3_conv2 (Conv2D)        (None, 56, 56, 256)       590080
_________________________________________________________________
block3_conv3 (Conv2D)        (None, 56, 56, 256)       590080
_________________________________________________________________
block3_pool (MaxPooling2D)   (None, 28, 28, 256)       0
_________________________________________________________________
block4_conv1 (Conv2D)        (None, 28, 28, 512)       1180160
_________________________________________________________________
block4_conv2 (Conv2D)        (None, 28, 28, 512)       2359808
_________________________________________________________________
block4_conv3 (Conv2D)        (None, 28, 28, 512)       2359808
_________________________________________________________________
block4_pool (MaxPooling2D)   (None, 14, 14, 512)       0
_________________________________________________________________
block5_conv1 (Conv2D)        (None, 14, 14, 512)       2359808
_________________________________________________________________
block5_conv2 (Conv2D)        (None, 14, 14, 512)       2359808
_________________________________________________________________
block5_conv3 (Conv2D)        (None, 14, 14, 512)       2359808
_________________________________________________________________
block5_pool (MaxPooling2D)   (None, 7, 7, 512)         0
_________________________________________________________________
flatten (Flatten)            (None, 25088)             0
_________________________________________________________________
fc1 (Dense)                  (None, 4096)              102764544
_________________________________________________________________
fc2 (Dense)                  (None, 4096)              16781312
_________________________________________________________________
dense_1 (Dense)              (None, 10)                40970
=================================================================
Total params: 134,301,514
Trainable params: 40,970
Non-trainable params: 134,260,544
_________________________________________________________________
```

VGG-16 has 16 layers comprised of Convolutional layers, Max Pooling layers, Activation layers, Fully connected layers. There are 13 convolutional layers, 5 Max Pooling layers and 3 Dense layers which sums up to 21 layers but only 16 weight layers. Convolution layer 1 has number of filters as 64 while Convolution layer 2 has 128 filters, Convolution layer 3 has 256 filters while Convolution layer 4 and Convolution layer 5 has 512 filters.

Input layer works on 224*224 size of images hence our dataset images of 28*28 needs to be reshaped. In order to avoid over-fitting of data and optimize results without any biasing training data is split between test data and validation set i.e. 2000 images in validation set and 80000 images in testing set along with their labels. The data is distributed randomly in order to preserve the randomness of dataset. For cross validation, data is further split in batches within training, testing and validation data randomly. For training data and testing data batch size is chosen to be 10, for validation data, batch size is chosen to be 4. VGG-16's output layer has 1000 labels originally (as it was trained on ImageNet dataset which has 1000 class labels), it is modified to 10 output class labels. To compare the results on same grounds, Adam optimizer and categorical crossentropy is used for optimization and evaluation of loss (as used in 3 layer CNN). The model provides an accuracy of 94% with 0.19 loss, which is significantly better than training a convolutional neural network from scratch.

5 Results and Discussion

The better results are obtained, retraining an already trained data, however chances of over-fitting are fairly high in retraining the same model. An accuracy of 90% is achieved after re-training 2 layer CNN model on the same time, however it violates the concept of Machine Learning, as the basic idea in Machine Learning is to have better predictions on new data than on old data.

Model	Accuracy	Loss
2 Layer CNN	87%	0.27
VGG-16	94%	0.19

Better results can be achieved by increasing number of hidden layers of neural network as here we have used only 1 hidden layer. Learning rate used in VGG-16 model is 0.0001. We evaluated accuracy and loss values on different learning rates ranges from 0.001 to 0.0001. There was not a significant difference among values which can used by online stores. A very low learning rate progresses the training slowly as convergence is slow. On the other hand, if learning rate (generally represented by α), cost function may not decrease on every iteration and may not converge. Learning rate is one of the hyper parameters for this model.

6 Conclusion

We have evaluated performance of a 2 layer neural network and predefined VGG-16 on an imgeset comprised of 70000 gray-scale images having 10 output labels. The scope of future work can be focused on different factors like:

- Increasing number of layers in CNN model.
- Evaluation of performances can be played around on different sizes of epochs, batch sizes, filter kernels of hidden layers, activation functions used.
- Tweaking more than one layer(not just output layer).

References

1. Simonyan, K., Zisserman, A.: Very deep convolutional networks for large scale. In: Conference ICLR (2015)
2. He, K., Zhang, X., Ren, S., Sun, J.: Deep residual learning for image recognition. In: Computer Vision and Pattern Recognition (2015)
3. Szegedy, C., Vanhoucke, V., Ioffe, S., Shlens, J., Wojna, Z.: Rethinking the inception architecture for computer vision. In: Computer Vision and Pattern Recognition (2015)
4. Kryvobokov, M., Wilhelmsson, M.: Analysing location attributes with a hedonic model for apartment prices in donetsk, Ukraine. Int. J. Strateg. Property Manag. **11**(3), 157–178 (2007)
5. Qi, X., Liao, R., Jia, J., Fidler, S., Urtasun, R.: 3D graph neural networks for RGBD semantic segmentation. In: IEEE International Conference on Computer Vision (ICCV) (2017)
6. Behera, A., Gidney, A.G., Wharton, Z., Robinson, D.P., Quinn, K.: A CNN model for head pose recognition using wholes and regions. In: 2019 14th IEEE International Conference on Automatic Face & Gesture Recognition (2019)
7. Russakovsky, O.: ImageNet large scale visual recognition challenge. Int. J. Comput. Vis. **115**, 211–252 (2014). ISSN 1573–1405
8. Krizhevsky, A., Sutskever, I., Hinton, G.: Large, deep convolutional neural network (2012)
9. Zeiler, M.D., Fergus, R.: Visualizing and understanding convolutional neural networks (2013)
10. Goodfellow, I., Bengio, Y., Courville, A.: Deep Learning. MIT Press, Cambridge (2016). http://www.deeplearningbook.org
11. Seo, Y., Shin, K.S.: Hierarchical convolutional neural networks for fashion image classification. Exp. Syst. Appl. **116**, 328–339 (2019). ISSN 0957–4174

Image Recoloring of Art Paintings for the Color Blind Guided by Semantic Segmentation

Stamatis Chatzistamatis(✉), Anastasios Rigos, and George E. Tsekouras

Department of Cultural Technology and Communication, University of the Aegean, University Hill, 81100 Mytilene, Lesvos Island, Greece
{stami,a.rigos}@aegean.gr, gtsek@ct.aegean.gr

Abstract. This paper introduces a semantic-segmentation guided image recoloring approach of digitized art paintings to enhance the color perception of color- blind people that suffer from protanopia and deuteranopia. Semantic segmentation using transfer learning between natural images and art paintings is applied to extract annotated color information. By using a standard technique, the annotated colors are transformed to simulate the effects of protanopia and deuteranopia. Then, a specialized objective function is minimized to recolor only the colors that are significantly different from the respective simulated ones, because these colors are perceived as confusing by the color blind. The effectiveness of the proposed method is demonstrated through its comparison with other algorithms in several experimental cases.

Keywords: Color vision deficiency · Digitized art paintings · Image recoloring · Semantic segmentation · Deep network

1 Introduction

The human color vision system generates the color perception by using three types of photoreceptor cells, called cones, to perform photon absorption: the L-cones, the M-cones, and the S-cones. The L-cones correspond to the red color, the M-cones to the green color, and the S-cones to the blue color. Malfunction of one or more photoreceptors results in color vision deficiency (CVD), also called color blindness, which consists of three types: the monochromacy, the dichromacy, and the anomalous trichromacy [16, 17, 20]. The most challenging CVD is the dichromacy, which embraces three categories [5, 16, 20]: (a) protanopia caused by the absence of L-cones, (b) deuteranopia caused by the absence of M-cones, and (c) tritanopia caused by the absence of S-cones. The protanopes and deuteranopes cannot distinguish between red and green, while the tritanopes between blue and yellow.

People with strong CVDs face difficulties in daily life, where problematic color perception becomes annoying or even critical (e.g. road signs), making their accessibility in colored content a challenge. Regarding this issue, the accessibility of color-blind people in cultural content, such as art paintings, has been acknowledged as an important demand by worldwide organizations dealing with the CVDs and cultural organizations such as museums, as well [7, 10, 12]. Many color-blind people are at a disadvantage when choosing to study or enjoy art paintings because they can only discern a confusing set of objects and colors.

So far, a wide variety of image recoloring methods has been proposed to enhance the color perception of the color-blind [16]. Hassan and Paramersan [5] set up the image recoloring in the XYZ color space utilizing three steps namely, color normalization, angular color rotation, and color un-normalization. Huang et al. [8] performed the color enhancement by extracting key colors and determining an optimal mapping to maintain the contrast between pairs of those colors. In [9], special requirements were quantified by minimizing an objective function in the CIE Lab space. Rani and Rajeev [14] assisted deuteranopic viewers by enhancing the contrast between adjacent shades.

Although too much effort has been put on the recoloring of natural images, there are relatively few works that consider the case study of digitized art painting images. Due to the complexity of such kind of images, maintaining a color natural appearance of the recolored image is a very challenging problem [1, 18]. The requirement of color naturalness focuses on minimizing the perceptual difference between the colors in the original image and the respective modified colors in the recolored image [16].

In this paper, we introduce a novel approach that attempts to meet the requirement of naturalness, regarding the protanopia and deuteranopia CVDs. A transfer learning based semantic image segmentation algorithm is implemented to extract annotated color information of the original image. The semantic segmentation is implemented by introducing a framework for transferring learning from a Mask RCNN network [3, 15], trained on available large collections of labeled natural images, to the context of art paintings. Then, the colors identified above are transformed to simulate the corresponding color blind perception [20]. The above information is further processed by a specialized objective function, which is minimized to obtain the recolored art painting.

The material is organized as follows. Section 2 describes the proposed algorithm in detail. Section 3 illustrates the simulation results and the respective analysis. Finally, the paper concludes in Sect. 4.

2 The Proposed Recoloring Method

The flowsheet of the algorithm is illustrated in Fig. 1. Given an RGB color $\boldsymbol{C} = (C_R\ C_G\ C_B)^T$, with $C_R, C_G, C_B \in [0, 255]$, its simulation to protanopia or deuteranopia is denoted as $\boldsymbol{C}_D = (C_{R,D}\ C_{G,D}\ C_{B,D})^T$, where subscript D describes the protanopia or deuteranopia.

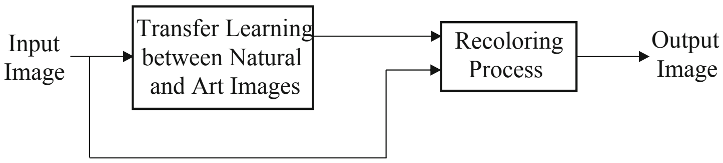

Fig. 1. The basic algorithmic steps of the recoloring process.

The vector $\boldsymbol{C}_D$ is calculated by matrix transformations that involve the XYZ and LMS color spaces, where the transformations are functionally represented $\boldsymbol{C}_D = f_D(\boldsymbol{C})$. For a detailed description of the color simulation procedure, the interested reader is referred to [20].

2.1 Semantic Segmentation Using Transfer Learning Between Natural and Art Digitized Paintings

R-CNN [3] is one of the first deep learning networks inspired by AlexNet [11] and it uses segments of that network with minor changes. Network's functionality is improved using the Selective Search [19] technique to perform object recognition in the image instead of classifying the whole image as one object. After identifying the regions of interest (RoIs) with bounding boxes, a processed version of AlexNet is used to classify the object. At the last level of the network, a support vector machine (SVM) categorizes the object into a class. However, after executing the network's training process, one more step takes place to optimize the rectangular boundaries, which is considered a simple regression problem. In a nutshell, it gets as input the bounding boxes of the objects and improves them. The main drawback of the R-CNN is the utilization of many feed-forward iterations ($\sim$2 K) of AlexNet for each RoI, and separately trains the three subsequent models: (a) CNN for extracting image features, (b) SVM, and (c) a simple regression model to improve the bounding boxes.

Fast R-CNN [2] was implemented to solve these problems and accelerate the R-CNN. It performs only one feed-forward pass of the CNN throughout the image and then pools on every bounding box (named Region of Interest Pooling - RoIPool). Then, it integrates all the aforementioned three models on a common network, where the regression takes place in parallel with the classification which is carried out by Softmax classifier instead of the SVM, taking as an input the result of the RoIPool layer. The next improved network is the Faster R-CNN which uses a Region Proposal Network (RPN) to accomplish the tasks of the Selective Search algorithm. The latest suggestion based on R-CNN is the Mask R-CNN which is the Faster R-CNN [15] with the exception that instead of bounding boxes it detects the real contours (i.e. masks) of the objects in the image. To achieve this, a parallel branch of the network is responsible for classifying the pixels into objects. Each mask is classified into two classes using binary regression rather than Softmax.

The above-mentioned deep learning algorithms were able to achieve very good results on classification problems after trained on large datasets. The lack of available training data in many domains such as medical images and art images is a well-known problem in the scientific community. That problem is addressed by the transfer learning mechanism [4, 21]. The main idea behind that approach is to train a machine learning framework on a new task while exploiting the knowledge acquired by the framework in a previously related task.

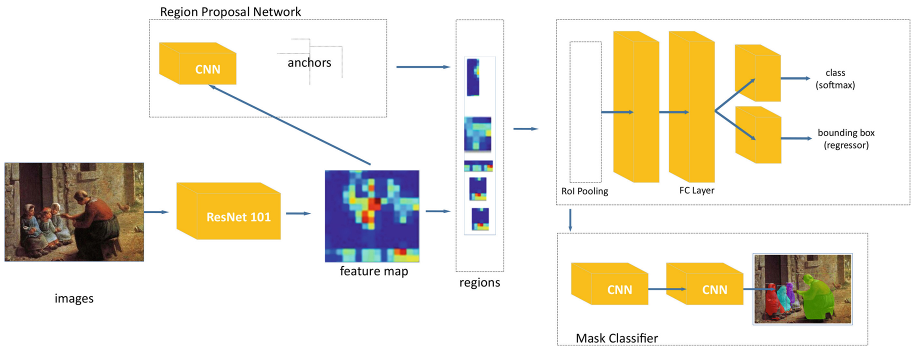

Fig. 2. The basic structure of the transfer learning based semantic segmentation scheme.

The flowsheet of the network used in this paper is depicted in Fig. 2. We use Matterport's[1] implementation of Mask-RCNN for training nine classes of art paintings images with seventy-five annotated images in each class. Firstly, data preprocessing is carried out in terms of image augmentation. The key point is to follow a set process of taking in existing images from our training dataset and apply some image transformation operations to them. Specifically, regarding each image, a horizontal flip is performed, the image is randomly cropped to a scale between 0.9 and 1 times the original dimension, a Gaussian blur with random standard deviation is applied, the contrast is adjusted, the brightness is adjusted, and a series of random affine transformations are also applied so each image has dimensions 500×500. The nine trained classes are: person, boat, bird, horse, bowl, chair, table, vase and fruit.

The ResNet101 architecture [6] is used as a backbone model to extract relevant features from the input image. Instead of using the pre-trained weights for MS COCO[2], we initialize the weights of our backbone model using weights pre-trained on Imagenet[3]. The backbone model serves as a feature extractor, where the early layers detect low-level features (edges and corners), and later layers successively detect higher-level features (person, boat, etc.). To fine-tune the model pre-trained on Imagenet, we train only the model heads and the layers from ResNet101 level 4 and up for the remaining epochs, because we reuse the weights of the model learned to extract features from natural images. The image is converted from a tensor of shape (500, 500, 3) to a feature map of shape (32, 32, 2048). The extracted feature map is then fed into a Region

1 https://github.com/matterport/Mask_RCNN.

2 http://cocodataset.org/.

3 http://www.image-net.org/.

Proposal Network (RPN) [15]. The RPN scans regions of the feature map with sliding bounding boxes, trying to determine regions that contain objects. For each box, called anchor, the RPN assigns an anchor class (i.e. possible object, not an object or neutral). A proposal layer then picks the anchors most likely to contain an object and refine the anchor box to fit the object more closely, obtaining the RoIs. For each region that contains an object selected by the RoI classifier, the model generates 28 × 28 masks.

2.2 Image Recoloring

The chosen color space is the RGB space. Let us denote the input image as $\boldsymbol{I} = [\boldsymbol{p}_{ij}]\ (1 \le i \le N;\ 1 \le j \le K)$ where $\boldsymbol{p}_{ij}$ symbolizes the RGB color vector of the (i, j) image pixel, and $N \times K$ is the image size. The pixels of the input image are divided into two disjoint sets namely, T_V and T_U. The set T_V includes all pixels that belong to the objects identified by the semantic segmentation algorithm, while the set T_U includes the rest of the pixels. Next, we form the set $S_V = \left\{\boldsymbol{C}_{V,1}, \boldsymbol{C}_{V,2}, \ldots, \boldsymbol{C}_{V,|S_V|}\right\}$ that includes the distinct colors of T_V, and the set $S_U = \left\{\boldsymbol{C}_{U,1}, \boldsymbol{C}_{U,2}, \ldots, \boldsymbol{C}_{U,|S_U|}\right\}$ that includes the distinct colors of T_U, where $|\bullet|$ stands for the set cardinality. Colors in S_V are transformed to simulate the dichromacy effect, $\boldsymbol{C}_{k,D} = f_D(\boldsymbol{C}_k)\ (k = 1, 2, \ldots, |S_V|)$. By appropriately choosing $\phi > 1$ (trial and error), if for some k it holds $\left\|\boldsymbol{C}_k - \boldsymbol{C}_{k,D}\right\| < \phi$ the colors $\boldsymbol{C}_k$ and $\boldsymbol{C}_{k,D}$ are similar, meaning that dichromats do not confuse the color $\boldsymbol{C}_k$. Therefore, this color must remain intact. All colors of S_V satisfying the above condition are transferred to the set S_U. This updating mechanism reads as

$$\forall \boldsymbol{C}_k \in S_V :\ \left\|\boldsymbol{C}_k - \boldsymbol{C}_{k,D}\right\| < \phi \ \rightarrow\ S_V = S_V - \{\boldsymbol{C}_k\} \ \wedge\ S_U = S_U \cup \{\boldsymbol{C}_k\}. \quad (1)$$

After the end of the updating process, colors belonging to the set S_U will remain intact, whereas the colors belonging to the set S_V will be appropriately modified to enhance their perception by the color blind.

Next, the fuzzy c-means is used to divide the elements of S_V in n_1 clusters with centers $\boldsymbol{V} = \{\boldsymbol{v}_1, \boldsymbol{v}_2, \ldots, \boldsymbol{v}_{n_1}\}$, and the elements of S_U in n_2 clusters with centers $\boldsymbol{U} = \{\boldsymbol{\upsilon}_1, \boldsymbol{\upsilon}_2, \ldots, \boldsymbol{\upsilon}_{n_2}\}$. The cluster centers are called *key colors*. The target is to obtain a recoloring set $\boldsymbol{V}_{rec} = \left\{\boldsymbol{v}_{rec,1}, \boldsymbol{v}_{rec,2} \ldots, \boldsymbol{v}_{rec,n_1}\right\}$ of the set $\boldsymbol{V}$.

The error vector between the key color $\boldsymbol{v}_i$ and its simulation $f_D(\boldsymbol{v}_i)$ is: $\boldsymbol{er}_i = \boldsymbol{v}_i - f_D(\boldsymbol{v}_i)\ \ (i = 1, 2, \ldots, n_1)$. Then, the recoloring process of $\boldsymbol{v}_i$ is [1, 18].

$$\boldsymbol{v}_{rec,i} = \boldsymbol{v}_i + \boldsymbol{M}_{D,i}\,\boldsymbol{er}_i \quad (2)$$

$$\text{with} \qquad \boldsymbol{M}_{D,i} = \begin{bmatrix} \alpha & \mu_{D,i,3} & 0 \\ \mu_{D,i,1} & \beta & 0 \\ \mu_{D,i,2} & \mu_{D,i,4} & 1 \end{bmatrix} \quad (3)$$

In the case of protanopia, $\alpha \in [-1, 0]$, $\beta = 1$, and $\mu_{D,i,3} = \mu_{D,i,4} = 0$ are prefixed, while $\mu_{D,i,1}$ and $\mu_{D,i,2}$ are adjustable positive parameters. In the case of deuteranopia,

$\alpha = 1$, $\beta \in [-1, 0]$ and $\mu_{D,i,1} = \mu_{D,i,2} = 0$ are prefixed, while $\mu_{D,i,3}$, $\mu_{D,i,4}$ are adjustable positive parameters. Considering protanopia, the implementation of (2) along with the respective matrix in (3) leads to a reduction of the Red in favor of G and B, obtaining less saturated red/oranges and more saturated greens, increasing the contrast and therefore, decreasing color confusion of a protanope viewer. In the case of deuteranopia, the above process leads to the reduction of green in favor of red and blue colors obtaining similar results. In both cases, the color confusion is alleviated.

Given two key colors $\boldsymbol{v}_i \in \boldsymbol{V}$ and $\boldsymbol{\upsilon}_i \in \boldsymbol{U}$, their distance is $\left\|\boldsymbol{v}_i - \boldsymbol{\upsilon}_j\right\|$. After transforming the key color $\boldsymbol{v}_i$ into $\boldsymbol{v}_{rec,i}$, the distance between $\boldsymbol{v}_{rec,i}$ and $\boldsymbol{\upsilon}_i$ as seen by a dichromat is $\left\|f_D(\boldsymbol{v}_{rec,i}) - f_D(\boldsymbol{\upsilon}_j)\right\|$. The objective is to keep the above distances as similar as possible so that the dichromat will be able to perceive the differences between colors in a similar way as the normal color vision viewer. Thus, summing over all pairs.

$$E_1 = \frac{1}{n_1 n_2} \sum_{i=1}^{n_1} \sum_{j=1}^{n_2} \left| \left\|\boldsymbol{v}_i - \boldsymbol{\upsilon}_j\right\| - \left\|f(\boldsymbol{v}_{rec,i}) - f(\boldsymbol{\upsilon}_j)\right\| \right| \tag{4}$$

Following the same approach for all color pairs in the set $\boldsymbol{V}$ we arrive at

$$E_2 = \frac{1}{n_1^2} \sum_{i=1}^{n_1} \sum_{j=1}^{n_1} \left| \left\|\boldsymbol{v}_i - \boldsymbol{v}_j\right\| - \left\|f(\boldsymbol{v}_{rec,i}) - f(\boldsymbol{v}_{rec,j})\right\| \right|. \tag{5}$$

It can be easily seen that minimizing E_1 and E_2 enhances the contrast between the objects identified by the semantic segmentation when compared each other and when compared with the rest of the image regions. To further preserve the naturalness the $\boldsymbol{v}_{rec,i}$ must be as close to $\boldsymbol{v}_i$ as possible. To do so, we use the next error function.

$$E_3 = \frac{1}{n_1} \sum_{i=1}^{n_1} \left\|\boldsymbol{v}_i - \boldsymbol{v}_{rec,i}\right\| \tag{6}$$

The overall objective function reads as

$$E = E_1 + E_2 + \gamma E_3 \tag{7}$$

where γ is a regularization factor that takes positive values and is used to obtain a counterbalance between the distinct parts of the function E.

The function E is optimized with respect to the parameters $\mu_{D,i,1}$, $\mu_{D,i,2}$ for protanopia, and $\mu_{D,i,3}$, $\mu_{D,i,4}$ for deuteranopia. In each case, the total number of adjusted parameters is $2n_1$. To perform the minimization, we employ the well-known differential evolution (DE) algorithm [13]. The DE comprises three evolving learning phases: the mutation, crossover and selection. There are two parameters that must be defined namely, the $F_{FR} \in (0,\ 1]$ that controls the rate at which the population evolves, and the $C_{FR} \in [0,\ 1]$ that controls the fraction of the parameter values copied from one generation to the next. A detailed description of DE is provided in [13].

The above procedure obtains the matrices $\boldsymbol{M}_{D,i}\,(i = 1, 2, \ldots, n_1)$ that minimize the function E. Each matrix corresponds to one key color of the set $\boldsymbol{V}$. The recoloring process of the image pixels $\boldsymbol{p}_{ij}\ (1 \le i \le N;\ 1 \le j \le K)$ is described next. If $\boldsymbol{p}_{ij} \in S_V$ then this pixel must be modified. The methodology of Vienot et al. [20] is applied to obtain the simulated color $f_D(\boldsymbol{p}_{ij})$ and calculate the corresponding error vector using Eq. (1): $\boldsymbol{er}_{ij} = \boldsymbol{p}_{ij} - f_D(\boldsymbol{p}_{ij})$. The closest key color to $\boldsymbol{p}_{ij}$ is denoted as $\boldsymbol{v}_{\ell_0}$ and defined as: $\left\|\boldsymbol{p}_{ij} - \boldsymbol{v}_{\ell_0}\right\| = \min\limits_{1 \le \ell \le n_1}\left\{\left\|\boldsymbol{p}_{ij} - \boldsymbol{v}_{\ell}\right\|\right\}$, with $\boldsymbol{v}_{\ell_0} \in \boldsymbol{V}$. Then, the recoloring of $\boldsymbol{p}_{ij}$ is carried out in terms of Eq. (2).

$$\boldsymbol{p}_{rec,ij} = \boldsymbol{p}_{ij} + \boldsymbol{M}_{D,\ell_0}\,\boldsymbol{er}_{ij} \tag{8}$$

Finally, all pixels of the input image with colors belonging to the set S_V are appropriately recolored, while the rest are kept intact. The impact of this effect is that the number of elaborated pixels reduces and therefore, the naturalness of the recolored image increases because the number of modified pixels is kept to a minimum.

3 Simulation Experiments

In this section, six art paintings are used to perform several experiments for protanopia and deuteranopia. The paintings are presented in Fig. 3. The proposed method is compared to two recoloring algorithms. The first was developed by Huang et al. in [8] and concerns both protanopia and deuteranopia. The second was developed by Rani and Rajeev in [14] and concerns only the deuteranopia. The performance index to conduct the comparison is the naturalness index [9].

$$J = \frac{1}{N\,K}\sum_{i=1}^{N}\sum_{j=1}^{K}\left\|\boldsymbol{p}_{ij} - \boldsymbol{p}_{rec,ij}\right\| \tag{9}$$

For our experiments we set $\phi = 11$, meaning that all color combinations belonging to sphere with radius 11 are consider similar to the color located at the center of that sphere. An odd number is selected to achieve uniformity in R, G, and B axis. The numbers of key colors for the sets $\boldsymbol{V}$ and $\boldsymbol{U}$ are $n_1 = n_2 = 12$. Thus, in total there are 24 key color. Based on trial and error approach, in the case of protanopia we select $\alpha = -0.5$, and in the case of deuteranopia $\beta = -0.5$. The domain of values for the adjustable parameters $\mu_{D,i,1}$, $\mu_{D,i,2}$, $\mu_{D,i,3}$, and $\mu_{D,i,4}$ is the interval [0, 1].

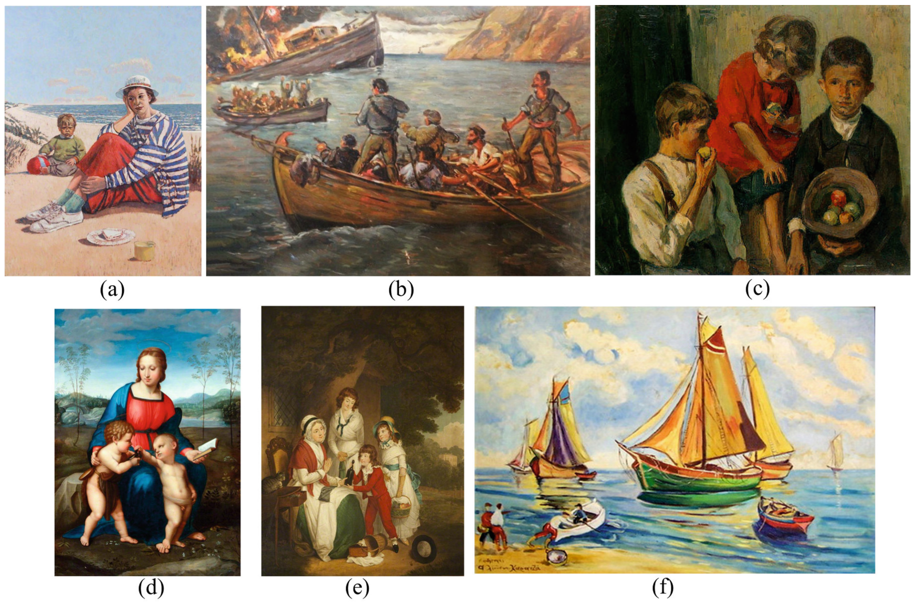

Fig. 3. (a) Painting 1 (by Terence Clarke), (b) painting 2 (by Stratis Axiotis), (c) painting 3 (by Ektor Doukas), (d) painting 4 (by Raphael), (e) painting 5 (by William Redmore Bigg), and (f) painting 6 (by Angeliki Leousi-Karatza).

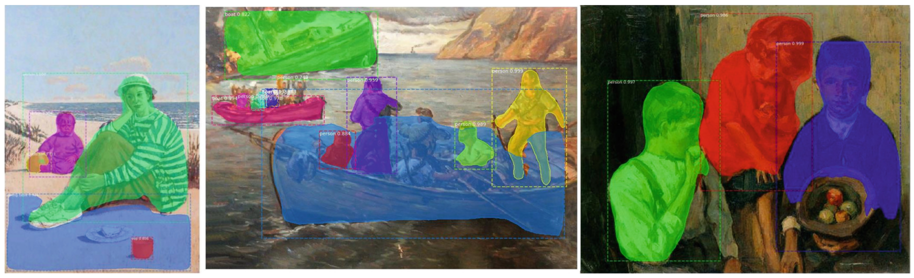

Fig. 4. Semantic segmentation results for the first three paintings of Fig. 3.

For the differential evolution the parameters are: $F_{FR} = 0.8$, $C_{FR} = 0.9$, the population size is equal to 50, and the maximum number of iterations $t_{\max} = 100$. As far as the parameter setting of the other two methods is concerned, it is the same as reported in the respective references.

The results of the transfer learning-based semantic segmentation for the first three paintings are illustrated in Fig. 4. It can be easily seen that the obtained object recognition is sufficiently accurate.

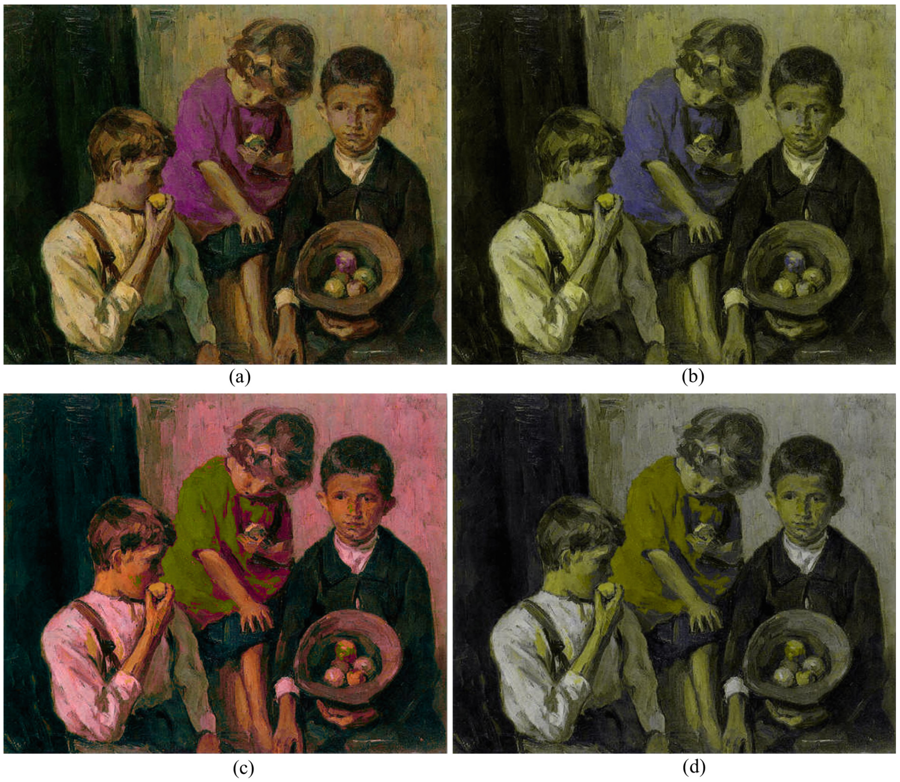

Fig. 5. Results on painting 3 (protanopia): (a) recolored (proposed method), (b) recolored as seen by a protanope (proposed method), (c) recolored (method of Huang et al. [8]), (d) recolored as seen by a protanope (method of Huang et al. [8]).

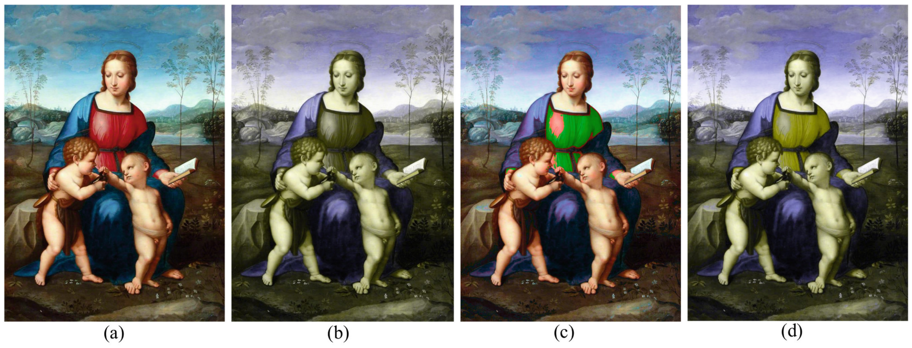

Fig. 6. Results on painting 4 (protanopia): (a) recolored (proposed method), (b) recolored as seen by a protanope (proposed method), (c) recolored (method of Huang et al. [8]), (d) recolored as seen by a protanope (method of Huang et al. [8]).

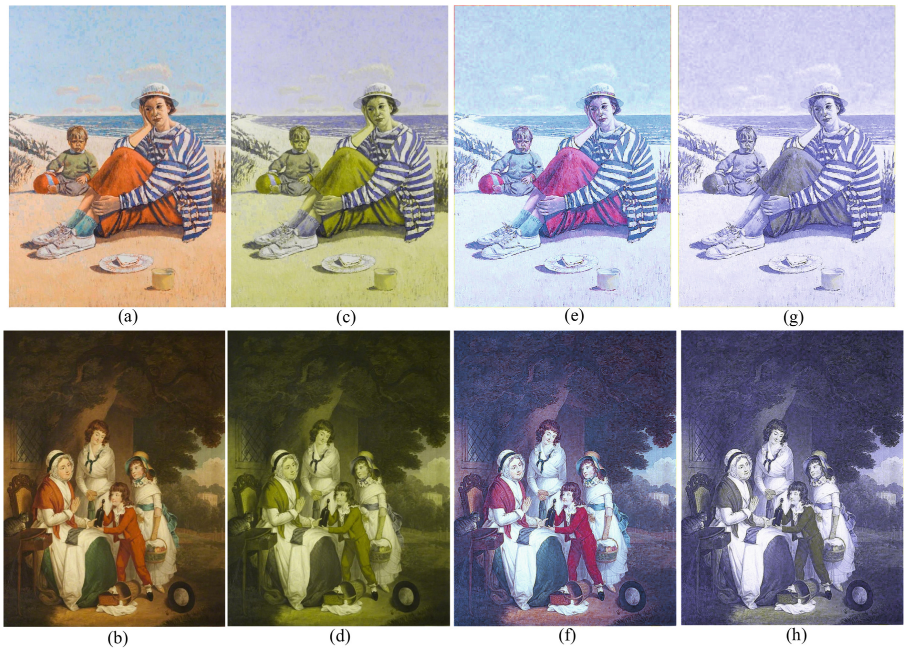

Fig. 7. Results on paintings 1 and 5 (deuteranopia): (a) and (b) recolored (proposed method), (c) and (d) recolored as seen by a deuteranope (proposed method), (e) and (f) recolored (method of Rani and Rajeev [14]), (g) and (h) recolored as seen by a deuteranope (method of Rani and Rajeev [14]).

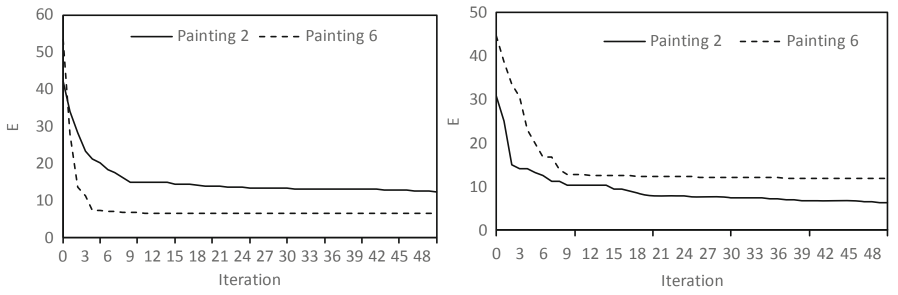

Fig. 8. Dynamic behavior of the objective function E during the application of the DE algorithm for the paintings 2 and 6 in the cases of protanopia (left figure) and deuteranopia (right figure).

Figures 5 and 6 visualize the recolored and the corresponding protanope simulations for paintings 3 and 4, as they are obtained by the proposed algorithm and the method in [8]. Note that the recolored paintings obtained by our approach use colors that are more similar to the respective colors of the original paintings reported in Fig. 3.

The same visual characteristics are observed in Fig. 7, where the proposed method is compared with the recoloring algorithm developed in [14], regarding the case of deuteranopia for the paintings 1 and 5.

Figure 8 depicts the minimization of E as a function of the iteration during the DE implementation for the paintings 2 and 6.

Table 1. Values of the naturalness index (J) obtained by the three algorithms for the six images regarding the cases of protanopia and deuteranopia (best values for each case are in bold fonts).

Paintings	Protanopia		Deuteranopia		
	Proposed	Huang et al. [8]	Proposed	Huang et al. [8]	Rani and Rajeev [14]
1	**3.7168**	12.3482	**8.7589**	13.8699	87.8429
2	**9.0473**	9.8727	**5.0898**	5.1581	25.8787
3	**7.4945**	20.0707	5.8445	**2.1712**	77.3267
4	**5.5553**	23.8336	9.3129	**3.3042**	83.9168
5	**3.9349**	14.6587	**18.5893**	63.8226	90.4925
6	**1.9294**	22.8655	**8.0602**	9.3072	89.9749

Quantitative comparative results in terms of the naturalness index given in Eq. (9) are reported in Table 1. The results of this table are quite convincing since, apart from two experimental cases in deuteranopia (paintings 3 and 4), the proposed algorithm significantly outperforms the other two algorithms. The main conclusion extracted from this table is that the naturalness index is sufficiently minimized by the proposed recoloring approach, yielding colors that are not curious for a normal color vision viewer, while maintaining an aesthetic result for the dichromat viewers, also. This fact is supported by both the visual and quantitative results.

4 Conclusions

The problem investigated in this paper was the recoloring of digitized art paintings in order to improve the color perception of dichromat viewers that suffer from protanopia or deuteranopia. Initially, a transfer learning based semantic segmentation mechanism was applied to extract meaningful color information. The colors of the objects recognized by the deep network were simulated to match the way a dichromat perceives them. Based on the above information, the pixels of the input image were divided into two sets. The first set included colors that must be recolored, whereas the second one included colors that remained intact. This process reduces the number of modified pixels yielding a recolored image that retains its natural appearance. Then, a specially designed objective function was minimized using differential evolution. The optimization parameters are elements of a matrix transformation involved in the recoloring process. The structure of the objective function favored the selection of colors that keep similar the color differences in the original and the dichromat simulation of the recolored image. The method was tested in several experimental cases. The simulation results indicated that the proposed methodology can naturally modify the original colors enhancing the perception of color blind viewers.

Future efforts could extend the present algorithm by developing more sophisticated learning approaches and effective color transformations in order to enhance the protanopia, deuteranopia, and tritanopia effects and the color adaptation procedures, as well.

Acknowledgments. This research is co-financed by Greece and the European Union (European Social Fund-ESF) through the Operational Programme "Human Resources Development, Education and Lifelong Learning 2014–2020" in the context of the project "Color perception enhancement in digitized art paintings for people with Color Vision Deficiency" (MIS 5047115).

References

1. Doliotis, P., Tsekouras, G.E., Anagnostopoulos, C.N., Athitsos, V.: Intelligent modification of colors in digitized paintings for enhancing the visual perception of color-blind viewers. In: The Proceedings of the 5th International Conference on Artificial Intelligence Applications and Innovations, pp. 293–301 (2009)
2. Girshick, R.: Fast R-CNN. In: The Proceedings of the 2015 IEEE International Conference on Computer Vision (ICCV), Santiago, Chile, pp. 1440–1448 (2015)
3. Girshick, R., Donahue, J., Darrell, T., Malik, J.: Rich feature hierarchies for accurate object detection and semantic segmentation. In: The Proceedings of the 2014 IEEE Conference on Computer Vision and Pattern Recognition (CVPR), Columbus, OH, USA, pp. 580–587 (2014)
4. Gonthier, N., Gousseau, Y., Ladja, S., Bonfait, O.: Weakly supervised object detection in artworks. In: The Proceedings of the 2018 European Conference on Computer Vision (ECCV 2018), Munich, Germany, pp. 692–709 (2018)
5. Hassan, M.F., Paramesran, R.: Naturalness preserving image recoloring method for people with red–green deficiency. Sig. Process. Image Commun. **57**, 126–133 (2017)
6. He, K., Zhang, X., Ren, S., Sun, J.: Deep residual learning for image recognition. In: The Proceedings of the 2016 IEEE Conference on Computer Vision and Pattern Recognition (CVPR), Las Vegas, NV, USA, pp. 770–778 (2016)
7. Ho, G.W.: Color, vision, and art: teaching, learning, and making art with color blind awareness. M.Sc. thesis, University of Florida (2014)
8. Huang, J-B., Chen, C.S., Jen, T.S., Wang, S.J.: Image recolorization for the color blind. In: The Proceedings of the 2009 IEEE International Conference on Acoustics, Speech and Signal Processing (ICASSP 2009), pp. 1161–1164 (2009)
9. Huang, J.-B., Tseng, Y.-C., Wu, S.-I., Wang, S.-J.: Information preserving color transformation for protanopia and deuteranopia. IEEE Signal Process. Lett. **14**(10), 711–714 (2007)
10. Johnston-Feller, R.: Color Science in the Examination Museum Objects. The Getty Conservation Institute, Los Angeles (2001)
11. Krizhevsky, A., Sutskever, I., Hinton, G.E.: ImageNet classification with deep convolutional neural networks. Commun. ACM **60**(6), 84–90 (2017)
12. Marmor, M.F., Lanthony, P.: The dilemma of color deficiency and art. Surv. Ophthalmol. **45** (5), 407–414 (2001)
13. Price, K.V., Storn, R.M., Lampinen, J.A.: Differential Evolution: A Practical Approach to Global Optimization. Springer, Berlin (2005)

14. Rani, S.S., Rajeev, R.: Colour transformation for deuteranopic viewers. Int. J. Control Theor. Appl. **9**(10), 4527–4535 (2016)
15. Ren, S., He, K., Girshick, R., Sun, J.: Faster R-CNN: towards real-time object detection with region proposal networks. IEEE Trans. Pattern Anal. Mach. Intell. **39**(6), 1137–1149 (2017)
16. Ribeiro, M., Gomes, A.J.P.: Recoloring algorithms for colorblind people: a survey. ACM Comput. Surv. **52**(4), 72:1–72:37 (2019)
17. Stockman, A., Sharpe, L.T.: The spectral sensitivities of the middle- and long-wavelength-sensitive cones derived from measurements in observers of known genotype. Vision. Res. **40**, 1711–1737 (2000)
18. Tsekouras, G.E., Chatzistamatis, S., Anagnostopoulos, C.N., Makris, D.: Color adaptation for protanopia using differential evolution-based fuzzy clustering: a case study in digitized paintings. In: The Poceedings of the 2018 IEEE Conference on Evolving and Adaptive Intelligent Systems (EAIS 2018), Rhodes Island, Greece (2018)
19. Uijlings, J.R.R., van de Sande, K.E.A., Gevers, T., Smeulders, A.W.M.: Selective search for object recognition. Int. J. Comput. Vision **104**, 154–171 (2013)
20. Vienot, F., Brettel, H., Mollon, J.: Digital video colourmaps for checking the legibility of displays by dichromats. Color Res. Appl. **24**(4), 243–252 (1999)
21. Yin, R., Monson, E., Honig, E., Daubechies, I., Maggioni, M.: Object recognition in art drawings: transfer of a neural network. In: The Proceedings of the 2016 IEEE International Conference on Acoustics, Speech and Signal Processing (ICASSP), Shanghai, China (2016)

Large-Scale Geospatial Data Analysis: Geographic Object-Based Scene Classification in Remote Sensing Images by GIS and Deep Residual Learning

Konstantinos Demertzis[1], Lazaros Iliadis[1](✉), and Elias Pimenidis[2]

[1] School of Engineering, Democritus University of Thrace, 67100 Xanthi, PC, Greece
kdemertz@fmenr.duth.gr, liliadis@civil.duth.gr
[2] University of the West of England Bristol, FET-Computer Science and Creative Technologies, Bristol, UK
Elias.Pimenidis@uwe.ac.uk

Abstract. Recent advances in optical sensor technologies and Geoinformatics, can support very large scale high definition, used for multispectral and panchromatic images. This capability allows the use of remote sensing for the observation of complex earth ecosystems. Application areas include, sustainability of biodiversity, precision agriculture, land, crops and parasites management. Moreover, it supports advanced quantitative studies of biophysical and biogeochemical cycles, in costal or inland waters. The requirement for precise and effective scene classification, can significantly contribute towards the development of new types of decision support systems. This offers considerable advantages to business, science and engineering. This research paper proposes a novel and effective approach based on geographic *object-based* scene classification in remote sensing images. More specifically, it introduces an important upgrade of the well-known *Residual Neural Network* (*ResNet*) architecture. The omission of some layers in the early stages of training, achieves an effective simplification of the network, by eliminating the "*Vanishing Gradient Problem*" (VGP) which causes efficiency limitations in other "*Deep Learning*" (DEL) architectures. The use of the *Softmax* activation function instead of the *Sigmoid* in the last layer, is the most important innovation of the proposed system. The *ResNet* has been trained using the novel *AdaBound* algorithm that employs dynamic bounds on the employed learning rates. The result is the employment of a smooth transition of the stochastic gradient descent, tackling the noise dispersed points of misclassification with great precision. This is something that other spectral classification methods cannot handle. The proposed algorithm was successfully tested, in scene identification from remote sensing images. This confirms that it could be further used in advanced level processes for *Large-Scale Geospatial Data Analysis*, such as cross-border classification, recognition and monitoring of certain patterns and multi-sensor data fusion.

Keywords: Geospatial Data · GIS · Remote Sensing · Scene Classification · Residual Neural Networks · Vanishing Gradient Problem

L. Iliadis et al. (Eds.): EANN 2020, INNS 2, pp. 274–291, 2020.
https://doi.org/10.1007/978-3-030-48791-1_21

1 Introduction

1.1 Scene Classification and Machine Learning

The rapid advances of digital and communication technologies combined with recent developments in optical sensor technologies have resulted in major changes in the way that we monitor land. This is due to the availability of many different systems that offer high spectral image analysis of the earth's surface (e.g. Multispectral, Hyperspectral [1], Panchromatic and Synthetic Aperture Radar) [2]. Despite such advances, the effective comprehension of the semantic content of such images is still a major challenge and a significant research topic. More specifically, scene classification, aims to achieve automatic semantic tagging of each remote sensing object. This process is content-based and it is one of the most critical problems in *Geoinformatics*. It is very important in a wide range of applications such as, the design and the management of land resources, the applications of precision agriculture, the monitoring of complex ecosystems, the sustainable management of biodiversity and the recording of nature destruction and traffic control.

The past few decades have seen the development of various methods of *Scene Classification* (SCC) based on remote sensing. The early SCC methods were primarily based on low level features or heuristics, which focused on colour, texture, and shape. It is worth mentioning Color Histogram (CH), Histogram of Oriented Gradients (HOG), Local Binary Pattern (LBP), Scale Invariant Feature Transform (SIFT) and Gabor filters Grey Level Co-occurrence Matrix (GLCM) [3]. These methods perform well with images of uniform texture, but their ability to identify more complex scenes is poor. The design of features by humans, affects the effectiveness of the above models considerably. On the other hand, methods based on middle level features, can produce a holistic representation of a scene, which is developed through local visual features such as SIFT, CH, or LBP of local image patches. The deployment of a system capable to develop middle level features, starts with the extraction of the local features of the image, and continues with the codification that can lead to an intermediate representation. The most well-known and widely used model for classifying images of middle level is the *Bag of Visual Words* (BoVW) due to its simplicity and effectiveness [5]. Despite having evolved through considerable improvements in the effectiveness of classification, the techniques based on BoVW have not seen further development and utilisation due to their limitations in representing scenes of high resolution.

Deep Learning (DL) is a branch of computational intelligence that utilises a series of algorithms in attempting to model data of high levels of abstraction. This is achieved by using a multilevel processing architecture, based on consecutive linear and non-linear transformations. It is part of the group of learning techniques that exploit data representations to explain and extract optimal results. In the case of image classification they can produce spatial information such as, edges, shapes and relevant chromatic regions.

Deep Learning Architectures use distributed representation whose main hypothesis is that the observed data are extracted from the interaction of factors grouped in levels.

DL adds the assumption that these levels of factors are either the result of abstraction or synthesis of various scales, depending on their volume and size. Such architectures explore the idea of a hierarchical decomposition of the factors from a high to a low level, with the more abstract concepts drawn from the lowest levels. Thus, they are hierarchically distributed according to levels of abstraction, creating the conditions for selecting the most suitable features of the learning process.

Using the above processes, DL architectures and more specifically Deep Neural Networks (DNN), have achieved impressive performance in many remote sensing applications such as, the accurate representation of features in image classification, the identification of objects and their semantic segmentation. DNN, simulate processes of human vision. Multiple operational levels and intermediate representations are created from image capture in the human eye's retina caused by the reaction of muscles. Such process relies in the transformation of every intermediary unit of input representation into a representation at a higher level. The features at higher level are more generic and less changeable, while those of lower level support the classification of inputs. Their effectiveness can be interpreted based on the *Universal Approximation Theorem* which refers to the potential of a neural structure to approximate continuous functions and the Probabilistic Inference which assumes the activation of non-linearity as a cumulative distribution function [5].

In DNN, every hidden layer trains a discreet group of features resulting from the output of the previous layer. The functioning of such a network allows for the analysis of the most complex features as they recompose and decompose from layer to layer. Such a feature is called a hierarchy. As the decomposition of information increases the complexity of the system hierarchically, it offers the ability to process high level data through non-linear functions. Such networks are suitable for the discovery of non-structured data, for revealing latent structures in unlabelled data and the handling of other problematic structures. Even miniscule similarities or anomalies that these might entail can be identified.

Despite all their important functionality and their advantages, the gradients of the loss function approximate zero, when layers that use activation functions are added neural network architectures. This may cause considerable difficulties in the training of the network, almost to the point of not being capable of training at all, depending on the number of hidden layers that are added. The above is a major vulnerability of deep learning neural networks, called *Vanishing Gradient Problem* (VGP) [6].

2 Theoretical Background

2.1 Facing the Vanishing Gradient Problem

In *Machine Learning* the VGP problem pauses a problem in the constriction of neural networks with gradient-based learning methods and backpropagation. In such methods, each of the weights receives, at each iteration, an analogue update with the partial derivative of the error function in relation to the weight it currently uses. In some cases though, the gradient is insignificantly low effectively preventing the weight to change its value. In the worst case, this could prevent the neural network in completing its training [7]. The following Eq. 1, corresponds to a sigmoid activation function (SGA).

$$S(a) = \frac{1}{1 + e^{-a}} \tag{1}$$

It compresses and projects a large range of inputs to a relative small vector space e.g. [0, 1]. Thus, a large change of the input to the sigmoid activation function, corresponds to a small change in its output. Thus the partial derivative becomes extremely small. It is worth noting that when the inputs to the SGA increase, i.e. when |x| increases or decreases, the partial derivative moves towards zero. The above properties of the sigmoid activation function are ideal for the representation of probabilities and classification procedures. However, both the Sigmoid and the Tangent Hyperbolic (TanH) activation functions, have decreased in popularity recently due to the VGP problem [7].

Let us assume a neural network (NN) with 4 hidden layers with a single neuron at each layer. In the above NN the activity of each neuron depends on the activity of that in the previous layer. More specifically the activity of each neuron depends on that of the previous, multiplied by a given weight. This value is propagated via an activation function (the input is a case of special exemption from the above rule). The margin of error *J* at the end of the network shows the total error of the system. The backpropagation process is executed to modify the weights via *Gradient Descent* in such a way as to minimise the value of *J*. To calculate the first weight derivative, the chain rule to backpropagate is used as follows:

$$\frac{\partial error}{\partial w_1} = \frac{\partial error}{\partial output} * \frac{\partial output}{\partial hidden_2} * \frac{\partial hidden_2}{\partial hidden_1} * \frac{\partial hidden_1}{\partial w_1} \tag{2}$$

Subsequently the derivatives are used repetitively until the lowest point has been reached using gradient descent following a specific Learning Rate. The first derivative is used for the activation of the second hidden layer as it is given below. This is performed using the sigmoid activation function (from the output to hidden$_2$) based on the equations below:

$$z_1 = hidden_2 * w_3 \tag{3}$$

$$\frac{\partial output}{\partial hidden_2} = \frac{\partial Sigmoid(z_1)}{\partial z_1} w_3 \tag{4}$$

Similarly the second derivative is used for the propagation from the hidden$_2$ to the hidden$_1$ layer:

$$z_2 = hidden_1 * w_2 \tag{5}$$

$$\frac{\partial hidden_2}{\partial hidden_1} = \frac{\partial Sigmoid(z_2)}{\partial z_2} w_2 \tag{6}$$

In both cases the propagated values contain the derivatives of the sigmoid activation function. This can collectively be expressed as follows:

$$\frac{\partial output}{\partial hidden_2}\frac{\partial hidden_2}{\partial hidden_1} = \frac{\partial Sigmoid(z_1)}{\partial z_1} w_3 * \frac{\partial Sigmoid(z_2)}{\partial z_2} w_2 \tag{7}$$

Both the values of the Sigmoid (z_1) and Sigmoid (z_2), are less than 0.25. The weights w_1, w_2, w_3, are initialised by the Gauss method so that they can have a mean value equal to 0 and standard deviation equal to 1. Therefore every $\|w_i\|$ is smaller than 1. Thus for the calculation of the derivatives we multiply numbers that are less than 1 and 0.25. Given that two numbers in the range [0, 1] are multiplied, the result will always be a smaller value, e.g. 1/3*1/3 = 1/9. Thus, multiplying such small numbers many times, results in a gradient that is so small that will force the network to stop the learning process. The various terms used in such a multiplication is shown in (8) below:

$$\frac{\partial output}{\partial hidden_2}\frac{\partial hidden_2}{\partial hidden_1} = \overset{<1/4}{\frac{\partial Sigmoid(z_1)}{\partial z_1}} \overset{<1}{w_3} * \overset{<1/4}{\frac{\partial Sigmoid(z_2)}{\partial z_2}} \overset{<1}{w_2} \tag{8}$$

In networks with a small number of layers, employing Sigmoid activation functions is not considered a major problem, whereas in multi-layered architectures it could cause major disruption to the normal and effective training of the network.

Totally, four types of solutions for the VGP problem have been proposed in the literature [8]:

a) Methods that do not use gradients such as *Simulated Annealing*, *Multi-Grid Random Search* and *Random Weight Guessing*. Generally the Global Search Methods (GSM) work well in the case of simple problems with long term dependencies. Simple problems can be resolved with networks that use only a few parameters and do not require complex calculations. Such solutions are characterized as *Flat Minima* situations where the network is attempting to solve the problem using a simple architecture. The weights' interconnection levels, are included in a very specific vector space with the error being almost constant. This can only cover a small range of problems, therefore the use of *Flat Minima* is not recommended as a general solution.
b) Methods that enforce higher gradients. Higher gradients can be reinforced by using optimization methods. These are considered time consuming and computationally costly. Furthermore, they appear to have problems in learning to store accurate information, related to the real value of classification.
c) Methods that operate on higher levels. They employ the *Rectified Linear Unit* (ReLU) activation functions that do not yield small derivatives:

$$ReLU(x) = max(0, x) \quad \text{or} \quad ReLU(x) = \begin{cases} 0 \, if \, x < 0 \\ x \, if \, x \geq 0 \end{cases} \tag{9}$$

In some cases though, the ReLU neurons can be forced to situations in which they become inactive for all inputs. In such cases, none of the gradients backpropagate via the neuron, resulting in the neuron being stuck in an interminable inactive condition and effectively dies. This category also includes methods that attempt to solve the problem by following an intuitive process, via the use of high level parameters, such as metadata. These cases also fail in yielding solid and generalizing solutions.

d) Methods that use special architectures. The most important solutions for the VGP problem have been proposed via the use of ResNets [9]. This addresses the stagnation of multiple layer levels even when the size of the network exceeds the 150 layers.

3 The Employed Residual Neural Networks

ResNets, are brain inspired. They are utilizing “skip connections-shortcuts”, in order to jump over some layers. They operate similarly to the Convolutional Neural Networks (CNN), however in ResNets the input is provided sequentially at the exit of the hidden layers, if they are in a certain distance from each other.

In the majority of neural networks, one layer feeds the very next one. In a ResNet that consists of several blocks, every single layer feeds the successive one, but at the same time it provides input to a layer which is located 2 maybe 3 positions far (it skips the order as in Fig. 1). Many linearly interconnected Residual Blocks (REB) constitute a Residual Neural Network. The values of REB parameters are determined based on the network’s structure. They aim at modelling a high level of abstraction of the incoming samples, using multiple stacked non-linear transformations. Their architecture assumes the following characteristics, namely: *Local Receptive Fields* (LRF), *Weight Sharing* (WS), *Spatial Subsampling* (SpaSu), *Feature Combination* (FC) [10].

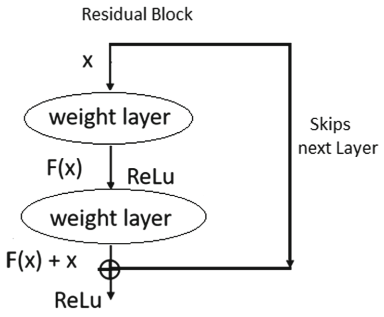

Fig. 1. Image of a Residual Block. Several of them are forming a Residual Neural Net

Essentially, ResNet architecture consists of a set of levels that are characterized by different functionality. They can be configured through their parameters and hyperparameters. The purpose is to convert an input volume into an output one, through a differential function. Interconnection based on the *Residual Block* parameter, determines the overall architecture of the network. The levels of neurons commonly used fall into the following basic categories, namely: *Convolutional Layers* (CL), *Fully Connected Layer* (FCL), *Pooling Layers* (PL), *Dropout Layer* (DRL), *Feed-Forward Layer* (FFL). After any level architecture and sequence, all of the top-level neurons are input to an FFL array or any similar forward-current array [10]. The *Loss Function* (LF) aims to attribute the classification error, which is the difference between the prediction output and the known desired output during the training process.

As noted above, the substantial difference between CNNs and ResNets is the sequential addition of the input to the output of the hidden layers, provided that the hidden layers are at certain distance apart. The Residual Block consists of a set of CLs defined by architectural standardization (usually 2). The input vector x of the Block is stored in a local buffer and after passing all levels of the Block, it is added to the output of F(x) + x. The increased output is presented as input to the next *Residual Block* and so on [10]. In the case of single skips we can use the notation l-2 to l. More specifically, let $W^{l-1,l}$ be the weight vector for connection weights from layer l-1 to l and let $W^{l-2,l}$ be the weight vector for weights from layer l-2 to l. Thus, the forward propagation through the use of the activation function would be the following [9]:

$$a^l = g\left(W^{l-1,l} \cdot a^{l-1} + \beta^l + W^{l-2,l} \cdot a^{l-2}\right) = g\left(Z^l + W^{l-2,l} \cdot a^{l-2}\right) \tag{10}$$

Where, a^l is the output of neurons in layer *l, g* is the activation function for layer *l,* $W^{l-1,l}$ is the weight matrix for neurons between layer *l-1* and *l.* Also, $W^{l-2,l}$ is the weight matrix for neurons between layer *l-2* to *l* and

$$Z^l = W^{l-1,l} \cdot a^{l-1} + \beta^l. \tag{11}$$

ResNets, are inspired by the function of pyramidal cells in the cerebral cortex of the brain, where forward skips take place in many layers. This forward propagation process is expressed by the following equation:

$$a^l = g\left(Z^l + \sum\nolimits_{k=2}^{\mathrm{K}} W^{l-k,l} \cdot a^{l-k}\right) \tag{12}$$

where k-1 is the number of skips.

In backward propagation through the activation function, the *Normal Path* is described by Eq. 13 and the *Skip Paths* by Eq. 14:

$$\Delta w^{l-1,l} = -\eta \frac{\partial E^l}{\partial w^{l-1,l}} = -\eta \alpha^{l-1} \cdot \delta^l \tag{13}$$

$$\Delta w^{l-2,l} = -\eta \frac{\partial E^l}{\partial w^{l-2,l}} = -\eta \alpha^{l-2} \cdot \delta^l \tag{14}$$

Where η is the learning rate, δ^l is the error signal of neurons at layer l and α^l is the activation of neurons at layer l. For the case of a ResNet using forward propagation, the above equations are transformed as follows:

$$\Delta w^{l-k,l} = -\eta \frac{\partial E^l}{\partial w^{l-k,l}} = -\eta \alpha^{l-k} \cdot \delta^l \tag{15}$$

This residual connection does not go through activation functions that "squash" the derivatives, resulting in a higher overall derivative of the block.

4 Literature Review

Inspired by the success of deep learning in the field of computer vision, several related studies have been conducted suggesting various DL architectures for the analysis of ultrasonic data, which have admittedly provided new impetus to this field. The authors of [11] use a hybrid method which combines stacked *Autoencoder*, *Principle Component Analysis* (PCA), and *Logistic Regression* to perform hyperspectral data classification. Tao et al. [12] use a sparse stacked *Autoencoder* to efficiently represent features from unmarked spatial data, and then learned features are fed into a linear SVM for hyperspectral data classification. Various 1D [13] and 2D [14] CNN architectures have been proposed from time to time to encode spectral and spatial information. The latest and most sophisticated proposal concerns 3D CNN [15] in which the third dimension refers to the time axis resulting in a spatio-temporal architecture in the spectral classification. In 3D CNNs, the convolution functions are spatial-spectral, whereas in 2D CNNs, they are spatial only. Compared to 1D and 2D CNNs, 3D CNNs can better spectral information thanks to 3D convolution functions.

Trying to exploit the particularities and advantages of unsupervised learning, the authors [16] propose an unsupervised CNN architecture to perform learning of spectral-spatial features. This is performed by using sparse learning to estimate the network's weights in a greedy layer-wise fashion instead of an end-to-end approach. The algorithm is rooted on sparse representations and enforces both population and lifetime sparsity of the extracted features, simultaneously. They successfully illustrate the expressive power of the extracted representations in several scenarios: classification of aerial scenes, as well as land-use classification in very high resolution or land-cover classification from multi- and hyperspectral images [4].

The proposed algorithm clearly outperforms PCA. The results have shown that single-layer CNNs can extract powerful discriminative features only when the receptive field accounts for neighboring pixels. They are preferred when the classification requires high resolution and detailed results. However, Deep architectures significantly outperform single-layer variants, capturing increasing levels of abstraction and complexity throughout the feature hierarchy.

In [17] authors propose a Deep Recurrent Neural Network model with a new activation function (*parametric rectified Tanh – PRetanh*). The proposed activation function makes it possible to use fairly high learning rates without the risk of divergence during the training procedure. Moreover, a modified gated recurrent unit, which uses PRetanh for hidden representation, is adopted to construct the recurrent layer in the network to efficiently process hyperspectral data and reduce the total number of parameters.

All of the above architectures have major malfunctions and are hampered by the VGP problem, which generally disrupts deep approaches. He et al. [9] tried to overcome this problem by employing the idea of very deep networks by proposing the 152-layers ResNet, which allowed CNNs to grow much deeper without suffering the problem of vanishing/exploding gradients. The authors provide an in-depth analysis about the degradation problem, i.e., simply increasing the number of layers in plain networks results in higher training and test errors.

It is suggested that it is easier to optimize the residual mapping in the ResNet than to optimize the original, unreferenced mapping in the conventional CNNs. In essence, instead of learning a direct map from low-quality inputs to high-quality outputs, the CNN is tasked with learning the residual, i.e., the difference between the low and high-quality signals, which typically represents missing high-frequency information, at least for the case of super-resolution. To allow networks to capture and extract features from multiple scale, skip connections between different layers have also been considered and are now part of state-of-the-art approaches.

The authors of [18], are proposing a novel network architecture, which is a fully Convolutional/Deconvolutional network, for unsupervised spectral–spatial feature learning of hyperspectral images, which is able to be trained in an end-to-end manner. Specifically, the proposed architecture, is based on the so-called *encoder–decoder* paradigm. The input 3-D hyperspectral patch is first transformed into a typically lower dimensional space via a convolutional sub-network (encoder). Then it is expanded to reproduce the initial data by a *de-convolutional sub-network* (decoder).

However, during the experiments, we have found out, that such a network is not easy to be optimized. Although the proposed network has not been explicitly designed for the task of object detection, we have observed that the target object can be localized by the activated or suppressed pixels in some specific learned feature maps of the first residual block. This makes it possible to achieve the unsupervised object detection in hyperspectral images. Experimental results also demonstrate that the features learned by the proposed unsupervised network can be used for the hyperspectral image classification task, and the obtained classification results are competitive compared with the other supervised approaches.

5 The Introduced Methodology

The methodology that is introduced by this research paper, is based on the Convolutional/Deconvolutional (CN/DC) Network architecture that has been used by Mou et al. [18]. The above authors have proposed a fully CN/DC network approach, in which the desired output is the input data itself. Specifically, the introduced model, consists of two parts as its name typically states, namely the Convolutional and Deconvolutional subsystem. The first subsystem corresponds to an encoder that transforms the input characteristics xi into an abstract representation of intermediate features hi.

The corresponding Deconvolutional subset, plays the role of the decoder that reproduces in the original xi input data, the encrypted, intermediate hi features. Essentially the CN/DC network with Residual Learning is a modular network architecture that stacks residual blocks. Similar to Convolutional blocks, a Residual block consists of several Convolutional layers that have the same feature map size and the same number of filters. Their function performs the following calculation.

$$\phi_n = g(\varphi_n) + F(\varphi_n; \Theta_n) \tag{16}$$

$$\varphi_{n+1} = f(\phi_n) \tag{17}$$

Where φ_n refers to feature maps, Θ_n to a collection of weights associated with residual block, F is a residual function and f is the activation function. The corresponding function g, is fixed to an identity mapping:

$$g(\varphi_n) = \varphi_n \tag{18}$$

If *f* is a linear activation function and $\varphi_{(\mathrm{n}+1)} = \varphi_\mathrm{n}$, the output for the nth residual block is calculated by Eqs. (16) and (17) so that:

$$\varphi_{\mathrm{n}+1} = \varphi_\mathrm{n} + \mathrm{F}(\varphi_\mathrm{n}; \Theta_\mathrm{n}) \tag{19}$$

The following Eq. 20 is recursively produced:

$$\varphi_{n+2} = \varphi_{n+1} + F\left(\varphi_{n+1}; \Theta_{n+1}\right) = \varphi_n + F(\varphi_n; \Theta_n) + F\left(\varphi_{n+1}; \Theta_{n+1}\right) \tag{20}$$

The recurrence formula below, is obtained for any shallower block *n* and any deeper block *L*.

$$\varphi_\mathrm{L} = \varphi_\mathrm{n} + \sum\nolimits_{\mathrm{i-n}}^{\mathrm{L-1}} \mathrm{F}(\varphi_\mathrm{i}; \Theta_\mathrm{i}) \tag{21}$$

The way residual learning helps in the effective training of the deep network in question, is found in the rules of backpropagation, where E stands for the loss function:

$$\frac{\partial \mathrm{E}}{\partial \varphi_\mathrm{n}} = \frac{\partial \mathrm{E}}{\partial \varphi_\mathrm{L}} \frac{\partial \varphi_\mathrm{L}}{\partial \varphi_\mathrm{n}} = \frac{\partial \mathrm{E}}{\partial \varphi_\mathrm{L}} \left(1 + \frac{\partial}{\partial \varphi_\mathrm{n}} \sum\nolimits_{\mathrm{i}=1}^{\mathrm{L-1}} \mathrm{F}(\varphi_\mathrm{i}; \Theta_\mathrm{i})\right) \tag{22}$$

In this way, the classification information of a layer in the network does not disappear even when the trainable weights are arbitrarily small, which is the key to make the training in the deep network possible. Also, in order to be able to successfully complete the processes performed by the Convolutional/Deconvolutional subsystems, the need for a pooling layer is imperative. However, the pooling layer leads to a reduced resolution of feature maps. This recreates the original input data to Deconvolutional, through an Unpooling process, in order to separate the feature maps, that is, to increase their spatial range, as opposed to the concentration applied by the Convolutional web.

It should be noted that using *Max-Pooling* indices the system is able to record the position of the maximum value in each local concentration area while concentrating in the Convolutional sub-net. Recently, an advanced version of the *max* and *argmax* functions was presented [19]. It can receive not only the maximum value in the field of indicators of a maximum concentration layer, but the corresponding index of this value as well [19]. Specifically, these two functions can be calculated as follows:

$$\mu = \sum\nolimits_v z(i,j) \frac{exp(az(i,j))}{\sum\nolimits_v exp(az(i,j))} \approx max_v z(i,j) \tag{23}$$

$$\mu = \sum\nolimits_v [i,j]^T \frac{exp(az(i,j))}{\sum\nolimits_v exp(az(i,j))} \approx argmax_v z(i,j) \tag{24}$$

It is a fact, that with the use of the *max* and *argmax* functions, the *max-poling* indices can be obtained in any pooling layer. Then, by performing interpolation in the *Unpooling* layers of the *Deconvolutional* sub-network, the interconnected values which are transferred by the *max-pooling* indices can be successfully handled. The use of *max-pooling* indices allows for a more accurate display of location information and allows feature maps to record detailed information about input features.

6 The Geographic Object-Based Scene Classification Algorithm

This research paper suggests an important modification that upgrades the ResNet architecture discussed above, which employs the Softmax activation function, instead of the Sigmoid at its last level. According to the introduced novel approach, the fully Residual Network is trained using the novel AdaBound algorithm that employs dynamic bounds on their learning rates. It achieves a smooth transition to the stochastic Gradient Descent, which accurately addresses the noisy scattered misspellings that other spectral classification methods cannot handle. As it has already been said, the following Softmax activation function which maps the non-normalized output of a neural network to a probability distribution over predicted output classes, was used instead of the Sigmoid, in the last CL [10]:

$$\sigma(z)_i = \frac{e^{z_i}}{\sum_{j=1}^{k} e^{z_j}}, \quad i = 1, \ldots, k \quad z = (z_1, \ldots, z_k) \in R^k \tag{25}$$

Where, zj is every element of the input vector z, $\sigma(z)$ is the output vector and the sum of its components $\sigma(z)_i$ is equal to 1.

The choice of the *Softmax* was based on the fact that it performs better on multi-classification problems, like the one under consideration. On the other hand, the *Sigmoid* is suitable on binary classification tasks. In the case of *Softmax*, the sum of probabilities is equal to 1 whereas in Sigmoid it does not have to be equal to 1. Finally for the *Softmax*, the highest value has the highest probability, whereas in the *Sigmoid*, the highest value has a high probability but not the highest. The fully residual network was trained using the novel *AdaBound* algorithm [20] that employs dynamic bounds on their learning rates. It achieves a smooth transition to stochastic gradient descent. The following algorithm 1, (in the form of pseudocode) presents the *AdaBound* function [20]:

Algorithm 1. AdaBound

```
Input: $x_1 \in F$, initial step size $\alpha, \{\beta_{1t}\}_{t=1}^{T}, \beta_2$ lower bound function $\eta_l$, upper bound function $\eta_u$
1: Set $m_0 = 0, u_0 = 0$
2: for $t = 1$ to T do
3:     $g_t = \nabla f_t(x_t)$
4:     $m_t = \beta_{1t} m_{t-1} + (1 - \beta_{1t}) g_t$
5:     $u_t = \beta_2 u_{t-1} + (1 - \beta_2) g_t^2$ and $V_t = diag(u_t)$
6:     $\hat{\eta}_t = Clip\left(\frac{a}{\sqrt{V_t}}, \eta_l(t), \eta_u(t)\right)$ and $\eta_t = \frac{\hat{\eta}_t}{\sqrt{t}}$
7:     $x_{t+1} = \prod_{f,diag(\eta_t^{-1})}(x_t - \eta_t \cdot m_t)$
8: end for
```

Compared with other approaches, the *AdaBound* method has two advantages. First, there exists a fixed turning point to distinguish, in the simple ADAM algorithm and the SGD is uncertain. So the *Adabound* addresses this problem with a continuous transforming procedure rather than a "hard" switch. Second, the *AdaBound* introduces an extra hyperparameter to decide the switching time, which is not very easy to fine-tune. In general, the use of the *AdaBound* algorithm has a high convergence speed compared to stochastic gradient descent models and it exceeds the poor generalization ability of adaptive approaches. Moreover, it has dynamic limits on the learning rate, in order to achieve the highest accuracy for the dataset under consideration [20].

7 The Data Experiments and Results

The dataset used in this research, includes images taken from the Reflective Optics System Imaging Spectrometer (ROSIS) covering the Engineering School at the University of Pavia [21]. The available training samples belong to nine categories that are mainly related to land cover items. Each image is 610×340 pixels with a resolution of 1.3 m per pixel. Ultrasound imaging consists of 115 spectral channels ranging from 430 to 860 nm of which only 103 were used in the work as 12 were removed due to noise.

For the network configuration, we leverage convolutional filters with a very small receptive field of 3×3. In addition, the convolutional stride is fixed to 1 pixel; the spatial padding is also 1 pixel. Max-pooling is performed over 3×3 pixel windows with stride 3. All the convolutional layers are using ReLU as an activation function except for the last layer that uses Softmax. The fully residual network was trained using the novel AdaBound algorithm [9] and all the suggested default parameters were used for all the following experiments. Once the training of the residual network is complete, we can start to fine-tune the network for hyperspectral data classification. We have made use of stochastic gradient descent with a fairly low learning rate equal to 0.0001.

The following criteria were used to evaluate the performance of the geographic object-based scene classification algorithms in remote sensing images [22]:

a) Overall Accuracy (OA): This metric represents the number of samples that are classified correctly, divided by the number of test samples. b) Average Accuracy (AA): This index shows the average accuracy of the classifications of all categories. c) Kappa coefficient: This is a statistical measurement that provides information on the level of agreement between the truth map and the final classification map. It takes into account the percentage of agreement which could be expected only chance. In general, it is considered to be a more robust index than a simple percent agreement calculation, since k takes into account the agreement occurring by chance.

In addition, in order to evaluate the importance of the classification accuracy derived from different approaches, a McNemar statistical test is performed [23]:

$$z_{12} = \frac{f_{12} - f_{21}}{\sqrt{f_{12} + f_{21}}} \tag{26}$$

Where f_{ij} is the number of correctly classified samples in the ith classification and of the incorrectly classified in the jth classification. The McNemar's test is based on the standardized normal test statistic and therefore, the null hypothesis, which is "*no significant difference*," is rejected at the widely used $p = 0.05(|z| > 1.96)$ level of significance. This assessment test, determines the significance of the differences between the classification accuracy values obtained by the proposed model, versus the accuracy values obtained by other examined approaches.

To validate the effectiveness of the proposed architecture, the method is compared with the most widely used supervised deep learning models which are summarized as follows:

a. 1-D CNN: The 1-D CNN network architecture was designed as in [24] and includes an input layer, a convolutional layer, a max-pooling layer, a fully connected layer, and an output layer. The number of convolutional filters is 20, the length of each filter is 11 and the pooling size 3. Finally, 100 hidden units are contained in the fully connected layer.
b. 2-D CNN: The 2-D CNN architecture was designed as in [15]. It contains three convolutional layers equipped with 4×4, 5×5 and 4×4 convolutional filters, respectively. The 2-D CNN architecture was designed as in [15]. It contains three convolutional layers equipped with 4×4, 5×5 and 4×4 convolutional filters, respectively.
c. The Convolutional layers - except for the latter - are followed by max-pooling layers. In addition, the numbers of convolutional filters for CL are 32, 64 and 128, respectively.
d. Simple Convolutional/Deconvolutional network: The simple Convolutional/Deconvolutional network with simple convolutional blocks and the Unpooling function are applied in the cases of [25,26].

e. Residual Convolutional/Deconvolutional network: It is an architecture using residual blocks and a more precise Unpooling function, as presented in [18].

***Optimized Residual Convolutional/Deconvolutional* (ORCD) network**
It is the improved version of the above architecture which was presented in this research paper. It differs in the fact that it uses the *Softmax* activation function in the last convolutional layer and that its fully residual network is trained using the novel AdaBound algorithm. This is achieved by employing dynamic bounds on the learning rates, which results in a smooth transition to stochastic gradient descent. This method shows great efficacy while maintaining advantageous properties of adaptive learning, such as rapid initial progress and hyperparameter insensitivity. Note that, we have used the standard types of training and testing samples in order make the proposed approach fully comparable with other classifiers in the literature.

The ORCD network was trained using the *AdaBound* algorithm, and all the suggested default parameters were used for all the following experiments. The number of Convolutional filters (CF), increases towards deeper layers of the convolutional subnetworks: There were 64 CF in the first residual block, 128 in the following block, and 256 in the last one. This rule is turned over for the *Deconvolutional sub-network*. All of the convolutional layers are with ReLU as activation function except the last layer that uses the *Softmax*.

All weight matrices in the network and the bias vectors are initialized with a uniform distribution, and their values are initialized in the range [−0.1, 0.1]. The number of the unlabeled data samples of the Pavia University that were used for training the network is 10000. These unlabeled samples are randomly selected from the whole set of images.

In the *Optimized Residual Convolutional/Deconvolutional* network, the hyperspectral data are normalized in the closed interval [0, 1]. Then, all of the weights are updated during the training procedure. Once the training of the network is completed, the *fine-tuning* process for hyperspectral data classification follows. The *stochastic gradient descent* with a fairly low learning rate of 0.0001 has been employed, for the fine tuning of the network. During this process, a percentage equal to 10% of both hyperspectral data sets, has been randomly selected as the validation set.

That is, during fine-tuning, 90% of the dataset has been used for learning and the remaining 10% of the available data samples served as the validation set, to perform tuning of the *hyper-parameters*, such as the numbers of convolutional filters in the convolutional layers. All of the test samples were used to evaluate the final performance of the learned *spectral–spatial feature representations* and the *fine-tuned network* was used to perform the classification.

The following Table 1 shows the classification maps using the *Pavia University* data set and the comparison of the accuracies between the classifiers *1-D CNN, 2-D CNN, Simple Convolutional/Deconvolutional Network (Simple C/D N), Residual C/D N* and the proposed *Optimized R C/D N*.

Trying to evaluate the above algorithms based on the obtained results, it is easy to conclude that the proposed ORCD *Network* outperforms the competing Deep Learning approaches for the *OA, AA*, and *Kappa* evaluation indices.

Table 1. Comparison of the accuracies between the classifiers

Class No	Class Name	1D CNN	2D CNN	Simple C/D N	Residual C/D N	Optimized R C/D N*
1	Asphalt	83.73	69.25	82.81	78.99	**86.59**
2	Meadows	65.70	93.39	97.11	**97.16**	97.01
3	Gravel	67.03	63.13	60.31	61.46	**69.97**
4	Trees	94.03	94.39	95.59	**95.76**	94.91
5	Metal Sheets	99.41	**100**	97.55	97.77	98.83
6	Bare Soil	**96.30**	49.06	59.38	59.46	69.87
7	Bitumen	**93.83**	72.26	78.42	79.50	86.49
8	Bricks	93.56	94.32	96.50	96.82	**96.85**
9	Shadows	**99.79**	93.77	92.29	92.40	97.71
OA	–	79.28	82.66	87.82	87.39	**90.51**
AA	–	88.15	81.06	84.44	84.37	**88.69**
Kappa	–	0.7423	0.7688	0.8363	0.8308	**0.8482**
Significance	–	31.362	31.464	23.178	22.232	21.871

The proposed method produces extremely accurate results without repeated problems of undetermined cause, because all of the features in the considered dataset are handled very efficiently. In addition, one of the key advantages gained from the results is the high reliability, resulting from the high kappa values (maximum reliability if $k \geq 0.81$). This can be considered as the result of data processing that allows the most reliable relevant data for the forthcoming forecasts. The above Table 1, also provides information on the results of the *McNemar* test to assess the significance of the difference between the classification accuracy of the proposed network and the other approaches considered. The results of the *McNemar* test, have proven that there exist statistically significant differences among the results obtained by the employed methods. More specifically, the differences between the 1D and 2D CNN with the rest of them are quite high, whereas there are minor but significant differences between the Optimized R C/D N (our proposed approach) and the Residual.

8 Discussion - Conclusions

This research proposes an innovative and highly effective geographic object-based scene classification system in remote sensing images, using an innovative Residual Neural Network (ResNet) architecture. This approach eliminates VGP as it is using Softmax activation function instead of Sigmoid on the last layer of the network. The fully residual network was trained using the novel AdaBound algorithm that employs dynamic bounds on their learning rates. It achieves a smooth transition to stochastic gradient descent, and it precisely addresses the noisy scattering points of misclassification that other spectral classification methods cannot handle properly.

Its implementation is based on the optimal use and combination for the first time in the literature, of two highly efficient and fast learning processes (Softmax activation function and AdaBound algorithm), which create an integrated intelligent system.

This network also remarkably implements a Large-Scale Geospatial Data Analysis approach that attempts to balance latency, throughput, and fault-tolerance using ResNet while simultaneously exploiting learning processes optimally and as efficiently as possible. The reliability of the proposed network has been successfully tested in the recognition of scenes from remote sensing photographs, which suggests that it can be used in higher level Geospatial Data Analysis processes. Such cases are the classification, the recognition and monitoring of specific standards, and the fusion of multi-sensor data.

Suggestions for the evolution and future improvements of this network should focus on further optimizing the parameters of the algorithms used in ResNet architecture. This will be done in order to achieve an even more efficient, more accurate and faster categorization process using a heuristic approach [27] or customization of the algorithm with the use of Spiking Neural Networks [28]. It would also be important to study the extension of this system by implementing the Lamda architecture [29] in an environment of parallel and distributed big data analysis systems (Hadoop). Finally, an additional target that could be considered in the direction of future expansion concerns the operation of the network by methods of self-improvement [30] and redefinition of its parameters in meta-learning. This can fully automate the geographic object-based scene classification process in remote sensing images.

References

1. Plaza, A., Plaza, J., Paz, A., Sanchez, S.: Parallel hyperspectral image and signal processing. IEEE Sign. Process. Mag. **28**, 119–126 (2011)
2. Hubert, M.J., Carole, E.: Airborne SAR-efficient signal processing for very high resolution. Proc. IEEE **101**, 784–797 (2013)
3. Zhang, W., Tang, P., Zhao, L.: Remote sensing image scene classification using CNN-CapsNet. Remote Sens. MDPI **11**(5), 494 (2019). https://doi.org/10.3390/rs11050494
4. Yang, Y., Newsam, S.: Bag-of-visual-words and spatial extensions for land-use classification. In: Proceedings of the 18th SIGSPATIAL International Conference on Advances in Geographic Information Systems, San Jose, CA, USA, pp. 270–279 (2010)
5. Penatti, O.A., Nogueira, K., dos Santos, J. A.: Do deep features generalize from everyday objects to remote sensing and aerial scenes domains? In: Proceedings of the IEEE Conference on Computer Vision and Pattern Recognition Workshops, Boston, MA, USA, pp. 44–51 (2015)
6. Schmidhuber, J.: Deep learning in neural networks: an overview. Neu. Netw. **61**, 85–117 (2015)
7. Hochreiter, S., Bengio, Y., Frasconi, P., Schmidhuber, J.: Gradient Flow in Recurrent Nets: The Difficulty Of Learning Long-term Dependencies. IEEE Press, New York (2001)
8. Kolen, J.F., Kremer, S.C.: Gradient flow in recurrent nets: the difficulty of learning long-term dependencies. In: A Field Guide to Dynamical Recurrent Networks, pp. 237–243. IEEE, (2001)

9. He, K., Zhang, X., Ren, S., Sun, J.: Deep residual learning for image recognition (2015). arXiv:1512.03385
10. Goodfellow, I., Bengio, Y., Courville, A.: Deep Learning. MIT Press, Cambridge (2016)
11. Chen, Y., Lin, Z., Zhao, X., Wang, G., Gu, Y.: Deep learning-based classification of hyperspectral data. IEEE J. Appl. Earth Obs. Remote Sens. **7**(6), 2094–2107 (2014)
12. Tao, C., Pan, H., Li, Y., Zou, Z.: Unsupervised spectral-spatial feature learning with stacked sparse autoencoder for hyperspectral imagery classification. IEEE Explore Geosci. Remote Sens. **8**(6), 2381–2392 (2015)
13. Kussul, N., Lavreniuk, M., Skakun, S., Shelestov, A.: Deep learning classification of land cover and crop types using remote sensing data. IEEE Explore Geosci. Remote Sens. **14**(5), 778–782 (2017)
14. Makantasis, K., Karantzalos, K., Doulamis, A., Doulamis, N.: Deep supervised learning for hyperspectral data classification through convolutional neural networks. In: Geoscience & Remote Sensing (2015)
15. Chen, Y., Jiang, H., Li, C., Jia, X., Ghamisi, P.: Deep feature extraction and classification of hyperspectral images based on CNN. IEEE Trans. Geosci. Remote Sens. **54**(10), 6232–6251 (2016)
16. Romero, A., Gatta, C., Camps-Valls, G.: Unsupervised deep feature extraction for remote sensing image classification. IEEE Trans. Geosci. Remote Sens. **54**(3), 1349–1362 (2016)
17. Mou, L., Ghamisi, P., Zhu, X.: Deep recurrent neural networks for hyperspectral image classification. IEEE Trans. Geosci. Remote Sens. **55**(7), 3639–3655 (2017)
18. Mou, L., Ghamisi, P., Zhu, X.: Unsupervised spectral-spatial feature learning via deep residual conv–deconv network for hyperspectral image classification. IEEE Trans. Geosci. Remote Sens. **56**(1), 391–406 (2018)
19. Glorot X., Bengio Y.: Understanding the difficulty of training deep feedforward neural networks. In: Proceedings International Conference Artificial Intelligence Statistics, pp. 249–256 (2010)
20. Luo, L., Xiong, Y., Liu, Y., Sun, X.: Adaptive gradient methods with dynamic bound of learning rate (2019). arXiv:1902.09843
21. Grana, M., Veganzons, M.A., Ayerdi, B.: Hyperspectral remote sensing scenes (2020). http://www.ehu.eus/ccwintco/index.php/Hyperspectral_Remote_Sensing_Scenes. Grupo De Inteligencia, Computacional
22. Fawcett, T.: An introduction to ROC analysis. Pattern Recogn. Lett. **27**, 861–874 (2006)
23. Agresti, A.: Categorical Data Analysis, p. 413. Wiley, Hoboken (2002). ISBN 978-0-471-36093-3
24. Hu, W., Huang, Y., Wei, L., Zhang, F., Li, H.: Deep convolutional neural networks for hyperspectral image classification. J. Sens. S.I. Deep Learn. Remote Sens. Image Underst., art. no. 258619 (2015)
25. Dosovitskiy, A., Springenberg, J. T., Brox, T.: Learning to generate chairs, tables and cars with convolutional networks. In: Proceedings IEEE Conference Computer Vision Pattern Recognition, pp. 1538–1546 (2015)
26. Dosovitskiy, A., Fischer, P., Springenberg, J.T., Riedmiller, M., Brox, T.: Discriminative unsupervised feature learning with exemplar convolutional neural networks. IEEE Trans. Pattern Anal. Mach. Intell. **38**(9), 1734–1747 (2016)
27. Demertzis, K., Iliadis, L.: Adaptive elitist differential evolution extreme learning machines on big data: intelligent recognition of invasive species. In: Proceedings of the INNS Conference Advances in Big Data, Advances in Intelligent Systems and Computing, vol. 529. Springer, Heidelberg (2016)

28. Demertzis, K., Iliadis, L., Anezakis, V.: A deep spiking machine-hearing system for the case of invasive fish species. In: Proceedings IEEE-SMC Innovations in Intelligent Systems & Applications (INISTA), pp. 23–28 (2017)
29. Demertzis, K., Tziritas, N., Kikiras, P., Sanchez, S.L., Iliadis, L.: The next generation cognitive security operations center: adaptive analytic lambda architecture for efficient defense against adversarial attacks. Big Data Cogn. Comput. **3**, 6 (2019). https://doi.org/10.3390/bdcc3010006
30. Demertzis, K., Iliadis, L.S., Anezakis, V.D.: Extreme deep learning in biosecurity: the case of machine hearing for marine species identification. J. Inf. Telecommun., 1–19 (2018). Taylor & Francis

Semantic Segmentation of Vineyard Images Using Convolutional Neural Networks

Theofanis Kalampokas, Konstantinos Tziridis, Alexandros Nikolaou, Eleni Vrochidou, George A. Papakostas(✉), Theodore Pachidis, and Vassilis G. Kaburlasos

Human-Machines Interaction Laboratory (HUMAIN-Lab), International Hellenic University, Agios Loukas 65404, Kavala, Greece
{theokala, kenaaske, alexniko, evrochid, gpapak, pated, vgkabs}@teiemt.gr

Abstract. This paper aims to study the segmentation demands of vineyard images using Convolutional Neural Networks (CNNs). To this end, eleven CNN models able to provide semantic segmented images are examined as part of the sensing subsystem of an autonomous agricultural robot. The task is challenging due to the similar color between grapes, leaves and image's background. Moreover, the lack of controlled lighting conditions results in varying color representation of grapes and leaves. The studied CNN model architectures combine three different feature learning sub-networks, with five meta-architectures for segmentation purposes. Investigation on three different datasets consisting of vineyard images of grape clusters and leaves, provided segmentation results, by mean pixel intersection over union (IU) performance index, of up to 87.89% for grape clusters and 83.45% for leaves, for the case of ResNet50_FRRN and MobileNetV2_PSPNet model, respectively. Comparative results reveal the efficacy of CNNs to separate grape clusters and leaves from image's background. Thus, the proposed models can be used for in-field applications for real-time localization of grapes and leaves, towards automation of harvest, green harvest and defoliation agricultural activities by an autonomous robot.

Keywords: Semantic segmentation · Convolutional neural network · Computer vision · Deep learning · Precision agriculture · Harvesting robot

1 Introduction

Robotics are entering the agricultural fields in slow but persistent way [1]. Most researches are testing agricultural robotics, namely *Agrobots*, in controlled environments such as greenhouses, while little has been done in real-field applications [2, 3]. This work investigates the segmentation task of grapes clusters and leaves, based on CNNs, to be integrated into an agrobot for in-field grape harvesting tasks. Convolutional neural networks (CNNs) are a class of deep neural networks for visual imagery analysis, mainly for object recognition and classification [4, 5]. Over many benchmark datasets, CNNs have demonstrated their capability to advance the state-of-the-art accuracies of object recognition [6, 7]. The capacity of a CNN can be controlled by varying their depth and breadth, estimating the stationary characteristics of images and the locality of pixel dependencies [8]. Visual object recognition is a basic task in remote sensing that finds among others, application in agriculture [3, 9], with our special interest focused on *viniculture*.

Convolutional neural networks have been applied to viticulture [10–16]. In [11] a benchmark hyperspectral dataset of grape images is employed to test a five-layer CNN for object identification. Hyperspectral images of grapes are used in [13], with a deep CNN, which extracts spectral-spatial information of hyperspectral images using a limited number of samples. Also in [16], hyperspectral images of grapes are tested with a CNN architecture to predict class-related results. In [10], an automated image-based workflow is developed quantifying inflorescences and single flowers images of grapevines. Image regions depicting inflorescences are identified and localized by segmenting the images into classes using a Fully Convolutional Network (FCN). Morphological and color features of grapes are used in [12] for ripeness estimation with a CNN. In a recent work [14] satellite image data is used to identify a vineyard, integrating the Continuous Wavelet Transform (CWT) and a CNN. A CNN is used to estimate vineyard grape yield in [15], by measuring the weight of grapes on a vine from an image with relatively good accuracy.

In this work, the recent advances in handling uncertainties during a segmentation task in vineyard images, using CNNs are investigated. More specifically, eleven CNN deep pixel-to-pixel architectures are applied in three sets of RGB images of red grapes, white grapes and a mixture of both kinds of grapes. The proposed architectures are derived from combining three different types of feature learning sub-networks with five different types of classification sub-networks.

This work examines and adopts existing methods on plant phenotyping using visual imaging and furthers the capabilities of in-field image classification. The modular design of the proposed models points out new combinations of segmentation architectures that fit the problem under study, i.e. grape and leaves segmentation. Thus, it paves the way forward for an autonomous robot to discriminate grapes and leaves on the spot, towards automating agricultural tasks such as harvest, green harvest and defoliation.

The rest of the paper is structured as follows. In Sect. 2 the image datasets and the examined CNN models are presented. Results are discussed in Sect. 3. Section 4 concludes by summarizing the contribution of this work and future research directions.

2 Materials and Methods

This section summarizes the main materials used to execute the proposed study as well as briefly describes the applied methods.

2.1 Image Datasets

Three datasets are used to evaluate the CNN models under investigation; dataset 1 consists of 274 images of white grapes and leaves, dataset 2 consists of 259 images of red grapes and leaves and dataset 3 is derived by combining dataset 1 and 2. Images of dataset 1 are captured by an RGB high resolution Samsung Mirrorless camera (NX500), while images of dataset 2 are captured by a USB 3.0 high resolution Thorlabs camera (DCC3240C) with lens C-MOUNT 12 mm (MVL12M23). All images are taken from three vineyards of well-known North Greek wine producers as part of a national research program [17] and are available to the public upon request. Two different types of cameras are used to test the performance of the models for the different equipment of the research program, since two RGB cameras will be mounted on the harvesting robot; one on the vehicle and one on the robotic arm that will approach the grape clusters to complete the agricultural tasks. Moreover, images of different quality comprise each dataset. The different quality of datasets is intentional, in order to test the performance of the networks under varying conditions and point out the most robust among them. In-field applications are characterized by unstable and varying conditions resulting in a lack of consistency in capturing the images to be used. In our case, for example, one of the cameras will be mounted on the moving, i.e. non-stable, robotic arm of the ground harvesting vehicle. This will lead to images of different characteristics i.e. varying illuminations, different viewing angles etc. These characteristics are the difficulties and challenges that the Agrobot will encounter in the real-field application, and therefore need to be explored. The original datasets are augmented in order to generate sufficient number of images for training the CNN models, as described in the next section. All the captured images have been annotated (ground truth) in order the pixels to belong to one of 3 classes, namely grapes, leaves and background. Ground truth images are constructed using the LabelMe annotation tool [18]. The details of each dataset are summarized below.

Dataset 1. Dataset 1 consists of 274 images of white grapes, augmented to 1370. The initial dataset contains 1064 white grape clusters and 1192 leaves. Dataset 1 consists of images of single isolated grape clusters, without any overlapping.

Dataset 2. Dataset 2 consists of 259 images of red grapes, augmented to 1295. The initial dataset contains 1282 red grape clusters and 1264 leaves. Dataset 2 consists of images of many and overlapping grape clusters or with dense leave coverage.

Dataset 3. Dataset 3 is the merge of datasets 1 and 2 (2665 augmented images).

2.2 Data Augmentation

The most common method to reduce overfitting on image data is to artificially augment the dataset using label-preserving transformations [19, 20]. Traditional transformations consist of using a combination of affine transformations to manipulate the training data. We employ four distinct forms of data augmentation that allow transformed images to be produced from the original images with minimum computations; flip, rotate, shift and shearing. For each input image, four duplicated images, 60% transformed compared to the original, are generated. Original image and duplicates are fed into the CNN models. Thus, for a dataset of N images size, the final size of the augmented dataset is 5N (N + 4N).

2.3 Examined Models

Convolutional neural networks are trainable multistage architectures [21]. The input and output of each stage are sets of arrays. At the output, each array represents a feature extended at all locations on the input. Typically, each stage is composed of three layers; a filter-bank layer, a non-linearity layer and a feature pooling layer [4]. The 3-layer stages that form the feature learning network, are followed by a classification module, as shown in Fig. 1. In this work, three feature learning networks are combined with five classification convents, where it is possible, by forming eleven models that are evaluated for the problem under study; optimal in-field localization of grape clusters and leaves by a harvesting robot.

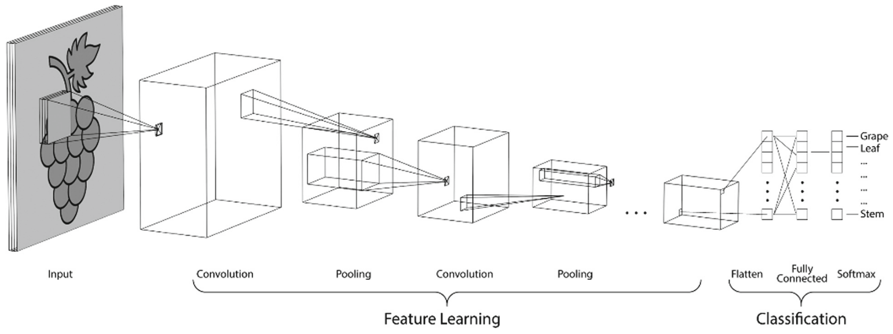

Fig. 1. Typical structure of a CNN.

Feature Learning Networks. In a typical CNN architecture, initial layers deal with feature learning (Fig. 1). First layer includes a set of independent filters that are randomly initialized. At this point, the network learns from the data and detects low-level features such as edges are curves. An activation function is also applied to the feature maps to increase non-linearity in the network. The pooling layer reduces the spatial size of input representation, the number of parameters and thus, the overall required computations. Herein, three CNN architectures are examined, the *VGG16*, the *ResNet50* and *MobilNetV2*.

- VGG16 is a very deep convolutional neural network with 16 layers for large-scale image classification [22].
- ResNet50 is a very deep 50-layer convolutional neural network. ResNets can handle more layers by having lower complexity than VGG networks [23].
- MobileNetV2 introduces a new CNN layer, the inverted residual and linear bottleneck layer, enabling high accuracies in mobile and embedded vision applications [24], with lower complexity.

Classification Convents. The last layer of the typical CNN architecture comprised a fully connected classification scheme, namely a meta-architecture (Fig. 1). Artificial Neural Networks (ANN) are added to combine the image features into attributes.

Backpropagation minimizes the errors and weights are adjusted to optimize the models' performance. In this work five meta-architectures able to provide class label for each input image's pixel and thus performing semantic segmentation of the vineyard images, are examined, as listed below.

– *FPN*. The Feature Pyramid Network [25] creates a feature pyramid that has strong semantics at all scales. The main idea relies on an architecture that combines low-resolution, semantically strong features with high-resolution, semantically weak features via a top-down pathway and lateral connections.
– *FCN8*. In a Fully Connected Network [5] the fully connected layers for the image classification are replaced by multiple convolutional layers and decoder layers, forming two phases; the feature extraction phase and the decoder phase, resulting into a classification model that assigns a class label in each pixel of the image.
– *U-Net*. The U-Net architecture represents a method of decoding, that up-samples features by using transposed convolution for each down-sampling stage. The main idea is to increase the network with successive layers where pooling operations are replaced by up-sampling operations. U-Net is a modified and extended version of FCN such that it works with very few training images and yields more precise segmentations [26].
– *PSPNet*. Pyramid Scene Parsing Network extends the pixel-level-feature to the specially designed global pyramid pooling one. The local and global clues together make the final prediction more reliable [27].
– *FRRN*. Full-Resolution Residual Network exhibits strong localization and recognition performance. A multi-scale context is combined with pixel-level accuracy by using two processing streams within FRRN; one that carries information at the full image resolution and one that undergoes a sequence of pooling operation. The two streams are coupled at the full image resolution using residuals [28].

3 Results and Discussion

Eleven CNN based semantic segmentation models, derived by combining the above-mentioned feature learning sub-networks and classification met-architectures, were evaluated with dataset 1, 2 and 3. The experimental results of the conducted study, along with the experimental setup are summarized in this section.

3.1 Experimental Setup

To evaluate the examined models, the labeled datasets are divided into training and testing sets. For all datasets, the testing set consists of 20 images while the rest of the images are used for training. For all experiments, categorical weighted cross entropy Loss is used [29]. ADADELTA optimizer learning rate [30] is set to 1.0. ADADELTA is selected due to its capability to dynamically adapt the learning rate during the training process. Batch size is 12 for all models. All models are trained for 200 epochs. All methods were implemented in Python 3.7 using TensorFlow and Keras, on a computer equipped with Nvidia RTX 2070 GPU.

3.2 Results

Results are reported for the three datasets under study. The performance of each model is evaluated by the mean intersection over union (IU) on the testing set for the three classes of each dataset (Tables 1, 2 and 3) and their average. Moreover, Loss, F1-score and average IU for all models during training in each dataset (Tables 4, 5 and 6), are also presented.

The experimental results regarding the testing set are summarized in Tables 1, 2 and 3. The best performance network for dataset 1 is MobileNetV2_PSPNet, which achieves IU of 87.79% and 83.45%, for grapes and leaves, respectively. The best average performance for all classes is achieved by the same network, which reaches a state-of-the art average IU 88.21%.

Table 1. IU (%) on the testing set for dataset 1.

CNN models	IU grapes	IU leaves	IU background	Average IU
VGG16_FPN	83.09	72.90	89.60	81.86
VGG16_FCN8	81.47	63.58	87.90	77.65
VGG16_U-Net	81.96	65.47	88.26	78.56
VGG16_PSPNet	86.00	78.83	91.98	85.60
ResNet50_FPN	78.90	66.94	87.26	77.70
ResNet50_U-Net	80.57	67.29	87.73	78.53
ResNet50_PSPNet	82.01	71.36	89.35	80.90
ResNet50_FRRN	79.10	70.07	85.80	78.32
MobileNetV2_FPN	87.07	78.62	92.29	85.99
MobileNetV2_U-Net	86.76	78.63	92.22	85.87
MobileNetV2_PSPNet	**87.79**	**83.45**	**93.4**	**88.21**

Table 2. IU (%) on the testing set for dataset 2.

CNN models	IU grapes	IU leaves	IU background	Average IU
VGG16_FPN	67.15	56.99	77.33	67.15
VGG16_FCN8	65.42	52.04	73.80	63.73
VGG16_U-Net	66.08	57.17	77.13	66.79
VGG16_PSPNet	68.35	57.40	76.62	67.45
ResNet50_FPN	64.56	53.28	75.92	64.58
ResNet50_U-Net	66.84	56.34	76.12	66.43
ResNet50_PSPNet	57.42	44.17	73.43	58.34
ResNet50_FRRN	**79.51**	59.04	72.69	**70.41**
MobileNetV2_FPN	65.85	**59.27**	76.52	67.21
MobileNetV2_U-Net	68.91	58.11	**77.44**	68.15
MobileNetV2_PSPNet	64.10	54.74	74.79	64.54

Table 3. IU (%) on the testing set for dataset 3.

CNN models	IU grapes	IU leaves	IU background	Average IU
VGG16_FPN	71.32	61.09	79.41	70.60
VGG16_FCN8	71.08	58.89	78.35	69.44
VGG16_U-Net	68.40	55.83	78.46	67.56
VGG16_PSPNet	68.07	61.24	80.51	69.94
ResNet50_FPN	68.07	54.41	77.89	66.79
ResNet50_U-Net	69.14	54.34	78.04	67.17
ResNet50_PSPNet	70.07	58.45	80.04	69.52
ResNet50_FRRN	**87.89**	62.19	**89.77**	**79.95**
MobileNetV2_FPN	75.76	**64.12**	82.83	74.23
MobileNetV2_U-Net	75.88	64.10	83.75	74.57
MobileNetV2_PSPNet	74.04	64.37	83.07	73.82

For dataset 2, the best performance is achieved by combinations ResNet50_FRRN (IU 79.51%), MobileNetV2_FPN (IU 59.27%) for grapes and leaves segmentation respectively, while for all classes an IU 77.44% is reached by MobileNetV2_U-Net. For dataset 3, the models ResNet50_FRRN (IU 87.89%), MobileNetV2_FPN (IU 64.12%) shown the best accuracy for grapes and leaves segmentation, respectively, with the former being the best performed model on average (IU 79.95%).

Table 4, 5 and 6 summarize the models' performance in terms of Loss, F1-score and IU on the training set for each dataset. For dataset 1, best scores are achieved by MobileNetV2_U-Net, providing 0.039 Loss, 97.47% F1-score and 95.09% IU. For dataset 2, VGG16_FPN model (0.065 Loss, 96.15% F1-score and 92.69% IU) shown the best performance.

Table 4. Loss, F1-score and IU on the training set for dataset 1.

CNN models	Loss	F1-score (%)	Average IU (%)
VGG16_FPN	0.087	95	90.66
VGG16_FCN8	0.125	92.13	91.13
VGG16_U-Net	0.088	95.02	90.60
VGG16_PSPNet	0.114	93.60	88.09
ResNet50_FPN	0.117	92.14	84.12
ResNet50_U-Net	0.095	93.18	89.57
ResNet50_PSPNet	0.189	90.64	83.08
ResNet50_FRRN	0.176	80.56	89.63
MobileNetV2_FPN	0.039	97.59	95.33
MobileNetV2_U-Net	**0.039**	**97.47**	**95.09**
MobileNetV2_PSPNet	0.079	95.35	91.20

Table 5. Loss, F1-score and IU on the training set for dataset 2.

CNN models	Loss	F1-score (%)	Average IU (%)
VGG16_FPN	**0.065**	**96.15**	**92.69**
VGG16_FCN8	0.270	92.11	89.41
VGG16_U-Net	0.069	95.80	92.06
VGG16_PSPNet	0.114	93.31	87.96
ResNet50_FPN	0.071	95.80	92.04
ResNet50_U-Net	0.077	95.39	91.33
ResNet50_PSPNet	0.150	91.80	85.15
ResNet50_FRRN	0.089	95.40	86.17
MobileNetV2_FPN	0.102	94.14	89.12
MobileNetV2_U-Net	0.103	93.88	88.70
MobileNetV2_PSPNet	0.199	89.80	81.82

Table 6. Loss, F1-score and IU on the training set for dataset 3.

CNN models	Loss	F1-score (%)	Average IU (%)
VGG16_FPN	0.143	93.44	91.61
VGG16_FCN8	0.291	88.67	87.30
VGG16_U-Net	0.141	92.91	86.89
VGG16_PSPNet	0.189	90.64	83.08
ResNet50_FPN	0.168	91.53	84.59
ResNet50_U-Net	0.153	92.27	85.80
ResNet50_PSPNet	0.103	94.48	89.64
ResNet50_FRRN	0.379	**96.73**	**92.56**
MobileNetV2_FPN	**0.100**	94.16	89.11
MobileNetV2_U-Net	0.079	95.20	90.96
MobileNetV2_PSPNet	0.151	91.95	85.31

For dataset 3, lower Loss (0.100) was achieved by MobileNetV2_FPN, while the best F1-score (96.73%) and IU 92.56% reached by ResNet50_FRRN model. From the Table 1, 2, 3, 4, 5 and 6, it is obvious that the performance of the models is higher for dataset 1, then dataset 2. This is attributed to the different quality of the images between datasets 1 and 2.

From the overall experimental results, it seems that in most cases models based on MobileNetV2 network reach comparatively high or higher performances. More specific U-Net, PSPNet and FRRN meta-architectures with MobileNetV2 and ResNet50 achieved the biggest scores in general, for both grapes and leaves classes. However, the highest performance (average IU) is achieved with MobileNetV2_PSPNet (88.21%). This can be attributed to the fact that PSPNet needs image resolution divisible by 48, e.g. 192 $\times$ 192, 240 $\times$ 240, 288 $\times$ 288 etc. In our case, all networks were trained with image size of 224 $\times$ 224, while the nearest permissible resolution to that, that is 240 $\times$ 240, was used

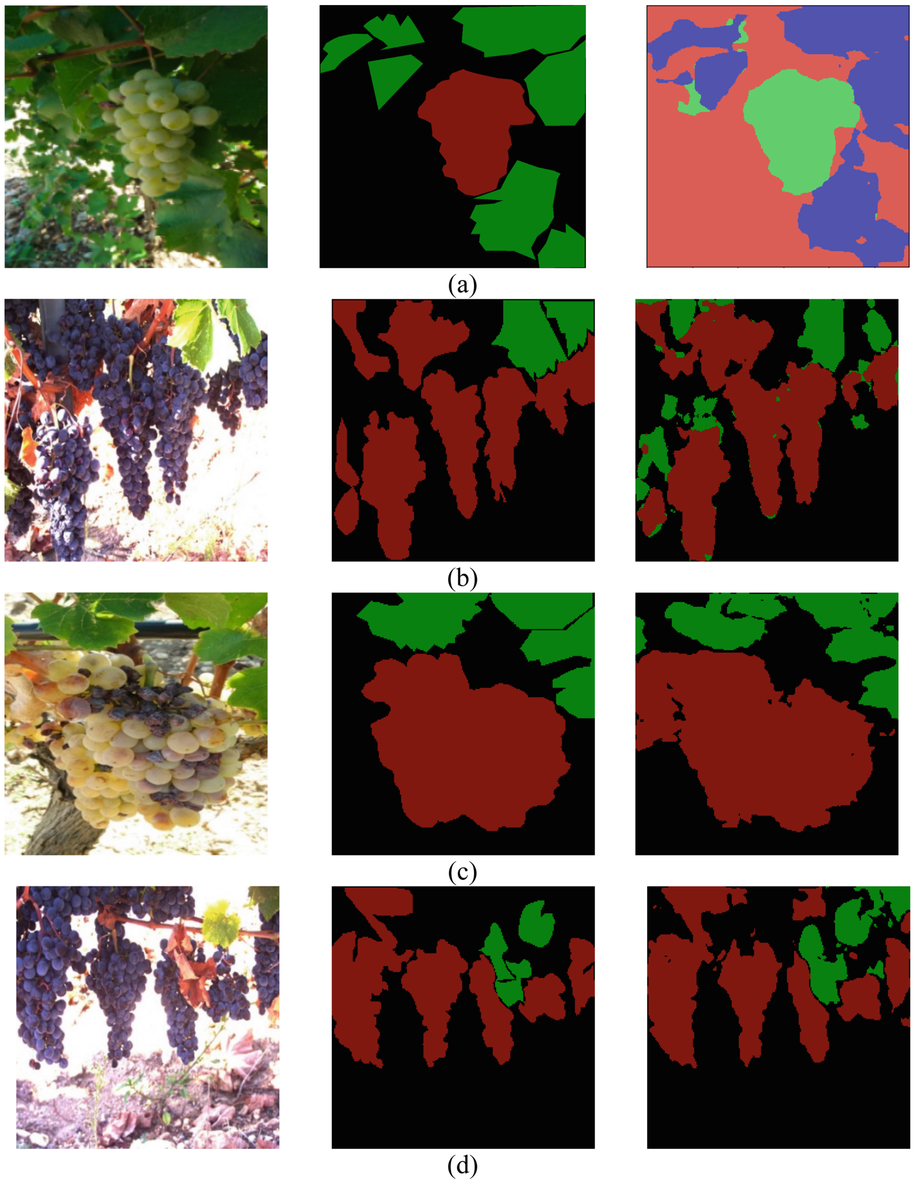

Fig. 2. Qualitative results from the testing (a) dataset 1 with MobilNetV2_PSPNet model, (b) dataset 2 with ResNet50_FRRN model and (c), (d) dataset 3 with ResNet50_FRRN model. From left to right: input RGB image, ground truth image and segmented image.

for the PSPNet. As it comes to the restriction of the 224 $\times$ 224 resolution for the rest of the models, this is due to the fact that our datasets consist of an insufficient number of photos to train the models from the beginning, so pretrained models, that required image size of 224 $\times$ 224, where used. When comparing the examined networks in terms of computational time, all models need 26–32 s average time per epoch, while the three combinations with MobileNetV2 need less time; 14–21 s average time per epoch. This is due to the light weighted architecture of MobileNetV2. Time is crucial when it comes to real-time applications, especially in our case, where the optimal model is intended to run on a Jetson TX2 for in-field segmentation by a harvesting robot. Figure 2 displays the image of each dataset from the testing dataset with the best segmented performance in terms of average IU, as reported in Tables 1, 2 and 3, alongside the corresponding ground truth image and the segmented final image.

4 Conclusions

In this paper, the task of semantic segmentation of vineyard images using convolutional neural networks was studied. For this purpose, a modular design framework that enables the creative combination of three different feature learning sub-networks and five meta-architectures was applied. In total, eleven different models were evaluated to three datasets with vineyard images and they compared to each other in terms of segmentation accuracy. The applied benchmarking framework provides researchers and practitioners with a means to evaluate design choices for their task in the frame of viniculture, and more particularly for grape and leaves segmentation. The latter segmentation task is the first step for the development of an autonomous robot able to discriminate grapes and leaves on the spot, towards automating agricultural tasks such as harvest, green harvest and defoliation. Future work includes training and testing the networks using more in-field images captured from the mounted cameras of the Agrobot.

Acknowledgment. This research has been co-financed by the European Union and Greek national funds through the Operational Program Competitiveness, Entrepreneurship and Innovation, under the call RESEARCH – CREATE – INNOVATE (project code: T1EDK-00300).

References

1. Xue, J., Zhang, L., Grift, T.E.: Variable field-of-view machine vision based row guidance of an agricultural robot. Comput. Electron. Agric. **84**, 85–91 (2012). https://doi.org/10.1016/j.compag.2012.02.009
2. Søgaard, H.T., Lund, I.: Application accuracy of a machine vision-controlled robotic micro-dosing system. Biosyst. Eng. **96**, 315–322 (2007). https://doi.org/10.1016/j.biosystemseng.2006.11.009
3. Mavridou, E., Vrochidou, E., Papakostas, G.A., Pachidis, T., Kaburlasos, V.G.: Machine vision systems in precision agriculture for crop farming. J. Imaging **5**, 89 (2019). https://doi.org/10.3390/jimaging5120089
4. LeCun, Y., Kavukcuoglu, K., Farabet, C.: Convolutional networks and applications in vision. In: Proceedings of 2010 IEEE International Symposium on Circuits and Systems, pp. 253–256. IEEE (2010). https://doi.org/10.1109/ISCAS.2010.5537907
5. Long, J., Shelhamer, E., Darrell, T.: Fully convolutional networks for semantic segmentation. In: 2015 IEEE Conference on Computer Vision and Pattern Recognition (CVPR), pp. 3431–3440. IEEE (2015). https://doi.org/10.1109/CVPR.2015.7298965

6. Chatfield, K., Simonyan, K., Vedaldi, A., Zisserman, A.: Return of the devil in the details: delving deep into convolutional nets. In: Proceedings of the British Machine Vision Conference 2014, pp. 6.1–6.12. British Machine Vision Association (2014). https://doi.org/10.5244/C.28.6
7. Szegedy, C., Wei Liu, Yangqing Jia, Sermanet, P., Reed, S., Anguelov, D., Erhan, D., Vanhoucke, V., Rabinovich, A.: Going deeper with convolutions. In: 2015 IEEE Conference on Computer Vision and Pattern Recognition (CVPR), pp. 1–9. IEEE (2015). https://doi.org/10.1109/CVPR.2015.7298594
8. Krizhevsky, A., Sutskever, I., Hinton, G.E.: ImageNet classification with deep convolutional neural networks. Commun. ACM **60**, 84–90 (2017). https://doi.org/10.1145/3065386
9. Badeka, E., Kalabokas, T., Tziridis, K., Nicolaou, A., Vrochidou, E., Mavridou, E., Papakostas, G.A., Pachidis, T.: Grapes visual segmentation for harvesting robots using local texture descriptors. In: 12th International Conference on Computer Vision Systems (ICVS 2019), pp. 98–109 (2019). https://doi.org/10.1007/978-3-030-34995-0_9
10. Rudolph, R., Herzog, K., Töpfer, R., Steinhage, V.: Efficient identification, localization and quantification of grapevine inflorescences and flowers in unprepared field images using fully convolutional networks. Vitis J. Grapevine Res. **58**(3), 95–104 (2019). https://doi.org/10.5073/vitis.2019.58.95-104
11. Mei, S., Ji, J., Bi, Q., Hou, J., Du, Q., Li, W.: Integrating spectral and spatial information into deep convolutional neural networks for hyperspectral classification. In: 2016 IEEE International Geoscience and Remote Sensing Symposium (IGARSS), pp. 5067–5070. IEEE (2016). https://doi.org/10.1109/IGARSS.2016.7730321
12. Kangune, K., Kulkarni, V., Kosamkar, P.: Grapes ripeness estimation using convolutional neural network and support vector machine. In: 2019 Global Conference for Advancement in Technology (GCAT), pp. 1–5. IEEE (2019). https://doi.org/10.1109/GCAT47503.2019.8978341
13. . Li, N., Wang, C., Zhao, H., Gong, X., Wang, D.: A novel deep convolutional neural network for spectral-spatial classification of hyperspectral data. Int. Arch. Photogramm. Remote Sens. Spat. Inf. Sci. ISPRS Arch. **42**, 897–900 (2018). https://doi.org/10.5194/isprs-archives-XLII-3-897-2018
14. Zhao, L., Li, Q., Zhang, Y., Wang, H., Du, X.: Integrating the continuous wavelet transform and a convolutional neural network to identify vineyard using time series satellite images. Remote Sens. **11**, 2641 (2019). https://doi.org/10.3390/rs11222641
15. Monga, T.: Estimating vineyard grape yield from images. In: Lecture Notes in Computer Science (Lecture Notes in Artificial Intelligence and Lecture Notes in Bioinformatics), pp. 339–343 (2018). https://doi.org/10.1007/978-3-319-89656-4_37
16. Yu, S., Jia, S., Xu, C.: Convolutional neural networks for hyperspectral image classification. Neurocomputing **219**, 88–98 (2017). https://doi.org/10.1016/j.neucom.2016.09.010
17. Personalized Optimal Grape Harvest by Autonomous Robot (POGHAR). http://evtar.eu/
18. Russell, B.C., Torralba, A., Murphy, K.P., Freeman, W.T.: Labelme: a database and web-based tool for image annotation. Int. J. Comput. Vis. **77**, 157–173 (2008). https://doi.org/10.1007/s11263-007-0090-8
19. Wong, S.C., Gatt, A., Stamatescu, V., McDonnell, M.D.: Understanding data augmentation for classification: when to warp? In: 2016 International Conference on Digital Image Computing: Techniques and Applications (DICTA), pp. 1–6. IEEE (2016). https://doi.org/10.1109/DICTA.2016.7797091
20. Mikolajczyk, A., Grochowski, M.: Data augmentation for improving deep learning in image classification problem. In: 2018 International Interdisciplinary Ph.D. Workshop (IIPhDW), pp. 117–122. IEEE (2018). https://doi.org/10.1109/IIPHDW.2018.8388338

21. Gatys, L.A., Ecker, A.S., Bethge, M.: Image style transfer using convolutional neural networks. In: 2016 IEEE Conference on Computer Vision and Pattern Recognition (CVPR), pp. 2414–2423. IEEE (2016). https://doi.org/10.1109/CVPR.2016.265
22. Simonyan, K., Zisserman, A.: Very Deep Convolutional Networks for Large-Scale Image Recognition. In: 3rd International Conference Learning Representations, ICLR 2015, Conference Track Proceedings (2014)
23. He, K., Zhang, X., Ren, S., Sun, J.: Deep residual learning for image recognition. In: 2016 IEEE Conference on Computer Vision and Pattern Recognition (CVPR), pp. 770–778. IEEE (2016). https://doi.org/10.1109/CVPR.2016.90
24. Sandler, M., Howard, A., Zhu, M., Zhmoginov, A., Chen, L.-C.: Mobilenetv2: inverted residuals and linear bottlenecks. In: 2018 IEEE/CVF Conference on Computer Vision and Pattern Recognition, pp. 4510–4520. IEEE (2018). https://doi.org/10.1109/CVPR.2018.00474
25. Lin, T.-Y., Dollar, P., Girshick, R., He, K., Hariharan, B., Belongie, S.: Feature pyramid networks for object detection. In: 2017 IEEE Conference on Computer Vision and Pattern Recognition (CVPR), pp. 936–944. IEEE (2017). https://doi.org/10.1109/CVPR.2017.106
26. Ronneberger, O., Fischer, P., Brox, T.: U-Net: convolutional networks for biomedical image segmentation. In: Lecture Notes in Computer Science (Lecture Notes in Artificial Intelligence and Lecture Notes in Bioinformatics), pp. 234–241 (2015). https://doi.org/10.1007/978-3-319-24574-4_28
27. Zhao, H., Shi, J., Qi, X., Wang, X., Jia, J.: Pyramid scene parsing network. In: 2017 IEEE Conference on Computer Vision and Pattern Recognition (CVPR), pp. 6230–6239. IEEE (2017). https://doi.org/10.1109/CVPR.2017.660
28. Pohlen, T., Hermans, A., Mathias, M., Leibe, B.: Full-resolution residual networks for semantic segmentation in street scenes. In: 2017 IEEE Conference on Computer Vision and Pattern Recognition (CVPR), pp. 3309–3318. IEEE (2017). https://doi.org/10.1109/CVPR.2017.353
29. Siam, M., Gamal, M., Abdel-Razek, M., Yogamani, S., Jagersand, M.: RTseg: real-time semantic segmentation comparative study. In: 2018 25th IEEE International Conference on Image Processing (ICIP), pp. 1603–1607. IEEE (2018). https://doi.org/10.1109/ICIP.2018.8451495
30. Zeiler, M.D.: ADADELTA: an adaptive learning rate method (2012)

Towards a Reliable Face Recognition System

Adamu Ali-Gombe[1](✉), Eyad Elyan[1], and Johan Zwiegelaar[2]

[1] Robert Gordon University, Aberdeen, UK
{a.ali-gombe,e.elyan}@rgu.ac.uk
[2] Mintra Group, Oslo, Norway
johan.zwiegelaar@mintragroup.com
https://www.rgu.ac.uk, https://www.mintragroup.com

Abstract. Face Recognition (FR) is an important area in computer vision with many applications such as security and automated border controls. The recent advancements in this domain have pushed the performance of models to human-level accuracy. However, the varying conditions in the real-world expose more challenges for their adoption. In this paper, we investigate the performance of these models. We analyze the performance of a cross-section of face detection and recognition models. Experiments were carried out without any preprocessing on three state-of-the-art face detection methods namely HOG, YOLO and MTCNN, and three recognition models namely, VGGface2, FaceNet and Arcface. Our results indicated that there is a significant reliance by these methods on preprocessing for optimum performance.

Keywords: Face detection · Face recognition · Deep learning · YOLO

1 Introduction

Face detection and recognition have numerous real-world applications such as person identification and tracking. The real-world environment is typically unconstrained and has been the attention of the computer vision community for some time now. Despite exceeding human performances on test data, FR models hardly meet the requirements in the real-world [28]. Thus, preprocessing steps such as pose augmentation and illumination normalization continue to be crucial especially in mismatched conditions [16]. However, extra preprocessing steps could add delays to real-time recognition.

Majority of the established deep learning face recognition systems consist of three modules namely, a detector module, a pre-processing module and a recognition module [17,19,23]. Established detections model such as Viola and Jones [25], Bob [3] and fiducial detectors [23] are employed to localize the

Supported by InnovateUK, Mintra Group and Robert Gordon University.

L. Iliadis et al. (Eds.): EANN 2020, INNS 2, pp. 304–316, 2020.
https://doi.org/10.1007/978-3-030-48791-1_23

required face area before a recognition model is used. This makes the process reliant on the accuracy of the detection model. The stand-out face recognition models that reported close to or better than human performances are Deepface [17], DeepID [21], VGGFace [5], SpereFace [15], ArcFace [7], CosFace [26] and FaceNet [23].

Although some of the results reported are close to perfect, it was discovered when testing is done at scale, these models' performances degrade considerably [11]. Moreover, these tests were carried out in controlled environments and most of these datasets were carefully curated. Furthermore, the bias in data collection such as ethnicity and race creates skewed model performances [1,2,30]. Again, recognition across wide age gaps is still challenging even for state-of-the-art models with near-perfect results. Other challenges include disguise or individual appearance and variations such as beard, facial expression, and others. Pictorial conditions such as illumination, pose, occlusion due to dressing (wearing a cap or eyeglasses), image quality, etc. [16] and Face spoofing [4] are all considered challenging problems to state-of-the-art FR systems.

In this paper, we perform face detection and recognition using state-of-art models and demonstrate that despite the great successes, challenges still exist in deploying these models in the real-world. Our experiments highlight these challenges and we show that without preprocessing and post-processing such as alignment, illumination normalization and frontalization, models under-performs below the reported results.

The rest of the paper is organised as follows. In Sect. 2, related literature is reviewed and discussed. Section 3 presents the methods used in this work. Section 4 discusses in details experimental set-up and the datasets used. Findings are discussed in Sect. 5. Finally, we conclude and suggest future directions in Sect. 6.

2 Related Works

2.1 Face Detection

While face detection can be achieved using a general detection framework such as Histogram of Oriented Gradients (HOG) [6], You Look Only Once (YOLO) [18], Single Shot Detector (SSD) [14], Region Convolution Neural Network (R-CNN) [9], Max Margin Object Detection (MMOD) [12]; there are specialized face detection frameworks like Multi-Task Cascade CNN (MTCNN) [31], retina face [8] and Face Attention Networks (FAN) [27] built specifically for this purpose. Both categories have merits and the choice of a detector will depend on the application or nature of the data available. That said, specialized detectors benefit from the inclusion of ad-hoc detection pipelines with little to no overhead such as facial landmark detection that could be beneficial in post-processing. Face detection techniques such as HOG, Haar cascade are considered traditional machine learning approaches. Recent face detection techniques such as YOLO, use deep learning model or a Convolutional Neural Network (CNN) as the backbone model. The shift in trend is that fact that traditional approaches require features to be extracted before a machine learning classifier such as an SVM could be trained. Thus, features engineering reduces the generalization of these approaches. Whereas deep learning approaches learn features directly from pixel values over many training iterations thereby, generalizing better to unseen samples.

Haar cascades method [25] is one of the early successes in face detection systems and remains a popular choice. This method introduces the concept of integral images which is calculated based on region neighborhood. Similarly, HOG divides the image into cells with discrete angular bins of gradient orientations. Both are effective and fast but are affected by pose and occlusion or partial face view. These techniques are best suited for frontal faces with fewer pose effects.

Cascade CNN [13] are quite efficient in detecting faces with high visual variation such as pose and facial expressions. This approach performs detection in three different stages at different scales. A combined six CNN are used with three CNNs to determine face candidates and the other three CNNs are for bounding box calibration. Multi-Task Cascade CNN (MTCNN) is an extension of cascade CNN. While both use a cascade of CNNs, MTCNN is much faster and more accurate than the former. RetinaFace [8] added a self-supervised signal using 3D dense face regression alongside identity classification, face and facial landmark regression. According to the authors, the intuition is that since mask prediction in Mask-RCNN improved localization, then additional supervisory signal will be just as important in face localization. RetinaFace is a one-stage detector i.e faces are detected in a single go with no branches or sub-networks. Face Attention Network (FAN) [27] adds attention mechanism using a RetinaNet structure with a novel anchor assignment strategy.

Apart from generalizing better, deep learning methods enhance performances through preprocesses such as augmentation, random cropping, hard mining of samples, negative detection and others. Günther *et al.* [10] observed that on open-set detection challenge using UCCS dataset, both TinyFaces, Cascade CNN, YOLO, LBF and LgfNet performed well on face detection. The models were able to detect at least 33000 of the 36153 labeled test faces. However, the authors observed this was at the expense of high false detections. Generally, there is a trade-off between speed and accuracy when choosing a detector. Deep learning-based detectors are more accurate but are slower than traditional approaches such as HOG, but traditional approaches are less accurate. The difference in prediction time could be negligible when experimenting with few images or locally but when providing services at scale or remotely, this may be a factor to consider.

2.2 Face Recognition

Face recognition is achieved using a machine learning model by training on either engineered features or raw pixel values. A face recognition model learns an embedding function that brings together similar identities closer in the embedding space irrespective of the image conditions. Deep models in FR share a lot of commonalities and mostly use standards CNNs (such as ResNet, VGG, SENet) as their backbone. Regardless of the model used, deep learning approaches use a classifier [5] on identification task or a distance metric when verification is the task [19].

DeepFace recognition [23] presented an improved recognition approach using 3D face alignment and frontalization technique. The facial alignment was guided by 6 fiducial points and refined by a Support Vector Regressor (SVR). DeepFace achieved identification task using a softmax and the learned model was used as a Siamese network with a chi-squared (χ^2) distance metric as the objective in a verification task. An extension of DeepFace was presented in DeepFace2 [24] which extend the process with bootstrapping (semantic bootstrapping). similarly, VGGface [5] and VGGface2 [17] were trained using softmax.

Deep IDentity features (DeepID) [21] learned identity-related features in a multi-class identification task using multiple CNNs (60). DeepID features are 160-D each and were combined with features from other networks ($160 \times 2 \times 60$). Faces were detected using fiducial detectors and the CNNs were trained on multiple face region crops. DeepID features were found to generalize well to face verification even to unseen faces. This was extended to DeepID2 [20] and DeepID2+ [22] with better network architecture, bigger hidden representations and supervision in convolution layers.

FaceNet [19] used triplet loss with Euclidean distance to train an inception model in image recognition. The approach implemented a triplet batch of two matching pairs and a non-matching sample. To choose the right pairs, FaceNet developed a novel negative exemplar mining of the most difficult triplets during training. In the Euclidean space, identical faces were held at smaller margins while different faces were pushed apart. FaceNet turned out to be highly invariant to illumination and pose on test images.

Arcface [7] utilizes an additive angular margin in obtaining highly discriminative features in face recognition. Essentially, this approaches uses centers which are determined by employing the weights of the last fully connected layer and the embedding after normalization. Extensive experiments were performed on many public datasets and the results obtained showed better performances than other existing approaches. Closely related to this are Sphereface [15] and Cosface [26].

The recent deep models use similar backbones and what differentiates them most is the training protocol. Some employ a different training function such as a softmax or additive angular margin loss or even a distance measure. All these approaches present compelling evidence on the choices made. These choices in some literature show some dependency on the task, for instance, FaceNet employed a triplet loss on their verification task which is quite logical. However, VGGface2 was trained using softmax but the model also showed comparable results on verification when the model was used as a face features and a face similarity is evaluated.

3 Methods

Three detector models considered in this paper, these are; YOLO, MTCNN and HOG. The choice of these is to compare the performance of a general-purpose detector, a specialized detector, and a mix of deep learning model and traditional machine learning models. Three face recognition models were considered namely: VGG2faces, Arcface and Facenet, All of which are deep models. Thus, this gives us a cross-section of loss flavors that is; a VGG2face trained using softmax, an Arcface model trained using additive angular margin and a Facenet trained on triplet loss.

The first detector considered is HOG. HOG is a general detector and relies on image structure to perform detection. HOG first divides the images into local regions/grids and evaluate the gradient and orientation of pixels within these regions. Then a histogram is generated from each region. Gradients are changes in intensities along the x and y directions both of which are evaluated to be the magnitude at that pixel. The orientation is the gradients angle. An image histogram is then generated from each region/grid using these two values. Gradient normalization is usually applied to minimize the effect of illumination in the process. Equations 1, 2, 3, 4 shows how the total gradient and orientation angle is calculated.

$$g_{x_i} = x_{(i+1)} - x_{(i-1)} \tag{1}$$

$$g_{y_i} = y_{(i+1)} - y_{(i-1)} \tag{2}$$

$$G = \sqrt{g_{x_i}^2 + g_{y_i}^2} \tag{3}$$

$$\phi = \arctan(g_{y_i}/g_{x_i}) \tag{4}$$

The second detector is YOLO which uses a CNN backbone and detect/classify objects in a single pass. This feature improves the speed of detection in real-time application. YOLO performs detection by subdividing an image into grid cells. Each grid cell outputs a bounding box, a confidence score and a class. The confidence is a measure of how accurate the model thinks an object exists within the cell. The bounding box is center of the object with width and height relative to the entire image. The cumulative loss is calculated as shown in Eq. 5.

$$
\begin{aligned}
L = \lambda_{coord} \sum_{i=0}^{s^2} \sum_{j=0}^{B} l_{ij}^{obj} [(x_i - \hat{x_i})^2 + (y_i - \hat{y_i})^2] \\
+\lambda_{coord} \sum_{i=0}^{s^2} \sum_{j=0}^{B} l_{ij}^{obj} [(\sqrt{w_i} - \sqrt{\hat{w_i}})^2 + (\sqrt{h_i} - \sqrt{\hat{h_i}})^2] \\
+ \sum_{i=0}^{s^2} \sum_{j=0}^{B} l_{ij}^{obj} (C_i - \hat{C_i})^2 \\
+\lambda_{noobj} \sum_{i=0}^{s^2} \sum_{j=0}^{B} l_{ij}^{noobj} (C_i - \hat{C_i})^2 \\
+ \sum_{i=0}^{s^2} l_i^{obj} \sum_{c \in classes} (p_i(c) - \hat{p_i}(c))^2
\end{aligned}
\tag{5}
$$

Where l_i^{obj} denotes the presence of object in cell i, l_{ij}^{obj} the jth bounding box in cell i, C is a set of classes with $p(c)$ probability, B is the set of bounding boxes, S^2 is the grids and x, y, w, h are coordinates.

Our final detector is MTCNN. This method employs online hard mining of samples to improve detection. These samples are positive face samples, negative face samples and partial faces. Detection is achieved in three-stages with three different CNNs from a coarse to fine-grained detection (P-Net, R-Net and O-Net). The first stage, P-Net, proposes candidate faces which are graded using bounding box regression and Non-Maxima Suppression (NMS) to get the high likely face candidates. The second stage is used to isolate false candidates through NMS and bounding box regression. The final stage applies supervision in learning the correct face regions. The supervision signal is a face classification and the overall loss is the sum of the Eqs. 6 and 7.

$$L_i^{det} = -(y_i^{det} \log(p_i) + 1 - y_i^{det}(1 - \log(p_i))) \tag{6}$$

$$l_i^{box} = ||\hat{y}_i^{box} - y_i^{box}||_2^2 \tag{7}$$

where y_i are ground truths and $p_i, \hat{y}$ are the network outputs.

3.1 Face Recognition

Different loss functions are employed in this domain that captures the similarities between image pairs or sometimes the popular probabilistic based softmax functions. The basic idea in these losses is somewhat similar but newer losses provide better parameter handling and samples combination [28]. Losses may be task-dependent, that is whether the target is an open-set or a closed-set recognition.

VGGface2 relies on a simple softmax classifier to train a ResNet for face identification task. Because of the size of the network and dataset, VGGFace learns to separate samples of different identities and brings closet samples from the same identity in the embedding space.

FaceNet uses a triplet loss to achieve face verification. The triplet loss function makes use of an anchor image x^a, positive image x^p and a negative image x^n. The loss maximizes the distance between the anchor and a negative image while minimizing the distance between the anchor and the positive sample. However, the models require the right anchor, positive, negative batch combinations for best performance. Equation 8 shows how the triplet loss is evaluated.

$$L = ||f(x_i^a) - f(x_i^p)||_2^2 + \alpha < ||f(x_i^a) - f(x_i^n)||_2^2 \tag{8}$$

Where α is a margin hyper-parameter.

Arcface uses an additive angular margin to penalizes the loss based on a geodesic distance between samples in a hyper-sphere using an arc-cosine function. This is an extension of angular softmax. Angular softmax (A-softmax) [26] adds a constraint in the hypersphere to learn better discriminative features in face recognition. A-softmax is more efficient than traditional softmax because it adopts a different decision boundary for each class. Equation 9 shows how the additive angular margin is calculated.

$$L_{arcface} = -\frac{1}{N}\sum_{i=1}^{N}\log\frac{e^{s(\cos(\theta_{y_i}+m))}}{e^{s(\cos(\theta_{y_i}+m))}+\sum_{i=i,j\neq y_i}^{n}e^{s\cos\theta_j}} \tag{9}$$

Where s is the scale of the embedding and m is the margin (kept at 0.5).

4 Experiment

4.1 Datasets

Experiments were carried on two datasets namely, Wider face [29] & VGG2 [5]. Wider face is a popular benchmark for face detection in an uncontrolled environment. It contains faces with high variations in scale, pose, occlusion and illumination. The choice of the dataset is because it captures all the ideal scenarios for a face detection task in the wild. Wider face contains 32,203 images with 393,703 labeled faces. The dataset is split into a train, validation and a test set (40-10-50 split). The train set was used to train detectors and the validation set was kept as a hold out for evaluation. Results were reported on the validation set because we do not have access to the test set ground truth.

VGG2 Dataset is a large scale face recognition dataset with about 3.3 m images. Images are taken in a more controlled environment but some pictures contain multiple faces, occlusion and varying light conditions. VGG2 has many samples per identity. The dataset is split across 8631 identities in the training set and 500 identities in the test set. Both of these sets are disjoint, making the dataset ideal for facial verification task. For our recognition task, the test set is kept as a hold-out for evaluation.

4.2 Experimental Set-Up

The detector models (HOG, MTCNN, YOLO) were trained using wider face dataset. Our HOG detector is based on the implementation in Dlib library, details can be found here[1]. Wider Face annotations were converted to XML using a python script. For MTCNN, we used a pre-trained model available at[2] which was also trained on wider face. YOLO version 3 model was trained on Wider Face following the protocol specified in[3]. Annotations were first converted to YOLO standards then, new filters and anchor boxes were evaluated before training. We used a batch size of 64 and subdivision of 16, and training was stopped when the loss remained unchanged for many iterations. In all experiments, no further pre-processing was applied to data apart from augmentation and sampling/mining techniques peculiar to the models. The models were evaluated on the test set on the number of correctly detected faces and a positive detection is considered if the IOU is over 0.4.

The recognition models (Arcface, VGGFace and FaceNet) were trained on VGG2 dataset. Prior to training, the face area was cropped out from the images using the bounding box information provided. All models were trained using a ResNet-50 backbone. The Arcface model was obtained from the authors official GitHub repository[4]. No age prediction or LFW dataset verification was employed during training. We only used a validation set for verification after 2000 batches. The training was terminated when the error rate was less than zero when the validation and training accuracies are almost the same. We trained FaceNet model using the Arcface repository but changed the loss function to a triplet loss and all other settings remain thesame. We used a pre-trained VGGface model from[5] which was trained on thesame dataset and ResNet-50 model. These models were evaluated on face crops from the test data with no further facial alignment or augmentation done. This is to give us a better understanding of the actual performance or effect of the approaches used in training the models.

Testing was carried out by generating image pairs from the test set. Using ten folds, a total of 100k pairs were generated with 50% negative matches in the pairs. The models were evaluated by measuring the True Accept Rate (TAR), False Accept Rate (FAR) and False Reject Rate (FRR). These metrics were calculated using Eqs. 10, 11 and 12. At test time, the models were used to extract facial embeddings from pairs. A correct match is measured using cosine similarity between these facial embeddings. A threshold of 0.5 was chosen and all faces with similarity less than or equal to the threshold are considered a match. The threshold value was chosen from repeated experimentation.

$$TAR = \frac{matches}{samplesize} \tag{10}$$

1 https://github.com/davisking/dlib.
2 https://pypi.org/project/mtcnn/.
3 https://github.com/pjreddie/darknet.
4 https://github.com/deepinsight/insightface.
5 https://github.com/WeidiXie/Keras-VGGFace2-ResNet50.

$$FAR = \frac{falseacceptance}{samplesize} \tag{11}$$

$$FRR = \frac{falserejections}{samplesize} \tag{12}$$

5 Discussion

Table 1 shows the detection performances from each model. HOG detection had the lowest false detection rate of 1.32% with YOLO and MTCNN at 8.95% and 5.04% respectively. This is not surprising given the number of detected samples. HOG detector struggled to detect face because of the varying image conditions in the dataset. As seen in Fig. 1, HOG detector is affected significantly by scale, pose and occlusion.

YOLO is a general detector but shows robustness in this challenging domain. YOLO performed significantly better than HOG. From the sample detection in Fig. 1, we can see that Partial face view or partial occlusion do not affect YOLO. However, it struggles with considerable occlusion. Also, it had the worst false detection rate among the models. This may indicate that it sometimes finds it difficult to distinguish the background from faces. YOLO re-scale images in training and this is meant to improve detection of smaller objects. But we discovered that some small and blurry faces were also missed.

MTCNN detected more faces than the other detectors in this experiment. It also had a low false detection rate which demonstrates the benefits of training on negative samples. The model is also not affected by scale or partial occlusion. However, we observed that there were instances when partial faces were missed.

Generally, all the models show good IOU on the detected faces. The high average IOU returned by these models suggest reliability in these challenging circumstances. That said, none of the detectors achieved over 50% detection with IOU threshold of over 0.4.

Table 1. Face detection performances

Model	Ground truth	Detected faces	False detections	Average IOU
HOG	39708	5774	76	0.69
YOLO	39708	14846	1328	0.62
MTCNN	39708	17047	860	0.73

Table 2. Face recognition performances

Model	TAR	FAR	FRR
VGGface2	86.27	0.15	13.58
FaceNet	84.97	0.13	14.90
Arcface	88.13	1.25	10.62

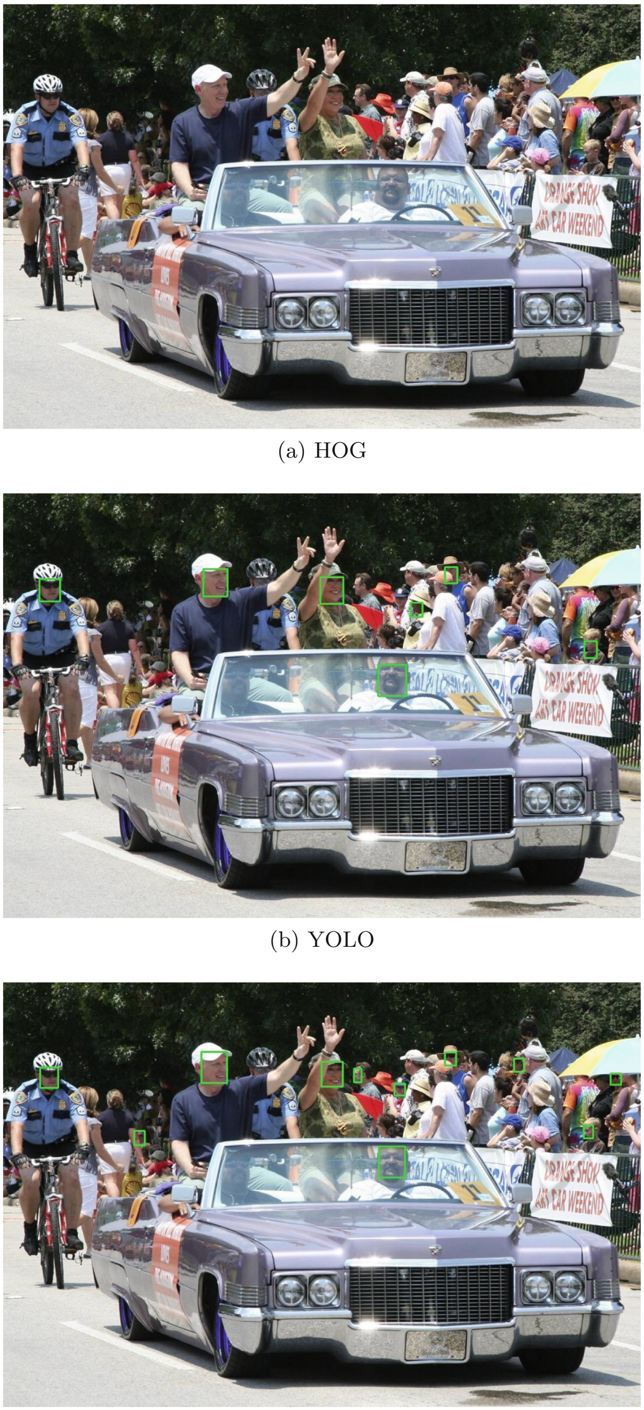

(a) HOG

(b) YOLO

(c) MTCNN

Fig. 1. Sample face detection output from the three detection models

Tables 2 shows the performances of the face recognition models. All models had a very low false acceptance rate. This points to the facts that there was a clear separation of dissimilar samples by the models in the embedding space. However, the number of false rejections is significantly high. This is could be associated with the varying image conditions in the dataset used. We observed that some of the false rejection were due to pose angle and partial faces.

In this experiment, both VGGface2 and Arcface generated better embeddings than FaceNet. This shows that the two models trained using variants of softmax produced better facial features that the model trained on triplets. But this was at the expense of a slightly higher false acceptance rate. That said, the performances were generally below expectations and demonstrate the reliance of these model of preprocessing to achieve optimum performances.

Furthermore, one may argue that the metric or threshold value chosen could have played a part. However, when face alignment was introduced as a preprocessing step in a different experiment, the TAR increased by almost 9% across board. Thus, there is little connection between the threshold or metric and the performance. And this indicates that preprocessing continue to be significant in face recognition models.

6 Conclusion

In this paper, we analyze the performances of established face detection and recognition models. Experiments were conducted to compare models trained on a common dataset and the same recognition task. The performances of these models were evaluated using different metrics and the results indicated that optimum performance can be obtained only when extra preprocessing steps are carried out. These techniques are domain-specific and may create an overhead on the overall system and this may hinder their uses in real-time applications. This work opens a new research direction on the need for methods that rely less on preprocessing for optimum performances.

References

1. Ali-Gombe, A., Elyan, E.: MFC-GAN: class-imbalanced dataset classification using multiple fake class generative adversarial network. Neurocomputing **361**, 212–221 (2019)
2. Ali-Gombe, A., Elyan, E., Jayne, C.: Multiple fake classes GAN for data augmentation in face image dataset. In: 2019 International Joint Conference on Neural Networks (IJCNN)
3. Anjos, A., El-Shafey, L., Wallace, R., Günther, M., McCool, C., Marcel, S.: Bob: a free signal processing and machine learning toolbox for researchers. In: Proceedings of the 20th ACM International Conference on Multimedia. ACM (2012)
4. Boulkenafet, Z., Komulainen, J., Hadid, A.: Face spoofing detection using colour texture analysis. IEEE Trans. Inf. Forensics Secur. **11**, 1818–1830 (2016)
5. Cao, Q., Shen, L., Xie, W., Parkhi, O.M., Zisserman, A.: VGGFace2: a dataset for recognising faces across pose and age. In: 13th IEEE International Conference on Automatic Face and Gesture Recognition (FG 2018) (2018)

6. Dalal, N., Triggs, B.: Histograms of oriented gradients for human detection. In: IEEE Computer Society Conference on Computer Vision & Pattern Recognition (2005)
7. Deng, J., Guo, J., Xue, N., Zafeiriou, S.: ArcFace: additive angular margin loss for deep face recognition. In: Proceedings of the IEEE Conference on CVPR (2019)
8. Deng, J., Guo, J., Zhou, Y., Yu, J., Kotsia, I., Zafeiriou, S.: RetinaFace: single-stage dense face localisation in the wild. arXiv preprint arXiv:1905.00641 (2019)
9. Girshick, R., Donahue, J., Darrell, T., Malik, J.: Region-based convolutional networks for accurate object detection and segmentation. IEEE Trans. Pattern Anal. Mach. Intell. **38**, 142–158 (2015)
10. Günther, M., et al.: Unconstrained face detection and open-set face recognition challenge. In: IEEE International Joint Conference on Biometrics (IJCB) (2017)
11. Kemelmacher-Shlizerman, I., Seitz, S.M., Miller, D., Brossard, E.: The MegaFace benchmark: 1 million faces for recognition at scale. In: Proceedings of the IEEE Conference on Computer Vision and Pattern Recognition (2016)
12. King, D.E.: Max-margin object detection. arXiv preprint arXiv:1502.00046 (2015)
13. Li, H., Lin, Z., Shen, X., Brandt, J., Hua, G.: A convolutional neural network cascade for face detection. In: Proceedings of the IEEE Conference on Computer Vision and Pattern Recognition (2015)
14. Liu, W., Anguelov, D., Erhan, D., Szegedy, C., Reed, S., Fu, C.Y., Berg, A.C.: SSD: Single shot multibox detector. In: European Conference on Computer Vision (2016)
15. Liu, W., Wen, Y., Yu, Z., Li, M., Raj, B., Song, L.: SphereFace: deep hypersphere embedding for face recognition. In: Proceedings of the IEEE Conference on Computer Vision and Pattern Recognition (2017)
16. Mehdipour Ghazi, M., Kemal Ekenel, H.: A comprehensive analysis of deep learning based representation for face recognition. In: Proceedings of the IEEE Conference on Computer Vision and Pattern Recognition Workshops, pp. 34–41 (2016)
17. Parkhi, O.M., Vedaldi, A., Zisserman, A., et al.: Deep face recognition. In: BMVC, vol. 1, p. 6 (2015)
18. Redmon, J., Divvala, S., Girshick, R., Farhadi, A.: You only look once: unified, real-time object detection. In: Proceedings of the IEEE Conference on Computer Vision and Pattern Recognition (2016)
19. Schroff, F., Kalenichenko, D., Philbin, J.: Facenet: a unified embedding for face recognition and clustering. In: Proceedings of the IEEE Conference on Computer Vision and Pattern Recognition, pp. 815–823 (2015)
20. Sun, Y., Chen, Y., Wang, X., Tang, X.: Deep learning face representation by joint identification-verification. In: Advances in Neural Information Processing Systems, pp. 1988–1996 (2014)
21. Sun, Y., Wang, X., Tang, X.: Deep learning face representation from predicting 10,000 classes. In: Proceedings of the IEEE Conference on Computer Vision and Pattern Recognition, pp. 1891–1898 (2014)
22. Sun, Y., Wang, X., Tang, X.: Deeply learned face representations are sparse, selective, and robust. In: Proceedings of the IEEE Conference on Computer Vision and Pattern Recognition, pp. 2892–2900 (2015)
23. Taigman, Y., Yang, M., Ranzato, M., Wolf, L.: DeepFace: closing the gap to human-level performance in face verification. In: Proceedings of the IEEE Conference on Computer Vision and Pattern Recognition, pp. 1701–1708 (2014)
24. Taigman, Y., Yang, M., Ranzato, M., Wolf, L.: Web-scale training for face identification. In: Proceedings of the IEEE Conference on CVPR (2015)

25. Viola, P., Jones, M.J.: Robust real-time face detection. Int. J. Comput. Vis. **57**(2), 137–154 (2004)
26. Wang, H., Wang, Y., Zhou, Z., Ji, X., Gong, D., Zhou, J., Li, Z., Liu, W.: CosFace: large margin cosine loss for deep face recognition. In: Proceedings of the IEEE Conference on Computer Vision and Pattern Recognition (2018)
27. Wang, J., Yuan, Y., Yu, G.: Face attention network: an effective face detector for the occluded faces. arXiv preprint arXiv:1711.07246 (2017)
28. Wang, M., Deng, W.: Deep face recognition: a survey. arXiv:1804.06655 (2018)
29. Yang, S., Luo, P., Loy, C.C., Tang, X.: Wider face: a face detection benchmark. In: IEEE Conference on Computer Vision and Pattern Recognition (CVPR) (2016)
30. Zeng, Y., Lu, E., Sun, Y., Tian, R.: Responsible facial recognition and beyond. arXiv preprint arXiv:1909.12935 (2019)
31. Zhang, K., Zhang, Z., Li, Z., Qiao, Y.: Joint face detection and alignment using multitask cascaded convolutional networks. IEEE Signal Process. Lett. **23**, 1499–1503 (2016)

Machine Learning in Medical Systems and Applications

Automated Screening of Patients for Dietician Referral

Kamran Soomro and Elias Pimenidis(✉)

Computer Science Research Centre, University of the West of England, Bristol, UK
{kamran.soomro,elias.pimenidis}@uwe.ac.uk

Abstract. Critical Care Units (CCU) in a hospital treat the severely sick patients that need constant monitoring and close medical attention. Feeding patients, enteral feeding in particular, is a critical and continuous process. Monitoring patients, managing their feeding and referring to a dietician is a key factor in CCUs. Screening patients for referral to a dietician in a CCU is an error-prone and complicated task. One of the main challenges in this regard is that the data needed to screen patients is scattered among many different variables and textual forms. The number of patients being treated in the CCU is also a significant problem since it becomes difficult for the staff to keep track of the needs of all patients. Therefore, an automated screening tool can support effectively the feeding process and contribute considerably towards improving the quality and consistency of patient care. In this paper we present early stages of a project that aims at using machine learning techniques to help CCU consultants to automatically screen patients for dietician referral.

Keywords: Automated patient screening · CCU screening · Dietician referral · Patient data processing

1 Introduction

This paper presents the early stages of a project that aims at using Artificial Intelligence to analyse data collected in the critical care units (or intensive care units) of a National Health Service (NHS) hospital in the UK. Critical Care Units (CCUs) are where the sickest patients are admitted and where large amounts of detailed clinical data are collected (usually hourly) for the duration of the patient's stay. Most CCUs, have moved from paper to clinical information systems to capture data from the patients' monitor, ventilator and other equipment into an extensive database. Currently, CCUs are not using these systems and data to their advantage, with much of the captured data left unanalysed. In an era of limited NHS resources, these digital resources have the potential to both optimise patient outcomes and make systems more efficient and effective.

Supported by the University of the West of England, Bristol.

Data analysis and machine learning systems have been used widely in CCUs, primarily to automate processes where problems are well known and fully defined, and there the deliverables to efficiency and accuracy achieved are well within the expected levels [1,7].

CCUs aim to optimise the patients' survival, clinical outcomes and to reduce harm caused by therapies. All CCUs have recognised targets to improve outcomes, such as maintaining an optimal sedation level, maintaining lung volumes delivered by the ventilator within a specific range and delivering a minimum amount of nutrition to patients whilst they are critically ill. Yet, these targets are often not achieved. This study aims to use these common targets to assess the feasibility of using this clinical data routinely collected can be used to improve the achievement of these targets.

The aim of this project is to determine how routine clinical data collected in CCUs can be used to optimise patient outcomes by augmenting clinician decision making and altering clinician behaviour to optimise patient clinical outcomes.

This study will focus on optimising three common clinical targets: sedation level, mechanical ventilation and enteral nutrition in patients of all ages requiring intensive care. These interventions have been selected because they can be defined regardless of age; and are known to be poorly met in practice [8,9]. Data produced by the clinical information system at the CCUs has been studied to determine its quality and suitability for exposure to advanced analysis techniques. Data has been filtered and cleaned to develop a suitable experimental repository that is compatible with further analysis techniques. The data will be mined to reveal potential associations that will enhance the detail, quality and significance of the information that could be passed on to the clinicians at the CCUs.

1.1 Aims and Project Plan

The collected data has been formatted in a way that allows for it to be uniform, easily stored and accessed in an efficient way. The formatting and cleaning of the data will allow for the results of processing to return outputs that are consistent in the nature and format of the output, can be interpreted consistently over the same organisational criteria, guaranteeing that outcomes are compatible throughout time. This phase will determine which of the data elements produced by the clinical information system will be useful for further processing and suitable for delivering coherent outcomes. All patient data has been anonymised in accordance to the ethics of the NHS in the UK and in accordance to the UK Data Protection Act which encompasses the GDPR.

Data will be stored in repositories that are only accessible to the members of the team of this project. The processing at this initial stage will involve data mining techniques that will aim to reveal hidden associations within the data. These will be explored as to being consistent over time, i.e. the same types of associations confirmed over different data batches. The analysis will also explore the logic of the associations revealed as to whether these are relevant to the aims of the clinicians, i.e. whether the extracted context in the data associations is suitable to support decision making in the target areas that have been identified for this project. These conclusions will allow, the members of the project team working on the analysis of the data, to carefully select among the data produced those elements that will support meaningful further processing. Thus, the volume of data that will be utilised for the next stage of the research will be those reduced to those data that will contribute directly to meeting the aims of this project, by processing via advanced Artificial Intelligence techniques.

For the next phase of the work, different machine learning techniques and algorithms will be utilised. The aim here will be to process the data items selected in the previous phase of the analysis to allow the work team and the participating clinicians to assess the efficiency and effectiveness of these techniques and algorithms. The data that has been cleaned, prepared and formatted at the initial phase will be split into training and test sections, with the formal used to train the machine learning algorithms and the latter to attempt to reproduce known results. The accuracy and efficiency, of the algorithms that will be exposed to this experimental data, will be assessed by the project team. Decisions as to the usefulness of each of the techniques explored will be made; if deemed necessary, the clinicians will provide additional patient case data to assist resolving the suitability of these techniques. On completion of this phase of processing and testing, results and conclusions will be reviewed by the project team to assess their usefulness and the potential of expanding this research further to a full scale system. Such a system will be engaged to process data in real time and aim to support decisions made by the clinicians, by drawing away the complexity of processing rich and voluminous data and providing the benefits of data associations that will support faster and more accurate decision making the CCU clinicians.

One of the most urgent needs in any CCU is that of screening and managing a patient's enteral feeding [4]. There could be complications in a patient's health that could lead to a reaction to feeding at any time during the day. These would in turn lead to decisions in changing the patient's feeding patterns, stopping feeding temporarily, or referring the patient to a dietician for further assessment. Screening is complicated due to the sources and types of data that have to be considered at very frequent intervals, the number of nursing staff available to do so and the impact it could have on the overall treatment of the patient. This has been identified as a first priority in this project.

2 The Problem

After consultation with CCU consultants, one of the problems identified to be targeted within this project is the screening of patients for referral to dieticians. The main problem in this regard is that there are numerous factors to consider. These include:

1) Patient Body Mass Index less than 18.5 kg/m^2.
2) Patient received little or no nutrition for 5 days or more.

3) Patient has been admitted in critical care ≥3 days and receiving enteral tube feeding as per protocol.
4) Patient received Jejunal tube feeding.
5) Patient received renal replacement therapy (intermittent or continuous) 3 days or more.
6) Patient has liver disease.
7) Patient has Pancreatitis.
8) Patient has Chyle leak.
9) Patient has significant short bowel resections and/or high output ileostomy.
10) Pressure has ulcer category 2 or above.
11) Health professionals have concerns regarding nutrition.

Determining whether a patient needs referral to a dietician requires subjective assessment by the clinicians based on these factors. The issue is further complicated by the fact that this information is not directly recorded. It either needs to be inferred from various attributes recorded in the patient history or from the text-based patient history. For example, whether a patient has liver disease or not is not directly recorded anywhere. A consultant can look at an attribute such as the patient's Albumin or Bilirubin levels and determine that the patient has liver problems, though this would still not indicate if the problems are chronic or acute [3]. That aspect is only recorded in the patient history.

The aforementioned complications present significant challenges in the automation of the nutritional screening process. Therefore, the first challenge in developing such a system is to synthesise the variables that can be fed into an appropriate learning algorithm. Different approaches could be adopted for this purpose. For example, for determining the presence of liver disease, one approach could be to perform a fuzzy word match to search the patient history for text related to liver disease. This text could then be analysing using natural language processing to determine if the patient has acute or chronic liver disease. Another approach could be to analyse the patient's Albumin and Bilirubin levels within the algorithm and determine if there are indications of liver disease. However, this approach has the potential pitfall that it analysing such measurements usually requires expert knowledge.

3 The Data

The CCU data is recorded in a Microsoft SQL Server database using a meta-model specifically developed to store the information. Each patient is afforded a *PatientID* upon first encounter with the NHS. Thereafter, each patient visit is recorded as a separate *encounter* with a unique *EncounterID*. This helps to keep track of each unique visit by the patient to the NHS, which may be spread out over time and for different healthcare issues. The NHS database contains a predefined list of *interventions* that may be applied to patients, identified by a unique *InterventionID*. Each intervention further has different *attributes* that can be recorded, each with its own *AttributeID*s. For example, two sample interventions along with their attributes are shown in Fig. 1.

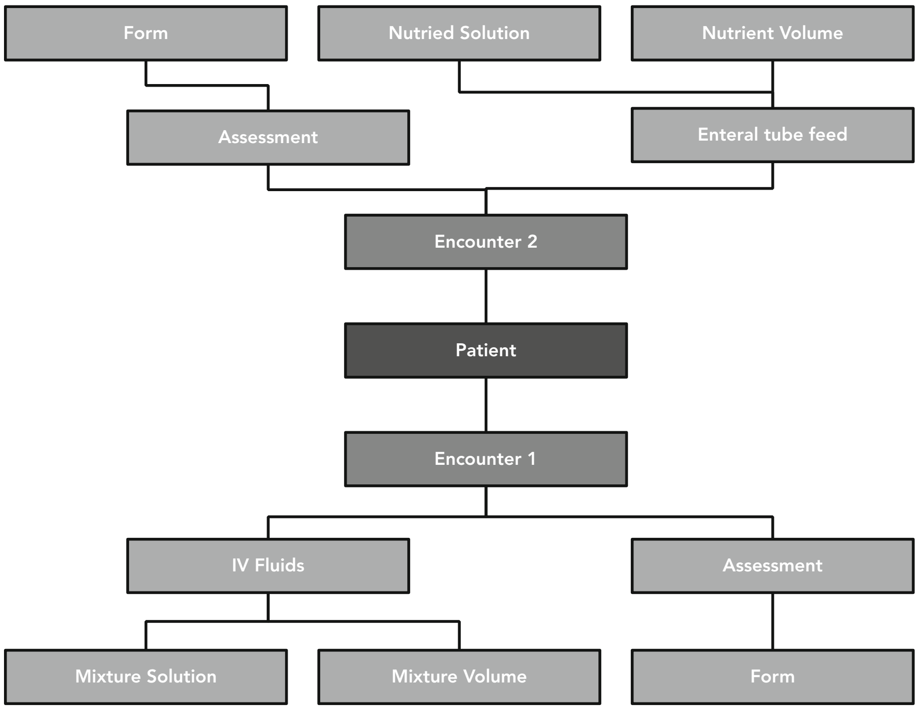

Fig. 1. Simplified NHS data model.

In total the database comprises about 250 GB consisting of data of approximately 5,000 patients. Each *encounter* also has a free-form text field associated with it that contains the CCU consultant's notes about the patient. Furthermore, various patient measurements are also recorded such as weight, height, age, initial diagnosis etc. Some patient attributes such as height and weight are recorded only upon admission and/or discharge and additionally as needed. Other attributes, such as blood pressure, heart rate etc are automatically recorded more frequently by the monitoring equipment on the beds. The exact frequency can be set by the CCU consultants such as half hourly, hourly, daily etc. For the purposes of this project, the complexity arises from the fact that much of the information is recorded in the free-form text fields and is not directly recorded anywhere. For example, to determine whether a patient has received little or no nutrition over the past 5 days, we face the same challenge as with determining if the patient has liver disease. We could either aggregate the nutritional intake information recorded in the database, or use natural language processing techniques to extract the same information from the free-form text field. For the former, there are additional issues such as classifying the nutrition as too little or sufficient. Another issue is that the nutritional intake information is not recorded as a single intervention, but in many different interventions. Careful study and foresight is required to accurately extract the necessary information.

4 Future Work

Going forward we need to carefully consider the aforementioned challenges, and devise appropriate strategies and solutions to address them. Various researchers have attempted to solve these problems in various ways. Some researchers have chosen to adopt a statistical approach [2,6,11]. Others have attempted to use natural language processing to perform real-time screening of patients based on their history [5,10]. However, there appears to be a lack of utilisation of other machine-learning techniques for patient screening. We propose that other techniques such as neural networks can also be used to effectively screen patients for dietician referral. A significant challenge in this regard would be synthesis of the required data for input into the learning algorithm. These aspects will be explored further in the coming months.

Acknowledgements. We would like to acknowledge the support and help provided by Dr Chris McWilliams, Clinicians, Consultants, and other clinical researchers from the Critical Care Unit at Bristol Royal Infirmary.

References

1. Ghassemi, M., Celi, L.A., Stone, D.J.: State of the art review: the data revolution in critical care. In: Vincent, J.L. (ed.) Annual Update in Intensive Care and Emergency Medicine 2015, vol. 2015, pp. 573–586. Springer, Cham (2015)
2. González, C., García-Berrocal, B., Pérez, M., Navajo, J.A., Herraez, O., González-Buitrago, J.M.: Laboratory screening of connective tissue diseases by a new automated ENA screening assay (EliA Symphony) in clinically defined patients. Clinica Chim. Acta **359**(1–2), 109–114 (2005). https://doi.org/10.1016/j.cccn.2005.03.042
3. Hall, P., Cash, J.: What is the real function of the liver 'function' tests? Ulster Med. J. **81**(1), 30–36 (2012)
4. Hansen, C.C., Dissanaike, S.: Nutrition in the intensive care unit. Southwest Respir. Crit. Care Chron. **3**(10), 10–16 (2015). https://pulmonarychronicles.com/index.php/pulmonarychronicles/article/view/195
5. He, Q., Veldkamp, B.P., Glas, C.A.W., de Vries, T.: Automated assessment of patients' self-narratives for posttraumatic stress disorder screening using natural language processing and text mining. Assessment **24**(2), 157–172 (2017). https://doi.org/10.1177/1073191115602551
6. Jeong, S., Yang, H., Hwang, H.: Evaluation of an automated connective tissue disease screening assay in Korean patients with systemic rheumatic diseases. PLOS ONE **12**(3), e0173597 (2017). https://doi.org/10.1371/journal.pone.0173597
7. Lovejoy, C.A., Buch, V., Maruthappu, M.: Artificial intelligence in the intensive care unit. Crit. Care **23**(1), 7 (2019). https://doi.org/10.1186/s13054-018-2301-9
8. Mehta, N.M., Bechard, L.J., Cahill, N., Wang, M., Day, A., Duggan, C.P., Heyland, D.K.: Nutritional practices and their relationship to clinical outcomes in critically ill children–an international multicenter cohort study. Crit. Care Med. **40**(7), 2204–2211 (2012). https://doi.org/10.1097/CCM.0b013e31824e18a8
9. Nassar, A.P., Zampieri, F.G., Salluh, J.I., Bozza, F.A., Machado, F.R., Guimarães, H.P., Damiani, L.P., Cavalcanti, A.B.: Organizational factors associated with target sedation on the first 48 h of mechanical ventilation: an analysis of checklist-ICU database. Crit. Care **23**(1), 34 (2019). https://doi.org/10.1186/s13054-019-2323-y

10. Ni, Y., Bermudez, M., Kennebeck, S., Liddy-Hicks, S., Dexheimer, J.: A real-time automated patient screening system for clinical trials eligibility in an emergency department: design and evaluation. JMIR Med. Inf. **7**(3), e14185 (2019). https://doi.org/10.2196/14185
11. Valentine, N.A., Alhawassi, T.M., Roberts, G.W., Vora, P.P., Stranks, S.N., Doogue, M.P.: Detecting undiagnosed diabetes using glycated haemoglobin: an automated screening test in hospitalised patients. Med. J. Aust. **194**(4), 160–164 (2011). https://doi.org/10.5694/j.1326-5377.2011.tb03762.x

Drug2vec: A Drug Embedding Method with Drug-Drug Interaction as the Context

Pengfei Liu, Xubin Zheng, Man-Hon Wong, and Kwong-Sak Leung(✉)

The Chinese University of Hong Kong, Shatin, Hong Kong SAR, China
{pfliu,xbzheng,mhwong,ksleung}@cse.cuhk.edu.hk

Abstract. The combinatorial pharmacological effects of drugs are influenced by the complex interactions among them. When the patient is allergic to some drugs, the combination of drugs have to be changed. Based on that, we put forward a linear-algebra-equation query task. In this paper, we propose a model called Drug2vec that approximates the relationship among drugs and can solve the linear-algebra-equation query task. For example, we can find drugs with the following relationship: *drug A + drug B = drug C*. Drug2vec applies a three-layer neural network, which firstly projects a drug into an embedded space and then retrieves another drug that interacts with it. Experimental results show that Drug2vec can approximate the relationship among drugs to linear equations, and the drugs that fit a linear equation have connections with respect to their structures. We also propose a metric called AUE (area under the enrichment curve) to evaluate the performance of our model. Drug2vec can predict drug-drug interactions with high accuracy, and the AUE can be 0.96 in the normal test. The AUE score of Drug2vec can be greatly increased with linear modification in the blind test.

Keywords: Deep learning · Drug-drug interaction · Drug discovery

1 Introduction

Drug combinatorial therapy plays an important role in modern medical healthcare as it can provide more comprehensive treatment for patients. In many cases, patients are treated with multiple medicines at the same time. Some patients may be allergic to some drugs and the drug combination should be replaced. Hence, it is important to search for new drug combinatorial treatment and provide suggestions for physician. Analyzing drug-drug interaction (DDI) via *in vivo* and *in vitro* methods are accurate and reliable, however, they are also relatively expensive, time consuming and even involves moral considerations [14]. On the other

P. Liu, X. Zheng—Both authors contributed equally to the work.

hand, estimating drug-drug interaction *in silico* is much more convenient, expeditious and economical. Therefore, we come up with a task called linear-algebra-equation query in drug-drug interaction analysis via computational method.

In this paper, we proposed a model called Drug2vec that can estimate the drug-drug interaction. It can be applied to do linear-algebra-equation query and to predict drug-drug interaction. Linear-algebra-equation query is a task that finds a set of drugs that have relationship described by a linear algebra equation. For example, we want to find *drug A, B, C* that meet the requirement represent by an equation: *drug A + drug B = drug D*. The query relation among drugs is presented as a linear algebra equation. That is why we call it linear-algebra-equation query.

Our model is inspired by the Word2vec model in natural language processing (NLP)[5]. Word2vec is a three-layer neural network with only one hidden layer. It breaks long sentences into word pairs within local contexts. Then a one-hot representation of the word pairs is projected to a lower-dimensional vector in a smaller embedded space. This vector is called embedded vector. Word2vec model is of critical importance in NLP as it simplifies the relationship among words.

Drug2vec has the same structure as word2vec, in which there is only one hidden layer and no activation or pooling function is applied. The context for Drug2vec is defined as the DDI network. Similar to what word2vec achieves in NLP, Drug2vec can represent drugs as vectors and approximate the relationships among drugs to simple linear algebra equations. The new representative vectors can also be applied to predict DDI with high accuracy. However, when dealing with a new drug that has never met before, the model does not perform well. In that case, we apply linear repair method in our model to make the whole model more robust.

In this paper, Drug2vec is implemented using Pytorch (version 1.00) which is a widely used package in deep learning. All the codes and data are available online: https://github.com/Lowpassfilter/Drug2vec.

The rest of this paper is arranged as follows: the related works in DDI analysis are given in Sect. 2, and the linear-algebra-equation task and the details of Drug2vec model are discussed in Sect. 3. Section 4 is about the evaluation method for Drug2vec, and the experimental results and discussion are given in Sect. 5. In the end, we draw a conclusion of this work in Sect. 6.

2 Related Works

The field of computer-aided drug-drug interaction (DDI) analysis has been explored for a few years. The most effective methods developed in the recent year can be classified as matrix factorization (MF) approach or neural network approach. For example, in [12] the authors applied a semi-non-negative matrix factorization for DDI prediction. The values in the low-ranked decomposed matrix are restricted to be non-negative to provide better understandability. Deep learning is known for its ability to comprehend relationship among high dimensional data. It is quite suitable for understanding the complex interaction among drugs. [7] built an 8 layers fully connected neural network for DDI and drug-food interactions. The authors also conducted experiments on Drugbank and gave detailed statistics for this database. [15] designed a position aware multi-task deep neural network and outperformed the state of the art in DDI Extraction Challenge 2013.

The word2vec technique in natural language processing (NLP) gradually shows its power in cheminformatics and bioinformatics in the recent years. [1] proposed ProtVec to represent the amino-acid sequences and applied it to do protein family classification. [10] and [8] applied word2vec to find the adverse drug reactions from Twitter data or medical records. Later on Mol2vec was introduced in [2] to learn vector representations of the molecular substructures. The compounds encoded vectors were then combined with supervised machine learning methods to predict compound properties. In [3] FP2VEC was proposed to obtain the embedding vector of compounds for their quantitative structure-activity relationship (QSAR) model in order to predict properties of chemical compounds. [13] introduced IVS2vec and dense fully connected neural network (DFCNN) to predict whether a molecule can bind the potential targets or not.

Despite the success of applying word2vec, there are still works that have not done yet. Firstly, the word2vec focuses on representing the complex relationships among words, but till now, the applications in bioinformatics are only focus on classification tasks. We believe that the word2vec can do more. We came up with an idea to represent the complex relationship among drugs and furthermore to deal with the linear-algebra-equation query task. Secondly, the word2vec has not been applied for DDI analysis. Therefore, in this paper, we define a linear-algebra-equation query task and then propose the Drug2vec model, a derivative of word2vec for this task and DDI analysis.

3 Drug2vec

The idea behind Drug2vec is inspired by the word2vec technique in natural language processing (NLP) area. In this section, the linear-algebra-equation query is firstly defined and then the word2vec is briefly introduced. After that, the Drug2vec is explained in details including how it works and how to solve the linear-algebra-equation query task. However, there is limitation of the neural network in the model. Therefore, we include the matrix factorization (MF) in our Drug2vec model for the so-called blind test.

3.1 Linear-Algebra-Equation Query

In drug therapy, some patients may be allergic to some drugs. In that situation, the doctor have to find other drugs that have the similar pharmacological effect. If combinatorial therapy is applied, the situation may become more complicated, because the doctor may have to use another combination of different drugs. For example, omeprazole, clarithromycin and amoxicillin are used to treat the helicobacter pylori. Sometimes the patient may be allergic to amoxicillin and then this drug combination have to be changed.

For replacing one drug, if we describe it in a linear algebra equation, it would be:

$$DrugA = DrugB \tag{1}$$

If it is a combination of drugs, it can also be described in linear algebra equation. For example,

$$DrugA + DrugB = DrugC \tag{2}$$

Generally speaking, we can describe the relationships among drugs via linear algebra equation. As mentioned above, in some real-world situations, we may want to find out which drugs have that kind of relationship described as specific linear algebra equations. Therefore, we come up with a task that is finding drugs interaction or combination given the relationship described in linear algebra equations. It is like searching for records that meet the relationship requirements. Therefore, we name it linear-algebra-equation query.

3.2 Drug2vec Architecture

Although word2vec is initially invented to handle sequential data, it can be modified and applied in approximating the DDI. The definition of context is the key in word2vec. It chops the long word sequences into short overlapped segments and extracts the local relationship among words in each segment. A similar concept of context can be defined for DDI and an example is showed in Fig. 1 (a).

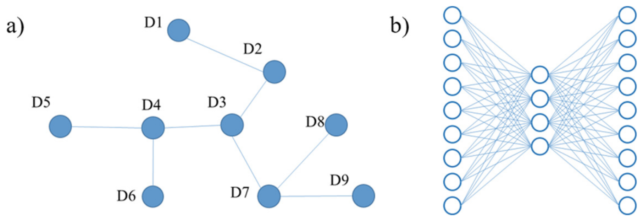

Fig. 1. (a) an example context for the drug-drug interaction network (b) network architecture for Drug2vec method

In DDI networks, the context for each drug within a radius of n can be defined as drugs that can be reached with no more than n steps from it. For example, in Fig. 1 (a), the context for $D2$ with radius 2 is $D1$, $D3$, $D4$, $D7$. For every drug in the context, it composes a drug pair with the central drug. All those drug pairs are used to train the model Drug2vec.

The goal of Drug2vec is to approximate the relationships among drugs and to represent them using linear algebra equations so that we can use it to trace the drugs with relationships described in linear algebra equations. We apply a three-layer neural network to capture the linear relationship. The network structure of Drug2vec is showed in Fig. 1 (b). The first layer is the input layer, where the number of neurons equals the total number of drugs. A drug is represented as a one-hot vector in the input layer. The length of the vector equals to the number of drugs. For each drug, only the value that refer to the drug is 1 while all the other values equal to 0. In Fig. 1 (a), $D2$ is represented as [0, 1, 0, 0, 0, 0, 0, 0, 0]. The middle layer, also called the hidden layer, is the embedding vector space. A drug's one-hot vector is projected to this space, the dimension of which is number of neurons in the hidden layer. The vector obtained in this layer is called the embedded vector or encoded vector. The output layer is of the same size as the input layer. Each neuron in the output layer corresponds to a drug. The output is a one-hot vector in which different indexes representing different drugs. The value corresponding to the drug that have interactions with the input drug is expected to be 1. All the other values equal to 0.

In order to ensure strict linear property of the model, non-linear operations are not used in the network, such as pooling, normalization, or activation function like sigmoid and ReLU [6]. It is important to ensure the network has strict linear relations. Otherwise, it cannot fit the linear algebra relationship very well.

3.3 Drug2vec for Linear-Algebra-Equation Query

The procedures to tackle the linear-algebra-equation query via Drug2vec are described as follows.

- Drug2vec is trained using all the drug pairs to learn to encode a drug into a vector while preserving the relationship between different drugs. The three-layer neural network is obtained that fits the training data most.
- Encode each drug into the corresponding vector in the hidden layer of Drug2vec.
- Fit encoded vectors into the linear algebra equation and look for the drugs that suit the equation best. Because of the limited computational power, we test Drug2vec with the following 3 linear algebra equations:

$$\text{linear relationships} = \begin{cases} A = B \\ A + B = C \\ A + B = C + D \end{cases} \tag{3}$$

We choose the drugs combination with the least L2 loss as the best fitting drugs. As for (3), the L2 loss functions are:

$$\begin{aligned} &L2\ Loss_1 = (f(A) - f(B))^2 \\ &L2\ Loss_2 = (f(A) + f(B) - f(C))^2 \\ &L2\ Loss_3 = (f(A) + f(B) - f(C) - f(D))^2 \end{aligned} \tag{4}$$

where $f(.)$ represent the encoding of the drug.

3.4 Drug2vec for Predicting Drug-Drug Interaction

Drug2vec can also be applied to predict the interactions between drugs. For each drug, the output of the three-layer neural network is a vector that has the same length as the number of drugs. The values in the vector are expected to be approximately 1 at the positions of the interactive drugs, and close to 0 at the positions representing the non-interactive drugs.

In new drug discovery, researchers may produce drugs that have never been seen before. In that case, the neural network may not work well, because the neuron of the drug has never been active during the training process. The three layer neural network can be explained in a more mathematical way as shown in Fig. 2 (a). Suppose the one-hot vector for drug is $d = \{s_1, s_2, ..., s_n\} \subset R^n$, where $s_i \in 0, 1$ and n is the number of drugs. For a drug interaction pair (d_i, d_j), the neural network is actually looking for two matrix $U \subset R^{n\times m}$ and $V \subset R^{m\times n}$, so that $d_i UV = d_j$, where m is the size of the embedded space. The input d_i is a one-shot vector that represents a drug. The linear transformation between the input layer and the hidden layer can be regard as a matrix U. The ith row in the trained matrix U should actually be the embedded vector for drug i. The matrix V represents the transformation between encoded vector of the drug and the output d_j. If the drugs never appear in the training stage, the corresponding rows in U never get trained and keep the initial random values. Then the outputs for the unseen drugs is meaningless. In that situation, the neural network architecture does not work well. Hence, Drug2vec model includes the linear repair method to approximate the untrained rows in U.

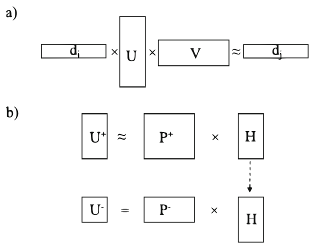

Fig. 2. Drug2vec can be interpreted in a matrix operation view, so that a linear repair method can be defined for the blind test. (a) a matrix perspective to understand Drug2vec (b) an illustration of linear repair method for the blind test

The idea of linear repair method is shown in Fig. 2 (b). Suppose the rows corresponding to the training drugs in U compose a new matrix U^+, and the rows corresponding to the new drugs compose another new matrix U^-. We introduce the feature matrix for training drugs denoted as P^+, and the feature matrix for new drugs denoted as P^-. Using linear regression, a matrix H can be obtained to transfer P^+ to U^+ with the minimal loss shown below:

$$\left\|U^+ - HP^+\right\|_2 \tag{5}$$

H can also be applied to transfer P^- into a new matrix U^* which is an approximation to U^-:

$$U^* = HP^- \tag{6}$$

When facing a new drug, Drug2vec applies the approximate matrix U^* to repair U of the neural network model. More specifically, the U^- in U is replaced by U^*.

4 Evaluation

There are two objectives of the Drug2vec model. One is to solve the linear-algebra-equation query task, the other is to predict a drug-drug interaction. Therefore, two groups of experiments are conducted to test the performance of Drug2vec.

For the linear-algebra-equation query, Drug2vec is applied to retrieve drugs among the dataset that have the relationship shown as 3 linear-algebra-equation in 3. Then the structure of the drugs is displayed to see whether the drugs retrieved by Drug2vec meet the requirement.

To predict drug-drug interaction, the output of Drug2vec is not a number indicating the probability of the interaction between two drugs. It is a vector whose nearest neighbors indicate interactive drugs. Because there are still interactions among drugs unknown, we cannot decide whether it has interaction if we find the nearest neighboring drug not marked as interactive in the dataset. In that case, we had better evaluate the ability of the model to find existing interaction regardless of the false positive. Moreover, having interaction or not depends on the Euclidean distance from the output vector to the one-hot vector representing a drug. If the output vector is close to a drug, then the drug will be regard as having interaction with the input drug in Drug2vec model. If we choose the closest 20% drugs as interactive drugs, the result will be different from choosing the top 5%. Therefore, it is not applicable to use the metrics in classification to measure the prediction ability in Drug2vec, such as AUROC or AUPR.

To evaluate Drug2vec quantitatively, we define a new metric called area under the enrichment curve (AUE), which is similar to AUROC. The horizontal axis in the enrichment curve is the percentage of the nearest drugs that are predicted as interactive with the input drug. The vertical axis represents the percentage of the testing drugs whose interactive drugs are found. The area under the enrichment curve (AUE) measures how well Drug2vec can find the interactive drugs in a given searching range. The enrichment curve looks similar to the receiver operating curve which starts from the bottom left corner to top right corner. However, the meaning is different. The AUE focuses more on the ability of finding the interaction within the nearest neighborhood of the output vector.

When testing the prediction accuracy of Drug2vec, there are two different settings, which are the normal test and the blind test. In the normal test, drugs can exist in the training and testing set at the same time, and the AUE score can be directly used to measure the performance of Drug2vec. In the blind test, drugs are divided into a big set and a small set. The interactions within the big set are used as training set, and the interactions across the two sets are used as testing set. In the blind test, a drug cannot exist in training and testing set at the same time. The blind test is to simulate the ability of predicting interactions for a new drug. In that situation, the linear repair method is included to enhance the prediction ability of Drug2vec.

5 Experimental Result

5.1 Dataset and Prepossessing

Drugs and their interaction information are downloaded from Drugbank [11], and are prepossessed based on the method reported in [12]. Initially, 2329 drugs are downloaded from Drugbank. 603 of them are selected and the drugs with incomplete information are abandoned. After that, those drugs without the off-label side effects in OFF-SIDES [9], or without chemical structures are further removed. The final drug interaction network contains 568 drugs and $21,351$ interactions among them. Among these interactions, $16,757$ of them are enhancive DDIs and are regarded as the enhancive network in this paper. On the other hand, 4594 of them are degressive DDIs and are regarded as the degressive network in this paper. If the type of DDIs is not considered, the $21,351$ DDIs are regarded as the binary network. Then the context of each drug can be obtained and moreover the pair drugs can be used for training the Drug2vec. From the view of graphics, the enhancive network consists of 2 disconnected components and the degressive network consists of 27 disconnected components which is more fragmental.

The canonical SMILES, drug structure images of the 568 drugs are downloaded from PubChem [4], a comprehensive public online database for molecules. Drugbank provides drug names and drug CIDs that can be retrieved from PubChem. While the names and CIDs of some drugs provided in Drugbank are not consistent in PubChem. On that occasion, CIDs are used with a higher priority. Besides, each drug has an 881-dimensional structural feature vector and a 9149-dimensional OFFSIDES feature vector.

5.2 Result of Linear-Algebra Equation Query

Drug2vec is tested to show its capacity to retrieve drugs for linear-algebra-equation query. Drug2vec is trained on the complete set of the drug pairs for 100 epochs. Then, the one-hot representations of the 568 drugs are put into Drug2vec and their embedded vectors in the hidden layers are saved. After that, these 568 embedded vectors of drugs are fed into three linear-algebra-equation queries in 3 respectively. The most suitable combinations of drugs that meet the linear-algebra-equation requirement are retrieved using L2 loss shown in 4. The structures of the best drug combinations are shown in Fig. 3.

Figure 3 (a) is the result for equation $A = B$. It can be seen that when structures of the retrieved drugs are extremely similar to each other with only

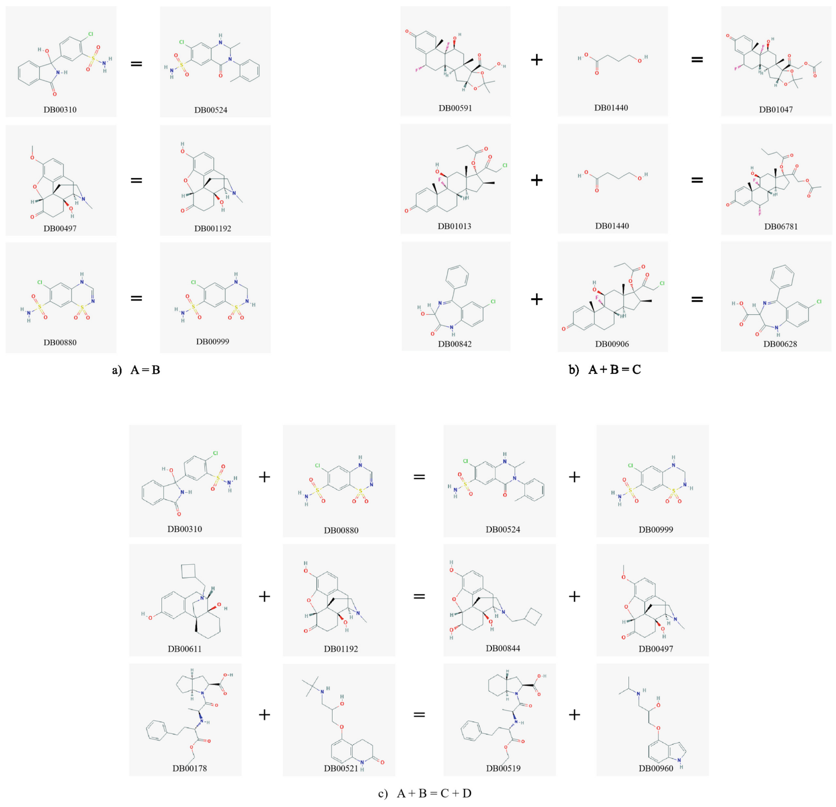

Fig. 3. Samples of the best drug combinations retrieved by Drug2vec for three linear-algebra-equation queries: (a) $A = B$, (b) $A+B = C$, (c) $A+B = C+D$. The structure of the drugs are downloaded from Pubchem, and the number at the bottom of each drug is their corresponding drug IDs in DrugBank.

one atom different. For example, the carbon "C" in drug with ID DB00310 is replaced by nitrogen "N" in DB00524. The drug with ID DB00999 is with one more hydrogen "H" than DB00880. The drugs DB00497 and DB01192 are exactly similar.

Figure 3 (b) shows the result for equation $A + B = C$. It can be seen that relationship among these drug can be interpreted as "transferring the aldehyde (-CHO) from one drug to another". In Fig. 3 (b), drug DB01440 (gamma-Hydroxybutyric acid) appear in the top two drug combinations for this linear-algebra-equation query. Its aldehyde is transferred to an existing drug and form another drugs. Same thing happens in the third example, where the aldehyde from drug DB00906 is added to DB00842 to form drug DB00628.

Figure 3 (c) is the result for equation $A + B = C + D$. This equation quite resembles the combination of the first equation $A = C$ and $B = D$. In the third combination in Fig. 3 (c), drug DB00178 is similar to DB00519, while drug DB0

0521 is akin to DB00960. Thus, drug DB00178 plus drug DB00521 is similar to drug DB00960 plus drug DB00519.

5.3 Performance of Predicting Drug-Drug Interaction

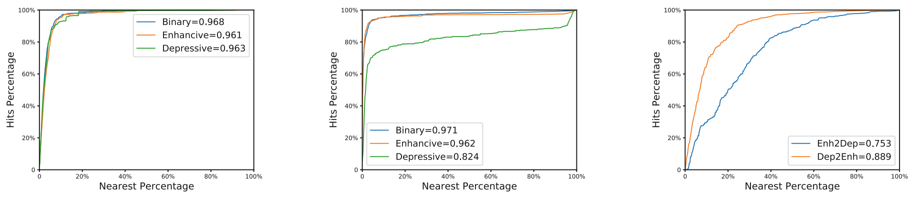

(a) Normal test (b) Blind test (c) Cross test

Fig. 4. Enrichment curves of Drug2vec in (a) Normal test, (b) Blind test and (c) Cross test. The horizontal line is the percentage of drugs that predicted to be connected with the input drug, and the vertical line is the percentage of input drugs whose neighboring drugs are found.

For drug-drug interaction (DDI) prediction, the normal test and the blind test are conducted for three DDI networks, binary network, enhancive network and depressive network. Besides, the cross test is proposed here to see whether the knowledge learnt by Drug2vec can be transferred. In the cross test, Drug2vec is trained on the enhancive network and testing on the depressive network, and vice versa. The cross test is designed to check whether the knowledge that Drug2vec learned from one network can transfer to another network.

In the normal test, 90% of the DDIs are randomly chosen as the training set and 10% are left as the testing set. Drug2vec is trained on the training set for several rounds and tested on the testing set. The performance on the testing set is used to evaluate the model. The number of rounds is chosen manually and is less than 10 for most experiments. The performance in the normal test for the three networks is showed in Fig. 4 (a), in which the AUE score is 0.968 for the binary network, 0.961 for the enhancive network, and 0.963 for the depressive network. This result shows that Drug2vec performs consistently well in DDI prediction in the normal test.

In the blind test, 90% of drugs are randomly selected and the DDIs within these drugs are used as the training set. The DDI pairs between those drugs and the remaining 10% drugs are used for testing. In the blind test, linear repair are included. From Fig. 4 (b) we can see that Drug2vec can achieve relatively high performance in the blind test for the binary network and the enhancive network. But for the depressive network, the AUE score is 0.824, which is less than in the normal test. Moreover, experiments are also conducted to test the performance of Drug2vec with linear repair and without linear repair. The result is shown in Table 1. As we expect, without linear repair the AUE score is just around 0.5.

The reason is discussed before that the parameters associated with testing drugs in the neural network have never been trained. Using linear repair will fix the problem.

In the cross test, the training set and the testing set are chosen based on the type of DDIs. Firstly, Drug2vec is trained on the enhancive network and tested on the degressive network. Then, Drug2vec is trained and tested in the other way round. The result of the cross test is shown in Fig. 4 (c). The AUE score of learning depressive to predict enhancive is 0.889, and the AUE score of learning enhancive to predict depressive is 0.753. The knowledge of one network can partially transfer to another. The score is not so high as in the normal test or the blind test. It is probably because the enhancive network and the depressive network have different properties. So estimating from one to the other is a really difficult task.

Table 1. Linear repair AUE for the blind test.

Blind type	Without linear repair	With linear repair
Binary	0.51 ± 0.02	0.971 ± 0.03
Positive	0.51 ± 0.02	0.969 ± 0.04
Negative	0.51 ± 0.02	0.824 ± 0.03

6 Conclusions

In this paper, we put forward a linear-algebra-equation query task and then propose a model Drug2vec to solve it. Drug2vec can simplify the relationship among drugs using drug-drug interaction as the context. Drug2vec embeds the one-hot representation of a drug into a low-dimensional vector. The embedded vector of drug can approximate the linear-algebra relationship of drug. After that, the embedded vector is restored to the interactive drug. Hence, Drug2vec can also be applied for predicting drug-drug interaction.

The experimental results show that Drug2vec can retrieve drugs with relationship described by linear-algebra equations. Furthermore, Drug2vec is able to find the interactive drugs for a given drug with high accuracy. The AUE score can be around 0.96.

Acknowledgement. The authors sincerely thank Prof. Shi from the Northwestern Polytechnical University to share their drugs date to us, which accelerated the production of this paper.

References

1. Asgari, E., Mofrad, M.R.: Continuous distributed representation of biological sequences for deep proteomics and genomics. PloS one **10**(11), e0141287 (2015)

2. Jaeger, S., Fulle, S., Turk, S.: Mol2vec: unsupervised machine learning approach with chemical intuition. J. Chem. Inf. Model. **58**(1), 27–35 (2018)
3. Jeon, W., Kim, D.: FP2VEC: a new molecular featurizer for learning molecular properties. Bioinformatics **35**, 4979–4985 (2019)
4. Kim, S., Thiessen, P.A., Bolton, E.E., Chen, J., Fu, G., Gindulyte, A., Han, L., He, J., He, S., Shoemaker, B.A., et al.: Pubchem substance and compound databases. Nucleic Acids Res. **44**(D1), D1202–D1213 (2015)
5. Mikolov, T., Sutskever, I., Chen, K., Corrado, G.S., Dean, J.: Distributed representations of words and phrases and their compositionality. In: Advances in Neural Information Processing Systems, pp. 3111–3119 (2013)
6. Ramachandran, P., Zoph, B., Le, Q.V.: Searching for activation functions. arXiv preprint arXiv:1710.05941 (2017)
7. Ryu, J.Y., Kim, H.U., Lee, S.Y.: Deep learning improves prediction of drug-drug and drug-food interactions. Proc. Nat. Acad. Sci. **115**(18), E4304–E4311 (2018)
8. Tafti, A.P., Badger, J., LaRose, E., Shirzadi, E., Mahnke, A., Mayer, J., Ye, Z., Page, D., Peissig, P.: Adverse drug event discovery using biomedical literature: a big data neural network adventure. JMIR Med. Inform. **5**(4), e51 (2017)
9. Tatonetti, N.P., Patrick, P.Y., Daneshjou, R., Altman, R.B.: Data-driven prediction of drug effects and interactions. Sci. Transl. Med. **4**(125), 12ra31–12ra31 (2012)
10. Wang, C., Singh, O., Dai, H., Jonnagaddala, J., Jue, T.R., Iqbal, U., Su, E., Abdul, S.S., Li, J.: NTTMUNSW system for adverse drug reactions extraction in Twitter data. In: Proceedings of the Social Media Mining Shared Task Workshop at the Pacific Symposium on Biocomputing, pp. 4–8 (2016)
11. Wishart, D.S., Feunang, Y.D., Guo, A.C., Lo, E.J., Marcu, A., Grant, J.R., Sajed, T., Johnson, D., Li, C., Sayeeda, Z., et al.: Drugbank 5.0: a major update to the drugbank database for 2018. Nucleic Acids Res. **46**(D1), D1074–D1082 (2017)
12. Yu, H., Mao, K.T., Shi, J.Y., Huang, H., Chen, Z., Dong, K., Yiu, S.M.: Predicting and understanding comprehensive drug-drug interactions via semi-nonnegative matrix factorization. BMC Syst. Biol. **12**(1), 14 (2018)
13. Zhang, H., Liao, L., Cai, Y., Hu, Y., Wang, H.: IVS2vec: a tool of inverse virtual screening based on word2vec and deep learning techniques. Methods **166**, 57–65 (2019)
14. Zhang, P., Wang, F., Hu, J., Sorrentino, R.: Label propagation prediction of drug-drug interactions based on clinical side effects. Sci. Rep. **5**, 12339 (2015)
15. Zhou, D., Miao, L., He, Y.: Position-aware deep multi-task learning for drug-drug interaction extraction. Artif. Intell. Med. **87**, 1–8 (2018)

Feature Selection with Artificial Bee Colony Algorithms for Classifying Parkinson's Diseases

Rafet Durgut[1], Yusuf Yargı Baydilli[1], and Mehmet Emin Aydin[2](✉)

[1] Department of Computing Engineering, Karabuk University, Karabuk, Turkey
{rafetdurgut,yusufbaydilli}@karabuk.edu.tr

[2] Department of Computer Science and Creative Technologies, UWE Bristol, Bristol, UK
mehmet.aydin@uwe.ac.uk

Abstract. Parkinson's is a brain disease that affects the quality of human life significantly with very slow progresses. It is known that early diagnosis is of great importance to arrange relevant and efficient treatments. Data analytics and particularly predictive approaches such as machine learning techniques can be efficiently used for earlier diagonosis. As a typical big data problem, the number of features in the collected data of Parkinson's symptoms per case matters crucially. It is known that the higher the number of features considered the more complexities incur in the handling algorithms. This leads to the dimensionality problem of datasets, which requires optimisation to overcome the trade-off between complexity and accuracy. In this study, artificial bee colony-based feature selection methods are employed in order to select the most prominent features for successful Parkinson's Disease classification over the datasets. The optimised set of features were used in training and testing *k nearest neigbourhood* algorithm, and then verifed with *support vector machine* algorithm over the public dataset. This study demonstrates that binary versions of artificial bee colony algorithms can be significanlty successful in feature selection in comparison to the relevant literature.

Keywords: Parkinson's disease classification · Speech analysis · Feature selection · Artificial bee colony

1 Introduction

According to a report published in 2015, 6.2 million people globally suffer from Parkinson's Disease (PD), and about 177 thousand of these cases have resulted in death [1]. Although the main reasons leading to the emergence of PD are not fully known and there is no known cure, it is possible to apply some treatments to improve the symptoms observed in the patient [2]. In this way, it is aimed that the patient lives its remaining life with a relatively higher standard. From this point of view, early diagnosis of the disease is very important. The fact that the disease has a neurodegenerative structure, that is, targets motor reflexes, negatively affecting the patient's movement and mental activities, makes it possible to diagnose the disease through the tests carried out [3]. One of these tests is "speech analysis". Findings such as phonetic and speech disorders observed in PD patients, even, the onset of some deformations before the PD clinically diagnosed, reveal that this test is highly effective for early diagnosis [4]. Besides, this test is very simple and cheap. So, it provides that PD can be diagnosed by medical personnel as soon as possible [5].

In the first of the studies that developed a Computer-aided Diagnosis (CAD) model with the results obtained from these tests, Little et al. [5] tried to detect the dysphonia that occurred in Parkinson's patients through the phonations obtained from 31 patients. The authors who trained Support Vector Machine (SVM) using the uncorrelated features in the dataset, stated that they achieved 91.4% classification success. As of this date, many researchers have carried out studies to select the most suitable features in the related dataset and to increase the classification success by using different machine learning algorithms [6]. For example, Das [7] used Artificial Neural Networks (ANN) and raise the classification success rate to 92.9%. Li et al. [9] used SVM and fuzzy-based non-linear method and reported their classification success as 93.47%. In their studies, Chen et al. [10] performed feature selection and achieved 96.47% classification accuracy with the hybrid extreme learning machine. On the other hand, Zuo et al. [11] achieved 97.47% success rate using fuzzy k-Nearest Neighbor (k-NN) method improved with Particle Swarm Optimization (PSO). Finally, Gük [12] was able to increase the classification score to 98.46% by using rotation-forest ensemble k-NN.

Since speech analysis has an important place in the classification of PD, Sakar et al. [13] have brought a new dataset to the literature. The authors who examined 40 subjects (20 Parkinson's patients, 20 normal) in their study, took samples of words and sentences as well as the vowel letter 'a'. At the end of the study, they reported that vowel samples had more distinctive features than word and sentence samples. They trained a SVM using the features extracted from the samples and achieved 77.5% classification success as a result. In the other studies performed on this dataset; while Zhang et al. [14] employed ensemble learning with the multi-edit-nearest-neighbor algorithm, Abrol et al. [15] used the kernel sparse greedy algorithm. Abrol et al. was able to increase classification success up to 99.4%.

As seen in the literature, the studies mostly propose hybrid feature selection and machine learning approaches for higher success in classifications in expense of various aspects. It is observed that the high success rates achieved by the researchers seem proportional to the cross-validation methods used (e.g. Leave-one-out CV or 10-fold CV), which imples that different samples from the same cases are used for both training and validation purposes. Obviously, this is a tricky approach that has potiantial to undermine the real success level with respect to generalisation of the learning approaches [16]. In addition, the datasets used in the studies underconsideration contain samples from a small number of cases and need wider range os samples from larger dataset highly accurate early diagnosis of PD. Sakar et al. [17] have created a dataset consisting of 252 cases for this purpose. The dataset covers a wide range of features including the basic features, many additional discriminative features extracted from the audio signals using various techniques. The corresponding study reports a wideer use of feature selection and machine learning techniques to hit the performance of 86% by SVM over 50 efficiently selected features.

The motivation of this study is to enhance the efficency and performance of classifiers, particularly *k nearest heighbourhood (k-NN)* via efficent feature selection using the varients of one of the prominent and recent swarm intelligence approaches; *artificial bee colony (ABC)* algorithms. This is due to the attractive performance of binary versions of ABC in the recent publications. At the end of the study, the classification success was observed with competetive results and verified with SVM, too.

The rest of the paper is organised as follows: Sect. 2 reviews and introduces feature selection while Sect. 3 overviews the original and binary versions of ABC algorithm. The experimental results are provided and discussed with relevant works in Sect. 4 and 5, respectfully, while the study is concluded in Sect. 6.

2 Feature Selection

Feature selection is one very prominant areas of data analysis and machine learning, which plays crutial role in the success of the approches with respect ot algorithmic complexity and the accuracy of the results. Big data studies emerge to particularly take care this very issue in data analysis due to the fact that the size of data tables, particularly the number of columns/attributes, hugely matters in processing. However, each attribute in a dataset may not promise significant contribution to classification success. It is a fact that excessive number of features enlarges the problem size and, subsequently, causes higher complexity on machine learning algorithms that tackle the provided classification problems. On the contrary, reduced number of features ends up with underfitting and lower accuracy in results. Hence, feature selection turns in a crutial optimisation problem in which the complexity is minimised without compromising accuracy once the most relevant and impactful features are optimally selected. This helps chose a sub-set of all features, which provide a stable classification on the test data [18].

One of the methods used in feature selection is to develop a search strategy in the features in the dataset. In this way, it is aimed to raise the classification success to the highest possible point by selecting sub-sets from the features pool. Since brute-force searching will result in serious time and computational complexity, researchers develop strategies continuously to speed up this process through heuristic methods [19,20]. In this study, ABC-based search strategy was implemented in 756 features of the dataset. The fitness value of each solution was calculated by the k-NN algorithm. The validation of the training phase was provided by the LOSOCV method as seen in Fig. 1.

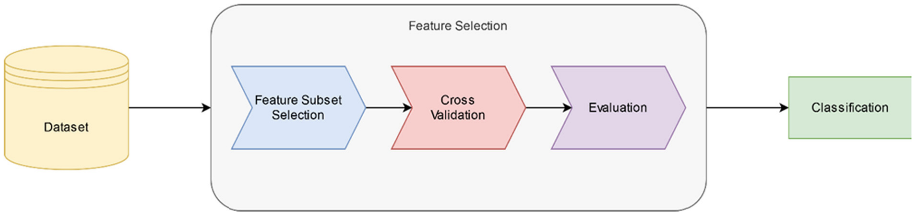

Fig. 1. Flowchart of the feature selection and classification process

3 Artificial Bee Colony (ABC) Algorithms for Feature Selection

The artificial bee colony (ABC) algorithm is one of recently developed swarm intelligence approaches inspired of food search behaviors of the honey bee swarms. The original algorithm has been developed by Karaboğa [21], which imitates the collective behaviour of honey bees within their hives. The algorithm implies use of two types of bees within the hive; employed and onlooker bees. These social insects fulfil collective behaviour in three different phases as modeled into this approach, where first phase imposes each employed bee to improve its own food source, while the second phase involves each onlooker bee to look for improving the quality of its own food source. In the final phase, an exploration is initiated for new food sources by onlooker bees, subsequently transorfmed into scout bees, if non-adequate improvement is achieved. Further investigations and enhamncements for functional optimisation problems are reported in [8].

The conceptualisation of the ABC algorithm translates the natural processes and activities into algorithmic components and functionalities, where "food source" is translated into a "feasible solution" denoted with $\mathbf{x}_i$, while "nectar amount" is recognised as the fitness of a solution denoted by $F(\mathbf{x}_i)$ as given in Eq. 1.

$$F(\mathbf{x}_i) = \begin{cases} \frac{1}{1+f(\mathbf{x}_i)} & f(\mathbf{x}_i) \geq 0 \\ 1 + |f(\mathbf{x}_i)| & \text{otherwise} \end{cases} \tag{1}$$

The probability of a particular food source to be selected through the process of ABC algorithm is calculated with Eq. 2, while a neighbouring solution such as $\mathbf{x}_n = \mathbf{x}_i + \mathbf{v}_i$ generated using Eq. 3

$$p(\mathbf{x}_i) = \frac{F(\mathbf{x}_i)}{\sum_{j=1}^{N} F(\mathbf{x}_j)} \tag{2}$$

$$\mathbf{v}_i = \mathbf{x}_i + \phi_i(\mathbf{x}_i - \mathbf{x}_n) \tag{3}$$

where $\mathbf{x}_i, \mathbf{x}_n, \mathbf{v}_i$ in the equations refer to the current solution, neighbor solution and candidate solution, respectively. ϕ_i is a randomly generated number in the scale of $[-1, 1]$. $i = 1, 2 \ldots, N$ indicates the index of the food source, where N

indicates the number of food sources. On the other hand, the scout bees can be genereted using Eq. 4 when no improvement is realised by onlooker bees.

$$x_{i,j} = LB_j + rand(0,1) \times (UB_j - LB_j) \tag{4}$$

where, $x_{i,j}$ is the j^{th} decision variable as the member of $\mathbf{x}_i$ solution vector; $j = 1, 2, .., D$ is the index, D is the total number of decision variables, LB and UB are the upper and lower boundary values defined for the decision variable.

Feature selection is a binary optimization problem, but, the ordinary ABC algorithm is developed for the continuous domains. The ABC version for solving binary problems is suggested in [22], where Eq. 3 and Eq. 4 are replaced with Eq. 5, based on Bernoulli process, as given below.

$$x_{i,j} = \begin{cases} 0 & rand < 0.5 \\ 1 & \text{otherwise} \end{cases} \tag{5}$$

The following four methods are different variants of developed ABC for binary optimization problems and used for feature selection purposes as reported below.

A. BinABC (ABCv1) Algorithm has been proposed by Kiran et al. [23] imposing Eq. 6 to replace Eq. 3 in which XOR logical operator is used to produce neighbour solutions noting that the variables provided in Eq. 3 as in vector form while are in Eq. 6 as scalar form. The parameter of ϑ is used as the logical NOT operator with which neighbour generation is applied alongside a pre-set threshold value (e.g. 0.5), if the resulted vaule is to be taken or its complement as the output value.

$$v_{i,j} = x_{i,j} \oplus \vartheta(x_{i,j} \oplus x_{n,j}) \tag{6}$$

Table 1. XOR based neighborhood operation.

Current solution ($x_{i,j}$)	Neighbor solution ($x_{n,j}$)	XOR operation ($x_{i,j} \oplus x_{n,j}$)	State 1 ($\vartheta < 0.5$)	State 2 ($\vartheta \geq 0.5$)	State 1 ($v_{i,j}$)	State 2 ($v_{i,j}$)
0	0	0	1	0	1	0
0	1	1	0	1	0	1
1	0	1	0	1	1	0
1	1	0	1	0	0	1

As the procedure can be seen in Table 1, XOR operator is applied to current,$x_{i,j}$, and neighbor, $x_{i,j}$, solutions, then the output value is negated if $\vartheta < 0.5$, kept as is, otherwise. Afterwards, XOR is re-applied to the current solution, $x_{i,j}$ and the output value filtered with ϑ for the final output value, $v_{i,j}$.

B. DisABC (ABCv2) Algorithm is proposed by Kashan et al. [24] which uses a similarity measure calculated by Eq. 7 in which the similarity of the bits in two compared solutions plays the key role. A dissimilarity measure, which names the algorithm, is subsequently calculated for this version of the algorithm in order to be used for neighbour solution generation. As the approach imposes, a new solution, was generated by Eq. 4 previously for non-binary problems, is now replaced with Eq. 7, which calculates Jaccard's similarity constant together with Eq. 8.

$$sim(x_i, x_j) = \frac{M_{11}}{M_{01} + M_{10} + M_{11}} \tag{7}$$

$$dissim(x_i, x_j) = 1 - sim(x_i, x_j) \tag{8}$$

where M_{11} is the number of 1 bits in both x_i and x_n at the same positions, while M_{01} and M_{10} are determined, accordingly. Eq. 9 declares that the dissimilarity of the current solution with the neighbour-to-be is an approximate of the dissimilarity of two existing solutions, x_i and x_j, normalised with ϕ while Eq. 10 presents a minimisation model with a number of constraints, which imples that the new solution to-be, v_i, is expected to satisfy the constraints and let the objective function be minimum.

$$dissim(v_i, x_i) \approx \phi \times dissim(x_i, x_j) \tag{9}$$

$$\min \quad |dissim(v_i, x_i) - \phi \times dissim(x_i, x_j)| \tag{10}$$

Subject to:

$$\begin{aligned} M_{11} + M_{01} &= n_1 \\ M_{10} &\leq n_0 \\ \{M_{10}, M_{11}, M_{01}\} &\geq 0 \text{ and } \in \mathbb{Z} \end{aligned}$$

where ϕ is a random positive value, n_1 and n_0 represent the number of bits with a value of 1 and 0 in the current solution, x_i. The aim in here is to determine the closest possible minimum value according to the difference between the candidate solution and the current solution. Detailed information and examples can be found in [24].

C. Improved BinABC (ABCv3) ABC algorithm updates the value of only one decision variable among D number of decision variables per iteration, while various other swarm intelligence algorithms propose updating multiple variables within the complete vector of decision variables. Obviously, there is a trade-off between exploration and exploitation balance to handle while attemting the updates.

This binary version of the ABC, as discussed in [26], attempts to balance exploration and exploitation with an exponantially calculated rate, d_t as in Eq. 11.

$$d_t = rand(0, \alpha) + e^{-(\frac{t}{t_{max}}) \times 0.1 \times D} + 1 \tag{11}$$

where, the α is randomly determined perturbation number, D is the problem dimension, number of decison variables, and t and t_{max} indicate the current and maximum number of iterations, respectively. It is worthwhile to note that d_t will decrease with growing t, which means that the exploration is higher in earlier iterations while exploitation gets stronger in later iterations. That is believed to help keep the balance explained above.

The neighbourhood operator in Eq. 6 proposed by Kıran et al. [23] is revised to be used in this version due to the fact that ϑ is originally setup with 0.5 in Eq. 6 as the exploitation factor. This pre-set fixed threshold weakens the exploitation as it involves a more random process. Eq. 12 proposes a new way to determine ϑ. This rule allocates 0 to ϑ if the new solution is worse, otherwise, it is updated depending on the iteration.

$$\vartheta = \begin{cases} Q_{max} - (\frac{Q_{max} - Q_{min}}{t_{max}}) \times t & F(x_n) < F(x_i) \\ 0 & \text{otherwise} \end{cases} \tag{12}$$

where Q_{max} and Q_{min} represent the upper and lower limits of the defined range, respectively [25].

D. NBABC (ABCv4) In this binary ABC (NBABC) version that proposed by Santana et al. [26], it is ensured the influencing of the specified number of decision variables during the implementation of the neighborhood operator. Trough the *max_dim* parameter in the algorithm, the maximum number of dimension values is determined in each iteration. The pseudo code of the neighborhood operator is as follows:

Algorithm 1: NBABC Algorithm

```
   Input: $\mathbf{x}_i$
1  Select $x_j$ where $i \neq j$                    /* A new Food Source */
2  Set The number of selected dimensions ($max\_dim \times D$)
3  Select random dimensions for the food source (Dims)
4  Foreach $d \in Dims$ do
5      if $x_{i,d} = x_{j,d}$ then
6          $v_{i,d} = x_{i,d}$
7      end
8      else
9          $v_{i,d} = x_{j,d}$
10     end
11 Return $v_i$
```

4 Experimental Results

The following experimental study has been fulfilled to test the algorithms underconsideration for feature selection purposes. The dataset created by Sakar et al. [17] has been widely used. This dataset contains samples from 188 Parkinson's patients and 64 healthy cases. While constructing the dataset, the voice of patients for the vowel 'a' was recorded 3 times from each case, hence, $252 \times 3 = 756$ audio signals were obtained. In addition to the baseline features of audio signals, feature extraction was made through many techniques (e.g. Time Frequency Measures, Mel Frequency Cepstral Coefficients, Wavelet Transform Based Features, Vocal Fold Features, Tunable Q-Factor Wavelet Transform Based Features). Thus, they were able to create a dataset including a total of 754 feature vectors.

The algorithmic hyper parameters considered through out of these experimentations have been tabulated in Table 2 per algorithm.

Table 2. Control parameters of algorithms

	ABCv1	ABCv2	ABCv3	ABCv4
Population Size	20	20	20	20
Max number of Function Evaluation	1000	1000	1000	1000
max_dim	-	-	-	0.1
ϕ_{max}/Q_{max}	-	0.9	0.3	-
ϕ_{min}/Q_{min}	-	0.1	0.1	-
Limit	100	100	100	100

Table 3 shows the success metrics on each feature category. Since the Bandwidth features in the dataset are few, all methods achieved the best results. When the algorithms run using the TQWT features that have the highest number of features, ABCv2, ABCv3 and ABCv4 showed the best performance according to calculated mean and maximum success values. Although ABCv2 performed the best on the Wavelet Transform features according to the mean results, ABCv3 and ABCv4 achieved the maximum success value. For MFCC features, ABCv4 algorithm achieved the highest scores for both mean and maximum results. Finally, ABCv2 performed better than other methods for Baseline and Vocal Fold features.

From this part of the study, it can be concluded that the MFCC features contain the most qualified features to distinguish between classes. Therefore, all four algorithms showed the best performance on these features. Another important point is that although the number of these features is 84, the algorithms have achieved the highest results with an average of 40.

In the second stage of the study, classification was performed with SVM using the features selected for k-NN algorithm. That was to verify how robust was ABC-based feature selection. As can be seen from Table 4, the features selected

Table 3. Feature selection with k-NN results.

		Baseline (26 Features)			Bandwidth (8 Features)			Vocal Fold (22 Features)			MFCC (84 Features)			WT Applied to F0 (182 Features)			TQWT (432 Features)		
		ACC	**F1**	**MCC**	**ACC**	**F1**	**MCC**	**ACC**	**F1**	**MCC**	**ACC**	**F1**	**MCC**	**ACC**	**F1**	**MCC**	**ACC**	**F1**	**MCC**
ABCv1	*Mean*	0.79	0.87	0.39	**0.77**	**0.86**	**0.30**	0.80	0.88	0.41	0.85	0.90	0.56	0.77	0.85	0.31	0.84	0.90	0.55
	Max	0.83	0.89	0.49	**0.77**	**0.86**	**0.30**	0.81	0.89	0.45	0.87	0.92	0.63	0.79	0.87	0.37	0.86	0.91	0.59
ABCv2	*Mean*	**0.82**	**0.89**	**0.48**	**0.77**	**0.86**	**0.30**	**0.82**	**0.89**	**0.46**	0.85	0.91	0.58	**0.79**	**0.87**	**0.37**	**0.85**	**0.91**	**0.58**
	Max	0.83	0.89	0.49	**0.77**	**0.86**	**0.30**	0.83	0.89	0.49	0.86	0.91	0.61	0.79	0.87	0.39	0.86	0.91	0.61
ABCv3	*Mean*	0.80	0.87	0.40	**0.77**	**0.86**	**0.30**	0.80	0.88	0.41	0.85	0.91	0.58	0.78	0.86	0.34	**0.85**	**0.91**	**0.58**
	Max	0.83	0.89	0.49	**0.77**	**0.86**	**0.30**	0.82	0.89	0.48	0.87	0.92	0.62	0.80	0.88	0.42	0.86	0.91	0.60
ABCv4	*Mean*	0.80	0.88	0.42	**0.77**	**0.86**	**0.30**	0.81	0.88	0.44	**0.86**	**0.91**	**0.59**	0.78	0.86	0.36	**0.85**	**0.91**	**0.59**
	Max	0.83	0.89	0.49	**0.77**	**0.86**	**0.30**	0.82	0.89	0.48	0.87	0.92	0.64	0.80	0.87	0.40	0.87	0.92	0.63

Table 4. SVM results for selected features

		Baseline (26 Features)			Bandwidth (8 Features)			Vocal Fold (22 Features)			MFCC (84 Features)			WT Applied to F0 (182 Features)			TQWT (432 Features)		
		ACC	**F1**	**MCC**	**ACC**	**F1**	**MCC**	**ACC**	**F1**	**MCC**	**ACC**	**F1**	**MCC**	**ACC**	**F1**	**MCC**	**ACC**	**F1**	**MCC**
ABCv1	*Mean*	0.79	0.87	0.35	**0.77**	**0.86**	**0.29**	0.76	0.86	0.27	0.82	0.89	0.50	0.76	0.86	0.24	0.82	0.89	0.49
	Max	0.82	0.89	0.46	**0.77**	**0.86**	**0.29**	0.78	0.87	0.34	0.85	0.91	0.59	0.77	0.86	0.29	0.85	0.90	0.56
ABCv2	*Mean*	0.76	0.85	0.28	**0.77**	**0.86**	**0.29**	0.73	0.83	0.18	**0.84**	**0.90**	**0.54**	**0.77**	**0.86**	**0.25**	**0.83**	**0.89**	**0.51**
	Max	0.76	0.85	0.28	**0.77**	**0.86**	**0.29**	0.73	0.83	0.18	0.84	0.90	0.54	0.77	0.86	0.25	0.83	0.89	0.51
ABCv3	*Mean*	**0.79**	**0.87**	**0.37**	**0.77**	**0.86**	**0.29**	0.76	0.85	0.26	0.83	0.89	0.51	0.76	0.86	0.24	0.82	0.89	0.48
	Max	0.83	0.90	0.51	**0.77**	**0.86**	**0.29**	0.79	0.87	0.38	0.88	0.92	0.66	0.78	0.87	0.32	0.84	0.90	0.55
ABCv4	*Mean*	0.79	0.87	0.36	**0.77**	**0.86**	**0.29**	**0.77**	**0.86**	**0.30**	0.83	0.89	0.52	0.76	0.86	0.24	0.82	0.89	0.48
	Max	0.82	0.89	0.48	**0.77**	**0.86**	**0.29**	0.79	0.87	0.36	0.86	0.91	0.60	0.77	0.86	0.29	0.84	0.90	0.55

by ABCv3 algorithm gave the best results according to the maximum success criteria. However, according to the mean success criteria, ABCv2 and ABCv4 were able to compete with ABCv3.

The fact that SVM algorithm, which is trained with 35 features selected by ABCv3 algorithm, produces higher results compared to k-NN, shows that SVM algorithm is a more successful classification algorithm than k-NN. On the other hand, it can be concluded that the features selected by the binary ABC algorithms create a reasonable and fair benchmark environment for classification algorithms. Moreover, it is possible to achieve higher successes by using SVM instead of k-NN while calculating fitness values in the feature selection stage of ABC algorithms.

5 Related Works and Discussions

Since the dataset used in this study has been made public, several studies have been carried out to improve the classification successes. For example, Altay and Atlas [27] used two different evolutionary algorithms in their work. Badem et al. [28] employed ABC algorithm for feature selection. Tuncer and Dogan [29] performed feature extraction with Singular Value Decomposition (SVD) and feature selection with Neighborhood Component Analysis (NCA). In the classification phase, they used SVM. Castro et al. [30] provided classification with ANN. Finally, Tuncer et al. [31] extracted features from the dataset using minimum average maximum tree and SVD, and then performed classification with k-NN. It was observed that some of their results remian better in accuracy than our score. However, with closer look into the details, it was seen that the 10-fold CV method was used during the training and validation phase. But, as mentioned in the work by Sakar et al. [17], using this kind of cross-validation cannot provide generalization for all subjects and causes in biased results. Therefore, it is found unfair to make a comparison between the results in [31] and our study's. For this reason, our results are evaluated with the results obtained in the original study, namely the study using LOSOCV (Leave-One-Subject-Out Cross Validation). The relevant comparison is as in Table 5 below.

Table 5. Comparison of the results with the original study

	Feature selection algorithm	# of features	Classification algorithm	Acc. (mean)	Acc. (max)
Sakar et al	mRMR	50	SVM	-	0.84
This study	ABCv$	39	k-NN	0.86	0.87
	ABCv5	35	SVM	0.83	0.88

In general, it is observed that the MFCC features in the Parkinson dataset are the best definitive and the most discriminative features for classification. In this respect, it can be concluded that the MFCC features will provide more stable and successful results in more comprehensive Parkinson datasets to be created in the future. However, as seen in the original study, the classification success rate achieved using only MFCC features remained at the level of 0.84. This leads to the question of whether or not more successful results can be obtained through feature selection algorithms.

In their study, Sakar et al. [17] stated that the highest score was obtained with an SVM trained with 50 features selected from all features (756). However, as can be seen in Table 5, when evaluated on the basis of mean values, it can be observed that the NBABC (ABCv4) algorithm can achieve more successful results with less features (0.86). When the algorithms were evaluated in terms of the maximum success rate, all algorithms except disABC (ABCv2) produced the highest accuracy value (0.87). Moreover, if SVM is trained with the selected features, it has been observed that the success rates can be increased a little more. Accordingly, improved binABC (ABCv3) algorithm obtained the highest success value (0.88). As a result, it can be said that thanks to the feature selection to be applied in Parkinson datasets, higher successes can be achieved and binary ABC methods are highly capable in this task.

6 Conclusions

The datasets of Parkinson's sympthoms collated provide great support to study data-driven computational approaches if they are helpful in diagnosis of the disease. The dimensionality problem of such datasets has to be eased before devicing automatic methods to help medical staff. One of the collated datasets are of sound samples they receive from patients through signal processing techniques to apply speech analysis, which help understand any anomlies detected. Machine learning techniques are prominantly used in predictive analysis of the data for diagnosis purposes. However, the dimansionality problem matters and the number of features has to be studied and optimsed accordingly.

In this study, the variants of binary ABC algorithms have been studied for feature selection and dimensionality problem of the datasets underconsideration, which includes 756 features. In the first stage of the study, feature selection was made using four different binary ABC algorithms, and the success values of the selected features were evaluated with the k-NN algorithm. In the second stage of the study, SVMs were trained with the selected features and it was seen that the selected features could increase the classification success compared to the original study. Thus, it has been shown that effective results can be achieved in PD classification by the methods used in the study.

References

1. Wang, H., et al.: Global, regional, and national life expectancy, all-cause mortality, and cause-specific mortality for 249 causes of death, 1980–2015: a systematic analysis for the Global Burden of Disease Study 2015. Lancet **388**(10053), 1459–1544 (2016)

2. Oertel, W.H.: Recent advances in treating Parkinson's disease. F1000Research, 6 Mar 2017
3. Massano, J., Bhatia, K.P.: Clinical approach to Parkinson's disease: features, diagnosis, and principles of management. Cold Spring Harb. Perspect. Med. **2**(6), a008870 (2012)
4. Little, M.A., McSharry, P.E., Roberts, S.J., Costello, D.A., Moroz, I.M.: Exploiting nonlinear recurrence and fractal scaling properties for voice disorder detection. BioMed. Eng. OnLine **6**(1), 1–19 (2007)
5. Little, M.A., McSharry, P.E., Hunter, E.J., Spielman, J., Ramig, L.O.: Suitability of dysphonia measurements for telemonitoring of Parkinson's disease. IEEE Trans. Biomed. Eng. **56**(4), 1015–1022 (2009)
6. Cai, Z., et al.: An intelligent Parkinson's disease diagnostic system based on a chaotic bacterial foraging optimization enhanced fuzzy KNN approach. Comput. Math. Methods Med. **1–24**, 2018 (2018)
7. Das, R.: A comparison of multiple classification methods for diagnosis of Parkinson's disease. Expert Syst. Appl. **37**(2), 1568–1572 (2010)
8. Düğnci, M., Aydin, M.E.: A honeybees-inspired heuristic algorithm for numerical optimisation. Neural Comput. Appl. 1-15 (2019)
9. Li, D.C., Liu, C.W., Hu, S.C.: A fuzzy-based data transformation for feature extraction to increase classification performance with small medical data sets. Artif. Intell. Med. **52**(1), 45–52 (2011)
10. Chen, H.L., Wang, G., Ma, C., Cai, Z.N., Liu, W.B., Wang, S.J.: An efficient hybrid kernel extreme learning machine approach for early diagnosis of Parkinson's disease. Neurocomputing **184**, 131–144 (2016)
11. Zuo, W.L., Wang, Z.Y., Liu, T., Chen, H.L.: Effective detection of Parkinson's disease using an adaptive fuzzy k-nearest neighbor approach. Biomed. Signal Process. Control **8**(4), 364–373 (2013)
12. Gük, M.: An ensemble of k-nearest neighbours algorithm for detection of Parkinson's disease. Int. J. Syst. Sci. **46**(6), 1108–1112 (2015)
13. Sakar, B.E., et al.: Collection and analysis of a Parkinson speech dataset with multiple types of sound recordings. IEEE J. Biomed. Health Inf. **17**(4), 828–834 (2013)
14. Zhang, H.-H., et al.: Classification of Parkinson's disease utilizing multi-edit nearest-neighbor and ensemble learning algorithms with speech samples. BioMed. Eng. OnLine **15**(1), 122 (2016)
15. Abrol, V., Sharma, P., Sao, A.K.: Greedy dictionary learning for kernel sparse representation based classifier. Pattern Recogn. Lett. **78**, 64–69 (2016)
16. Refaeilzadeh, P., Tang, L., Liu, H.: Cross-validation. In: Encyclopedia of Database Systems, pp. 532–538, Springer, Berlin (2009)
17. Sakar, C.O., et al.: A comparative analysis of speech signal processing algorithms for Parkinson's disease classification and the use of the tunable Q-factor wavelet transform. Appl. Soft Comput. **74**, 255–263 (2019)
18. Cai, J., Luo, J., Wang, S., Yang, S.: Feature selection in machine learning: a new perspective. Neurocomputing **300**, 70–79 (2018)
19. Yusta, S.C.: Different metaheuristic strategies to solve the feature selection problem. Pattern Recogn. Lett. **30**(5), 525–534 (2009)
20. Nguyen, B.H., Xue, B., Zhang, M.: A survey on swarm intelligence approaches to feature selection in data mining. Swarm Evol. Comput. **54**, 100663 (2020)
21. Karaboga, D., Basturk, B.: A powerful and efficient algorithm for numerical function optimization: artificial bee colony (ABC) algorithm. J. Glob. Optim. **39**(3), 459–471 (2007)

22. Karaboga, D., Gorkemli, B., Ozturk, C., Karaboga, N.: A comprehensive survey: artificial bee colony (ABC) algorithm and applications. Artif. Intell. Rev. **42**(1), 21–57 (2014)
23. Kiran, M.S., Gunduz, M.: XOR-based artificial bee colony algorithm for binary optimization. Turk. J. Electr. Eng. Comput. Sci. **21**, 2307–2328 (2013)
24. Kashan, M.H., Nahavandi, N., Kashan, A.H.: DisABC: A new artificial bee colony algorithm for binary optimization. Appl. Soft Comput. **12**(1), 342–352 (2012)
25. Durgut, R.: Improved binary artificial bee colony algorithm. arXiv preprint arXiv:2003.11641
26. Santana, C.J., Macedo, M., Siqueira, H., Gokhale, A., Bastos-Filho, C.J.A.: A novel binary artificial bee colony algorithm. Future Gener. Comput. Syst. **98**, 180–196 (2019)
27. Altay, E. V., Alatas, B. : Multi-objective association analysis of Parkinson disease with intelligent optimization algorithms. In: Proceedings of the 1st International Informatics and Software Engineering Conference (UBMYK), pp. 1–6, Ankara, Turkey (2019)
28. Badem, H., Turkusagi, D., Caliskan, A., Çil, Z.A.: Feature selection based on artificial bee colony for Parkinson disease diagnosis. In: Medical Technologies Congress (TIPTEKNO), İzmir. Turkey **2019**, 1–4 (2019)
29. Tuncer, T., Dogan, S.: A novel octopus based Parkinson's disease and gender recognition method using vowels. Appl. Acoust. **155**, 75–83 (2019)
30. Castro, C., Vargas-Viveros, E., Sanchez, A., Gutierrez-Lopez, E., Flores, D.L.: Parkinson's disease classification using artificial neural networks. In: VIII Latin American Conference on Biomedical Engineering and XLII National Conference on Biomedical Engineering, Cancun, Mexico, pp. 1060–1065 (2020)
31. Tuncer, T., Dogan, S., Acharya, U.R.: Automated detection of Parkinson's disease using minimum average maximum tree and singular value decomposition method with vowels. Biocybern. Biomed. Eng. **40**(1), 211–220 (2020)

Medical Knowledge-Based Deep Learning Framework for Disease Prediction on Unstructured Radiology Free-Text Reports Under Low Data Condition

Shashank Shetty[1](✉), V. S. Ananthanarayana[1], and Ajit Mahale[2]

[1] Department of Information Technology, National Institute of Technology Karnataka, Mangalore, India
shashankshetty06@gmail.com, anvs@nitk.ac.in

[2] Department of Radiology, Kasturba Medical College, MAHE, Mangalore, Karnataka, India
ajit.mahale@manipal.edu
http://nitk.edu.in/

Abstract. There has been increasing popularity in medical text mining due to its vast applications in the field of disease prediction and clinical Recommendation systems. Radiology reports possess rich information depicting radiologists investigations on the health conditions of the patients in associated radiology images. However, radiology reports exist in a free-text unstructured format consisting of valuable information for disease prediction. This information cannot be easily retrieved and utilized for prediction without suitable text mining techniques. The medical dataset available in the current procedure is small, domain-specific and restricted to the institution. However, data is one of the critical factors to power Machine Learning (ML) and Deep Learning (DL) models. To overcome the above challenge of predicting disease in the low data condition, we present a practical Deep Learning framework that combines a Knowledge Base (KB) with the Deep Learning for accurate text mining and predicting the lung diseases from the unstructured radiology free-text reports. We adopt Glove word embeddings with the KB trained on large corpus for effective text modelling. Further, we incorporate Convolutional Neural Network-based Discriminative Dimensionality Reduction (CNN-DDR) to obtain the most discriminative feature vector. Finally, a fully connected Deep Neural Network (DNN) is leveraged as the prediction model to detect the diseases. We applied the proposed framework to predict the lung diseases on radiology reports from both publicly available Indiana University (IU) dataset [6] and data collected from the private hospital. We benchmark the performance of the proposed framework, which outperforms against the standard ML Techniques.

Keywords: Clinical recommendation systems · Deep learning · Disease prediction · Knowledge base · Unstructured text mining

1 Introduction

Radiology is an essential medical discipline and central to modern healthcare, that provides comprehensive insights for disease detection, staging and treatment planning through medical imaging such as Chest X-Ray (CXR) and Computed Tomography (CT). Medical radiology reports are the processed data prepared by the radiologist from the raw images comprising of valuable prognostic informations that are yet to be investigated for predictive analytics applications like disease predictions. The radiologist or critical care physicians classify and predict the diseases from the report manually. Automating the process when there is more number of patients with higher risk will assist the clinicians with lesser experience to input their observations and obtain the predicted outcome. However, the diagnostic report exists in the unstructured free-text format making it inaccessible and challenging for automatic analysis. Radiology report comprises of finding section outlining the detailed medical examination containing both regular and irregular features, an impression section signifying the concluding remarks containing key observations and other sections like details of patients and indications. Out of these sections, the finding section is considered as an essential module, due to the coverage of major details of the organs, detection of any abnormalities and possible diseases. Other than the common NLP challenges, some of the significant challenges faced in radiology text report mining are: detection or identification of findings (normal or abnormal) and lack of publicly available medical datasets.

The unstructured radiology free-text report classification can be divided into two categories: Rule-based methods [7,10] and conventional ML-based methods [4,15]. The Rule-based approaches typically rely on traditional pattern matching with the pre-defined medical terms determined by radiologists or general medical terminologies extracted from the standard healthcare ontologies such as SNOMED CT[1]. The main disadvantage of rule-based approaches is the effectiveness of the system rely on the accuracy of the pre-defined patterns or the medical keywords. The ML-based techniques classify reports based on the medical features learned from the labelled reports [4,15]. Currently, the DL techniques have given promising results in the general text classification tasks such as sentimental analysis and relation extractions from the free-text [9,12]. The success of DL techniques in various applications has inspired us to apply it on clinical decision making by predicting diseases from radiology reports.

Word Embedding technique such as Global Vector (GloVe) [14] map every word to the dense and real-valued vector space that captures its meaning and syntactic properties of the words in raw corpus. Generally, the bigger the size of the corpora, superior is the quality of the learned word embeddings. But, there is a need for more time and considerable resources to train the larger corpora [13]. Thus, various groups and labs have released their learned word embeddings trained on the massive corpora [14]. Traditionally, word embeddings are determined at the word level from the medical corpus of unlabelled unstructured text

[1] http://www.snomed.org/.

considering only the implicit semantics of the words, neglecting the valuable information accessible in domain-specific medical resources [4]. Recently, few studies have implied that incorporating domain knowledge, or KB with the text corpus can benefit the improvement of word embeddings quality [3]. We use the embeddings trained on massive medical corpora as a medical Knowledge-base to enrich the effectiveness of word embeddings learnt from the radiology medical corpus. By leveraging Knowledge-base, the rare medical words can be acquired, projecting the word embeddings in more discriminative direction, strengthening the salient information and decreasing the noise. Due to the insufficient benchmark studies on publicly accessible data [4,7,10,15], there is a need to establish a best prediction techniques on radiology reports. Hence, we have leveraged the publicly available corpus: IU dataset as well as real-time data and benchmarked the results against the standard ML Techniques. In this research, we address the challenge of low data situation in the medical radiology report dataset by adapting the medical KB at the text feature extraction stage. We present an intelligent medical knowledge-based framework for disease classification and prediction on Unstructured Radiology Reports under Low data Conditions.

1.1 Motivations and Contributions

Most of the existing Clinical Decision Support or recommendation Systems utilizes only numerical or structured data. However, there is limited work on unstructured data like radiology free-text reports that as a good source of information for the prediction of diseases. Medical cohorts available in current practice is small, domain-specific and are limited to the medical institutes causing "low data situation" effecting the performance of DL models. Henceforth, motivation of this research work is to handle the unstructured radiology report in the low data situation and predict the disease outcomes. The main contribution of this research work is summarized as follows:

– We point out the significance of incorporating Knowledge-based Medical Text modelling with CNN-DDR and DNN for classifying and predicting diseases in Radiology Reports in low data environment.
– We carry out comprehensive analysis on two medical datasets (i.e., publicly available IU dataset and real-time corpus collected from the private medical institute) to illustrate the competency and rationality of the proposed DL Framework and benchmarked against the standard ML Techniques. To the best of our knowledge, this is the first work leveraging radiology data collected from Indian Private Hospital.
– We examine the effectiveness of incorporating Knowledge-base in enhancing the performance of the overall framework.

2 Proposed Methodology

The proposed Knowledge-based Deep Learning framework for Disease prediction from the unstructured radiology reports is shown in Fig. 1. As an overview,

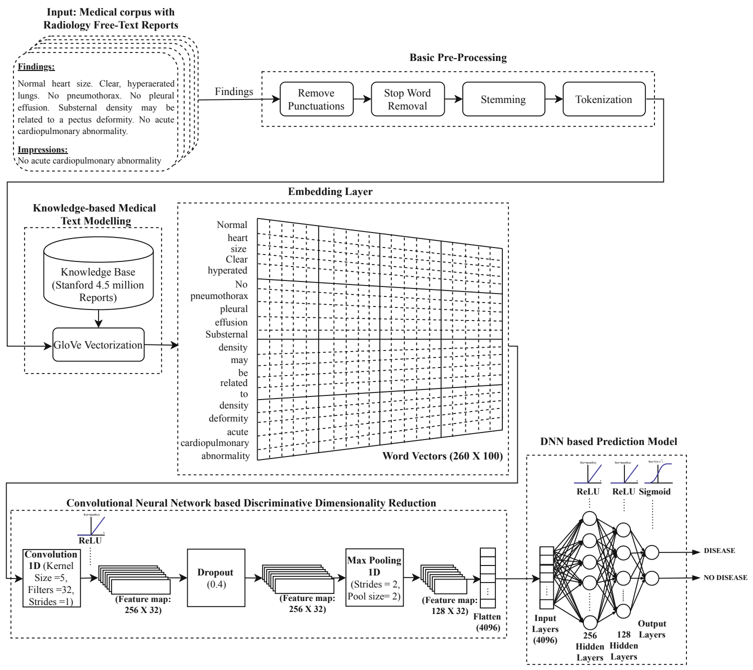
Input: Medical corpus with Radiology Free-Text Reports
Findings:
Normal heart size. Clear, hyperaerated lungs. No pneumothorax. No pleural effusion. Substernal density may be related to a pectus deformity. No acute cardiopulmonary abnormality.
Impressions:
No acute cardiopulmonary abnormality
Findings
Basic Pre-Processing
Remove Punctuations
Stop Word Removal
Stemming
Tokenization
Knowledge-based Medical Text Modelling
Knowledge Base (Stanford 4.5 million Reports)
GloVe Vectorization
Embedding Layer
Normal heart size Clear hyperated No pneumothorax pleural effusion Substernal density may be related to density deformity acute cardiopulmonary abnormality
Word Vectors (260 X 100)
Convolutional Neural Network based Discriminative Dimensionality Reduction
ReLU
Convolution 1D (Kernel Size =5, Filters =32, Strides =1)
(Feature map: 256 X 32)
Dropout (0.4)
(Feature map: 256 X 32)
Max Pooling 1D (Strides = 2, Pool size= 2)
(Feature map: 128 X 32)
Flatten (4096)
DNN based Prediction Model
ReLU
ReLU
Sigmoid
Input Layers (4096)
256 Hidden Layers
128 Hidden Layers
Output Layers
DISEASE
NO DISEASE

Fig. 1. Medical Knowledge-based Deep Learning Framework

the radiology findings are pre-processed to obtain the essential latent medical concepts. The word embeddings are learnt from the medical words by applying customized knowledge-based Medical Text modelling. Dense word embeddings obtained are mapped to the medical words from the findings in the Embedding Layer. Most Discriminative features are extracted by reducing the dimension using the CNN-DDR. Finally, the flattened discriminative features are fed to the DNN for predicting the disease outcome.

2.1 Basic Pre-processing

The radiology findings are extracted from the medical corpus and these findings are passed through a series of NLP tasks such as removing punctuation's; stop words to retain only essential medical words and filter insignificant words and symbols. Stemming helps in clearing away the suffixes and retains only the root word. During the Tokenization phase, the medical findings are divided into smaller units called tokens. Next, the tokens are processed through Knowledge-based Medical Text modelling phase to obtain the latent medical information.

2.2 Knowledge-Based Medical Text Modelling (KB-MTM)

In the proposed model, the word embeddings are jointly learnt from both the medical corpus and the KB. Firstly, we will revisit the GloVe that creates the base for the medical corpus-based objective function, and in the next section, we will derive the improved objective function from the KB.

i. Global Vectors (GloVe) for Vectorization: GloVe [14] word embedding model uses statistical information generated from the global word-word co-occurrence matrix to obtain the word vectors from the text corpus. In particular, given a medical radiology Corpus MC, GloVe initializes by building the Word-word co-occurrence matrix X, where the *target word* is depicted by the row and the *context word* is depicted by the column. Given a medical corpus with n words, the co-occurence matrix will be nxn. The X_{ij} denotes the tabular entries, that is the total occurrences of the context medical word $\tilde{mw}_j$ appears in the target medical word mw_i in the medical corpus MC. Let V represent the Vocabulary, the collection of all the words in the medical corpora. For a given medical word mw_i, GloVe model instigates by learning word embeddings or word vectors mv_i, $\tilde{mv}_i \in \mathbb{R}^d$ considering it as a target word mw_i or the context word $\tilde{mw}_i$ respectively and the dimensionality d is the user defined hyper-parameter.

The probability of context medical word $\tilde{mw}_j$ given the target medical word mw_i is given by $P(j|i) = X_{ij} \Big/ X_i$. Where, X_i is the total occurrence of target word mw_i in the MC. For instance, $mv_i^T \cdot \tilde{mv}_i$ gives the similarity between the two medical words mw_i and $\tilde{mw}_j$. We have to learn the medical word vectors that are true to the global word-word co-occurrence matrix given by,

$$mv_i^T \cdot \tilde{mv}_j = logP(j|i) = log(X_{ij}) - log(X_i) \tag{1}$$

Similarly $X_{ij} = X_{ji}$,

$$mv_j^T \cdot \tilde{mv}_i = logP(i|j) = log(X_{ij}) - log(X_j) \tag{2}$$

Adding Eq. (1) and Eq. (2). Since, $mv_i^T \cdot \tilde{mv}_j = mv_j^T \cdot \tilde{mv}_i$, we get

$$2mv_i^T \cdot \tilde{mv}_j = 2log(X_{ij}) - log(X_i) - log(X_j) \tag{3}$$

In the Eq. (3), the left hand side are the learnable parameters and the right hand side are the counts learnt from the medical corpus. Since $log(X_i)$ and $log(X_j)$ rely only on the medical words mw_i and $\tilde{mw}_j$, we consider them as the biases particular to the medical word that will be learned.

$$mv_i^T \cdot \tilde{mv}_j = log(X_{ij}) - b_i - b_j \tag{4}$$

$$mv_i^T \cdot \tilde{mv}_j + b_i + b_j = log(X_{ij}) \tag{5}$$

Where, b_i and b_j are the scalar biased real-valued terms associated with mw_i and $\tilde{mw}_j$ respectively. The objective function of the GloVe Embedding method minimizes the weighed least square errors with weighting function f:

$$J_{MC} = \sum_{i,j=1}^{V} f(X_{ij})(R^{MC} + b_i + \tilde{b_j} - log(X_{ij}))^2 \tag{6}$$

Here, $R^{MC} = mv_i^T \cdot \tilde{mv_j}$, is the scalar vaiue obtained by the inner dot product between the transpose of target word vector mv_i and the context word vector $\tilde{mv_j}$ from *MC*. The $f(X_{ij})$ is the weighting function that allocates lower weights for frequent co-occurrences to prevent from skewing of objective function due to over-emphasizing of most common word pairs and is given by:

$$f(m) = \begin{cases} (\frac{m}{m_{max}})^{\alpha} & \text{if } m < m_{max} \\ 1 & \text{otherwise} \end{cases} \tag{7}$$

As per [14], the effectiveness of the model relies on the cutoff. So, m_{max} is set to 100 and α to 3/4. The objective function defined from the medical corpus in Eq. (6) aim to learn the co-occurrence between the two medical words mw_i and $\tilde{mw_j}$ by minimizing the squared difference between the inner dot product and the logarithm of the co-occurences between the medical words in the matrix X.

ii. Integrating Medical Knowledge Base to GloVe: GloVe is the word embeddings technique that learns only from the corpus and does not use any existing KB's. Henceforth, failing to learn embeddings from the rare words and faces a significant challenge in capturing the semantics, which is essential in medical text mining. Likewise, the medical dataset available will be domain-specific restricted to private medical institute and small in number, causing a considerable challenge to learn word embeddings due to the smaller vocabulary size. To deal with this issue, we incorporate learnt word embeddings as a KB during the text modelling of the medical corpus. Given a Medical Knowledge Base *MKB*, we derive the objective function J_{MKB} that considers the semantic relation R(mw_i, $\tilde{mw_j}$) between the corresponding target and context medical words mw_i and $\tilde{mw_j}$ respectively. We use learnt word embeddings trained on 4.5 million Stanford reports [17] as a concrete case for KB in this experiment. There are no rigid rules to use any specific KB. However we can utilize any KB that derives meaningful connection between the medical words.

Let $R^{MKB} = kv_i^T \cdot \tilde{kv_j}$ be the scalar vaiue obtained by the inner dot product between the transpose of target word knowledge vector kv_i and the context word knowledge vector $\tilde{kv_j}$ from MKB corresponding to the words mw_i and $\tilde{mw_j}$ in the *MC*. The Medical Knowledge-based objective function can be described as follows:

$$J_{MKB} = \sum_{i,j=1}^{V} f(X_{ij})(R^{MKB} + b_i + \tilde{b_j} - log(X_{ij}))^2 \tag{8}$$

Where, b_i and b_j are the scalar biased real-valued terms associated with mw_i and $\tilde{mw_i}$ respectively. The Medical Knowledge-based objective function defined by Eq. (8) learns the co-occurrence between the two medical words mw_i and $\tilde{mw_j}$ by minimizing the squared difference between the inner dot product of knowldege vectors derived from the *MKB* and the logarithm of the co-occurences between the words mw_i and $\tilde{mw_j}$ in the matrix X.

iii. Embedding Layer: The Embedding layer is loaded with the pre-trained word embedding weights obtained from the huge corpus and the word embeddings for each medical words in the training medical corpus is learned.

The medical findings are of different length and are padded to have the same length. Matrix Multiplication of one hot vector of each word in a vocabulary and Embedding Weight Matrix returns the corresponding matrix of the medical words in a given corpus as the output of Embedding Layer (i.e., hidden layer). Here, Embedding weight Matrix is treated as a look-up table, where the hidden layer output can be obtained by look-up operation with the encoded integer of the medical word. The complete pre-trained medical KB is loaded as a dictionary of 260 padded words to produce the embedding matrix of word vectors with output dimension 100. The algorithm for proposed KB-MTM is mentioned in the Sect. A.

2.3 Convolutional Neural Network Based Discriminative Dimentionality Reduction (CNN-DDR)

We have proposed CNN-DDR technique with the objective of reducing the storage and computational costs, by learning from the high dimensional embeddings into low dimensional representation, such that the most discriminative features are retained. The architecture employed for CNN-DDR is a modified version of CNN architecture [5]. Let $mx_i \in \mathbb{R}^d$ denote i-th medical word in the sentence (i.e., findings) of d-dimensional word vector. Here, we consider 100 dimension word vectors for each medical word (i.e., $d = 100$). The medical sentence (i.e., findings from the radiology report) of length k (i.e., $k = 260$) with padding when required is represented as: $mx_{1:k} = mx_1 \oplus mx_2 \oplus ... \oplus mx_k$. Here, $\oplus$ represent the concatenation operator. Let the concatenation of the medical words $mx_i, mx_{i+1}, ..., mx_{i+j}$ be represented as $mx_{i:i+j}$. Let $W \in \mathbb{R}^{pd}$ be the filter involved in convolution operation applied to the window of p medical words to generate the Discriminative features. We leverage 32 filters of window size 5 (i.e., $p = 5$). For instance, from the window of medical words $mx_{i:i+p-1}$, the new discriminative medical feature mc_i is produced and is represented by $mc_i = f(W \cdot mx_{i:i+p-1} + b)$., where b is a bias term, $b \in \mathbb{R}$.

Rectified Linear Unit (ReLU) [1] activation function, f with filter W is employed on each available window of medical words $\{mx_{1:p}, mx_{2:p+1}, ..., mx_{k-p+1:k}\}$ to generate the feature map, $mc = [mc_1, mc_2, ..., mc_{k-p+1}]$, here $mc \in \mathbb{R}^{k-p+1}$. Later, we apply dropout mechanism [9] after the first layer of convolution operation for regularization and addressing overfitting problem. Dropout mechanism is utilized to avoid co-adaptation at the Hidden layer by randomly dropping out a few units at the time of the training process. Let $z = [\tilde{mc}_1, \tilde{mc}_2, ..., \tilde{mc}_n]$ be the penultimate layer and n be the number of filters. Let y be the output of forward propagation in the CNN and is represented by $y = W \cdot z + b$. When the dropout operation is applied at the penultimate layer, $y = W \cdot (z \otimes \delta_i) + b$, where $\delta_i \in \mathbb{R}^n$ is the Bernoulli random variables that drops the i^{th} neuron with the probability (p_i) of being 1 and $\otimes$ denote the element-wise multiplication operator. Regularizing the convolution layer with the dropout probability gives the maximum robustness to the overfitting. For our experiment, based on a grid search approach [2], dropout probability of 0.4 is applied after the first hidden layer to restrain the model from overfitting.

Let $\tilde{y} = [\tilde{y_1}, \tilde{y_2}, ..., \tilde{y}_L]$, where $L = k-p+1$ be the feature map generated from the Dropout Layer. Max-pooling [5] is used to down sample the input features by reducing the dimensionality of the feature map. The main aim is to learn the most discriminative features with the maximum value for every feature map. Max-pooling produces the discriminative feature map $y^{'}$ by applying the strides s and pooling window size pw on the feature map $\tilde{y}$. Let $||$ be the customized concatenation operation and Max-pooling operation is applied to every possible windows on the feature map $\tilde{y}$ to produce, $y^{'} = ||_{i=1,i=i+s}^{L-pw+1} max\{\tilde{y}_{i:i+pw-1}\}$, where $y^{'} \in \mathbb{R}^n$. For instance in our case, we have applied pool window size, *pw=2* and strides, *s=2* on feature map of length, *L=256*. Initially, i will be equal to 1 and incremented with the number of strides till it reaches *L-pw+1*. The discriminative feature map obtained is $y^{'}_{1:128} = max\{\tilde{y}_{1:2}\} \oplus max\{\tilde{y}_{3:4}\} \oplus ... \oplus max\{\tilde{y}_{255:256}\}$. The feature maps obtained from the max-pooling layer containing discriminative features is flattened into channel dimension and is given as the input to the prediction model.

2.4 DNN Based Prediction Model

DNN [9] is applied in the proposed framework for predicting the disease exists or not in the Radiology report. DNN is typically a multi-layer neural network, influenced by a biological neural network consisting of a collection of connected modules named neurons. DNN's comprises of multiple such connected units between the input and output layers. The flattened discriminative features $y^{'} \in \mathbb{R}^n$ obtained from the CNN-DDR module is given as the input to fully connected four layered DNN for predicting whether disease exists or not in the radiology reports. The basic operation performed by DNN on the flattened discriminative features are forward propagation or inference represented as,

$$y^{'}_{i+1} = h(W_i \cdot y'_i + b_i), \tag{9}$$

where $W_{i=0,1,2}$ are the weight arrays and $b_{i=0,1,2}$ are the bias of the DNN Layers. Here, *h()* is the non-linear function applied on every element of the feature vector. Non-linear function, ReLU is applied at the penultimate layers and the Sigmoid operation for the binary classification at the output layers. For our experiment, based on a grid search approach [2], dropout probability of 0.2 is applied after the first hidden layer to restrain the model from overfitting.

3 Experimental Results and Evaluation

3.1 Datasets and Cohort Selection

Thorough investigation was conducted on two medical datasets: medical expert labelled publicly accessible radiology cohort of IU Dataset [6] and real-time data collected from KMC Hospital (Mangalore, India) (Ethics approval was granted by the Institutional Ethics Committee (IEC), Kasturba Medical College (KMC), Mangalore to leverage the de-identified data for the research purpose). The radiology reports collected are de-identified and categorized as either "normal" (i.e., cases with no acute abnormality or any active diseases) or "abnormal" (i.e., cases with acute pulmonary abnormalities such as Cardiomegaly, Pulmonary atelectasis, Pleural effusion, Opacity/lung base, Calcified granuloma, etc.). IU dataset [6] is the manually labelled publicly available dataset consisting of de-identified clinical radiology images paired up with the diagnostic reports. Most of the existing works on IU dataset are cross-modal retrieval (i.e., report generation) from images [11,16]. The dataset is unseen in terms of radiology report classification and disease prediction. We selected 3638 radiology reports comprising of *Findings* and reports with missing *findings* are removed. The Medical Subject Heading (MeSH) indexing is leveraged to find the ground truth annotation and based on the MeSH terms, the reports are categorized into two classes "normal" and "abnormal". The final annotated data is manually validated by an experienced radiologist to verify the correctness of the annotations. Table 1 depicts the summary statistics of both the datasets.

Table 1. Cohort statistics: Radiology reports from two Institutions

Characteristic	IU dataset	KMC dataset
Total # of Radiology Reports	3996	502
Total # of Final Cohort selected	3638	502
Total # of Sentences	11541	3649
Total # of Words	91171	17198
Total # of Vocabulary	1568	393
Total # of Training set	3274	452
Total # of test set	364	50
% of Normal cases	38%	52%
% of Abnormal cases	62%	48%

3.2 Benchmarking the Proposed Prediction Model Against the State-of-the-Art Machine Learning Techniques

In order to comprehensively validate the proposed Medical knowledge-based Deep Learning framework, we leverage various traditional ML techniques such as Support Vector Machine (SVM), K-Nearest Neighbour (KNN), Random Forest (RF), Logistic Regression (LR) and AdaBoost classifier (AB) [8]. For our experiment, we have used the NVIDIA Tesla M40 server with 24 GB GPU, 3 TB Hard disk, 128 GB RAM and Ubuntu server Operating System. The radiology corpora are divided into training and test set. The Medical Knowledge-based Deep Learning model was trained for 100 epochs and 10-fold stratified cross-validation is applied to examine the proposed model. The findings extracted from the report are preprocessed and padded with the input size of 260. The proposed KB-MTM is applied to the free-text to obtain the word vectors of size $260 \times 100 = 26000$. The CNN-DDR is utilized to produce the most discriminative medical features of size 4096. Further, the DNN based prediction model is employed on the low dimensional features extracted from CNN-DDR to detect the pathology present on the reports. Also, these KB features were tested on traditional ML techniques for validation. The grid search technique [2] is used to choose the optimal hyperparameters for fine-tuning of the model parameter setting. Empirically, the classical ANN with one hidden layer was tested, and it did not perform well compared to the DNN with two hidden layers. We implemented the proposed model using a well-known deep learning framework, Tensorflow [9]. The following are the hyperparameters set for CNN-DDR and DNN model: Kernel Size:5, filter size:32, strides:1, dropout probability: 0.4, pool size:2 and learning rate: 0.001. We have also utilized Adam optimizer and binary cross-entropy as the loss function. The benchmark results are presented in Table 2 for IU and KMC Hospital dataset. The performance and the quality of the disease prediction were examined with the following five metrics: accuracy, precision, recall, F1 score and Matthews correlation coefficient (MCC) [8]. The proposed model with KB achieves high precision signifies that most cases belonging to the "abnormal" class are detected, which is the main objective of our disease prediction model. We have measured the F1-Score and MCC, which are also an essential evaluation metrics in our experiment, as our data exhibit class imbalance problem (i.e., In IU dataset, the pathology or abnormal class are in more significant number compared to the normal class; refer Table 1). The proposed model with KB has the staggering improvement in F1-Score and MCC for IU dataset. The higher value of F1-Score and MCC of the proposed Knowledge-based Deep Learning model on both dataset signifies that even if there was a class imbalance, the model was able to accurately classify. It is observed that RF with KB has produced good results after the proposed model for KMC dataset. It is due to the ensemble of decision trees generated by RF on the feature vectors obtained from KB-MTM is more discriminative for predicting disease compared to DNN without KB. However, the proposed DNN with KB features outperforms RF with KB features and other traditional ML models in terms of performance for both the dataset.

3.3 Effect of Knowledge-Based Medical Text Modelling

We have also examined the effect of customized KB-MTM compared with the Glove word embedding, as shown in Fig. 2a and Fig. 2b respectively. There is a significant increase of 3% and 2% in terms of accuracy, precision, recall, F1 score and around 7% and 3% improvement in MCC for IU dataset and KMC dataset respectively. The results depict that incorporating KB with the word-embedding models significantly increases the performance of the disease prediction due to the knowledge gained from the word embeddings trained on the large corpora.

Table 2. Benchmarking the proposed DNN model with and without KB against the State-of-the-Art ML Model for IU and KMC Hospital Dataset

Models	Indiana University Dataset					KMC Hospital Dataset				
	Acc.	Pre.	Recall	F-Sc.	MCC	Acc.	Pre.	Recall	F-Sc.	MCC
SVM	73.75%	0.732	0.737	0.597	0.415	76.16%	0.786	0.762	0.797	0.529
KNN	77.16%	0.780	0.772	0.705	0.521	88.88%	0.892	0.889	0.895	0.777
RF	86.36%	0.873	0.864	0.787	0.708	93.53%	0.942	0.935	0.937	0.873
LR	79.74%	0.795	0.797	0.704	0.555	88.88%	0.892	0.889	0.896	0.777
GB	76.55%	0.779	0.766	0.591	0.482	88.28%	0.889	0.883	0.891	0.765
DNN-KB ***(Proposed)***	**87.27%**	**0.874**	**0.873**	**0.813**	**0.723**	**92.53%**	**0.927**	**0.925**	**0.929**	**0.850**
DNN+KB ***(Proposed)***	**90.40%**	**0.908**	**0.904**	**0.858**	**0.794**	**94.13%**	**0.947**	**0.941**	**0.944**	**0.883**

Note: Acc.=Accuracy, Pre.=Precision, F-Sc.=F1-Score, DNN-KB=DNN without KB, DNN+KB=DNN with KB

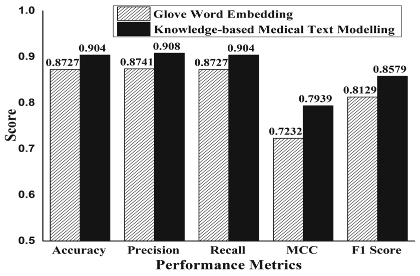

(a) Indiana university dataset

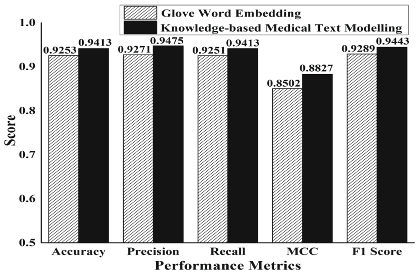

(b) KMC Hospital dataset

Fig. 2. Effectiveness of proposed KB-MTM compared to the GloVe Embeddings

4 Conclusion and Future Work

As an outline, we have proposed the Medical Knowledge-based Deep Learning framework for predicting the lung diseases from the radiology reports at low data condition. We have found that there is no adequate literature for comparing the prediction techniques on radiology reports. Hence, we have benchmarked our results in comparison with the Standard ML Techniques on publicly available IU dataset and real-time collected dataset from the KMC Hospital. To the best of our knowledge, this is the first work on the disease prediction from the radiology reports collected from Indian private Hospital. To overcome the issue of handling the scarce data situation in the prediction models, the KB-MTM is proposed to incorporate the trained word embeddings from the large medical corpora. It is observed that integrating knowledge-base trained on a large corpus of radiology reports has increased the performance of the proposed prediction model. When we benchmark against the standard ML techniques, our proposed Medical Knowledge-based Deep Learning framework outperforms by 4–17% and 1–18% in terms of accuracy on IU and KMC Hospital dataset, respectively.

In future work, we would like to explore the DL architecture for enhancing the disease prediction accuracy. We would further like to analyze the multi-class classification of abnormal classes to group of pathologies.

Acknowledgement. We thank the Department of Information Technology, NITK Surathkal for providing resources for this research. We are grateful to KMC Hospital, Mangalore for granting access to the de-identified radiology reports for this research (*Ref. IEC KMC MLR 01-2020/80 dated 15.01.2020*).

A Appendix

Algorithm 1: Knowledge-based Medical Text Modelling

```
Input: Medical-Knowledge-Base: Pre-Trained Word embeddings on 4.5 million Stanford
       Radiology Report, Medical-Corpus: Unstructured Radiology Reports
Output: A Text Model trained on Unstructured Radiology Report Corpus with Word
        Embedding Representation
initialization;
Function Clean($S$):
    Remove the Punctuation from $S$.
    Remove Stopwords from $S$.
    Stemming operation is applied on $S$ to remove suffix.
    return $S$;
End Function
Function Tokenize(Medical-Corpus):
    for each findings $f_i \in$ Medical-Corpus do
        Cleaned-Findings $\longleftarrow$ Clean($f_i$);
        tokens $\longleftarrow$ Cleaned-Findings are split into tokens;
    end
    return tokens;
End Function
Function Convert-Word-to-Embeddings(Medical-Corpus):
    - Tokenized-Docs $\longleftarrow$ Tokenize(Medical-Corpus)
    - Let $v_1, v_2, \ldots, v_n$ be the Unique medical words (i.e., Vocabulary) obtained from the
    $Tokenized - Docs$.
    - Generate one hot vector $hv_{i:n}$ for each word in a Vocabulary $v_{i:n}$.
    - Let $k$ be the input length of each $Tokenized - Docs$ (Pad the documents if necessary.
    - Generate the knowledge-based word embeddings.
      • The co-occurrence between the two medical words are learnt by the objective
      function defined in the Eq. (8) using Stochastic Gradient Descent by minimizing
      the $kv_i$, $\tilde{kv_j}$, $b_i$ and $\tilde{b_j}$ from the large corpus (refer Eq. (8) for term details).
      • Load the Medical-Knowledge-Base as the Embedding Weight Matrix with
      $d$-dimension word knowledge vectors $kv^1_{i:d}, kv^2_{i:d}, \ldots, kv^k_{i:d} = kv^{j:k}_{i:d}$,
      (where, $i = 1, 2, \ldots, d$) for all the medical words $k$.
    - The corresponding matrix is obtained by matrix multiplication (denoted by $\times$)
    between one hot vector of each word in a vocabulary and Embedding Weight Matrix
    through Embedding Layer with input size $k$ and the output dimension $d$ is,
    $\tilde{kv}^{j:k}_{i:d} \longleftarrow hv_{i:n} \times kv^{j:k}_{i:d}$
    return Word Vectors $\tilde{kv}^{j:k}_{i:d}$ of size $k \times d$
End Function
```

References

1. Agarap, A.F.: Deep learning using rectified linear units (relu). CoRR abs/1803.08375, March 2018
2. Bergstra, J., Bengio, Y.: Random search for hyper-parameter optimization. J. Mach. Learn. Res. **13**, 281–305 (2012)

3. Cao, Y., Huang, L., Ji, H., Chen, X., Li, J.: Bridge text and knowledge by learning multi-prototype entity mention embedding, pp. 1623–1633. ACL (2017)
4. Castro, S., Tseytlin, E., Medvedeva, O., Mitchell, K., Visweswaran, S., Bekhuis, T., Jacobson, R.: Automated annotation and classification of BI-RADS assessment from radiology reports. J. Biomed. Inform. **69**, 177–187 (2017)
5. Collobert, R., Weston, J., Bottou, L., Karlen, M., Kavukcuoglu, K., Kuksa, P.P.: Natural language processing (almost) from scratch. CoRR (2011)
6. Demner-Fushman, D., Kohli, M.D., Rosenman, M.B., Shooshan, S.E., Rodriguez, L., Antani, S.K., Thoma, G.R., McDonald, C.J.: Preparing a collection of radiology examinations for distribution and retrieval. JAMIA **23**(2), 304–10 (2016)
7. Dutta, S., Long, W.J., Brown, D.F., Reisner, A.T.: Automated detection using natural language processing of radiologists recommendations for additional imaging of incidental findings. Ann. Emerg. Med. **62**(2), 162–169 (2013)
8. Flach, P.: Machine Learning: The Art and Science of Algorithms That Make Sense of Data. Cambridge University Press, Cambridge (2012)
9. Goodfellow, I., Bengio, Y., Courville, A.: Deep Learning. The MIT Press, Cambridge (2016)
10. Hassanpour, S., Bay, G., Langlotz, C.: Characterization of change and significance for clinical findings in radiology reports through natural language processing. J. Digit. Imaging **30**, 314–322 (2017)
11. Liu, G., Hsu, T.H., McDermott, M.B.A., Boag, W., Weng, W., Szolovits, P., Ghassemi, M.: Clinically accurate chest x-ray report generation. CoRR (2019)
12. Santos, I., Nedjah, N., Mourelle, L.: Sentiment analysis using convolutional neural network with fastText embeddings, pp. 1–5, November 2017. https://doi.org/10.1109/LA-CCI.2017.8285683
13. Patel, K., Patel, D., Golakiya, M., Bhattacharyya, P., Birari, N.: Adapting pre-trained word embeddings for use in medical coding, pp. 302–306. ACL (2017)
14. Pennington, J., Socher, R., Manning, C.: Glove: Global vectors for word representation, pp. 1532–1543. Association for Computational Linguistics, October 2014
15. Trivedi, H., Mesterhazy, J., Laguna, B., Vu, T., Sohn, J.: Automatic determination of the need for intravenous contrast in musculoskeletal MRI examinations using IBM Watson's natural language processing algorithm. J. Digit. Imaging **31**(2), 245–251 (2017)
16. Xue, Y., Xu, T., Rodney Long, L., Xue, Z., Antani, S., Thoma, G.R., Huang, X.: Multimodal recurrent model with attention for automated radiology report generation, pp. 457–466. Springer International Publishing, Cham (2018)
17. Zhang, Y., Ding, D.Y., Qian, T., Manning, C.D., Langlotz, C.P.: Learning to summarize radiology findings. CoRR (2018)

Multidataset Incremental Training for Optic Disc Segmentation

Javier Civit-Masot[1](✉), Antonis Billis[2], MJ Dominguez-Morales[1], Saturnino Vicente-Diaz[1], and Anton Civit[1]

[1] Escuela Superior de Ingenieria Informatica, University of Seville, Seville, Spain
{jcivit,mdominguez,satur,civit}@atc.us.es

[2] Lab of Medical Physics, Aristotle University of Thessaloniky, Thessaloniky, Greece
ampillis@med.auth.gr

Abstract. When convolutional neural networks are applied to image segmentation results depend greatly on the data sets used to train the networks. Cloud providers support multi GPU and TPU virtual machines making the idea of cloud-based segmentation as service attractive. In this paper we study the problem of building a segmentation service, where images would come from different acquisition instruments, by training a generalized U-Net with images from a single or several datasets. We also study the possibility of training with a single instrument and perform quick retrains when more data is available. As our example we perform segmentation of Optic Disc in fundus images which is useful for glaucoma diagnosis. We use two publicly available data sets (RIM-One V3, DRISHTI) for individual, mixed or incremental training. We show that multidataset or incremental training can produce results that are similar to those published by researchers who use the same dataset for both training and validation.

Keywords: Deep learning · Eye fundus image segmentation · Multiple dataset training · Incremental training · Glaucoma

1 Introduction

Glaucoma is a disabling decease that can lead to blindness in about 2 to 5% of the cases and sight impairment in 10% of the cases [19]. Although Loss of vision can occur even with the best treatment, correct therapy and follow-up will stabilize the majority of patients with glaucoma.

The key to detection and management of glaucoma is understanding how to examine the optic disc (OD) [4]. The OD is an oval 'plughole' down which the retinal nerve fibres descend through a sheet known as the lamina cribrosa. The retinal nerve fibres are then bundled together to form the optic nerve. The optic cup (OC) is the white, cup-like area in the center of the optic disc. The tissue between the border of the cup and the disc is the neuroretinal rim. This tissue consists mainly of nerve fibers with some glial cells and is usually pink. Most normal discs are more vertically oval and their cup more horizontally oval. A typical retina fundus image is shown in Fig. 1.

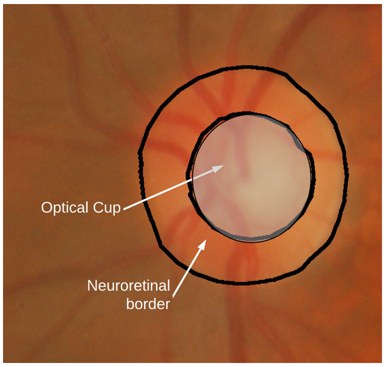

Fig. 1. Optic disc and cup

Several indicators are used to aid the diagnosis of glaucoma from fundus eye images. The cup to disc ratio (CDR) [18] which is the rate between the diameters of the optic disc and cup is the most widely used. In the mean CDRs of the glaucoma and normal eyes were 0.65 ± 0.13 and 0.39 ± 0.15, respectively allowing CDR to be used as a diagnostic aid. Another diagnostic approach is based on the rule based on the shape of the neuroretinal RIM. According to this rule in normal eyes, the thickness of the neuroretinal rim along the cardinal meridians of the OD decreases in the order inferior (I) $>$ superior (S) $>$ nasal (N) $>$ temporal (T) [9]. In any case accurate OC/OD segmentation is required to be able to apply these techniques. This segmentation is an error prone process even for expert ophthalmologists specially in typical work overloaded scenarios.

Thus machine learning (ML) approaches are attractive for fundus image segmentation. Segmentation methodologies are based in three possible approaches [24]: Form matching based on random forests, support vector machines or K-means [14]; techniques based on transformations and active contours [3] oe Deep learning-based methods [1,21,22,26].

There are two scenarios for using image segmentation tools in a clinical set up. In the first one the tool is marketed by the provider of the image acquisition instrument. In this case we can train using images captured with the instrument linked to the tool. In a second scenario the segmentation is implemented as a service and has to be able to segment images from different clinics acquired with different instruments. Some approaches have been proposed for combined dataset training e.g. [5], however, they have not been applied, to medical image segmentation. Some previous works [1,21] have used different data sets but they train and test with each set independently. In [8] authors use several datasets but training is always performed with a combined dataset and, thus, it does not show the influence of performing single or multidataset training.

The objective of this paper is to study the problems that we would face to implement fundus segmentation as a service. For this purpose we will first find a suitable architecture for fundus image segmentation. Then we will train the system using a single data set and use it to predict over images from that set and images acquired with other instruments. After this we will use a mixed training dataset combining images from the different datasets, train our net with it and use it to make predictions on the different testing datasets. Finally we will study the realistic approach for clinical practice, i.e., to train with what is available and later do retraining when more data becomes available.

2 Materials and Methods

Implementation. Selection of Architectures for Segmentation. U-Net is a widely used fully convolutional neural network introduced in [20]. It has been widely used in image segmentation applications including several works related to ophthalmologic images including OD segmentation [21], retinal vessel segmentation [16] and diabetic retinopathy diagnosis [2]. In this work tools were developed to generalize U-Net models to allow rapid implementation in cloud-based GPU and TPU [10] architectures. We use a Keras [7] Tensorflow 2.1 implementation on the Google Collaboratory Python notebook environment.

In this section we will establish a methodology to select a generalized U-Net that correctly segments the OD. For this purpose we will train using combined datasets leaving the comparison of this approach with other alternatives for later sections.

Our networks are optimized versions of the U-Net proposed in [21]. Among the modifications are the use of a different image generator that produces the larger image batches for TPU training by means of static and dynamic data augmentation [27]. Also, to be able to modify our U-Net structure without recoding, we use a highly parameterizable U-Net recursive model. With this model we can change the depth and width of the net, the possibility of batch normalization, the use of upsampling or transpose convolution and the width ratio between successive layers known as increment ratio (IR). IR [13] is widely used as an effective pruning method.

We select network with the smallest IR and, thus, the one with less trainable parameters when two networks produce similar results. Although we train and make predictions in the web pruning improves time and reduces operating costs. The reduction of the initial network width and its depth are alternatives that we also explore.

We use 96 image batches for both training and testing, and train for 15 epoch using 100 training steps and 30 test steps per time. We use an Adam optimization algorithm with a learning rate of 0.0008. These values have proven suitable for TPU and GPU based training and provide good results with training times of less than 30 min for the TPU implementation.

Regarding the data sets, we use the publicly available RIM-ONE v3 and DRISHTI fundus image data sets. RIM ONE-v3 [12], form the MIAG group at the University of La Laguna (Spain), consists of 159 images labeled by expert ophthalmologists for OD/OC. DRISHTI-GS [23], from Aravind Eye Hospital, Madurai (India), consists of 101 images also labeled for OC/OD. In Fig. 2 we can see that the images that come from both data sets have very different characteristics.

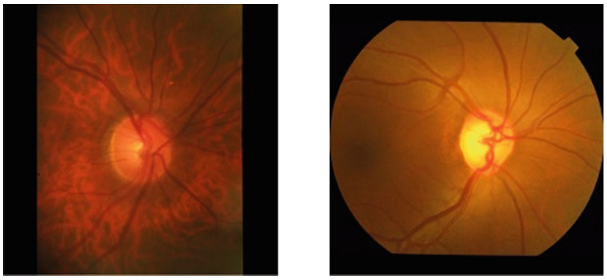
Fig. 2. Images RIM ONE (left) and DRISHTI (right) datasets

Figure 3 shows the used segmentation methodology. We start by trimming and resizing the images in the data sets by removing a 10% border on all edges of the image to reduce the black borders. After this, we resize the images to 128×128 pixels and perform a limited clip contrast histogram equalization. After, we split the data sets. For each set, we use 75% of the images for training and 25% for validation. Next, we perform, for each data set, static data augmentation by creating images with modified brightness and different contrast parameters. Later, we merge the data from the different sets. In the merging process, we perform data replication and random combustion to provide longer vectors as input for our dynamic image generators. Image generators [6] increase the data by performing random rotations, moving, zooming and flipping over the images of the extended merged data set.

Dice coefficient [11] is used to estimate the similarity between the correct and predicted disc. This figure of merit, also known as F1 score, is widely used and allows us to compare our results with those from other works. Dice coefficient is defined as:

$$DC = \frac{2TP}{2TP + FP + FN} \tag{1}$$

In this equation TP indicates true positives, FP false positives, and FN false negatives.

2.1 Instrument Based Versus Cloud-Based Segmentation

To show the results obtained when training with data from a single instrument or when training as a service, we will first train the system using a single data set and use it to predict images from other sets. After this we will use last section's mixed data set to train our network and use it to make the same predictions. In this section we use a generalized 6-layer U-Net which had good results in the previous section. It has only 40 channels in the first layer and the layer IR is 1.1. Given that we also resize the images in the sets to 128×128, the number of trainable parameters is less than 1 million.

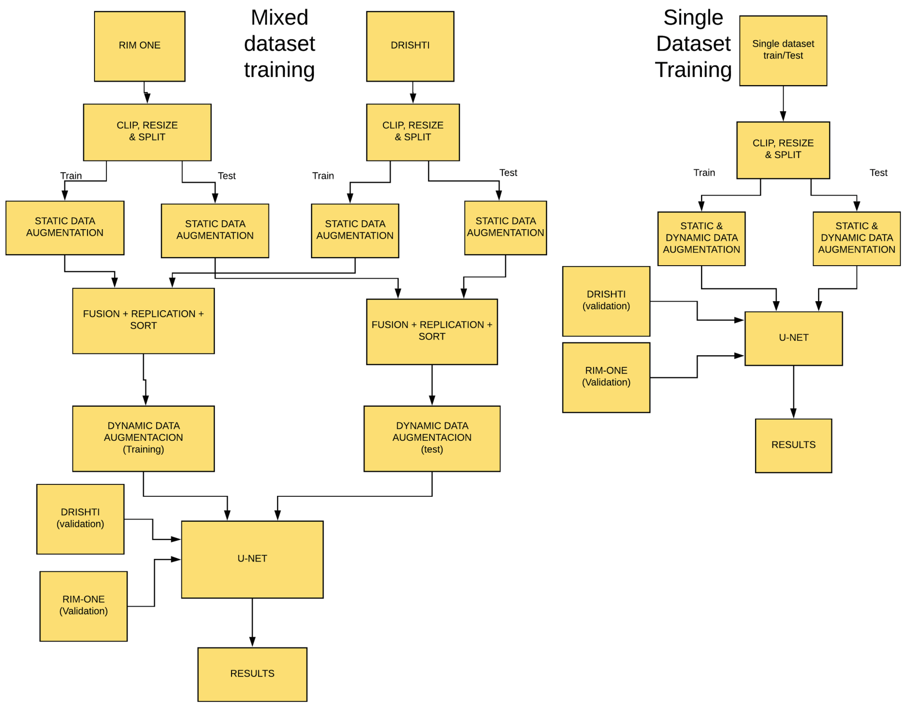

Fig. 3. Segmentation methodology

2.2 Study of the Viability of Incremental Learning

An interesting alternative, essential to implement cloud services, is to train initially with the available data and later modify the weights incrementally as we have data from new instruments. In this section, we will first train the system using a single data set and make predictions as stated above. Subsequently we will perform a short retraining (3 epochs) using images from the other data set and study the influence on the results. Thus, we test the feasibility of an incremental training using the resources and networks that we would deploy to implement a web service for segmentation of fundus images. This methodology is different from that used in other papers (e.g., [1,21,22,26]), where data from a single source are used for both training and testing.

We compare our work with those works that use deep learning for OD segmentation and use the DRISHTI or RIM-ONE data set. Zilly et al. [26] use a light three-layer CNN including sophisticated pre and postprocessing and apply it independently to both data sets. Sevastopolsky [21] uses a very light U-Net and provides results for RIM ONE. Al-Bander [1] uses a heavily modified, dense U-Net and provides results for both data sets. Shankaranarayana [22] uses a residual U-Net and provides results for RIM ONE.

3 Results

3.1 Network Selection

Regarding disk segmentation (Table 1), for our experiments we initially used a network that is very similar to the original U-Net: 5 stages and default drop-out rates (0.3). We use transpose convolution since direct subsampling is not currently compatible with TPUs.

Table 1. Disk segmentation results for different network architectures.

D/W/IR	Train/Test	Best/Worst/Std.	RRP	MTP
5/32/1.5	0.94/0.91	0.99/0.69/0.07	95	3.5
5/40/1.2	0.90/0.79	0.98/0.64/0.09	95	1.1
6/40/1.3	0.95/0.91	0.98/0.64/0.09	96	3.3
6/40/1.1	0.95/0.91	0.97/0.59/0.09	95	.9
7/40/1.2	0.95/0.92	0.98/0.61/0.11	97	2.6
7/64/1.3	0.96/0.94	0.99/0.62/0.08	97	14

Table 1 shows Dice coefficients for train and for test sets for various evaluated U-Net alternatives. The first row of the table defines the main parameters of the architecture, that is, the network depth (D), the number of filters in the first layer (W), and the IR. As an example, 6/40/1.1 means that we use a generalized 6-layer U-Net with 40 channels in the first layer and an IR of 1.1. This network is shown in Fig. 4.

In addition to this base case we provide data for pruned networks where we try to obtain the same or greater performance with a smaller number of parameters. To achieve this goal, we decrease the IR while increasing the number of filters in the first layer, the depth of the network or both. The MTP column in Table 1 shows the millions of trainable parameters in the network. For each network architecture, we provide the mean Dice coefficient for the training and test sets, the Dice coefficient for the best and worst predicted images in the test set and the Dice standard deviation over the test set.

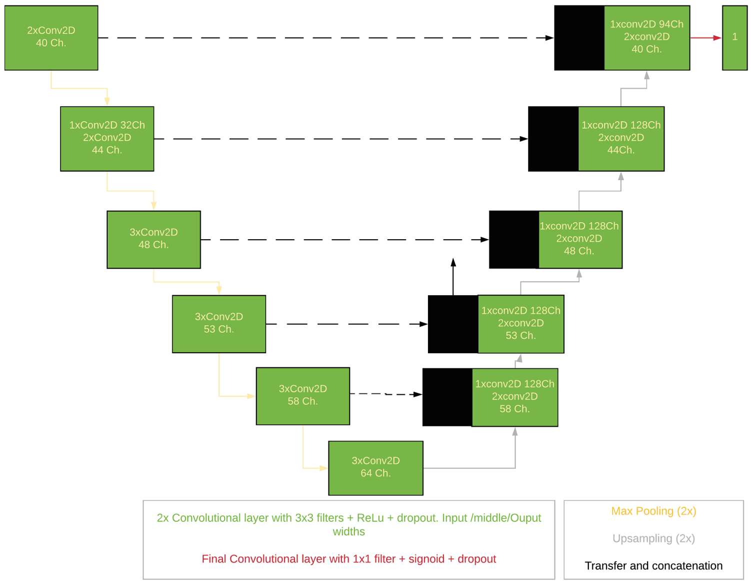

Fig. 4. Generalized 6 layer 6/40/1.1 U-Net architecture

Real disk shapes are not circular, but are approximately elliptical. In general, the ratio of the horizontal cup and disc diameters is larger than that of the diameters in the horizontal direction [17], however, in most of the works on the subject including all those mentioned in Table 2 the CDR is calculated using the mean diameters of the OC and OD. Although there are several possible interpretations of the average diameter, they have small differences with the real fundus images. In this paper we consider that the average radius of the OD is the square root of its area divided by π. We define a new parameter (Radio Ratio-RRP parameter) that is very useful for estimating the accuracy of the CDR. This parameter is defined as the percentage of test images for which the predicted disk radius has less than 10% error compared to the average radius of the ground truth. As an example, for the deepest network in the table, for 97% of the images our estimate of the radius has an error below 10% (RRP = 97).

We can see that deep networks with few parameters such as 6/40/1.1, which has less than 1M trainable parameters, achieve good results for disk segmentation. In this specific case, it achieves a RRP of 95. We will use this architecture for all the experiments in the rest of this paper. As a reference, we include in the Table 1 a very wide and deep network (7/64/1.3) with more than 14 million parameters. Although the performance of this network is better than in any other case, the small improvement does not justify the additional complexity of the network.

3.2 Disk Segmentation with Multiple Datasets

We want to discover how our system behaves when training with the combined data set and compare these results with those obtained when a single data set (i.e. RIM ONE or DRISHTI) is used to train the system. We will also compare the results with those obtained by other researchers. Table 2 shows Disk segmentation results for the three scenarios in this section. In the first two we train using a single data set and validate using the part of that data set that is not used for training and the other data set, while in the last scenario we train and validate with a mixed data set. Our scenarios are as follows:

– 75% of the DRISHTI data set is used for training and validation is done first with the rest of DRISHTI and then with the RIM ONE data set.
– 75% of the RIM ONE data set is used for training and validation is carried out with the rest of the RIM ONE data set and the DRISHTI data set.
– 75% of a mixed data set is used to train the networks and then we validate with the rest of the mixed data set.

We can see in Table 2 that, with our 6-layer network in the scenarios in which we train with a single data set the results when testing with images of that data set are good with Dice coefficients greater than 0.98 (DRISHTI) and 0.96 (RIM1). However, when we validate these networks with the other set, the results are below 0.66 or even 0.50 in some cases. In the third scenario in which we train with a mixed data set, we get results that are more similar when we test with images that come from both data sets. In this case, we obtain a Dice of 0.96 for the DRISHTI test subset and 0.87 for the RIM ONE subset.

Table 2. Multiple/single set dice coefficients.

Author	DRI	RIM
Zilly et al. [26]	0.97	-
Al-Bander [1]	0.95	0.90
Sevastopolsky [21]	-	0.94
Shankaranarayana et al. [22]	-	0.98
Drishti trained	0.98	0.50
RIM trained	0.66	0.97
Multi-dataset	0.96	0.87

In Table 2 we also results of previously referenced works which have trained and tested with each data set independently. Thus, they are related to our first two scenarios but they never test a network trained with one data set with images from another. Although we use networks with a small number of parameters, when we train with a single set we obtain results similar to those obtained by other papers. When training with DRISHTI, we obtained a Dice value of 0.98.

This value is slightly higher than 0.97 [26]. In the RIM ONE trained case, we get a dice value of 0.97 which compares well with 0.98 [1].

The most significant results in the Table 2 come from what can't be obtained in other studies, i.e., when we train with a dataset and predict using data from another source. In this case, we always get poor prediction results. This demonstrates that it is not feasible to create a service using training data captured with a single acquisition device. We also see in Table 2 that when you train with a combined data set, the network produces good results for both data sets, although not as good as when the training and prediction sets are part of the same set of data.

Regarding the clinically significant RRP parameter (Table 3), in the first two scenarios almost all radios for the test data are predicted with less than 10% error when compared to the segmentation done by ophthalmologists. However, the prediction for the other data set is much worse and, in some cases, we never get errors below 10%. This situation improves significantly when we train with a mixed data set.

Table 3. Radio ratio parameter.

	DRI	RIM
Drishti trained	100	38
RIM ONE trained	62	100
Multi-dataset	100	82

3.3 Incremental Training Results

We want to find out how our system behaves, when training with one set and then retraining lightly with some data from the other, and see if the results similar to those obtained when a single set of data is used (i.e. RIM ONE or DRISHTI) to train the system. Table 4 shows the results of disk segmentation for our two cases. On the first train, we use only DRISHTI data and validate using remaining of that data set and RIM ONE. In the second scenario, we make a brief retrain (3 epochs) using RIM ONE and the data set. Our scenarios are defined as follows:

- 75% of DRISHTI is used for training and validation is carried out first with the rest DRISHTI and then with the complete RIM ONE.
- 75% of RIM ONE is used to retrain the network and then we validate with the test part of both sets.

We can see in Table 4 that when we train with DRISHTI the tests with images from that same data set obtain very good Dice values. Specifically, we obtain an average Dice of 0.98 (DRISHTI) but only 0.64 (RIM1). The situation is worse than it seems as in the worst case for some RIM images the segmentation does not produce any pixels.

Table 4. Segmentation dice with retraining

Author	DRI	RIM
Zilly et al. [26]	0.97	-
Al-Bander [1]	0.95	0.90
Sevastopolsky [21]	-	0.94
Shankaranarayana et al. [22]	-	0.98
Drishti trained	0.98	0.64
RIM retrained	0.89	0.80

When we retrain the network with the other data set, the Dice values are 0.89 (DRISHTI) and 0.80 (RIM). For the worst case, we get a Dice of 0.69. Therefore, we can see that with a light retraining, the network can quickly learn the specific characteristics of the second data set. In Table 4 we include results of the other papers analyzed before. When we train with a single set of data, we obtain results for that set that are similar to those obtained by other papers. When training with the DRISHTI data set, we obtained a dice value of 0.98 for OD segmentation. This value is slightly above 0.97 [26]. As in the previous section the most significant results in Table 4 come from what is not available from other studies. The results obtained when we do a quick retraining show that, in this case, we get good prediction results for all test images.

4 Conclusions

We have been able to demonstrate that through the use of data from different data sets, adequate image preprocessing and significant data augmentation, we have been able to perform disk segmentation obtaining results with a performance similar to those obtained by other authors who use a single set for training and testing.

The use of a generalized configurable U-net recursive model allows us to easily train and test any U-Net configuration without having to make any changes to the code. This allows great flexibility for testing different architectures. We have tested networks with 4 to 7 layers, from 32 to 92 input channels, and with IR from 1.1 to 2.0. The number of parameters has varied from 0.9 to 44 million. Several U-Net architectures have been proven suitable for disk segmentation.

We have shown that by performing a rapid retraining with data from a new data set, and by preprocessing images and performing data augmentation, we can implement disk segmentation with performance equivalent to that reported by researchers using a single set for both training and testing.

4.1 Future Work

There are many possibilities to expand this work in the future. Among other possible topics, it would be interesting to implement modifications to always produce disc shapes that are acceptable to ophthalmologists. The automation of architecture configuration parameters and the use of other CNN architectures in parallel for the direct detection of glaucoma.

This work shows the importance of retraining by adding new sources to the segmentation system. In a real clinical service scenario, we would have to start training the network with the initially available data and retrain it when new images become available. The possibility of improving the network architecture by including residual blocks [25] or the combination of these blocks and a conventional U-Net [15] has proven effective in several segmentation applications and could potentially improve the performance of our process. The robustness of these networks when analyzing images from many different instruments remains an open problem for the future.

References

1. Al-Bander, B., Williams, B., Al-Nuaimy, W., Al-Taee, M., Pratt, H., Zheng, Y.: Dense fully convolutional segmentation of the optic disc and cup in colour fundus for glaucoma diagnosis. Symmetry **10**(4), 87 (2018)
2. Aujih, A., Izhar, L., Mériaudeau, F., Shapiai, M.I.: Analysis of retinal vessel segmentation with deep learning and its effect on diabetic retinopathy classification. In: 2018 International Conference on Intelligent and Advanced System (ICIAS), pp. 1–6. IEEE (2018)
3. Bhat, S.H., Kumar, P.: Segmentation of optic disc by localized active contour model in retinal fundus image. In: Smart Innovations in Communication and Computational Sciences, pp. 35–44. Springer (2019)
4. Bourne, R.R.: The optic nerve head in glaucoma. Community Eye Health **19**(59), 44 (2006)
5. Choi, Y., Choi, M., Kim, M., Ha, J.W., Kim, S., Choo, J.: Stargan: Unified generative adversarial networks for multi-domain image-to-image translation. In: Proceedings of the IEEE Conference on Computer Vision and Pattern Recognition, pp. 8789–8797 (2018)
6. Chollet, F.: Building powerful image classification models using very little data. Keras Blog (2016)
7. Chollet, F.: Deep Learning with Python, 1st edn. Manning Publications Co., Greenwich (2017)
8. Civit-Masot, J., Luna-Perejón, F., Vicente-Díaz, S., Rodríguez Corral, J.M., Civit, A.: TPU cloud-based generalized U-net for eye fundus image segmentation. IEEE Access **7**, 142379–142387 (2019). https://doi.org/10.1109/ACCESS.2019.2944692
9. Das, P., Nirmala, S., Medhi, J.P.: Diagnosis of glaucoma using CDR and NRR area in retina images. Netw. Model. Anal. Health Inform. Bioinform. **5**(1), 3 (2016)
10. Dean, J., Patterson, D., Young, C.: A new golden age in computer architecture: empowering the machine-learning revolution. IEEE Micro **38**(2), 21–29 (2018)
11. Dice, L.R.: Measures of the amount of ecologic association between species. Ecology **26**(3), 297–302 (1945)
12. Fumero, F., Alayón, S., Sanchez, J.L., Sigut, J., Gonzalez-Hernandez, M.: Rim-one: an open retinal image database for optic nerve evaluation. In: 2011 24th International Symposium on Computer-Based Medical Systems (CBMS), pp. 1–6. IEEE (2011)

13. Howard, A.G., Zhu, M., Chen, B., Kalenichenko, D., Wang, W., Weyand, T., Andreetto, M., Adam, H.: Mobilenets: Efficient convolutional neural networks for mobile vision applications. arXiv preprint arXiv:1704.04861 (2017)
14. Kim, S.J., Cho, K.J., Oh, S.: Development of machine learning models for diagnosis of glaucoma. PLoS One **12**(5), e0177726 (2017)
15. Kim, S., Bae, W., Masuda, K., Chung, C., Hwang, D.: Fine-grain segmentation of the intervertebral discs from MR spine images using deep convolutional neural networks: BSU-Net. Appl. Sci. **8**(9), 1656 (2018)
16. Lian, S., Li, L., Lian, G., Xiao, X., Luo, Z., Li, S.: A global and local enhanced residual u-net for accurate retinal vessel segmentation. IEEE/ACM Trans. Comput. Biol. Bioinform. (2019)
17. Lingam, C.L., Mansberger, S., Miglior, S., Paranhos, A., Pasquale, L.R., Susanna Jr., R., Wang, N.: 4. risk factors (ocular). Diagnosis of Primary Open Angle Glaucoma: WGA consensus series-10, vol. 10, p. 127 (2017)
18. MacIver, S., MacDonald, D., Prokopich, C.L.: Screening, diagnosis, and management of open angle glaucoma. Can. J. Optom. **79**(1), 5–71 (2017)
19. Quigley, H.A., Broman, A.T.: The number of people with glaucoma worldwide in 2010 and 2020. Br. J. Ophthalmol. **90**(3), 262–267 (2006)
20. Ronneberger, O., Fischer, P., Brox, T.: U-net: convolutional networks for biomedical image segmentation. In: International Conference on Medical Image Computing and Computer-Assisted Intervention, pp. 234–241. Springer (2015)
21. Sevastopolsky, A.: Optic disc and cup segmentation methods for glaucoma detection with modification of U-net convolutional neural network. Pattern Recogn. Image Anal. **27**(3), 618–624 (2017)
22. Shankaranarayana, S.M., Ram, K., Mitra, K., Sivaprakasam, M.: Joint optic disc and cup segmentation using fully convolutional and adversarial networks. In: Fetal, Infant and Ophthalmic Medical Image Analysis, OMIA 2017, pp. 168–176. Springer International Publishing (2017)
23. Sivaswamy, J., Krishnadas, S., Joshi, G.D., Jain, M., Tabish, A.U.S.: Drishti-GS: retinal image dataset for Optic Nerve Head (ONH) segmentation. In: 2014 IEEE 11th International Symposium on Biomedical Imaging (ISBI), pp. 53–56. IEEE (2014)
24. Thakur, N., Juneja, M.: Survey on segmentation and classification approaches of optic cup and optic disc for diagnosis of glaucoma. Biomed. Signal Process. Control **42**, 162–189 (2018)
25. Xiuqin, P., Zhang, Q., Zhang, H., Li, S.: A fundus retinal vessels segmentation scheme based on the improved deep learning U-net model. IEEE Access **7**, 122634–122643 (2019). https://doi.org/10.1109/ACCESS.2019.2935138
26. Zilly, J., Buhmann, J.M., Mahapatra, D.: Glaucoma detection using entropy sampling and ensemble learning for automatic optic cup and disc segmentation. Comput. Med. Imaging Graph. **55**, 28–41 (2017)
27. Zoph, B., Cubuk, E.D., Ghiasi, G., Lin, T.Y., Shlens, J., Le, Q.V.: Learning data augmentation strategies for object detection. arXiv preprint arXiv:1906.11172 (2019)

On Image Prefiltering for Skin Lesion Characterization Utilizing Deep Transfer Learning

K. Delibasis[1](✉), S. V. Georgakopoulos[1], S. K. Tasoulis[1], I. Maglogiannis[2], and V. P. Plagianakos[1]

[1] Department of Computer Science and Biomedical Informatics, University of Thessaly, Papassiopoulou 2-4, Lamia 35100, Greece
{kdelimpasis,spirosgeorg,stasoulis,vpp}@uth.gr

[2] Department of Digital Systems, University of Piraeus, Grigoriou Lampraki 126, Piraeus 18532, Greece
imaglo@unipi.gr

Abstract. Skin cancer is one of the most diagnosed cancers according to the World Health Organization and one of the most malignant. Unfortunately, still the available annotated data are in most cases not enough to successfully train deep learning algorithms that would allow highly accurate predictions. In this paper, we propose the utilization of transfer learning to fine-tune the parameters at the very last layers of a pre-trained a deep learning neural network. We expect that a limited number of skin lesion images is enough to affect significantly the later data-specific layers. Furthermore, we propose a pre-process step for skin lesion images that segments and crops the lesion, whereas smooths the effect of image masking, thus enhancing the network's classification capabilities. The reported results are very promising, since the overall accuracy, as well as the accuracy of individual class classification improved in 7 out of the 8 classes, suggesting future developments in medical diagnosis through pre-trained deep learning models and specialized image prefiltering.

Keywords: Convolutional Neural Networks (CNN) · Skin Lesion Classification · Cancer detection · Image pre-processing

1 Introduction and Related Work

Skin cancer is one of the most frequently diagnosed cancers according to the World Health Organization [1] and one of the most malignant. There are many types of skin carcinomas, with "melanoma" having the highest rate of mortality [16], while "basal cell carcinoma" being the most common skin cancer with lower mortality. Trained machine learning computational tools capable of discriminating between normal skin images and images of skin cancer is crucial.

The task of further discriminating types of cancer can be much more challenging but still of great importance, since different types of cancer are characterized by significantly different mortality rates.

In the literature, there have also been unsupervised methods able to provide such discrimination in their pattern findings [19], [2] indicating class separability to some degree. His prior knowledge justifies the use of supervised methods that are able to achieve much higher accuracy in similar complexity tasks [13]. The most recent advances in supervised approaches use Convolutional Neural Networks variants for both segmentation and classification of skin images.

The utilization of filtertering is widely adopted by supervised methods aiming to extract appropriate features for training a classifier [14]. Even in the case of state-of-the-art supervised methods such as the Convolutional Neural Networks (CNNs) that are able to construct the most relevant features for each problem, the use of global image filters significantly improves CNN performance in some cases [7]. A common use of filters on CNN is when artifacts occur within an image [8]. In particular, pre-processing of dermoscopy images for lesion classification is very common. In [15] the authors proposed a method for detecting the lesion type, where a pre-process stage for removing the hairs from the skin and the lesion is performed. Next the deep transfer learning approach is used to fine-tune the pre-trained model Alexnet [9] using dermoscopy images. Deep transfer learning is a recent popular approach used in medical imaging where knowledge is transferred from pre-trained models using large-scale data into new models [18].

However, recent findings [7] show that CNN models trained to classify general purpose images can achieve higher classification performance when compared with pre-trained models on medical domain problems. In [10] the authors examined the transfer learning approach for skin cancer classification employing several state-of-the-art architectures (VGG-16, ResNet50, ResNet101, Inception-v3) trained on the popular ImageNet dataset. It was shown that the fine-tuned VGG-16 model outperformed the rest of the CNNs under comparison.

In this work, we deal with the problem of classifying dermoscopy images into different skin cancer types. Our aim is to investigate the effect of prior lesion segmentation on the classification performance of a CNN and to derive an optimal way of incorporating the segmentation information into the image dataset without inducing artifacts that may affect the features learn by the CNN. More specifically, it is expected that, since the segmentation is a masking operation, it produces strong edges at the lesion border, which represent irrelevant information that may deteriorate the performance of the CNN classifier. However, if the mask-generated edges are filtered-out from the image dataset, the clipping and segmentation process should preclude irrelevant image information and consequently increase the achieved classification accuracy. To this end, we propose a pre-process filtering method that minimizes the artificial edges after lesion segmentation. Then, we use the deep transfer learning methodology where a deep learning model is fine-tuned by the aforementioned images. Comparative results confirm the superiority of including image segmentation and clipping in conjunction with the image filtering to suppress the segmentation-related edges.

2 Methodology

Motivated by [7], the proposed methodology is based on fine-tuning a pre-trained CNN model. More precisely, we evaluate a model, is trained using the well-established ImageNet dataset that consists of real world images, and subsequently fine tune it with dermoscopy images, which have been segmented and prepossessed using the proposed approach, to remove the background of the lesion.

The preprocessing step consists of two main parts. In the first part the segmentation of the lesion from the background skin takes place, while in the second part we proceed to the filtering of the edges induced by the aforementioned lesionsegmentation. In Fig. 1 the workflow of the proposed methodology is presented. More precisely, the original input dermoscopy image is segmented through a trained CNN [12] producing a binary mask. The resulting segmentation mask is applied on the original dermoscopy image, filtering-out the background, while retaining the lesion. However the lesion boundary edges introduced through this procedure are expected to prevent the efficient training of the CNN. To avoid this side effect, we filter the images by filling the zero-valued pixels of segmented image appropriate image values of the lesion edges. In the final step, the pre-processed images are used to fine-tune the pre-trained CNN model towards real-world object classification.

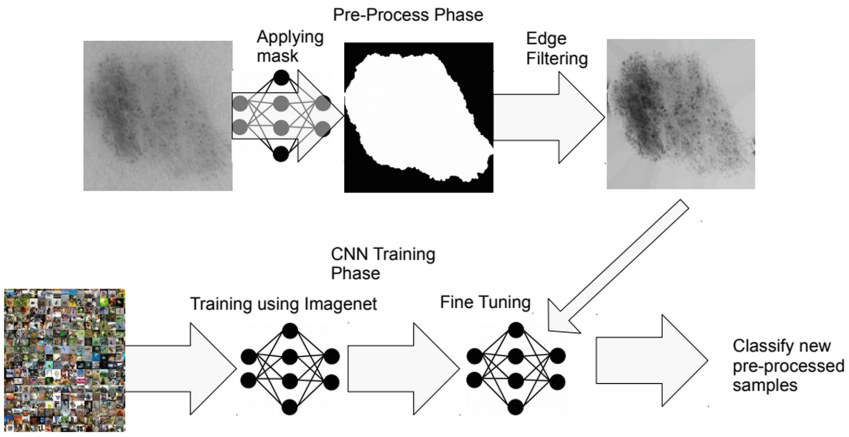

Fig. 1. An overview of the proposed approach

2.1 Image Preprocessing

Lesion Segmentation

Lesion segmentation in a dermosopy image involves the separation of the skin lesion from the surrounding skin and the creation of the corresponding binary masks. Several methodologies are reported in the literature concerning lesion segmentation [11].

The preprocessing phase of the proposed workflow creates such binary skin lesion masks. In this study the methodology based on adaptive thresholding published in [12] was utilized. Nevertheless, the proposed methodology can exploit any other similar algorithm.

Image Cropping, Masking and Filtering

After lesion segmentation, cropping is performed to extract the image patch that will be input to the CNN. Since the CNN requires input of standard dimensions, the original image patch is cropped as a square, masked using the segmentation result and rescaled to the desired dimensions, using the standard bicubic interpolation. It is however reasonable to assume that the strong edge introduced by binary masking can induce irrelevant features during the deep learning process, thus deteriorate the performance of the CNN (Fig. 2). In order to test this assumption and improve the classification accuracy, we propose a special preprocessing of the input image mask that retains the image information, whereas minimizing the artificial edges due to cropping and masking.

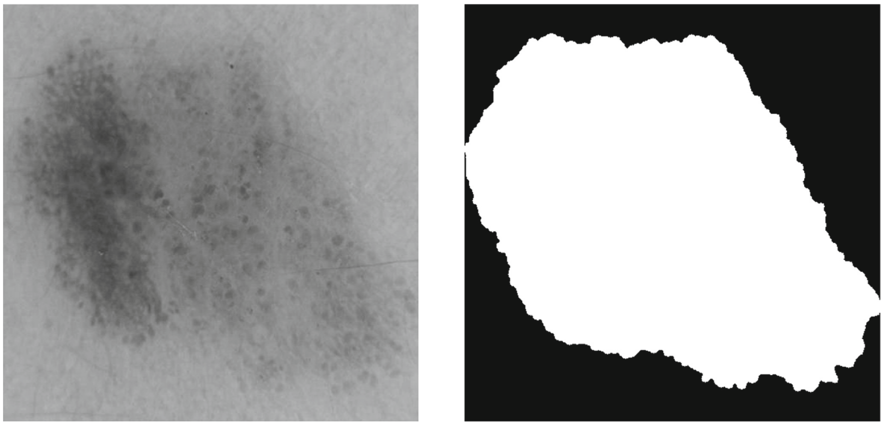

Fig. 2. A typical example of cropped image, I_c (left) and the corresponding segmented image, B_c (right)

Let I be the original RGB dermoscopy image that is decomposed into its three color channels and B_c the square binary segmented image, cropped round the detected lesion. The following steps are applied to each masked and cropped color channel I_c. Let us also denote by g_σ the 2-dimensional Gaussian kernel with standard deviation equal to σ. The proposed pre-processing algorithm is described in the following steps.

$$J_l = J * g_\sigma$$

A typical example of J and J_l is shown in Fig. 3

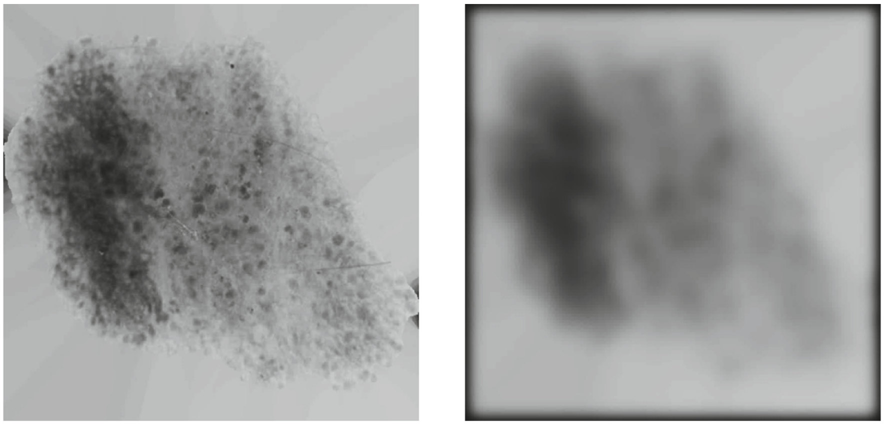

Fig. 3. Typical examples of the images of step 3 of the preprocessing algorithm. The J image in the left, the blurred image J_l in the right.

Step 1. The masked and cropped image is convolved with g_σ to produce a smoother version: $I_g = I_c * g_\sigma$

Step 2. The Distance Transform is applied to B_c, yielding for each zero-valued pixel in B_c the distance from the nearest non-zero (boundary) pixel, as well as the coordinates of the nearest pixel $(p_{i,j}, q_{i,j})$.

Step 3. An intermediate image is generated as following,

$$J(i,j) = \begin{cases} I_c(i,j) & B_c(i,j) > 0 \\ I_g(p_{i,j}, q_{i,j}) & B_c(i,j) = 0 \end{cases}$$

According to its definition, this image is identical to I_c at the non-zero pixels of the B_c, whereas the rest of its pixels hold the value of the nearest boundary pixel of the smoothed, cropped image I_g. As it can be visually observed, this image (J) is prone to radial edges, thus the preceding convolution with the Gaussian is employed to smoothing of the boundary values and smear the radial edges. Please note that this smoothing is applied to the boundary values that are replicated in the zero-valued pixels of the Bc image and does not affect the pixels inside the lesion (where $B_c > 0$). Furthermore, the aforementioned image

J is also convolved with a Gaussian kernel to blur the radial edges. In this case also, the blurring is applied on the zero valued pixels of the B_c without affecting the useful image part. The following equation it is utilized:

Step 4. The final image is composed by the pixels of Ic that have non-zero values in Bc and the blurred pixels of J1 that have zero values in Bc. In order to avoid a sharp image value change at the border, an image mask M is constructed as following:

$$M = max(d_{max} - DT(B_c), 0)\frac{1}{d_{max}}$$

It can be confirmed that by its definition, mask M has a value of 1 at the non-zero pixels of B_c, zero value at the zero-valued pixels of B_c that lie at a distance equal to or greater than d_{max} pixels from the border of B_c and linearly varying values at the rest of the pixels (the zero pixels of Bc that lie closer than d_{max} to the border of B_c). Then the final cropped and masked image, which will be used as input to the CNN, is defined as:

$$I_p = (1 - M)J + I_c$$

A typical example of mask M and the resulting image I_p is shown in Fig. 4. It becomes obvious that the finally cropped image contains unaltered the pixels of the lesion, whereas the masked-out pixels are smoothed, without noticeable transition at the lesion contour that may interfere with the image features that are automatically generated by the CNN. The above steps are repeated for all three color channels and the RGB smoothed cropped image is finally constructed.

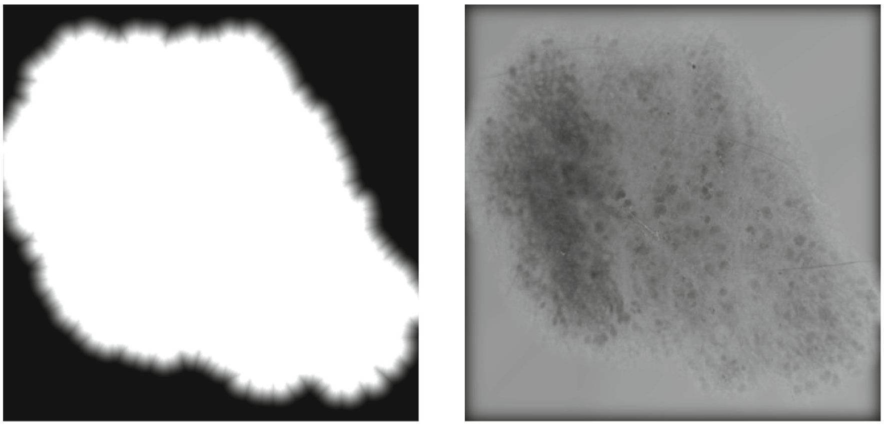

Fig. 4. A typical example of the image mask M (left) and the final cropped and masked image, after the application of filtering (right).

2.2 Convolutional Neural Networks Fine-Tuning

The processed dermoscopy images can be fed to a CNN for training. However, most medical image datasets are highly unbalanced with some classes, being dominant with respect to the number of samples they contain. Even the use of dataset augmentation techniques do not allow for proper CNN-training from scratch.

We deal with this problem leveraging knowledge from an already trained network in order to fine-tune the model and achieve highly accurate results. This technique usually referred to as transfer learning, is based on the assumption that the knowledge of a model which is capable of solving a problem in a specific domain can be used as a baseline for a model to solve an image classification problem in another domain. Adopting this strategy we select the well-established architecture VGG-16 [17] trained on the ImageNet dataset [6] as baseline to our model. The VGG-16 consisted of 13 convolutional layers, two fully-connected layers and one output layer with 1000 neurons equal to the number of classes of the ImageNet dataset. For the task at hand, the number of the classes is significantly lower, therefore the output layer is replaced by 9 neurons, according to the number of lesion types found in our dataset.

Next, we fine-tune the aforementioned pre-trained VGG-16 model by adapting its baseline knowledge to the medical domain of interest and finally classify the lesions. Since the CNN have internal structures which tend to learn generic features on their first layers such as color blobs, Gabor filters etc [21]; we choose to keep all the kernel weights of the convolutional layers that contain generic purpose information. As such, fine-tuning is performed only for the weights of the fully-connected layers and the output layer. We use a small learning rate parameter value equal to 0.001 for fine-tuning, since the pre-trained weights are expected to be more relevant than the randomly initialized weights and thus they need to adapt smoothly. Finally, we use the Stochastic Gradient Descent algorithm for the training [3] for 100 epochs with input batch size equal to 64 images. The dermoscopy images are resized to 224×224 as required by the VGG-16 architecture.

3 Experimental Results

We begin our experimental analysis by describing the specification of the dataset used for evaluation. Then we proceed by examining the various aspects of the proposed methodology. For this purpose we employ the original fine-tuned VGG-16 model along with both the original dermoscopy images and the images that have been preprocessed removing the background skin from the lesion.

3.1 Dataset Description and Image Classification Experiments

The dataset evaluated in this work is the train dataset, obtained from the International Skin Imaging Collaboration (ISIC) [20], [5] 2019 dataset, which contains

25.331 clinical dermoscopy images of skin lesions, of eight (8) different malignant and benign classes, along with their labels. The image classes labeled in this dataset and their population is given in Table 1.

Table 1. The number of samples per class (lesion type) of ISIC dataset.

Lesion	Number of samples
Melanoma	4522
Melanocytic nevus	12875
Basal cell carcinoma	3323
Actinic keratosis	867
Benign keratosis	2624
Dermatofibroma	239
Vascular lesion	253
Squamous cell carcinoma	628

As described above, the VGG deep learning model, pre-trained on the Imagenet dataset is subjected to transfer learning, under three experiments that are performed and compared in terms of classification accuracy, using the available dermoscopy image dataset, processed as following:

1. The original images of the dataset are used for training and testing.
2. The original images of the dataset are masked and clipped.
3. The original images are masked, clipped and finally processed using the filter described in Sect. 2.

3.2 Evaluation and Results

This section is devoted to the evaluation of the effectiveness of the preprocessing methodology on dermoscopy images for training a CNN through transfer learning against using the original images or the images for which the background skin has been simply masked-out. For this purpose, the described CNN model, VGG-16, has been fine-tuned separately using all three variations of input images through the process described in the previous Subsect. 3.1.

The evaluation of image classification is performed by 10-fold cross validation, applied to each class separately, due to increased class asymmetry. For the same reason, the performance of the different CNN models is evaluated using the accuracy measure along with the balanced accuracy [4], which is the mean accuracy of the model for each individual category of lesion.

In a baseline examination, the training of a CNN from scratch using augmentation techniques achieves mean accuracy below 60%. In contrast, as shown in Table 2 all aforementioned versions that utilize transfer learning as it is described

Table 2. The accuracy and the balance accuracy of the examined methods using cross validation 10-fold.

	Proposed method (masked, clipped and filtered images)	Original images	Segmented and Clipped images
Accuracy	**85.3**%	82%	76.1%
Ballanced accuracy	**73.6**%	70.8%	61.6%

Table 3. The classification accuracy of the different image processing methods for each lesion using the VGG-16 with transfer learning.

	Proposed method (masked, clipped and filtered images)	Original images	Segmented and Clipped images
Melanoma	**77**%	70%	63%
Melanocytic nevus	**94**%	91%	89%
Basal cell carcinoma	**87**%	83%	73%
Actinic keratosis	**62**%	59%	48%
Benign keratosis	**68**%	66%	53%
Dermatofibroma	**59**%	56%	38%
Vascular lesion	**78**%	77%	73%
Squamous cell carcinoma	59%	**61**%	50

Table 4. The Recall and Precision measures of 10-fold cross validation of the proposed method.

	Proposed method (masked, clipped and filtered images)	
	Precision	Recall
Melanoma	87%	82%
Melanocytic nevus	90%	94%
Basal cell carcinoma	82%	86%
Actinic keratosis	64%	68%
Benign keratosis	76%	70%
Dermatofibroma	74%	61%
Vascular lesion	96%	80%
Squamous cell carcinoma	78%	59%

in Sect. 2, perform significantly better. In more detail, Table 3 reports the accuracy and balanced accuracy of the three described techniques. As shown, the proposed method achieves the most accurate classification with respect to both metrics. Interestingly, we observe that the usage of the segmented images for training the CNN model provide lower classification accuracy than using the original images. This behavior indicates that the strong edges resulting from the lesion segmentation have an adverse effect on the performance of the CNN. It may be assumed that the CNN model tends to learn the shape of the lesion, instead of extracting the useful image features, which are related to the discrimination of the lesions. Furthermore, we conclude that the skin beyond the lesion does not contribute to classification, probably due to the irrelevant information it contains such as hairs etc. The proposed image pocessing approach seems to bypass this drawback by managing to remove the original human skin, while adding a blurring effect to minimize side effects of this procedure. In Table 4 is presented the recall and precision measures of the proposed methodology for each lesion.

4 Conclusion

This study utilized an extensive, multi-class image dermoscopy dataset to evaluate the effect of transfer learning and special image preprocessing on the classification accuracy achieved by a well-established deep learning model (VGG-16). Results show that transfer learning is essential for increasing the accuracy to acceptable levels, even in this case of a dataset with relatively high population of images (more than 25.000). The inclusion of lesion segmentation alone is not beneficial for the classification task, since the resulting accuracy deteriorated, probably due to the artificial boundary edges that are introduced during the masking process. Finally, the design of an elaborate image pre-processing filter that leaves intact the lesion pixel values and fills the rest of the mask pixels with appropriate values that smooth the boundary effect, proved beneficial, since it increased the overall 10-fold classification accuracy from 70.8% to 73.6%. Furthermore, it increased the accuracy of 7 out of the 8 lesion classes. The remaining class "squamous cell carcinoma" showed a marginal reduction of classification accuracy from 61% to 59%. More importantly, the accuracy for the classification of melanoma (the class of the highest malignancy) showed significant increase from 70% to 77%.

Acknowledgment. This project has received funding from the Hellenic Foundation for Research and Innovation (HFRI) and the General Secretariat for Research and Technology (GSRT), under grant agreement No 1901. We gratefully acknowledge the support of NVIDIA Corporation with the donation of the Titan X Pascal GPU used for this research.

References

1. https://www.who.int/uv/faq/skincancer/en/index1.html
2. Abbas, Q., Fondón, I., Rashid, M.: Unsupervised skin lesions borderdetection via two-dimensional image analysis. Comput. Methods Prog. Biomed. **104**(3), e1–e15 (2011). https://doi.org/10.1016/j.cmpb.2010.06.016
3. Bottou, L.: On-line learning and stochastic approximations. In: In On-line Learning in Neural Networks, pp. 9–42. Cambridge University Press, Cambridge (1998)
4. Brodersen, K.H., Ong, C.S., Stephan, K.E., Buhmann, J.M.: The balanced accuracy and its posterior distribution. In: 2010 20th International Conference on Pattern Recognition, pp. 3121–3124 (2010)
5. Codella, N.C.F., Gutman, D., Celebi, M.E., Helba, B., Marchetti, M.A., Dusza, S.W., Kalloo, A., Liopyris, K., Mishra, N., Kittler, H., Halpern, A.: Skin lesion analysis toward melanoma detection: a challenge at the 2017 international symposium on biomedical imaging (isbi), hosted by the international skin imaging collaboration (isic) (2017)
6. Deng, J., Dong, W., Socher, R., Li, L.J., Li, K., Fei-Fei, L.: ImageNet: a large-scale hierarchical image database. In: CVPR09 (2009)
7. Georgakopoulos, S.V., Kottari, K., Delibasis, K., Plagianakos, V.P., Maglogiannis, I.: Improving the performance of convolutional neural networkfor skin image classification using the response of image analysis filters. Neural Comput. Appl. **31**(6), 1805–1822 (2019). https://doi.org/10.1007/s00521-018-3711-y
8. Jafari, M.H., Nasr-Esfahani, E., Karimi, N., Soroushmehr, S.M.R., Samavi, S., Najarian, K.: Extraction of skin lesions from non-dermoscopic images using deep learning (2016). arXiv: 1609.02374
9. Krizhevsky, A., Sutskever, I., Hinton, G.E.: Imagenet classification with deep convolutional neural networks. In: Pereira, F., Burges, C.J.C., Bottou, L., Weinberger, K.Q. (eds.) Advances in Neural Information Processing Systems, vol. 25, pp. 1097–1105. Curran Associates Inc., New York (2012)
10. Li, Y., Shen, L.: Skin lesion analysis towards melanoma detection using deep learning network. Sensors **18**(2), 556 (2018). https://www.mdpi.com/1424-8220/18/2/556
11. Maglogiannis, I., Doukas, C.N.: Overview of advanced computer vision systems for skin lesions characterization. IEEE Trans. Inf. Technol. Biomed. **13**(5), 721–733 (2009)
12. Maglogiannis, I., Zafiropoulos, E., Kyranoudis, C.: Intelligent segmentation and classification of pigmented skin lesions in dermatological images. In: Antoniou, G., Potamias, G., Spyropoulos, C., Plexousakis, D. (eds.) Advances in Artificial Intelligence, pp. 214–223. Springer, Heidelberg (2006)
13. Mhaske, H.R., Phalke, D.A.: Melanoma skin cancer detection and classification based on supervised and unsupervised learning. In: 2013 International Conference on Circuits, Controls and Communications (CCUBE), pp. 1–5 (2013)
14. Oliveira, R., Filho, M., Papa, J., Pereira, A., Manuel, J., Tavares, J.: Computational methods for the image segmentation of pigmented skin lesions: a review. Comput. Methods Programs Biomed. **131**, 127–141 (2016)
15. Salido, J.A., Ruiz, C.: Using deep learning for melanoma detection in dermoscopy images. Int. J. Mach. Learn. Comput. **8**, 61–68 (2018). https://doi.org/10.18178/ijmlc.2018.8.1.664
16. Siegel, R.L., Miller, K.D., Fedewa, S.A., Ahnen, D.J., Meester, R.G.S., Barzi, A., Jemal, A.: Colorectal cancer statistics, 2017. CA: Cancer J. Clin. **67**(3), 177–193 (2017)

17. Simonyan, K., Zisserman, A.: Very deep convolutional networks for large-scale image recognition. In: International Conference on Learning Representations (2015)
18. Talo, M., Baloglu, U.B., Yıldırım, Ö., Acharya, U.R.: Application of deep transfer learning for automated brain abnormality classification using mr images. Cogn. Syst. Res. **54**, 176–188 (2019)
19. Tasoulis, S.K., Doukas, C.N., Maglogiannis, I., Plagianakos, V.P.: Skin lesions characterisation utilising clustering algorithms. In: Konstantopoulos, S., Perantonis, S., Karkaletsis, V., Spyropoulos, C.D., Vouros, G. (eds.) Artificial Intelligence: Theories, Models and Applications, pp. 243–253. Springer, Heidelberg (2010)
20. Tschandl, P., Rosendahl, C., Kittler, H.: The ham10000 dataset: a large collection of multi-source dermatoscopic images of common pigmented skin lesions. Sci. Data **5**, 180161 (2018)
21. Yosinski, J., Clune, J., Bengio, Y., Lipson, H.: How transferable are features in deep neural networks? In: Advance in Neural Information Processing System, vol. 27, pp. 3320–3328 (2014)

Identification of Eyelid Basal Cell Carcinoma Using Artificial Neural Networks

Evagelos Georgios Chatzopoulos[1], George Anastassopoulos[2,3], Efstathios Detorakis[4], and Adam Adamopoulos[1](✉)

[1] Laboratory of Medical Physics, Department of Medicine, Democritus University of Thrace, Komotini, Greece
tsohoulis@gmail.com, adam@med.duth.gr

[2] Laboratory of Medical Informatics, Department of Medicine, Democritus University of Thrace, Komotini, Greece
anasta@med.duth.gr

[3] Department of Electrical and Computer Engineering, University of Patras, Patras, Greece

[4] Clinic of Ophthalmology, Department of Medicine, University of Crete, Heraklion, Greece
detorakis@gmail.com

Abstract. First results of the classification of the eyelid Basal Cell Carcinoma using Artificial Neural Networks are presented. Full, or half-face photographs of healthy subjects and patients suffering from eyelid Basal Cell Carcinoma were used to train and validate Artificial Neural Networks for the purpose of pattern recognition, identification and classification. The efficiency of the algorithm was tested using various training methods and it was evaluated using the accuracy score, that is, the ration of the number of the correctly classified cases over the total number of cases under examination. With respect to the accuracy, the proposed algorithm reached up to 100% performance. The algorithm is accompanied by a specifically designed and developed user friendly Graphical User Interface.

Keywords: Eyelid Basal Cell Carcinoma · Pattern recognition · Artificial Neural Networks

1 Introduction

Basal Cell Carcinoma (BCC) is defined as a slowly growing, locally expanding, malignant epidermal tumor [1–3]. It is the most common type of skin cancer as over 70% of cases are related to it. In fact, 90% of BCC concern the head and neck area, while 10% of cases occur in the eyelid, which confirms the relationship between BCC and sun exposure [4–7]. Effective treatment of BCC in the ophthalmic region is achieved by a variety of methods and depends on both the characteristics of the BCC and the patient himself. Depending on the size, the topographic location of the tumor, the age and the general health condition of the patient, there is a wide variety of approaches aimed at correcting the eyelid deficit [8–13]. Of course, to understand the functional anatomy of the peripheral region, it is essential to understand the principles of repairing the eyelids. Appropriate treatment may consists of either surgical resection of the tumor or repair of the lesion through nonsurgical procedures, using state-of-the-art technologies such as subtractive cryotherapy and photodynamic therapy. In addition, it is possible to use modern pharmaceutical preparations such as imikumimod 5% cream, as well as the use of multiple interventions to repair eyelid defects [14–16].

In order to select the most appropriate therapeutic technique, it is necessary to classify the tumors into specific categories according to their characteristics and through clinical control of the patient. Balancing tumor removal techniques, combined with functionality of the surgical site and cosmetic repair of the lesion, make the therapeutic approach applied successful. While there are a variety of invasive and non-invasive techniques to repair BCC in the eyelid, the choice of a more appropriate method that will lead to treatment is a complicated process. Due to the fact that there are so many types of BCC, identification and classification are difficult tasks and depend on many factors. For this reason, as in many areas of medicine for diagnostic support [17–21], in the present work it was developed an Artificial Intelligence (AI) system that can distinguish cases of BCC in order to support physicians in decision making and to confirm or assist timely and valid diagnosis. The proposed AI system is based on Artificial Neural Networks (ANN), a method that, along with fuzzy systems, as well as, evolutionary optimization algorithms can be utilized for face identification, detection and recognition [22–28].

The purpose of this work is to develop an intelligent pattern recognition system for identifying eyelid BCC from a patient's full or half-face photograph. To accomplish this task, ANN were constructed and trained to identify and classify face photographs of normal subjects and photographs of eyelid BCC patients. To gain user-friendliness the developed algorithms are executed under a specially designed Graphical User Interface (GUI). The performance of the developed ANN were evaluated with respect to their classification accuracy score. The obtained results indicated that AI systems based on ANN can favorably be utilized for eyelid BCC identification and classification.

2 Material and Methods

The material used for the present work consisted of full or half-face photographs of normal subjects and eyelid BCC patients. Image files were saved in raw, jpeg and tiff format. The preprocessing procedure consisted of two steps. At the first step a special function script was developed and utilized in order to convert all photographs to the same size varying in the range of 200 $\times$ 200 pixels up to 1000 $\times$ 1000 pixels. At the second step images were turned from RGB format to grayscale for purpose of the faster execution of the learning algorithm, without missing any vital information. Representative examples of images of a normal and two pathological cases are shown in Fig. 1.

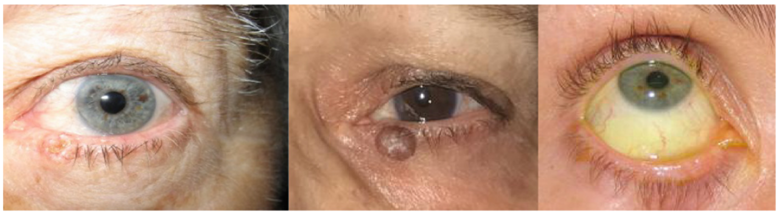

Fig. 1. Photograph of a normal subject eyelid (left) and two eyelid BCC cases (middle and right).

The overall purpose of this study was to develop a pattern recognition algorithm that would detect, identify and classify the presence of eyelid BCC in a patient's face photograph with the use of ANN. For purpose of convenience a suitable GUI was developed which allows the user either to train ANN by selecting a large set of images from the patients' database, or, to pick and upload a specific image and request from the system to identify and classify it, by providing an answer to the question of whether it corresponds to an eyelid BCC case or not. The ANN algorithms and the GUI were developed using the Matlab programming environment [29].

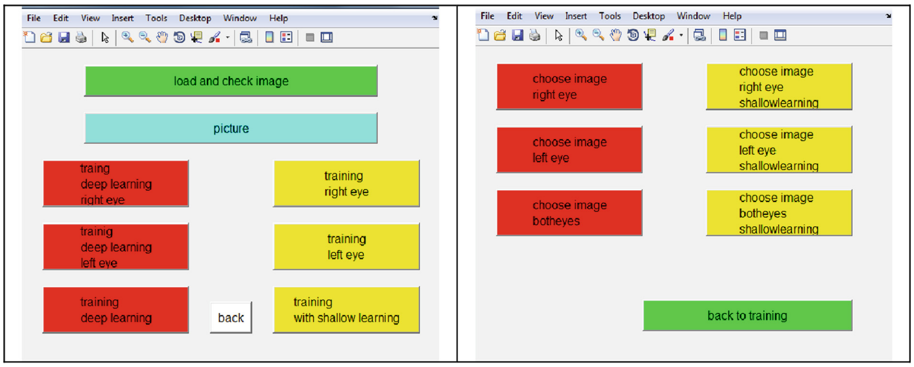
File Edit View Insert Tools Desktop Window Help
load and check image
picture
traing deep learning right eye
training right eye
trainig deep learning left eye
training left eye
training deep learning
back
training with shallow learning
File Edit View Insert Tools Desktop Window Help
choose image right eye
choose image right eye shallowlearning
choose image left eye
choose image left eye shallowlearning
choose image botheyes
choose image botheyes shallowlearning
back to training

Scr. 1. Screenshots of GUI at the ANN training procedure (left) and at the specific case image selection procedure (right).

During the ANN training procedure, three options were provided: (i) right-eye training, (ii) left-eye training, and (iii) both-eye training. In the first two cases the algorithm uploads the corresponding images (right-eye or left-eye respectively) from the patients' database. In the last case the image was splitted in a right and a left part, each one containing the corresponding eye and then the right-eye training algorithm or the left-eye training algorithm was invoked, depending on the eye of interest. Screenshots of the GUI training procedure representation and the image selection of the specific case under consideration are shown in Scr. 1. Parameters that define the architecture of the ANN, namely, number of neural layers, number of neurons per layers, as well as the functional parameters of the ANN like percentage of training, testing and validation subsets over the total set of samples, training methods, number of training epochs and termination conditions, were user defined, through selections provided by the GUI.

As it was mentioned in the previous section, the performance of the ANN was evaluated in terms of the accuracy of classification. By denoting as TP, FP, TN and FN the number of cases that were classified by the algorithms as true positive, false positive, true negative and false negative respectively, the *accuracy* (*ACC*) of the classification method is given by the expression:

$$ACC = \frac{TP + TN}{TP + TN + FP + FN} \tag{1}$$

i.e., *ACC* is the ratio of the number of correctly classified cases over the total number of cases. Accuracy-Loss diagrams were generated during the training procedure of the ANN.

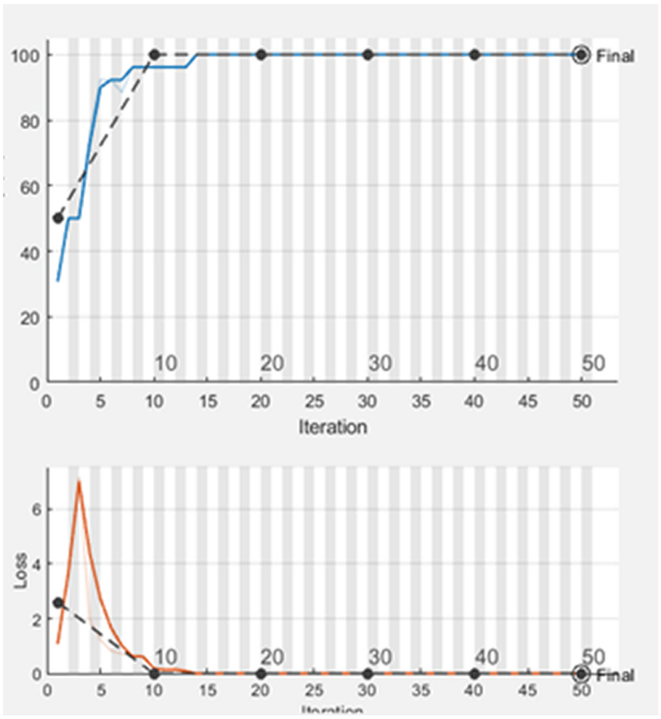

Scr. 2. Accuracy diagram and Loss diagram using the SGDM training method for the training (solid lines) and the validation procedure (dotted lined).

3 Results

Numerous computer experiments were conducted using the proposed algorithms in order to evaluate their performance and efficiency. Screenshot of the obtained Accuracy-Loss diagrams obtained by training the ANN using the Stochastic Gradient Descent with Momentum optimizer (SGDM) in the training method [30, 31] are shown in Scr. 2, where the ANN managed to reach accuracy up to 100% and to zero classification error. The corresponding results that were obtained using the Root Mean Square Propagation optimizer (RMSProp) in the training method [32] are shown in Scr. 3, where again the ANN succeeded to achieve accuracy up to 100% and zero error.

In Scr. 4, the representative results are presented with respect to the classification of a specific case by a trained ANN. These classification results refer to a full-face photograph of a normal subject and the right eye of a eyelid BCC patient that were selected to be identified and classified by the algorithm using SGDM. The algorithm at a first step splitted the full-face photograph of the normal subject to a right and a left part and subsequently examined if either the right or the left eyelid is pathological, concluding to a true negative answer for both eyelids. On the other hand, the case of the right eye of the eyelid BCC patient was classified as true positive by the algorithm.

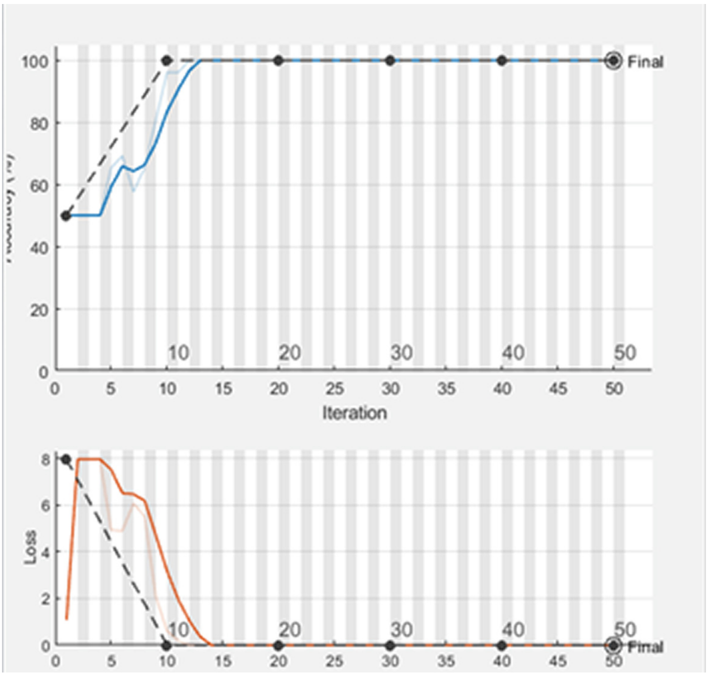

Scr. 3. Accuracy diagram and Loss diagram using the RMSProp training method for the training (solid lines) and the validation procedure (dotted lined).

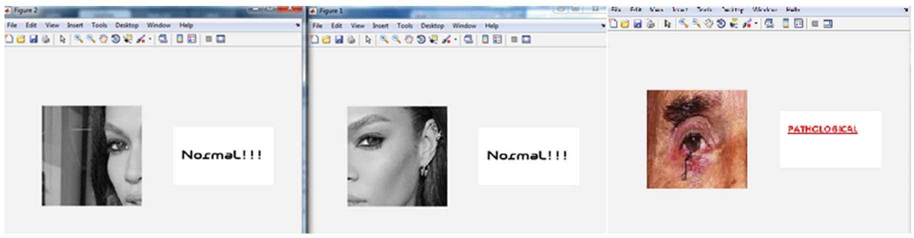
Figure 2
File Edit View Insert Tools Desktop Window Help
Normal!!!
Figure 1
File Edit View Insert Tools Desktop Window Help
Normal!!!
PATHOLOGICAL

Scr. 4. Left and middle: true negative classification of a full-face photograph of a normal subject (splitted in right and left part by the algorithm during preprocessing). Right: true positive classification of the right half-face photograph of an eyelid BCC patient.

4 Discussion

In this work, the first results of an intelligent pattern recognition algorithm for the identification and classification of eyelid BCC were presented. AI classification algorithms were developed based on ANN and were applied on face photographs of normal subjects and eyelid BCC patients. The algorithms were executed under a specially designed user-friendly GUI. To our knowledge it is the first time that such a task is accomplished. A large number of computer experiments indicated that ANN can account for the identification and classification of eyelid BCC, reaching performance efficiency that topped up to 100%. In future work, the proposed algorithms will be used on a larger patients' database that is constructed with the collaboration of the Clinic of Ophthalmology of the University of Crete and Deep Learning Neural Network algorithms will be used. Deep Learning algorithms has been proven very efficient in the recent past to accomplish tasks referring to pattern recognition in general, and specifically to image classification and face identification and recognition [33–35]. In addition to the present work, a wider variety of ANN training and learning algorithms and Deep Learning algorithms based on Convolution Neural Networks (CNN) will be utilized for purpose of comparison among these methods.

References

1. Telfer, N.R., Colver, G.B., Bowers, P.W.: Guidelines for the management of basal cell carcinoma. Br. J. Dermatol. **141**, 415–423 (1999)
2. Preston, D.S., Stern, R.S.: Nonmelanoma cancers of the skin. N. Eng. J. Med. **327**, 1649–1662 (1992)
3. Miller, S.J.: Biology of basal cell carcinoma (Part I). J. Am. Acad. Dermatol. **24**, 1–13 (1991)
4. Salomon, J., Bieniek, A., Baran, E., Szepietowski, J.C.: Basal cell carcinoma on the eyelids: own experience. Dermatol. Surg. **24**, 1–13 (1991)
5. Goldberg, D.P.: Assessment and surgical treatment of basal cell skin cancer. Clin. Plast. Surg. **24**, 673–686 (1997)
6. Duong, H.Q., Copeland, R.: Basal cell carcinoma, eyelid. Emedicine (2001)

7. Green, A.: Changing patterns in incidence of non-melanoma skin cancer. Epithelial Cell Biol. **1**, 47–51 (1992)
8. Allali, J., D'Hermies, F., Renard, G.: Basal cell carcinomas of the eyelids. Ophthalmologica **219**, 57–71 (2005)
9. Gaughan, L.J., Bergeron, J.R., Mullins, J.F.: Giant basal cell epithelioma developing in acute burn site. Arch. Dermatol. **99**(5), 594–595 (1969)
10. Margolis, M.H.: Superficial multicentric basal cell epithelioma arising in thermal burn scar. Arch. Dermatol. **102**(4), 474–476 (1970)
11. Anderson, N.P., Anderson, H.E.: Development of basal cell epithelioma as a consequence of radiodermatitis. AMA Arch. Dermatol. Syphilol. **63**(5), 586–596 (1951)
12. Gilbody, J.S., Aitken, J., Green, A.: What causes basal cell carcinoma to be the commonest cancer? Aust. J. Public Health **18**, 218–221 (1994)
13. Gilde, K.: Malignant tumors of the skin. Orv. Hetil. **147**(48), 2321–2330 (2006)
14. Schulze, H.J., Cribier, B., Requena, L.: Imiquimod 5% cream for the treatment of superficial basal cell carcinoma: results from a randomized vehicle-controlled phase III study in Europe. Br. J. Dermatol. **152**(5), 939–947 (2005)
15. Warren, R.C.; Nerad, J.A.: Micrographic (Mohs') surgery in the management of periocular basal cell epitheliomas. Arch. Ophthalmol. **108**(6), 845–850 (1990)
16. Lindgren, G., Larko, O.: Long-term follow-up of cryosurgery of basal cell carcinoma of the eyelid. J. Am. Acad. Dermatol. **36**, 742–746 (1997)
17. Mantzaris, D., Anastassopoulos, G., Adamopoulos, A.: Genetic algorithm pruning of probabilistic neural networks in medical disease estimation. Neural Netw. **24**(8), 831–835 (2011)
18. Stephanakis, I.M., Iliou, T., Anastassopoulos, G.: Mutual information algorithms for optimal attribute selection in data driven partitions of databases. Evolving Systems (2018). https://doi.org/10.1007/s12530-018-9237-9
19. Stephanakis, I.M., Anastassopoulos, G.C.: A multiplicative multilinear model for inter-camera prediction in free view 3D systems. J. Eng. Intell. Syst. **21**(2/3), 193–207 (2013)
20. Stephanakis, I.M., Anastassopoulos, G.C., Iliadis, L.: A self-organizing feature map (SOFM) model based on aggregate-ordering of local color vectors according to block similarity measures. Neurocomput. J. **107**, 97–107 (2013)
21. Stephanakis, I.M., Iliou, T., Anastassopoulos, G.: Information feature selection: using local attribute selections to represent connected distributions in complex datasets. In: Boracchi, G., Iliadis, L., Jayne, C., Likas, A. (eds.) Engineering Applications of Neural Networks. EANN 2017, Communications in Computer and Information Science, vol. 744, pp. 441–450. Springer, Cham (2017)
22. Vaillant, R., Monrocq, C., Le Cun, Y.: Original approach for the localisation of objects in images. IEE Proc. Vis. Image Sign. Process. **141**(4), 245–250 (1994)
23. Le Cun, Y., Bottou, L., Bengio, Y., Haffner, P.: Gradient-based learning applied to document recognition. Proc. IEEE **86**(11), 2278–2324 (1998)
24. Owley, H., Baluja, S., Kanade, T.: Neural network-based face detection. IEEE Trans. Pattern Anal. Mach. Intell. **20**(1), 23–38 (1998)
25. Hjelmas, E., Low, B.K.: Face detection: a survey. Comput. Vis. Image Underst. **83**(3), 236–274 (2001)
26. Zhao, W., Chellappa, R., Phillips, P.J., Rosenfeld, A.: Face recognition: a literature survey. ACM Comput. Surv. (CSUR) **35**(4), 399–458 (2003)
27. Tolba, A.S., El-Baz, A.H., El-Harby, A.A.: Face recognition: a literature review. Int. J. Sign. Process. **2**(2), 88–103 (2006)
28. Zhang C., Zhang, Z.: A survey of recent advances in face detection. Technical report, Microsoft Research (2010)

29. Matlab homepage. https://www.mathworks.com/products/matlab.html
30. Qian, N.: On the momentum term in gradient descent learning algorithms. Neural Netw. **12**(1), 145–151 (1999)
31. Sutskever, I., Martens, J., Dahl, G.E., Hinton, G.E.: On the importance of initialization and momentum in deep learning. In: ICML, vol. 3, no. 28, pp. 1139-1147 (2013)
32. Wilson, A.C., Roelofs, R., Stern, M., Srebro, N., Recht, B.: The marginal value of adaptive gradient methods in machine learning. In: Bengio, S., Wallach, H., Larochelle, H., Grauman, K., Cesa-Bianchi, N., Garnett, R. (eds.) 31st Conference on Neural Information Processing Systems (NIPS 2017), Long Beach, CA, USA (2017)
33. Krizhevsky, A., Sutskever, I., Hinton, G.E. Imagenet classification with deep convolutional neural networks. In: Advances in neural information processing systems, pp. 1097–1105 (2012)
34. Russakovsky, O., Deng, J., Su, H., Krause, J., Satheesh, S., Ma, S., Huang, Z., Karpathy, A., Khosla, A., Bernstein, M., Berg, A., Fe-Fei, L.: Imagenet large scale visual recognition challenge. Int. J. Comput. Vis. **115**(3), 1–42 (2014)
35. Bengio, Y., Goodfellow, I.J., Courville, A.: Deep Learning. MIT Press, Cambridge (2015)

Fuzzy Logic Modeling

Application of Algorithmic Fuzzy Implications on Climatic Data

Stefanos Makariadis, Georgios Souliotis, and Basil K. Papadopoulos(✉)

Department of Civil Engineering Section of Mathematics and Informatics, Democritus University of Thrace, 67100 Kimeria, Greece
{smakaria,gsouliot,papadob}@civil.duth.gr

Abstract. In this paper we present a new Fuzzy Implication Generator via Fuzzy Negations which was generated via conical sections, in combination with the well-known Fuzzy Conjunction T-norm = min. Among these implications we choose the most appropriate one, after comparing them with the empiristic implication, which was created with the help of real temperature and humidity data from the Hellenic Meteorological Service. The use of the empiristic implication is based on real data and also it reduces the volume of the data but without cancelling them. Finally, the pseudo-code, which was used in the programming part of the paper, uses the new Fuzzy Implication Generator and approaches the empiristic implication satisfactorily which is our final goal.

Keywords: Fuzzy implication · Empiristic implication · Fuzzy negation via conical sections

1 Introduction

The Theory of Fuzzy Implications and Fuzzy Negations plays an important role in many applications of fuzzy logic, such as approximate reasoning, formal methods of proof, inference systems, decision support systems (cf [2] and [5]). Recognizing the above important role of Fuzzy Implications and Fuzzy Negations, we tried to construct Fuzzy implications from Fuzzy negations, so that we could change the implication with one parameter, thus giving an algorithmic procedure of the "if......then......" rule. The tools for this construction, namely a fuzzy implication generator, were mainly the conclusions of (cf [11]) and in particular the following formula 1

$$N(x) = \sqrt{(a^2-1)x^2+1} + ax, \quad x \in [0,1], \quad a \leq 0. \tag{1}$$

producing fuzzy negations via conical sections and Corollary 2.5.31. (see [1]). The combination of these two through the fuzzy conjunction T-norm = min gave us an algorithmic procedure for the evaluation of the best implication with respect to the problem data. For the evaluation of the best implication we used the empiristic implication (see [8]) as a comparison measurement. The empiristic implication does not satisfy any of the properties of the fuzzy implications and has no specific formula, meaning it is not a function. However, the choice of this particular implication was not random as it was based on its ability to be directly calculated by the empirical data without being affected by the amount of the data.

The paper follows the following structure: The section Preliminaries presents the theoretical background of the paper, such as the definitions of the Fuzzy Implications, Fuzzy Negations and Triangular norms. The section Main Results shows the implication which is constructed by a strong fuzzy negation and a t-norm with $T_M(x, y) = \min\{x, y\}$. Next, the empiristic implication and the algorithm for its calculation are presented. The data used are real, such as the average monthly temperature and the average monthly relative humidity, two of the most important climatic variables in meteorology (see [4]). Furthermore, the algorithmic process for finding the best fuzzy implication among the empiristic implication, the three known implications from the literature (Kleen-Dienes, Lukasiewicz, Reichenbach) (see [1]) and the constructed parametric implication is analysed. The calculation of the implications with the use of data was done in the Matlab programming environment. We present the documentation of the Matlab code which was used to calculate the implications.

2 Preliminaries

The following short theoretical background is important in order to understand this paper.

2.1 Fuzzy Implication

In the literature we can find several different definitions of fuzzy implications. In this paper we will use the following one, which is equivalent to the definition proposed by Kitainik [6], (see also [3] and [1]).

Definition 1. *A function* $I : [0, 1]x[0, 1] \to [0, 1]$ *is called a fuzzy implication if for all* $x, x_1, x_2, y, y_1, y_2 \in [0, 1]$ *the following conditions are satisfied:*
$(I1)$ $x_1 \le x_2$ *then* $I(x_1, y) \ge I(x_2, y)$, *i.e,* $I(\cdot, y)$ *is decreasing,*
$(I2)$ $y_1 \le y_2$ *then* $I(x, y_1) \le I(x, y_2)$, *i.e.,* $I(x, \cdot)$ *is increasing,*
$(I3)$ $I(0, 0) = 1$
$(I4)$ $I(1, 1) = 1$
$(I5)$ $I(1, 0) = 0$

Example 1. *Some examples of Fuzzy Implications are given below:*
Kleene-Dienes: $I_{KD}(x, y) = \max\{1 - x, y\}$
Lukasiewicz: $I_{LK}(x, y) = \min\{1, 1 - x + y\}$
Reichenbach: $I_{RC}(x, y) = 1 - x + x \cdot y$

2.2 Fuzzy Negations

The following definitions and examples can be found [1,3,9], and [10].

Definition 2. *A function* $N : (0,1) \to [0,1]$ *is called a Fuzzy negation if*
$(N1)$ $N(0) = 1,\ N(1) = 0$
$(N2)$ *N is decreasing*

Definition 3. *A fuzzy negation N is called strict if, in addition,*
(N3) N is strictly decreasing,
(N4) N is continuous,
A fuzzy negation N is called strong if the following property is met,
$(N5)$ $N(N(x)) = x,\ \ x \in [0,1]$

Example 2. *Examples of Fuzzy Negations are given below.*
$N_K(x) = 1 - x^2,$ *strict*
$N_R(x) = 1 - \sqrt{x},$ *strict*
$N^{\lambda}(x) = \frac{1-x}{1+\lambda x},\ \ \lambda \in (-1,+\infty)$ *strong Sugeno class*
$N^{W}(x) = (1 - x^{w})^{\frac{1}{w}},\ \ w \in (0,+\infty)$ *strong Yager class*

Remark 1. The paper [11] proves a new family of strong fuzzy negations, which is produced by conical sections and is given from the Eq. (1), which will play a key role in building the algorithmic procedure we propose in the section Main Results.

2.3 Triangular Norms (Conjunctions)

The Triangular norms were introduced by Menger [9] and were later reconstructed by Schweizer and Sklar [10] in the form they have today. In essence, they are a generalization of the classical binary conjunction ($\wedge$) into a fuzzy intersection. The following definition can be found in the monograph by Klement et. al [7], (see also [1]).

Definition 4. *A function* $T : [0,1]^2 \to [0,1]$ *is called triangular norms shortly t- norm, if it satisfies, for all* $x, y \in [0,1]$*, the following conditions:*
$(T1)$ $T(x,y) = T(y,x)$ (*commutativity*)
$(T2)$ $T(x,T(y,z)) = T(T(x,y),z)$
$(T3)$ *if* $y \leq z,$ *then* $T(x,y) \leq T(x,z)$ (*monotonicity*)
$(T4)$ $T(x,1) = x$ (*boundary condition*)

Table 1 lists a few of the common t-norms.

In the paper we will use the most basic of all t-norms, which is the minimum

$$T_M(x,y) = \min\{x,y\} \tag{2}$$

Table 1. Table basic t-norms

Minimum	$T_M(x,y) = \min\{x,y\}$
Algebraic product	$T_p(x,y) = x \cdot y$
Lukasiewicz	$T_{LK}(x,y) = \max(x+y-1,0)$
Active product	$T_D(x,y) = \begin{cases} 0 & x,y \in [0,1) \\ min(x,y) & otherwise \end{cases}$
Nilpotent minimum	$T_{nM}(x,y) = \begin{cases} 0 & x+y \leq 1 \\ min(x,y) & otherwise \end{cases}$

3 Main Results

3.1 Construction of Fuzzy Implications via Strong Negations

The main purpose of this work is to create a two plays function that satisfies Definition 1, utilizing the temperature and humidity data given by the Hellenic National Meteorological Service. That is, the construction of an implication that gives the degree of truth of the two variables, the temperature and the humidity. To achieve this, the two variables are normalized with the help of fuzzy sets. In this way the temperature gets values of [0, 1] and the humidity gets values of [0, 1], which is the degree of truth of the two variables. For example, if the temperature between $[21°, 31°]$ degrees is considered high, then it has a degree of truth 1. And similarly if the humidity between [40%, 50%] is considered low, then it has a degree of truth of 0.7. Our goal is to construct an implication that gives the degree of truth, as does the statement below:

"If the temperature is high, then the humidity is low."

To what degree of truth can we respond to this statement?

This is our intention, that is, to find an implication that is close enough to the correlation of the two variables, the temperature and the humidity, as are shown in our data. But to find such an implication there must be a comparison measure, that is, we want from our data to ensure the degree of truth of the temperature and the humidity pair as they are given. The comparison measure in the present work is the empiristic implication that uses all the data in order to produce a table in which in the first row and the first column there will be the data grouped into classes and in each cell there will be the corresponding degree of truth of the data. Then, we compare each of the Kleen-Dienes, Lukasiewicz, Reichenbach (see [1]) and the parametric implications which will be generated, with the empiristic one, using the square error of the difference of the aforementioned implication tables from the empiristic implication table.

The smallest square error will give the best implication.

In book [1], and in particular in Corollary (2.5.31), the implication generated by a strong fuzzy negation and a t-norm is examined and the formula

$$I(x,y) = N(T(x,N(y))), \;\; x,y \in [0,1] \tag{3}$$

is proposed. Using the above implication (3) (see 3) with t-norm (2) (see 2) and the formula (1) (see 1) with parameter α and after the appropriate calculations, the following equation occurs.

$$I(x,y) = \sqrt{(a^2-1)\,.\left(\min\left(x, \sqrt{(a^2-1)\,y^2+1}+ay\right)\right)^2+1} \\ +a.\min\left(x, \sqrt{(a^2-1)\,y^2+1}+ay\right), y \in [0,1], a \le 0 \qquad \text{(equation a)}$$

The above implication of (equation a), which is a new generator fuzzy implications, is important because it has the parameter α which helps us to use the implication on our data and at the same time examine for which value of α we have the best approach. Hence, an algorithmic process of finding a better implication is created which will play an important role in the course of the paper.

3.2 Empiristic Implication

In order to be able to estimate which of the proposed implications approaches the pairs (Temperature, humidity) of the Hellenic Meteorological Service, we need to have a comparison measurement. In this paper we use the empiristic implication as a measure see [8]. The empiristic implication will be presented while explaining the steps of the algorithm, based on our data, which derive from the Hellenic Meteorological Service and are the average monthly temperature and the average monthly humidity of the last five years from the 13 regions of Greece (see Fig. 1, Fig. 2).

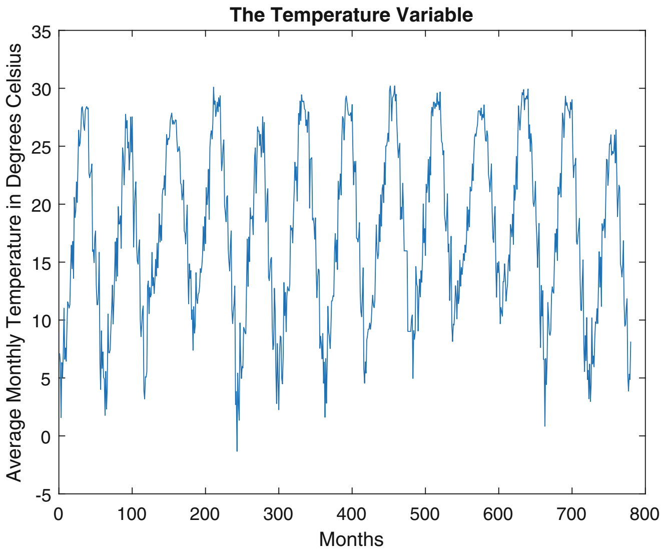

Fig. 1. Temperature variable

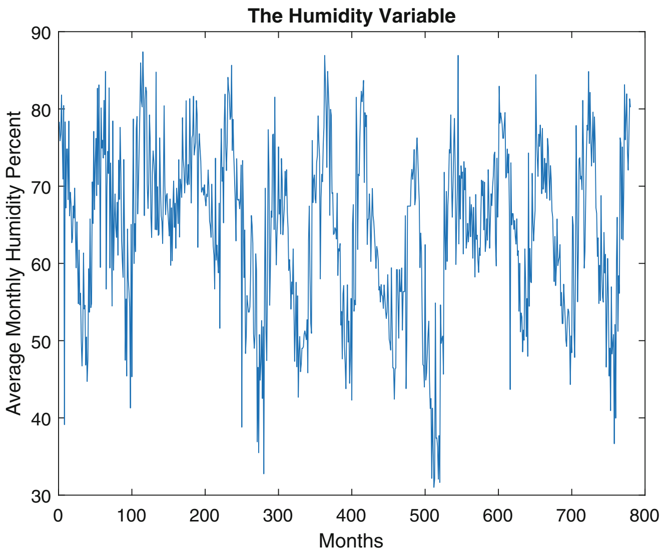

Fig. 2. The humidity variable

Our goal is to find which implication approaches best our data dependence (temperature and humidity), giving us as a result the degree of the true coexistence of the two corresponding values. For example, we would like to see the degree of truth of the statement:

if the temperature is 20 °C then the humidity is 60%

First, we find the table representing the empiristic implication. For the construction of the empiristic implication, we divide the 780 temperature and relative humidity data into 11 classes with the use of the Sturges type

$$c = 1 + \log_2 n \overset{n=780}{\Leftrightarrow} c = 1 + \log_2(780) \Leftrightarrow c = 1 + \frac{\log(780)}{\log(2)} \Leftrightarrow c = 10.6 \qquad (4)$$

after first placing them in ascending order. Each class has its median as a representative. This is how we create the empiristic implication table, which has the medians of the humidity classes in the first row while the medians of the temperature classes are in the first column. Each cell of the table is divided by the sum of the column in which it belongs. In this way, we have in each cell the degree of the truth of the coexistence of the values of the corresponding column and row of the cell (see Table 2). Then we normalize the temperature and the humidity medians. Next, we check first whether the three known implications (Kleen-Dienes, Lukasiewicz, Reichenbach) (see [1]) approach the table above. Then, we examine the norm of each of the above implications with the empirical implication. The results are as follows.

Table 2. Table of the empiristic implication

0.0282	0	0.0141	0.0423	0.0282	0.0563	0.1127	0.1127	0.1831	0.1972	0.2286
0.0141	0	0.0141	0.0704	0.0563	0.0845	0.1972	0.0704	0.1268	0.2113	0.1571
0	0	0	0.0563	0.0423	0.1127	0.0986	0.1408	0.1127	0.1408	0.3000
0	0.0141	0.0423	0.0563	0.0704	0.1408	0.0986	0.1408	0.1831	0.1690	0.0857
0.0141	0.0423	0.0845	0.0423	0.1268	0.0986	0.0845	0.1549	0.1268	0.1127	0.1143
0.0423	0.0282	0.1408	0.0845	0.1972	0.0563	0.0423	0.1690	0.0563	0.1127	0.0714
0.0563	0.0563	0.1268	0.1268	0.1268	0.1690	0.1127	0.0845	0.0704	0.0423	0.0286
0.0845	0.1268	0.1831	0.1972	0.0845	0.0986	0.0845	0.0423	0.0704	0.0141	0.0143
0.1127	0.2254	0.1408	0.1127	0.1127	0.1268	0.0845	0.0282	0.0563	0	0
0.2676	0.1690	0.1549	0.1549	0.0704	0.0423	0.0704	0.0563	0.0141	0	0
0.3803	0.3380	0.0986	0.0563	0.0845	0.0141	0.0141	0	0	0	0

The Results of the Norms. The squared error of the two implications (empiristic and Kleen-Dienes) gives the result is 6.2465.

The squared error of the two implications (empiristic and Kleen-Dienes) gives the result is 8.7386.

The squared error of the two implications (empiristic and Kleen-Dienes) gives the result is 7.4448.

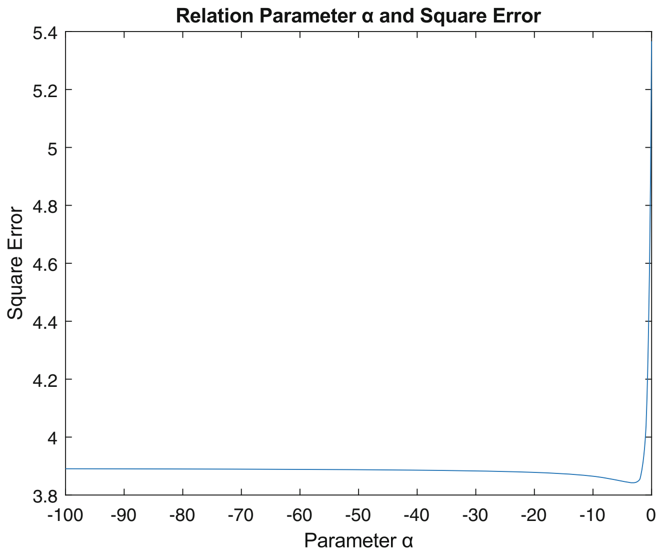

Fig. 3. Relation parameter α and square error.

After the examination of the three implications is completed, we proceed to find the best parameter $a \leq 0$ that we have from the (equation a). We have the best approach for the value $\alpha = -3$ and with a very good approach the squared error of the two implications (empiristic and Kleen-Dienes) gives the result is 3.8425 (see Fig. 3).

Remark 2. To achieve our goal, that is, to approach the empiristic implication table, we used 3 linguistic variables (low, medium and high) for temperature and humidity respectively.
$[a, b, c, d] = [-1.33\ -1.33\ 7\ 12]$ is low temperature
$[a, b, c, d] = [10\ 13\ 15\ 18]$ is medium temperature
$[a, b, c, d] = [16\ 21\ 30.21\ 30.21]$ is high temperature
$[a, b, c, d] = [31.01\ 31.01\ 40\ 45]$ is low humidity
$[a, b, c, d] = [43\ 50\ 60\ 65]$ is medium humidity
$[a, b, c, d] = [64\ 75\ 87.39\ 87.39]$ is high humidity
(see Fig. 4, Fig. 5). Also, to avoid the property of the implication I (0,1) = 1, which reinforces the falsehood, we tried to obtain the values of $x \neq 0$.

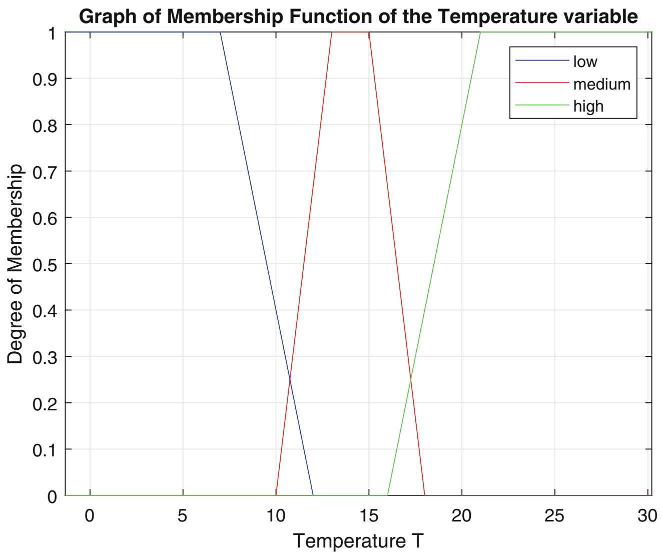

Fig. 4. Membership function of the temperature.

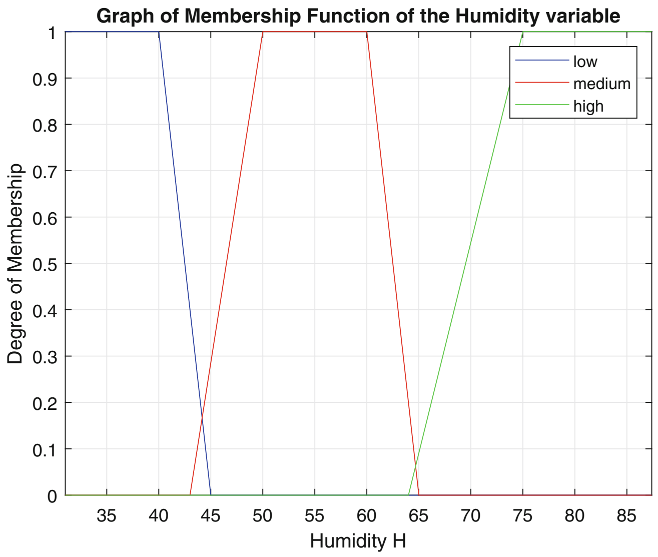

Fig. 5. Membership function of the humidity.

3.3 The Documentation of the Matlab Code

The data are in the file Data.xlsx. Our application includes a case study, which uses real climatic data (average monthly temperature and average monthly relative humidity) of the last five years 2015–2019 from the 13 regions of Greece for the 12 months of each year and evaluates the empiristic implication, with fuzzy implications we created. The application was implemented in Matlab R2018b and includes the steps:

1. We load the data onto the program, which creates two 780×1 tables. The lines in the tables are the 780 observations and the columns in the tables are the temperature and relative humidity variables. Temperature, Humidity.
2. We find the minimum and maximum values of the columns that make up the range of the variables.
3. We have the original table with the first column is X and the second is Y.
4. We add to this table a column which is the increment number in order not to miss the original pairs (xi, yi). The column we add is the third one.
5. Later, we create a different table for X together with its increment number and a different one for Y. Then, we have the initial position for each X and Y so we sort in ascending order according to the values. We notice that in the first column we have X and Y in ascending order and in the second column their position in the original data.
6. We normalize using trapezoidal membership functions
7. We apply the Sturges rule: (see 4) in order to divide the sorted data columns in classes.

8. Next, we create 11 classes for each sorted table.
9. We add the classes to the third column in the sorted tables. The format of the sorted tables is: the first column has X in ascending order, the second column has the initial position and the third column has the class.
10. Then, we sort the above two tables by increment number to get the data back to their original position along with their classes.
11. We put the above tables in a table where the first column is X, the second is the class of X, the third is Y and the fourth is the class of Y.
12. We create a Zero Table. The table will be a column larger and a column smaller to place the medians.
13. Finally, we create the table we want without adding values to the first row and column.
14. We create medians for the classes of X and place them in the Final Table.
15. We create medians for the classes of Y and place them in the Final Table.
16. The Final Table has the medians of the classes of Y as its first row and the medians of the classes of X as its first column.
17. We create a new table who has the first row and the first column with medians.
18. We form the rest of the table by calling the function of parametric implication.
19. The table imp1 is the table of the empiristic implication.
20. We will check three well-known implications with the data we have.
21. The first is Kleen-Dienes (see Examples1.)
22. Table A is an 11×1 column table containing the temperature medians.
23. Table B is a 1×11 row table containing the humidity medians.
24. Table A1 is an 11×1 column table containing the nondimensionalized values of the temperature medians.
25. Table B1 is a 1×11 row table containing the nondimensionalized values of humidity medians.
26. The final table of Kleen-Dienes implication is imp2 and the control of the norm of the two implications (empiristic and Kleen-Dienes) is nor1 = norm (imp1-imp2).
27. The second implication is Lukasiewicz (see Examples1.)
28. The final table of the Lukasiewicz implication is imp3 and the control of the norm of the two implications (empiristic and Lukasiewicz) is nor2 = norm (imp1-imp3).
29. The third implication is Reichenbach (see Examples1.)
30. The final table of Reichenbach's implication is imp4 and the control of the norm of the two implications (empiristic and Reichenbach) is nor3 = norm (imp1-imp4).
31. The final table of Parametric's implication is OtherTable and the control of the norm of the two implications (empiristic and Parametric) is nor4 = norm (imp1-OtherTable).

4 Conclusions

It is now evident that the type of the strong fuzzy negations that are generated via conical sections, combined with the fuzzy conjunction (T-norm = min), give us a robust algorithmic process of finding the more appropriate fuzzy implication. So we see that a purely mathematical process and even a geometric one is a powerful tool when it is well supported to achieve approximate reasoning. In addition, a thorough and careful study of the data in the correct order will greatly reduce the computational complexity. Our future research on the applications of fuzzy implications will continue with the aim of achieving better results of the convergence of the empiristic implication and the implications the strong fuzzy negations that are generated via conical sections.

Acknowledgements. We would like to thank the Hellenic National Meteorological Service for the quick reply to our request for the concession of the climatic data of the last five years, in order to be used in the present paper (see [4]).

References

1. Baczynski, M., Jayaram, B.: Fuzzy Implications. Springer-Verlag, Heidelberg (2008). https://doi.org/10.1007/978-3-540-69082-5_1
2. Fodor, J.C.: Contrapositive symmetry of fuzzy implications. Fuzzy Sets Syst. **69**, 141–156 (1995)
3. Fodor, J.C., Roubens, M.: Fuzzy preference Modelling and Multicriteria Decision Support. Kluwer, Dordrecht (1994)
4. Hellenic National Meteorological Service. http://www.hnms.gr/emy/el/climatology/climatology_month
5. Jenei, S.: A new approach for interpolation and extrapolation of compact fuzzy quantities. The one dimensional case. In: Klement, E.P., Stout, L.N. (eds.) Proceedings of the 21th Linz Seminar on Fuzzy Set Theory, Linz, Austria, pp. 13–18 (2000)
6. Kitainik, L.: Fuzzy Decision Procedures with Binary Relations. Kluwer, Dordrecht (1993)
7. Klement, E.P., Mesiar, R., Pap, E.: Triangular Norms. Kluwer, Dordrecht (2000)
8. Mattas, K., Papadopoulos, B.: Fuzzy empiristic implication, a new approach. In: Mattas, K., Papadopoulos, B. (eds.) Modern Discrete Mathematics and Analysis, SOIA. Springer Optimization and Its Applications, vol. 131, pp. 317–331 (2018)
9. Menger, K.: Statistical metrics. Proc. Nat. Acad. Sci. USA **28**, 535–537 (1942)
10. Schweizer, B., Sklar, A.: Probabilistic Metric Spaces. North-Holland, New York (1983)
11. Souliotis, G., Papadopoulos, B.: An algorithm for producing fuzzy negations via conical sections. Algorithms **12**(5), 89 (2019). https://doi.org/10.3390/a12050089

Fuzzy Logic Application to Searchable Cryptography

Hassan B. Kazemian[1](✉) and Yang Ma[2]

[1] School of Computing and Digital Media, London Metropolitan University, London, UK
h.kazemian@londonmet.ac.uk

[2] Underwriters Laboratories, UK Security Lab, Basingstoke, UK
Yang.Ma@ul.com

Abstract. Public Key Encryption with Keyword Search (PEKS) allows users to search encrypted files by a specific keyword without compromising the original data security. Almost all current PEKS schemes enable users to search exact keyword only instead of imprecise keyword (such as "latest", "biggest", etc.). Therefore, if the keyword is fuzzy, these PEKS schemes will be terminated and then report errors. Besides, some PEKS schemes are not secure mainly because they are vulnerable to Off-line Keyword Guessing Attack (OKGA). This research paper incorporates with Mamdani Fuzzy Inference System to PEKS for supporting Fuzzy Keyword Search. Secondly, the proposed scheme is proved to be semantic secure under the random oracle models so that it is able to resist OKGA. In addition, the new scheme allows users to search multiple keywords and therefore, it could be applied to the general public networks.

Keywords: Public Key Encryption with Keyword Search (PEKS) · Off-line Keyword Guessing Attack (OKGA) · Mamdani Fuzzy Inference System

1 Introduction

The rising popularity of cloud computing attracts companies and individuals to upload their data into the online trusted servers (i.e. cloud servers). It brings about substantial merits, such as saving local memory and reducing maintenance fee, etc. How to keep data security becomes an intractable problem. Interestingly, Public Key Encryption with Keyword Search (PEKS) protects information security and data transmission security.

Boneh et al. [1] defined the first PEKS scheme in 2004 which requires a secure channel (i.e. Secure Sockets Layer) between the server and the receiver. But building a secure channel is much expensive and unrealistic in some cases. Besides, Byun et al. [3] pointed out that the first PEKS was compromising from Off-line Keyword Guessing Attack (OKGA). In 2008, Baek et al. [2] proposed a new PEKS scheme to remove the secure channel from the first PEKS system.

L. Iliadis et al. (Eds.): EANN 2020, INNS 2, pp. 410–422, 2020.
https://doi.org/10.1007/978-3-030-48791-1_32

But, Yau et al. [4] also found that Baek et al.'s PEKS suffers OKGA. Tang et al. [5] introduced a new PEKS scheme resisting OKGA, but the encryption algorithm is complex. Soon later, Rhee et al. [6] defined the concept of Trapdoor Indistinguishability to PEKS (called dPEKS) for preventing OKGA. However, dPEKS scheme is able to search single keyword only instead of multiple keywords so that it may not be applied to the general public networks. Meanwhile, Baek et al.'s proposed MPEKS [2] scheme to solve multiple keywords search problem. However, MPEKS also needs a secure channel. Later on, Wang et al. [7] came up with a Secure Channel Free MPEKS system to remove the secure channel and support multiple keywords search, but it suffers OKGA. Recently, PEKS witnesses a dramatic development and becomes much security and functionalities.

In practice, several keywords are distilled to represent the whole document instead of one keyword only. Besides, the user may type imprecise keyword for searching, such as "latest", "biggest", etc. Due to PEKS ciphertext may contain fuzzy keyword leading to system errors, therefore, Mamdani Fuzzy Inference method could be perfectly applied to PEKS scheme in order to solve fuzzy keyword search problem. In 1973, Lotifi Zadeh's [8] came up with new fuzzy algorithms to analyse complex systems and decision processes. Later, Ebrahim Mamdani [9] revisited Lotifi's approach and then proposed an inference system to control a steam engine and boiler combination based on linguistic rules from human knowledge. However, Mamdani-style inference is not computationally efficient, Michio Sugeno [10] proposed a new fuzzy inference using a single spike (a singleton) as the rule consequent. Recently, Fuzzy sets theory has been applied successfully in many areas. Singh et al. [11] pointed out fuzzy systems could applied to classification, modelling control problems. Lermontov et al. [12] analysed water quality using fuzzy set. Meanwhile, Marchini et al. [13] proposed a framework for fuzzy indices of environmental conditions.

This paper formally defines a new PEKS scheme named *Public Key Encryption with Multi-keywords Search using Mamdani System (m-PEMKS)* and then presents a concrete construction of it. Besides, m-PEMKS is proved to be semantic secure under random oracle models so that it could resist OKGA. In addition, the proposed scheme incorporates with Mamdani System to solve fuzzy keyword search problem, which is the first paper combining Fuzzy Logic and PEKS.

2 Methodology

2.1 Bilinear Pairings

Let G_1 be an additive cyclic group and G_T be a multiplicative cyclic group. g is a generator of G_1 and a prime number p is the order of G_1. Suppose a and b are the elements in Z_p. A bilinear pairing can be regarded as a map $e : G_1 \times G_1 \rightarrow G_T$, which has the following properties:

i. Bilinear: $e(aU, bV) = e(U, V)^{ab}$ for all $U, V \in G_1$ and $a, b \in Z_p$.
ii. Computable: $e(U, V) \in G_T$ is computable in a polynomial time algorithm, for any $U, V \in G_1$.
iii. Non-degenerate: $e(U, V) \neq 1$.

2.2 The Bilinear Diffie-Hellman (BDH) Assumption

Given g, xg, yg, zg as input (where $x, y, z \in Z_p$), compute $e(g, g)^{xyz} \in G_T$. An algorithm A has an advantage ε in solving BDH assumption in G_1, if $Pr[A(g, xg, yg, zg) = e(g, g)^{xyz}] \geq \varepsilon$. It is shown that BDH assumption holds in G_1 if no t time algorithm has an advantage at least ε in solving BDH assumption in G_1.

2.3 The 1-Bilinear Diffie-Hellman Inversion (1-BDHI) Assumption

Given g, xg as input (where $x \in Z_p$), compute $e(g, g)^{\frac{1}{x}}$. An algorithm A has an advantage in solving 1-BDHI assumption in G_1, if $Pr[A(g, xg) = e(g, g)^{\frac{1}{x}}] \geq \varepsilon$. It is shown that 1-BDHI assumption holds in G_1 if no t time algorithm has an advantage at least ε in solving 1-BDHI assumption in G_1.

2.4 Fuzzy Rule Based Model

The fuzzy rule based model has four steps as follows:

1. *Fuzzification of the input variables:* The aim of this step is transforming crisp inputs into fuzzy inputs by the membership functions.
2. *Rules evaluation:* The fuzzified inputs are applied to the antecedents of the fuzzy rules and then apply "AND" operation to these rule antecedents.
3. *Aggregation of the rule outputs:* The membership functions of all rule consequents previously clipped or scaled are combined into a single fuzzy set.
4. *Defuzzification:* The defuzzification method, center of gravity (COG), is utilized to transform fuzzy outputs into crisp outputs.

3 Public Key Encryption with Multi-keywords Search Using Mamdani System

Let sender, server and receiver be three parties in PEKS scheme. The sender is a party who runs PEKS algorithm to create a Searchable ciphertext. Besides, the receiver is a party who executes Trapdoor algorithm to create a Trapdoor query. Once the server receives the encrypted messages from the sender and the receiver, it will run Test algorithm to estimate whether two ciphertexts contain the same keyword or not, and replies to the receiver in the end.

3.1 Formal Definition of m-PEMKS

The proposed scheme has eight Probabilistic Polynomial Time algorithms:

1. $KeyGen_{Param-PEMKS}(1^{\varsigma})$: Input 1^{ς} for generating a common parameter cp.
2. $KeyGen_{Param-RSA}(k)$: Input k for generating a global parameter gp.
3. $KeyGen_{Server-PEMKS}(cp)$: Input cp and then produce a public and private PEMKS key pair $(pk_{Ser-PEMKS}, sk_{Ser-PEMKS})$ of the server.

4. $KeyGen_{Server-RSA}(gp)$: Input gp and then produce a public and private RSA key pair ($pk_{Ser-RSA}$, $sk_{Ser-RSA}$) of the server.
5. $KeyGen_{Receiver-PEMKS}(cp)$: Input cp and then produce a public and private PEMKS key pair ($pk_{Rec-PEMKS}$, $sk_{Rec-PEMKS}$) of the receiver.
6. $Encryption(pk_{Ser-PEMKS}, pk_{Rec-PEMKS}, pk_{Ser-RSA}, W)$: A searchable encryption $E = (E_1, E_2) =$ SCF-PEMKS$(pk_{Ser-PEMKS}, pk_{Rec-PEMKS}, W_{part1})\|RSA(pk_{Ser-RSA}, W_{part2})$ is created, where $W = (W_{part1}, W_{part2}) = [(w_1, w_2, ..., w_n); w_{n+1}]$.
7. $Request(pk_{Ser-PEMKS}, sk_{Rec-PEMKS}, pk_{Ser-RSA}, W)$: A trapdoor request $R = (R_1, R_2) =$ Trapdoor$(pk_{Ser-PEMKS}, sk_{Rec-PEMKS}, W_{part1})\|$ RSA$(pk_{Ser-RSA}, W_{part2})$ is created, where $W = (W_{part1}, W_{part2}) = [(w_1, w_2, ..., w_m); w_{fuzzy}]$.
8. $Test(E, R, sk_{Ser-PEMKS}, sk_{Ser-RSA})$: Test algorithm contains two parts: Exact Match and Fuzzy Match.

For Exact Match: Input the server's PEMKS private key $sk_{Ser-PEMKS}$, an encryption $E_1 =$ SCF-PEMKS$(pk_{Ser-PEMKS}, pk_{Rec-PEMKS}, W_{part1})$ and a request $R_1 =$ Trapdoor$(pk_{Ser-PEMKS}, sk_{Rec-PEMKS}, W^*_{part1})$. If $W^*_{part1} \in W_{part1}$, the system will go to Fuzzy Match. Otherwise, the system will terminate.

For Fuzzy Match: Input the server's RSA private key $sk_{Ser-RSA}$, an encryption $E_2 =$ RSA$(pk_{Ser-RSA}, W_{part2})$ and a request $R_2 =$ RSA$(pk_{Ser-RSA}, W^*_{part2})$. Then, the server decrypts E_2 and R_2 to obtain W_{part2} and W^*_{part2}. Let W^*_{part2} and W_{part2} be the conclusion and the condition of the rules in Mamdani system. Next, the encrypted file is filtered by Mamdani system and the server will reply to the receiver in the end.

3.2 The Concrete Construction of m-PEMKS

The details of m-PEMKS are listed in the following (Fig. 1):

1. $KeyGen_{Param-PEMKS}(1^{\varsigma})$: Let G_1 be an additive cyclic group and G_T be a multiplicative cyclic group. g is a random generator of G_1 whose order is a prime number p. A bilinear pairing is a map $e : G_1 \times G_1 \rightarrow G_T$. Let $H : \{0,1\}^{\circ} \rightarrow G_1$ and $H^* : G_T \rightarrow \{0,1\}^{\bullet}$ be two specific hash functions. This algorithm returns the common parameter $cp = \{g, p, G_1, G_T, e, H, H^*\}$.
2. $KeyGen_{Param-RSA}(K)$: Randomly select prime numbers u and v (where $u \neq v$) and calculate $L = u \times v$ and $\phi(L) = (u-1) \times (v-1)$.
3. $KeyGen_{Server-PEMKS}(cp)$: The server randomly chooses $a \in Z_p$ and then computes $A = aP$. Besides, the server chooses $B \in G_1$ uniformly at random. Therefore, the server's PEMKS public key is $pk_{Ser-PEMKS} = (cp, A, B)$ and the PEMKS private key is $sk_{Ser-PEMKS} = (cp, a)$.
4. $KeyGen_{Server-RSA}(gp)$: The server randomly selects $x \in Z_q$, where $gcd(\phi(L), x) = 1$ and $1 < x < \phi(L)$. Next, the server calculates y by $y \equiv x^{-1}(mod \phi(L))$. Therefore, the server's RSA public key is $pk_{Ser-RSA} = (x, L)$ and the private key is $sk_{Ser-RSA} = (y, L)$.

5. $KeyGen_{Receiver-PEMKS}(cp)$: The receiver randomly chooses $c \in Z_p$ and then computes $C = cP$. Therefore, the receiver's PEMKS public key is $pk_{Rec-PEMKS} = (cp, C)$ and the PEMKS private key is $sk_{Rec} = (cp, c)$.
6. $Encryption(pk_{Ser-PEMKS}, pk_{Rec-PEMKS}, pk_{Ser-RSA}, W)$: The sender randomly chooses $t \in Z_p$ and a keyword-vector $W{=}(W_{part1}, W_{part2}){=}[(w_1, w_2, ..., w_n); w_{n+1}]$. The sender then computes a searchable encryption $E = (E_1, E_2) = [(M, N_1, N_2, ..., N_n); N_{n+1}] = [(tA, H^*(D_1), H^*(D_2), ..., H^*(D_n)); (w_{n+1})^x mod\, L]$, where $D_1 = e(H(w_1), C)^t$,$D_2 = e(H(w_2), C)^t$,...,$D_n = e(H(w_n), C)^t$.
7. $Request(pk_{Ser-PEMKS}, sk_{Rec-PEMKS}, pk_{Ser-RSA}, W)$: The receiver randomly chooses $t^* \in Z_p$ and a keyword-vector $W{=}(W_{part1}, W_{part2}){=}[(w_1, w_2, ..., w_m); w_{fuzzy}]$. The receiver then computes $R = (R_1, R_2) = [(Z, T_1, T_2, ..., T_m), T_{fuzzy}] = [(e(A, t^*B), cH(w_1) \oplus e(A, B)^{t^*+c}, cH(w_2) \oplus e(A, B)^{t^*+c}, ..., cH(w_{m-1}) \oplus e(A, B)^{t^*+c}); (w_{fuzzy})^x mod\, L]$.
8. $Test(E, R, sk_{Ser-PEMKS}, sk_{Ser-RSA})$: For $i \in \{1, 2, ..., n\}$ and $j \in \{1, 2, ..., m\}$, where $j \leq i$.

(i) *For Exact Match*: Firstly, the server calculates
$T_{w_1} = T_1 \oplus Z \bullet e(aB, C) = cH(w_1^*), ...,$
$T_{w_j} = T_j \oplus Z \bullet e(aB, C) = cH(w_j^*), ...,$
$T_{w_m} = T_m \oplus Z \bullet e(aB, C) = cH(w_m^*)$
Then, the server checks whether $H^*[e(T_{w_j}, \frac{M}{a})] = N_i$ or not. If "yes", the system will go to Fuzzy Match. Otherwise, the system will terminate.

(ii) *For Fuzzy Match*: The server decrypts w_{n+1} and w_{fuzzy} from $\{[(w_{n+1})^x mod\, L]^y mod\, L\}$ and $\{[(w_{fuzzy})^x mod\, L]^y mod\, L\}$. Let w_{fuzzy} and w_{n+1} be the conclusion and condition of the rules in Mamdani system.

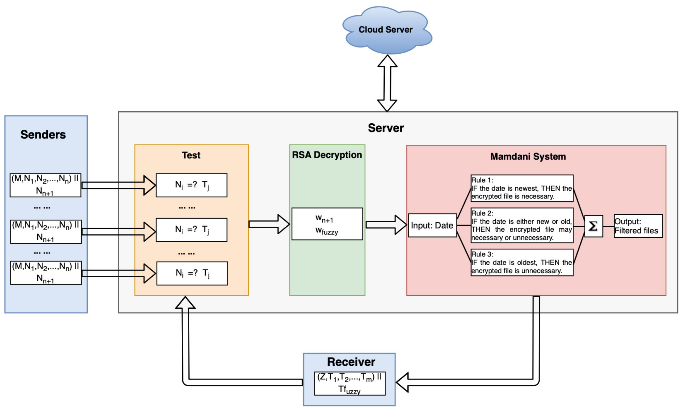
Cloud Server
Server
Senders
(M,N1,N2,...,Nn) II Nn+1
(M,N1,N2,...,Nn) II Nn+1
(M,N1,N2,...,Nn) II Nn+1
Test
Ni =? Tj
Ni =? Tj
Ni =? Tj
RSA Decryption
wn+1
wfuzzy
Mamdani System
Input: Date
Rule 1: IF the date is newest, THEN the encrypted file is necessary.
Rule 2: IF the date is either new or old, THEN the encrypted file may necessary or unnecessary.
Rule 3: IF the date is oldest, THEN the encrypted file is unnecessary.
Σ
Output: Filtered files
Receiver
(Z,T1,T2,...,Tm) II Tfuzzy

Fig. 1. The concrete construction of m-PEMKS

Without loss of generality, suppose w_{fuzzy} is the keyword "latest" while w_{n+1} stands for a set of "DATE". Therefore, three rules can be defined in the following:
Rule1: IF DATE is oldest, THEN the encrypted file is unnecessary.
Rule2: IF DATE is newest, THEN the encrypted file is necessary.
Rule3: IF DATE is either new or old, THEN the encrypted file may necessary or may unnecessary.

3.3 The Correctness of m-PEMKS

For Exact Match: for $i \in \{1, 2, ..., n\}$ and $j \in \{1, 2, ..., m\}$, the proposed scheme is completely correct in the following:
Firstly,
$T_{w_j} = T_j \oplus Z \bullet e(aB, C) = cH(w_j^*) \oplus e(A, B)^{t^*+c} \oplus e(A, t^*B) \bullet e(aB, cP) = cH(w_j^*) \oplus e(A, B)^{t^*+c} \oplus e(A, B)^{t^*} \bullet e(A, B)^c = cH(w_j^*) \oplus e(A, B)^{t^*+c} \oplus e(A, B)^{t^*+c} = cH(w_j^*)$
Then,
$H^*[e(T_{w_j}, \frac{M}{a})] = H^*[e(cH(w_j^*), \frac{tA}{a})] = H^*[e(cH(w_j^*), tP)] = H^*[e(H(w_j^*), C)^t] = N_i$

For Fuzzy Match: this algorithm is still correct due to the properties of Mamdani Fuzzy Inference System.

3.4 The Security Analysis of m-PEMKS

The proposed scheme contains two cryptographic algorithms: PEKS and RSA. The security of proposed scheme mainly relies on Ciphertext Indistinguishability of Chosen Plaintext Attack (IND-CPA) and Trapdoor Indistinguishability of Chosen Plaintext Attack (Trapdoor-IND-CPA).

IND-CPA security is that a malicious server (**Game1**) could not decide which PEMKS ciphertext contains which encrypted keyword, if it has not received the Trapdoor containing the given keyword. Besides, if a malicious receiver (**Game2**) that has not obtained the server's PEMKS private key cannot check whether PEMKS ciphertext and Trapdoor have the same keyword, even if he/she intercepts all Trapdoors for any specific keyword. For **Trapdoor-IND-CPA** security, it is an outside attacker excluding the server and the receiver (**Game3**) cannot differentiate any difference between Trapdoors containing the same keyword. To conclude, the proposed scheme satisfies Ciphertext Indistinguishability and Trapdoor Indistinguishability against a Chosen Plaintext Attack (CPA).

Theorem 1. The m-PEMKS above is IND-CPA secure against CPA in Game1 under the random oracle model assuming that BDH assumption is intractable.

Game 1: **A** is supposed to be a malicious server.

Proof: Suppose that **E** has $(g, p, G_1, G_T, e, xg, yg, zg)$ as an input of BDH assumption whose running time is bounded by T. **E**'s aim is to calculate a BDH key $e(g,g)^{xyz}$ of xg, yg and zg using **A**'s IND-CPA. Besides, **A** asks for at most h and h^* times for the queries of H and H^* hash functions.

Setup Simulation
E firstly sets $C = xg$ and randomly selects $a \in Z_p$ and then calculates $A = ag$. **E** also picks up $B \in G_1$ uniformly at random. After that, **A** obtains the common parameter $(g, p, G_1, G_T, e, H, H^*)$, the server's PEMKS public key (cp, A, B) and PEMKS private key (cp, a) and the receiver's PEMKS public key (cp, C). Besides, **E** chooses two hash functions H and H^* in the following:

– **A** can query a keyword w_i to H function at any time. To respond, **E** searches *H_List* for a tuple $(w_i, F_i, f_i, \theta_i)$ and the *H_List* is empty in original. If the tuple exists, **A** will receive $H(w_i) = F_i$ as a response. Otherwise, **E** does the following steps:

i. **E** picks up a coin θ_i uniformly at random and then calculates $Pr[\theta_i = 0] = \frac{1}{h+1}$.
ii. **E** selects $f_i \in Z_p$ uniformly at random. If $\theta_i = 0$, **E** will calculate $F_i = yg + f_i g$. If $\theta_i = 1$, **E** will calculate $F_i = f_i g$.
iii. **E** returns F_i as an answer to **A** and adds $(w_i, F_i, f_i, \theta_i)$ into *H_List*.

– **A** queries D_i to H^* function at any time. Then, **E** searches *H^*_List* for a tuple (D_i, N_i). If the tuple exists, **A** will receive N_i as a response. Otherwise, **E** selects $N_i \in \{0,1\}^\bullet$ uniformly at random and then returns it to **A** and also adds (D_i, N_i) into *H^*_List*.

Phase 1–1 Simulation (Trapdoor queries)
A issues a query for the trapdoor corresponding to the keyword-vector $W_l = (w^*_{l1}, w^*_{l2}, ..., w^*_{lm})$. To respond, **E** executes the following steps:

– **E** randomly selects $i' \in \{1, 2, ..., m\}$
– **E** runs the above algorithms for simulating H function to create a tuple $(w_{li'}, F_{li'}, f_{li'}, \theta_{li'})$. If $\theta_{li'} = 0$, **E** will output "Suspend" and terminate the system. Otherwise, **E** conducts the following:

• **E** selects $t^* \in Z_p$ and then computes $T_1 = f_{l1}C \oplus e(A,B)^{t^*+x} = f_{l1}xg \oplus e(A,B)^{t^*+x} = xF_{l1} \oplus e(A,B)^{t^*+x} = xH(w_{l1}) \oplus e(A,B)^{t^*+x}$, $T_2 = xH(w_{l2}) \oplus e(A,B)^{t^*+x}$,...,$T_m = xH(w_{lm})$ and $Z = e(A, t^*B)$. Therefore, $T_W = (Z, T_1, T_2, ..., T_m)$.

Challenge Simulation
A sends $W_0 = (w_{01}, w_{02}, ..., w_{0n})$ and $W_1 = (w_{11}, w_{12}, ..., w_{1n})$ to **E**. Once **E** receives the target keyword-vector pair, he/she does the following:

- **E** randomly selects $i \in \{1, 2, ..., n\}$.
- **E** runs the above algorithms for simulating H function to obtain two vectors of tuples $(W^*_{0i}, F^*_{0i}, f^*_{0i}, \theta^*_{0i})$ and $(W^*_{1i}, F^*_{1i}, f^*_{1i}, \theta^*_{1i})$. If θ^*_{0i} and θ^*_{1i} are equal to 1, **E** will output "Suspend" and terminate the system. Otherwise, **E** runs the above algorithms for simulating H function at $2(n-1)$ times to obtain two vectors of tuples $((w^*_{01}, F^*_{01}, f^*_{01}, \theta^*_{01}), ..., (w^*_{0i-1}, F^*_{0i-1}, f^*_{0i-1}, \theta^*_{0i-1}), (w^*_{0i+1}, F^*_{0i+1}, f^*_{0i+1}, \theta^*_{0i+1}), ..., (w^*_{0n}, F^*_{0n}, f^*_{0n}, \theta^*_{0n}))$ and $((w^*_{11}, F^*_{11}, f^*_{11}, \theta^*_{11}), ..., (w^*_{1i-1}, F^*_{1i-1}, f^*_{1i-1}, \theta^*_{1i-1}), (w^*_{1i+1}, F^*_{1i+1}, f^*_{1i+1}, \theta^*_{1i+1}), ..., (w^*_{1n}, F^*_{1n}, f^*_{1n}, \theta^*_{1n}))$. If θ^*_{0i} and θ^*_{1i} are equal to 0 for all $i = 0, ..., i-1, i+1, ..., n$, **E** will output "Suspend" and terminate the system. Otherwise, **E** does the following:
- **E** chooses $\beta \in \{0, 1\}$ uniformly at random.
- **E** chooses $N_i \in \{0, 1\}^\bullet$ uniformly at random and creates a target SCF-PEMKS

Ciphertext $S^* = (M^*, N^*_1, N^*_2, ..., N^*_n) = (zA, H^*[J_1], H^*[J_2], ..., H^*[J_n])$ So, $S^* = (M^*, N^*_1, ..., N^*_{i-1}, N^*_{i+1}, ..., N^*_n) = (zA, H^*[e(H(w_{\beta_1}), C)^z], ..., H^*[e(H(w_{\beta_{i-1}}), C)^z], H^*[e(H(w_{\beta_1+1}), C)^z], ..., H^*[e(H(w_{\beta_n}), C)^z])$
Note that $J_i = e(H(w_{\beta_i}), C)^z = e(yg + f_{\beta_i}g, xg)^z = e(yg, xg)^z \bullet e(f_{\beta_i}g, xg)^z = e(g, g)^{xyz} \bullet e(zg, xg)^{f_{\beta i}}$
Note also that $e(f_{\gamma_i}g, xg)^z = e(f_{\gamma_i}g, C)^z = e(H(w_{\gamma_i}), C)^z$

Phase 1–2 Simulation (Trapdoor queries)
A can continue to ask **E** for Trapdoor queries for the keyword-vector W_i. **E** answers to **A** as in Phase 1–1, as long as $w_i \notin W_0, W_1$.
Guess
A outputs the guess $\beta^* \in \{0, 1\}$. Then, **E** selects d in the list for H^* function and returns $\frac{d_{\beta^*_i}}{e(zg,xg)^{f_{\beta^*_i}}}$ as its guess for BDH key.

Analysis of Game 1. Let *Event1* and *Event2* be events that **E** does not suspend during Phase 1–1 and Phase 1–2 (Trapdoor queries) and **E** does not suspend during Challenge Simulation respectively. Therefore, the probability of *Event1* happening is at least $[(1-\frac{1}{h+1})^m]^h \geq \frac{1}{e^m}$. Besides, the probability of *Event2* happening is at least $(1-\frac{1}{h+1})^{2(n-1)}\{1-(1-\frac{1}{h+1})^2\} \geq (\frac{1}{h+1}) \bullet (\frac{h}{h+1})^{2(n-1)}$. In addition, let $Hybrid_r$ for $r \in \{1, 2, ..., n\}$ be an *event* that the attacker **A** can successfully guess the keyword of the left part of a "hybrid" PEMKS Ciphertext formed with r, coordinates from W_β followed by $(n-r)$ coordinates from $W_{1-\beta}$. Consequently, $Pr[Event3] = 2\Sigma^n_{k=1}(Pr[Hybrid_r] - Pr[Hybrid_{r-1}]) = 2(Pr[Hybrid_r] - Pr[Hybrid_0]) = 2\varepsilon$. However, the probability that **A** requests a query for either $H^*(e(H(W^*_{0i}), C)^z)$ or $H^*(e(H(W^*_{1i}), C)^z)$ is at least 2ε, so the probability that **A** issues a query for $H^*(e(H(W^*_i), C)^z)$ is at least ε. In total, **E**'s success probability ε^* is $(\frac{h}{h+1})^{2(n-1)} \bullet \frac{\varepsilon}{e^m(h+1)h^*}$, which is negligible.

Theorem 2. The m-PEMKS above is IND-CPA secure against CPA in Game2 under the random oracle model assuming that 1-BDHI assumption is intractable.

Game 2: **A** is supposed to be a malicious receiver.

Proof: Suppose that **E** has (g, p, G_1, G_T, e, xg) as an input of 1-BDHI assumption whose running time is bounded by T. **E**'s aim is to calculate a 1-BDHI key $e(g,g)^{\frac{1}{x}}$ of xg using **A**'s IND-CPA. Besides, **A** asks for at most h and h^* times for the queries of H and H^* hash functions.

Setup Simulation
E firstly sets $A = xg$ and $B \in G_1$. **E** also selects $c \in Z_p$ uniformly at random and calculates $C = cP$. Then, **A** obtains the common parameter $(g, p, G_1, G_T, e, H, H^*)$, the server's PEMKS public key (cp, A, B), the receiver's PEMKS public key (cp, C) and PEMKS private key (cp, c). Besides, **E** chooses two hash functions H and H^* in the following:

- **A** can query a keyword w_i to H function at any time. To respond, **E** selects $f_i \in Z_p$ uniformly at random and then calculates $F_i = f_i g$ and finally returns F_i as a response to **A**.
- **A** can query D_i to H^* function at any time. Then, **E** searches *H^*_List* for a tuple (D_i, N_i). If the tuple exists, **A** will receive N_i as a response. Otherwise, **E** selects $N_i \in \{0,1\}^\bullet$ uniformly at random and then sends it to **A**. **E** also adds (D_i, N_i) into *H^*_List*.

Challenge Simulation
A sends $(W_{0i}^*, F_{0i}^*, f_{0i}^*, \theta_{0i}^*)$ and $(W_{1i}^*, F_{1i}^*, f_{1i}^*, \theta_{1i}^*)$ to **E**, where $W_0^* = (w_{01}, w_{02}, ..., w_{0n})$ and $W_1^* = (w_{11}, w_{12}, ..., w_{1n})$. **E** randomly chooses $\beta \in \{0,1\}$ and $N_i \in \{0,1\}^\bullet$. Then, **E** creates a target PEMKS Ciphertext $S^* = (M^*, N_1^*, N_2^*, ..., N_n^*) = (\psi xg, H^*[J_1], H^*[J_2], ..., H^*[J_n])$
So, $S^* = (M^*, N_1^*, N_2^*, ..., N_n^*) = (\psi xg, H^*(e(H(w_{\beta_1}), C)^\psi), H^*(e(H(w_{\beta_2}), C)^\psi), ..., H^*(e(H(w_{\beta_n}), C)^\psi))$
Notice that $e(H(w_{\beta_i^*}), C)^\psi) = e(f_i g, cg)^\psi = e(g,g)^{\psi \cdot f_i c}$.

Guess
A outputs the guess $\beta^* \in \{0,1\}$. Then, **E** returns $\psi = \frac{1}{x \cdot f_i c}$ as the guess for 1-BDHI key.

Analysis of Game 2. Let *Event4* and *Event5* be events that **E** does not suspend during Challenge Simulation and **A** does not issue a query for either one of $H^*(e(H(W_{0i}^*), C)^\psi)$ or $H^*(e(H(W_{1i}^*), C)^\psi)$ respectively. So, the probability of *Event4* happening is equal to 1. Besides, according to Bayes's rule and the definition above, the probability of *Event5* happening is at least 2ε and therefore, the probability that **A** issues a query for $H^*(e(H(W_i^*), C)^\psi)$ is at least ε. Therefore, $e(H(W_j^*), C)^\psi = e(g,g)^{\psi \cdot f_i c}$ will appear in H*_List. Due to **A** asks for at most h^* times H^* hash function queries, the probability that **E** selects the correct answer is at least $\frac{1}{h^*}$. In total, E's success probability ε^* is $\frac{\varepsilon}{h^*}$, which is negligible.

Theorem 3. The m-PEMKS above is Trapdoor-IND-CPA secure against CPA in Game3 under the random oracle model assuming that BDH assumption is intractable.

Game 3: **A** is supposed to be an outside attacker excluding the server and the receiver.

Proof: Suppose that **E** has $(g, p, G_1, G_T, e, xg, yg, zg)$ as an input of BDH assumption whose running time is bounded by T. **E**'s aim is to calculate a BDH key $e(g,g)^{xyz}$ of xg, yg and zg using **A**'s Trapdoor-IND-CPA. Besides, **A** asks for at most h and h^* times for the queries of H and H^* hash functions.

Setup Simulation
E firstly sets $A = xg, B = yg$, $C = zg$ and returns (cp, A, B) as the server's PEMKS public key and (cp, C) as the receiver's PEMKS public key. **E** also chooses two H and H^* hash functions at random.
Phase 3–1 Simulation (Trapdoor queries)
A issues a query for the trapdoor corresponding the keyword-vector W_i, where $i \in \{1, 2, ..., m\}$. To respond, **E** chooses $t^* \in Z_p$ uniformly at random. Then, **E** computes $T_1 = zH(w_{i1}) \oplus e(yg, xg)^{t^*+z}, T_2 = zH(w_{i2}) \oplus e(yg, xg)^{t^*+z}, ..., T_m = zH(w_{im}) \oplus e(yg, xg)^{t^*+z}$ and $Z = e(t^* yg, xg)$. So $T_W = (Z, T_1, T_2, ..., T_m)$. Finally, **E** returns T_W to **A**.
Challenge Simulation
A sends (W_0^*, W_1^*) to **E**, where $W_0^* = (w_{01}, w_{02}, ..., w_{0m})$, $W_1^* = (w_{11}, w_{12}, ..., w_{1m})$. **E** creates the challenge Trapdoor request as follows:
E randomly selects a bit $\beta \in \{0, 1\}$. Therefore, $T_1 = zH(w_{\beta_1^*}) \oplus e(yg, xg)^{t^*+z} = zH(w_{\beta_1^*}) \oplus e(g,g)^{xyz} \bullet e(g,g)^{xyt^*}, T_2 = zH(w_{\beta_2^*}) \oplus e(g,g)^{xyz} \bullet e(g,g)^{xyt^*}, ..., T_m = zH(w_{\beta_m^*}) \oplus e(g,g)^{xyz} \bullet e(g,g)^{xyt^*}$, $R = e(t^* yg, xg)$.
Phase 3–2 Simulation (Trapdoor queries)
A can continue to ask Trapdoor queries for the keyword-vector W_i. While, **E** answers to **A** as in Phase 3–1, as long as $W_i \neq W_0, W_1$.
Guess
A outputs the guess $\beta^* \in \{0, 1\}$. If $\beta = \beta^*$, **E** outputs "yes", otherwise, **E** outputs "no".

Analysis of Game 3. Due to **A** is a malicious outside attacker, he/she cannot distinguish any difference between two Trapdoors even though these two Trapdoors have the same keyword. The reason is that **E** randomly chooses $t^* \in Z_p$ and t^* changes every time leading to $T_i = cH(w_{\beta i}) \oplus e(A, B)^{t^*+c}$ changes every time. Even if two Trapdoors have the same keyword, the results are still different because of t^*. Therefore, the key part of Trapdoor Indistinguishability in this proposed scheme is the confidentiality of $e(A, B)^{t^*+c}$.

Suppose the attacker **A** obtains the value of $e(A, B)^{t^*+c}$, he/she can distinguish whether two Trapdoors have the same keyword. The reason is that the attacker **A** only calculates one extra XOR operation as $T_i = cH(w_{\beta i}) \oplus e(A, B)^{t^*+c} \oplus e(A, B)^{t^*+c} = cH(w_{\beta i})$. Therefore, the attack **A** can distinguish that $T_{w_{0i}} = cH(w_{0i})$ and $T_{w_{1i}} = cH(w_{1i})$ are equal as long as $w_{0i} = w_{1i}$. Consequently, the attack A could distinguish two Trapdoors T_{W_0} and T_{W_1}. However, according to Challenge Simulation in Game3, it is easy to acquire $e(A, B)^{t^*+c} = e(g,g)^{xyz} \bullet e(g,g)^{xyt^*}$, which satisfies BDH assumption. Hence, the attacker **A** cannot calculate the value of $e(A,B)^{t^*+c}$ and therefore, it cannot compute $T_i = cH(w_{\beta i}) \oplus e(A,B)^{t^*+c}$.

4 The Performance of m-PEMKS

The proposed system is implemented by JAVA, which requires two libraries in the following: JPBC library [14] and jFuzzyLogic library [15,16].

The proposed scheme applies the Single Input Single Output (SISO) Mamdani Fuzzy Inference System. The is because of the properties of Artificial Intelligence and Cryptography. Artificial Intelligence explores and analyses the data for discovering the relationships between the different data sets. On the contrary, the purpose of cryptography is hiding as much as possible information. Besides, the input value of Mamdani system is plaintext. Therefore, if m-PEMKS applies Two or More Input Single Out (T/MISO) Mamdani Fuzzy Inference System, sufficient data will be exposed to the public networks and therefore, crackers are able to launch attacks to recover more information. Figure 2 shows the membership functions for an example of searching "latest" financial reports and Fig. 3 shows the assessed value for each input. More specially, three senders upload the financial reports with different dates to the server by m-PEMKS system. Once the server receives them, it will run *Test* algorithm incorporating with SISO Mamdani Fuzzy Inference System to filter the "latest" reports. By Fig. 3, it can be seen that the first report partly belongs to the old and acceptable financial report while the second report belongs to the acceptable financial report. However, the third report completely belongs to the "latest" financial report.

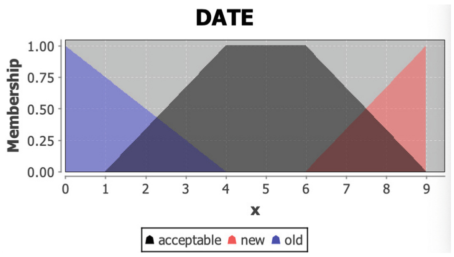

Fig. 2. Membership functions for an example of searching "latest" financial reports

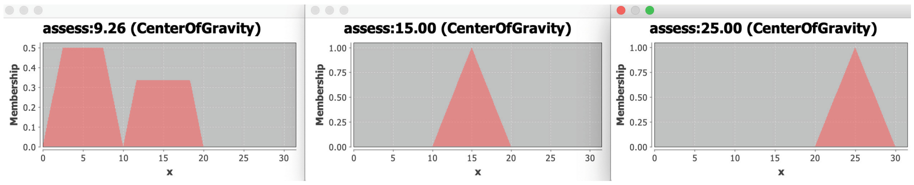

Fig. 3. Assessed values for an example of searching "latest" financial reports

5 Conclusion

In this paper, a novel and a robust *Public Key Encryption with Multiple Keywords Search using Mamdani System(m-PEMKS)* scheme is presented. The new scheme is proved to be semantic secure in the random oracle models under BDH and 1-BDHI assumptions and also satisfies the properties of Ciphertext Indistinguishability and Trapdoor Indistinguishability and therefore, it is able to resist Off-line Keyword Guessing Attack. Furthermore, Single Input Single Output Mamdani technique is applied to m-PEMKS so that it has the ability to solve fuzzy and imprecise keywords, such as "latest" and "tallest", etc., as described in the paper.

References

1. Boneh, D., Di Crescenzo, G., Ostrovsky, R., Persiano, G.: Public key encryption with keyword search. In: Advances in Cryptology - EUROCRYPT, pp. 506–522 (2004)
2. Baek, J., Safavi-Naini, R., Susilo, W.: Public key encryption with keyword search revisited. In: Computational Science and its Applications? ICCSA 2008, pp. 1249–1259 (2008)
3. Byun, J., Rhee, H., Park, H., Lee, D.: Off-line keyword guessing attacks on recent keyword search schemes over encrypted data. Lecture Notes in Computer Science, pp. 75–83 (2006)
4. Yau, W., Heng, S., Goi, B.: Off-line keyword guessing attacks on recent public key encryption with keyword search schemes. Lecture Notes in Computer Science, pp. 100–105 (2008)
5. Tang, Q., Chen, L.: Public-key encryption with registered keyword search. In: Public Key Infrastructures, Services and Applications, pp. 163–178 (2010)
6. Rhee, H., Park, J., Susilo, W., Lee, D.: Trapdoor security in a searchable public-key encryption scheme with a designated tester. J. Syst. Softw. **83**(5), 763–771 (2010)
7. Wang, T., Au, M., Wu, W.: An efficient secure channel free searchable encryption scheme with multiple keywords. In: Network and System Security, vol. 9955, pp. 251–265 (2016)
8. Zadeh, L.: Outline of a new approach to the analysis of complex systems and decision processes. IEEE Trans. Syst. Man Cybern SMC **3**(1), 28–44 (1973)
9. Mamdani, E.H., Assilian, S.: An experiment in linguistic synthesis with a fuzzy logic controller. Int. J. Man-Mach. Stud. **7**(1), 1–13 (1975)
10. Takagi, T., Sugeno, M.: Fuzzy identification of systems and its applications to modeling and control. IEEE Trans. Syst. Man Cybern. **15**, 116–132 (1985)
11. Singh, J., Singh, N., Sharma, J.K.: Fuzzy modeling and identification of intelligent control for refrigeration compressor. J. Sci. Ind. Res. **65**, 22–30 (2006)
12. Lermontov, A., Yokoyama, L., Lermontov, M., Machado, M.A.S.: River quality analysis using fuzzy water quality index: Ribeira do Iguape river watershed, Brazil. Ecol. Indic. **9**, 1188–1197 (2009)
13. Marchini, A., Facchinetti, T., Mistri, M.: F-IND: a framework to design fuzzy indices of environmental conditions. Ecol. Indic. **9**, 485–496 (2009)
14. De Caro, A., Iovino, V.: JPBC: Java pairing based cryptography. In: 2011 IEEE Symposium on Computers and Communications (ISCC) (2011)

15. Cingolani, P., Alcalá-Fdez, J.: jFuzzyLogic: a Java library to design fuzzy logic controllers according to the standard for fuzzy control programming. Int. J. Comput. Intell. Syst. **6**(Supplement 1), 61–75 (2013)
16. Cingolani, P., Alcala-Fdez, J.: jFuzzyLogic: a robust and flexible Fuzzy-Logic inference system language implementation. In: 2012 IEEE International Conference on Fuzzy Systems (FUZZ-IEEE). IEEE (2012)

Personal Car Driver Black Box: A Wearable System for Data Log and Prediction Based on EVOS Paradigms

Mario Malcangi(✉)

Computer Science Department, Università degli Studi di Milano, Milan, Italy
malcangi@di.unimi.it

Abstract. Car driver's performance is affected by physiologic behavior, causing automotive accidents. A system that predicts incoming behaviors is proposed considering vital signs as data to infer by Evolving Systems (EVOS) paradigms and several behaviors as prediction targets. A black-box like approach is proposed. It implements data loging of the vital signs and it applies an evolving prediction paradigm. Long term data log enables post-event analysis and data set building for supervised learning for the prediction paradigms.

Keywords: EFuNN · Behavior's onset · Wearable systems · EVOS · Car driver's performance · Vital signs

1 Introduction

Several physiologic behaviors affect the car driver's performance and are the cause of automotive accidents: drosiness, fatigue, alcohol abuse, drug abuse, hyperarousal. [1]. The main investigation topic has concerned sleep onset prediction [2, 3], but effective solutions to this issue need to consider all the physiologic behavior and the vital signs that concur to affect the car driver's performance. Heart rate (HR) and its variability (HRV) are the primary vital signs correlated to driver behavior because they are under the control of the Autonomic Nervous System (ANS) that consists of two main divisions: the sympathetic (SNS) and the parasympathetic (PNS).

PNS controls the homeostasis and body's rest-and-digest response. SNS controls the body's fight-or-flight response. SNS and PNS execute antagonist control of body's functions: e.g. PNS decreases the HR and SNS increases HR. That is, when a subject is falling asleep or relaxed PNS is active and SNS is inactive, when the subject is awake or fatigued SNS is active and PNS is inactive [2, 3].

Because HR and HRV reflects the ANS activity, by measuring the HR and HRV vital signs is possible to know which one, PNS or SNS, is active, that is, if the subject is asleep or awake (fatigued or relaxed). The transition between PNS and SNS activity is when happens the behavior onset. The switching between PNS and SNS activity could be detected measuring the power spectrum density (PSD) of the HRV time-series sequences: SNS modulates HRV's low frequencies (0.04–0.15 Hz) and PNS modulates HRV's high frequencies (0.18–0.4 Hz) [6].

ANS also controls other physiologic body functions, such as respiration, contraction of muscles, release of adrenaline so that other vital signs could be measured to predict the subject's physiologic behavior: e.g. bio-impedance, temperature, muscle's activity. Measuring vital signs and executing prediction on such measurements can lead to develop a system that predicts subject's behavior and do him aware about incoming unwanted physiologic status such as sleep onset or loss of attention when he is involved in critical activities (e.g. car driving).

A variety of technologies have been investigated to the purpose of maintaining alertness in car driving activity, most of them with limited success [4]. A popular approach to the issue consists in measuring and predicting from movements mainly related to arms (actigraphy) [5]. This is hardcomputing-based and do not measure other physiologic parameters.

In our investigation we had an holistic approach combining the measurement of most of the vital signs in a softcomputing-based paradigm for prediction in evolving mode and online.

1.1 EVOS Paradigms

Prediction from physical data like vital signs is a challenge because the fuzzy nature of such data. Evolving brain-inspired paradigms demonstrated to perform well when applied to real data [7]. Best performing and optimal paradigms are the Evolving Fuzzy Neural Networks (EFuNNs) and Evolving Spiking Neural Networks (ESNNs).

EFuNN [8] is an implementation of the Evolving Connectionist Systems (ECOSs), a class of neural networks that combine the adaptive/evolving learning capability of neural networks with the approximate reasoning and linguistic feature representation of fuzzy logic.

ECOSs, because based on local learning, is characterized by:

- Fast learning
- Real-time adaptation
- Evolving
- Spatio-temporal representation.

These peculiarities fits well the wearable system-oriented applications.

ESNNs are further development of ECOSs where the neuron's model is the biological neuron and its synapses, the spiking neuron [9]. This assumes that the information is represented as trains of spikes over time. The spiking neuron accumulates input information (spikes) and emits at its axon a spike when a threshold exceeded.

ESNNs are brain-inspired neural networks that are characterized by:

- Fast learning
- Real-time adaptation
- Evolving
- Spatio-temporal representation.

These fits well the requirements of the wearable system-oriented applications.

1.2 Wearable Technologies and Vital Signs Measurements

Vital signs measurement when became common practice as uninvasive wearable technology was released by electronic industries [10]. After a first generation of wearable electronics was released for sport performance monitoring (chest belts), a second generation made available wrist wearable (watch-like) and finger wearable sensors-based on photodetecting technology that enabled the deployment of uninvasive applications in medical and consumer fields [11].

Photodetector sensing is an optimal alternative to electrodes-based bioelectric measurements (ECG). Photodetectors are a Light Emitting Diodes (LEDs) technology combined with PhotoDiode (PD) technology that enable to record the Heart Rate (HR) by the PhotoPlethysmoGram (PPG). PPG method is uninvasive and reliable because the sensor don't require electrical coupling with the person's body (skin) requiring the application of conductive gel or pasta for optimal conductivity.

Another important wearable technology advancement was been the AnalogFront-End (AFE) deployment on a Chip Scale Package (CSP), a less than 1 mm $\times$ 1 mm $\times$ 0.1 mm thin package developed by Analog Devices Inc. (ADI), and CSP deployment of a 32-bit microcomputer developed by (Freescale, NXP). These technologies enable complex tasks such as ultra-small and noisy signal amplification and processing with very low-power consumption (nanoWatt).

The availability of RadioFrequency (RF) communication such as a sub-1 GHz RF Transceiver ultra-low power (under 10 nA), CSP packaged, developed by Microsemi Corp. completed the wearable technology's mosaic.

The last step in this wearable technology innovation was system integration in System-on-Chip (SoC) scale devices that deploy all the required technologies (sensing, signal processing, communication) in a small device that can be hosted in a small wearable case like a watch or a bracelet [12].

Bluetooth Low Energy (BLE) was also available at very small integration scale and available for the development of the personal wireless area network and targeted to wearable device's connectivity in medical and fitness applications.

2 System Framework

The proposed Personal Car Driver Black Box is a wearable system consisting of an analog subsystem (sensors and amplifiers), of a mixed-signal subsystem (Analog to Digital Converters (ADCs)) and of a digital subsystem (Microcontroller Unit (MCU), an embedded memory (eM), a wireless communication) (Fig. 1).

The analog subsystem consists of a set of uninvasive sensors such as metal surface contact electrodes, photosensors, thermistor, inertial sensors (accelerometer, gyroscope), connected to an analog-front-end (AFE) for signal conditioning (amplification, filtering, impedance adaptation).

The vital signs captured and conditioned by the analog subsystem are then applied to the mixed-signal subsystem (ADC) to be sampled and quantized as data streams.

The data streams are processed by the digital subsystem that runs the learning and prediction paradigm, and are stored on a nonvolatile memory (NVM).

All the subsystems consist of state of the art wearable ultra-embedded microelectronics (ultra-low power, ultra-small, ultra-low cost). All the electronics is packaged in a watch-like case, so the noninvasiveness's requirement was accomplished.

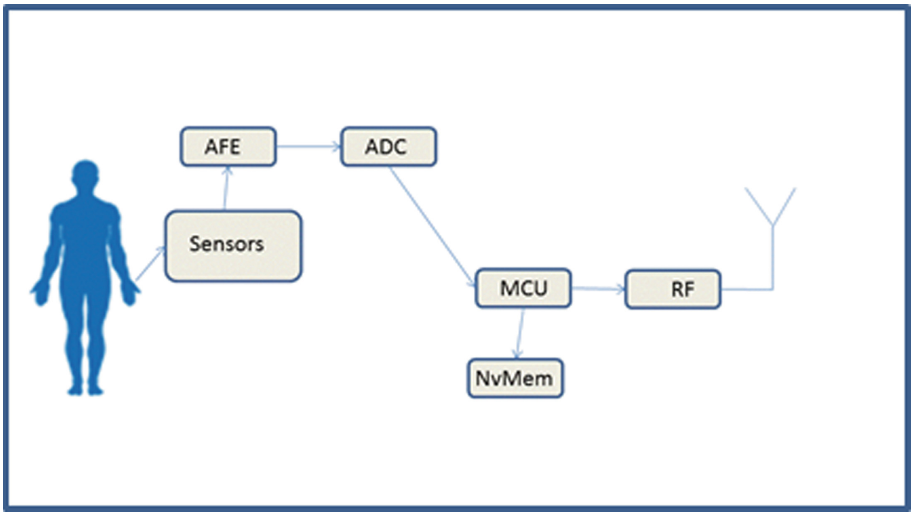

Fig. 1. Personal Car Driver Black Box system architecture

3 Prediction Paradigm

The reference prediction paradigm is the Evolving Fuzzy Neural Network (EFuNN). EFuNN's peculiarities such as adaptability to new data of unknown distribution, avoiding of catastrophic forgetting, fast adaptation (one step-learning), linguistically meaningful information representation and online learning concur to accomplish the prediction requirements for a personal behavior prediction system based on vital signs measurements.

EFuNN is a predictive paradigm that belongs to the Evolving Connectionist Systems (ECOSs), a class of modular connectionist-based systems that evolve continuously their structure and functionality, self-organizing, adapting interactively from incoming data.

EFuNN is a five layers Feed-Forward Artificial Neural Network (ANN) (Fig. 2) that implements fuzzy rules and a fuzzy logic inference engine in connectionist mode by four layer of connections. This architecture enables the EFuNN to infer by rules and to learn by data.

The first layer inputs the crisp data. The second layer encodes the membership functions that fuzzify the crisp data from the first layer. The third layer encodes the fuzzy rules that connect the inputs to the outputs. The fourth layer implements the defuzzification of the output data. The fifth layer is the final output (crisp) (Fig. 2).

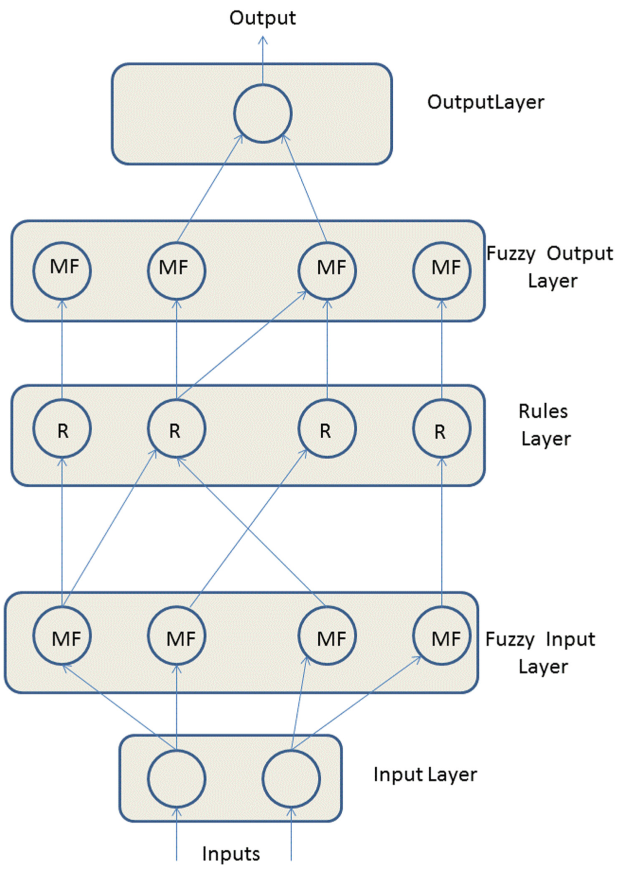

Fig. 2. EFuNN five layers feed forward ANN architecture.

4 Data Set

To train and test the EFuNN a dataset was collected by sensors data measuring vital signs (Heart rate, movements). The dataset consists of values of heart rate and movement at time (t − n) as input variables, with the fatigue level at the moment (t) as an output variable (label).

To train and test the EFuNN the simulation environment NEUCOM [13] was been used that requires a set of patterns of labeled data such as:

H_1 M_1 H_2 M_2 H_3 M_3 H_4 M_4 H_5 M_5 H_6 M_6 … H_j M_j … H_N M_N L_n
H_j : i-th amplitude of the i-th sample of the n-th HR measure
M_j : j-th amplitude of the j-th sample of the n-th Movement measure
L_n : n-th label associated to the n-th sequence.

The dataset was built by collecting the HR and movement measurements of a driver, labeling two fatigue behavioral conditions: (low, severe) (Fig. 3) [14].

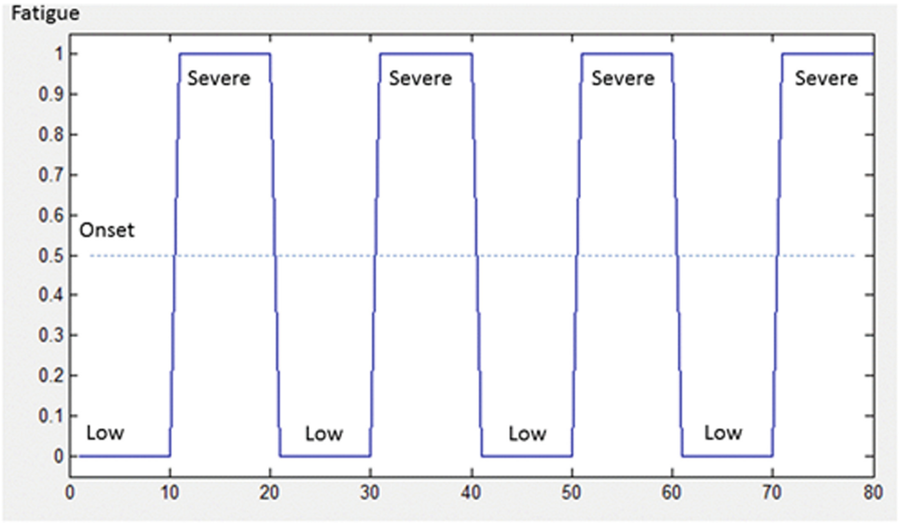

Fig. 3. Dataset to train and test the EFuNN's prediction paradigm.

5 Training and Test

To train the EFuNN the fatigue dataset was been applied to the NEUCOM simulation environment by splitting randomly it in two sub-datasets (80% for training purpose, 20% for test purpose) (Fig. 4).

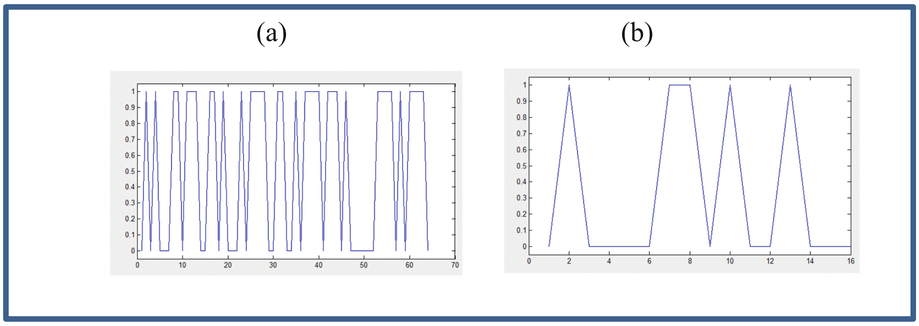

Fig. 4. Dataset to train and test the EFuNN's prediction paradigm. (a) Train: random split (80%), (b) Test: random split (20%).

After training the EFuNN's setup is as follow with three membership functions (triangular):

Sensitivity Threshold: 0.9
Error Threshold: 0.1
Number of Membership Functions: 3

Learning rate for: W1: 0.1
Learning Rate for W2: 0.1
Pruning: On
Node age: 60
Aggregation: On

At the end of training a set of six rules resulted. Follows the Rule 4:

if
[Var 1] –> (MF 1) @ 0.000 & (MF 2) @ 0.091 & (MF 3) @ 0.909
[Var 2] –> (MF 1) @ 0.000 & (MF 2) @ 0.091 & (MF 3) @ 0.909
[Var 3] –> (MF 1) @ 0.000 & (MF 2) @ 0.100 & (MF 3) @ 0.900
[Var 4] –> (MF 1) @ 0.000 & (MF 2) @ 0.091 & (MF 3) @ 0.909
then Output for (MF 1) @ 0.000 Output for (MF 2) @ 0.091 Output for (MF 3) @ 0.909

After training was executed (Fig. 5) the prediction capabilities of the EFuNN was tested by 20% dataset (Fig. 6). The test confirmed the EFuNN capability to predict the fatigue onset from HR and movements measurements captured by the wearable device (Fig. 6 and Fig. 7).

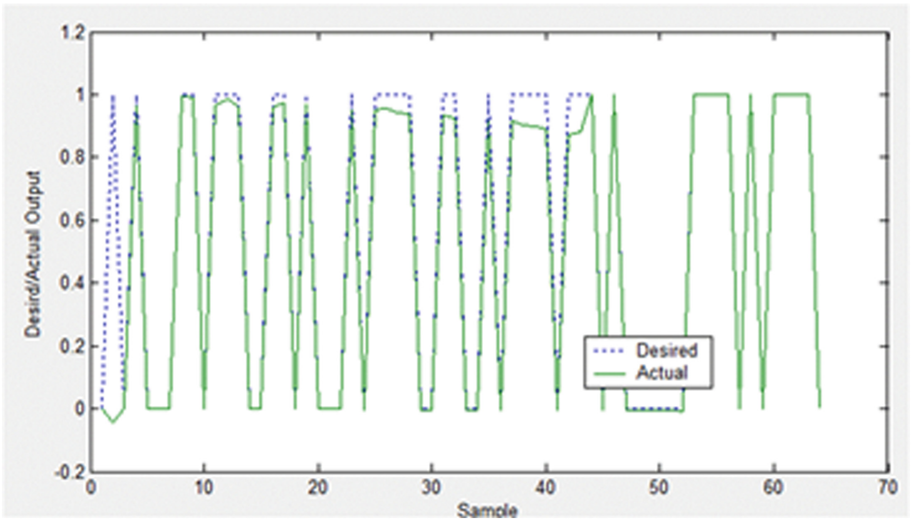

Fig. 5. EFuNN's train with the 80% random splitted dataset

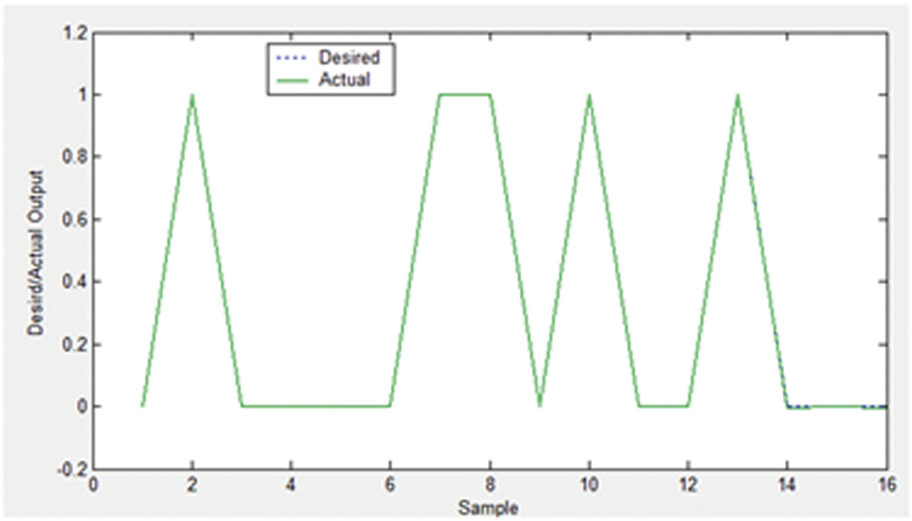

Fig. 6. EFuNN's test after test with 20% random splitted dataset.

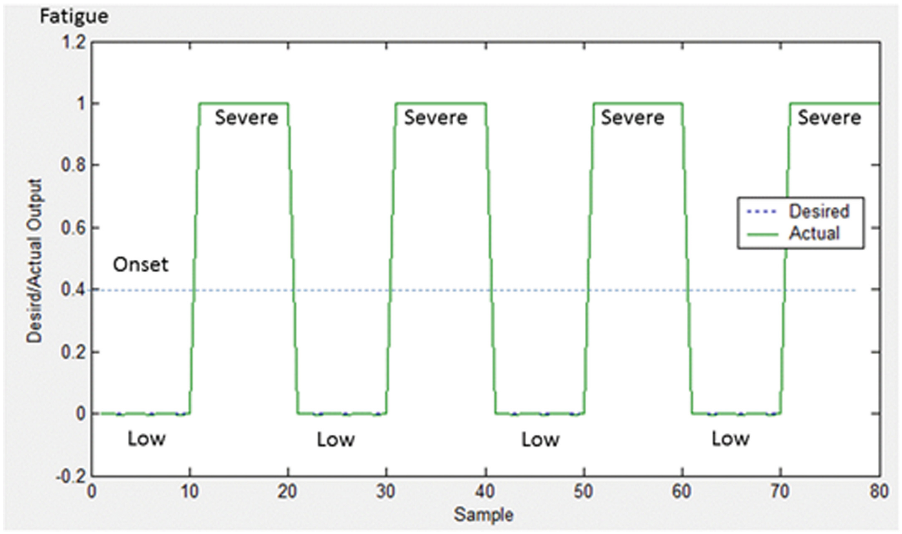

Fig. 7. EFuNN's after test with full dataset

6 Conclusion and Discussion

The modeling and the tests executed on different behavioral status of the car driver confirmed that the method could be applied to several risky behavioral condition to warn the driver about his ability to continue to drive (safe/risky). Because several vital signs measurements concur to assess the driver condition, a data fusion strategy need to be investigated, considering it one of the capabilities embedded in the EFuNN paradigm.

Another topic to be elaborated on is the continuous data gathering targeted to post event analysis and dataset building (black box mode).

References

1. NHTSA: Drowsy driving. Published by NHTSA's National Center for Statistics and Analysis. 1200 New Jersey Avenue SE, Washington, DC 20590 (2011)
2. Malcangi, M., Smirne, S.: Fuzzy-logic inference for early detection of sleep onset. Neural Comput. Appl. **27**, 41–50 (2015)
3. Dorfman, G.F., Baharav, A., Cahan, C., Akselrod, S.: Early detection of falling asleep at the wheel: a heart rate variability approach. Comput. Cardiol. **35**, 1109–1112 (2008)
4. Stutts, J.C.: Sleep Deprivation Countermeasures. National Academy Press, Wascinton D.C. (2000)
5. Straczkiewicz, M., Urbanek, J.K., Crainiceanu, C.M., Harezlak, J.: Automatic car driving detection using raw accelerometry data. Physiol. Meas. **37**(10), 1757–1769 (2016)
6. Quintana, S.D., Heathers, J.A.J.: Considerations in the assessment of heart rate variability in behavioral research. Front. Psychol. **5**, 805 (2014)
7. Malcangi, M.: Applying evolutionary methods for early prediction of sleep onset. Neural Comput. Appl. **27**, 1165–1173 (2016). https://doi.org/10.1007/s00521-015-1928-6
8. Kasabov, N.: Evolving fuzzy neural network – algorithms, applications and biological motivation. In: Yamakawa, T., Matsumoto, G. (eds.) Methodologies for Conception, Design and Application of the Soft Computing. World Computing, pp. 271–274 (1998)
9. Kasabov, N.: Time-Space, Spiking Neural Networks and Brain-Inspired Artificial Intelligence. Springer Series on Neurosystems. Springer, Berlin (2019)
10. Broeders, J.H.: Wearable electronic devices monitor vital signs activity level and more. Analog Dialog (December 2014)
11. Palhmi, J., Broeders, J.H.: Optical integration without compromises (1995). https://www.analog.com/en/technical-articles/optical-integration-without-compromises.html
12. Broeders, J.H.: The sensors behind the GEN II wearable device, Technical Article, https://www.analog.com/media/en/technical-documentation/tech-articles/the-sensors-behind-the-GEN-II-wearable-device.pdf
13. https://Kedri.aut.nz/areas-of-expertise/data-mining-and-support/neucom
14. Sahayadhas, A., Sundaraj, K., Murugappan, M.: Detecting driver drowsiness based on sensors: a review. Sensors **12**, 16937–16953 (2012)

Learning/Clustering

Instance Weighted Clustering: Local Outlier Factor and K-Means

Paul Moggridge(✉), Na Helian, Yi Sun, Mariana Lilley, and Vito Veneziano

The University of Hertfordshire, Hatfield, UK
p.moggridge@herts.ac.uk

Abstract. Clustering is an established unsupervised learning method. Substantial research has been carried out in the area of feature weighting, as well instance selection for clustering. Some work has paid attention to instance weighted clustering algorithms using various instance weighting metrics based on distance information, geometric information and entropy information. However, little research has made use of instance density information to weight instances. In this paper we use density to define instance weights. We propose two novel instance weighted clustering algorithms based on Local Outlier Factor and compare them against plain k-means and traditional instance selection.

Keywords: Machine learning · Unsupervised learning · Instance weighting

1 Introduction

In the area of Data Mining, clustering is one type of unsupervised learning that involves finding groups of similar instances in data. Arguably the most popular clustering algorithm is k-means [11]. This algorithm partitions instances into a given number of clusters k. K-means iteratively assigns instances to clusters based on their distance to the centroids of the clusters, the centroids' positions are then recalculated to be the means of instances in their respective clusters.

Instance selection is a well established technique. It is often used for removing instances that are outliers. Feature weighting (also referred to as "attribute weighting") is an ongoing area of research. In Feature weighting the features of a dataset are weighted based on their various metrics typically related to how much they enhance the accuracy of the main data mining activity. Inspired by instance selection and feature weighting, Instance weighting assigns a weight to each of the instances in a dataset. Considering outliers for example, from a statistics' perspective, outlierness is a scale rather a boolean property, so it makes sense to use weighting rather than selection in response.

Thanks you to Innovate UK for your support.

Hawkins defines an outlier as "an observation which deviates so much from the other observations as to arouse suspicions that it was generated by a different mechanism" [9]. Outlier accommodation is enabling algorithms to accommodate outliers, it is the opposite of outlier diagnosis, where outliers are identified and removed before processing. Instance Weighting can provide a way for clustering algorithms to accommodate outliers, by adjusting how much to learn from outlying instances. This is important since clustering algorithms, such as k-means can be adversely effected by the presence of outliers in a dataset. Whilst it is true that some types and severities of outlier should be fully discarded, some types and severities of outliers may be best partially retained for the clustering process to learn from. This is especially important when the total number of instances is low.

This paper is structured as follows. Section 2 presents the related work. Section 3 describes our two novel instance weighted clustering algorithms. Section 4 is the methodology, experimental results and discussion of our findings. Finally, Sect. 5 draws conclusions from our findings and presents our recommendations for future work.

2 Related Work

Nock and Neilsen's [12] research is inspired by boosting algorithms (from supervised learning) and k harmonic means clustering [15]. They are the first to formalise a boosting based approach, their solution penalises bad clustering accuracy by updating the instance weights. Their algorithm gives more weight to data points that are not well modelled. Their approach could be described as a statistics based approach. Their paper investigates, for which scenarios, instance weighting improves the accuracy of clustering and if instance weighting can reduce initialisation sensitivity. They investigate applying instance weighting on multiple algorithms including k-means, fuzzy k-means, harmonic k-means and Exception Maximisation and prove the applicability of instance weighting to a range of algorithms. Their research shows that instance weighting could speed up the clustering algorithms. They highlight the growing attention around weighted iterative clustering algorithms in unsupervised learning. In our research we have applied a simpler method, but used a density based technique. We also investigate the benefit of instance weighting and how instance weighting can address the presence of outliers in a dataset.

Sample Weighted Clustering by Jian Yu et al. weights instances using a probability distribution derived from an information theory approach [14]. They point out that there is little research on sample (another name of instance) weighted clustering compared to feature weighted clustering. Like our work they investigate the benefit instance weighting for datasets with outliers wrapping the popular k-means algorithm. They highlight that just one outlier can adversely effect the clustering output of k-means, fuzzy c-means and expectation maximisation. Their information theory based approach produces promising results which are robust to outliers across a variety of datasets. They also found their weighting also made their algorithm less sensitive to initialisation.

Lei Gu's research uses geometric based weighting that also takes local neighbour information into account [7]. Their approach uses two weighting schemes per cluster. One scheme for points close to the center of the clusters and another scheme for ambiguous points near the clusters boundaries. Their algorithm outperforms Jain Yu et al.'s algorithm (described in the previous paragraph) for accuracy. Lei Gu's research also considers non image segmentation based clustering problems.

Hammerly and Elkan's research [8] investigates the k harmonic mean algorithm [15]. They found that it produces better accuracy than k-means and show that having a non-constant (iterative) weight function is also useful. They point out many wrapper based solutions have been proposed, such as random restart, optimising the initialisation and optimising k-selection around clustering, but less research has been put into wrappers which iteratively effect the clustering. Hammerly and Elkan point out the benefit of wrapper methods is that they can often be simultaneously applied.

In Adaptive Nonparametric Clustering by Efimov et al. [6] the weightings are assigned to both the instances and features w_{ij} rather than just w_i (instance weighting) or just w_j (feature weighting). The idea of their algorithm is to look for structures in the clustering, for example, slopes away from local homogeneity. Their approach has several strengths, their algorithm supports manifold clustering and is robust against outliers. Another useful property of their algorithm is the lack of a tunable parameter, which many algorithms has. Their paper does not attempt generalise or suggest the possibility of applying their method as a wrapper method.

Jain provides an overview of clustering discussing the key issues in designing clustering algorithms, and points out some of the emerging and useful research directions [10]. Jain's paper outlines six problems/research areas, one of which is "A fundamental issue related to clustering is its stability or consistency. A good clustering principle should result in a data partitioning that is stable with respect to perturbations in the data. We need to develop clustering methods that lead to stable solutions". This is the problem our research considers solving through instance weighting. Their review paper also points out challenges related semi-supervised clustering (however, we are not considering semi-supervised clustering in this paper), one challenge in the area of semi-supervised clustering is "how to provide the side information". Instance weighting is one possible solution to this problem, our algorithm could be adapted to work in a hybrid mode. Also, with regard to semi-supervised learning it is highlighted that it is desirable to have approach which avoids changing clustering existing algorithms, and instead wrap around them.

Instance weighting is an established technique but there is much less research compared feature weighting. For instance, in recent and comprehensive literature, for example, Data Clutering [1] instance weighting is not mentioned. However, instance weighting is a promising technique and can provide several enhancements to several existing clustering algorithms. Instance weighting is also an increasingly important technique, on the popular dataset website UCI

[5], the average size of the datasets in terms of instances is increasing. Instance weighting like ours makes clustering more robust leading towards an increasingly automated knowledge discovery process by reducing the requirement for preprocessing of data.

Some work has paid attention to instance weighted clustering algorithms using various instance weighting metrics based on distance information, geometric information and entropy information. However, little research has made use of instance density information to weight instances. In this paper we use density to define instance weights, develops clustering methods that lead to stable solutions by using instance density information to weight instances.

2.1 Local Outlier Factor

Local Outlier Factor (LOF) is an outlier detection algorithm which provides a measure of outlierness. LOF works by comparing the density of an instance to that of its neighbours [3]. Equations (1), (2) and (3)[1] show how to calculate the LOF of a point A. A represents the point we are calculating the local density of. k represents the number of neighbours to consider. $k-distance$ is the distance from a given point to its k^{th} furthest point. $N_K(A)$ is the set of k nearest neighbours to A.

$$reachability-distance_k(A,B) = \max\{k-distance(B), d(A,B)\} \tag{1}$$

$$\text{lrd}_k(A) := 1/\left(\frac{\sum_{B\in N_k(A)} \text{reachability-distance}_k(A,B)}{|N_k(A)|}\right) \tag{2}$$

$$\text{LOF}_k(A) := \frac{\sum_{B\in N_k(A)} \frac{\text{lrd}(B)}{\text{lrd}(A)}}{|N_k(A)|} = \frac{\sum_{B\in N_k(A)} \text{lrd}(B)}{|N_k(A)|}/\text{lrd}(A) \tag{3}$$

Consider the example dataset in Fig. 1 (left), the data point at location $(5,5)$ labelled a is moderately outlying. *k-distance* is the distance to the k^{th} furthest point, so if $k=3$, then k^{th} nearest neighbour of a would be the point at location $(1,1)$ labelled b. If point a is within the k neighbours of point b (See Fig. 1 (right)) the $reachability-distance_k(a,b)$ will be the $k-distance$ of b, the distance to the k^{th} further point $(2,1)$ from b. Otherwise, it will be the real distance of a and b. So in Fig. 1 it is **not** within the k neighbours of point b so in this case it is the real distance between a and b.

To get the lrd (local reachability density) for the point a, we will first calculate the reachability distance of a to all its k nearest neighbours and take the average of that number. The lrd is then simply the inverse of that average. Since a is not the third nearest point to b see Fig. 1 (right), the reachability distance in this case is always the actual distance. A value greater than one indicates a lower density (thus the instance is outlier). A value one indicates similar density to neighbours. Less than one indicates a higher density. So low density becomes a high LOF score highlighting a instance as an outlier.

[1] https://en.wikipedia.org/wiki/Local_outlier_factor.

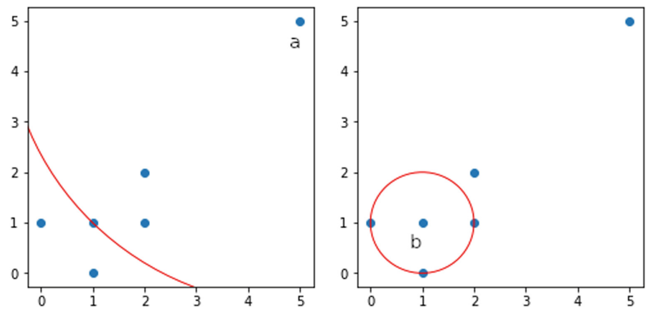

Fig. 1. Calculating the reachability distance.

One of properties that makes LOF ideal is that the LOF algorithm can work on datasets with clusters of different densities and instance count. As long as the number of k neighbours is below the number of instances in the smallest cluster. This is advantageous since it places little restriction on the dataset to which the weighted clustering algorithm can be applied to. However, one possible drawback to the LOF algorithm is its time complexity of $O(n^2)$, where n is the data size. However, there is existing work speeding up LOF using GPU acceleration [2].

3 Proposed Methods

We have proposed two novel algorithms based on k-means, Local Outlier Factor Instance Weighted K-Means (LOFIWKM) and Iterative Local Outlier Factor Instance Weighted K-Means (ILOFIWKM). LOFIWKM calculates the weights over the **whole dataset once upon initialisation**, whereas ILOFIWKM calculates the weights **for each cluster upon each iteration**. The weights generated by executing the LOF algorithm are used when calculating means for the positions of the new centroids in the k-means algorithm. In Fig. 3 the weights are represented by black circles, where the smaller the circle the higher the weight.

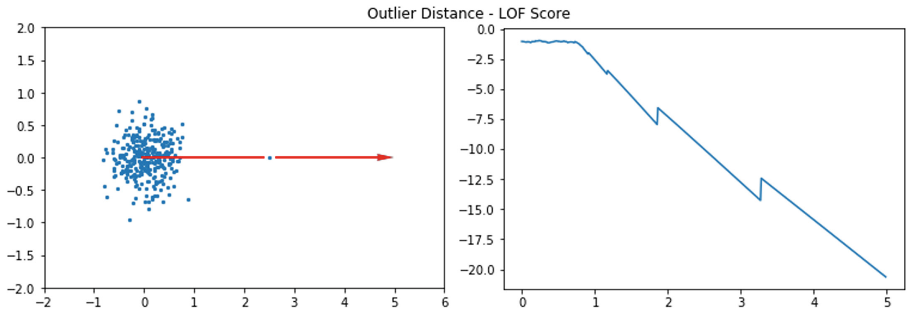

Fig. 2. Demonstrating the LOF scores.

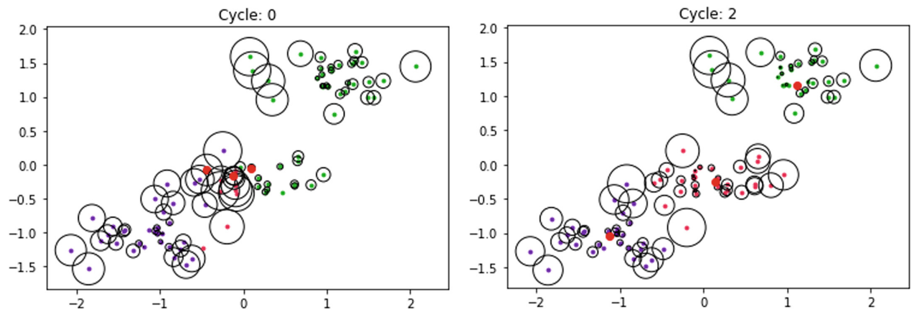

Fig. 3. The I LOF IW K-Means showing different how weights change as the algorithm executes.

More formally, LOFIWKM, starts by calculates the LOF score of every instance considering the whole dataset. Taking the whole dataset into consideration, we highlight outliers relative to the whole dataset. Then as per k-means, centroids are initialised. However, our algorithm uses a weighted random initialisation based on LOF scores and instance positions. Then as per k-means, instances are assigned to the centroids they are closest to. Then as per k-means, the algorithm iterates until converged (there is no more reassignments of instance between clusters) or a max allowed iterations is met. Then, the algorithm calculates the new positions of the centroids based on its' instances, taking a weighted average using normalised LOF scores as weights to moderate the impact of the instance positions on the mean. Then as per k-means instances are assigned the new centroid they are nearest to. Figure 1 shows a formal description of the algorithm where, Dataset of instances = D_i, $D = \{D_1,\ D_2\ \ldots\ D_i\ D_N\}$. LOF Scores for each instance in the dataset = LOF_i, $LOF = \{LOF_1,\ LOF_2,\ \ldots\ LOF_i,\ LOF_N\}$. Clusters corresponding the K value entered = C_k, $C = \{C_1,\ C_2\ \ldots\ C_k, C_K\}$ a centroid has a position and collection of instances. The number of iterations/k-means cycles = c.

ILOFIWKM operates the same as LOFIWKM upto the end of iteration step. Then the algorithm LOF score of every instance running the LOF algorithm per cluster and normalising the LOF scores per cluster. Figure 2 shows a formal description of the algorithm.

Algorithm 1. LOFIWKM

```
Calculate $LOF$ for $D$
for all $w$ in $LOF$ do
    Assign $\frac{w-min(LOF)}{max(LOF)-min(LOF)}$ to $w^*$
end for
Assign $LOF^*$ to $LOF$
Use $LOF$ weighted random to select $K$ positions from $D$ assign to $C$
for all $i$ in $D$ do
    Assign $i$ to $k$ according to $\min(dist(i, C))$
end for
Assign 0 to $c$
while $C$ not converged or $c \leq c^{max}$ do
    for all $k$ in $C$ do
        Assign $\frac{\sum_{k_N}^{k_0} i \cdot w}{\sum_{k_N}^{k_0} w}$ to $k$
    end for
    for all $i$ in $D$ do
        Assign $i$ to $k$ where $\min(dist(i, C))$
    end for
    Assign $c + 1$ to $c$
end while
```

4 Experimentation

The purpose of the proposed algorithms is to improve k-means ability to handle outliers. Two variables, count of outliers and range of outliers are experimented with, furthermore the two new algorithms were compared against plain k-means. All experiments are repeated 175 times as the algorithms and the synthetic dataset generation are both stochastic. The outliers are generated using a uniform distribution over a given range, and appended to the dataset. Both synthetic and real world datasets are experimented on. All datasets used included their ground truths and this was used assess clustering accuracy using ARI (Adjusted Random Index). The ARI computes a similarity measure between clusterings by considering all pairs of instances and counting pairs that are assigned in the same or different clusters in the predicted and true clusterings.

The experiments use the scikit-learn libraries where possible [13] to speed development and aid repeatability. Most notably scikit-learn's LOF implementation was used for calculating the measures of outlyingness. Furthermore, scikit-learn's Blobs Dataset Generator, Standard Scaler, PCA and Adjusted Random Index were utilised. For the k-means algorithm, our own python implementation was used and updated to create the novel algorithms. This ensures that the only difference between k-means and our instance weighted k-means algorithms was changes described in this paper.

For each run of the experiments the dataset was regenerated. The synthetic blob datasets (noise = 0.3) are generated with 90 instances, 2 features and 3 clusters of equal sizes. For the outlier count various amounts of outliers were tested: 5, 10, 15, 20, 25. For the outlier range experiment, various ranges were tested: 20, 40, 60, 80, 100, the (dataset with outliers spans a range of 10 in either axis) (Fig. 4).

Algorithm 2. ILOFIWKM

```
Calculate $LOF$ for $D$
for all $w$ in $LOF$ do
    Assign $\frac{w-min(LOF)}{max(LOF)-min(LOF)}$ to $w^*$
end for
Use $LOF$ weighted random to select $K$ positions from $D$ assign to $C$
for all $i$ in $D$ do
    Assign $i$ to $k$ according to $\min(dist(i, C))$
end for
Assign 0 to $c$
while $C$ not converged or $c \leq c^{max}$ do
    for all $k$ in $C$ do
        Assign $\frac{\sum_{k_N}^{k_0} i \cdot w}{\sum_{k_N}^{k_0} w}$ to $k$
    end for
    for all $i$ in $D$ do
        Assign $i$ to $k$ where $\min(dist(i, C))$
    end for
    for all $C$ do
        Partially recalculate $LOF$ for $i$ in $k$
        for all $w$ in $k$ do
            Assign $\frac{w-min(LOF)}{max(LOF)-min(LOF)}$ to $w^*$
        end for
    end for
    Assign $c + 1$ to $c$
end while
```

Also experiments are conducted on a real world dataset containing 210 instances, 7 features and 3 clusters the measurements are of damaged wheat kernels of 3 different varieties [4]. The dataset was obtained via the UCI Machine Learning Repository [5] (Fig. 5).

4.1 Outlier Count and Range Synthetic Dataset Results

Figure 6 shows positive results for density based instance weighted clustering. The instance weighted algorithms were able to achieve better clustering accuracy

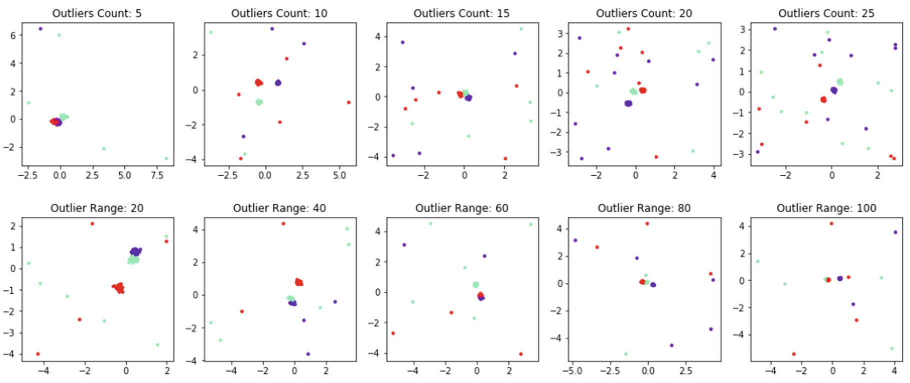

Fig. 4. A sample of the blobs datasets.

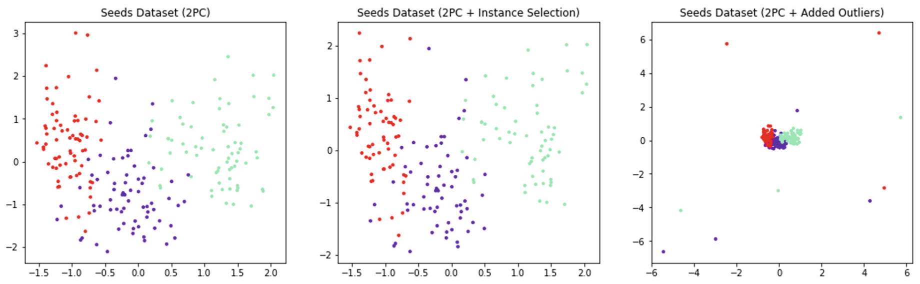

Fig. 5. The seeds datasets.

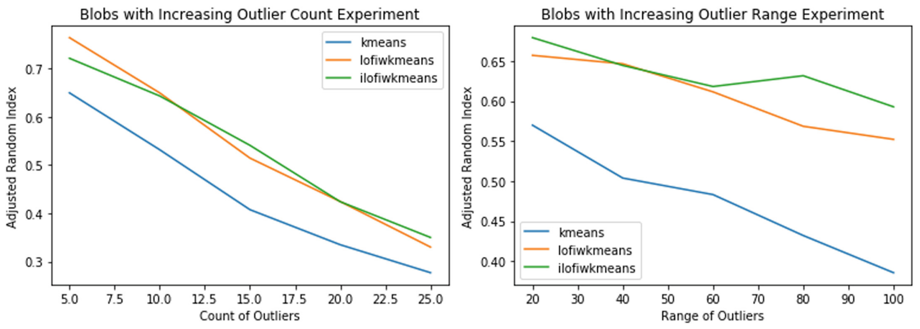

Fig. 6. Adjusted Random Index scores for the blobs datasets

than k-means. In Fig. 6 on the left, the impact of increasing the count outliers can be seen. In Fig. 6 on the right, the impact of creating increasingly distance outliers is shown. The accuracy of k-means quickly deteriorates as the outliers get distant. The LOFIWKM and ILOFIWKM algorithms are not as strongly effected by the presence of increasing distant outliers. Across both experiments, a minimal gain can be seen in using the iterative version, ILOFIWKM.

4.2 Real World Dataset Results

In Fig. 7 instance weighting is compared with instance selection. The three groups of columns show different conditions of the dataset. Left shows the results with dataset having additional synthetic outliers added. Center shows the results of the algorithms having the outliers removed (i.e. Instance Selection). The outliers were removed using the LOF algorithm with the same neighbours count as in LOFIWKM algorithms (neighbours = 5). The outlier contamination value was set to 0.1 to remove the most outlying 10% of the dataset. Finally right shows results for the original dataset. We can compare instance weighting to instance selection by comparing the right group's LOFIWKM result to the central group's k-means result. It can be seen that instance weighting slightly outperformed instance selection in ARI score, however only slightly. It can also been seen that

ILOFIWKM and LOFIWKM provided a large benefit on the original dataset and the with additional outliers added compared to k-means. Our results mirror tests on the seeds dataset in Lei Gu's research were weighting also enhance clustering accuracy [7].

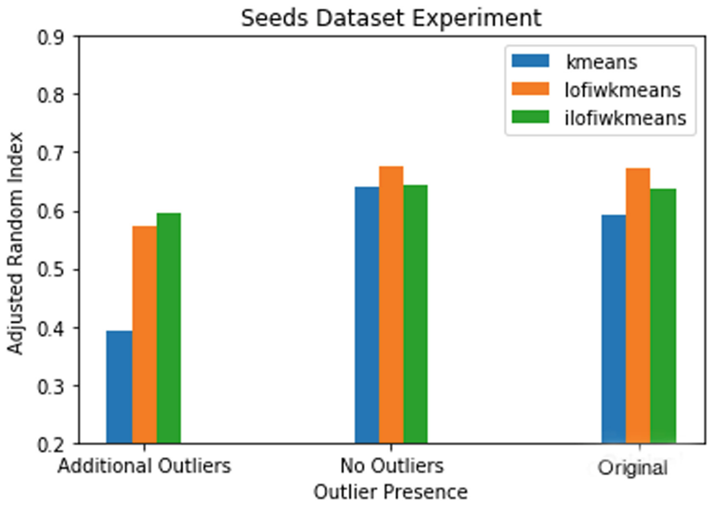

Fig. 7. Adjusted Random Index scores for the seeds dataset

5 Conclusion and Future Work

In conclusion, this paper has shown that instance weighting can help mitigate the effect of outliers on both a synthetic and a real world dataset.

In this paper we only investigated k-means which has a hard membership function and the LOF algorithm. However, there is likely more useful combinations to be found. Hammerly and Elkan found that varying weights did improve the performance of hard membership function algorithms (i.e. k-means) [8]. However, Nock and Neilsen's research confirmed instance weighting to be more advantageous for clustering algorithms with soft membership functions such as fuzzy k-means [12]. A future work of this paper should be to investigate soft membership function algorithms.

Our modifications were made to a basic version of the k-means algorithm. However, it would be possible to combine the LOF instance weighting with a version of k-means which has more optimisations or is being used in conjunction with wrapper functions. Furthermore, with instance weighting there is potential to simultaneously apply multiple instance weights which could prove to increase robustness or accuracy.

The time complexity LOFIWKM is equivalent to LOF instance selection $O(n^2)$ plus k-means $O(n)$, however ILOFIWKM is significantly more costly taking the complexity of k-means plus the execution of the LOF algorithm per cluster (for each clusters instances), further experimentation may prove that ILOFIWKM may be not suitable for large datasets, without optimisation of the LOF algorithm, such as, the research by Alshawabkeh et al. [2].

Future work also includes testing the algorithms with a more thorough outlier generation process. In this paper we added instances from a uniform distribution, centred on the dataset. This had two disadvantages, firstly this method possibly does not highlight one of the advantages of instance weighting. Instance weighting has the potential to retain some of the information an outlier presents, since the "outliers" are uniformly random these benefits are negated. Secondarily, it is possible that when generating the "outliers" that a proportion of fall within a normal range and end up not being outliers.

Currently our algorithm requires parameter selection of k clusters and the size of the LOF neighbourhood. Other algorithms [7,14] require some parameter selection with the exception of the state of the art [6]. It would be clearly better to not require the parameter selection and it does seem possible to automate the selection of these parameters.

References

1. Aggarwal, C.C., Reddy, C.K.: Data Clustering: Algorithms and Applications, 1st edn. Chapman Hall CRC, Boca Raton (2013)
2. Alshawabkeh, M., Jang, B., Kaeli, D.: Accelerating the local outlier factor algorithm on a GPU for intrusion detection systems. In: Proceedings of the 3rd Workshop on General-Purpose Computation on Graphics Processing Units, pp. 104–110 (2010)
3. Breunig, M.M., Kriegel, H.P., Ng, R.T., Sander, J.: LOF: identifying density-based local outliers. In: ACM Sigmod Record, vol. 29, pp. 93–104. ACM (2000)
4. Charytanowicz, M., Niewczas, J., Kulczycki, P., Kowalski, P.A., Łukasik, S., Żak, S.: Complete gradient clustering algorithm for features analysis of x-ray images. In: Information Technologies in Biomedicine, pp. 15–24. Springer (2010)
5. Dua, D., Graff, C.: UCI machine learning repository (2017). http://archive.ics.uci.edu/ml
6. Efimov, K., Adamyan, L., Spokoiny, V.: Adaptive nonparametric clustering. IEEE Trans. Inf. Theory **65**(8), 4875–4892 (2019)
7. Gu, L.: A novel sample weighting k-means clustering algorithm based on angles information. In: 2016 International Joint Conference on Neural Networks (IJCNN), pp. 3697–3702. IEEE (2016)
8. Hamerly, G., Elkan, C.: Alternatives to the k-means algorithm that find better clusterings. In: Proceedings of the Eleventh International Conference on Information and Knowledge Management, pp. 600–607 (2002)
9. Hawkins, D.M.: Identification of outliers, vol. 11. Springer (1980)
10. Jain, A.K.: Data clustering: 50 years beyond k-means. Pattern Recogn. Lett. **31**(8), 651–666 (2010)
11. Lloyd, S.: Least squares quantization in PCM. IEEE Trans. Inf. Theory **28**(2), 129–137 (1982)

12. Nock, R., Nielsen, F.: On weighting clustering. IEEE Trans. Pattern Anal. Mach. Intell. **28**(8), 1223–1235 (2006)
13. Pedregosa, F., Varoquaux, G., Gramfort, A., Michel, V., Thirion, B., Grisel, O., Blondel, M., Prettenhofer, P., Weiss, R., Dubourg, V., Vanderplas, J., Passos, A., Cournapeau, D., Brucher, M., Perrot, M., Duchesnay, E.: Scikit-learn: machine learning in python. J. Mach. Learn. Res. **12**, 2825–2830 (2011)
14. Yu, J., Yang, M.S., Lee, E.S.: Sample-weighted clustering methods. Comput. Math. Appl. **62**(5), 2200–2208 (2011)
15. Zhang, B.: Generalized k-harmonic means. Hewlett-Packard Laboratories Technical Report (2000)

Detecting Pattern Efficiently with Don't Cares

Hayam Alamro[1,2](✉) and Costas Iliopoulos[1]

[1] Department of Informatics, King's College London, London, UK
{hayam.alamro,costas.iliopoulos}@kcl.ac.uk
[2] Department of Information Systems, Princess Nourah Bint Abdulrahman University, Riyadh, Kingdom of Saudi Arabia

Abstract. In this paper, we introduce our efficient simple method which can locate all occurrences of pattern P of k subpatterns with "don't cares" of length m in text S of length n. Our algorithm employs advanced data structure and the *Kangaroo* method, which can be applied to selected suffixes of the *suffix tree* of S to answer subsequent queries in $O(k)$ time using a predefined computational method to find all occurrences of pattern P with "don't cares" in text S in a fast and effective manner.

Keywords: Pattern · Don't cares · Detect

1 Introduction

Pattern matching is the problem of string matching which is to find the location(s) of a given word, the pattern within another one, the text [15,16]. The classical pattern matching problem is to find all the occurrences of a given pattern P of length m in a text S of length n, both being sequences of characters drawn from a finite character set Σ. This problem is interesting as a fundamental computer science problem and is a basic need of many applications, such as text retrieval, music retrieval, computational biology, data mining, network security, among many others. Solutions to the pattern matching in strings can be roughly classified into two categories, window shifts and automaton, and text indexing [14]. In the first one, the pattern is examined using a window shift where the window slides along the text from left to right according to the window rules of each algorithm, such that the found location is reported after a whole match with the corresponding pattern. The algorithms that are adopted this approach are *Brute-force* algorithm, *Karp-Rabin* algorithm [25] and *Boyer-Moore* algorithm [6] which works on skipping a large portion of the text while searching a pattern, which helps in speeding up the searching process. The *KMP* is the first linear-time pattern matching algorithm, which stores the information of matching to prevent a backward shift to improve the search time with the help of the failure function [26]. Also, the *Aho-Corasick* algorithm [1], which is

L. Iliadis et al. (Eds.): EANN 2020, INNS 2, pp. 447–459, 2020.
https://doi.org/10.1007/978-3-030-48791-1_35

an improved version of the *KMP* algorithm and based on the automaton approach, preprocesses the keywords (dictionary strings) then search for the keywords simultaneously which runs in time proportional to the sum of the lengths of the keywords. At the multi-pattern matching level, Commentz-Walter [13] presented an algorithm which is a combination of the Boyer-Moore and Aho-Corasick, and Wu-Manber [36] also uses the idea of Boyer-Moore in addition to building three tables (SHIFT, HASH, and PREFIX) to determine how many characters should be skipped and which pattern is a candidate for the match. The other pattern matching solutions involve building an index for a text such that the occurrences of a query pattern can be reported, where the data structure contains all the suffixes of the text. *Suffix tree* and *Suffix array* are data structures for text indexing, linear space, and hold the compact representation of the text suffixes. Recently, classical string indexing problems are extended to address the patterns with more complicated forms, such as don't cares characters, gaps and errors to meet many applications needs in reality. A *don't care* character means that this position of the pattern can match any character in the text and is denoted with '*'. Don't care is also called wildcard [5] or gap [32]. A Suffix tree is an efficient data structure as it stores the suffixes of a given string in linear space and time, and is useful in various applications concerning string matching like finding longest common prefix, repeated substrings and antiperiods of a string. The majority of applications that use complex patterns like don't cares characters, focus on non-indexing data structure where the text is not preprocessed in advance, while few of them adopted this approach as we will see in the next section. Hence, in this paper, we propose an algorithm that is simple and efficient in terms of using text indexing data structure without using additional data structures. The algorithm is based on preprocessing the text using a suffix tree without using a generalization suffix tree, and instead, it applies the Kangaroo method which is enabled by a predefined computational method. The contributions of this paper as follows:

1. To innovate an efficient and simple approach that can locate all occurrences of a given pattern P of length m in a text S of length n, where pattern P is defined over the alphabet $\Sigma \cup \{*\}$ and text S is sequences of characters drawn from a finite character set Σ.
2. To achieve the following specific contribution: propose an efficient algorithm which relies on constructing the *suffix tree* T for the text S without using a generalization *suffix tree* concept of $(P + S)$, instead, it applies the *Kangaroo* method on selected suffixes of the *suffix tree* of S using a predefined computational method to find all occurrences of pattern P in a fast and effective manner.

The rest of the paper as follows. In Sect. 2, the related work about pattern matching with don't cares is described. In Sect. 3, we introduce background concepts and definitions, and formally define the problem we address. In Sect. 4, we detailed our approach in detecting pattern with "don't cares" and present our algorithm. In Sect. 5, we conclude.

2 Related Work

Pattern matching has been generalized to searching in the presence of errors, e.g. Hamming distance [4,20,28], edit distance [11,28,33]. These variations of the original problem are known as approximate pattern matching. Fischer and Paterson [19] introduced the solution for the pattern matching with don't cares based on Fast Fourier Transform (FFT) and presented the algorithm that runs in $O(n \log m \log |\Sigma|)$ time. Subsequently, Indyk [23] gave a randomized algorithm which removed the dependency on the alphabet and involved convolution, running in time $O(n \log n)$. Afterward, Kalai [24] presented a slightly faster and simpler randomised algorithm as it uses a single simple convolution based on the simple randomized fingerprinting algorithm of Karp and Rabin [25] and runs in $O(n \log m)$. Finally, Cole and Hariharan in [12], solved the long lasting open problem of removing the dependency on $|\Sigma|$ in the algorithm and presented a deterministic $O(n \log m)$ time algorithm which also used convolution. Chen et al. [7] presented SAIL algorithm that conducts two phases (forward and backward) to return each matching substring of P in T in $O(n + klmg)$ time complexity, where k is the frequency of P's last character occurring in T, l is a user defined maximum length for each matching substring, and g is the maximum difference between the user defined maximum length and the minimum number of wildcard characters between two consecutive letters in P. Pinter [31] on the other hand avoided the use of convolution and used the Aho-Corasick algorithm [1] to solve the problem. The running time of Pinter's algorithm is $O(n+m+\alpha)$, where α is the total number of occurrences of the component subpatterns. However, Pinter's technique cannot be used to index the text. Furthermore, Cole and Lewenstein [10] also presented an algorithm to solve this problem considering a centroid path decomposition on tree T. The algorithm in [10] first prepossesses the text in $O(n \log Kn + n \log |\Sigma|)$ time to build a data structure of size $O(n \log Kn)$ which answers subsequent queries in time $O(2K \log \log n + m + |occ(P)|)$. Here K is the number of don't cares in the pattern and $occ(P)$ denotes the set of occurrences of the pattern in the text. Philip et al. [5] used the ART decomposition introduced by [3] to decompose the tree into a single top tree and a number bottom trees, and used the LCP data structure by [10] to report the occurrences of P in T. Rahman et al. [32] presented an algorithm where they prepossess the text in optimal $O(n)$ time and can answer subsequent queries in $O(m + \alpha \log \log n)$ time. Thereafter, Iliopoulos and Rahman [22] presented algorithms for pattern matching which can solve the problem of pattern matching with don't cares in $O(n + m + \alpha)$ time, where α is the total number of occurrences of the component subpatterns. Lam et al. [27] make use of [22] to find a set of candidate positions in T which are a superset of all matches of P in T, then the algorithm verifies whether each of them is real or not. Clifford and Porat [9] presented a filtering based algorithm for the k mismatch pattern with don't care symbols in either pattern P or text T and bounded with k mismatch and runs in $(nm^{1/3}k^{1/3} \log^{2/3} m)$. Subsequently, Clifford et al. [8] presented two solutions for pattern matching with don't cares and bounded with k mismatches. The first solution uses a randomized algorithm that works in $(n(k+\ logm \log k) \log n)$ time, and the second solution uses a deterministic algorithm which runs in $(nkpoly\log m)$ time and based on k selectors to find k mismatch problem with don't cares. Nicolae and Rajasekaran [30] gave two algorithms for pattern matching with k mismatches and don't cares in the pattern. The first one runs in $O(n\sqrt{(q+k)\log m})$ time, and the second one runs in $O(\sqrt[3]{qk\log^2 m}+n\sqrt{k\log m})$ time. Finally, Liu et al. [29] proposed two suffix tree-based algorithm (MMST-S and MMST-L) to solve variable length wildcards, according to the length of exact characters in a pattern. The algorithms involve three phases: the first phase includes constructing the suffix tree, the second phase for preprocessing the multipattern by sorting them which requires to split the exact characters into groups and gaps and then classified them according to the alphabetical order of each character in MMST-S and according to the last exact characters' group in MMST-L approach, finally, they are solved using the proposed algorithms. Most relevant to our work is the work of Iliopoulos and Rahman [22] as the algorithm based on text indexing approach by building a suffix array for the text T, then, it works on dividing the pattern P into l groups of sub-patterns, where each sub-pattern P_i is a string over the alphabet Σ and $1 \leq i \leq l-1$. For each sub-pattern, there is parameter k_i which indicates the number of don't cares characters between P_i and P_{i+1}. The algorithm in [22] computes the occurrences of $occ(P_i)$ using $SA(T)$ and for each occurrence position $(r \in occ(P_i))$, the algorithm uses two arrays (*val* and *permitted*) which computes the accumulated length of each sub-pattern P_i in *val* array first, then uses that array in *permitted* array to check each candidate position is an occurrence position for the pattern P. This is done, after comparing the result of the checking with the total number of the subpatterns each time a new candidate position is tested, which requires the algorithm to test all the subpatterns of P to decide whether it has an occurrence in the text or not. However, comparing to our work, this paper focuses on innovating simple, less complicated and efficient algorithm that can exactly locate all occurrences of a given pattern P of length m with don't cares characters in a text S of length n based on selected suffixes of the *suffix tree* of S using a predefined simple equation to enable the *Kangaroo* method without using additional data structures. Furthermore, the test for each P comes logically coherent and sequential such that the test starts from the first subpattern of P, then it moves to the next subpattern as long as the previous test was successful, otherwise, it stops testing the remaining subpatterns of P to save the time of the algorithm and report that pattern does not exist.

3 Background and Problem Definition

3.1 Background

String and Substring. Let $S = S[1, n]$ be a string of length $|S| = n$ over an alphabet Σ of size $|\Sigma| = \sigma$. The empty string ε is the string of length 0. For $1 \leq i \leq j \leq n$, $S[i]$ denotes the ith symbol of S, and $S[i \dots j]$ the contiguous sequence of symbols (called *factor* or *substring*) $S[i]S[i+1]\dots S[j]$. A substring

$S[i \dots j]$ is a suffix of S if $j = n$ and it is a prefix of S if $i = 1$. A string p is a *repeat* of $S \iff p$ has at least two occurrences in S. In addition p is said to be *right-maximal* in $S \iff$ there exist two positions $i < j$ such that $S[i, i + |p| - 1] = S[j, j + |p| - 1] = p$ and either $j + |p| = n + 1$ or $S[i, i + |p|] \neq S[j, j + |p|]$ [15,21].

Suffix Tree. The *suffix tree* T for a string S of length n over the alphabet Σ is a rooted directed compacted trie built on the set of suffixes of S. The suffix tree has n leaves and its internal nodes have at least two children whiles its edges are labelled with substrings of S. The labels of all outgoing edges from a given node start with a different character. All leaves of the suffix tree are labelled with an integer i, where $i \in \{1 \dots n\}$ and the concatenation of the labels on the edges from the root to the leaf gives us the suffix of S which starts at position i. The nodes of the (non-compacted) trie which have branching nodes and leaves of the tree are called *explicit nodes*, while the others are called *implicit nodes*. The occurrence of a substring P in S is represented on T by either an explicit node or implicit node and called the *locus* of P. The *suffix tree* T can be constructed in $O(n)$ time and space. In order to have one-to-one correspondence between the suffixes of S and the leaves of T, a character $\$ \notin \Sigma$ is added to the end of the label edge for each suffix i to ensure that no suffix is a prefix of another suffix. To each node α in T is also associated an interval of leaves $[i..j]$, where $[i..j]$ is the set of labels of the leaves that have α as an ancestor (or the interval $[i..i]$ if α is a leaf labelled by i). The intervals associated with the children of α (if α is an internal node) form a partition of the interval associated with α (the intervals are disjoints sub-intervals of $[i..j]$ and their union equals $[i..j]$). For any internal node α in the *suffix tree* T, the concatenation of all edge labels in the path from the root to the node α is denoted by $\bar{\alpha}$ and the string depth of a node α is denoted by $|\bar{\alpha}|$ [2,17,21].

Definition 1. *The Lowest Common Ancestor (LCA) of two nodes u and v in a tree T is defined as the deepest node in T that is an ancestor of both u and v. This node, denote it by α, lies on all root to u and on all root to v path [18].*

Pattern Matching. In what follows, we assume that we are given a text S of length n and a pattern P of length m. The classical matching problem consists in locating all occurrences of P in S, that is, all possible i such that for all $j \in [1, m]$, $S[i + j - 1] = P[j]$. This problem has been extended by introducing "don't care" character as follows:

Definition 2. *A don't care character, denoted by '$*$' is a character such that $* \notin \Sigma$ and matches any character $\sigma \in \Sigma$ for all $\sigma \in \Sigma$ [22].*

3.2 Problem Definition

Given a text S over the alphabet Σ and a pattern P over the alphabet $\Sigma \cup \{*\}$. The problem is to find all the occurrences of P in S.

Example 1. Consider that we have the following text S over the alphabet Σ and a pattern of actions P over the alphabet $\Sigma \cup \{*\}$:

$S = ABXABGCABGCAFFBYBGAFABGCAFFBY$
$P = AB * CA * *BY$

As we note from the example, '$*$' can match any action in S, therefore the pattern of actions P has two occurrences in S at positions 7 and 20. Note that indexing the text starts from 0. Before describing our proposed solution, we will start by stating some useful lemmas.

Lemma 1. *Two sub-strings $S[i, i+d-1]$ and $S[j, j+d-1]$ are equal $\iff$ they have the same locus in the suffix tree of S [2].*

Example 2. Consider the sequence S in example 1, and the pattern $P = ABGCAFFBY$. The pattern P has two occurrences in S at positions 7 and 20 ($S[7, 15], S[20, 28]$) and have the same locus on the suffix tree (Fig. 1) at suffixes 7 and 20.

Lemma 2. *If X is a subsequence of sequence S, then X is the deepest non leaf node from the root node, and X must be the longest common subsequence or the longest repeat subsequence [29].*

Example 3. As shown in Fig. 1, the subsequence $X = AB$ is the deepest non leaf node from the root node, and the longest common subsequence of length 2 for the suffixes $(0, 7, 20, 3)$. This also means that the subsequence X occurred 4 times in S.

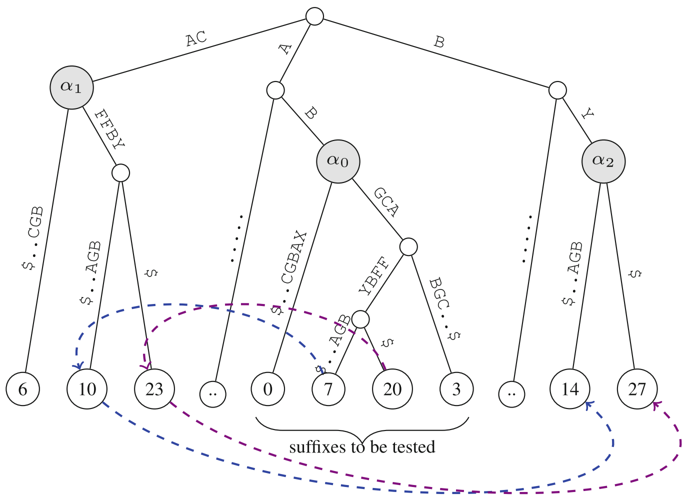

Fig. 1. Sub-tree of the suffix tree of the text S (see Example 1) and illustration of locating occurrences of the pattern $P = AB * CA * *BY$ in S using our method. The occurrences of pattern P in S are at (7 and 20).

Table 1. P_α array of pattern $P = AB * CA * *BY$

j	$\bar{\alpha}_j$	$\lvert\bar{\alpha}_j\rvert$	δ_j
0	AB	2	1
1	CA	2	2
2	BY	2	0

4 Detecting Pattern with "Don't Cares"

In a pattern with "don't cares" characters problem, we are given a string S of length n over the alphabet Σ and a pattern P of length m over the alphabet $\Sigma \cup \{*\}$ and have to find all occurrences of P in S efficiently. This problem can be solved using the *suffix tree* of S and *Kangaroo method* to find all occurrences of P with its sub-patterns in S. To find a pattern P with "don't cares" characters, it will be useful to define a pattern P having "don't cares" characters as follows:

Definition 3. *A pattern P with "don't cares" characters is a pattern consists of k subpatterns, where each subpattern P_j is a string over the alphabet $\Sigma \cup \{*\}$. For each $0 \leq j \leq k-1$, we have a pair $(|\bar{\alpha}_j|, \delta_j)$, where $|\bar{\alpha}_j|$ is the letters string length starting at position 0 at P_j and $\in \Sigma$, and δ_j is the "don't cares characters" length followed $|\bar{\alpha}_j|$ at P_j.*

For example: suppose we have $P = AB*CA**BY$. We divide P into P_k sub-patterns as follows:

$$\text{AB}^*\text{CA}^{**}\text{BY} = P_0P_1P_2 = (|\bar{\alpha}_0|, \delta_0)(|\bar{\alpha}_1|, \delta_1)(|\bar{\alpha}_2|, \delta_2) = (2,1)(2,2)(2,0)$$

4.1 Kangaroo Method

Kangaroo approach is commonly used in string pattern matching with at most k mismatches. The *Kangaroo* method is usually used with a generalization *suffix tree* of $(P + T)$ and works on matching strings by using LCA (Lowest Common Ancestor) query on the *suffix tree.* More precisely, to match pattern P with text T_i with at most k mismatches, the LCP (Longest Common Prefix) between P and T_i is found by using LCA query in the suffix tree between the nodes representing P and T_i. The LCP ends either at the first mismatch between P and T_i at position q of P or one of the strings terminates. The first mismatch can be skipped using a *Kangaroo* jump in $O(1)$ time. To allow for another mismatch, another *Kangaroo* jump should be done from the suffix $q+1$ of P and suffix $i+q-1$ of T on the *suffix tree.* We continue on doing *Kangaroo* jumps until we hit the maximum number of mismatches in $O(k)$ time or one of the strings terminates [37]. Our algorithm uses a new simple and efficient approach such that it relies on constructing a suffix tree T for the text S only without using the generalization concept of $(P + T)$, and instead, the algorithm applies the *Kangaroo* jumps on chosen suffixes of the *suffix tree* using a predefined computational method to find all occurrences of the pattern P with "don't cares" in S, in a fast and effective manner.

4.2 Detecting Pattern with "Don't Cares"

The proposed algorithm starts by preprocessing the *suffix tree* T of text S and decomposing pattern P into k subpatterns $(P_0 \ldots P_{k-1})$ such that each subpattern consists of a pair $(|\bar{\alpha}_j|, \delta_j)$, where $|\bar{\alpha}_j|$ represents the letters string length of P_j over the alphabet Σ, δ_j represents the '*' length at P_j and k is the number of subpatterns, (see Algorithm 1 Step 2). The algorithm also, constructs an array P_α

of length k at the preprocessing phase which retains the letters of each subpattern P_j that corresponds to the label $\bar{\alpha}_j$ on the *suffix tree*, the label length $|\bar{\alpha}_j|$, the '*' length δ_j and indexed with a value of j, (see Table 1 for illustration). The algorithm proceeds into k phases. At the first phase, the algorithm traces the *suffix tree* T of S starting from the root to find the locus of the first subpattern α_0 of the label $P_\alpha[0,0]$, which is of length $|\bar{\alpha}_0|$. If the locus α_0 is found, the algorithm locates its associated suffixes interval $[i_s, i_e]$ such that α_0 is its ancestor and represents the longest common prefix for those suffixes (lemma 2), see (Steps 4–8). The associated suffixes interval $[i_s, i_e]$ represents the possible suffixes that the pattern P with "don't cares" characters occurs at one or more of them. To check the occurrence of pattern P, the remaining subpatterns $(P_1 \dots P_{k-1})$ of P should be found on the tree. To do so, for each $l \in [i_s, i_e]$, the algorithm applies the *Kangaroo* method (Steps 10–11) such that it starts from the suffix l and find the next suffix d of the subpattern P_1 by adding the suffix number l to the label length $|\bar{\alpha}_0|$ and "don't cares" length δ_0 on the tree as follows:

$$l + |\bar{\alpha}_0| + \delta_0 = d$$

Next, the algorithm jumps to the suffix d, where $d \in [1 \dots n]$ suffixes of the tree and a query runs at this suffix starting from the root of T to test the label existence of the next subpattern $P_\alpha[1,0]$ where its locus is α_1 and of length $|\bar{\alpha}_1|$. If the returned result of the query is true, then a second *Kangaroo* jump should be done at the suffix (d) to go to the next suffix $(d+1)$ to test the next subpattern P_{j+1} by adding the suffix number d to the label length of the previous subpattern $|\bar{\alpha}_j|$ and "don't cares" length δ_j on the tree as follows (Steps 16–29):

$$d + |\bar{\alpha}_j| + \delta_j = d + 1$$

The algorithm will continue to do this procedure until it achieves the query of the last subpattern P_{k-1} and an occurrence is reported at l (Steps 30–33). At any phase the algorithm fails in testing l such that the query returns false, the algorithm stops testing l (Steps 26–27) and proceeds to test the next l in the suffixes interval $[i_s, i_e]$ which saves the time of the algorithm and can find all occurrences of the pattern P in a faster and effective way. Figure 1 illustrates our algorithm in finding the occurrence(s) of pattern P on the suffix tree of text S (which is given in Example 1). At this example, the algorithm divides pattern P into 3 subpatterns and builds the *suffix tree* of S as a preliminary stage. Then, starts with the first subpattern P_0 to find its locus on the *suffix tree* which is denoted by α_0 and represents the label at $P_\alpha[0,0]$. Afterwards, it locates its associated suffixes subset where "AB" is its ancestor which are $[0,7,20,3]$. Then, for each $l \in [0,7,20,3]$, the algorithm conducts a testing for the occurrence of pattern P using the equation in (Algorithm 1 Step 19) where it calculates the next suffix that the algorithm should jump to test the next subpattern existence. This can be done by adding the length of $|\bar{\alpha}_{j-1}|$ and δ_{j-1} to the current suffix being tested. At our example, pattern P has two occurrences at suffix 7 (which its *Kangaroo* jumps illustrated using blue dotted curve) and at suffix 20 (which its *Kangaroo* jumps illustrated using violet dotted curve) but has no occurrence at suffixes 0 and 3. For further clarification, at suffix 7, the algorithm computes the next suffix d to jump which is 10 $(7 + 2 + 1)$, and it inquiries the occurrence of the subpattern $P_\alpha[1, 0]$ at suffix 10 which is found at locus α_1. Next, a second jump should be done to the next suffix $d+1$ which is 14 $(10+2+2)$ and a second query at this suffix runs to test the existence of $P_\alpha[2, 0]$ where the returned result is true and the locus is α_2. At the end, an occurrence of the pattern P is reported at the current suffix l being tested which is 7. The efficiency of our algorithm lies on testing only subset of the suffixes of the suffix tree T of S. In addition to, testing only the alphabetic part of each subpattern without caring of "don't cares" symbols, which shortens the search process and thus reduces the search time. Furthermore, the test for each pattern P in terms of its subpatterns is conducting sequentially such that the pattern test starts from the first subpattern of P, then it moves to the next subpattern as long as the previous test was successful, otherwise, it does not require completion of the remaining subpatterns, which improves the search efficiency. We have thus obtained the following theorems.

Algorithm 1. Detect Pattern P with Don't Cares in text S

```
Input: Text string $S$, Pattern $P$ with Don't Cares
Output: $P\_occ[]$: all suffixes where $P$ has an occurrence in $S$

1: procedure LOCATE PATTERN $P$ WITH DON'T CARES IN TEXT $S$
2: ▷ Phase 0: (Preprocessing)
      – Build Suffix Tree $T$ of $S$
      – Decompose pattern $P$ into sub-patterns $(P_0 \dots P_{k-1})$, where each $P_j = (|\bar{\alpha}_j|, \delta_j)$ and $0 \le j \le k-1$,
        $k$ = no. of sub-patterns
      – Build an array $P_\alpha$ indexed $j = (0 \dots k-1)$, where $P_\alpha[j,0] = \bar{\alpha}_j$, $P_\alpha[j,1] = |\bar{\alpha}_j|$ and $P_\alpha[j,2] = \delta_j$
3: ▷ Phase 1: (Find Occ $(P_0)$)
4:    Start from the root $T$
5:    Find the locus $\alpha_0$ of $P_\alpha[0,0]$
6:    if (found) then
7:        Locate the associated suffixes interval $[i_s, i_e]$ where the locus $\alpha_0$ is its ancestor
8:        $occ \leftarrow 0$
9:        // Find all occurrences of $P$ in $S$
10:        for each $l \in [i_s, i_e]$
11:        go to Phase 2
12:    else                                                    ▷ $P$ is not found
13:        exit matching
14:    end if
15: ▷ Phase 2: (Find Occ $(P_1 \dots P_{k-1})$)
16:    $j \leftarrow 1$
17:    $d_0 \leftarrow l$
18:    while $(j \le k-1)$ do
19:        $d_1 \leftarrow d_0 + |\bar{\alpha}_{j-1}| + \delta_{j-1}$        ▷ $d_1 \leftarrow d_0 + P_\alpha[j-1,1] + P_\alpha[j-1,2]$
20:        go to suffix $(d_1)$                                 ▷ Kangaroo jump
21:        Start from the root $T$
22:        Find the locus $\alpha_j$ of $P_\alpha[j,0]$
23:        if (found) then
24:            $j \leftarrow j+1$
25:            $d_0 \leftarrow d_1$
26:        else
27:            exit                 ▷ there is no occurrence for pattern $P$ at suffix $l$
28:        end if
29:    end while
30:    if $(j = k)$ then
31:        $P\_occ[occ] \leftarrow l$                  ▷ there is an occurrence at suffix $l$
32:        $occ \leftarrow occ + 1$
33:    end if
34: end procedure
```

Theorem 1. *Given a text S over the alphabet Σ of length n and a pattern P over the alphabet $\Sigma \cup \{*\}$ of length m, we can compute the occurrence of P in S in $O(n+m+k)$ time complexity, where k is the total number of the subpatterns of P.* □

Proof. Let us analyse the time complexity of Algorithm 1. *Phase* 0, is the preprocessing stage which consists of constructing the suffix tree of sequence S of length n in $O(n)$ linear time and space using linear algorithm [35], decomposing pattern P of length m into k subpatterns in $O(m)$ time, and then storing them in an indexed two dimensional array P_α of length k which requires $3k$ space as each subpattern is split into ($|\bar{\alpha}|$ and δ) with $\bar{\alpha}$. Given that, the time requires to access an index array is $O(1)$ time, and the time requires to answer the lowest common ancestor (LCA) on the suffix tree is $O(1)$ time [34], we analyse the rest of the algorithm as follows. At *Phase* 1, after the algorithm finds the locus of the first subpattern P_0 of P of length $|\bar{\alpha_0}|$, it uses the (for) loop to test l selected suffixes of the suffix tree in $O(l)$ time. For each l tested, *Phase* 2 should be implemented to find the occurrences of remaining subpatterns $(P_1 \dots P_{k-1})$. Here, we have three possibilities. **Case 1**, the pattern P is exist in the text and therefore the (while) loop will be executed $(k-1)$ times which is the case for finding the pattern in the text. Knowing that $(k-1)$ kangaroo jumps should be executed at this case, where at each kangaroo jump, the algorithm runs the LCA query at the current suffix that it moved to in total $O(k-1)$ time. Therefore, the time required for this case is $O(k-1)$. **Case 2**, when only the first q subpatterns are found, the algorithm will exit the while loop after testing subpattern $(q+1)$ which means that there is no occurrence for the pattern P in S. Therefore, the time required for this case is $O(q)$. **Case 3**, When only the first subpattern P_0 is located at phase 1, but there is no occurrence for the remaining $(k-1)$ subpatterns. At this case, the (while) loop will be executed only once at phase 2, and the time is $O(1)$ which is considered as an efficient time for the execution time when the pattern is not part of the text, and the algorithm requires no completion on testing the remaining of subpatterns which saves the time of the algorithm. Therefore, the time required for this case is $O(1)$ time. Since we are interested in the degree of the function $f(n)$ for the algorithm which is related to the execution time of the statements inside the (for) loop, we will ignore l. Hence, the time complexity of Algorithm 1 is $O(n+m+k)$ for the **Case 1**, $O(n+m+q)$ for the **Case 2** and $O(n+m)$ for the **Case 3**. □

According to Theorem 1, we can conclude our next theorem to find all occurrences of pattern P with "don't cares" in text S as follows.

Theorem 2. *Given a text S over the alphabet Σ of length n and a pattern P over the alphabet $\Sigma \cup \{*\}$ of length m, we can compute all occurrences of P in S in $O(n+m+k+occ(P))$ time complexity, where k is the total number of the subpatterns of P and $occ(P)$ is the total number of occurrences of P in S.* □

5 Conclusion

We have introduced our simple and efficient method which can find all the occurrences of pattern P with "don't cares" in text S. This problem is interesting as a fundamental computer science problem and is a basic need for many applications which are concerned with the occurrence of the subsequence of the original pattern sequence. In response, we designed our algorithm using linear space and time data structure with help of the *Kangaroo* method such that be able to test only selected suffixes of the *suffix tree* of S in a fast and effective way. Comparing to the work in [22] and to the others described in the related work, our algorithm adopted the logical sequential approach for testing each pattern P such that the test starts from the first subpattern of P, then it moves to the next subpattern as long as the previous test was successful which saves the time of the algorithm and speeds up the locating process. The interesting issues that will be studied in our future work are, improving our work to detect patterns with "don't cares" and errors from the text, and detecting patterns from a text contains "don't cares" characters, while maintaining our goal of the algorithm simplicity and efficiency.

References

1. Aho, A.V., Corasick, M.J.: Efficient string matching: an aid to bibliographic search. Commun. ACM **18**(6), 333–340 (1975)
2. Alamro, H., Badkobeh, G., Belazzougui, D., Iliopoulos, C.S., Puglisi, S.J.: Computing the antiperiod (s) of a string. In: 30th Annual Symposium on Combinatorial Pattern Matching (CPM 2019). Schloss Dagstuhl-Leibniz-Zentrum fuer Informatik (2019)
3. Alstrup, S., Husfeldt, T., Rauhe, T.: Marked ancestor problems. In: Proceedings 39th Annual Symposium on Foundations of Computer Science (Cat. no. 98CB36280), pp. 534–543. IEEE (1998)
4. Amir, A., Lewenstein, M., Porat, E.: Faster algorithms for string matching with k mismatches. J. Algorithms **50**(2), 257–275 (2004)
5. Bille, P., Gørtz, I.L., Vildhøj, H.W., Vind, S.: String indexing for patterns with wildcards. Theory Comput. Syst. **55**(1), 41–60 (2014)
6. Boyer, R.S., Moore, J.S.: A fast string searching algorithm. Commun. ACM **20**(10), 762–772 (1977). https://doi.org/10.1145/359842.359859
7. Chen, G., Wu, X., Zhu, X., Arslan, A.N., He, Y.: Efficient string matching with wildcards and length constraints. Knowl. Inf. Syst. **10**(4), 399–419 (2006)
8. Clifford, R., Efremenko, K., Porat, E., Rothschild, A.: Pattern matching with don't cares and few errors. J. Comput. Syst. Sci. **76**(2), 115–124 (2010)
9. Clifford, R., Porat, E.: A filtering algorithm for k-mismatch with don't cares. In: International Symposium on String Processing and Information Retrieval, pp. 130–136. Springer (2007)
10. Cole, R., Gottlieb, L.A., Lewenstein, M.: Dictionary matching and indexing with errors and don't cares. In: Proceedings of the Thirty-Sixth Annual ACM Symposium on Theory of Computing, pp. 91–100 (2004)
11. Cole, R., Hariharan, R.: Approximate string matching: a simpler faster algorithm. SIAM J. Comput. **31**(6), 1761–1782 (2002)

12. Cole, R., Hariharan, R.: Verifying candidate matches in sparse and wildcard matching. In: Proceedings of the Thirty-Fourth Annual ACM Symposium on Theory of Computing, pp. 592–601 (2002)
13. Commentz-Walter, B.: A string matching algorithm fast on the average. In: International Colloquium on Automata, Languages, and Programming, pp. 118–132. Springer (1979)
14. Crochemore, M., Hancart, C.: Pattern matching in strings. In: Mikhail, J.A. (ed.) Algorithms and Theory of Computation Handbook, pp. 11.1–11.28. CRC Press (1998). https://hal-upec-upem.archives-ouvertes.fr/hal-00620790
15. Crochemore, M., Hancart, C., Lecroq, T.: Algorithms on Strings. Cambridge University Press, Cambridge (2007)
16. Crochemore, M., Perrin, D.: Pattern matching in strings. In: Image Analysis and Processing II, pp. 67–79. Springer (1988)
17. Farach, M.: Optimal suffix tree construction with large alphabets. In: Proceedings 38th Annual Symposium on Foundations of Computer Science, pp. 137–143. IEEE (1997)
18. Fischer, J., Huson, D.H.: New common ancestor problems in trees and directed acyclic graphs. Inf. Process. Lett. **110**(8–9), 331–335 (2010)
19. Fischer, M.J., Paterson, M.S.: String-matching and other products. Tech. rep. Massachusetts Institute of Technology, Cambridge Project MAC (1974)
20. Galil, Z., Giancarlo, R.: Improved string matching with k mismatches. ACM SIGACT News **17**(4), 52–54 (1986)
21. Gusfield, D.: Algorithms on stings, trees, and sequences: computer science and computational biology. ACM SIGACT News **28**(4), 41–60 (1997)
22. Iliopoulos, C.S., Rahman, M.S.: Pattern matching algorithms with don't cares. In: Proceedings of 33rd SOFSEM, pp. 116–126 (2007)
23. Indyk, P.: Faster algorithms for string matching problems: matching the convolution bound. In: Proceedings 39th Annual Symposium on Foundations of Computer Science (Cat. no. 98CB36280), pp. 166–173. IEEE (1998)
24. Kalai, A.T.: Efficient pattern-matching with don't cares. In: SODA 2002 Proceedings of the Thirteenth Annual ACM-SIAM Symposium on Discrete Algorithms, pp. 655–656. ACM Press (January 2002). https://www.microsoft.com/en-us/research/publication/efficient-pattern-matching-dont-cares/
25. Karp, R.M., Rabin, M.O.: Efficient randomized pattern-matching algorithms. IBM J. Res. Dev. **31**(2), 249–260 (1987)
26. Knuth, D.E., Morris Jr., J.H., Pratt, V.R.: Fast pattern matching in strings. SIAM J. Comput. **6**(2), 323–350 (1977)
27. Lam, T.W., Sung, W.K., Tam, S.L., Yiu, S.M.: Space efficient indexes for string matching with don't cares. In: International Symposium on Algorithms and Computation, pp. 846–857. Springer (2007)
28. Landau, G.M., Vishkin, U.: Fast parallel and serial approximate string matching. J. Algorithms **10**(2), 157–169 (1989)
29. Liu, N., Xie, F., Wu, X.: Multi-pattern matching with variable-length wildcards using suffix tree. Pattern Anal. Appl. **21**(4), 1151–1165 (2018)
30. Nicolae, M., Rajasekaran, S.: On pattern matching with k mismatches and few don't cares. Inf. Process. Lett. **118**, 78–82 (2017)
31. Pinter, R.Y.: Efficient string matching with don't-care patterns. In: Combinatorial Algorithms on Words, pp. 11–29. Springer (1985)
32. Rahman, M.S., Iliopoulos, C.S., Lee, I., Mohamed, M., Smyth, W.F.: Finding patterns with variable length gaps or don't cares. In: International Computing and Combinatorics Conference, pp. 146–155. Springer (2006)

33. Sahinalp, S.C., Vishkin, U.: Efficient approximate and dynamic matching of patterns using a labeling paradigm. In: Proceedings of 37th Conference on Foundations of Computer Science, pp. 320–328. IEEE (1996)
34. Sung, W.K.: Algorithms in Bioinformatics: A Practical Introduction. CRC Press, Boca Raton (2009)
35. Ukkonen, E.: On-line construction of suffix trees. Algorithmica **14**(3), 249–260 (1995)
36. Wu, S., Manber, U., et al.: A fast algorithm for multi-pattern searching. University of Arizona, Department of Computer Science (1994)
37. Ziviani, N., Baeza-Yates, R.: String processing and information retrieval. In: 14th International Symposium, SPIRE 2007 Santiago, Chile, October 29–31, 2007 Proceedings, vol. 4726. Springer (2007)

Eye Movement Data Analysis

Olga Georgieva[1(✉)], Nadejda Bocheva[2], Bilyana Genova[2], and Miroslava Stefanova[2]

[1] Faculty of Mathematics and Informatics, Sofia University "St. Kliment Ohridski", 5 James Bourchier Blvd., 1164 Sofia, Bulgaria
o.georgieva@fmi.uni-sofia.bg

[2] Institute of Neurobiology, Bulgarian Academy of Sciences, 1113 Sofia, Bulgaria
nadya@percept.bas.bg

Abstract. The aim of the present study is to investigate the separation abilities of three statistical parameters for grouping participants in the visual-motor experiment by their age and gender. These parameters represent different characteristics of the decision-making process and were determined by applying the hierarchical drift diffusion model to the response time and accuracy of the experimental data [1]. The objective function cluster analysis was applied to explore distinct data spaces formed by the parameters' data. The ability for grouping is assessed and interpreted according to the differences in the subjects' capabilities to perform the visuo-motor task. The study compares the conclusions based by drift-diffusion model using Bayesian parameter estimation with those based on the cluster analysis in terms of ability to distinguish the performance of different age groups. The investigation of gender effects are uniquely investigated by cluster analysis technique.

Keywords: Decision making · Visuo-motor task · Cluster analysis · Fuzzy clustering

1 Introduction

A significant part of the brain studies concerns the revealing existing dependencies of the biosignal parameters. The common implementation base of these purposes is the new generation of communication devices as well as the new information technologies. The problem of research is to investigate and apply an appropriate algorithm for data processing enabling information retrieval in order to bring significant information about the existing dependencies of the brain activity [10, 12].

The potential of the unsupervised learning algorithms as cluster analysis could be considered as possible alternative for biosignal discrimination. These methods are powerful in dealing with complex and uncertain information. They find groups within the data and thus conclude about existing relations and features among them. Different brain states have been benefited by this approach as a basis for theoretical and experimental evidence for a scientific forecast of the human condition [10, 11].

The process of human decision making involves a multitude of processes - from coding stimulus information to organizing a response based on the decision choice. A successful approach to separate the contribution of these processes is the drift diffusion model [5–9]. The model is applicable for two-choice decision tasks and assumes that the decision is reached by sequential accumulation of evidence in support of the two decision choices. It combines the information about the accuracy and the speed of performance and decomposes the processes not related to the decision in a separate parameter (t-c) that describes the time needed to code the stimulus information and prepare the response. The model assumes that the evidence in support of the two possible choices accumulates in time and this process is noisy. The speed of evidence accumulation depends on the task difficulty and is characterized by a parameter labelled drift rate (v-c). An additional parameter (a-c) describes the balance between the accuracy and speed of the response representing the decision boundary between the two choices – if this boundary is large, more time is needed to make a choice, however, the probability of accidental errors diminishes. If there is no imbalance in stimulus presentation or a bias in selecting one choice more often, the starting point of evidence accumulation is at the middle of the boundary between the two choices. However, all main parameters of the model have variability due to instability to keep a constant criterion in the decision process, the random variations in evidence accumulation from trial to trial and the variability in the non-decision processes.

A Python toolbox named Hierarchical Drift Diffusion Model (HDDM) [13] applies the drift-diffusion model by using Bayesian parameter estimation. It is flexible, allows estimation of both individual and group parameters, tolerates missing values and requires less data to estimate model parameters. However, coding mixed-effects models with the toolbox is a challenge. In certain cases, it is quite difficult to evaluate the interaction of between-subject factors. More complex models are also time-consuming.

In this study we try to evaluate whether, based on the parameters evaluated by HDDM, it is possible to estimate the contribution of other between-subject factors, not included in the analysis and to obtain additional information about different characteristics of the stimulus conditions or experimental groups. The first part of the study compares the conclusions based on the hypothesis testing in the HDDM with those based on the application of a methodology by clustering algorithm about the informativeness of different experimental conditions and respective parameters of the drift diffusion model. The assessment focuses the ability to distinguish the performance of different age groups. The last study part extracts information about gender effects and their interaction with age that were not assessed by the HDDM.

2 Data Description

Data from four types of visual experiments have been examined. Three types of movements and one static condition were used. The stimuli were the so-called glass patterns. They are generated by repeating the initial dot pattern after being transformed by a certain rule e.g. all points are offset or rotated at a certain angle or offset from the center of the set. In this way a pattern is formed in which each point is paired with another. In our experiments, the points were offset from a given center, but it was displaced from the mid-point of the image in a horizontal direction. The pairs of dots are relatively close together (at a distance of 60 pixels = 2 cm) and rotated in such a way that if connected with a line, most lines would intersect at the displaced center of the pattern. Out of 25 pairs of points (50 points in total) 18 pointed to the center of the pattern, and 7 pairs were randomly oriented (this is called coherence of 72%). This description corresponds to the static condition in the experiments.

The other conditions used are combined, flicker and motion. In all of them the lifetime of the dots was three frames (100 ms). In the flicker condition, one-third of the pairs are re-generated elsewhere on every frame keeping their initial orientation. This gives the impression of movement, but it is not related to the orientation of the pairs. In the combined condition, the pairs move in the direction of their orientation, so that those pointing to the center of the set move away from it and the others (7) move in a random direction. Again, each frame updates the position of one-third of the pairs. In motion condition, there are no pairs, and 18 $\times$ 2 (36) points in the pattern move away from a common center, while the remaining 7 $\times$ 2 (14) move randomly.

Data of 35 observers participating in the four experiments were collected. The subjects are classified in three age groups: 12 young (19 to 34 years, median = 23 years); 11 middle aged (36 to 52 years, median = 44 years); 12 old (57 to 84 years, median = 72) having a parity representation of both sexes in each group. Each pattern was presented to each participant 20 times in random order. Each condition was performed on a separate day. The task of the participants was to determine whether the center of the patterns was to the left or to the right of the screen. They had to make a saccade to the perceived pattern center and to press a mouse button according to their decision.

3 Methodology

The present study aims to analyze the capabilities to extract information based on statistical parameters, which represent the relationship between the accuracy of the response and the response time when examining data from eye saccade movements in the visuo-motor task. The problem needs to explore different spaces formed by these data in order to answer which parameters best define the difference between the age groups, as well as to assess the impact of the gender on their performance abilities.

For this search the raw data of the four experiments were processed to calculate the statistical characteristics related to decisions in a two-choice task determined by applying the HDDM to the response time and accuracy of the experimental task [1]. These parameters represent different properties of the decision-making process:

A) Time data not related to decision making processes, t-c. It represents the time needed for coding the stimulus information and for organizing motor response.
B) Boundary between the two alternatives, a-c in decision. This parameter represents the individual willingness for higher accuracy or faster speed.
C) Rate of accumulation of evidence about the two alternatives, v-c.

Two types of data spaces could be organized to reveal different information:

1. The separation abilities of each parameter: t-c, a-c and v-c, could be investigated by processing the corresponding four-dimensional space formed by each parameter data obtained via all four experiments.
2. The distinguishing ability of each experiment namely static, combined, flicker and motion, could be discovered by processing the corresponding three-dimensional data space formed by the data of the parameters t-c, a-c and v-c obtained for the respective experiment.

Our understanding is that clustering based on the parameters data characterizes the decision-making process, whereas clustering by movement types - performance accuracy related to the task difficulty. Exploring the structure of these spaces by determining significant data groups we would be able to detect the influence of the separate characteristics of the calculated parameters as well as the condition - combined, motion, flicker, static on separating the contribution of the age and gender on the decision process. Due to the lack of a reference model, studies of these data spaces can be carried out using unsupervised learning methods as cluster analysis. For each formed data space the research procedure follows several steps:

a) Data clustering;
b) Evaluation of clustering quality to find the optimal number of clusters;
c) Comparative analysis of the obtained grouping;
d) Visualization and interpretation of the results.

According to the preliminary investigations the data do not present clear structure due to the complexity of the visuo-motor factors' dependencies. In this situation, an effective solution could be found by methods of objective function clustering. These are methods based on optimization of clustering criterion for desirable separation. The clusters are described by their center, which is a point in the data space that is most representative for the cluster in probabilistic sense. Further, we apply fuzzy clustering technique as a good opportunity to deal with uncertainty of the spaces. Its advantage is that it assesses belonging, as well as the degree of belonging to the distinct clusters.

Fuzzy-C-Means (FCM) Algorithm
Fuzzy clustering technique is particularly successful in partitioning not well separated data groups with vague and uncertain boundaries. Every point of the data space belongs to the clusters with degree of membership, which is a value between 0 and 1. If the data is close to the cluster center, the membership degree is closer to one. FCM is an objective function-based algorithm with clustering criteria J that minimizes the following sum [4]:

$$J = \sum_{i=1}^{c} \sum_{k=1}^{N} u_{ik}^{m} \|x_k - v_i\|^2, \qquad (1)$$

where u_{ik} denotes the membership degree of the data point x_k, $k = 1,\ldots, N$, to the i-th cluster center v_i, $i = 1,\ldots, c$. Here N is the number of data in the data space and c is the number of clusters. The coefficient $m \in [1, \infty)$ determines how much clusters may overlap and its default value is $m = 2$. As we don't have a preliminary knowledge about the shape and orientation of the searched clusters, Euclidean distance is incorporated as a data distance measure of (1).

Quality of Clustering
Several indexes are calculated to evaluate the quality of clustering:

1) Average within cluster distance (AWCD) value estimates the data distances to the cluster center in the clusters. Minimum value is preferred, however the "knee" principle is applied to determine the best clustering for a given data space.

$$AWCD = \frac{1}{c}\sum\nolimits_{i=1}^{c} \frac{\sum_{k=1}^{N} u_{ik}^{m} u \|x_k - v_i\|^m}{\sum_{k=1}^{N} u_{ik}^{m}} \tag{2}$$

2) Average partition density (APD) assesses the density of the clusters. An index measures the fuzziness of the partition but without considering the data set itself. Good partitions are indicated by large values of APD.

$$APD = \frac{1}{c}\sum\nolimits_{i=1}^{c} \frac{S_i}{\sum_{k=1}^{N} u_{ik}}, \tag{3}$$

where $S_i = \sum\limits_{k=1}^{N} u_{ik}$ for every point k that $(x_k - v_i)(x_k - v_i)^T < 1$.

3) The cluster volume, V_i, $i = 1,.., c$, is calculated by a sum of the memberships values that form the cluster. Maximum value indicates better clustering.

The AWCD, APD and V_i indexes are parameters that evaluate the quality of the obtained data grouping itself, but not the classification capabilities of the obtained grouping. In order to assess the extent to which the obtained clusters cover actually existing groups in data in terms to the age and gender, it is necessary to account for the degrees of affiliation of the subject data to each cluster presented. As all data belong to all clusters in order to evaluate the subject affiliation the maximum degree of membership is taken to determine the affiliation to a particular cluster.

4 Results and Analysis

Results of FCM application to the four-dimensional data spaces of each experimental parameter: t-c, a-c, v-c, are considered.

4.1 Age Grouping Assessment

The obtained values for AWCD and APD indexes allow to set appropriate data separation among division in 2, 3, 4 and 5 clusters as well as to compare the three studied data spaces t-c, a-c, v-c (Table 1). Best clustering in terms of group compactness, which means better informativeness, is identified in space t-c as the APD index takes highest values, followed by space v-c. The least informative is the space a-c. This result means that the parameter that could best distinguishes the age of the participants in a decision making task is the time needed for coding the stimulus information and for organizing motor response. The parameters that are directly involved in making a decision like the rate of evidence accumulation or the boundary between the two choices are less informative for this task.

The results of AWCD enable to set the proper number of clusters. However, this answer is not straightforward. By applying the knee method to all data spaces we found that most representative is clustering in 3 and 4 clusters. Bearing in mind the number of data, division in more than five clusters does not give reliable information.

Table 1. Clustering indexes results of the distinct parameters

Index \c	2	3	4	5
t-c data space				
AWCD	0,279133	0,179799	0,129162	0,053895
APD	0,887900	0,886915	0,910591	0,913007
a-c data space				
AWCD	0,710794	0,489768	0,377499	0,261670
APD	0,638586	0,766424	0,769378	0,779237
v-c data space				
AWCD	0,555400	0,351397	0,270981	0,217894
APD	0,752245	0,855247	0,827687	0,851103

Further consideration of t-c data space division as most informative one could reveal more existing dependences. Thus, when dividing into three clusters, the interpretability of the results is directly referred to the three studied age subjects groups, whereas at c = 4 three significant clusters and one of outliers could be discussed.

The coordinates of the cluster centers give us some more inside information about the obtained grouping (Table 2). For separation in three clusters, c = 3, the first cluster comprises most of the young and part of the middle aged adults, the second cluster includes part of the elderly people and the third - most of the elderly and part of the middle aged subjects. This division is not able to recognize the middle aged persons, whereas the two others – young and old, are well defined. The division in four clusters, c = 4, identifies well the young and old people as the first cluster comprises only young people and the fourth cluster includes only elderly people. The second cluster is formed mostly by middle aged; the third one is mostly formed by old subjects.

Table 2. Cluster centers of t-c parameter data clustering grouped into 3 and 4 clusters

c	Combined	Flicker	Motion	Static	c	Combined	Flicker	Motion	Static
1	0,3219	0,3314	0,3340	0,3264	1	0,2786	0,2589	0,2479	0,2534
2	0,9736	1,0641	1,3208	0,6849	2	0,3993	0,4169	0,4737	0,4298
3	0,5477	0,5353	0,5965	0,5439	3	0,5865	0,5795	0,6284	0,5729
	–	–	–	–	4	0,9609	1,0519	1,3070	0,7344

It could be summarized that the middle aged group is difficult to distinguish, especially when separation is in three clusters. The elderly group is more scattered than the young one in both clustering (Fig. 1). According to the cluster centers values, the dynamic conditions better distinguish participants then the static one. In particular, best one is motion condition, where no form information (e.g., orientation grouping) is presented. This implies that the absence of form information (no orientation grouping) in the visual motion task allows better separation of the age groups.

In order to assess the extent to which the obtained clusters cover actually existing data groups formed by the age and gender, it is necessary to account for the degrees of membership of each person's data to each cluster obtained. The maximum degree of membership determines the affiliation with a particular cluster. The affiliation of participants from different age groups to a cluster for each of the studied spaces in 4 clusters is presented in Figs. 1, 2 and 3, where young subjects' data are in pink, in green are data of the middle group and in blue – elderly subjects. Each examined person is represented by a line connecting it to the center of a cluster. The length of the line corresponds to the degree of membership to that cluster.

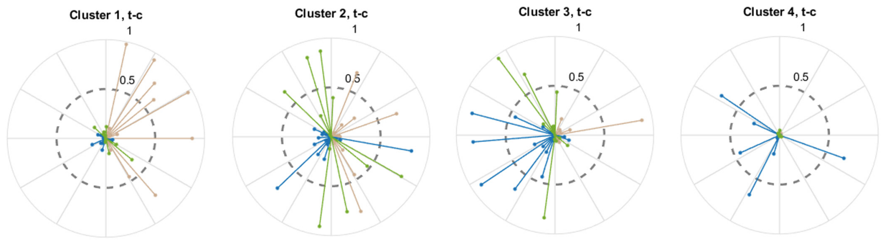

Fig. 1. Clustering in 4 clusters based on t-c: time unrelated to the decision-making process.

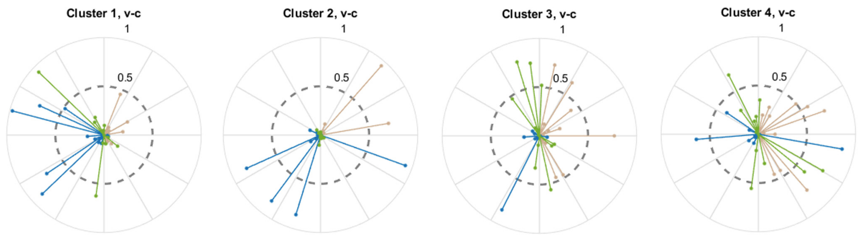

Fig. 2. Clustering in 4 clusters via v-c: rate of information accumulation for the two alternatives.

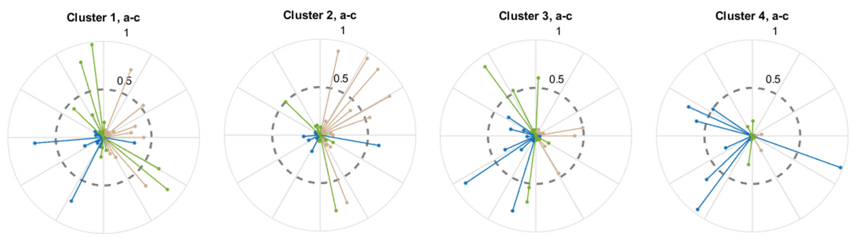

Fig. 3. Clustering in 4 clusters based on a-c: the boundary between the two alternatives

The results of three-dimensional spaces organized for the data of the different conditions of the experiments are less informative and will not be presented here.

4.2 Gender Grouping Assessment

The assessment of the gender differentiation of the subjects participated in the visual experiments can be done by the grouping of the four-dimensional space. For this purpose, the volume of clusters, V_i, $i = 1, c$ formed from the data for the two genders are compared. The respective relative volume values are calculated in order to account for the different number of female and male participants in each group.

Relative value of the cluster volumes of t-c data set separation shows that males are more represented in the clusters of young people and part of the middle-aged, whereas women predominantly form the cluster of elderly. The bold values at Table 3 present the highest volume for each gender for separation in 3 and 4 clusters, respectively.

Table 3. Relative values of the cluster volumes for the two genders of t-c data clustering

	c = 3			c = 4	
Cluster	Female	Male	Cluster	Female	Male
1	0,3019	**0,5844**	1	0,1598	0,3268
2	0,1544	0,0834	2	0,3178	**0,4033**
3	**0,5438**	0,3322	3	**0,3855**	0,2110
			4	0,1369	0,0589

By the same method the two genders are distinguished for each group separately (Table 4). Again, female are less likely to form the group of young people, while male are strongly represented in it: 0,559 vs. 0,8799 for division into 3 clusters and 0,3645 vs. 0,6945 for division into 4 clusters. Conversely, women more strongly form the elderly group, whereas male are less represented. These results are visible at Fig. 4a and b. The interaction between age and gender obtained here for a task of decision making based on dynamic visual information is in agreement with previous data analysis on motion direction discrimination [2].

Table 4. Relative volumes of clusters calculated for the two genders in t-c space; a) division in three clusters; b) division in four clusters

a)	Young		Middle aged		Elderly	
Cluster	Female	Male	Female	Male	Female	Male
1	**0,559**	**0,8799**	0,3104	**0,5859**	0,079	0,2384
2	0,0213	0,0191	0,0291	0,0211	0,3906	0,2105
3	0,4197	0,1011	**0,6605**	0,3931	**0,5304**	**0,5511**
b)	Young		Middle aged		Elderly	
Cluster	Female	Male	Female	Male	Female	Male
1	**0,3645**	**0,6957**	0,1048	0,0969	0,0443	0,0881
2	0,3223	0,2507	**0,4896**	**0,6369**	0,109	**0,3866**
3	0,2614	0,0444	0,3853	0,2572	**0,4891**	0,3669
4	0,0118	0,0092	0,0204	0,0091	0,3576	0,1585

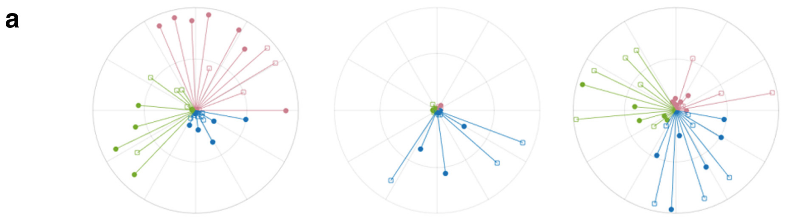

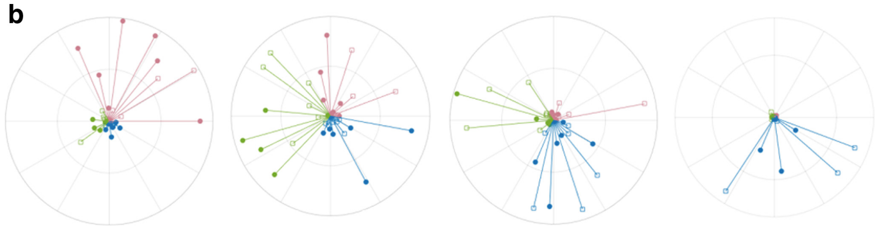

Fig. 4. a. Gender distribution for division into 3 clusters of t-c groups of young (pink), middle aged (green) and elderly (blue); female - empty square, male - filled circles. b. Gender distribution for division into 4 clusters of t-c groups of young (pink), middle aged (green) and elderly (blue); female - empty square, male - filled circles.

5 Conclusion

The results shown can be used to account for existing dependencies in the age and gender to deal with the visual decision making task. The accuracy of the responses for different types of stimuli and reaction time are accounted for. The results of separating the age groups based on the values of the parameters of the drift diffusion model are in agreement with the conclusions based on the probability to distinguish the three age groups in the different tasks obtained by the HDDM [1]. In our experimental condition the non-decision time provides better separation of the age groups than any other parameter. In single experiments Ratcliff and colleagues found that the boundary separation and the non-decision time distinguish most the young and the old participants [9]. They showed that the non-decision time is the parameter that correlates most between the different studies with the same participants. This result may imply that the non-decision time is the most stable individual characteristic of the participants in the two-choice decision tasks.

Our findings suggest that the differences in the experimental conditions in a common task significantly affect various aspects of the process of decision making and allow separating the participants in the experiments by some individual characteristics in the space of the HDDM parameters. The correspondence of the conclusions based on the HDDM and the clustering data of our study validates the possibility to complement the analysis of the subjects' performance in two-choice decision tasks by method based on fuzzy clustering analysis. The application of this approach provides additional information based on the cluster separation. It implies that in a visual task where the location of the pattern center could be determined by form cues (orientation), motion cues (direction of motion) or by their combination, the dynamic conditions provide better separation of the age groups. These conclusions are in agreement with the knowledge that static information is predominantly processed by the ventral pathway in the brain and dynamic information by the dorsal pathway [3]. The first pathway is slower and involves the recognition of images as the final stage of information processing, while the dorsal pathway is associated with determining the location of objects, their spatial location and their movement.

Our results also imply that between-factors not studied by HDDM can be evaluated based on the individual values of the parameters extracted from the model application. Clustering methodology is successful to the gender estimation obtaining results similar to our previous findings. This possibility allows the simplification of model coding and estimation by HDDM. Improvement of the interpretability of the clustering results is also expected by processing of the raw data recorded by the eye tracker.

Acknowledgement. This work was supported by the National Science Fund under Grant DN02/3/2016 "Modelling of voluntary saccadic eye movements during decision making" and by the Science Fund of Sofia University "St. Kliment Ohridski" under project no. 80-10-61/13.04.2020.

References

1. Bocheva, N., Genova, B., Stefanova, M.: Drift diffusion modeling of response time in heading estimation based on motion and form cues. Int. J. Biol. Biomed. Eng. **12**, 75–83 (2018)
2. Bocheva, N., Georgieva, O., Stefanova, M.: Data analysis of age-related changes in visual motion perception. In: ICAART, no. 1, pp. 556–561 (2011)
3. Goodale, M.A., Milner, A.D.: Separate visual pathways for perception and action. Trends Neurosci. **15**, 20–25 (1992)
4. Bezdek, J.C.: Pattern Recognition with Fuzzy Objective Function Algorithms. Plenum Press, NY (1981)

5. Ratcliff, R., Smith, P., Brown, S., MacKoon, G.: Diffusion decision model: current issues and history. Trends Cogn. Sci. **20**(4), 260–281 (2016)
6. Ratcliff, R., Smith, P.: Perceptual discrimination in static and dynamic noise: the temporal relation between perceptual encoding and decision-making. J. Exp. Psychol. Gen. **139**(1), 70–94 (2010)
7. Ratcliff, R.: A diffusion model account of response time and accuracy in a brightness discrimination task: fitting real data and failing to fit fake but plausible dat. Psychon. Bull. Rev. **9**, 278–291 (2002)
8. Ratcliff, R., MacKoon, G.: The diffusion decision model: theory and data for two-choice decision tasks. Neural Comput. **20**(4), 873–922 (2008)
9. Ratcliff, R., Thapar, A., MacKoon, G.: Aging and individual differences in rapid two-choice decisions. Psychon. Bull. Rev. **13**(4), 626–635 (2006)
10. Viswanathan, M., Whangbo, T.K., Yang, Y.K.: Data mining in ubiquitous healthcare. In: Kimito, F. (ed.) New Fundamental Technologies in Data Mining. InTech (2011). http://www.intechopen.com/books/newfundamentaltechnologies-in-data-mining/data-mining-inubiquitoushealthcare. ISBN:978-953-307-547-1
11. Di, W., Zhu, D.: Study on brainfag based on EEG signal analysis. In: Proceedings of ETP International Conference on Future Computer and Communication, pp. 134–137 (June 2009)
12. Calvo, R.A., D'Mello, S.K.: Affect detection: an interdisciplinary review of models, methods, and their applications. IEEE Trans. Affect Comput. **1**(1), 18–37 (2010)
13. Wiecki, T.V., Sofer, I., Frank, M.J.: HDDM: hierarchical Bayesian estimation of the drift-diffusion model in Python. Front. Neuroinform. **7**, 1–10 (2013)

Machine Learning for Neuro/Biological Modeling

Computational Complexity of Kabsch and Quaternion Based Algorithms for Molecular Superimposition in Computational Chemistry

Rafael Dolezal[1,2](✉), Katerina Fronckova[3], Ayca Kirimtat[1], and Ondrej Krejcar[1]

[1] Faculty of Informatics and Management, Center for Basic and Applied Research, University of Hradec Kralove, Rokitanskeho 62, 50003 Hradec Kralove, Czech Republic
rafael.dolezal@uhk.cz
[2] Biomedical Research Center, University Hospital Hradec Kralove, Sokolska 581, 500 05 Hradec Kralove, Czech Republic
[3] Department of Informatics and Quantitative Methods, University of Hradec Kralove, Rokitanskeho 62, 50003 Hradec Kralove, Czech Republic

Abstract. This work deals with the analysis of Kabsch and quaternion algorithms, which may be used for 3D superimposition of molecules by rigid roto-translation in computational chemistry and biology. Both algorithms, which are very important for *in silico* drug design, were studied from the point of view of their non-trivial mathematical structure. Their computational complexity was investigated by a superimposition of various random pseudo-molecules with 2 – 100,000 atoms in Matlab. It was found that both proposed algorithm implementations exhibit the same asymptotic time computational complexity of $O(n)$, with the quaternion algorithm involving a higher number of floating-point operations (FLOPs) and showing lower computational performance in terms of serial CPU time.

Keywords: Molecular superimposition · Computational complexity · Kabsch algorithm · Quaternions · Drug design

1 Introduction

Over the last few decades, rational approaches in computational chemistry, computational biology, bioinformatics, chemoinformatics and drug research have increasingly applied various algorithms, which can predict, under certain conditions, structures of chemical substances with the desired biological activity before they are synthesized and biologically tested on living organisms [1, 2]. This gradually leads to a qualitative departure from outdated drug development methods based on trial-and-error heuristic approaches towards cheaper, faster and more efficient ways of drug design using modern biomedical technologies. The impact of these applied information technologies is evidenced mainly by more than 200 drugs that have been successfully introduced into clinical trials with significant help of so-called computer-aided drug design (CADD) methods [3]. However, CADD methods are not widespread globally and their potential is not fully realized at present. On the other, CADD methods still present a challenge for computer scientists, since the required high accuracy in the desired predictions may be satisfied only by extremely demanding calculations.

From the vast number of different CADD methods (e.g. pharmacophore analysis, structure-activity relationships, molecular docking, molecular metadynamics, Free energy perturbation, core hopping, virtual screening, *ab initio* calculations), we will select and focus on a crucial problem of efficient superimposing two chemical molecules in a three-dimensional Euclidean space [4]. The superimposition of two molecules is an important computational operation performed, for example, to assess similarity of the electron density of chemical structures, to create a reference Cartesian system for molecular interaction fields in 3D structure-biological activity analyses (3D QSAR), or to quantify conformational changes of molecules in molecular dynamics studies [5, 6]. In a certain variation, the problem of the best superimposition of two structures is also encountered in bioinformatics, where it has a related principle of searching for similarities between text strings that represent the genetic code as a sequence of nucleic acids.

We will focus, in this work, on the presentation of the computational part of the roto-translation of molecules in the context of computational chemistry. The aim of this work will, thus, be to outline present techniques to superimpose two molecules that differ in a particular way (e.g. by the constitution, configuration, conformation, position and rotation in 3D space). We will try to define and interpret the problem from the point of view of theoretical computer science. This part will be followed by an overview of possible program implementations that superimpose two molecules and by an experimental analysis of their computational complexity in Matlab 2018. Although molecular superimposition has been to some extent reported in the literature, this work clearly proves and explains that the Kabsch algorithm is better for implementation in bioinformatics tasks than the quaternion based superimposition algorithm.

2 Problem Definition

At first, we introduce the problem of optimal superimposition of two molecules A and B by defining each molecule as a separate, rigid object in three-dimensional space. We will characterize each molecule in a simplified way as a point group in 3D space using Cartesian coordinates of all n atoms. We will use a matrix notation, where chemical symbols of the elements (Z, consisting of one or two characters) are in the first column and the Cartesian coordinates x, y and z, expressed in units Å (10^{-10} m) in the next three columns. We call this matrix molecular identity matrix $\mathbf{I}$ (1).

$$\mathbf{I} = \begin{bmatrix} Z_1 & x_1 & y_1 & z_1 \\ \vdots & \vdots & \vdots & \vdots \\ Z_n & x_n & y_n & z_n \end{bmatrix} \tag{1}$$

The simplest case of superimposing two identical molecules can be solved as a problem of minimizing the distances of the same atoms in their identity matrices $\mathbf{I_A}$ and $\mathbf{I_B}$ (Fig. 1). If two different molecules are to be superimposed, it is necessary to specify additional superimposition rules for two molecules in mathematical terms. For instance, it is possible to superimpose only some important atoms or groups of atoms in molecules (e.g. pharmacophores) or to add a factor that favors the closest superimposition of the atoms that are most chemically similar (e.g. bioisosteric groups, atoms in the same group of elements). In the special case of constitutional isomers (e.g. 1,4-dichlorobenzene and 1,3-dichlorobenzene, Fig. 1, right part), we can also use the same algorithm as in the case of the superimposition of identical molecules roto-translated in 3D space which minimizes Euclidian distances between the corresponding chemical elements in the identity matrices $\mathbf{I_A}$ and $\mathbf{I_B}$. In the case of "very" different molecules, it is therefore necessary to introduce similarity or priority criteria for matching atoms, but this is evidently an arbitrary condition that opens door to various solutions.

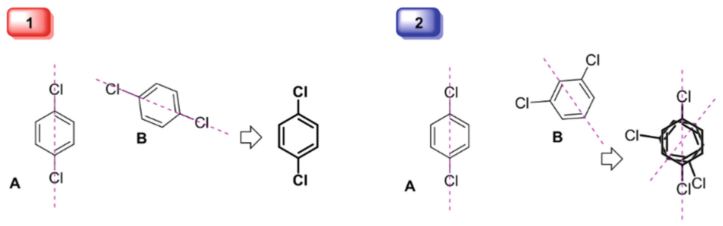

Fig. 1. A symbolic superimposition of two molecules in 2D space, which may be identical (1) or different (2).

Thus, the problem of superimposing two molecules is to minimize the distances of the same or similar atoms in the two molecules. In the case of superimposing so-called conformational isomers or proteins, root-mean-square distance (RMSD) is used to evaluate the achieved superimposition. When comparing conformers A and B, i.e. two molecules with the same identity and connectivity, the calculation of RMSD is given by Eq. (2):

$$\mathrm{RMSD} = \sqrt{\frac{1}{n}\sum\nolimits_{i=1}^{n} (x_i^A - x_i^B)^2 + (y_i^A - y_i^B)^2 + (z_i^A - z_i^B)^2} \tag{2}$$

where x_i, y_i and z_i represent coordinates of the same atoms in the identity matrices $\mathbf{I}$ of molecules A and B. The RMSD function in this definition can only be used to characterize a pair of the same molecules in a different conformations. For instance, RMSD can be utilized to compare results of X-ray analysis and molecular docking simulation of a drug-receptor complex. When calculating RMSD for two conformers, distances between two corresponding atoms in the identity matrices $\mathbf{I_A}$ and $\mathbf{I_B}$ are simply evaluated. In the case of two different molecules, RMSD could be alternatively calculated from all intermolecular atom pair distances. In such a case, the asymptotic time calculation complexity of the RMSD calculation has a value of $O(n \times m)$.

In practice, several simplifying rules can be applied to achieve lower complexity of RMSD calculations, because this measure should be simple in order to be utilized in superimposing algorithms as an objective function which should be minimized. Then the optimal superimposing algorithm can be selected for massive calculations with millions of molecules.

3 State of the Art

3D molecular superimposition currently plays an important role in studies of energetic, physical-chemical, and biological properties of chemical substances (e.g. small molecule drugs, proteins, nucleic acids). The basic difficulty in superimposing molecules is that there are many ways to superimpose molecules. This makes the problem inherently very complex, especially if the conformational flexibility is allowed. In practice, therefore, various heuristic approaches or sampling techniques are used to perform molecular superimposition.

In principle, molecular superimposition techniques can be divided into two basic categories: 1) comparing dimensionless atoms or groups of atoms (e.g. functional groups or pharmacophores); 2) comparing atoms or groups of atoms having a volume. From a computational point of view, the least squares methods, genetic algorithms, Monte Carlo algorithms, brute force algorithms or simulated annealing are used in practice to superimpose two molecules [7]. From a chemical point of view, superimposition methods can be divided into those that consider the simple qualitative identity of dimensionless atoms and those that are derived from maximizing the electron density overlap between two molecules [8]. In addition, various approximate superimposition algorithms that are inaccurate but very fast are used in practice (e.g. algorithms for projecting chemical structures into a symmetric icosahedron, maximization of molecular surface overlap). Other algorithms are based on the insertion of elastic bonds between similar atoms of the ordered molecules and subsequent geometrical minimizing the potential energy of the system thus defined. However, many of these algorithms are implemented in commercial programs for computational chemistry and revealing their structure or determining their asymptotic time complexity is quite demanding due to the unavailability of the program source codes [9].

Mathematically, the problem of superimposing two molecules is commonly solved by orthogonal rotation of one molecule, with RMSD being an objective function that needs to be minimized. In the case of protein alignment, RMSD is calculated only for alpha carbons of the same amino acids. Several least squares algorithms have been proposed to find a rotation that minimizes RMSD [10]. The most effective superimposition methods require finding the eigenvectors of a matrix of squares of interatomic distances (e.g. Kabsch method, Diamond method) [11, 12]. Currently, superimposing techniques are still evolving and turn out to be more computationally efficient than older matrix-based methods. For example, a quick and easy iterative Newton-Raphson (NR) superimposition method that determines the eigenvalues of the quadratic molecular distance matrix from its characteristic polynomial may be mentioned [13].

Based on the NR method, a quaternion based algorithm was lately proposed which seems to be very efficient and less complex in comparison to the Diamond algorithm [14]. Quaternion algorithms are utilized for example in molecular docking software to superimpose various molecules.

In the study, we will focus on two types of superimposing algorithms, namely on the Kabsch algorithm which uses 3 × 3 rotation matrices and on the quaternion method which applies 4 × 4 rotation matrices. We will try to briefly describe their computational complexity and compare them experimentally in Matlab. Up to our best knowledge, performance and scalability testing of both algorithms has not been published yet.

4 Methodology and Proposed Solutions

4.1 Formal Definition of Superimposition

Let us have two vectors $\pi = \{p_1, p_2, \ldots, p_n\}$ and $\rho = \{r_1, r_2, \ldots, r_n\}$, which denote two point groups with one-to-one correspondence. Each component p_i and r_i has three subcomponents: $(p_i(x), p_i(y), p_i(z))$, $(r_i(x), r_i(y), r_i(z))$. Assuming that the vectors π and ρ have properties of a rigid body, the superimposition problem can be defined as finding the optimal rotation matrix $\boldsymbol{R}$ and the translation vector t so that the following holds (3):

$$RMSD = \sqrt[2]{\frac{e}{n}}; e = \min|\mathbf{R}\pi + t - \rho|^2 = \min \sum\nolimits_{i=1}^{n} |\mathbf{R}p_i + t - r_i|^2. \tag{3}$$

The task defined in this way belongs to the problems of finding the least squares. It can be shown that the optimization of translation vector t is independent of rotation (4–6):

$$\frac{\partial e}{\partial t} = \frac{\partial}{\partial t} \sum\nolimits_{i=1}^{n} |\mathbf{R}p_i + t - r_i|^2 = \sum\nolimits_{i=1}^{n} 2\frac{\partial(\mathbf{R}p_i + t - r_i)}{\partial t}(\mathbf{R}p_i + t - r_i) = 0, \tag{4}$$

$$\frac{\partial e}{\partial t} = \sum\nolimits_{i=1}^{n} (\mathbf{R}p_i + t - r_i) = 0 \rightarrow t = \frac{\sum_{i=1}^{n} r_i}{n} - \mathbf{R}\frac{\sum_{i=1}^{n} p_i}{n}, \tag{5}$$

$$t = centroid(\pi) - \mathbf{R}centroid(\rho). \tag{6}$$

Importantly, the rotation of a centroid point is identity. It follows that after moving both vectors π and ρ to their centroids, the optimal superimposition can be simply found by rotating the vectors (7):

$$e = \min \sum\nolimits_{i=1}^{n} \left|\mathbf{R}p_i' - r_i'\right|^2, \text{where } p_i' = p_i - \frac{\sum_{i=1}^{n} p_i}{n} \text{and } r_i' = r_i - \frac{\sum_{i=1}^{n} r_i}{n}. \tag{7}$$

4.2 Kabsch Algorithm

In this subsection, our implementation of Kabsch algorithm is described. This algorithm was designed to minimize RMSD for two molecular systems A and B with defined atom one-to-one correspondence, which optimizes the rotation matrix **R** (8).

$$RMSD = \sqrt[2]{\frac{e}{n}}; e = \min\|\mathbf{I_B R} - \mathbf{I_A}\|^2. \tag{8}$$

The Kabsch algorithm can be separated into three main steps:

1. translation of the geometric center of molecule A (e.g. centroid) into the geometric center of molecule B,
2. calculation of the covariance matrix,
3. calculation of the optimal rotation matrix **R**.

Translation of molecule A requires the calculation of the geometric centers of molecules A and B. The calculation can be characterized by a simple algorithm whose time complexity is given by the number of atoms n in a given molecule, respectively in the corresponding identity matrix **I**, as $O(n)$.

```
function mid = ctrd(I,n) % I is an identity matrix
mid = [0, 0, 0];
for (int i = 1; i <= n; i++) {
   mid (1,1) = mid (1,1) + I(i,2);
   mid (1,2) = mid (1,2) + I(i,3);
   mid (1,3) = mid (1,3) + I(i,4);}
mid = mid./n;
```

The translation itself is accomplished by determining the translation vector t, which is subtracted from the coordinates of the mobile molecule B. Again, it is a calculation with time complexity of $O(n)$, which is dependent only on the number of atoms n in molecules A and B.

```
mid1 = ctrd(I_A,n); % I_A is the identity matrix of A
mid2 = ctrd (I_B,n);
t = mid2 - mid1,
function C = shift (I_B, n, t)
for (int i = 1; i <= n; i++) {
   I_B(i,2) = I_B(i,2) - t(1,1);
   I_B(i,3) = I_B(i,3) - t(1,2);
   I_B(i,4) = I_B(i,4) - t(1,3);}
C = sqrt(sum(t.*t)); % returning the magnitude of t
```

Calculating the covariance matrix **H** from the identity matrix of molecule A ($\mathbf{I_A}$) and the shifted molecule B ($\mathbf{I_B}$) is a mathematical operation that involves transposition and multiplication of the matrices ($\mathbf{H} = \mathbf{A^T B}$). Summing up the transposition and the product into one algorithm, this calculation shows an asymptotic time complexity of $O(n)$. At this point, the algorithm assumes that the matrices $\mathbf{I_A}$ and $\mathbf{I_B}$ contain the same number of n corresponding atoms (i.e. unmatched atoms have to be excluded from the calculation).

```
function H = covariance (I_A, I_B, n)
H = zeros(3,3);
for (int i = 2; i <= 4; i++) {
  for (int j = 2; j <= 4; j++) {
    for (int k = 1; k <=n; k++) {
    H(i-1,j-1) = H(i-1,j-1) + I_A(k,i)*I_B(k,j);}}}
```

However, it should be recalled here that iterative multiplication of square matrices that is performed in the covariance calculation has generally time computational complexity of *$O(n^3)$* due to three nested `for` loops, as seen in the above algorithm. However, in the above multiplication of matrices $n \times 3$, the asymptotic time complexity in the big O notation is only proportional to n. Regarding multiplication of matrices of different dimensions, there are currently algorithms the time complexity of which is proportional to n with an exponent between 2 and 3 (e.g. Strassen or CW-like algorithms).

The last step of the Kabsch algorithm is the calculation of the optimal rotation matrix **R**. This matrix can be calculated according to the following mathematical formula (9):

$$\mathbf{H} = \mathbf{USV^T}, d = \det\left(\mathbf{VU^T}\right), \mathbf{R} = \mathbf{V}\begin{pmatrix} 1 & 0 & 0 \\ 0 & 1 & 0 \\ 0 & 0 & d \end{pmatrix}\mathbf{U^T}. \tag{9}$$

Since the covariance matrix **H** has a dimension of 3×3 in this case, the calculation of the rotational matrix **R** by singular value decomposition (SVD), determinant calculation and matrix multiplication have a constant time complexity of *$O(1)$*. However, if the matrix **H** were generally of *$m \times n$* dimensions, the asymptotic time complexity of the SVD calculation would be of *$O(m^2n + mn^2)$* and the calculation of the determinant by the Bareiss algorithm of *$O(n^3)$*.

Importantly, the most complicated operation in superimposition of two molecules is calculation of the covariance matrix **H**, which is essentially based on matrix multiplication. Another question, however, is how effective the Kabsch algorithm is, for example, in achieving minimum RMSD.

4.3 Quaternion Algorithm

The quaternion algorithm is based on the same problem definition of superimposition as the Kabsch algorithm (see Eq. (8)). If we expand the Eq. (8), we get the relation (10), in which the center, linear and negative term causes a change in distance as a function of rotation. The other two quadratic terms are constant.

$$e = \min\|\mathbf{I_B R} - \mathbf{I_A}\|^2 = \sum\nolimits_{i=1}^{n} \|\mathbf{R}(b_i)\|^2 - 2\sum\nolimits_{i=1}^{n} \mathbf{R}(b_i)\cdot a_i + \sum\nolimits_{i=1}^{n} \|a_i\|^2. \tag{10}$$

The middle, non-quadratic term can be expressed using quaternion notation (11):

$$\sum\nolimits_{i=1}^{n} \mathbf{R}(b_i) \cdot a_i = \sum\nolimits_{i=1}^{n} q a_i q^* \cdot b_i = \sum\nolimits_{i=1}^{n} (q a_i) \cdot (b_i q). \tag{11}$$

The quaternion can be expressed as a four-component vector $q = (q_0, q_1, q_2, q_3)^{\mathrm{T}}$ or it can be expanded to a quaternion matrix **Q** with dimensions 4 × 4 (12):

$$\mathbf{Q} = \begin{pmatrix} q_0 & -q_1 & -q_2 & -q_3 \\ q_1 & q_0 & -q_3 & q_2 \\ q_2 & q_3 & q_0 & -q_1 \\ q_3 & -q_2 & q_1 & q_0 \end{pmatrix}. \tag{12}$$

Using the quaternion matrix form (12), the coordinate part of identity matrices for molecules A (e.g. **A**) and B (e.g. **B**) may be expressed as quaternions, whose first components will be zeros (13):

$$\mathbf{A_i} = \begin{pmatrix} 0 & -a_{i,x} & -a_{i,y} & -a_{i,z} \\ a_{i,x} & 0 & -a_{i,z} & a_{i,y} \\ a_{i,y} & a_{i,z} & 0 & -a_{i,x} \\ a_{i,z} & -a_{i,y} & a_{i,x} & 0 \end{pmatrix}, \mathbf{B_i} = \begin{pmatrix} 0 & -b_{i,x} & -b_{i,y} & -b_{i,z} \\ b_{i,x} & 0 & -b_{i,z} & b_{i,y} \\ b_{i,y} & b_{i,z} & 0 & -b_{i,x} \\ b_{i,z} & -b_{i,y} & b_{i,x} & 0 \end{pmatrix}. \tag{13}$$

By means of the quaternion definitions of molecules **A** and **B**, the rotation of the molecular system can be expressed as (14):

$$\sum\nolimits_{i=1}^{n} (\mathbf{A_i q}) \cdot (\mathbf{B_i q}) = \sum\nolimits_{i=1}^{n} \mathbf{q^T A_i^T B_i q} = \mathbf{q^T} \left(\sum\nolimits_{i=1}^{n} \mathbf{A_i^T B_i} \right) \mathbf{q}. \tag{14}$$

When we define these equations: $\mathbf{N_i} = \mathbf{A_i^T B_i}, \mathbf{N} = \sum\nolimits_{i=1}^{n} \mathbf{N_i}$, then we get the following relationship (15):

$$\mathbf{Nq} = \lambda \mathbf{q}, \tag{15}$$

where **N** is a symmetric matrix and its elements $\mathbf{N_i}$ are equal to (16):

$$\mathbf{N_i} = \begin{pmatrix} a_{x_i}b_{x_i} + a_{y_i}b_{y_i} + a_{z_i}b_{z_i} & a_{z_i}b_{y_i} - a_{y_i}b_{z_i} & a_{x_i}b_{z_i} - a_{z_i}b_{x_i} & a_{y_i}b_{x_i} - a_{x_i}b_{y_i} \\ a_{z_i}b_{y_i} - a_{y_i}b_{z_i} & a_{x_i}b_{x_i} - a_{y_i}b_{y_i} - a_{z_i}b_{z_i} & a_{y_i}b_{x_i} + a_{x_i}b_{y_i} & a_{x_i}b_{z_i} + a_{z_i}b_{x_i} \\ a_{x_i}b_{z_i} - a_{z_i}b_{x_i} & a_{y_i}b_{x_i} + a_{x_i}b_{y_i} & -a_{x_i}b_{x_i} + a_{y_i}b_{y_i} - a_{z_i}b_{z_i} & a_{z_i}b_{y_i} - a_{y_i}b_{z_i} \\ a_{y_i}b_{x_i} - a_{x_i}b_{y_i} & a_{x_i}b_{z_i} + a_{z_i}b_{x_i} & a_{z_i}b_{y_i} + a_{y_i}b_{z_i} & -a_{x_i}b_{x_i} - a_{y_i}b_{y_i} + a_{z_i}b_{z_i} \end{pmatrix}. \tag{16}$$

To simplify the calculation, let's define the paired products of the coordinates S_{xy} in A and B molecules using summations (17):

$$S_{xy} = \sum\nolimits_{i=1}^{n} a_{x_i} b_{y_i}. \tag{17}$$

Subsequently, we can express the total matrix **N** by summations S (18):

$$\mathbf{N} = \begin{pmatrix} S_{xx}+S_{yy}+S_{zz} & S_{zy}-S_{yz} & S_{xz}-S_{zx} & S_{yx}-S_{xy} \\ S_{zy}-S_{yz} & S_{xx}-S_{yy}-S_{zz} & S_{yx}+S_{xy} & S_{xz}+S_{zx} \\ S_{xz}-S_{zx} & S_{yx}+S_{xy} & -S_{xx}+S_{yy}-S_{zz} & S_{zy}-S_{yz} \\ S_{yx}-S_{xy} & S_{xz}+S_{zx} & S_{zy}+S_{yz} & -S_{xx}-S_{yy}+S_{zz} \end{pmatrix}. \quad (18)$$

If we diagonalize the matrix **N**, we obtain eigenvectors $\mathbf{v_i}$ and eigenvalues λ_i for which this holds (19):

$$\begin{aligned} \mathbf{q} = \sum_{i=1}^{4}\alpha_i v_i; \mathbf{Nq} = \sum_{i=1}^{4}\alpha_i\lambda_i v_i; \mathbf{q^T Nq} = \sum_{i=1}^{4}\alpha_i\lambda_i \mathbf{q^T} v_i \\ = \sum_{i=1}^{4}\alpha_i\lambda_i\left(\sum_{j=1}^{4}\alpha_j v_j^T\right)v_i. \end{aligned} \quad (19)$$

The eigenvector, which has the maximum eigenvalue (i.e. the maximum because we require the relationship (11) to have the maximum value and, due to its negative sign, to cause the lowest decrease in RMSD), represents quaternion elements that provide the most advantageous rotation minimizing RMSD. The characteristic polynomial of the matrix **N**, whose roots represent eigenvalues, can be expressed as follows (20–21):

$$\det|\mathbf{N}-\lambda\mathbf{I}| = p_0\lambda^4 + p_1\lambda^3 + p_2\lambda^2 + p_3\lambda + p_4 = 0, \quad (20)$$

$$(\lambda - e_1)(\lambda - e_2)(\lambda - e_3)(\lambda - e_4) = 0. \quad (21)$$

The roots of a characteristic polynomial can be obtained e.g. by the Ferrari method (22–25):

$$e_{1,2} = -\frac{p_1}{4p_0} - S \pm \frac{1}{2}\sqrt{-4S^2 - 2\alpha + \frac{\omega}{S}},\ e_{3,4} = -\frac{p_1}{4p_0} + S \pm \frac{1}{2}\sqrt{-4S^2 - 2\alpha + \frac{\omega}{S}}, \quad (22)$$

$$\alpha = \frac{8p_0p_2 - 3p_1^2}{8p_0^2}, \omega = \frac{p_1^3 - 4p_0p_1p_2 + 8p_0^2p_4}{8p_0^3},\ S = \frac{1}{2}\sqrt{-\frac{2}{3}\alpha + \frac{1}{3p_0}\left(Q + \frac{\Delta_0}{Q}\right)}, \quad (23)$$

$$Q = \sqrt[3]{\frac{\Delta_1 + \sqrt[2]{\Delta_1^2 - 4\Delta_0^3}}{2}}, \Delta_0 = p_2^2 - 3p_1p_3 + 12p_0p_4, \quad (24)$$

$$\Delta_1 = 2p_2 - 9p_1p_2p_3 + 27p_1^2p_4 + 27p_0p_3^2 - 72p_0p_2p_4 \quad (25)$$

When we define the relationships between the characteristic polynomial parameters and the elements of the matrix **N**, the following relationships hold (26–29):

$$p_0 = 1, p_1 = 0, \tag{26}$$

$$p_2 = -2\Big((S_{xx})^2 + (S_{xy})^2 + (S_{xz})^2 + (S_{yx})^2 + (S_{yy})^2 + (S_{yz})^2 + (S_{zx})^2 + (S_{zy})^2 + (S_{zz})^2\Big), \tag{27}$$

$$p_3 = -8\left(S_{xx}S_{yy}S_{zz} + S_{yz}S_{zx}S_{xy} + S_{xy}S_{yx}S_{xz}\right), \tag{28}$$

$$\begin{aligned} p_4 = {} & \Big((S_{xy})^2 + (S_{xz})^2 - (S_{yx})^2 - (S_{zx})^2\Big)^2 + \Big[-(S_{xx})^2 + (S_{yy})^2 + (S_{zz})^2 + (S_{yz})^2 \\ & + (S_{zy})^2 - 2(S_{yy}S_{zz} - S_{yz}S_{zy})\Big] \times \Big[-(S_{xx})^2 + (S_{yy})^2 + (S_{zz})^2 + (S_{yz})^2 + (S_{zy})^2 + 2(S_{yy}S_{zz} - S_{yz}S_{zy})\Big] \\ & + \left[-(S_{xz} + S_{zx})(S_{yz} - S_{zy}) + (S_{xy} - S_{yx})(S_{xx} - S_{yy} - S_{zz})\right] \times \left[-(S_{xz} - S_{zx})(S_{yz} + S_{zy})\right. \\ & \left. + (S_{xy} - S_{yx})(S_{xx} - S_{yy} + S_{zz})\right] + \left[-(S_{xz} + S_{zx})(S_{yz} + S_{zy})\right. \\ & \left. - (S_{xy} + S_{yx})(S_{xx} + S_{yy} - S_{zz})\right] \times \left[-(S_{xz} - S_{zx})(S_{yz} - S_{zy}) - (S_{xy} + S_{yx})(S_{xx} + S_{yy} + S_{zz})\right] \\ & + \left[(S_{xy} + S_{yx})(S_{yz} + S_{zy})\right. \\ & \left. + (S_{xy} + S_{zx})(S_{xx} - S_{yy} + S_{zz})\right] \times \left[-(S_{xy} - S_{yx})(S_{yz} - S_{zy})\right. \\ & \left. - (S_{xz} + S_{zx})(S_{xx} + S_{yy} + S_{zz})\right] + \left[(S_{xy} + S_{yx})(S_{yz} + S_{zy})\right. \\ & \left. + (S_{xz} + S_{zx})(S_{xx} - S_{yy} - S_{zz})\right] \times \left[-(S_{xy} - S_{yx})(S_{yz} - S_{zy}) + (S_{xz} + S_{zx})(S_{xx} + S_{yy} - S_{zz})\right]. \end{aligned} \tag{29}$$

The above equations represent a non-trivial mathematical way for finding the optimal rotational matrix **R** using quaternion calculus. If we look at these calculations from the informatics point of view, we can draw the following conclusions:

- The translation of the centers of molecules is the same in the quaternion algorithm as in the Kabsch algorithm,
- the most computationally intensive is finding a quaternion that maximizes expression (11),
- once the highest eigenvalue of the matrix **N** λ_{max} is found, the optimal quaternion can be found as eigenvector by solving the equation (e.g. by the Gaussian method) (30):

$$(\mathbf{N} - \lambda_{max}\mathbf{I})\mathbf{v} = 0. \tag{30}$$

Let us take a closer look at the time complexity of the steps involved in finding the optimal quaternion to minimize RMSD of two molecules by rotation. The expression (17) can be calculated by the following simple algorithm:

```
Sxy = 0;
for (int i = 1; i <= n, i++) {
   Sxy = Sxy + I_A(i,2)*I_B(i,3); }% I_A, I_B - identity matrices
```

The algorithm for calculating S_{ij} has an asymptotic time complexity of *O(n)*. However, S_{ij} has to be calculated for all variations from the set of *x*, *y*, *z* coordinates for molecules A and B, which are 3^2, (see (19)). Even though the above formula seems to be complicated, the complete quaternion rotation still retains the asymptotic time complexity of *O(n)*.

Similarly, all operations in (19–21) involve a constant number of algebraic operations and therefore they have an asymptotic time complexity equal to constant, that is, *O(1)*. It would be possible to prove that the Gaussian method for calculating eigenvectors of the matrix **N** also exhibits the asymptotic time complexity of *O(1)*. If we compare the Kabsch and quaternion algorithms, it follows that both algorithms have the same time complexity. However, it is obvious that the Kabsch algorithm includes fewer floating-point operations (FLOPs).

5 Results and Discussion

In this study, both the Kabsch and quaternion algorithms were implemented and tested to evaluate their computational complexity in Matlab 2018. Taking into account Matlab's publicly available M codes, custom algorithms for the Kabsch and quaternion based superimposition were developed which estimated the relationship between the time necessary to superimpose two molecules containing 2 – 100,000 randomly positioned atoms. During the tests, calculation wall-time and RMSD values were monitored. The following simple script for Matlab was designed for the tests:

```
function []=test (n) % n is the maximal number of atoms to test
for i=2:n
    A = rand (3,i); % generation of random pseudo-molecule
    B = rand (3,i);
    tic; % start of time measurement
    lrmsd_1(i-1) = kabsch(A,B); % evaluation of RMSD
    time(i-1)=toc; % stop of time measurement
    tic;
    lrmsd_2(i-1) = quaternion (A,B); % evaluation of RMSD
    time_b(i-1)=toc;
end
a = subplot(2,1,1);
plot(2:n,time,2:n,time_b);
legend(a, {'Kabsch','Quaternion'});
b = subplot(2,1,2);
plot(lrms_1,lrms_2);
legend(b, {'Kabsch vs. Quaternion'});
```

The calculations confirmed that when the number of atoms in molecules got increased from 2 to 10, the computational wall-time required by the quaternion algorithm was higher compared to that of the Kabsch algorithm (Fig. 2). Higher time demands of the quaternion algorithm indicate that this method involves a higher number of FLOPs. Regarding the resulting RMSD value, both algorithms give exactly the same results (e.g. R^2 = 1) when testing molecules with 2 to 10 atoms.

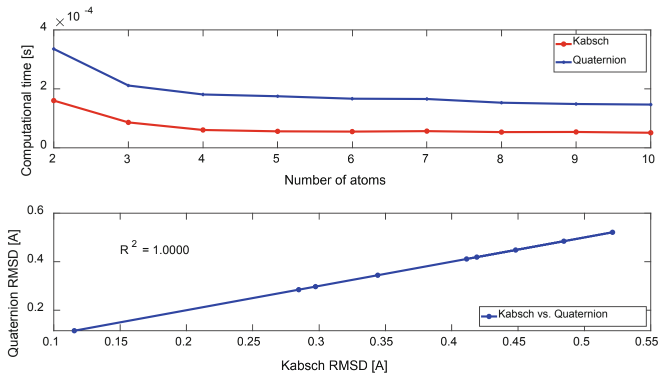

Fig. 2. Computational time to superimpose two molecules with random configuration of 2 - 10 atoms and the resulting RMSD by Kabsch and quaternion algorithms.

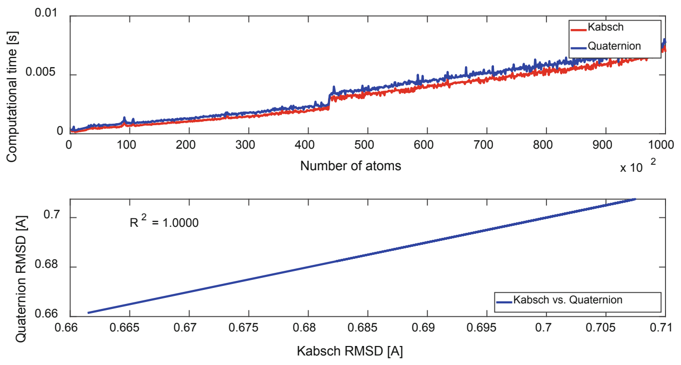

Fig. 3. Computational time to superimpose two molecules with random configuration of 2 – 100,000 atoms and the resulting RMSD by Kabsch and quaternion algorithms.

Testing computational time complexity for molecules with randomly generated 2 - 100,000 atoms proved that both algorithms have linear time complexity of *O(n)*, with the quaternion algorithm being more time consuming (Fig. 3). The RMSD values by both algorithms are exactly the same for molecules with up to 100,000 atoms.

A comparison of the Kabsch and quaternion algorithms shows that both have the same asymptotic time complexity of *O(n)*. The most demanding step in the Kabsch algorithm is the computation of the covariance matrix, in the case of the quaternion algorithm, it is the computation of the elements of the matrix **N**. Calculating diagonal matrices and determinants has a constant asymptotic complexity of *O(1)*, because they perform these operations on matrices of constant sizes.

However, in terms of the number of FLOPs, the two algorithms differ as the Kabsch algorithm comprises fewer FLOPs than the quaternion algorithm does. This result is clearly evident from the computational time testing, in which the quaternion algorithm requires constantly increased computational time to superimpose two molecules in comparison with the Kabsch algorithm. This is related to the fact that the Kabsch algorithm uses 3×3 rotation matrices, whereas the quaternion algorithm is loaded by calculating a 4×4 matrix $\mathbf{N}$. Overall, the quaternion algorithm appears to be less advantageous for molecule superimposition, which opposes the proposition by Popov [15].

6 Conclusions

The objective of this work is to briefly introduce the problem of rigid superimposing two molecules by roto-translation so that the molecule atoms get as close as possible to each other and the resulting RMSD has the lowest value. The analyzed Kabsch and quaternion algorithms for superimposition differ mainly in the methodology and in the number of mathematical steps performed. Importantly, it was found by analysis of the mathematical principles of the algorithms and confirmed by computer simulations in Matlab that both algorithms have the same, trivial asymptotic time complexity of *O(n)*. Nonetheless, application of the Kabsch algorithm should be prioritized for application in computational chemistry and biology, because it is less computationally demanding.

Acknowledgements. The work was supported by the Ministry of Education, Youth and Sports of Czech Republic (project ERDF no. CZ.02.1.01/0.0/0.0/18_069/0010054).

References

1. Dolezal, R., Ramalho, T., Franca, T.C., Kuca, K.: Parallel Flexible Molecular Docking in Computational Chemistry on High Performance Computing Clusters. In: Núñez, M., Nguyen. (eds.), LNCS, vol. 9330, pp. 418–427. Springer, Heidelberg (2015)
2. Bajorath, J.: Integration of virtual and high-throughput screening. Nat. Rev. Drug Discov. **1**, 882–894 (2002)
3. Kubinyi, H.: Success stories of computer-aided design. In: Computer Applications in Pharmaceutical Research and Development, pp. 377–724. Wiley, New Jersey (2006)
4. Veselovsky, A.V., Ivanov, A.S.: Strategy of computer-aided drug design. Curr. Drug Targets Infect. Disord. **3**, 33–40 (2003)
5. Taminau, J., Thijs, G., De Winter, H.: Pharao. J. Mol. Graph. Model. **27**, 161–169 (2008)
6. Tosco, P., Balle, T., Shiri, F.: Open3DALIGN. J. Com. Aid. Mol. Des. **25**, 777–783 (2011)
7. Taylor, W.R., May, A.C., Brown, N.P., Aszodi, A.: Protein structure: geometry, topology and classification. Reg. Prog. Phys. **64**, 517–590 (2001)
8. Carbó, R., Leyda, L., Arnau, M.: How similar is a molecule to another? Int. J. Quant. Chem. **17**, 1185–1189 (1980)
9. Sierk, M.L., Pearson, W.R.: Sensitivity and selectivity in protein structure comparison. Protein Sci. **13**, 773–785 (2004)
10. McLachlan, A.: Rapid comparison of protein structures. Acta Cryst. **38A**, 871–873 (1982)
11. Diamond, R.: A note on the rotational superposition problem. Acta Cryst. **44A**, 211–216 (1998)

12. Kabsch, W.: A discussion of the solution for the best rotation to relate two sets of vectors. Acta Cryst. **34A**, 827–828 (1978)
13. Ypma, T.: Historical development of the Newton-Raphson method. SIAM Rev. **37**, 531–551 (1995)
14. Theobald, D.L.: Rapid calculation of RMSDs using a quaternion-based characteristic polynomial. Acta Cryst. **61A**, 478–480 (2005)
15. Popov, P., Grudinin, S.: Rapid determination of RMSDs corresponding to macromolecular rigid body motions. J. Comput. Chem. **35**, 950–956 (2014)

Electronic Equivalent of Consciousness with Elementary Mental Process Model

Leonard Bernau(✉), Filip Paulu, and Jan Voves

FEE in Prague, Czech Technical University in Prague, Prague, Czechia
{polnirob,paulufil,voves}@fel.cvut.cz

Abstract. We present a project to design of the simplified model of thinking located in a little-explored field between neurobiology and psychology. While neurobiology in the incredibly complex microscopic system is dedicated to the structures and signals at the molecular level and the psychology is committed at the opposite extreme with highly sophisticated, they are very abstract and, therefore, difficult to grasp these wholes. There is a vast space between these two extremes. From the perspective of the inherent observers, it is investigable without overcoming the complexity of both points of interest. The primary goal of this research is to construct a multi-layer analog configuration space, the Electronic Equivalent of Consciousness (ECC), wherein the signals have the same properties (bioelectrical) as in the human brain.

Keywords: Neural network · Neurobiology · Electronics · Reticular formation · Neurohumoral process

1 Introduction

To create insight into the issue, it will follow the mental process in human from his point of view, as a human sees from his own subjective perspective. Thus creating an analogy subsequently usable for technological applications. our deepest pe A newborn baby is a highly plastic neural network (NN) defined by the 11 essential sensory inputs which are following: vision [17], hearing [37], smell [23], touch, heat, cold, pain [7], proprioception [39], vestibular sensor [18], interoreceptors [26] and taste [25]. All input signals are transformed via receptor systems into a bioelectric signal of a similar amplitude, which propagates across the NN at an average speed of 15–30 m/s [11,27], forming a signal object within the organic spatial structure where signals interfere with each other. The result of the harmonious constructive interference of these signals is a system of reflex actions that control the physiological functions of the body. They create an eleven-dimensional configuration space, formed by sensory inputs in the superposition, and they develop the mental activity. For the simplified model, we

Faculty of Electrical Engeneering, Czech Technical University in Prague, Czechia.

consider only optical VISUAL (V) and verbal AUDIO (A) signals. The anatomical region of this signal object with two parameters (A, V) in the human body is the reticular formation located in the extended spinal cord [24]. In the course of further development of the NN, a newborn encounters incoming signals A and V, which repeatedly assign the oral formulation A to each optical V signal and vice versa.

2 Introduction

To create insight into the issue, it will follow the mental process in human from his point of view, thus creating an analogy subsequently usable for technological applications. A newborn baby is a highly plastic neural network (NN) defined by the 11 essential sensory inputs which are following: vision [17], hearing [37], smell [23], touch, heat, cold, pain [7], proprioception [39], vestibular sensor [18], interoreceptors [26] and taste [25]. All input signals are transformed via receptor systems into a bioelectric signal of a similar amplitude, which propagates across the NN at an average speed of 15–30 m/s [11,27], forming a signal object within the organic spatial structure where signals interfere with each other. The result of the harmonious constructive interference of these signals is a system of reflex actions that control the physiological functions of the body. They create an eleven-dimensional configuration space, formed by sensory inputs in the superposition, and they develop the mental activity. For the simplified model, we consider only optical VISUAL (V) and verbal AUDIO (A) signals. The anatomical region of this signal object with two parameters (A, V) in the human body is the reticular formation located in the extended spinal cord [24]. In the course of further development of the NN, a newborn encounters incoming signals A and V, which repeatedly assign the oral formulation A to each optical V signal and vice versa.

An example of this process could be the mother's face in the visual field of the newborn (V), which is repeatedly interfered with the word the mother (A) [13,32]. This creates the AUDIO/VISUAL COMPLEX (AV), where the NN is gradually learned to assign a verbal (A) signal to the optical signal (V) of each person, object, situation and the phenomenon to verbal signal (A) and vice versa. When a particular AV complex is implemented into the NN, the NN completes the second component of AUDIO mother to mother face VISUAL and conversely. The gradual learning of the individual AV complexes arises in the NN with the 11- dimensional harmonic matrix of all acquired AV complexes and their interactions – the complex information (CI). The CI is a fundamental determining mechanism modifying the initially thoughtful responses to a superset of all relationships and interactions between all other implemented AV complexes. This superset is called, for this model, the cognitive resonance (CR). The continuous increase of the complexity of the CR develops the phenomenon of self-awareness and germination.

3 Hypotesis of Redundancy

Ongoing mental processes in the configuration space, nature creates an evolutionary extension of the original sensorimotor system to predict future events, which increases the ability to adapt to changing external conditions to improve survival chances. The complexity of human neurobiology is very redundant for the mental process because it is the consequence of all the demands which nature has for the human systems, as is described in [2,5]. The model of selective attention, the Intersensory Redundancy Hypothesis (IRH) [3,4], to explain how and under what conditions attention and perceptual processing are promoted to different aspects of events (amodal versus modality specific). Intersensory redundancy refers to the temporally synchronous and spatially collocated occurrence of the same information (e.g. rate, rhythm, duration, intensity shifts) across two or more senses. According to the IRH, intersensory redundancy is highly salient, it directs selective attention to the amodal aspects of events that are redundantly specified across the senses at the expense of nonredundantly specified information within the same event, particularly during early development.

The human bodies have to maintain homeostasis [22], neurohumoral regulation [14], obtain food, use movement, reproduce, grow up, control the immune system [28], breath. The fundamental principles based on our mental processes are significantly elementary. Therefore the construction of a device for creating a simulation of the simplified human conscious model does not have too extreme complexity.

4 Project Description

The primary goal of this research is to construct a multi-layer electronic analog configuration space wherein the incoming optical signals, in the first layer, form an input matrix which shifts the message of each point towards to the next layer at an average speed 15–30 m/s [11,27]. The distribution speed of signals between layers is 15–30 m/s [11,27]. By this method, a three-dimensional dynamic visual record of the current situation (V) (the analogy of short-term memory) is created. In parallel with the active optical 3D matrix, in individual layers, the acoustic signal is assigned for each point of the matrix separately, and their frequencies and amplitudes are partially summed. Thus each particular matrix point gets a unique dynamic address summed from the VISUAL for a pixel and the current AUDIO for the moment defined by each layer. Matrix points of all layers are created by AV complexes, which represent the input data for the superior NNs for further processing, as shown in Fig. 1.

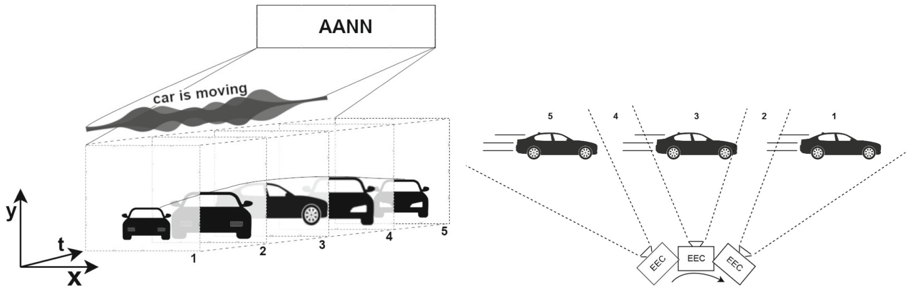

Fig. 1. Top: The schema of the situational processor, bottom: the situational model

4.1 Electronic Equivalent of Consciousness (EEC)

The EEC design does not replicate the human NN, but simulates the perception of spatial events over time, according to the subjective perception of the observer. The EEC creates a simplified dynamic model of a particular situation for the hierarchically superior networks. Figure 2 shows a functional block schema of the EEC. The optical input signal is connected to the first EEC layer (AVout) as a pixel array and proceeds at a speed of 15–30 m/s to the other layers [11,27]. Each point (pixel) of the layers is summed with an adjusted acoustic signal to the same amplitude. A spatial signal object is created, the situational processor, which contains the flow of each situation (complex information). The input optical signal in the layers is shifted in the space towards the rear (to the past), and for each point is summed the acoustic signal separately. A time delay of the visual flow (VISUAL) is created if the signals and their layering are slowed in the EEC structure. In the time delay, the visual flow (VISUAL) is associated with the acoustic signal of a verbal formulation. The result is the spatial signal object (complex information) where each situation is layered by a specific word formulation plus the accompanying AUDIO situation.

The configuration space, which simulates the situation as perceived in the user's consciousness, is created. Each point (pixel) in each layer is an input for the superior Analog Artificial Neural Networks audio and visual (AANN_A and AANN_V), which are learned by subtracting the dynamic variation of the whole situation from the AV complex. The AANN_V subtracts a dynamic variation of the acoustic signal (AUDIO) from the AVout complex and proposes to the next situation process AVin its own design of the Vin (VISUAL). AANN_A subtracts the dynamic visual signal variation (VISUAL) from the AVout complex and proposes to the next situation process AVin its design of the Ain (AUDIO). The AVin situation processor creates another AVcomplex which forms the simulation (model) of the observer imagination.

The Artificial Analog Neural Network decision ($\text{AANN}_{Decision}$), the highest hierarchically superior Analog Artificial Neural Network, performs the corrections comparisons (weight adjustment) in the AANNA and AANNV. The $\text{AANN}_{Decision}$ is a simulation of the decision-making process. In the learning

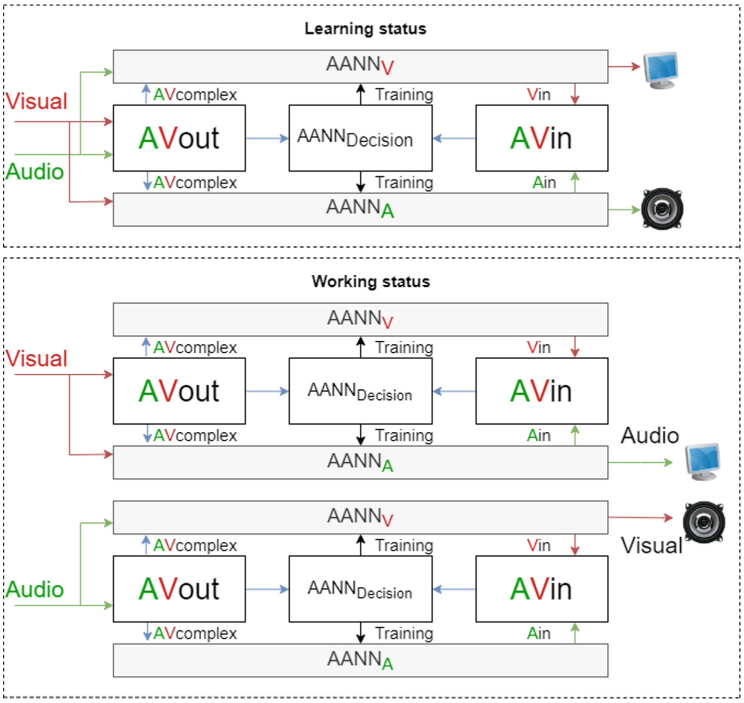

Fig. 2. Learning and working status block schema of the EEC.

status, the input of the AVout is an AUDIO signal simultaneously with the VISUAL signal. The AANN$_{Decision}$ includes the external signal for the network configuration, where the correction is performed between inputs of the AVout and the outputs AANNV and AANNA. In the working status, the AANN network performs the corrections automatically. The output of the learned device is a verbal formulation or an acoustic expression if the input is a visual signal of a particular situation. Verbal communication, which is the input of the learned device produces a visual representation of the output.

The VISUAL point P$_v$ is a tuple of three values where first is the luminance (cd/m^2), second the chrominance and third the saturation.

$$P_v = (v_{imunance} + v_{chrominance} + v_{saturation}) \tag{1}$$

The VISUAL screen is defined by

$$V = \begin{pmatrix} a_{1,1} & \cdots & a_{1,n} \\ \vdots & \ddots & \vdots \\ a_{m,1} & \cdots & a_{m,n} \end{pmatrix} = (a_{i,j}) \in P_v^{m \times n} \tag{2}$$

where V is the visual matrix of the VISUAL points array with size m $\times$ n. The AUDIO point P_a is a tuple of two values a_{left}, a_{right}, which represent 2 microphones.

$$P_a = (a_{left}, a_{right}) \tag{3}$$

The Timescreen S is a tuple of the VISUAL matrix and AUDIO point. In the Fig. 1 is shown the VISUAL input with the associated AUDIO input.

$$S = (V, P_a) \tag{4}$$

The EEC is formed by situations per time units. S_0 has speed 15–30 m/s [11, 27].

$$EEC = (S_0, S, ..., S_t) \tag{5}$$

The forward promotion y consists of a large number of neurons.

$$y = s\left(\sum_{i=1}^{n} w_i x_i\right) \tag{6}$$

The (NN) consists of neurons, as is described in [1,12]. There is y outputs of neuron, s is an activation function (sigmoid), w_i are weights (synapsis) and x_i are inputs of the neuron. These weights determine how the NN works. In the multilevel NN are outputs the inputs of the next layer.

The ($AANN_{Decision}$) decides the accurate of the imagination (AV_{inside}) and the output is the ERROR (E). Classical NN learns step by step according to the formula:

$$w_{t+1} = w_t - \eta \frac{\partial E}{\partial w_t} \tag{7}$$

where w_{t+1} - he weight in the time t + 1 time unit. The most widespread method of training the NN is backpropagation with gradient descendent, where each weight is updated by partial derivation of Error by the weight itself (8),

$$w_t = w_{t_0} - \eta \int_{t_0}^{t} \frac{\partial E}{\partial w_t} d\tau \tag{8}$$

where w_t = the weight in the time t and η shapes the learning rate [8].

The NNs are trained from continuous signal because the sampling of the signals causes loss of pieces of informations, and Von Neumann Bottleneck [33–35].

4.2 Possible Technological Realization

The selection of suitable technology is governed mainly by the price per mm2 of the proposed chip and by technology performance. One of the main criteria of nanotechnologies for the EEC development is the deacceleration of signals propagation in the material to 15–30 m/s [11,27].

One of the most widely used technologies for analog circuits is CMOS architecture. However, the individual pixels (neurons) are not physically separated from the others. The solution for manufacturing physical separation of the structure on the chip is to place the sensitive part (neuron) and electronic circuits on the same wafer. Silicon On Insulator (SOI) technology seems to be an ideal solution for this application [10]. The analog delay structures are included in SOI technology. The Buried Oxide (BOX) layer isolates the CMOS electronics implemented on a thin, low resistivity, epitaxial silicon layer from a thick, high resistivity handle wafer. The sensitive element (neuron) is integrated into the handle wafer, as illustrated in Fig. 3.

In contrast to other SOI technologies, the thick film SOI provides a double-well structure to shield the thin gate transistors from the BOX layer. The chosen technological process allows applying high bias voltages (up to 200 V), which are used to deplete the substrate partially and to fabricate devices with higher resistivity. At this time, there is no backside processing. Thus, the HV is applied from the top side using an ohmic contact. The pixel electronics are processed on a 3.5 μm thin epitaxial layer separated from the handle wafer by a 1 μm thin BOX layer. The electronics circuit of each pixel is located in an insulating substrate, which is surrounded by Deep Trench Insulation (DTI) [6].

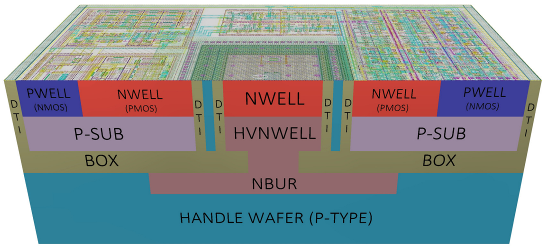

Fig. 3. Cross section of the SOI CMOS technology. The sensitive part of a pixel (neuron) is in the middle separated from electronics by DTI. The pixel is separated from the other by the DTI [6].

5 Conclusion

Although the artificial intelligence (AI) is an excessively evolving field with a partial performance, which dramatically exceeds our abilities (chess, voice recognition, faces), its real cognitive abilities are confronted with fundamental limits. The AI is currently unable to understand humor, read between the lines, and has no hint of self-awareness. The reason is that the mathematical models and systems of the current AI have no question of consciousness in their structure.

It is precisely the question of the inclusion of consciousness into the fundamental innovations of the AI field. The AI which is described in this paper is applicable in medicine [15], economy [20], sociology [40], education and music [19], music composition [38], emotional computation [36], philosophy [31] and many other research areas. The simplified model of human thinking and the ensuing development of its electronics equivalent (EEC) might be able to bring new technological applications. Many articles deal with the problem of sensorimotor transformation [9,21,30], however, the innovative approach of this project corresponds to questions of the perception and the consciousness of humans [29] and animals [16].

Acknowledgments. Research described in the paper was supported by the Czech Technical University grant SGS20/176/OHK3/3T/133 and Nadace Science 21 foundation.

References

1. Almási, A.D., Woźniak, S., Cristea, V., Leblebici, Y., Engbersen, T.: Review of advances in neural networks: neural design technology stack. Neurocomputing **174**, 31–41 (2016)
2. Aylett, M., Turk, A.: The smooth signal redundancy hypothesis: a functional explanation for relationships between redundancy, prosodic prominence, and duration in spontaneous speech. Lang. Speech **47**(1), 31–56 (2004)
3. Bahrick, L., Lickliter, R.: Intersensory redundancy guides attentional selectivity and perceptual learning in infancy. Dev. Psychol. **36**(2), 190–201 (2000). https://doi.org/10.1037//0012-1649.36.2.190
4. Bahrick, L., Lickliter, R.: Intersensory redundancy guides early perceptual and cognitive development. In: Kail, R.V. (ed.) Advances in Child Development and Behavior, vol. 30, pp. 153–187. Elsevier, Boston (2002)
5. Bahrick, L.E., Lickliter, R., Castellanos, I., Todd, J.T.: Intrasensory redundancy facilitates infant detection of tempo: extending predictions of the intersensory redundancy hypothesis. Infancy **20**(4), 377–404 (2015). https://doi.org/10.1111/infa.12081. https://onlinelibrary.wiley.com/doi/abs/10.1111/infa.12081
6. Benka, T., Havranek, M., Hejtmanek, M., Jakovenko, J., Janoska, Z., Marcisovska, M., Marcisovsky, M., Neue, G., Tomasek, L., Vrba, V.: Characterization of pixel sensor designed in 180 nm SOI CMOS technology. J. Instrum. **13**(1), C01025–C01025 (2018)
7. Cabibihan, J., Joshi, D., Srinivasa, Y.M., Chan, M.A., Muruganantham, A.: Illusory sense of human touch from a warm and soft artificial hand. IEEE Trans. Neural Syst. Rehabil. Eng. **23**(3), 517–527 (2015). https://doi.org/10.1109/TNSRE.2014.2360533
8. Chandra, B., Sharma, R.K.: Deep learning with adaptive learning rate using laplacian score. Expert Syst. Appl. **63**, 1–7 (2016). https://doi.org/10.1016/j.eswa.2016.05.022. http://www.sciencedirect.com/science/article/pii/S0957417416302470
9. Crochet, S., Lee, S.H., Petersen, C.C.: Neural circuits for goal-directed sensorimotor transformations. Trends Neurosci. **42**(1), 66–77 (2019). https://doi.org/10.1016/j.tins.2018.08.011. http://www.sciencedirect.com/science/article/pii/S0166223618302364

10. Dovhij, V., Holota, V., Kogut, I.: Architecture development and elements simulation of analytical microsystem-on-chip with "silicon-on-insulator" structures. In: 2016 13th International Conference on Modern Problems of Radio Engineering, Telecommunications and Computer Science (TCSET), pp. 368–372 (2016)
11. Drukarch, B., Holland, H.A., Velichkov, M., Geurts, J.J.G., Voorn, P., Glas, G., de Regt, H.W.: Thinking about the nerve impulse: a critical analysis of the electricity-centered conception of nerve excitability. Prog. Neurobiol. **169**, 172–185 (2018)
12. Duan, S., Hu, X., Dong, Z., Wang, L., Mazumder, P.: Memristor-based cellular nonlinear/neural network: design, analysis, and applications. IEEE Trans. Neural Netw. Learn. Syst. **26**(6), 1202–1213 (2014)
13. Futagi, Y.: Eye-hand-mouth coordination in the human newborn. Pediatr. Neurol. **75**, 43–47 (2017)
14. Golovin, M.S., Balioz, N.V., Krivoschekov, S.G., Aizman, R.I.: Integration of functional, psychophysiological, and biochemical processes in athletes after audiovisual stimulation. Hum. Physiol. **44**(1), 54–59 (2018)
15. Graham, S.A., Depp, C.A.: Artificial intelligence and risk prediction in geriatric mental health: what happens next? Int. Psychogeriatr. **31**(7), 921–923 (2019). https://doi.org/10.1017/S1041610219000954
16. Helmbrecht, T.O., dal Maschio, M., Donovan, J.C., Koutsouli, S., Baier, H.: Topography of a visuomotor transformation. Neuron **100**(6), 1429–1445.e4 (2018)
17. Hickey, C., Peelen, M.: Neural mechanisms of incentive salience in naturalistic human vision. Neuron **85**(3), 512–518 (2015). https://doi.org/10.1016/j.neuron.2014.12.049. http://www.sciencedirect.com/science/article/pii/S0896627314011581
18. Hitier, M., Sato, G., Zhang, Y.F., Zheng, Y., Besnard, S., Smith, P.F., Curthoys, I.S.: Anatomy and surgical approach of rat's vestibular sensors and nerves. J. Neurosci. Methods **270**, 1–8 (2016)
19. Holland, S.: Artificial intelligence, education and music: the use of artificial intelligence to encourage and facilitate music composition by novices (1989)
20. Huang, M.H., Rust, R., Maksimovic, V.: The feeling economy: managing in the next generation of artificial intelligence (AI). Calif. Manag. Rev. **61**(4), 43–65 (2019). https://doi.org/10.1177/0008125619863436
21. Huda, R., Goard, M.J., Pho, G.N., Sur, M.: Neural mechanisms of sensorimotor transformation and action selection. Eur. J. Neurosci. **49**(8), 1055–1060 (2019)
22. Iurlaro, M., von Meyenn, F., Reik, W.: Dna methylation homeostasis in human and mouse development. Curr. Opin. Genet. Dev. **43**, 101–109 (2017)
23. Jacobs, L.F.: Of space and smell: the strange evolution of the human nose. In: HRI 2017: Proceedings of the 2017 ACM/IEEE International Conference on Human-Robot Interaction, pp. 350–351. Association for Computing Machinery, New York (2017)
24. Jang, S.H., Kwon, H.G.: The ascending reticular activating system from pontine reticular formation to the hypothalamus in the human brain: a diffusion tensor imaging study. Neurosci. Lett. **590**, 58–61 (2015)
25. Ji, M., Su, X., Su, X., Chen, Y., Huang, W., Zhang, J., Gao, Z., Li, C., Lu, X.: Identification of novel compounds for human bitter taste receptors. Chem. Biol. Drug Des. **84**(1), 63–74 (2014)
26. Lazovic, B., Zlatkovic Svenda, M., Durmic, T., Stajic, Z., Duric, V., Zugic, V.: The regulation role of carotid body peripheral chemoreceptors in physiological and pathophysiological conditions. Med. pregl. **69**(11–12), 385–390 (2016)
27. Lima, P.M., Ford, N.J., Lumb, P.M.: Computational methods for a mathematical model of propagation of nerve impulses in myelinated axons. Appl. Numer. Math. **85**, 38–53 (2014)

28. Liston, A., Carr, E., Linterman, M.: Series: lifetime immunity shaping variation in the human immune system. Trends Immunol. **37**(10), 637–646 (2016)
29. Manson, G., Blouin, J., Kumawat, A., Crainic, V., Tremblay, L.: Rapid online corrections for upper limb reaches to perturbed somatosensory targets: evidence for non-visual sensorimotor transformation processes. Exp. Brain Res. **237**(3), 839–853 (2019)
30. Mayrhofer, J.M., El-Boustani, S., Foustoukos, G., Auffret, M., Tamura, K., Petersen, C.C.H.: Distinct contributions of whisker sensory cortex and tongue-jaw motor cortex in a goal-directed sensorimotor transformation. Neuron **103**(6), 1034–1043.e5 (2019)
31. McCarthy, J.: What has ai in common with philosophy? In: IJCAI, pp. 2041–2044 (1995)
32. Orioli, G., Bremner, A.J., Farroni, T.: Multisensory perception of looming and receding objects in human newborns. Curr. Biol. **28**(22), R1294–R1295 (2018)
33. Pham, H.L.: Characterisations of von neumann algebras. J. Math. Anal. Appl. **454**(2), 542–556 (2017)
34. Saini, S., Singh, P.: Von neumann stability of modified loop quantum cosmologies. Class. Quantum Gravity **36**(10), 105010 (2019)
35. Sebastian, A., Le Gallo, M., Eleftheriou, E.: Computational phase-change memory: beyond von neumann computing. J. Phys. D-Appl. Phys. **52**(44), 443002 (2019)
36. Sood, S.O.: Emotional computation in artificial intelligence education. In: AAAI (2008)
37. Sottek, R., Genuit, K.: Models of signal processing in human hearing. AEU - Int. J. Electron. Commun. **59**(3), 157–165 (2005). https://doi.org/10.1016/j.aeue.2005.03.016. http://www.sciencedirect.com/science/article/pii/S1434841105000701
38. Sterne, J., Razlogova, E.: Machine learning in context, or learning from LANDR: artificial intelligence and the platformization of music masterin. Soc. Media + Soc. **5**(2), 2056305119847525 (2019). https://doi.org/10.1177/2056305119847525
39. Tuthill, J.C., Azim, E.: Proprioception. Curr. Biol. **28**(5), R194–R203 (2018). https://doi.org/10.1016/j.cub.2018.01.064. http://www.sciencedirect.com/science/article/pii/S0960982218300976
40. Wu, W., Guo, Z., Zhou, X., Wu, H., Zhang, X., Lian, R., Wang, H.: Proactive human-machine conversation with explicit conversation goals (2019)

Metalearning-Non Linear Engineering Modelling

A Metalearning Study for Robust Nonlinear Regression

Jan Kalina(✉) and Petra Vidnerová

The Czech Academy of Sciences, Institute of Computer Science, Pod Vodárenskou věží 2, 182 07 Praha 8, Czech Republic
kalina@cs.cas.cz, petra@cs.cas.cz

Abstract. Metalearning is a methodology aiming at recommending the most suitable algorithm (or method) from several alternatives for a particular dataset. Its classification rule is learned over an available training database of datasets. It gradually penetrates to various applications in computer science and has also the potential to recommend the most suitable statistical estimator for a given dataset. We consider the nonlinear regression model. While there are some robust alternatives to the traditional (and very non-robust) nonlinear least squares available, it is not theoretically known which estimator performs the best for a particular dataset. In this work, we perform a metalearning study performed over 721 datasets predicting the best nonlinear regression estimator for an independent dataset. The estimators considered here include standard nonlinear least squares as well as its robust alternatives with a high breakdown point. On the whole, the presented study brings new arguments in favor of the nonlinear least weighted squares estimator, which is based on the idea to assign implicit weights to individual observations based on outlyingness of their residuals.

Keywords: Metalearning · Nonlinear regression · Robustness

1 Introduction

The aim of regression modeling is to explain a continuous response variable based on one or more independent variables (regressors), where the latter may be continuous and/or discrete, and thus to predict the response for individual fixed values of the regressors. Parametric estimators in the standard nonlinear regression model with a known regression function will considered in this paper.

Numerous estimation techniques for the nonlinear regression have established and successfully applied in economics, engineering, biomedicine etc. The most traditional tool here, i.e. the nonlinear least squares estimator, is well known to be too vulnerable to the presence of outlying measurements (outliers) in the data [19]. Therefore, robust alternatives to the least squares principle are highly

The work is supported by the projects 19-05704S (J. Kalina) and 18-23827S (P. Vidnerová) of the Czech Science Foundation.

desirable for the nonlinear regression model [2,17]. The concept of breakdown point as a measure of robustness suitable for nonlinear regression estimators was developed in [21]. Metalearning is a machine learning approach aiming at recommending the most suitable algorithm (or method) from several alternatives for a particular dataset. In the current paper, metalearning will be in the context of nonlinear regression with the aim to predict the best method for particular datasets not contained in the training database containing 721 datasets. Recommending a suitable estimator is even more important for the nonlinear regression for several reasons, namely due to the higher complexity of the model. Complications of nonlinear regression models namely include their bias, sensitivity to model specification, unknown properties for small sample sizes etc.

Section 2 of the paper recalls various estimators for the nonlinear regression model. Section 3 describes our metalearning study and its results are presented in Sect. 4. Finally, Sect. 5 concludes the paper.

2 Robust Estimation in Nonlinear Regression

Let us consider the nonlinear regression model

$$Y_i = f(\beta_1 X_{i1}, \dots, \beta_p X_{ip}) + e_i, \quad i = 1, \dots, n, \tag{1}$$

where f is a given continuous nonlinear function, $Y_1, \dots, Y_n$ is a continuous response, and $(X_{i1}, \dots, X_{ip})^T$ is the vector of regressors (independent variables) available for the i-th observation. We use the notation $e_1, \dots, e_n$ for random errors and X for the matrix with elements X_{ij}, where $i = 1, \dots, n$ and $j = 1, \dots, p$. The task is to estimate the parameters $\beta = (\beta_1, \dots, \beta_p)^T$. We stress here that the function f is specified. The most commonly used method for this estimation task is nonlinear least squares (NLS) estimator of β. Thus, the task is different from nonlinear regression tasks with an unknown f, which is a common situation in machine learning; in such a situation, multilayer perceptrons or support vector regression (SVR) [6] would be the commonly used tools for estimating the unknown nonlinear trend.

The NLS estimator is known to be vulnerable to the presence of outliers in the data [2,17]. Therefore, we recall several of its potential robust alternatives in this section, which are natural generalizations of robust estimators known in linear regression [7]. All of them will be used later in the metalearning study of Sect. 3.

2.1 Nonlinear Least Trimmed Squares

The nonlinear least trimmed squares (NLTS) estimator represents one of robust methods with a high breakdown point [21] and also an extension of the popular least trimmed squares from linear regression [16]. We denote by $\mathbb{R}$ the set of real numbers. Denoting the residual for any (fixed) $b = (b_1, \dots, b_p)^T \in \mathbb{R}^p$ as

$$u_i(b) = Y_i - f(b_1 X_{i1}, \dots, b_p X_{ip}), \quad i = 1, \dots, n, \tag{2}$$

squared residuals will be arranged in ascending order as

$$u^2_{(1)}(b) \leq u^2_{(2)}(b) \leq \cdots \leq u^2_{(n)}(b). \tag{3}$$

The user must specify a suitable value of the trimming constant h ($n/2 \leq h \leq n$). Then, the NLTS estimator b_{NLTS} of β is obtained as

$$\underset{b \in \mathbb{R}^p}{\arg\min} \sum_{i=1}^{h} u^2_{(i)}(b). \tag{4}$$

While it may be profitable to choose h to reflect the true percentage of contaminated data, we use here the very popular choice $h = \lfloor 3n/4 \rfloor$, where $\lfloor x \rfloor$ denotes the integer part of $x \in \mathbb{R}$ [7].

2.2 Nonlinear Least Weighted Squares

The nonlinear least weighted squares (NLWS) estimator represents an extension of the least weighted squares estimator from the linear regression [9,22,23] and at the same time a weighted analogy of the NLTS estimator. Let us assume the magnitudes $w_1, \ldots, w_n$ of nonnegative weights to be given. The NLWS estimator of the parameters in (1) is defined as

$$\underset{b \in \mathbb{R}^p}{\arg\min} \sum_{i=1}^{n} w_i u^2_{(i)}(b), \tag{5}$$

where the argument of the minimum is computed over all possible values of $b = (b_1, \ldots, b_p)^T$ and squared residuals are arranged as in (3).

The choice of weights has a determining influence on properties of the estimator [13]. If zero weights are assigned to outlying observations, then the estimator is ensured to be highly robust in terms of the breakdown point. The main reason for such robustness of the NLWS estimator is the implicitly weighted construction of the estimator itself, just like for the LWS estimator in the linear regression. Various weighting schemes will be described in Sect. 2.4. The NLWS algorithm may be computed by means of a generalization of the FAST-LTS algorithm of [18].

2.3 Nonlinear Regression Median

Regression quantiles represent a natural generalization of sample quantiles to the linear regression model. Their parameter $\alpha \in (0, 1)$, which corresponds to dividing the disturbances to $\alpha \cdot 100\%$ values below the regression quantile and the remaining $(1 - \alpha) \cdot 100\%$ values above the regression quantile. In general, regression quantiles represent an important tool of regression methodology, which is popular in economic applications. A natural extension of regression quantiles to nonlinear regression was investigated already in [15], while the most important special case remains to be the nonlinear regression median (NRM) with $\alpha = 1/2$.

2.4 Estimators Used in the Computation

We use the following seven available estimators, which will be denoted as estimators $1, \ldots, 7$. For each of the choices for the NLWS, we require a standard normalization of weights to $\sum_{i=1}^{n} w_i = 1$.

1. Nonlinear least squares (NLS).
2. Nonlinear regression median (NRM).
3. NLTS with h equal to $\lfloor 3n/4 \rfloor$.
4. NLWS with data-dependent adaptive weights of [4].
5. NLWS with linear weights
$$w_i = \frac{2(n+1-i)}{n(n+1)}, \quad i = 1, \ldots, n. \tag{6}$$
6. NLWS with trimmed linear weights
$$w_i = \frac{h-i+1}{h} I[i \leq h], \quad i = 1, \ldots, n, \tag{7}$$
where $I[.]$ denotes an indicator function and h equals again to $\lfloor 3n/4 \rfloor$.
7. NLWS with weights generated by the (strictly decreasing) logistic function
$$w_i = \left(1 + \exp\left\{\frac{i-n-1}{n}\right\}\right)^{-1}, \quad i = 1, \ldots, n. \tag{8}$$

2.5 Computational Complexity

The NLTS and NLWS estimators are computed (as already mentioned) by means of an adaptation of the FAST-LTS algorithm [18], which includes a selected number J of initial choices of p observations out of their total number n. Further, iterations are performed to permute the observations to order them according to the outlyingness of their residuals from the estimated trend. The computational complexity of the algorithm heavily depends on the choice of J. We believe this is the reason why the FAST-LTS has not been, to the best of our knowledge, analyzed in the literature in terms of computational complexity as a function of n and p. While the approximate computational complexity in terms of n and of the number of variables p is very difficult to evaluate here, it is mainly the repeated evaluation of the iterative part of the algorithm, which influences the complexity.

In addition, we are not aware of any study of computational aspects of the NLTS and NLWS estimators. There seem no recommendations for the choice of J. For the LTS in the linear regression model, $J = 500$ is advocated in the original paper [18]. However, it is clear that a larger J will be necessary in the nonlinear situation. The choice $J = 10\,000$ was proposed in [9], however without studying the effect of reducing J to smaller values. Therefore, we decided to use $J = 10\,000$ here for both the NLTS and NLWS, even at the price of high computational demands, while improving the speed was the main aim of our work. This gives a very high probability that the algorithm gives a reasonable approximation to the true value of the robust estimate.

Concerning the nonlinear regression median, its available algorithm based on the interior point method [15] stands on principles close to the algorithm for regression quantiles, which has been proven reliable in the linear regression model [14].

2.6 Illustration of Robust Nonlinear Regression

We randomly generate 70 observations following the Gompertz curve model

$$Y_i = \beta_1 + \beta_2 \exp\{\beta_3 + e^{\beta_4 X_i}\} + e_i, \quad i = 1, \ldots, n, \tag{9}$$

to illustrate the performance of the NLWS estimator with $\beta = (2, 1.5, -1, -1)^T$. The Gompertz growth curve is known as a model suitable e.g. for modeling of economic growth or as a consumption curve. The random error are generated as independent identically distributed random variables following the normal distribution $\mathsf{N}(0, \sigma^2)$ with $\sigma = 0.05$. Figure 1 (left) contains the plot of the response depending on the single regressor. To study the performance of various estimators under contamination, we performed an additional contamination by outliers as shown in Fig. 1 (right). Particularly, values in 10 observations with index $i = 10k$ for $k \in \{1, 2, \ldots, 7\}$ are increased by 1.

We used several estimates of regression parameters of the model (9) based on the simulated data set and the results are presented in Table 1. We are especially interested in implicitly weighted methods with a high breakdown point here. For raw (non-contaminated) data, all estimates are close to the true values of the parameters, while the NLS seems to be the most accurate estimate here. For contaminated data, the NLS estimates are heavily influenced by the contamination, but they are resistant for the other estimates, i.e. they are changed only slightly. From the practical point of view, using (any) robust method is more suitable compared to the non-robust NLS estimate. Such results reveal shows the added value of the robust approach in the nonlinear model in a unique way, because asymptotic interrelations of robust estimators (studied in [8] for the linear model) are not available for the nonlinear model.

Table 1. Estimated values of the vector of parameters $\beta = (2, 1.5, -1, -1)^T$ for raw and contaminated data of Sect. 2.6.

	Raw data				Contam. data			
	b_0	b_1	b_0	b_1	b_0	b_1	b_0	b_1
NLS	2.00	1.52	−0.98	−0.99	2.07	1.65	−0.97	−0.82
NLTS ($h = \lfloor 3n/4 \rfloor$)	1.98	1.55	−0.97	−0.94	1.98	1.57	−0.97	−0.90
NLWS (7)	1.97	1.55	−0.95	−0.93	2.01	1.56	−0.96	−0.92

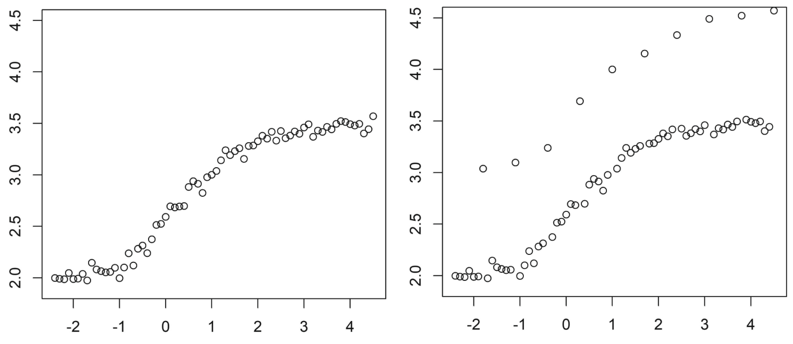

Fig. 1. Dataset from Sect. 2.6. Left: raw data. Right: contaminated data.

3 Description of the Metalearning Study

Metalearning is a computational approach allowing to exploit information from previously observed datasets and to extend them to new datasets [3]. It is popular for algorithm selection for optimization or classification tasks [20], although it may be also exploited for recommending the most suitable statistical estimator in regression context. In this paper, we describe our metalearning study with the aim to compare various nonlinear regression estimators. The study allows us also to detect the most relevant criteria for determining the most suitable weights for the NLWS.

In the primary learning part of the task, various nonlinear regression estimators are fitted for each of the given datasets and the best estimator is found using either the prediction mean square error or its robust version, described in Sect. 3.2. The subsequent secondary learning part has the aim to learn a classification rule allowing to predict the best regression method for a new dataset not present in the training database. Its input data are only selected features of individual datasets together with the result of the primary learning, which typically has the form of the index of the best method for each of the training datasets. In general, the user of metalearning must specify a list of essential components (parameters). We will now describe our choices for the primary and secondary parts of the metalearning task.

3.1 Data Acquisition

We work with the database of about 2000 real publicly available datasets available at the website [1]. The datasets come originally from various packages of R statistical software. The datasets come from different applications domains, e.g. there are datasets concerning economics, sociology, biomedicine, engineering etc.; a homogeneity of the datasets in terms of the domain application would be beneficial, but could be hardly acquired under our fully automatic process of downloading the datasets. On the other hand, such data acquisition ensures a desirable heterogeneity (diversity) of the datasets from the point of view of their statistical properties. To explain this, let us consider the skewness of residuals of the NLS estimator, considered as one of the features below in Sect. 3.4. If these residuals are heavily skewed and thus not likely to be considered as Gaussian, a highly robust estimator is more likely to be more suitable than the NLS. Thus, diverse statistical properties of the datasets is beneficial for the metalearning, because it allows to recommend the most suitable estimator correctly also for datasets with extreme characteristics.

First, we implemented an automated procedure for downloading each dataset and pre-processing the data from the internet. With the requirement to work with a large number of datasets effectively, the linux command line was used for an automatic manipulation with the datasets and particularly the command *wget* allowed us to download all the files in a CSV format. Then, the transformed datasets were loaded to Python. All the remaining manipulations and computations were implemented in Python, which gradually becomes a popular tool among data scientists thanks to numerous available packages for a more comfortable programming. The datasets were prepared to a format suitable for metalearning by means of a script exploiting packages Pandas and NumPy of Python. Each dataset is stored in a CVS file and is accompanied by a text description about the task of the analysis, number of observations and variables, and a link to a text description in a corresponding package of R software.

The sizes of the datasets were reduced in order to reduce the computational complexity of the datasets. Also this improves the homogeneity of the datasets (from the point of view of their sizes), which is desirable, as some of the features used below in Sect. 3.4 depend on the size of the dataset. To be specific, features in the form of p-values of hypothesis tests do not only depend on the violation of the null hypothesis, but also heavily depend on the size of the considered dataset, as the powers of these tests converge to 1 with an increasing size of the datasets. The reduction of their sizes is performed in the following way. If the number of observations in a particular dataset exceeded 100, we generated a random variable (say m) generated from the uniform distribution over the set $\{50, \ldots, 100\}$. Then, m observations were randomly selected from the dataset and retained, ignoring all remaining ones. In this way, sample sizes of individual datasets are diverse.

All observations with at least one missing value were omitted. While various automatic tools for perform imputation of missing values are available in R software, these would increase the computational costs even further, as the missing values appear in most of the datasets. Thus, we prefered reducing the sizes of the datasets, as explained in the previous paragraph.

Further, we performed an automatically detection of categorical variables. One of the remaining (i.e. continuous) variables was randomly chosen to be the response. Categorical variables such with 3 or more categories were omitted for the purpose of computational complexity. Binary variables were replaced by a single dummy variables, interpreted as indicators of the first group. We do not however keep all the variables. If a dataset contains more than 9 variables, some randomly chosen ones are omitted to have finally 9 variables; if there are binary regressors, these are omitted preferably. We consider the intercept in each of the datasets, i.e. a column with all ones was included to each dataset. Thus, the number of regressors (apart from intercept) is always between 1 and 9.

3.2 Data Pre-processing

In some of the datasets, regressors happen to be more or less multicollinear. We do not perform any special treatment, as prediction (rather than testing) in nonlinear regression is known not to suffer from multicollinearity. The computation of robust estimators of Sect. 3.3 seems resistant to multicollinearity as well. Nevertheless, to be sure, we computed each of the estimators for each of the datasets and if some warnings were reported, we omitted the whole dataset from the study. If the dataset after all these steps contains less than 20 observations or no regressor, it is omitted. Thus, the total number of datasets was reduced to the final number of 721. This is about 36% of the initial number of datasets in [1], which are to a large extent small and contain many missing values. The data acquisition and pre-processing often belongs to the most demanding tasks in applied machine learning problem and also in our study consumed most of the time and effort.

The response $Y_1, \dots, Y_n$ was transformed to contain values between 0 and 1 by the commonly used transform

$$Y_i \longmapsto \frac{Y_i - \min_i Y_i}{\max_i Y_i - \min_i Y_i}, \quad i = 1, \dots, n. \tag{10}$$

In the same way, all continuous regressors were transformed. Such transforms do not influence the prediction ability of the regression estimators, because all regression methods of this study are scale- and regression-equivariant, but do influence the features computed from each dataset. This is beneficial, as the original measurements differ greatly among datasets, as they also come from different fields and applications. On the whole, the fully automatic pre-processing has some disadvantages (e.g. the need for a random selection of the response), but a manual approach would not be feasible with this metalearning study, which is extraordinarily large (cf. [3,20]).

3.3 Primary Learning

In each of the 721 datasets, we consider the nonlinear model

$$Y_i = \beta_0 + \sum_{j=1}^{p} \beta_j X_{ij} + \sum_{j=1}^{p} \beta_{p+j} (X_{ij} - \bar{X}_j)^2 + e_i, \quad i = 1, \dots, n, \tag{11}$$

with the total number of $2p + 1$ regressors (which depend on the original p regressors), where the variables are centered using the mean of the j-th variable $\bar{X}_j$ (for $j = 1, \dots, p$) for the sake of numerical stability.

For the prediction measure, we use the (prediction) mean square error (MSE), which represents the most standard choice. We find the best method for each dataset using MSE in a leave-one-out cross validation, which represents a standard attempt for an independent validation. In addition, two possible robust alternatives are the trimmed mean square error (TMSE) and weighted mean square error (WMSE). To define them, we denote prediction errors as $r_1, \ldots, r_n$ and consider their ordered squared values $r^2_{(1)} \leq \cdots \leq r^2_{(n)}$. The user chooses h as integer between $n/2$ and h, and some non-negative weights $w_1, \ldots, w_n$. The robust error measures are defined as

$$TMSE = \frac{1}{h} \sum_{i=1}^{h} r^2_{(i)} \quad \text{and} \quad WMSE = \sum_{i=1}^{n} w_i r^2_{(i)}, \tag{12}$$

while we use the particular choices $h = \lfloor 3n/4 \rfloor$ for TMSE and trimmed linear weights (7) for WMSE.

3.4 Secondary Learning

The output of the primary learning is used in the form of the factor variable (index, indicator) of the best method for each of the datasets together with a list of features computed for each dataset. In the nonlinear model, we must consider the features for the metalearning rather carefully. For example, there is no meaningful analogue of the coefficient of determination in the nonlinear model. Other features must be evaluated for the NLS fit. Thus we came to selecting the following set of 9 features.

(A). The number of observations n,
(B). The number of regressors p (excluding the intercept),
(C). The ratio n/p,
(D). Condition number of the matrix $(X^T X)^{-1}$,
(E). P-value of the Shapiro-Wilk test of normality of NLS residuals,
(F). Skewness of residuals of the NLS,
(G). Kurtosis of residuals of the NLS,
(F). P-value of White's test of heteroscedasticity based on NLS residuals,
(I). P-value of the Wald test of linearity, i.e. of $H_0: \ \beta_{p+1} = \cdots = \beta_{2p} = 0$ in (11), based on NLS estimates of β.

For the subsequent metalearning task, which is a task of classification to 7 groups (i.e. finding the best among the 7 estimators of Sect. 2.4), we exploit various classification methods including support vector machines (SVM), a classification tree, k-nearest neighbors, and a multilayer perceptron with one hidden layer. We use also several other less known methods including a regularized version of linear discriminant analysis (LDA) denoted as SCRDA of [5], or a robust version of LDA denoted as linear MWCD classification [10].

4 Results

We used the R software for all the computations including necessary libraries (robustbase, quantreg, rda) for specific tasks such as robust estimation and classification. Our metalearning codes (for a preliminary version of the study) are presented on the website [11]. Using MSE in a leave-one-out cross validation study, the NLWS turns out to be the best estimator. The NLS yields the minimal prediction error for 23% of the datasets, the NRM for 20%, the NLTS in 26% and any of the versions of the NLWS in the remaining 31% of datasets. If TMSE is used, the NLWS becomes most successful for 35% and the NLTS for 39% of datasets. If WMSE is used, the NLWS becomes the best for 45% and the NLTS for 34% of datasets. In terms of these percentages, all the four choices of weights for the NLWS turn out to be roughly equally successful for any choice of the error measure.

Within the subsequent metalearning task, we computed various classifiers, while default settings of parameters was used for those computed using the R software. Hyperparameters for SVM or neural networks were estimated in a standard leave-one-out cross validation. The results are presented in Table 2 evaluated as the classification accuracy, i.e. ratio of correctly classified cases (datasets). The SVM classifier turns out to yield the best performance. The best result is obtained for the SVM with a Gaussian kernel for the TMSE; in this situation, the best regression method is found correctly in 71% of datasets. Because there are as many as 7 classes, the overall prediction ability is not very high. The most useful criteria for the choice of weights for the NLWS turn out to be heteroscedasticity and normality of the NLS residuals, which correspond to our intuition, because their heavy violation requires a strongly robust approach.

Table 2. Results of metalearning evaluated as the classification accuracy in a leave-one-out cross validation study. Three different prediction error measures are compared.

Classification method	Classification accuracy		
	MSE	TMSE	WMSE
Classification tree	0.35	0.45	0.47
k-nearest neighbor ($k = 3$)	0.56	0.61	0.64
LDA	0.60	0.68	0.65
SCRDA	0.60	0.68	0.66
Linear MWCD-classification	0.60	0.68	0.66
Multilayer perceptron	0.56	0.66	0.66
Logistic regression	0.56	0.67	0.69
SVM (linear)	0.60	0.69	0.70
SVM (Gaussian kernel)	0.64	0.71	0.70

5 Conclusions

In this paper, a metalearning study for finding the most suitable nonlinear regression estimator is presented. To our knowledge, this is the first metalearning study for nonlinear regression. The metalearning study presented here has the aim to construct a classification rule allowing to predict the most suitable nonlinear regression estimator for a particular dataset. For this purpose, we work with 721 real publicly available datasets. The NLWS seems to yield the best result for the majority of the datasets, while no weighting scheme is uniformly optimal over all datasets.

The results obtained here and presented in Table 1 are evaluated across all datasets, i.e. from various domains of applications (economy, sociology, biomedicine, engineering etc.). Concerning the analysis of a single dataset, the benefits of robust approaches (compared to the classical NLS) are also revealed here, i.e. the paper indicates the necessity of a robust approach for analyzing a dataset contaminated by more or less severe outliers. The NLTS and the nonlinear regression median have a weaker performance due to a low efficiency. Thus, the concept of efficiency (and not only the robustness) also seems to play a prominent role in the nonlinear regression modeling of real data. While the NLTS estimator has been already considered already in [4], the more novel NLWS estimator seems more promising as it has the ability to combine global and local robustness with efficiency. Robust prediction measures, and especially TMSE, are superior to the standard MSE.

The resulting metalearning is relatively successful in recommending the most suitable nonlinear regression estimator, even in spite of the difficulty of the secondary learning into as many as 7 groups. The results go far beyond those of [12], where only 30 datasets were considered.

As future research, we intend to work on the robustification of the whole metalearning process, which would bring very practical consequences to metalearning. Investigating computational aspects of the NLTS and NLWS estimators seem as a major open problem. After it becomes possible to reduce computational demands by improving the algorithm for their computation, our future aim remains to be a sophisticated (and computationally demanding) imputation of missing values. After the study being finalized, we also plan to make the database of 721 datasets to be made available in the github repository.

Acknowledgment. The authors would like to thank Aleš Neoral for help.

References

1. Arel-Bundock, V.: Website of datasets. https://vincentarelbundock.github.io/Rdatasets/datasets.html. Accessed 10 Sep 2019
2. Baldauf, M., Silva, J.M.C.S.: On the use of robust regression in econometrics. Econ. Let. **114**, 124–127 (2012)
3. Brazdil, P., Giraud-Carrier, C., Soares, C., Vilalta, E.: Metalearning: Applications to Data Mining. Springer, Berlin (2009)
4. Čížek, P.: Semiparametrically weighted robust estimation of regression models. Comput. Stat. Data An. **55**, 774–788 (2011)
5. Guo, Y., Hastie, T., Tibshirani, R.: Regularized discriminant analysis and its application in microarrays. Biostatistics **8**, 86–100 (2007)

6. Hastie, T., Tibshirani, R., Friedman, J.: The Elements of Statistical Learning. Springer, New York (2001)
7. Jurečková, J., Picek, J., Schindler, M.: Robust Statistical Methods with R, 2nd edn. CRC Press, Boca Raton (2019)
8. Jurečková, J., Sen, P.K., Picek, J.: Methodology in Robust and Nonparametric Statistics. CRC Press, Boca Raton (2013)
9. Kalina, J.: Highly robust methods in data mining. Serb. J. Manag. **8**, 9–24 (2013)
10. Kalina, J.: A robust pre-processing of BeadChip microarray images. Biocybern. Biomed. Eng. **38**, 556–563 (2018)
11. Kalina, J.: Metalearning for robust regression. https://github.com/jankalinaUI/Metalearning-for-robust-regression. Accessed 20 Oct 2019
12. Kalina, J., Peštová, B.: Robust regression estimators: a comparison of prediction performance. In: Proceedings of the 35th International Conference Mathematical Methods in Economics MME 2017, pp. 307–312. University of Hradec Králové, Hradec Králové (2017)
13. Kalina, J., Schlenker, A.: A robust supervised variable selection for noisy high-dimensional data. BioMed Res. Int. **2015**, 1–10 (2015). Article 320385
14. Koenker, R.: Quantile Regression. Cabridge University Press, Cambridge (2005)
15. Koenker, R., Park, B.J.: An interior point algorithm for nonlinear quantile regression. J. Econometrics **71**, 265–283 (1996)
16. Mount, D.M., Netanyahu, N.S., Piatko, C.D., Silverman, R., Wu, A.Y.: On the least trimmed squares estimator. Algorithmica **69**, 148–183 (2014)
17. Riazoshams, H., Midi, H.B., Sharipov, O.S.: The performance of robust two-stage estimator in nonlinear regression with autocorrelated error. Commun. Stat. Simulat. **39**, 1251–1268 (2010)
18. Rousseeuw, P.J., van Driessen, K.: Computing LTS regression for large datasets. Data Min. Knowl. Disc. **12**, 29–45 (2006)
19. Seber, G.A.F., Wild, C.J.: Nonlinear Regression. Wiley, New York (2003)
20. Smith-Miles, K., Baatar, D., Wreford, B., Lewis, R.: Towards objective measures of algorithm performance across instance space. Comput. Oper. Res. **45**, 12–24 (2014)
21. Stromberg, A.J., Ruppert, D.: Breakdown in nonlinear regression. J. Am. Stat. Assoc. **87**, 991–997 (1992)
22. Víšek, J.Á.: Robust error-term-scale estimate. In: Antoch, J., Hušková, M., Sen, P.K. (eds.) Nonparametrics and Robustness in Modern Statistical Inference and Time Series Analysis: A Festschrift in Honor of Professor Jana Jurečková. IMS Collections, **7**, pp. 254–267 (2010)
23. Víšek, J.Á.: Consistency of the least weighted squares under heteroscedasticity. Kybernetika **47**, 179–206 (2011)

An ASP-Based Approach for Phase Balancing in Power Electrical Systems

Theofanis Aravanis[1,2(✉)], Andreas Petratos[3], and Georgia Douklia[4]

[1] Department of Business Administration, School of Economics & Business, University of Patras, Patras, Greece
taravanis@upatras.gr

[2] Department of Mechanical Engineering, School of Engineering, University of the Peloponnese, Patras, Greece

[3] Elikonos 10, 263 31 Patras, Greece
andreas.petratos89@gmail.com

[4] Department of Mathematics, School of Natural Sciences, University of Patras, Patras, Greece
doukliageo10@gmail.com

Abstract. Unbalanced electrical loads on feeders of power electrical systems can cause serious problems, including power losses, significantly lower power quality, damaging of electrical equipment, and tripping of protective devices. Nevertheless, the problem of balancing such systems—which essentially is equivalent to the problem of integer partitioning—has proven to be NP-complete. Against this background, in this article, an algorithm based on the powerful, declarative framework of Answer Set Programming (ASP) is provided, that efficiently attacks practical instances of the phase-balancing problem. To the best of our knowledge, this is the first attempt of approaching this significant engineering problem by means of the ASP paradigm. The whole study indicates that the examined problem is of great interest from an algorithmic viewpoint, as well as an engineering application that highlights ASP's modelling methodology.

Keywords: Answer Set Programming · Power electrical systems · Phase-balancing problem · Energy distribution

1 Introduction

Modern power electrical systems demand high efficiency, robustness, and high-quality power supply for the consumers' sensitive electrical loads [3,12].

A typical three-phase 4-wire power system is depicted in Fig. 1. A three-phase alternating current (AC) source, connected as a wye (Y), feeds a three-phase wye (Y) connected, *linear* load.[1] Each (complex) impedance Z_a, Z_b and Z_c represents

[1] The current of a linear electrical load (e.g., resistor, motor, capacitor) is, at any time, *linearly proportional* to its voltage.

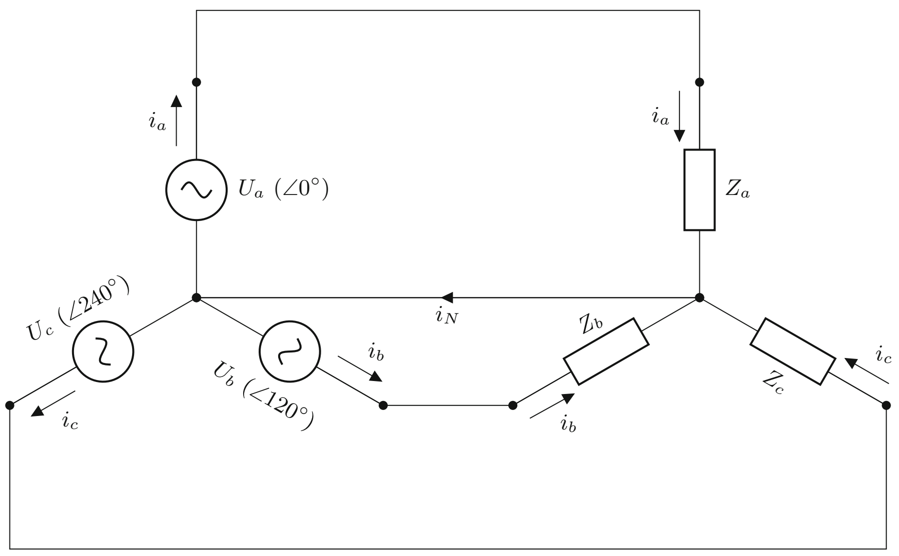

Fig. 1. A typical three-phase 4-wire power electrical system.

a single or, sometimes, a *cluster* of single-phase loads. Kirchhoff's Law enforces that the sum total of the phase currents i_a, i_b, i_c is equal to the current i_N of the neutral line; i.e., $i_a + i_b + i_c = i_N$.

For reasons that will become apparent in what follows, the ideal case is where the load is fully *balanced* (or *symmetric*), that is, $Z_a = Z_b = Z_c$, and the current i_N in the neutral line is zero (since $i_a + i_b + i_c = 0$). Nevertheless, achieving balance is not always an easy task, as the impedance of each phase is *changing frequently* over time (for instance, due to single-phase load variations), and the system drifts into *unbalance*; thus, $i_a + i_b + i_c \neq 0$. The goal of the network administrator is, therefore, to effectively distribute the loads in the first place, so that the minimum possible degree of unbalance to be achieved.

Unbalanced electrical loads of power electrical systems can cause numerous undesirable circumstances, including power losses, significantly lower power quality, damaging of electrical equipment, and tripping of protective devices [16].

The problem of phase balancing of feeders becomes even more demanding whenever a single-phase-to-ground fault has been occurred, and a *single-pole tripping* situation is ongoing, as depicted in Fig. 2. In this case, for as long as the faulted phase is out of service, and the total electrical load is served by the remaining two healthy phases, the feeder becomes significantly unbalanced. Given that faults of power electrical systems are predominantly single-phase-to-ground faults, the single-pole tripping situation is a quite often phenomenon [9].

In power systems where single-phase distribution transformers are utilized—a common practice in USA and Canada—the problem of phase balancing concerns HV/MV power transformers as well, since each single-phase distribution

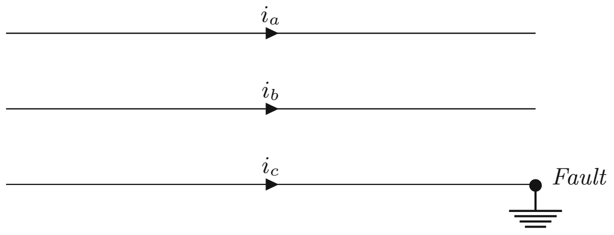

Fig. 2. A single-phase-to-ground fault in a three-phase power transmission line; only currents i_a and i_b reach the load, as i_c flows to the ground due to the fault.

transformer acts as a single-phase load for the HV/MV power transformers.[2] Therefore, a failure of the former can cause the unbalanced loading of the latter.

Against this background, an algorithm based on the powerful paradigm of *Answer Set Programming* (ASP) is provided in this article, that efficiently attacks practical instances of the phase-balancing problem. ASP is a modelling tool oriented towards difficult declaratively-specified search problems [7,8]. Despite the fact that it is a rather new programming framework, it has already successfully implemented to a plethora of real-world applications, including applications in science and humanities, industrial applications, data management and Artificial Intelligence [2].

Although there has been work made concerning phase balancing—the interested reader may, indicatively, refer to [10,13,16,17]—to the best of our knowledge, this is the first attempt of attacking this interesting search problem by means of ASP. As a matter of fact, this work constitutes a first step of our work-in-project according to which standard optimization problems in electrical engineering are addressed employing declarative problem-solving tools. It is noteworthy, lastly, that, as the phase-balancing problem is strongly related to power losses, the proposed algorithm is a useful tool for efficient energy management in any type of power transmission system, such as in *smart grids* [15]; see [14] for a study on phase balancing in a distribution smart grid.

For ease of presentation, throughout this work, we shall assume that each phase is compensated so that all three phases have the *same power factor*; i.e., $\texttt{arg}(Z_a) = \texttt{arg}(Z_b) = \texttt{arg}(Z_c)$.[3] For details on the structure and operation of power electrical systems, the interested reader is referred to [4,12].

The remainder of this paper is structured as follows: The next section introduces the problem of three-way integer partitioning, which, as it turns out, is equivalent to the phase-balancing problem. Section 3 presents the basic syntax and semantics of the ASP language, Sect. 4 introduces the alluded ASP-based algorithm, whereas, Sect. 5 conducts a brief experimental case study evaluating the proposed algorithm. The last two sections are devoted to a brief discussion and some concluding remarks.

[2] HV and MV stand for High-Voltage and Medium-Voltage, respectively.
[3] For a (non-zero) complex number z, $\texttt{arg}(z)$ denotes the argument of z.

2 The Integer Partitioning Problem

The problem of three-way integer partitioning is formally described as follows [11]:

> *Given a multiset of positive integers, the three-way integer partitioning problem is to divide them into three subsets, so that the sum of the numbers in each subset are as nearly equal as possible.*[4]

The integer partitioning problem has been shown to be NP-complete [5].

It turns out that the problem of three-way integer partitioning is *equivalent* to the three-phase-balancing problem, where each positive integer represents the *apparent power* of a load, and the three subsets correspond to the three phases of the feeder. Notice that, as $\texttt{arg}(Z_a) = \texttt{arg}(Z_b) = \texttt{arg}(Z_c)$, it is indifferent whether the apparent power, the impedance or the current of each load is utilized as the entity under partition.

Before presenting our ASP-based algorithm that addresses the phase-balancing problem, in the next section we introduce the basic syntax and semantics of the ASP language.

3 Answer Set Programming in a Nutshell

Answer Set Programming (alias, ASP) is a *declarative* problem-solving framework, that constitutes an easy and powerful modelling tool for *Knowledge Representation and Reasoning* applications (mainly, for solving NP-hard search problems) [7,8]. ASP's expressive power allows for a transparent and natural representation of the basic characteristics of the underlying problem.

The basic idea of ASP is to express a problem in a formal way, so that the *stable models* of its representation (alias, the *answer sets*) correspond to the solutions of the original problem. From a representational viewpoint, the *closed-world assumption* is adopted; that is, considering propositions as false, unless proved otherwise. In this sense, ASP can effectively capture *non-monotonicity*, a crucial feature for a wide range of applications.

In the rest of this section, we shall briefly review a subset of ASP's language that is sufficient for the purpose of this article, mainly borrowed from [1]; for more technical details on ASP, the reader is referred to [6].

3.1 Syntax

Definition 1 (Predicate Atom). *A predicate atom (or simply predicate) is denoted by $p(t_1, \ldots, t_n)$, where p is a predicate name, $t_1, \ldots, t_n$ are terms (constants or variables)—i.e., the arguments of predicate atoms—and the non-negative integer n is the arity of the predicate atom.*

[4] Recall that a multiset is a special type of set that allows for multiple instances for each of its elements.

Definition 2 (Conditional Atom). *A conditional atom is denoted by* $a_0 : a_1, \ldots, a_n$*, where every* a_i *for* $0 \leqslant i \leqslant n$ *is a predicate atom,* $a_1, \ldots, a_n$ *is the condition, and ':' resembles mathematical set notation.*

The purpose of ':' is to govern the instantiation of the "head literal" a_0, through the ones of $a_1, \ldots, a_n$. When a conditional atom is in the body of a rule, it expands conjunctively, whereas, when it is in the head of a rule, it expands disjunctively. If $n = 0$, we get a regular predicate atom, and denote it by a_0.

Definition 3 (ASP Logic Program). *An ASP logic program is a finite set of rules of the form:*

$$h_1; \ldots; h_m \leftarrow b_1, \ldots, b_n.$$

In the *head* of the rule, every h_j (for $1 \leqslant j \leqslant m$) is a predicate atom. In the *body* of the rule, every b_i (for $1 \leqslant i \leqslant n$) is a *literal* of the form a, `not` a, or $\neg a$, where a is a predicate atom, and the connectives '`not`' and '$\neg$' denote *default* and *classical* negation, respectively. Operators ';' and ',' express disjunctive and conjunctive connectives, respectively.

The rule is called *integrity constraint* if $m = 0$ (i.e., filters solution candidates, meaning that the literals in its body must *not jointly satisfied*), and *fact* if $m = 1$ and $n = 0$. In this latter case, the '$\leftarrow$' sign is usually omitted.

3.2 Semantics

Let $\mathbf{P}$ be an ASP logic program. The set of all constants that occur in $\mathbf{P}$ is called *Herbrand universe* of $\mathbf{P}$. The set of all predicate atoms constructible combining predicate names appearing in $\mathbf{P}$, with elements of the Herbrand universe of $\mathbf{P}$, is called *Herbrand base* of $\mathbf{P}$. A (Herbrand) *interpretation* $\mathcal{I}$ for $\mathbf{P}$ is a subset of the Herbrand base of $\mathbf{P}$ that contains all atoms interpreted as true by $\mathcal{I}$.

A rule is *ground* if it contains no variables. The *grounding* $\mathbf{P}^g$ of $\mathbf{P}$ is the set of all ground rules obtained by replacing all variables in each rule of $\mathbf{P}$ by all combinations of constants in the Herbrand universe. Given that an ASP logic program $\mathbf{P}$ with variables can be regarded as an abbreviation for $\mathbf{P}^g$, we henceforth concentrate on the propositional case.

Let $\mathcal{I}$ be an interpretation of $\mathbf{P}$. For a variable-free predicate atom a, $\mathcal{I} \models a$ iff $a \in \mathcal{I}$. For a default negated literal `not` a, $\mathcal{I} \models$ `not` a iff $\mathcal{I} \not\models a$, and for a classically negated literal $\neg a$, $\mathcal{I} \models \neg a$ iff $\neg a \in \mathcal{I}$.

A rule of $\mathbf{P}$ is satisfied by $\mathcal{I}$ if, for some h_j of the rule, $\mathcal{I} \models h_j$ whenever $\mathcal{I} \models b_i$, for all b_i of the rule. In this sense, an ASP logic program $\mathbf{P}$ is satisfied by $\mathcal{I}$ iff all rules of $\mathbf{P}$ are satisfied by $\mathcal{I}$.

Definition 4 (Model). *An interpretation* $\mathcal{I}$ *that satisfies an ASP logic program* $\mathbf{P}$ *is called a model of* $\mathbf{P}$*. A model of an ASP logic program* $\mathbf{P}$ *is a minimal model of* $\mathbf{P}$ *iff no proper subset of it satisfies* $\mathbf{P}$*.*

Those rules for which $\mathcal{I} \models b_i$, for all b_i, constitute the *reduct* $\mathbf{P}^{\mathcal{I}}$ of $\mathbf{P}$, with respect to $\mathcal{I}$.

Definition 5 (Answer Set—Stable Model). *An interpretation $\mathcal{I}$ is an answer set or stable model of an ASP logic program* $\mathbf{P}$ *iff* $\mathcal{I}$ *is a minimal model of the reduct* $\mathbf{P}^{\mathcal{I}}$.

4 The ASP-Based Algorithm

This section is devoted to the presentation of the alluded ASP-based algorithm that minimizes the degree of unbalance on feeders. The approach that the algorithm follows is the automated generation of *optimal* solutions for the declaratively-specified phase-balancing (search) problem. The source code of the program is presented subsequently in Listing 1, whereas, the predicates used are explained in Table 1.

```
 1  phase(a).  phase(b).  phase(c).

 2  l(1,25).  l(2,10).  ...  l(n,30).

 3  { line(F,l(N,W)) } :- phase(F), l(N,W).
 4  :- line(F1,l(N,_)), line(F2,l(N,_)), F1 != F2.
 5  :- not line(_,l(N,W)), l(N,W).
 6  :- not line(F,_), phase(F).

 7  line_load(F,S) :- phase(F), S = #sum{ P,N : line(F,l(N,P)) }.
 8  balanced(S/3) :- S = #sum{ P,N : l(N,P) }.
 9  error(F,|P-S|) :- phase(F), balanced(P), line_load(F,S).
10  total_error(S/3) :- S = #sum{ P,F : error(F,P) }.

11  #minimize { S : total_error(S) }.

12  #show line/2.  #show line_load/2.  #show total_error/1.
```

Listing 1. The ASP-based algorithm for the three-phase-balancing problem.

Some comments on the source code are in order. First of all, observe that a logic program consists of statements, all of which are terminated by a period '`.`'. Moreover, the connective '`:-`' can be read as '*if*'.

The algorithm takes as input the power S_i of each load i (for $1 \leqslant i \leqslant n$). Note that a cluster of loads can be, also, regarded as a single load.

Line 1 sets (in the form of facts) the three phases of the system, whereas, line 2 sets the available electrical loads, along with their power consumption (the number of phases and the power consumption of loads are indicative). Note that ASP's language supports only integer numbers (written as sequences of the digits $0 \ldots 9$), however, for all practical purposes of the examined application, the (potential) loss in precision is insignificant. Moreover, the load range can be set between 1 and 100, and larger loads range can be scaled accordingly to this range.

Table 1. Explanation of the predicates appearing in Listing 1.

Predicate name	Explanation
`phase/1`	Phase (a or b or c)
`l/2`	Number (i) and power (S_i) of an electrical load
`line/2`	Phase on which an electrical load is connected
`line_load/2`	Total power that each phase supplies
`balanced/1`	Balanced power (S_{bal})
`error/2`	Power error for each phase (ϵ_a or ϵ_b or ϵ_c)
`total_error/1`	Total power error (ϵ)

Line 3 generates solution candidates, by means of a *choice rule*. The idea of a choice rule is to express choices over subsets of atoms. Any subset of its head atoms can be included in an answer set, provided the body literals are satisfied.[5] Hence, in each solution candidate, arbitrary connections of each load to some phase(s) are made.

Line 4 is an integrity constraint which ensures that a load cannot be connected, simultaneously, to two distinct phases. In the same manner, line 5 ensures that every load is connected to at least one phase, and line 6 excludes phases without load. We note here that, unlike a variable name, whose recurrences within a rule refer to the same variable, the token '_' (not followed by any letter) stands for an anonymous variable that does not recur anywhere; one can view this as if a new variable name is invented on each occurrence of '_'.

Line 7 calculates the total power that each phase supplies. Line 8 calculates what we shall call *balanced power*. Balanced power, denoted S_{bal}, is the power of each phase when the three-phase load is perfectly balanced, and is calculated by the sum of the power of all electrical loads, divided by 3. In symbols:

$$S_{bal} = \frac{\sum_{i=1}^{n} S_i}{3} \tag{1}$$

Line 9 calculates the *power error* ϵ_x (where x stands for a phase a, b or c) for each one of the three phases; that is, the absolute value of the difference between S_{bal} and the total power that each phase supplies. Line 10 calculates the *total power error* ϵ; that is, the mean value of the errors of each phase. In symbols:

$$\epsilon = \frac{\epsilon_a + \epsilon_b + \epsilon_c}{3} \tag{2}$$

Line 11 is a minimization statement which generates the answer set with the minimum value of total power error ϵ. Lastly, line 12 indicates that only atoms over the predicates `line/2`, `line_load/2` and `total_error/1` ought to be printed.

[5] For instance, the logic program $\mathbf{P} = \{$ `a, {b} :- a` $\}$ has two answer sets; i.e., `{a}` and `{a,b}`.

Table 2. Computation time for indicative load distributions; the electrical loads are separated by semi-colons.

Loads distributions (kVA)	Total load (kVA)	Time (ms)
1; 5; 7; 10; 4; 8; 4; 1; 2; 3	45	410
11; 3; 3; 6; 5; 4; 7; 2; 1; 1	43	449
2; 4; 1; 10; 1; 4; 3; 2; 8; 13	48	550
6; 3; 9; 1; 5; 4; 3; 2; 1; 1	35	310
2; 4; 1; 2; 1; 5; 3; 7; 2; 14	41	406

5 Experimental Case Study

In order to test the performance of the proposed algorithm, indicative instances of the phase-balancing problem shall be considered in this section. The electrical system under investigation is assumed to be the electricity distribution network of Greece. The typical feeder of this network is a pole-mounted three-phase transformer, with the following technical characteristics: 50 kVA, 20/0.4 kV, Dyn1, 4%.

We consider 10 electrical loads (or cluster of loads). The computation time for indicative (random) load distributions of the electrical system is presented in Table 2. All computations were performed on an Intel© Core$^{\text{TM}}$ i5-2410M CPU @ 2.30 GHz machine, with 4 GB RAM available, using Clingo (version 4.5.4).[6]

The results obtained by Clingo for the first electrical load distribution are reported subsequently.

```
line(a,l(4,10))  line(a,l(5,4))

line(b,l(1,1))   line(b,l(3,7))   line(b,l(6,8))

line(c,l(2,5))   line(c,l(7,4))
line(c,l(8,1))   line(c,l(9,2))   line(c,l(10,3))

line_load(a,14)  line_load(b,16)  line_load(c,15)

total_error(0)
```

It is evident from Table 2 that the algorithm performs excellent for all practical instances of the problem; the time required to find the optimal solution for every considered scenario is in the order of *milliseconds* (ms). As it may be expected, its performance depends, not only on the total number of loads, but also on the loads distribution. In any case, if quality is what primarily matters, then lower performance can be tolerated, whereas, if protection is the main factor under consideration, then high performance seems to be imperative.

[6] https://potassco.org/clingo.

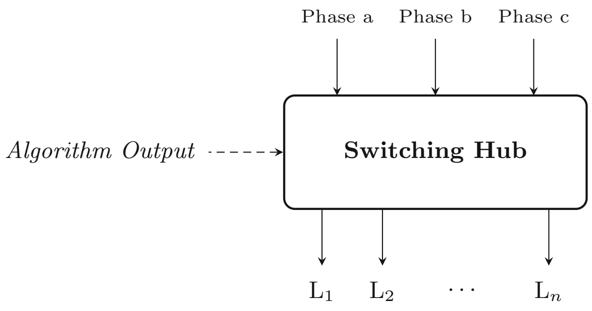

Fig. 3. The switching hub of the system. The hub implements the proper hard-wiring, so that each phase a, b or c of the feeder feeds the appropriate electrical load L_i (with $1 \leqslant i \leqslant n$), according to the output of Listing 1.

6 Discussion

In order for the results of the algorithm of Listing 1 to be practically implemented, a hardware installation in the form of *switching hub* is necessary, so that the appropriate connections between the three phases of the feeder and the available (clusters of) electrical loads to be employed (see Fig. 1). Such switching hub is depicted in Fig. 3, where the three phases of the feeder enter the hub which, given the output of the proposed algorithm, implements the proper hard-wiring so that each phase feeds the appropriate electrical load L_i (with $1 \leqslant i \leqslant n$).

7 Conclusion

In this article, we provided an ASP-based algorithm that efficiently attacks practical instances of the phase-balancing problem, a well-known NP-complete problem of power electrical systems. This is an interesting search problem from an algorithmic viewpoint, as well as an electrical-engineering application that highlights ASP's modelling methodology. The proposed algorithm aims to contribute to the development of a robust method for phase balancing in high-quality modern power electrical systems, given that unbalanced feeders may lead to a plethora of undesirable and harmful circumstances.

Following a line of research according to which standard optimization problems in electrical engineering are addressed by means of declarative problem-solving tools, future work is to be devoted to the study of the electricity cost-minimization problem with the aid of ASP.

Acknowledgements. The authors are grateful to the two anonymous reviewers for their valuable comments on this work.

References

1. Brenton, C., Faber, W., Batsakis, S.: Answer set programming for qualitative spatio-temporal reasoning: methods and experiments. In: Carro, M., King, A., Saeedloei, N., Vos, M.D. (eds.) Technical Communications of the 32nd International Conference on Logic Programming, ICLP 2016. Dagstuhl Publishing (2016)
2. Brewka, G., Eiter, T., Truszczyński, M.: Answer set programming at a glance. Commun. ACM **54**(12), 93–103 (2011)
3. Dugan, R., McGranaghan, M., Santoso, S., Beaty, H.W.: Electrical Power Systems Quality, 3rd edn. McGraw-Hill Education, New York (2012)
4. El-Hawary, M.E.: Electrical Energy Systems. CRC Press, Boca Raton (2018)
5. Garey, M.R., Johnson, D.S.: Computers and Intractability: A Guide to the Theory of NP-Completeness. W. H. Freeman, New York (1979)
6. Gebser, M., Kaminski, R., Kaufmann, B., Lindauer, M., Ostrowski, M., Romero, J., Schaub, T., Thiele, S.: Potassco User Guide, 2nd edn. University of Potsdam, Potassco (2017)
7. Gebser, M., Kaminski, R., Kaufmann, B., Schaub, T.: Answer Set Solving in Practice. Synthesis Lectures on Artificial Intelligence and Machine Learning. Morgan & Claypool Publishers, San Rafael (2012)
8. Gelfond, M.: Answer sets. In: van Harmelen, F., Lifschitz, V., Porter, B. (eds.) Handbook of Knowledge Representation, pp. 285–316. Elsevier Science, Amsterdam (2008)
9. Godoy, E., Celaya, A., Altuve, H.J., Fischer, N., Guzmán, A.: Tutorial on single-pole tripping and reclosing. In: Proceedings of the 39th Annual Western Protective Relay Conference (2012)
10. Gupta, N., Swarnkar, A., Niazi, K.R.: A novel strategy for phase balancing in three-phase four-wire distribution systems. In: 2011 IEEE Power and Energy Society General Meeting (2011)
11. Korf, R.E.: A complete anytime algorithm for number partitioning. Artif. Intell. **106**, 181–203 (1998)
12. Kothari, D.P., Nagrath, I.J.: Modern Power System Analysis, 4th edn. Tata McGraw Hill, New York (2011)
13. Lin, C.H., Chen, C.S., Chuang, H.J., Ho, C.Y.: Heuristic rule-based phase balancing of distribution systems by considering customer load patterns. IEEE Trans. Power Syst. **20**, 709–716 (2005)
14. Mansouri, K., Hamed, M.B., Sbita, L., Dhaoui, M.: Three-phase balancing in a LV distribution smart-grids using electrical load flow variation: "L.F.B.M.". In: Proceedings of the 16th International Conference on Sciences and Techniques of Automatic Control and Computer Engineering, STA 2015, pp. 427–431 (2015)
15. Momoh, J.A.: Smart Grid: Fundamentals of Design and Analysis, 1st edn. Wiley-IEEE Press, Hoboken (2012)
16. Wang, K., Skiena, S., Robertazzi, T.G.: Phase balancing algorithms. Electr. Power Syst. Res. **96**, 218–224 (2013)
17. Wang, W., Yu, N.: Phase balancing in power distribution network with data center. ACM SIGMETRICS Perform. Eval. Rev. **45**, 64–69 (2017)

Neural Networks Algorithmic Foundations

A New Lyapunov Analysis of Robust Stability of Neural Networks with Discrete Time Delays

Sabri Arik(✉)

Department of Computer Engineering, Faculty of Engineering, Istanbul University-Cerrahpasa, 34320 Avcilar, Istanbul, Turkey
ariks@istanbul.edu.tr

Abstract. This paper studies the global asymptotic robust stability of dynamical neural networks with discrete time delays under parameter uncertainties. By utilising the Lyapunov stability and Homeomorphic mapping theorems, a new sufficient condition is presented for the existence, uniqueness and global robust asymptotic stability of this class of neural systems with respect to the Lipschitz continuous activation functions. The proposed stability criterion is derived by employing a new type of Lyapunov functional and it unifies some of the key robust stability results obtained in the past literature.

Keywords: Delayed neural networks · Robust stability analysis · Homeomorphic mapping · Lyapunov functionals

1 Introduction

In the past years, dynamical neural networks have been successfully employed to solve real world engineering problems such as combinatorial optimization, image processing, pattern recognition, and associative memories. These applications usually require that the employed neural network must possess unique and globally asymptotically stable equilibrium points. Therefore, it is of great interest to carrying out the stability analysis of dynamical neural networks. Another important issue regarding stability of neural systems is the problem of time delays due to the finite switching speed of amplifiers during the neuronal signal transmission, which can have negative impact on the dynamical behaviours of the system. On the other hand, when electronically implementing neural systems, some external disturbances may cause undesired deviations in the values of the network parameters. Therefore, in order to conduct a complete and proper stability analysis of neural systems, the time delays and parameter uncertainties must be adequately introduced into the mathematical models of neural networks. This leads us to study the robust stability of neural networks in the presence of time delays. Recently, many papers have proposed various robust stability results for different types of delayed neural networks [1–20]. In this paper, by employing the Lyapunov stability and Homeomorphic mapping theorems, a new sufficient condition is obtained for the existence, uniqueness and global robust asymptotic stability of neural systems involving discrete time delays with respect to the Lipschitz continuous activation functions.

Notations: Let $v = (v_1, v_2, ..., v_n)^T$ be real vector and $Q = (q_{ij})_{n\times n}$ be a real matrix. $|v|$ will denote $|v| = (|v_1|, |v_2|, ..., |v_n|)^T$ and $|Q|$ will denote $|Q| = (|q_{ij}|)_{n\times n}$. If $P = (p_{ij})_{n\times n}$ and $Q = (q_{ij})_{n\times n}$ are two real matrices, then, $P \preceq Q$ will imply that $p_{ij} \le q_{ij}, i, j = 1, 2, ..., n$. The three commonly used vector norms for v and matrix norms for Q are as follows:

$$||v||_1 = \sum_{i=1}^{n} |v_i|,\ \ ||v||_2 = \sqrt{\sum_{i=1}^{n} v_i^2},\ \ ||v||_\infty = \max_{1\le i\le n} |v_i|$$

$$||Q||_1 = \max_{1\le i\le n} \sum_{j=1}^{n} |q_{ji}|, ||Q||_2 = [\lambda_{\max}(Q^TQ)]^{1/2}, ||Q||_\infty = \max_{1\le i\le n} \sum_{j=1}^{n} |q_{ij}|$$

This paper will consider the following neural network model with discrete time delays:

$$\frac{dx_i(t)}{dt} = -c_i x_i(t) + \sum_{j=1}^{n} a_{ij} f_j(x_j(t)) + \sum_{j=1}^{n} b_{ij} f_j(x_j(t-\tau_j)) + u_i, i = 1, 2, ..., n \quad (1)$$

where n is the number of the neurons, $x_i(t)$ denotes the state of the neuron i at time t, $f_i(\cdot)$ denote activation functions, a_{ij} and b_{ij} denote the strengths of connectivity between neurons j and i at time t and $t - \tau_j$, respectively; τ_j represents the time delay required in transmitting a signal from the neuron j to the neuron i, u_i is the constant input to the neuron i, the positive constant c_i is the charging rate for the neuron i.

The matrix-vector form of (1) is as follows:

$$\dot{x}(t) = -Cx(t) + Af(x(t)) + Bf(x(t-\tau)) + u \quad (2)$$

where $x(t) = (x_1(t), x_2(t), ..., x_n(t))^T$, $A = (a_{ij})_{n\times n}$, $B = (b_{ij})_{n\times n}$, $C = diag\ (c_i)$, $u = (u_1, u_2, ..., u_n)^T$, $f(x(t)) = (f_1(x_1(t)), f_2(x_2(t)), ..., f_n(x_n(t)))^T$ and $f(x(t-\tau)) = (f_1(x_1(t-\tau_1)), f_2(x_2(t-\tau_2)), ..., f_n(x_n(t-\tau_n)))^T$.

In order to study the stability of dynamical neural networks, we first require to define properties of the activation functions. In the current paper, the activation functions f_i will be choosen to be Lipschitz continuous. Lipschitz activation functions satisfy the following condition:

$$|f_i(x) - f_i(y)| \le \ell_i |x - y|,\ i = 1, 2, \cdots, n,\ \ \forall x, y \in R, x \ne y. \quad (3)$$

where ℓ_i are the Lipschitz constants.

When studying the robust stability of neural systems, it is customary to assume that the system matrices $A = (a_{ij})$, $B = (b_{ij})$ and $C = diag(c_i > 0)$ are defined in the following intervals:

$$\begin{aligned} C_I &:= \{C : 0 \prec \underline{C} \preceq C \preceq \overline{C}, i.e., 0 < \underline{c}_i \leq c_i \leq \overline{c}_i\} \\ A_I &:= \{A = (a_{ij}) : \underline{A} \preceq A \preceq \overline{A}, i.e., \underline{a}_{ij} \leq a_{ij} \leq \overline{a}_{ij}\} \\ B_I &:= \{B = (b_{ij}) : \underline{B} \preceq B \preceq \overline{B}, i.e., \underline{b}_{ij} \leq b_{ij} \leq \overline{b}_{ij}\} \end{aligned} \tag{4}$$

Note that (4) implies that the system matrices $A = (a_{ij})$, $B = (b_{ij})$ and $C = diag(c_i > 0)$ have the bounded norms. Therefore, in this paper, we will assume that the norms of the matrices $A = (a_{ij})$, $B = (b_{ij})$ and $C = diag(c_i > 0)$ are bounded. In other words, the matrices $A = (a_{ij})$, $B = (b_{ij})$ and $C = diag(c_i > 0)$ may have different upper bound norms. In the following, we unify the previous literature results which define various upper bound norms for the matrices intervalized in the form given in (4).

Lemma 1: Assume that the matrices A and B in (2) are defined within the intervals given by (4). Define $A^* = \frac{1}{2}(\overline{A} + \underline{A})$, $A_* = \frac{1}{2}(\overline{A} - \underline{A})$, $\hat{A} = (\hat{a}_{ij})_{n \times n}$ with $\hat{a}_{ij} = max\{|\underline{a}_{ij}|, |\overline{a}_{ij}|\}$, $B^* = \frac{1}{2}(\overline{B} + \underline{B})$, $B_* = \frac{1}{2}(\overline{B} - \underline{B})$, $\hat{B} = (\hat{b}_{ij})_{n \times n}$ with $\hat{b}_{ij} = max\{|\underline{b}_{ij}|, |\overline{b}_{ij}|\}$. Let

$$\begin{aligned} \sigma_1(A) &= \sqrt{\||{A^*}^T A^*| + 2|{A^*}^T|A_* + A_*^T A_*\|_2} \\ \sigma_2(A) &= \|A^*\|_2 + \|A_*\|_2 \\ \sigma_3(A) &= \sqrt{\|A^*\|_2^2 + \|A_*\|_2^2 + 2\|A_*^T|A^*|\|_2} \\ \sigma_4(A) &= \|\hat{A}\|_2 \end{aligned}$$

and

$$\begin{aligned} \sigma_1(B) &= \sqrt{\||{B^*}^T B^*| + 2|{B^*}^T|B_* + B_*^T B_*\|_2} \\ \sigma_2(B) &= \|B^*\|_2 + \|B_*\|_2 \\ \sigma_3(B) &= \sqrt{\|B^*\|_2^2 + \|B_*\|_2^2 + 2\|B_*^T|B^*|\|_2} \\ \sigma_4(B) &= \|\hat{B}\|_2 \end{aligned}$$

Then, the following conditions are satisfied:

$$\|A\|_2 \leq \sigma_m(A) = min\{\sigma_1(A), \sigma_2(A), \sigma_3(A), \sigma_4(A)\} \tag{5}$$

and

$$\|B\|_2 \leq \sigma_m(B) = min\{\sigma_1(B), \sigma_2(B), \sigma_3(B), \sigma_4(B)\} \tag{6}$$

We note here that the conditions $\|A\|_2 \leq \sigma_1(A)$, $\|A\|_2 \leq \sigma_2(A)$, $\|A\|_2 \leq \sigma_3(A)$ and $\|A\|_2 \leq \sigma_4(A)$ have been obtained in the references [1–3] and [4], respectively.

The following well known result provides an important toll for the analysis of the existence and uniqueness equilibrium point for nonlinear systems:

Lemma 6 [5]**:** If a map $H(x) \in C^0$ satisfies the conditions $H(x) \neq H(y)$ for all $x \neq y$ and $||H(x)|| \rightarrow \infty$ as $||x|| \rightarrow \infty$, then, $H(x)$ is homeomorphism of R^n.

2 Existence and Uniqueness Analysis of Equilibrium Point

In this section, we will present a new sufficient condition that ensures the existence and uniqueness of the equilibrium point of the neural network model (1).

Theorem 1: For the neural system defined by (1), let the activation functions $f_i(\cdot)$ satisfy (3) and the network matrices A, B and C satisfy (4). Then, the neural network model (1) has a unique equilibrium point for each u, if the following condition holds:

$$\Upsilon = \frac{c_m^2}{\ell_M^2} - \sigma_m^2(A) - \sigma_m^2(B) - 2\|\hat{A}^T \hat{B}\|_2 > 0$$

where $c_m = min\{\underline{c}_i\}$, $\ell_M = max\{\ell_i\}$, $\sigma_m(A) = min\{\sigma_1(A), \sigma_2(A), \sigma_3(A), \sigma_4(A)\}$ and $\sigma_m(B) = min\{\sigma_1(B), \sigma_2(B), \sigma_3(B), \sigma_4(B)\}$, $\hat{A} = (\hat{a}_{ij})_{n \times n}$ with $\hat{a}_{ij} = max\{|\underline{a}_{ij}|, |\overline{a}_{ij}|\}$ and $\hat{B} = (\hat{b}_{ij})_{n \times n}$ with $\hat{b}_{ij} = max\{|\underline{b}_{ij}|, |\overline{b}_{ij}|\}$.

Proof: In order to prove the existence and uniqueness of the equilibrium point, we will make use of the result of Lemma 6. For the neural network model (1), we can define the following associated map:

$$H(x) = -Cx + Af(x) + Bf(x) + u \tag{7}$$

$H(x) = 0$ implies that

$$-Cx + Af(x) + Bf(x) + u = 0$$

which is exactly the equilibrium equation of system (1). Therefore, every solution of $H(x) = 0$ is an equilibrium point of (1) since $H(x) = 0$ is equivalent to $\dot{x} = 0$. Therefore, the fact that $H(x)$ is homeomorphism of R^n will directly imply the the proof of Theorem 1. We will now show that the condition given Theorem 1 ensures that $H(x)$ is homeomorphism of R^n. Let $x \in R^n$ and $y \in R^n$ be two vectors such that $x \neq y$. Then, for $H(x)$ defined by (7), we can write

$$H(x) - H(y) = -C(x - y) + A(f(x) - f(y)) + B(f(x) - f(y)) \tag{8}$$

For the activation functions belonging to class $\mathcal{K}$, $x \neq y$ implies two distinct cases: $x \neq y$ and $f(x) - f(y) = 0$, or $x \neq y$ and $f(x) - f(y) \neq 0$. In the case of $x \neq y$ and $f(x) - f(y) = 0$, (8) takes the form

$$H(x) - H(y) = -C(x - y)$$

Since C is a positive diagonal matrix, $x - y \neq 0$ directly implies that $H(x) \neq H(y)$. Now consider the case where $x - y \neq 0$ and $f(x) - f(y) \neq 0$. In this case, from (8), we can derive the following

$$\begin{aligned}
&[2C(x-y) + H(x) - H(y)]^T[H(x) - H(y)] \\
&= [C(x-y) + A(f(x) - f(y)) + B(f(x) - f(y))]^T \\
&\quad \times[-C(x-y) + A(f(x) - f(y)) + B(f(x) - f(y))] \\
&= (x-y)^T C^2 (x-y) + (f(x) - f(y))^T A^T A(f(x) - f(y)) \\
&\quad +(f(x) - f(y))^T B^T B(f(x) - f(y)) + 2(f(x) - f(y))^T A^T B(f(x) - f(y)) \\
&\leq -c_m^2\|x-y\|_2^2 + \|A\|_2^2\|f(x) - f(y)\|_2^2 + \|B\|_2^2\|f(x) - f(y)\|_2^2 \\
&\quad +2|f(x) - f(y)|^T|A^T||B||f(x) - f(y)| \qquad (9)
\end{aligned}$$

From Lemma 1, we know that $\|A\|_2^2 \leq \sigma_m^2(A)$ and $\|B\|_2^2 \leq \sigma_m^2(B)$. Thus, (9) satisfies

$$\begin{aligned}
&[2C(x-y) + H(x) - H(y)]^T[H(x) - H(y)] \\
&\leq -c_m^2\|x-y\|_2^2 + \sigma_m^2(A)\|f(x) - f(y)\|_2^2 + \sigma_m^2(B)\|f(x) - f(y)\|_2^2 \\
&\quad +2|f(x) - f(y)|^T|A^T||B||f(x) - f(y)| \qquad (10)
\end{aligned}$$

Since $|A| \preceq \hat{A}$ and $|B| \preceq \hat{B}$, we can write the following inequality

$$\begin{aligned}
|f(x) - f(y)|^T|A^T||B||f(x) - f(y)| &\leq |f(x) - f(y)|^T|\hat{A}^T||\hat{B}||f(x) - f(y)| \\
&\leq \|\hat{A}^T\hat{B}||_2\|f(x) - f(y)\|_2^2 \qquad (11)
\end{aligned}$$

Using (11) in (10) leads to

$$\begin{aligned}
&[2C(x-y) + H(x) - H(y)]^T[H(x) - H(y)] \\
&\leq -c_m^2\|x-y\|_2^2 + \sigma_m^2(A)\|f(x) - f(y)\|_2^2 + \sigma_m^2(B)\|f(x) - f(y)\|_2^2 \\
&\quad +2\|\hat{A}^T\hat{B}||_2\|f(x) - f(y)\|_2^2 \qquad (12)
\end{aligned}$$

In the light of (3), we can write $\|f(x) - f(y)\|_2^2 \leq \ell_M^2\|x-y\|_2^2$. Hence, (12) takes the form:

$$\begin{aligned}
&[2C(x-y) + H(x) - H(y)]^T[H(x) - H(y)] \\
&\leq -c_m^2\|x-y\|_2^2 + \ell_M^2\sigma_m^2(A)\|x-y\|_2^2 + \ell_M^2\sigma_m^2(B)\|x-y\|_2^2 \\
&\quad +2\ell_M^2\|\hat{A}^T\hat{B}||_2\|x-y\|_2^2 \\
&= -\ell_M^2\Upsilon\|x-y\|_2^2 \qquad (13)
\end{aligned}$$

(13) can be written as

$$\begin{aligned}
&2(x-y)^T C(H(x) - H(y)) + (H(x)) - H(y))^T(H(x) - H(y)) \\
&\leq -\ell_M^2\Upsilon\|x-y\|_2^2 \qquad (14)
\end{aligned}$$

Since the term $(H(x)) - H(y))^T(H(x) - H(y)) \geq 0$, it follows from (14) that

$$2(x-y)^T C(H(x) - H(y)) \leq -\ell_M^2\Upsilon\|x-y\|_2^2 \qquad (15)$$

Since $\Upsilon > 0$, for $x - y \neq 0$, (15) implies that

$$2(x-y)^T C(H(x) - H(y)) < 0 \tag{16}$$

It can be directly concluded from (16) that $H(x) \neq H(y)$ for all $x \neq y$.

Letting $y = 0$ in (15) leads to

$$2x^T C(H(x) - H(0)) \leq -\ell_M^2 \Upsilon \|x\|_2^2 \tag{17}$$

Taking the absolute value of both sides of (17) yields:

$$2|x^T C(H(x) - H(0))| \geq \ell_M^2 \Upsilon \|x\|_2^2 \tag{18}$$

Form (18), the following can be written

$$2\|C\|_\infty \|x\|_\infty \|H(x) - H(0)\|_1 \geq \ell_M^2 \Upsilon \|x\|_2^2 \tag{19}$$

Since $\|x\|_\infty \leq \|x\|_2$ and $\|H(x) - H(0)\|_1 \leq \|H(x)\|_1 + \|H(0)\|_1$, we obtain from (19) that

$$\|H(x)\|_1 \geq \frac{\ell_M^2 \Upsilon \|x\|_2}{2\|C\|_\infty} - \|H(0)\|_1 \tag{20}$$

Since, $\|C\|_\infty$ and $\|H(0)\|_1$ are real finite values, it directly follows from (20) that $\|H(x)\| \to \infty$ as $\|x\| \to \infty$. Thus, the proof of Theorem 1 is complete.

3 Stability Analysis of Equilibrium Point

In this section, it will be shown that the condition obtained in Theorems 1 for the existence and uniqueness of the equilibrium point also implies the asymptotic stability of equilibrium point of neural system (1). Let x^* denote the equilibrium point of neural network model (1). By using the transformation $z_i(\cdot) = x_i(\cdot) - x_i^*, \;\; i = 1, 2, ..., n$, system (1) can be put into the following form:

$$\dot{z}_i(t) = -c_i z_i(t) + \sum_{j=1}^{n} a_{ij} g_j(z_j(t)) + \sum_{j=1}^{n} b_{ij} g_j(z_j(t - \tau_j)) \tag{21}$$

where $g_i(z_i(t)) = f_i(z_i(t) + x_i^*) - f_i(x_i^*), \forall i$. Note that neural system (21) inherits the assumption given by (3), namely,

$$|g_i(z_i(t))| \leq \ell_i |z_i(t)|, \; \forall i. \tag{22}$$

The stability of the origin of the transformed system (21) is equivalent to the stability of the equilibrium point x^* of (1). Therefore, we will establish the stability of the origin of system (21) instead of considering the stability of the equilibrium point of system (1).

System (21) can be written in the form:

$$\dot{z}(t) = -Cz(t) + Ag(z(t)) + Bg(z(t - \tau)) \tag{23}$$

with $z(t) = (z_1(t), z_2(t), ..., z_n(t))^T$, $g(z(t)) = (g_1(z_1(t)), g_2(z_2(t)), ..., g_n(z_n(t)))^T$ and $g(z(t - \tau)) = (g_1(z_1(t - \tau_1)), g_2(z_2(t - \tau_2)), ..., g_n(z_n(t - \tau_n)))^T$.

We can now proceed with the following result:

Theorem 2: For the neural system defined by (21), let the activation functions $g_i(\cdot)$ satisfy (22) and the network matrices A, B and C satisfy (4). Then, the origin of neural network model (21) is globally asymptotically stable, if the following condition holds:

$$\Upsilon = \frac{c_m^2}{\ell_M^2} - \sigma_m^2(A) - \sigma_m^2(B) - 2\|\hat{A}^T\hat{B}\|_2 > 0$$

where $c_m = min\{\underline{c}_i\}$, $\ell_M = max\{\ell_i\}$, $\sigma_m(A) = min\{\sigma_1(A), \sigma_2(A), \sigma_3(A), \sigma_4(A)\}$ and $\sigma_m(B) = min\{\sigma_1(B), \sigma_2(B), \sigma_3(B), \sigma_4(B)\}$, $\hat{A} = (\hat{a}_{ij})_{n\times n}$ with $\hat{a}_{ij} = max\{|\underline{a}_{ij}|, |\overline{a}_{ij}|\}$ and $\hat{B} = (\hat{b}_{ij})_{n\times n}$ with $\hat{b}_{ij} = max\{|\underline{b}_{ij}|, |\overline{b}_{ij}|\}$.

Proof: We employ the following Lyapunov functional [21]:

$$\begin{aligned} V(z(t)) = &\sum_{i=1}^{n} c_i z_i^2(t) + \sum_{i=1}^{n}\int_{t-\tau_i}^{t} \dot{z}_i^2(s)ds + \alpha\sum_{i=1}^{n}\int_{t-\tau_i}^{t} g_i^2(z_i(s))ds \\ &+ \beta\sum_{i=1}^{n}\int_{t-\tau_i}^{t} z_i^2(s)ds \end{aligned}$$

where α and β are some positive constant whose values will be obtained in what follows. The time derivative of the functional along the trajectories of system (23) is obtained as follows

$$\begin{aligned} \dot{V}(z(t)) &= \sum_{i=1}^{n} 2c_i z_i(t)\dot{z}_i(t) + \sum_{i=1}^{n}\dot{z}_i^2(t) - \sum_{i=1}^{n}\dot{z}_i^2(t-\tau_i) \\ &\quad +\alpha\sum_{i=1}^{n} g_i^2(z_i(t)) - \alpha\sum_{i=1}^{n} g_i^2(z_i(t-\tau_i)) + \beta\sum_{i=1}^{n} z_i^2(t) - \beta\sum_{i=1}^{n} z_i^2(t-\tau_i) \\ &= \sum_{i=1}^{n}(2c_i z_i(t) + \dot{z}_i(t))\dot{z}_i(t) - \sum_{i=1}^{n}\dot{z}_i^2(t-\tau_i) \\ &\quad +\alpha\sum_{i=1}^{n} g_i^2(z_i(t)) - \alpha\sum_{i=1}^{n} g_i^2(z_i(t-\tau_i)) + \beta\sum_{i=1}^{n} z_i^2(t) - \beta\sum_{i=1}^{n} z_i^2(t-\tau_i) \\ &= \sum_{i=1}^{n}[(c_i z_i(t) + \sum_{j=1}^{n} a_{ij}g_j(z_j(t)) + \sum_{j=1}^{n} b_{ij}g_j(z_j(t-\tau_j))) \\ &\quad \times(-c_i z_i(t) + \sum_{j=1}^{n} a_{ij}g_j(z_j(t)) + \sum_{j=1}^{n} b_{ij}g_j(z_j(t-\tau_j)))] \\ &\quad -\sum_{i=1}^{n}\dot{z}_i^2(t-\tau_i) + \alpha\sum_{i=1}^{n} g_i^2(z_i(t)) - \alpha\sum_{i=1}^{n} g_i^2(z_i(t-\tau_i)) \end{aligned}$$

$$
\begin{aligned}
&+\beta\sum_{i=1}^{n} z_i^2(t)-\beta\sum_{i=1}^{n} z_i^2(t-\tau_i)\\
\leq &\sum_{i=1}^{n}[(c_i z_i(t)+\sum_{j=1}^{n} a_{ij}g_j(z_j(t))+\sum_{j=1}^{n} b_{ij}g_j(z_j(t-\tau_j)))\\
&\times(-c_i z_i(t)+\sum_{j=1}^{n} a_{ij}g_j(z_j(t))+\sum_{j=1}^{n} b_{ij}g_j(z_j(t-\tau_j)))]\\
&+\alpha\sum_{i=1}^{n} g_i^2(z_i(t))-\alpha\sum_{i=1}^{n} g_i^2(z_i(t-\tau_i))+\beta\sum_{i=1}^{n} z_i^2(t)-\beta\sum_{i=1}^{n} z_i^2(t-\tau_i)\\
= &\sum_{i=1}^{n}[-c_i^2 z_i^2(t)+(\sum_{j=1}^{n} a_{ij}g_j(z_j(t)))(\sum_{j=1}^{n} a_{ij}g_j(z_j(t)))\\
&+(\sum_{j=1}^{n} b_{ij}g_j(z_j(t-\tau_j))))(\sum_{j=1}^{n} b_{ij}g_j(z_j(t-\tau_j))))\\
&+2(\sum_{j=1}^{n} a_{ij}g_j(z_j(t)))(\sum_{j=1}^{n} b_{ij}g_j(z_j(t-\tau_j))))]\\
&+\alpha\sum_{i=1}^{n} g_i^2(z_i(t))-\alpha\sum_{i=1}^{n} g_i^2(z_i(t-\tau_i))+\beta\sum_{i=1}^{n} z_i^2(t)-\beta\sum_{i=1}^{n} z_i^2(t-\tau_i)\\
= &-\sum_{i=1}^{n} c_i^2 z_i^2(t)+\sum_{i=1}^{n}(\sum_{j=1}^{n} a_{ij}g_j(z_j(t)))(\sum_{j=1}^{n} a_{ij}g_j(z_j(t)))\\
&+\sum_{i=1}^{n}(\sum_{j=1}^{n} b_{ij}g_j(z_j(t-\tau_j))))(\sum_{j=1}^{n} b_{ij}g_j(z_j(t-\tau_j))))\\
&+2\sum_{i=1}^{n}(\sum_{j=1}^{n} a_{ij}g_j(z_j(t)))(\sum_{j=1}^{n} b_{ij}g_j(z_j(t-\tau_j))))+\alpha\sum_{i=1}^{n} g_i^2(z_i(t))\\
&-\alpha\sum_{i=1}^{n} g_i^2(z_i(t-\tau_i))+\beta\sum_{i=1}^{n} z_i^2(t)-\beta\sum_{i=1}^{n} z_i^2(t-\tau_i) \qquad (24)
\end{aligned}
$$

(24) can be written as

$$
\begin{aligned}
\dot V(z(t)) \leq &-z^T(t)C^2 z(t)+g^T(z(t))A^TAg(z(t))\\
&+g^T(z(t-\tau))B^TBg(z(t-\tau))+2g^T(z(t))A^TBg(z(t-\tau))\\
&+\alpha g^T(z(t))g(z(t)-\alpha g^T(z(t-\tau))g(z(t-\tau))\\
\leq &-z^T(t)C^2 z(t)+g^T(z(t))A^TAg(z(t))\\
&+g^T(z(t-\tau))B^TBg(z(t-\tau))+2|g^T(z(t))||A^T||B||g(z(t-\tau))|\\
&+\alpha g^T(z(t))g(z(t)-\alpha g^T(z(t-\tau))g(z(t-\tau))\\
&+\beta z^T(t)z(t)-\beta z^T(t-\tau)z(t-\tau) \qquad (25)
\end{aligned}
$$

Since $|A| \preceq \hat{A}$ and $|B| \preceq \hat{B}$, (25) can be written in the form:

$$\begin{aligned}\dot{V}(z(t)) \leq & -z^T(t)C^2z(t) + g^T(z(t))A^TAg(z(t)) \\ & +g^T(z(t-\tau))B^TBg(z(t-\tau)) + 2|g^T(z(t))|\hat{A}^T\hat{B}|g(z(t-\tau))| \\ & +\alpha g^T(z(t))g(z(t) - \alpha g^T(z(t-\tau))g(z(t-\tau)) \\ \leq & -c_m^2\|z(t)\|_2^2 + \|A\|_2^2\|g(z(t))\|_2^2 + \|B\|_2^2\|g(z(t-\tau))\|_2^2 \\ & +2\|\hat{A}^T\hat{B}||_2\|g(z(t))\|_2\|g(z(t-\tau))\|_2 \\ & +\alpha g^T(z(t))g(z(t) - \alpha g^T(z(t-\tau))g(z(t-\tau)) \\ & +\beta z^T(t)z(t) - \beta z^T(t-\tau)z(t-\tau)\end{aligned} \tag{26}$$

Since $\|A\|_2 \leq \sigma_m(A)$ and $\|B\|_2 \leq \sigma_m(B)$, (26) leads to

$$\begin{aligned}\dot{V}(z(t)) \leq & -c_m^2\|z(t)\|_2^2 + \sigma_m^2(A)\|g(z(t))\|_2^2 + \sigma_m^2(B)\|g(z(t-\tau))\|_2^2 \\ & +\|\hat{A}^T\hat{B}||_2(\|g(z(t))\|_2^2 + \|g(z(t-\tau))\|_2^2) \\ & +\alpha g^T(z(t))g(z(t) - \alpha g^T(z(t-\tau))g(z(t-\tau)) \\ = & -c_m^2\|z(t)\|_2^2 + \sigma_m^2(A)\|g(z(t))\|_2^2 + \sigma_m^2(B)\|g(z(t-\tau))\|_2^2 \\ & +\|\hat{A}^T\hat{B}||_2\|g(z(t))\|_2^2 + \|\hat{A}^T\hat{B}||_2\|g(z(t-\tau))\|_2^2 \\ & -\alpha\|g^T(z(t-\tau))\|_2^2 \\ & +\beta z^T(t)z(t) - \beta z^T(t-\tau)z(t-\tau)\end{aligned} \tag{27}$$

If we choose $\alpha = \sigma_m^2(B) + \|\hat{A}^T\hat{B}||_2$, then (27) takes the form

$$\begin{aligned}\dot{V}(z(t)) = & -c_m^2\|z(t)\|_2^2 + \sigma_m^2(A)\|g(z(t))\|_2^2 + \|\hat{A}^T\hat{B}||_2\|g(z(t))\|_2^2 \\ & +(\sigma_m^2(B) + \|\hat{A}^T\hat{B}||_2)\|g^T(z(t))\|_2^2 \\ = & -c_m^2\|z(t)\|_2^2 + \sigma_m^2(A)\|g(z(t))\|_2^2 + \sigma_m^2(B)\|g(z(t))\|_2^2 \\ & +2\|\hat{A}^T\hat{B}||_2\|g(z(t))\|_2^2 + \beta\|z(t)\|_2^2\end{aligned} \tag{28}$$

In the light of (22), we can write $\|g(z(t))\|_2^2 \leq \ell_M^2\|z(t)\|_2^2$. Hence, (28) becomes:

$$\begin{aligned}\dot{V}(z(t)) \leq & (-c_m^2 + (\sigma_m^2(A) + \sigma_m^2(B) + 2\|\hat{A}^T\hat{B}||_2)\ell_M^2)\|z(t)\|_2^2 + \beta\|z(t)\|_2^2 \\ = & -\ell_M^2(\frac{c_m^2}{\ell_M^2} - \sigma_m^2(A) - \sigma_m^2(B) - 2\|\hat{A}^T\hat{B}||_2)\|z(t)\|_2^2 + \beta\|z(t)\|_2^2 \\ = & -\ell_M^2\Upsilon\|z(t)\|_2^2 + \beta\|z(t)\|_2^2 = -(\ell_M^2\Upsilon - \beta)\|z(t)\|_2^2\end{aligned} \tag{29}$$

It can be seen from (29) that, if $\beta < \ell_M^2\Upsilon$, then $\dot{V}(z(t)) < 0$ for all $z(t) \neq 0$. Let $z(t) = 0$. In this case, from (26), we have

$$\dot{V}(z(t)) \leq \|B\|_2^2\|g(z(t-\tau))\|_2^2 - \alpha\|g(z(t-\tau))\|_2^2 - \beta\|z(t-\tau)\|_2^2 \tag{30}$$

Since $\alpha > \|B\|_2^2$, it follows from (30) that

$$\dot{V}(z(t)) \leq -\beta\|z(t-\tau)\|_2^2 \tag{31}$$

(31) implies that $\dot{V}(z(t))$ is negative definite for all $z(t-\tau) \neq 0$. Let $z(t) = 0$ and $z(t-\tau) = 0$ in which case $\dot{z}(t) = 0$, implying that

$$\dot{V}(z(t)) = -\sum_{i=1}^{n} \dot{z}_i^2(t-\tau_i) = -\dot{z}^T(t-\tau)\dot{z}(t-\tau) \tag{32}$$

(32) implies that $\dot{V}(z(t)) < 0$ for all $\dot{z}(t-\tau) \neq 0$. Hence, we observe that $\dot{V}(z(t)) = 0$ if and only if $z(t) = z(t-\tau) = \dot{z}(t) = \dot{z}(t-\tau) = 0$, otherwise $\dot{V}(z(t)) < 0$. In addition, $V(z(t))$ is radially unbounded since $V(z(t)) \to \infty$ as $\|z(t)\| \to \infty$. Thus, the origin of (21) is globally asymptotically robust stable.

4 A Numerical Example and Comparisons

In this section, a numerical example is given to make a comparison between the result of this paper and the previous literature results. We first unify the robust stability results obtained in [1–4] and [6–8] in the following theorem:

Theorem 3: For system (21), let the activation functions $g_i(\cdot)$ satisfy (22) and the network matrices A, B and C satisfy (4). Then, the origin of (21) is globally asymptotically stable, if the following condition holds:

$$\Delta = \frac{c_m}{\ell_M} - \sigma_m(A) - \sigma_m(B) > 0$$

where $c_m = min\{\underline{c}_i\}$, $\ell_M = max\{\ell_i\}$, $\sigma_m(A) = min\{\sigma_1(A), \sigma_2(A), \sigma_3(A), \sigma_4(A)\}$ and $\sigma_m(B) = min\{\sigma_1(B), \sigma_2(B), \sigma_3(B), \sigma_4(B)\}$.

$$\underline{A} = \begin{bmatrix} -1 & -1 & -1 & -1 \\ -1 & -1 & -1 & -1 \\ -1 & -1 & -1 & -1 \\ -1 & -1 & -1 & -1 \end{bmatrix}, \overline{A} = \begin{bmatrix} 1 & 1 & 1 & 1 \\ 1 & 1 & 1 & 1 \\ 1 & 1 & 1 & 1 \\ 1 & 1 & 1 & 1 \end{bmatrix}, \underline{B} = \begin{bmatrix} -3 & -3 & -3 & -3 \\ -3 & -3 & -3 & -3 \\ -2 & -2 & -2 & -2 \\ -2 & -2 & -2 & -2 \end{bmatrix}, \overline{B} = \begin{bmatrix} 3 & 3 & 3 & 3 \\ 3 & 3 & 3 & 3 \\ 2 & 2 & 2 & 2 \\ 2 & 2 & 2 & 2 \end{bmatrix},$$

$$\underline{c}_1 = \underline{c}_2 = \underline{c}_3 = \underline{c}_4 = c_m, \quad \ell_1 = \ell_2 = \ell_3 = \ell_4 = 1$$

We obtain the following matrices:

$$A^* = B^* = \begin{bmatrix} 0 & 0 & 0 & 0 \\ 0 & 0 & 0 & 0 \\ 0 & 0 & 0 & 0 \\ 0 & 0 & 0 & 0 \end{bmatrix}, A_* = \hat{A} = \begin{bmatrix} 1 & 1 & 1 & 1 \\ 1 & 1 & 1 & 1 \\ 1 & 1 & 1 & 1 \\ 1 & 1 & 1 & 1 \end{bmatrix}, B_* = \hat{B} = \begin{bmatrix} 3 & 3 & 3 & 3 \\ 3 & 3 & 3 & 3 \\ 2 & 2 & 2 & 2 \\ 2 & 2 & 2 & 2 \end{bmatrix}$$

We have $\|\hat{A}^T\hat{B}\|_2 = 40$, $\sigma_1(A) = \sigma_2(A) = \sigma_3(A) = \sigma_4(A) = 4$ and $\sigma_m(A) = 4$, $\sigma_1(B) = \sigma_2(B) = \sigma_3(B) = \sigma_4(B) = 10.198$ and $\sigma_m(B) = 10.198$.

Applying the result of Theorem 3 to this example yields

$$\Delta = \frac{c_m}{\ell_M} - \sigma_m(A) - \sigma_m(B) = c_m - 14.198 > 0$$

from which the robust stability condition is obtained as $c_m > 14.198$. When applying the result of Theorem 3 to this example, we get that

$$\Upsilon = \frac{c_m^2}{\ell_M^2} - \sigma_m^2(A) - \sigma_m^2(B) - 2\|\hat{A}^T\hat{B}\|_2 = c_m^2 - 16 - 104 - 80 = c_m^2 - 200 > 0$$

from which the robust stability condition is obtained as $c_m > 14.140$. Thus, for the parameters of this example, Theorem 2 yields a weaker robust stability condition than the robust stability condition stated in Theorem 3.

5 Conclusion

This paper has studied the global asymptotic robust stability of delayed neural networks with the uncertain system matrices having the bounded norms and presented a novel sufficient condition for the existence, uniqueness and global asymptotic stability of the equilibrium point with respect to the Lipschitz activation functions. By giving a numerical example, the proposed result has been shown to be a new sufficient condition when compared with previously reported corresponding robust stability results.

Acknowledgements. This study was funded by Scientific Research Projects Coordination Unit of Istanbul University-Cerrahpasa. Project numbers: BYP-2020-34652

References

1. Faydasicok, O., Arik, S.: A new upper bound for the norm of interval matrices with application to robust stability analysis of delayed neural networks. Neural Netw. **44**, 64–71 (2013)
2. Cao, J., Huang, D.S., Qu, Y.: Global robust stability of delayed recurrent neural networks. Chaos, SolitonsFractals **23**(1), 221–229 (2005)
3. Ensari, T., Arik, S.: New results for robust stability of dynamical neural networks with discrete time delays. Expert Syst. Appl. **37**, 5925–5930 (2010)
4. Singh, V.: Global robust stability of delayed neural networks: Estimating upper limit of norm of delayed connection weight matrix. Chaos, Solitons Fractals **32**, 259–263 (2007)
5. Forti, M., Tesi, A.: New conditions for global stability of neural networks with applications to linear and quadratic programming problems. IEEE Trans. Circuits Syst. I: Regul. Pap. **42**, 354–365 (1995)
6. Ozcan, N., Arik, S.: Global robust stability analysis of neural networks with multiple time delays. IEEE Trans. Circuits Syst. I: Regul. Pap. **53**, 166–176 (2006)
7. Yucel, E., Arik, S.: Novel results for global robust stability of delayed neural networks. Chaos, Solitons Fractals **39**, 1604–1614 (2009)
8. Samli, R., Yucel, E.: Global robust stability analysis of uncertain neural networks with time varying delays. Neurocomputing **167**, 371–377 (2015)
9. Shao, J.L., Huang, T.Z., Zhou, S.: Some improved criteria for global robust exponential stability of neural networks with time-varying delays. Commun. Nonlinear Sci. Numer. Simul. **15**, 3782–3794 (2010)

10. Qi, H.: New sufficient conditions for global robust stability of delayed neural networks. IEEE Trans. Circuits Syst. I: Regul. Pap. **54**(5), 1131–1141 (2007)
11. Qiu, J., Zhang, J., Wang, J., Xia, Y., Shi, P.: A new global robust stability criteria for uncertain neural networks with fast time-varying delays. Chaos, Solitons Fractals **37**(2), 360–368 (2008)
12. Kwon, O.M., Park, J.H., Lee, S.M., Cha, E.J.: Analysis on delay-dependent stability for neural networks with time-varying delays. Neurocomputing **103**, 114–120 (2013)
13. Zhang, H., Wang, Z., Liu, D.: Robust stability analysis for interval Cohen-Grossberg neural networks with unknown time-varying delays. IEEE Trans. Neural Netw. **19**(11), 1942–1955 (2008)
14. Zhu, Q., Cao, J.: Robust exponential stability of Markovian jump impulsive stochastic Cohen-Grossberg neural networks with mixed time delays. IEEE Trans. Neural Netw. **21**(8), 1314–1325 (2010)
15. Huang, H., Feng, G., Cao, J.: Robust state estimation for uncertain neural networks with time-varying delay. IEEE Trans. Neural Netw. **19**(8), 1329–1339 (2008)
16. Huang, T., Li, C., Duan, S., Starzyk, J.A.: Robust exponential stability of uncertain delayed neural networks with stochastic perturbation and impulse effects. IEEE Trans. Neural Netw. Learn. Syst. **23**(6), 866–875 (2012)
17. Zhang, H., Wang, Z., Liu, D.: Global asymptotic stability and robust stability of a class of Cohen-Rossberg neural networks with mixed delays. IEEE Trans. Circuits Syst. I: Regul. Pap. **56**(3), 616–629 (2009)
18. Hu, S., Wang, J.: Global robust stability of a class of discrete-time interval neural networks. IEEE Trans. Circuits Syst. I: Regul. Pap. **53**(1), 129–138 (2006)
19. Wu, Z.G., Shi, P., Su, H., Chu, J.: Passivity analysis for discrete-time stochastic Markovian jump neural networks with mixed time delays. IEEE Trans. Neural Netw. **22**(10), 1566–1575 (2011)
20. Zhang, H., Liu, Z., Huang, G.B.: Novel delay-dependent robust stability analysis for switched neutral-type neural networks with time-varying delays via SC technique. IEEE Trans. Syst. Man, Cybern. Part B: (Cybern.) **40**(6), 1480–1491 (2012)
21. Arik, S.: An analysis of stability of neutral-type neural systems with constant time delays. J. Franklin Inst. **351**(11), 4949–4959 (2014)

Generalized Entropy Loss Function in Neural Network: Variable's Importance and Sensitivity Analysis

Krzysztof Gajowniczek(✉) and Tomasz Ząbkowski

Warsaw University of Life Sciences,
Nowoursynowska 159, 02-776 Warsaw, Poland
{krzysztof_gajowniczek, tomasz_zabkowski}@ssgw.edu.pl

Abstract. Artificial neural networks are powerful tools for data analysis and are particularly suitable for modelling relationships between variables for best prediction of an outcome. A large number of error functions have been proposed in the literature to achieve a better predictive power of a neural network. Only a few works employ Tsallis statistics, although the method itself has been successfully applied in other machine learning techniques. This paper undertakes the effort to examine various characteristics of the q-generalized function based on Tsallis entropy as an alternative loss measure in neural networks. To achieve this goal, we will explore various methods that can be used to interpret supervised neural network models. These methods can be used to visualize the model using the neural network interpretation diagram, assess the importance of variables by disaggregating the model's weights (Olden's and Garson's algorithms) and perform a sensitivity analysis of model responses to input variables (Lek's profile).

Keywords: Generalized entropy · Neural networks · Sensitivity analysis · Variable's importance

1 Introduction

Artificial intelligence (AI) methods, especially those based on machine learning methods, are rapidly becoming essential for the analysis of complex data. Artificial neural networks (ANNs) are highly parametrized, non-linear models with sets of processing units called neurons that can be used to approximate the relationship between the input and the output signals of a complex system [1]. They have been extensively and successfully applied in areas such as pattern recognition, signal processing, and system control in a number of real-world problems including engineering, medicine, or business [2–4].

In general, neural networks must determine the required mapping of input to output variables to solve a given problem during iterative training process. The main goal of the training is to find the correct weights values between the inputs and the outputs of the layers that minimize some predefined loss function (also called error measure) [5]. For the successful application it is important to train the network with a loss function that reflects the objective of the problem. For instance, the mean square error (MSE) is the most commonly used function, however it is not necessarily the best function for classification tasks. Consequently, a number of alternative loss functions have been investigated, and for the classification tasks the cross entropy loss function is considered as more appropriate [6].

In this article we make an effort to investigate an extension of the cross entropy loss function, which is a q-generalized loss function based on Tsallis statistics [7]. We will explore the properties of the proposed loss function and measure the performance of the neural network by assessing the variables' importance through a sensitivity analysis of response variable to changes in the input variables.

Although ANNs can be seen as powerful predictive tools compared to more conventional models such as linear or logistic regression, they are also criticized as 'black boxes', because ANN based models are hard to interpret and it is difficult to determine which features are most important for the problem and how they are related to the modelled phenomenon. To address this weakness, we will present several methods that will help broad audience to understand various aspects of the final neural network model outcome. For this purpose a Garson and Olden algorithms will be used to assess the importance of each input variable and the Lek's profile will be used to evaluate the effects of input variables by returning a plot of model predictions across the range of values for each variable [1, 8].

In particular, using artificially simulated data with the known underlying structure, we aim to answer the following research questions:

- What is the effect of the q-parameter in the proposed loss function on the various properties of the neural network?
- To what extent is it possible to analyse various characteristics of the neural network?

The remainder of this paper is organized as follows: Sect. 2 provides an overview of the similar research problems as well as the theoretical frameworks of the generalized entropy and artificial neural networks. In Sect. 3, the research framework was outlined, including the details of numerical implementation, artificial dataset and model performance measures. Section 4 outlines the experiments and presents the discussion of the results. The paper ends with concluding remarks in Sect. 5.

2 Theoretical Background

2.1 Artificial Neural Networks

Artificial neural networks are a set of algorithms created to mimic the human brain, that are designed to recognize patterns. They interpret input data through a kind of machine perception, labelling or clustering raw input. The patterns they recognize are numerical, contained in vectors, into which all real-world data, be it images, sound, text or time series, must be translated [9]. Usually ANNs are composed of several layers (e.g. multilayer perceptron; MLP) [10]. The layers are made of nodes. A node is just a place where computation happens, loosely patterned on a neuron in the human brain, which fires when it encounters sufficient stimuli. A node combines input from the data with a set of coefficients, or weights, that either amplify or dampen that input, thereby assigning significance to inputs with regard to the task the algorithm is trying to learn. These input-weight products are summed and then the sum is passed through a node's so-called activation function, to determine whether and to what extent that signal should progress further through the network to affect the ultimate outcome [11].

In general, artificial neural network (MLP) with a one hidden layer consisting of J hidden neurons and p input neurons (neurons from each layer activated by the logistic function f) estimates the following function:

$$ANN = f\left(w_0 + \sum\nolimits_{j=1}^{J} w_j f\left(w_{0j} + \sum\nolimits_{i=1}^{p} w_{ij} x_i\right)\right), \tag{1}$$

where w_0 stands for the bias synaptic weight of the output neuron, w_{0j} stands for the bias synaptic weight of the j-th hidden neuron, x_i stands for the i input feature, w_j stands for the weight corresponding to the synapse starting at the j-th hidden neuron and leading to the output neuron and w_{ij} stands for the weight of the i-th neuron from the input layer to the j neuron from the hidden layer [6].

ANNs are matched to data by learning algorithms during the iterative training process by the use of a given output, which is compared to the predicted output and the adjustment of all parameters. The parameters of ANNs are their weights. A common learning algorithm is the resilient backpropagation algorithm [12] that modifies neural network weights to find a local minimum (in ideal case a global minimum) of some predefined loss function E, which is, in this article, the function defined in the Eqs. 3 and 4.

2.2 Generalized Entropy

Information entropy introduced by Shannon [13] is the average rate at which information is produced by a stochastic source of data (or equivalently unpredictability of a particular event/state). The value of the entropy depends on two parameters: (1) disorder (uncertainty) and it is maximum when the probability of every possible states are equal; (2) number of possible events.

Standard Shannon entropy assumes a compromise contributions from the main mass of the distribution and the tail. To control both parameters, a generalization was proposed by Tsallis [7], defined as:

$$H_{T_q} = \frac{1}{q-1}\left(1 - \sum\nolimits_{i=1}^{n} t_i^q\right), \tag{2}$$

where t_i is the probability of occurrence of an event x_i being an element of a random variable X that can take values $x_1, \ldots, x_n$, and q is the adjustable generalization parameter. Using this generalized entropy with $q > 1$, high probability events contribute to the entropy value more than these with low probability. Therefore, the higher the value of q, the greater is the share of highly probable events in the final result.

ANNs require loss function that accepts target variable and its predicted value. To estimate this loss the Kullback-Leibler (K-L) divergence measuring distance between two distributions can be used. Generally K-L divergence measures the inefficiency of assuming that the distribution is $\{y_i\}$, when the true distribution is $\{t_i\}$. For the same reason, the mutual entropy of Tsallis is a generalization of K-L entropy, the latter being only a limiting case of the former for $q \to 1$. The mutual entropy of Tsallis refers to two probability distributions $\{t_i\}$ and $\{y_i\}$, $(i = 1, \ldots, n)$, over the same alphabet, and is defined as [5]:

$$H_{T_q}(t||y) = \frac{1}{1-q}\left(1 - \sum\nolimits_{i=1}^{n} t_i^q y_i^{1-q}\right). \tag{3}$$

The loss function being minimized during the training should accept input data, output data and the parameter vector. Based on these, a given loss function returns both the current loss and its gradients. For this reason, the loss function that implements Tsallis mutual entropy is defined as follows [5]:

$$E(t, y, q) = \frac{1}{1-q}\left(1 - t^q y^{1-q} - (1-t)^q (1-y)^{1-q}\right), \tag{4}$$

where (as previously) t and y stand for the true value and output of a given neural network respectively. Moreover q stands for the current value of the q-parameter and the gradient of the loss function defined as:

$$\frac{\partial}{\partial y} E(t, y, q) = (-(y-1)y)^{-q}(y^q(1-t)^q - (1-y)^q t^q), \tag{5}$$

is required for any gradient-based optimization algorithms.

2.3 Related Works on Variable's Importance

Machine learning systems are increasingly capable of solving many complex problems in many disciplines. Unfortunately, these systems remain characteristically opaque as these are difficult to look inside so the underlying relations between the input variables and the output cannot be easily captured.

In the last decades, several methods have been proposed to measure the importance of input variables, which basically apply some changes into input values and checks what happens to the output. In some methods called pruning, the approach is to eliminate irrelevant input e.g. [14–16], where the most significant input variables are determined first and, then these which are below a threshold are excluded from the neural network. This minimizes redundancy and allows to limit the size of the network.

There are some methods, as opposite to pruning methods, which aim to capture the relative contribution or the contribution profile of the input factors. For instance partial derivatives method by Dimopoulos et al. [17], which consists in calculating the partial derivatives of the output with respect to each input variable.

Some approaches are called ‘weights’ methods as these apply a computation using the connection weights. For example, Garson [18] proposed a method of partitioning the ANN connection weights in order to determine the relative importance of each input variable within the network. The same idea has been modified and applied by Goh [19]. In the case of a single layer of hidden units, the equation is:

$$Q_{ik} = \frac{\sum_{j=1}^{J} \left| w_{ij} v_{jk} \right| / \sum_{r=1}^{p} \left| w_{rj} \right|}{\sum_{i=1}^{p} \sum_{j=1}^{J} \left(\left| w_{ij} v_{jk} \right| / \sum_{r=1}^{p} \left| w_{rj} \right| \right)}, \tag{6}$$

where w_{ij} is the connection weight between the input i-th neuron and the j-th hidden neuron, v_{jk} is the connection weight between the j-th hidden neuron and the k-th output neuron, and $\sum\limits_{r=1}^{p} \left| w_{rj} \right|$ is the sum of the connection weights between the p input neurons (features) and the j-th hidden neuron. Q_{ik} represents the percentage of influence of the input variable on the output. In order to avoid the counteracting influence due to positive and negatives values, all connection weights were given their absolute values in the modified Garson algorithm.

Similarly, the Olden’s algorithm [20], which, in comparison to the Garson’s method, uses the product of the raw connection weights between each input and the output neuron and sums the product across all hidden neurons. An advantage of this approach is that relative contributions of each connection weight are maintained in terms of both, magnitude and sign, as compared to Garson’s algorithm which considers only the absolute magnitude.

An alternative approach to assess the relationship of variables in the neural network is Lek’s profile method [21]. The profile method is fundamentally different from Garson’s, Olden’s algorithms or pruning methods, as it is to assess the behaviour of target across different values of the input variables [8].

The Lek’s profile method evaluates the effects of each input feature by returning a model forecast graph across the range of values for this variable. The remaining features are kept constant when assessing the effects of each input variable. This method provides two options for setting fixed values of other invaluable features. The first option holds invaluable features at different quantiles such as minimum, 20th percentile, median or maximum. The second option clusters the invaluable features according to their natural grouping defined by data. Covariance among the variables may present unlikely scenarios if all invaluable features are kept at the same level. In other words high values for one features may be unlikely with high values for other features. This approach holds invaluable features at means defined by natural clusters in the data using k-means clustering algorithm.

The relationship between an outcome and the predictor may vary, taking into account the context of other variables (i.e. the presence of interactions) and sensitivities may vary at different points in the surface, taking into account the ability of the model to describe non-linear relationships [1]. Basically, this method generates a partial derivative of the response for each investigated feature and can provide insight into these complex relationships described by the model. Unfortunately, the Lek’s profile is only applicable to models with continuous features.

This paper intends to deal with the problem of variables' importance ranking applicable to the neural networks that use generalized entropy loss functions. Specifically, Olden's and Garson's algorithms were tested followed by sensitivity analysis using Lek's profile as those are supposed to be helpful based on the literature review.

3 Research Framework and Settings

3.1 Artificial Dataset

To assess any statistical method it is desirable to carry out an appropriate simulation analysis which may give results where the true signal is known in advance. A good simulation system should test several different aspects of classification problems such as linear and nonlinear features, non-informative features and correlation among the features. The dataset simulation was prepared according to the process described by Gajowniczek et al. [5]. Based on this aforementioned framework in the current article the simulation system (*twoClassSim* function from the *caret* package [22]) models a logarithmic binary event (Bernoulli random target variable) as a function of real signals using additive sets of a few different types. The final set consists of the following features:

- Factor1 and Factor2 which are truly important features;
- Linear having linear relationship with the target variable;
- Nonlinear adding some fluctuation to the log-odds;
- Noise which is non-informative for the target variable.

The entire dataset consist of 10,000 observations while the class imbalance ratio for binary classification task is set at approx. 50–50%. Moreover, all aforementioned variables were normalized to the range [0,1].

3.2 Numerical Implementation

All numerical experiments presented below were prepared using R programming language [23] installed on Ubuntu 18.04 operating system on a personal computer equipped with Intel Core i7-9750H2.6 GHz processor (12 threads) and 32 GB of RAM. As stated previously the dataset was prepared using the *caret* package. Each ANN was built using *neuralnet* package [24] which allows for flexible settings through custom-choice of loss function (see Eq. 4 and 5). Each time the ANN had 5 input neurons (equal to the number of the investigated features), 4 hidden neurons and one output neuron. All neurons were activated by the logistic function and the maximum steps for the training of the ANN was set at 10,000 iterations. Since usually the standard Shannon entropy is used as a loss function (q equals 1), to investigate the influence of the q-parameter on the ANN's structure, we set this parameter at 0.000001 (due to the numerical issues in calculating Eq. 4 from now on we will use the abbreviation 0), 1.000001 (abbreviation 1; approximately equals Shannon entropy) and 2. Finally, to prepare the variable's importance plots and Lek's profiles we used the *NeuralNetTools* package [8].

4 Numerical Experiment

The weights connecting neurons in ANN are partially analogous to the coefficients in the generalized linear model. The combined impact of the weights on model forecasts represents the relative importance of the predictors in their relationship to the output variable. However, there are a number of weights that combine one predictor with the output in the ANN. The large number of adjustable weights in ANN makes it very flexible in modelling non-linear effects, but imposes challenges for the interpretation.

To overcome this issue one can calculate the importance of each predictor using Olden's and Garson's algorithms (please see Fig. 1). The Garson's method suggests that Factor2 (left part of the figure) has the strongest relationship with the output variable (followed by Factor1 and NonLinear), similar to a strong positive association shown with the Olden's method (right part of the figure). For both methods all features are ranked in the same order.

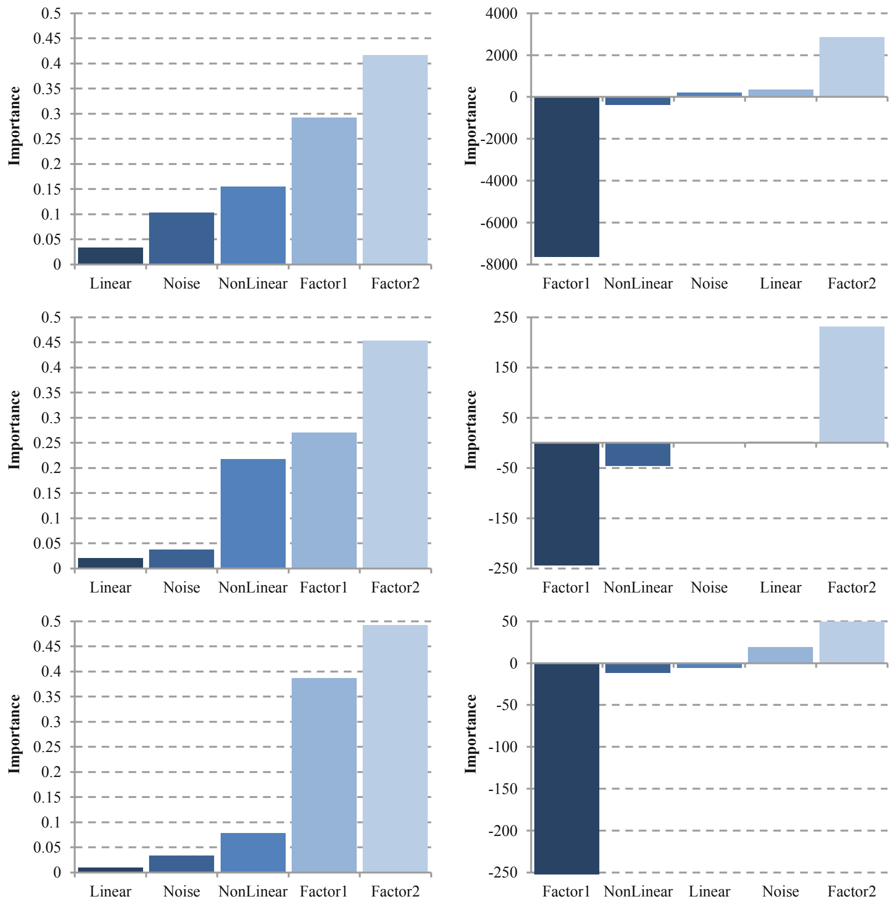

Fig. 1. Importance of each predictor using Garson's (left part) and Olden's (right part) for q-parameter set at 0 (upper part), 1 (middle part) and 2 (bottom part).

When analysing vertically the left part of the Fig. 1 it can be seen that *q*-parameter changes affect the validity of features. The relative importance of the most important feature (Factor2) increases from 0.42 (*q* equals 0 for the upper part of the figure) even up to 0.50 (*q* equals 2 for the bottom part of the figure). Simultaneously, the relative importance of other less important features (Linear and Noise) decreases even to 0.01-0.03. In total, the overall importance of the two most important features (which are truly relevant) becomes bigger and clearer from the initial value of about 0.71 even up to 0.89.

Right part of the Fig. 1 reveals that some features have positive and some negative impact on the target variable. Factor1 which is the second most important feature based on the Garson's method has very strong negative influence on the outcome variable based on the Olden's method. When using this method one can notice that when *q*-parameter increases from 0 to 2 the range/diversity of the relative importance flattens from the range 2500–(-7500) to the range 50–(-300). One more time the joint importance of Factor1 and Factor2 becomes bigger.

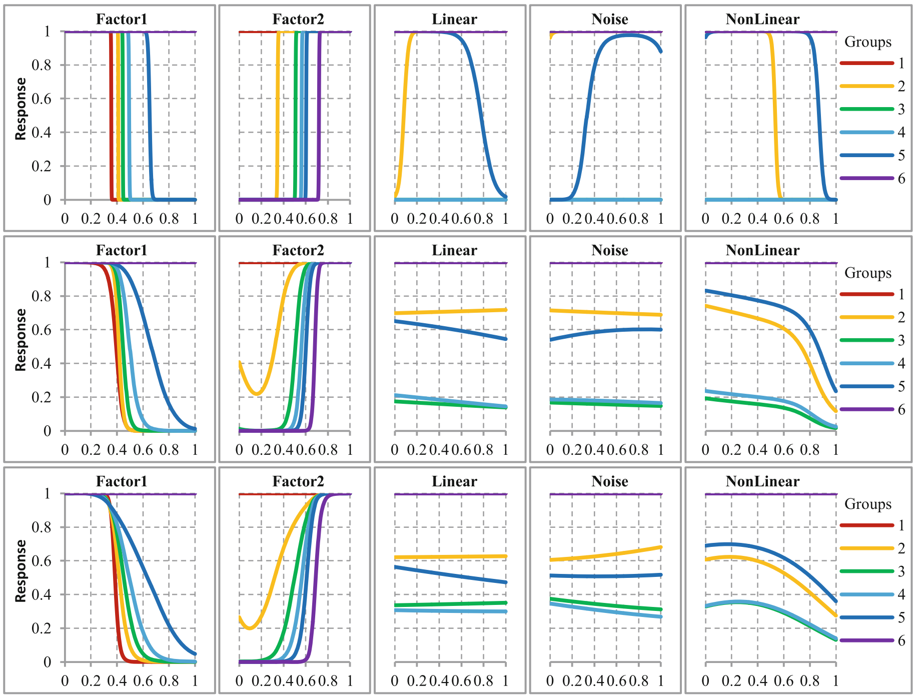

Fig. 2. Lek's profiles by holding other predictors at constant values of their minimum, 20th, 40th, 60th, 80th quantiles and the maximum algorithms for *q*-parameter set at 0 (upper part), 1 (middle part) and 2 (bottom part).

The results in Fig. 2 present Lek's profiles by holding other predictors at six different constant values i.e. their minimum (red colour), 20th, 40th, 60th, 80th quantiles (orange, green, cyan, and blue colours, respectively) and the maximum (purple colour). The horizontal axes present the whole range of each feature (as provided in Sect. 3.1 all the features were normalized) while the vertical axes show values of the response variable. Let's take first look on the most important variables presented in the upper part of the figure (q set at 0). The Olden's algorithm revealed that Factor1 and Factor2 have negative and positive influence on the target, respectively.

The Lek's profile shows the same relationship i.e. when the values of the Factor1 (x-axis) are increasing then the values of the outcome are decreasing from 1 to 0. This happens for the Factor1 values approx. between 0.3 and 0.7. In opposite, the behaviour of Factor2 is almost the same but has inverse relationship. In general, for both features the change is rapid i.e. all lines are almost vertical. For other three variables it can be seen that when other remaining variables are set at their minimums (group 1) or their 60th percentiles (group 4) there is no impact on the target variable (straight horizontal lines). On the other hand, the change is observed for group 5 (80th percentile; Noise) or for group 2 and 5 (20th and 80th percentiles; Linear and NonLinear).

When q-parameter is set at 1 or 2 (middle and bottom part of the Fig. 2) the influence on the outcome changes its behaviour and shape. Firstly, for Factor1 and Factor2 the change is not so rapid as previously i.e. curves are smoothed at the ends and are slightly tilted. Secondly, other three features lose their influence on the target and become almost horizontal.

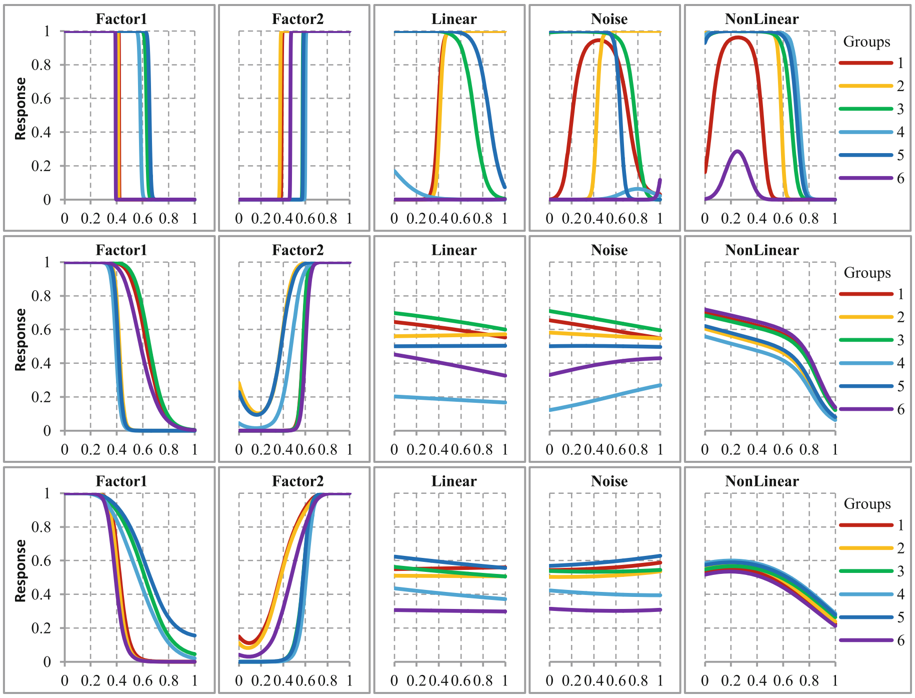

Fig. 3. Lek's profiles by holding other predictors at constant values at means defined by k-means algorithm for q-parameter set at 0 (upper part), 1 (middle part) and 2 (bottom part).

Results in Fig. 3 present Lek's profiles by holding other predictors at six different constant values (their means) defined by natural clusters in the data using k-means clustering algorithm.

The first difference is for Factor1 and Factor2 (upper part of the figure when q is set at 0). This time all curves changed their shapes (previously group 6 remained constant). This observation is also valid for three other features. Profile for the Linear confirms that this feature has straight influence on the outcome, i.e. target becomes either 0 or 1 after the change. Profiles for the Noise and for the NonLinear confirm that these features have variable impact on the outcome, especially for the group 1 and 6 which theoretically define the lowest and the biggest averages from the data.

Finally, with increased q-parameter to 1 or 2, in comparison to the Fig. 2, the similar behaviour can be observed. However, this time all curves for all features are squeezed next to each other more than before.

5 Conclusions

In this work, we have presented non-standard loss function based on the generalized (Tsallis) entropy measure and the methods to evaluate variable importance (Garson's, Olden's) and conduct a sensitivity analysis based on Lek's profiles. With our analysis we confirmed that the q-parameter within proposed loss function has an impact on different properties of the neural network, including variables importance and sensitivity of the neural network.

The analysis addresses the typical concern that supervised neural networks are black boxes that provide no information about underlying relationships between variables in the model. Importantly, we assessed the importance of a variables through disaggregating the model's weights and performed a sensitivity analysis providing meaningful interpretations that can enhance understanding of the relation between responses and input variables.

The future research will be focused on 1) examining the influence of the q-parameter on the final results provided by the ANN based models; 2) incorporating the generalized entropy loss function in other machine learning algorithms such as classification trees, random forests and support vector machines; 3) applications of the proposed interpretation/visualization methods (Garson's and Olden's algorithms, and Lek's profiles) to analyse various characteristics of other machine learning algorithms.

References

1. Zhang, Z., Beck, M.W., Winkler, D.A., Huang, B., Sibanda, W., Goyal, H.: Opening the black box of neural networks: methods for interpreting neural network models in clinical applications. Ann. Transl. Med. **6**(11), 216 (2018)
2. Gajowniczek, K., Orłowski, A., Ząbkowski, T.: Entropy based trees to support decision making for customer churn management. Acta Physica Polonica A **129**(5), 971–979 (2016)

3. Gajowniczek, K., Karpio, K., Łukasiewicz, P., Orłowski, A., Ząbkowski, T.: Q-entropy approach to selecting high income households. Acta Physica Polonica A **127**(3a), A38–A44 (2015)
4. Nafkha, R., Gajowniczek, K., Ząbkowski, T.: Do customers choose proper tariff? empirical analysis based on polish data using unsupervised techniques. Energies **11**(3), 514 (2018)
5. Gajowniczek, K., Orłowski, A., Ząbkowski, T.: Simulation study on the application of the generalized entropy concept in artificial neural networks. Entropy **20**(4), 249 (2018)
6. Golik, P., Doetsch, P., Ney, H.: Cross-entropy vs squared error training: a theoretical and experimental comparison. In: Proceedings of the 14th Annual Conference of the International Speech Communication Association "Interspeech-2013", Lyon, France, pp. 1756–1760 (2013)
7. Tsallis, C.: Introduction to Nonextensive Statistical Mechanics. Springer, New York (2009)
8. Beck, M.W.: NeuralNetTools: visualization and analysis tools for neural networks. J. Stat. Softw. **85**(11), 1–20 (2018)
9. Liu, W., Wang, Z., Liu, X., Zeng, N., Liu, Y., Alsaadi, F.E.: A survey of deep neural network architectures and their applications. Neurocomputing **234**, 11–26 (2017)
10. Gajowniczek, K., Ząbkowski, T.: Short term electricity forecasting based on user behavior from individual smart meter data. J. Intell. Fuzzy Syst. **30**(1), 223–234 (2016)
11. Rumelhart, D.E., Hinton, G.E., Williams, R.J.: Learning representations by BackPropagating errors. Nature **323**(6088), 533–536 (1986)
12. Riedmiller, M.: Rprop – Description and Implementation Details; Technical Report. University of Karlsruhe, Germany (1994)
13. Shannon, C.E.: A mathematical theory of communication. Bell Syst. Tech. J. **27**, 623–666 (1948)
14. Zurada, J.M., Malinowski, A., Cloete, I.: Sensitivity analysis for minimization of input data dimension for feedforward neural network. In: IEEE International Symposium on circuits and Systems, ISCAS1994, vol. 6. IEE Press, London (1994)
15. Engelbrecht, A.P., Cloete, I., Zurada, J.M.: Determining the significance of input parameters using sensitivity analysis. From natural to artificial neural computation, Springer, Malaga-Torremolinos (1995)
16. Kim, S.H., Yoon, C., Kim, B.J.: Structural monitoring system based on sensitivity analysis and a neural network. Comput.-Aided Civil Infrastruct. Eng. **155**, 309–318 (2000)
17. Dimopoulos, Y., Bourret, P., Lek, S.: Use of some sensitivity criteria for choosing networks with good generalization ability. Neural Process. Lett. **2**, 1–4 (1995)
18. Garson, G.D.: Interpreting neural network connection weights. Artif. Intell. Exp. **6**, 46–51 (1991)
19. Goh, A.T.C.: Back-propagation neural networks for modeling complex systems. Artif. Intell. Eng. **9**, 143–151 (1995)
20. Olden, J.D., Joy, M.K., Death, R.G.: An accurate comparison of methods for quantifying variable importance in artificial neural networks using simulated data. Ecol. Model. **178**(3–4), 389–397 (2004)
21. Lek, S., Delacoste, M., Baran, P., Dimopoulos, I., Lauga, J., Aulagnier, S.: Application of neural networks to modelling nonlinear relationships in ecology. Ecol. Model. **90**(1), 39–52 (1996)
22. Kuhn, M.: Building predictive models in R using the caret package. J. Stat. Softw. **28**(5), 1–26 (2008)
23. The R Development Core Team. R: A Language and Environment for Statistical Computing; R Foundation for Statistical Computing: Vienna, Austria (2014)
24. Fritsch, S., Guenther, F.: Neuralnet: training of neural networks. R Package Version 1.33.2016. https://CRAN.R-project.org/package=neuralnet. Accessed 10 Jan 2020

Robust Multilayer Perceptrons: Robust Loss Functions and Their Derivatives

Jan Kalina and Petra Vidnerová[(✉)]

The Czech Academy of Sciences, Institute of Computer Science,
Pod Vodárenskou věží 2, 182 07 Praha 8, Czech Republic
{kalina,petra}@cs.cas.cz

Abstract. Common types of artificial neural networks have been well known to suffer from the presence of outlying measurements (outliers) in the data. However, there are only a few available robust alternatives for training common form of neural networks. In this work, we investigate robust fitting of multilayer perceptrons, i.e. alternative approaches to the most common type of feedforward neural networks. Particularly, we consider robust neural networks based on the robust loss function of the least trimmed squares, for which we express formulas for derivatives of the loss functions. Some formulas, which are however incorrect, have been already available. Further, we consider a very recently proposed multilayer perceptron based on the loss function of the least weighted squares, which appears a promising highly robust approach. We also derive the derivatives of the loss functions, which are to the best of our knowledge a novel contribution of this paper. The derivatives may find applications in implementations of the robust neural networks, if a (gradient-based) backpropagation algorithm is used.

Keywords: Neural networks · Loss functions · Robust regression

1 Introduction

Neural networks represent a wide class of habitually used tools for the task of nonlinear regression. Numerous applications of estimation in nonlinear regression in various fields are nowadays solved by neural networks. Thus, they represent important exploratory tools of modern data analysis [15], particularly of exploratory data analysis (see e.g. [7]). However, the most commonly used methods for training regression neural networks based on the least squares criterion are biased under contaminated data [18] as well as vulnerable to adversarial examples.

Under the presence of outlying measurements (outliers) in the data, training multilayer perceptrons is known to be unreliable (biased). Such their non-robustness, caused by their minimization of the sum of squared residuals (see [11]

The research was financially supported by the projects GA19-05704S (J. Kalina) and GA18-23827S (P. Vidnerová) of the Czech Science Foundation.

for discussion), becomes even more severe for data with a very large number of regressors [3]. Therefore, researchers have recently become increasingly interested in proposing alternative robust (resistant) methods for training of multilayer perceptrons [2]. So far, only a few robust approaches for training for MLPs have been introduced and even smaller attention has been paid to a robustification of radial basis function (RBF) networks. Approaches replacing the common sum of squared residuals by a robust loss considered the loss functions corresponding to the median [1], least trimmed absolute value (LTA) estimator [17], or least trimmed squares (LTS) estimator [2,18]. The last two estimators were proposed for the model of the so-called contaminated normal distribution, assuming the residuals to come from a mixture of normally distributed errors with outliers, typically assumed to be normally distributed as well but with a (possibly much) larger variance than the majority of the data points. Other robust loss functions within multilayer perceptrons were examined in [13]. A different robust approach to neural networks based on finding the least outlying subset of observations but exploiting the standard loss minimizing the sum of least squares of residuals was proposed in [11], where also some other previous attempts for robustification of neural networks are cited. All these robust approaches were also verified to be meaningful in numerical experiments. Robust approaches to fitting neural networks were investigated also in the context of clustering (unsupervised learning), based on replacing means of clusters by other centroids (e.g. medoids [4]).

Here, we use the idea to replace the common loss function of multilayer perceptron by a robust version. On the whole, we consider here three particular loss functions for multilayer perceptrons, corresponding to

- Least squares (i.e. the most common form of the loss for multilayer perceptrons),
- Least trimmed squares (see Sect. 2),
- Least weighted squares (see Sect. 2).

As the main contribution, partial derivatives of the loss function with respect to each of the parameters are evaluated here for robust multilayer perceptrons. These are very useful, because the backpropagation algorithm for computing the robust neural networks requires them. We derive the derivatives for a particular architecture of the multilayer perceptron, while they can be extended in a straightforward way to more complex multilayer perceptrons. Nevertheless, we point out that the derivatives are difficult to find in the literature even for a standard multilayer perceptron with a loss based on minimizing the least squares criterion. Available robust estimators for linear regression and for the location model are recalled in Sect. 2 of this paper. Section 3 presents derivatives of standard as well as robust loss functions for a multilayer perceptron with one hidden layer. Section 4 concludes the paper.

2 Linear Model and Robust Estimation

This section recalls robust estimates in linear regression model (and the location model, which is its special case), which will serve as inspiration for the robust versions of neural networks studied later in Sect. 3. The standard linear regression model

$$Y_i = \beta_0 + \beta_1 X_{i1} + \cdots + \beta_p X_{ip} + e_i, \quad i = 1, \ldots, n, \tag{1}$$

considers n observations, for which a continuous response is explained by p regressors (independent variables, features) under the presence of random errors $e_1, \ldots, e_n$. The presence of the intercept β_0 in the model can be interpreted as the presence of a vector of ones in the design matrix X containing the elements X_{ij}. As the most common least squares estimator of $\beta = (\beta_0, \beta_1, \ldots, \beta_p)^T$ in (1) is vulnerable to the presence of outliers in the data, various robust alternatives have been proposed [8].

Robust statisticians have proposed a variety of estimation tools, which are resistant to the presence of outliers in the data. Such estimators are considered *highly* robust with respect to outliers, which have a high value of the breakdown point. We can say that the breakdown point, which represents a fundamental concept of robust statistics [8], is a measure of robustness of a statistical estimator of an unknown parameter. Formally, the finite-sample breakdown point evaluates the minimal fraction of data that can drive an estimator beyond all bounds when set to arbitrary values. Keeping in mind the high robustness, we decide for replacing the sum of squared residuals by loss functions of the least trimmed squares and least weighted squares estimators, which are known to yield reliable and resistant results over real data [10].

The least trimmed squares (LTS) estimator [16] represents a very popular regression estimator with a high breakdown point (cf. [8]). Consistency of the LTS and other properties were derived in [19]. Formally, the LTS estimate of β is obtained as

$$\arg\min_{b \in \mathbb{R}^{p+1}} \frac{1}{h} \sum_{i=1}^{h} u_{(i)}^2(b), \tag{2}$$

where the user must choose a fixed h fulfilling $n/2 \leq h < n$; here, $u_i(b)$ is a residual corresponding to the i-th observation for a given b, and we consider squared values arranged in ascending order denoted as $u_{(1)}^2(b) \leq \cdots \leq u_{(n)}^2(b)$. The LTS estimator may attain a high robustness but cannot achieve a high efficiency [19].

The least weighted squares (LWS) estimator [20] for the model (1), motivated by the idea to down-weight potential outliers, remains much less known compared to the LTS, although it has more appealing statistical properties. The definition of the LWS exploits the concept of weight function, which is defined as a function $\psi : [0,1] \to [0,1]$ under technical assumptions. The LWS estimator with a given ψ, which is able to much exceed the LTS in terms of efficiency, is defined as

$$\arg\min_{b \in \mathbb{R}^{p+1}} \sum_{k=1}^{n} \psi\left(\frac{k - 1/2}{n}\right) u_{(i)}^2(b). \tag{3}$$

We may refer to [20] and references cited therein for properties of the LWS; it may achieve a high breakdown point (with properly selected weights), robustness to heteroscedasticity, and efficiency for non-contaminated samples. The performance of the LWS on real data (see [9] and references cited therein) can be described as excellent. We also need to consider the location model, which is a special case of (1), in the form

$$Y_i = \mu + e_i, \quad i = 1, \dots, n \tag{4}$$

with a location parameter $\mu \in \mathbb{R}$. The LTS and LWS estimators are meaningful (and successful [9]) also under (4), while the LWS estimator in (4) inherits the appealing properties from (1).

3 Theoretical Results

This section presents partial derivatives of three loss functions for a particular architecture of a multilayer perceptron, i.e. assuming a single hidden layer. Their usefulness is discussed in Sect. 4.

3.1 Model and Notation

We assume that a continuous response variable $Y_i \in \mathbb{R}$ and a vector of regressors (independent variables) $X_i = (X_{i1}, \dots, X_{ip})^T \in \mathbb{R}^p$ are available for the total number of n observations. The regression modeling in the nonlinear model

$$Y_i = \varphi(X_i) + e_i, \quad i = 1, \dots, n, \tag{5}$$

with an unknown function φ and random errors $e_1, \dots, e_n$ will be performed using a multilayer perceptron (MLP) with a single hidden layer, which contains N hidden neurons.

The MLP estimates the response Y_i of the i-th observation by

$$\hat{Y}_i = \hat{Y}_i(c, \gamma, \omega) = g\left(\sum_{k=1}^{N} \gamma_k f\left(\sum_{j=1}^{p} \omega_{kj} X_{ij} + \omega_{k0}\right) + \gamma_0\right) + c, \quad i = 1, \dots, n, \tag{6}$$

where f and g must be specified (possibly nonlinear) functions. The formula (6) for computing the fitted values of the response considers two layers only however can be generalized for more layers easily. We use here a notation following [6], although other more or less different versions of notation may be used in this context as well. If g is an identity function, then of course $\gamma_0 + c$ represents a single parameter (intercept).

We estimate parameters c, $\gamma = (\gamma_0, \gamma_1, \dots, \gamma_N)^T$, and

$$\omega = (\omega_{10}, \dots, \omega_{N0}, \omega_{11}, \dots, \omega_{N1}, \dots, \omega_{1p}, \dots, \omega_{Np})^T \tag{7}$$

of (6) exploiting a (rather complicated) nonlinear optimization of a certain (selected) loss function. To simplify the notation, we further denote

$$\tau_i = \sum_{k=1}^{N} \gamma_k f\left(\sum_{j=1}^{p} \omega_{kj} X_{ij} + \omega_{k0}\right) + \gamma_0, \quad i = 1, \dots, n. \tag{8}$$

In the rest of the paper, we require that the derivatives of f and g exist. Under such (rather common) assumption, these derivatives will be denoted as f' and g', respectively. Although it is common in regression tasks to choose g in (6) as an identity function, which simplifies the computational efforts, we retain the general notation g here. Independently on the choice of the loss function we will use the notation $u_i = Y_i - \hat{Y}_i$ for residuals of the multilayer perceptron for $i = 1, \ldots, n$.

3.2 Derivatives of Fitted Values

As a preparatory result for further computations, we now derive independently on the choice of the loss function

$$\frac{\partial \hat{Y}_i}{\partial c}(c, \gamma, \omega) = 1, \quad i = 1, \ldots, n, \tag{9}$$

$$\frac{\partial \hat{Y}_i}{\partial \gamma_0}(c, \gamma, \omega) = g'(\tau_i), \quad i = 1, \ldots, n, \tag{10}$$

$$\frac{\partial \hat{Y}_i}{\partial \gamma_a}(c, \gamma, \omega) = g'(\tau_i) f\left(\sum_{j=1}^{p} \omega_{aj} X_{ij} + \omega_{a0}\right), \quad i = 1, \ldots, n, \quad a = 1, \ldots, N, \tag{11}$$

$$\frac{\partial \hat{Y}_i}{\partial \omega_{a0}}(c, \gamma, \omega) = \gamma_a g'(\tau_i) f'\left(\sum_{j=1}^{p} \omega_{aj} X_{ij} + \omega_{a0}\right), \quad i = 1, \ldots, n, \quad a = 1, \ldots, N, \tag{12}$$

and

$$\frac{\partial \hat{Y}_i}{\partial \omega_{ab}}(c, \gamma, \omega) = \gamma_a X_{ib} g'(\tau_i) f'\left(\sum_{j=1}^{p} \omega_{aj} X_{ij} + \omega_{a0}\right), \tag{13}$$

where $i = 1, \ldots, n$, $a = 1, \ldots, N$, and $b = 1, \ldots, p$.

These partial derivatives of (6) were derived by a repeatedly used chain rule for computing derivatives of a composite function. They are expressed as functions, i.e. depending on their parameters c, γ, and ω. Of course, computations with real data (e.g. within the neural network training) require to use estimated versions of these derivatives, which can be easily obtained by replacing c, γ, and ω by their estimates. We would like to point out that such estimates are always available within the backpropagation algorithm, because its user is required to specify initial estimates of these parameters. These partial derivatives appear in derivatives of the loss function, which will be now expressed for three different versions of the loss function, namely for the standard one based on least squares and for two robust alternatives.

3.3 Multilayer Perceptron with a Standard Loss

The most commonly used loss for multilayer perceptrons will be denoted as

$$\xi_1 = \xi_1(c, \gamma, \omega) = \frac{1}{n} \sum_{i=1}^{n} u_i^2, \tag{14}$$

which is known as the mean square error (MSE), corresponding to the least squares estimator in a location model. To estimate all parameters of (6), the common optimization criterion has the form

$$\arg \min_{c,\gamma,\omega} \xi_1(c, \gamma, \omega), \tag{15}$$

which is commonly solved by backpropagation. To derive the explicit expressions for partial derivatives, which are formulated below as a lemma, we will exploit the facts that e.g. it holds for $a = 1, \ldots, N$ that

$$\frac{\partial \xi_1}{\partial \gamma_a} = \frac{\partial}{\partial \gamma_a} \sum_{i=1}^{n} \left(Y_i - \hat{Y}_i\right)^2 = \sum_{i=1}^{n} \frac{\partial}{\partial \gamma_a} \left(Y_i - \hat{Y}_i\right)^2 = -2 \sum_{i=1}^{n} \left(Y_i - \hat{Y}_i\right) \frac{\partial \hat{Y}_i}{\partial \gamma_a}. \tag{16}$$

Lemma 1. *Under the notation of Sect. 3.1, it holds that*

(a)

$$\frac{\partial \xi_1}{\partial c}(c, \gamma, \omega) = -\frac{2}{n} \sum_{i=1}^{n} u_i, \tag{17}$$

(b)

$$\frac{\partial \xi_1}{\partial \gamma_0}(c, \gamma, \omega) = -\frac{2}{n} \sum_{i=1}^{n} u_i g'(\tau_i), \tag{18}$$

(c)

$$\frac{\partial \xi_1}{\partial \gamma_a}(c, \gamma, \omega) = -\frac{2}{n} \sum_{i=1}^{n} u_i g'(\tau_i) f \left(\sum_{j=1}^{p} \omega_{aj} X_{ij} + \omega_{a0} \right), \tag{19}$$

where $a = 1, \ldots, N$,

(d)

$$\frac{\partial \xi_1}{\partial \omega_{a0}}(c, \gamma, \omega) = -\frac{2}{n} \sum_{i=1}^{n} u_i \gamma_a g'(\tau_i) f' \left(\sum_{j=1}^{p} \omega_{aj} X_{ij} + \omega_{a0} \right), \tag{20}$$

where $a = 1, \ldots, N$,

(e)

$$\frac{\partial \xi_1}{\partial \omega_{ab}}(c, \gamma, \omega) = -\frac{2}{n} \sum_{i=1}^{n} u_i \gamma_a X_{ib} g'(\tau_i) f' \left(\sum_{j=1}^{p} \omega_{aj} X_{ij} + \omega_{a0} \right), \tag{21}$$

where $a = 1, \ldots, N$ and $b = 1, \ldots, p$.

It is rather surprising that we are not aware of the results of Lemma 1 being available anywhere in the literature. The formulas do not appear in standard textbooks (e.g. [6]), and texts on this topic available on the internet usually contain serious mistakes. Concerning the computations of the derivatives, Lemma 1 formulates them as depending on c, γ and ω, while the derivatives for numerical data can be estimated by using estimates of c, γ and ω, respectively.

3.4 LTS-loss in Linear Regression

The loss function of the LTS estimator in (1) is defined as

$$\xi_2 = \xi_2(\beta) = \frac{1}{h}\sum_{i=1}^{h} u_{(i)}^2. \tag{22}$$

To express its derivatives, we may recall the following result given on p. 7 of [19] stating that

$$\frac{\partial \xi_2}{\partial \beta}(\beta) = -\frac{2}{n}\sum_{i=1}^{n}\left[u_i(\beta)X_i \mathbb{1}[u_i^2(\beta) \leq u_{(h)}^2(\beta)]\right] \tag{23}$$

almost everywhere, where $u_i(\beta) = Y_i - X_i^T\beta$ for each i are residuals and $\mathbb{1}$ denotes an indicator function. The expression (23) contains $p+1$ particular derivatives for individual elements of β. In (23), the i-th squared residual is compared with the h-th largest *squared* residual. To conclude, the LTS estimator b_{LTS} in (1) can be computed (using now our notation) as the solution of the set of equations

$$\sum_{i=1}^{n} u_i(b)X_i \mathbb{1}[u_i^2(b) \leq u_{(h)}^2(b)] = 0, \tag{24}$$

where b is the $p+1$-dimensional variable.

3.5 Multilayer Perceptron with an LTS-loss

An MLP with the loss function corresponding to the LTS estimator was considered already in [17], where however the derivatives of the loss function are in our opinion incorrect. The same formulas were repeated in [18]. However, we must be much more careful in deriving the derivatives, which turn out to be have more complex formulas. Let us first consider the loss

$$\xi_2 = \xi_2(c, \gamma, \omega) = \frac{1}{h}\sum_{i=1}^{h} u_{(i)}^2, \tag{25}$$

where h is a specified constant fulfilling $n/2 \leq h < n$. The loss corresponds to the LTS estimator and thus we introduce the notation LTS-MLP for the (robust) multilayer perceptron with parameters estimated by the criterion

$$\arg\min_{c,\gamma,\omega} \xi_2(c, \gamma, \omega). \tag{26}$$

The derivatives of ξ_2 will be derived in an analogous way to the approach of Sect. 3.4.

Lemma 2. *We use the notation of Sect. 3.1. To avoid confusion, let us denote the residuals of the LTS-MLP as $\tilde{u} = \tilde{u}_i(c, \gamma, \omega)$ for $i = 1, \ldots, n$, to stress that they are functions of c, γ and ω. Let us further denote $\tilde{u}^2_{(1)} \leq \cdots \leq \tilde{u}^2_{(n)}$. It holds that*

(a)

$$\frac{\partial \xi_2}{\partial c}(c, \gamma, \omega) = -\frac{2}{h} \sum_{i=1}^{n} \tilde{u}_i \mathbb{1}[\tilde{u}_i^2 \leq \tilde{u}^2_{(h)}], \tag{27}$$

(b)

$$\frac{\partial \xi_2}{\partial \gamma_0}(c, \gamma, \omega) = -\frac{2}{h} \sum_{i=1}^{n} \tilde{u}_i \mathbb{1}[\tilde{u}_i^2 \leq \tilde{u}^2_{(h)}] g'(\tau_i), \tag{28}$$

(c)

$$\frac{\partial \xi_2}{\partial \gamma_a}(c, \gamma, \omega) = -\frac{2}{h} \sum_{i=1}^{n} \tilde{u}_i \mathbb{1}[\tilde{u}_i^2 \leq \tilde{u}^2_{(h)})] g'(\tau_i) f \left(\sum_{j=1}^{p} \omega_{aj} X_{ij} + \omega_{a0} \right), \tag{29}$$

where $a = 1, \ldots, N$,

(d)

$$\frac{\partial \xi_2}{\partial \omega_{a0}}(c, \gamma, \omega) = -\frac{2}{h} \sum_{i=1}^{n} \tilde{u}_i \mathbb{1}[\tilde{u}_i^2 \leq \tilde{u}^2_{(h)}] \gamma_a g'(\tau_i) f' \left(\sum_{j=1}^{p} \omega_{aj} X_{ij} + \omega_{a0} \right), \tag{30}$$

where $a = 1, \ldots, N$,

(e)

$$\frac{\partial \xi_2}{\partial \omega_{ab}}(c, \gamma, \omega) = -\frac{2}{h} \sum_{i=1}^{n} \tilde{u}_i \mathbb{1}[\tilde{u}_i^2 \leq \tilde{u}^2_{(h)}] \gamma_a X_{ib} g'(\tau_i) f' \left(\sum_{j=1}^{p} \omega_{aj} X_{ij} + \omega_{a0} \right), \tag{31}$$

where $a = 1, \ldots, N$ and $b = 1, \ldots, p$.

3.6 LWS-Loss in Linear Regression

Let us now consider the model (1) with the loss corresponding to an LWS estimator. The loss

$$\xi_3(\beta) = \sum_{i=1}^{n} \psi \left(\frac{i - 1/2}{n} \right) u^2_{(i)} \tag{32}$$

exploits a specified weight function ψ. Equivalently, we may express

$$\xi_3(\beta) = \sum_{i=1}^{n} w_i u^2_{(i)}, \tag{33}$$

where the weights are generated by ψ under a natural requirement $\sum_{i=1}^{n} w_i = 1$. The LWS estimator is defined by

$$\arg\min_{\beta} \xi_3(\beta). \tag{34}$$

The set of derivatives of the loss function in (1) has the form

$$\frac{\partial \xi_3}{\partial \beta} = -2 \sum_{i=1}^{n} X_i u_i \psi \left(\hat{F}^{(n)} \left(|u_i(\beta)| \right) \right), \tag{35}$$

where $\hat{F}^{(n)}$ denotes the empirical distribution function

$$\hat{F}^{(n)}(r) = \frac{1}{n} \sum_{j=1}^{n} \mathbb{1}[|u_j(\beta)| < r], \quad r \in \mathbb{R}; \tag{36}$$

a detailed proof was given on p. 183 of [20]. The special case for (4) again considers $X_i \equiv 1$ for each i. Let us consider the empirical distribution function

$$\hat{F}(r, b) = \frac{1}{n} \sum_{j=1}^{n} \mathbb{1}[|u_j(b)| < r], \quad r \in \mathbb{R}. \tag{37}$$

The LWS estimator b_{LWS} in (1) can be obtained as the solution of

$$\sum_{i=1}^{n} u_i(b) X_i \psi \left(\hat{F} \left(|u_i(b)|, b \right) \right) = 0, \tag{38}$$

which is a set of normal equations with the variable $b \in \mathbb{R}^{p+1}$. Here, $|u_i(b)|$ for each i plays the role of the threshold r from (37).

3.7 Multilayer Perceptron with An-LWS Loss

We introduce the notation LWS-MLP for the (robust) multilayer perceptron based on the robust loss function corresponding to the LWS estimator. Let us consider the loss

$$\xi_3(c, \gamma, \omega) = \sum_{i=1}^{n} \psi \left(\frac{i - 1/2}{n} \right) u_{(i)}^2, \tag{39}$$

formulated using a specified weight function ψ. The loss can be equivalently expressed as

$$\xi_3 = \xi_3(c, \gamma, \omega) = \sum_{i=1}^{n} w_i u_{(i)}^2, \tag{40}$$

if the weights are generated by ψ and again fulfil $\sum_{i=1}^{n} w_i = 1$. The loss corresponds to an LWS estimator and therefore we introduce the notation LWS-MLP for the (robust) multilayer perceptron with parameters given by

$$\arg\min_{c,\gamma,\omega} \xi_3(c, \gamma, \omega). \tag{41}$$

Our deriving the derivatives of ξ_3 is analogous to the reasoning of Sect. 3.6.

Lemma 3. *We use the notation of Sect. 3.1. Residuals of the multilayer perceptron will be denoted as $\tilde{u}_i = \tilde{u}_i(c, \gamma, \omega)$ and the corresponding empirical distribution function as*

$$\hat{F}(r) = \frac{1}{n} \sum_{i=1}^{n} \mathbb{1}[|\tilde{u}_i| < r], \quad r \in \mathbb{R}. \tag{42}$$

It holds that

(a)

$$\frac{\partial \xi_3}{\partial c}(c, \gamma, \omega) = -2 \sum_{i=1}^{n} \tilde{u}_i \psi \left(\hat{F}^{(n)}(|\tilde{u}_i|) \right), \tag{43}$$

(b)

$$\frac{\partial \xi_3}{\partial \gamma_0}(c, \gamma, \omega) = -2 \sum_{i=1}^{n} \tilde{u}_i \psi \left(\hat{F}^{(n)}(|\tilde{u}_i|) \right) g'(\tau_i), \tag{44}$$

(c)

$$\frac{\partial \xi_3}{\partial \gamma_a}(c, \gamma, \omega) = -2 \sum_{i=1}^{n} \tilde{u}_i \psi \left(\hat{F}^{(n)}(|\tilde{u}_i|) \right) g'(\tau_i) f \left(\sum_{j=1}^{p} \omega_{aj} X_{ij} + \omega_{a0} \right), \tag{45}$$

where $a = 1, \ldots, N$,

(d)

$$\frac{\partial \xi_3}{\partial \omega_{a0}}(c, \gamma, \omega) = -2 \sum_{i=1}^{n} \tilde{u}_i \gamma_a \psi \left(\hat{F}^{(n)}(|\tilde{u}_i|) \right) g'(\tau_i) f' \left(\sum_{j=1}^{p} \omega_{aj} X_{ij} + \omega_{a0} \right), \tag{46}$$

where $a = 1, \ldots, N$,

(e)

$$\frac{\partial \xi_3}{\partial \omega_{ab}}(c, \gamma, \omega) = -2 \sum_{i=1}^{n} \tilde{u}_i \gamma_a X_{ib} \psi \left(\hat{F}^{(n)}(|\tilde{u}_i|) \right) g'(\tau_i) f' \left(\sum_{j=1}^{p} \omega_{aj} X_{ij} + \omega_{a0} \right), \tag{47}$$

where $a = 1, \ldots, N, \quad b = 1, \ldots, p$.

3.8 Applications

Several datasets were analyzed by the presented robust neural networks (LTS-MLP and LWS-MLP) in [12]. In all datasets, which are contaminated by outliers, a robust mean square error was better (i.e. smaller) for all the robust MLPs than that of a plain MLP. This is true especially for simple artificial data and also the Boston housing dataset [5] and the Auto MPG dataset [5]. For the Boston housing dataset, some real estates in the very center of Boston are outlying, as they are small but extremely overpriced compared to those in the suburbs of the city. For the Auto MPG, we found those cars to be outlying for the model, which have a high weight and a high consumption. Other outliers can be identified as cars with a low weight, as there appears only a small percentage of them; such findings are in accordance with those of [14].

4 Conclusions

Standard training of neural networks, including their most common types, is vulnerable to the presence of outliers in the data and thus it is important to consider robustified versions instead. Due to a lack of reliable approaches, robustness in neural networks with respect to outliers remains a perspective topic in machine learning with a high potential to provide interesting applications in the analysis of contaminated data. In this paper, we focus on robust versions of multilayer perceptrons, i.e. alternative training techniques for the most common type of artificial neural networks. We propose an original robust multilayer perceptron based on the LWS loss.

We derive here derivatives of the loss functions based on the LTS and LWS estimates for a particular (rather simple) architecture of a multilayer perceptron. Our presenting this compact overview of derivatives needed for any available gradient-based optimization technique is motivated by an apparent mistake in the derivatives for a similar (although different) robust multilayer perceptron based on the LTA estimator in [18]. The main motivation for our deriving the derivatives is however their usefulness within the backpropagation algorithm, allowing to compute the robust neural networks. This paper does not however investigate any convergence issues of the proposed robust multilayer perceptron; to the best of our knowledge, convergence is not available for any other type of versions of neural networks, which are proposed as robust to the presence of outliers in the data. Implementing the LTS-MLP and LWS-MLP using the presented results is straightforward. Derivatives for more complex multilayer perceptrons, i.e. for networks with a larger number of hidden layers, can be obtained in an analogous way only with additional using the chain rule for computing derivatives.

While the presented results represent a theoretical foundation for our future research, there seems at the same time a gap of systematic comparisons of various different robust versions of neural networks over both real and simulated data. Such comparisons are intended to be a topic for our future work, because a statistical interpretation of the results of robust neural networks remains crucial.

Acknowledgments. The authors would like to thank David Coufal and Jiří Tumpach for discussion.

References

1. Aladag, C.H., Egrioglu, E., Yolcu, U.: Robust multilayer neural network based on median neuron model. Neural Comput. Appl. **24**, 945–956 (2014)

2. Beliakov, G., Kelarev, A., Yearwood, J.: Derivative-free optimization and neural networks for robust regression. Optimization **61**, 1467–1490 (2012)
3. Cisse, M., Bojanowski, P., Grave, E., Dauphin, Y., Usunier, N.: Parseval networks: improving robustness to adversarial examples. In: Proceedings of the 34th International Conference on Machine Learning ICML 2017, pp. 854–863 (2017)
4. D'Urso, P., Leski, J.M.: Fuzzy c-ordered medoids clustering for interval-valued data. Pattern Recogn. **58**, 49–67 (2016)
5. Frank, A., Asuncion, A.: UCI Machine Learning Repository. University of California, Irvine (2010). http://archive.ics.uci.edu/ml/
6. Haykin, S.O.: Neural Networks and Learning Machines: A Comprehensive Foundation, 2nd edn. Prentice Hall, Upper Saddle River (2009)
7. Henderson, D.J., Parmeter, C.F.: Applied Nonparametric Econometrics. Cambridge University Press, New York (2015)
8. Jurečková, J., Picek, J., Schindler, M.: Robust Statistical Methods with R, 2nd edn. Chapman & Hall/CRC, Boca Raton (2019)
9. Kalina, J.: A robust pre-processing of BeadChip microarray images. Biocybern. Biomed. Eng. **38**, 556–563 (2018)
10. Kalina, J., Schlenker, A.: A robust supervised variable selection for noisy high-dimensional data. BioMed Res. Int. **2015**, 1–10 (2015). Article no. 320385
11. Kalina, J., Vidnerová, P.: Robust training of radial basis function neural networks. In: Proceedings 18th International Conference ICAISC 2019. Lecture Notes in Computer Science, vol. 11508, pp. 113–124 (2019)
12. Kalina, J., Vidnerová, P.: On robust training of regression neural networks. In: Proceedings 5th International Workshop on Functional and Operatorial Statistics IWFOS (2020, accepted)
13. Kordos, M., Rusiecki, A.: Reducing noise impact on MLP training-techniques and algorithms to provide noise-robustness in MLP network training. Soft. Comput. **20**, 46–65 (2016)
14. Paulheim, H., Meusel, R.: A decomposition of the outlier detection problem into a set of supervised learning problems. Mach. Learn. **100**, 509–531 (2015)
15. Racine, J., Su, L., Ullah, A.: The Oxford Handbook of Applied Nonparametric and Semiparametric Econometrics and Statistics. Oxford University Press, Oxford (2014)
16. Rousseeuw, P.J., Van Driessen, K.: Computing LTS regression for large data sets. Data Min. Knowl. Disc. **12**, 29–45 (2006)
17. Rusiecki, A.: Robust learning algorithm based on LTA estimator. Neurocomputing **120**, 624–632 (2013)
18. Rusiecki, A., Kordos, M., Kamiński, T., Greń, K.: Training neural networks on noisy data. Lect. Notes Artif. Intell. **8467**, 131–142 (2014)
19. Víšek, J.Á.: The least trimmed squares. Part I: consistency. Kybernetika **42**, 1–36 (2006)
20. Víšek, J.Á.: Consistency of the least weighted squares under heteroscedasticity. Kybernetika **47**, 179–206 (2011)

Stability Analysis of Neutral-Type Hopfield Neural Networks with Multiple Delays

Ozlem Faydasicok(✉)

Department of Mathematics, Faculty of Science, Istanbul University, Istanbul, Turkey
kozlem@istanbul.edu.tr

Abstract. The main aim of this paper is to study the stability problem for neutral-type Hopfield neural networks possessing multiple time delays in the states of the neurons and multiple neutral delays in time derivative of states of the neurons. By using a suitable Lyapunov functional, a novel sufficient stability condition is obtained for global asymptotic stability of neutral-type neural networks with multiple delays. The derived stability criterion can be expressed in terms of the parameters of the neural network model which totally relies on some simple relationships established between the network parameters and it is completely independent of time delays and neutral delays. Hence, this new global asymptotic stability condition can be easily tested and verified by using some algebraic mathematical properties. We will also make a comparison between the result of this paper and previously published corresponding results. This comparison will indicate the advantages of our proposed stability condition over the previously reported stability conditions. Since obtaining stability conditions for neutral type neural networks with multiple delays is a difficult task to achieve due to the insufficient mathematical methods and techniques, the result given in this paper can be considered an important and alternative result for this class of neutral type neural systems.

Keywords: Neutral systems · Delayed neural networks · Stability analysis · Lyapunov functionals

1 Introduction

In recent years, various classes of neural networks have been studied by many researches to solve some important engineering problems such as optimization, signal processing, control problems, pattern recognition and associative memories [1–6]. In most of these applications, the designed neural networks are required be stable as the processed information is represented by the stable states of the neurons. Therefore, it is of great importance to carry out a proper stability analysis of dynamical behaviors of neural networks. On the other hand, when electronically implementing neural networks, due to the finite switching speed of amplifiers and the communication times among the neurons cause time delays, which can turn a stable neural network into an unstable neural network. These time delay parameters can effect the dynamical behaviours of neural networks. Hence, when analyzing the stability properties of dynamical neural networks, it is needed to consider the effect of the time delays on the dynamics of the designed neural network model. On the other hand, in order to evaluate the exact effect of time delays, the delays must also be introduced into the time derivatives of the states of the neurons. The neural networks having delays in both the states and the time derivative of the states are called neutral-type neural networks. This type of neural networks has been widely used to solve many engineering problems. Therefore, the stability of the class of neutral type neural networks has been studied by many researchers and a variety of important stability results have been proposed [7–32]. This paper will consider the neutral-type Hopfield neural networks involving multiple time delays in the states of the neurons and multiple neutral delays in time derivatives of the states of the neurons described by the following sets of differential equations:

$$\begin{aligned}\dot{x}_i(t) = -c_i x_i(t) + \sum_{j=1}^{n} a_{ij} f_j(x_j(t)) + \sum_{j=1}^{n} b_{ij} f_j(x_j(t-\tau_{ij})) + u_i \\ + \sum_{j=1}^{n} e_{ij} \dot{x}_j(t-\zeta_{ij}), \quad i = 1, \cdots, n. \qquad (1)\end{aligned}$$

where x_i represents the state of the ith neuron, c_i are some positive constants, the constant parameters a_{ij} and b_{ij} represent the strengths of the neuron interconnections. τ_{ij} $(1 \leq i, j \leq n)$ are the time delays and ζ_{ij} $(1 \leq i, j \leq n)$ are the neutral delays. The constants e_{ij} are coefficients of the time derivative of the delayed states. The $f_j(\cdot)$ represent the nonlinear neuron activation functions, and the constants u_i are some external inputs. In neural system (1), if we let $\tau = max\{\tau_{ij}\}$, $\zeta = max\{\zeta_{ij}\}$, $1 \leq i, j \leq n$, and $\delta = max\{\tau, \zeta\}$, then, the initial conditions of neural network model (1) are given by: $x_i(t) = \varphi_i(t)$ and $\dot{x}_i(t) = \vartheta_i(t) \in C([-\delta, 0], R)$, where $C([-\delta, 0], R)$ represents the set of all continuous functions from $[-\delta, 0]$ to R.

In the stability analysis of neutral network model defined by (1), it is important to first determine the characteristics of activation functions $f_i(x)$. In general, these activation functions are assumed to satisfied the following conditions:

$$|f_i(x) - f_i(y)| \leq \ell_i |x - y|, \; i = 1, 2, \cdots, n, \quad \forall x, y \in R, x \neq y. \qquad (2)$$

where ℓ_i are the Lipschitz constants.

2 Stability Analysis

This section is devoted to determining the criterion that establishes global stability of neutral-type delayed neural system described by (1). For the sake of simplicity of the proofs, the equilibrium points $x^* = (x_1^*, x_2^*, ..., x_n^*)^T$ possessed by (1) will be transferred to the origin. By defining $z(t) = x(t) - x^*$, we can deduce the following neutral-type neural system

$$\dot{z}_i(t) = -c_i z_i(t) + \sum_{j=1}^{n} a_{ij} g_j(z_j(t)) + \sum_{j=1}^{n} b_{ij} g_j(z_j(t-\tau_{ij})) + \sum_{j=1}^{n} e_{ij} \dot{z}_j(t-\zeta_{ij}),\ \forall i \quad (3)$$

where $g_i(z_i(t)) = f_i(z_i(t)+x_i^*) - f_i(x_i^*), \forall i$. Note that neutral-type neural system (3) inherits the assumption given by (2), namely,

$$|g_i(z_i(t))| \le \ell_i |z_i(t)|,\ \forall i. \quad (4)$$

It can now be proceeded further with the following theorem:

Theorem 1: For neutral-type neural system (3), let the activation functions satisfy (4). Then, the origin of neutral-type Hopfield neural network model (3) is globally asymptotically stable if there exist positive constants $p_1, p_2, ..., p_n$ and a positive constant $0 < \kappa < 1$ such that

$$\xi_i = p_i \frac{c_i}{\ell_i} - \sum_{j=1}^{n} p_j (|a_{ji}| + |b_{ji}|) > 0,\ \forall i$$

and

$$\eta_{ji} = \frac{\kappa}{n} p_i - p_j |e_{ji}| > 0,\ \forall i, j.$$

Then, the origin of system (3) is globally asymptotically stable.

Proof: We will construct the following positive definite Lyapunov functional

$$\begin{aligned} V(t) = {} & \sum_{i=1}^{n} p_i \Big(1 - \kappa sgn(z_i(t)) sgn(\dot{z}_i(t))\Big) sgn(z_i(t)) z_i(t) \\ & + \frac{1}{n}\kappa \sum_{i=1}^{n}\sum_{j=1}^{n} p_j \int_{t-\zeta_{ij}}^{t} |\dot{z}_j(s)| ds + \sum_{i=1}^{n}\sum_{j=1}^{n} p_i \int_{t-\tau_{ij}}^{t} |b_{ij}||g_j(z_j(s))| ds \\ & + \epsilon \sum_{i=1}^{n}\sum_{j=1}^{n} \int_{t-\tau_{ij}}^{t} |z_j(s)| ds \end{aligned} \quad (5)$$

where ϵ is a positive constant whose value will be obtained in what follows. The time derivative of $V(t)$ can be obtained as follows:

$$\begin{aligned}\dot{V}(t) = &\sum_{i=1}^{n} p_i\Big(1 - \kappa sgn(z_i(t))sgn(\dot{z}_i(t))\Big)sgn(z_i(t))\dot{z}_i(t)\\ &+\frac{1}{n}\kappa\sum_{i=1}^{n}\sum_{j=1}^{n} p_j|\dot{z}_j(t)| - \frac{1}{n}\kappa\sum_{i=1}^{n}\sum_{j=1}^{n} p_j|\dot{z}_j(t-\zeta_{ij})|\\ &+\sum_{i=1}^{n}\sum_{j=1}^{n} p_i|b_{ij}||g_j(z_j(t))| - \sum_{i=1}^{n}\sum_{j=1}^{n} p_i|b_{ij}||g_j(z_j(t-\tau_{ij}))|\\ &+\epsilon\sum_{i=1}^{n}\sum_{j=1}^{n}|z_j(t)| - \epsilon\sum_{i=1}^{n}\sum_{j=1}^{n}|z_j(t-\tau_{ij})| \end{aligned} \tag{6}$$

Since

$$\begin{aligned} &p_i\Big(1 - \kappa sgn(z_i(t))sgn(\dot{z}_i(t))\Big)sgn(z_i(t))\dot{z}_i(t)\\ &= p_i\Big(sgn(z_i(t)) - \kappa\Big(sgn(z_i(t))\Big)^2 sgn(\dot{z}_i(t))\Big)\dot{z}_i(t)\\ &= p_i sgn(z_i(t))\dot{z}_i(t) - p_i\kappa\Big(sgn(z_i(t))\Big)^2 sgn(\dot{z}_i(t))\dot{z}_i(t) \end{aligned} \tag{7}$$

and

$$\begin{aligned}\frac{1}{n}\kappa\sum_{i=1}^{n}\sum_{j=1}^{n} p_j|\dot{z}_j(t)| &= \frac{1}{n}\kappa\sum_{i=1}^{n}\sum_{j=1}^{n} p_i|\dot{z}_i(t)| = \kappa\sum_{i=1}^{n} p_i|\dot{z}_i(t)|\\ &= \kappa\sum_{i=1}^{n} p_i sgn(\dot{z}_i(t))\dot{z}_i(t)\end{aligned} \tag{8}$$

Using (7) and (8) in (6) results in

$$\begin{aligned}\dot{V}(t) = &\sum_{i=1}^{n} p_i sgn(z_i(t))\dot{z}_i(t) - \sum_{i=1}^{n} p_i\kappa\Big(sgn(z_i(t))\Big)^2 sgn(\dot{z}_i(t))\dot{z}_i(t)\\ &+\sum_{i=1}^{n} p_i\kappa sgn(\dot{z}_i(t))\dot{z}_i(t) - \frac{1}{n}\kappa\sum_{i=1}^{n}\sum_{j=1}^{n} p_j|\dot{z}_j(t-\zeta_{ij})|\\ &+\sum_{i=1}^{n}\sum_{j=1}^{n} p_i|b_{ij}||g_j(z_j(t))| - \sum_{i=1}^{n}\sum_{j=1}^{n} p_i|b_{ij}||g_j(z_j(t-\tau_{ij}))|\\ &+\epsilon\sum_{i=1}^{n}\sum_{j=1}^{n}|z_j(t)| - \epsilon\sum_{i=1}^{n}\sum_{j=1}^{n}|z_j(t-\tau_{ij})| \end{aligned} \tag{9}$$

Let

$$\begin{aligned}\upsilon_i(t) = &\, p_i sgn(z_i(t))\dot{z}_i(t) - p_i\kappa\Big(sgn(z_i(t))\Big)^2 sgn(\dot{z}_i(t))\dot{z}_i(t)\\ &+ p_i\kappa sgn(\dot{z}_i(t))\dot{z}_i(t),\;\; i = 1, 2, \cdot\cdot\cdot, n\end{aligned}$$

Then, (9) can be written as

$$\begin{aligned}\dot{V}(t) = &\sum_{i=1}^{n} \upsilon_i(t) - \frac{1}{n}\kappa \sum_{i=1}^{n}\sum_{j=1}^{n} p_j |\dot{z}_j(t-\zeta_{ij})| + \sum_{i=1}^{n}\sum_{j=1}^{n} p_i |b_{ij}||g_j(z_j(t))| \\ &- \sum_{i=1}^{n}\sum_{j=1}^{n} p_i |b_{ij}||g_j(z_j(t-\tau_{ij}))| + \epsilon \sum_{i=1}^{n}\sum_{j=1}^{n} (|z_j(t)| - |z_j(t-\tau_{ij})|) \quad (10)\end{aligned}$$

If $z_i(t) \neq 0$, then, $\Big(sgn(z_i(t))\Big)^2 = 1$. In this case, we obtain

$$\begin{aligned}\upsilon_i(t) &= p_i sgn(z_i(t))\dot{z}_i(t) \\ &= -p_i sgn(z_i(t)) c_i z_i(t) + \sum_{j=1}^{n} p_i sgn(z_i(t)) a_{ij} g_j(z_j(t)) \\ &\quad + \sum_{j=1}^{n} p_i sgn(z_i(t)) b_{ij} g_j(z_j(t-\tau_{ij})) + \sum_{j=1}^{n} p_i sgn(z_i(t)) e_{ij} \dot{z}_j(t-\zeta_{ij}) \\ &\leq -p_i c_i |z_i(t)| + \sum_{j=1}^{n} p_i |a_{ij}||g_j(z_j(t))| \\ &\quad + \sum_{j=1}^{n} p_i |b_{ij}||g_j(z_j(t-\tau_{ij}))| + \sum_{j=1}^{n} p_i |e_{ij}||\dot{z}_j(t-\zeta_{ij})|\end{aligned}$$

If $z_i(t) = 0$, then, $sgn(z_i(t)) = 0$. In this case, we obtain

$$\upsilon_i(t) = p_i \kappa sgn(\dot{z}_i(t))\dot{z}_i(t)$$

Since $\kappa < 1$, we get

$$\begin{aligned}\upsilon_i(t) &\leq p_i sgn(\dot{z}_i(t))\dot{z}_i(t) \\ &= -p_i sgn(\dot{z}_i(t)) c_i z_i(t) + \sum_{j=1}^{n} p_i sgn(\dot{z}_i(t)) a_{ij} g_j(z_j(t)) \\ &\quad + \sum_{j=1}^{n} p_i sgn(\dot{z}_i(t)) b_{ij} g_j(z_j(t-\tau_{ij})) + \sum_{j=1}^{n} p_i sgn(\dot{z}_i(t)) e_{ij} \dot{z}_j(t-\zeta_{ij}) \\ &\leq -p_i c_i |z_i(t)| + \sum_{j=1}^{n} p_i |a_{ij}||g_j(z_j(t))| \\ &\quad + \sum_{j=1}^{n} p_i |b_{ij}||g_j(z_j(t-\tau_{ij}))| + \sum_{j=1}^{n} p_i |e_{ij}||\dot{z}_j(t-\zeta_{ij})|\end{aligned}$$

Thus, for all $z_i(t) \in R$, the following holds:

$$\upsilon_i(t) \leq -p_i c_i |z_i(t)| + \sum_{j=1}^{n} p_i |a_{ij}||g_j(z_j(t))| + \sum_{j=1}^{n} p_i |b_{ij}||g_j(z_j(t-\tau_{ij}))| + \sum_{j=1}^{n} p_i |e_{ij}||\dot{z}_j(t-\zeta_{ij})| \tag{11}$$

Hence, using (11) in (10) yields

$$\begin{aligned}\dot{V}(t) \leq & -\sum_{i=1}^{n} p_i c_i |z_i(t)| + \sum_{i=1}^{n}\sum_{j=1}^{n} p_i |a_{ij}||g_j(z_j(t))| + \sum_{i=1}^{n}\sum_{j=1}^{n} p_i |b_{ij}||g_j(z_j(t-\tau_{ij}))| \\ & + \sum_{i=1}^{n}\sum_{j=1}^{n} p_i |e_{ij}||\dot{z}_j(t-\zeta_{ij})| - \frac{1}{n}\kappa \sum_{i=1}^{n}\sum_{j=1}^{n} p_j |\dot{z}_j(t-\zeta_{ij})| \\ & + \sum_{i=1}^{n}\sum_{j=1}^{n} p_i |b_{ij}||g_j(z_j(t))| - \sum_{i=1}^{n}\sum_{j=1}^{n} p_i |b_{ij}||g_j(z_j(t-\tau_{ij}))| \\ & + \epsilon \sum_{i=1}^{n}\sum_{j=1}^{n} |z_j(t)| - \epsilon \sum_{i=1}^{n}\sum_{j=1}^{n} |z_j(t-\tau_{ij})| \end{aligned} \tag{12}$$

(12) can be rewritten in the form:

$$\begin{aligned}\dot{V}(t) \leq & -\sum_{i=1}^{n} p_i c_i |z_i(t)| + \sum_{i=1}^{n}\sum_{j=1}^{n} p_i |a_{ij}||g_j(z_j(t))| + \sum_{i=1}^{n}\sum_{j=1}^{n} p_i |b_{ij}||g_j(z_j(t))| \\ & + \sum_{i=1}^{n}\sum_{j=1}^{n} p_i |e_{ij}||\dot{z}_j(t-\zeta_{ij})| - \frac{1}{n}\kappa \sum_{i=1}^{n}\sum_{j=1}^{n} p_j |\dot{z}_j(t-\zeta_{ij})| + \epsilon \sum_{i=1}^{n}\sum_{j=1}^{n} |z_j(t)| \\ = & -\sum_{i=1}^{n} p_i c_i |z_i(t)| + \sum_{i=1}^{n}\sum_{j=1}^{n} p_j |a_{ji}||g_i(z_i(t))| + \sum_{i=1}^{n}\sum_{j=1}^{n} p_j |b_{ji}||g_i(z_i(t))| \\ & + \sum_{i=1}^{n}\sum_{j=1}^{n} p_i |e_{ij}||\dot{z}_j(t-\zeta_{ij})| - \frac{1}{n}\kappa \sum_{i=1}^{n}\sum_{j=1}^{n} p_j |\dot{z}_j(t-\zeta_{ij})| + n\epsilon \sum_{i=1}^{n} |z_i(t)| \end{aligned} \tag{13}$$

Under the assumption given by (4), we can write (13) as follows:

$$\begin{aligned}\dot{V}(t) \leq & -\sum_{i=1}^{n} p_i c_i |z_i(t)| + \sum_{i=1}^{n}\sum_{j=1}^{n} \ell_i p_j |a_{ji}||z_i(t)| + \sum_{i=1}^{n}\sum_{j=1}^{n} \ell_i p_j |b_{ji}||z_i(t)| \\ & + \sum_{i=1}^{n}\sum_{j=1}^{n} p_i |e_{ij}||\dot{z}_j(t-\zeta_{ij})| - \frac{1}{n}\kappa \sum_{i=1}^{n}\sum_{j=1}^{n} p_j |\dot{z}_j(t-\zeta_{ij})| + n\epsilon \sum_{i=1}^{n} |z_i(t)| \\ = & -\sum_{i=1}^{n} (p_i c_i - \ell_i \sum_{j=1}^{n} p_j (|a_{ji}| + |b_{ji}|))|z_i(t)| \\ & - \sum_{i=1}^{n}\sum_{j=1}^{n} (\frac{\kappa}{n} p_i - p_j |e_{ji}|)|\dot{z}_i(t-\zeta_{ji})| + n\epsilon \sum_{i=1}^{n} |z_i(t)| \\ = & -\sum_{i=1}^{n} \xi_i |z_i(t)| - \sum_{i=1}^{n}\sum_{j=1}^{n} \eta_{ji} |\dot{z}_i(t-\zeta_{ji})| + n\epsilon \sum_{i=1}^{n} |z_i(t)| \end{aligned} \tag{14}$$

Since $\eta_{ji} > 0, \forall i, j$, (14) satisfies:

$$\begin{aligned}\dot{V}(t) & \leq -\sum_{i=1}^{n} \xi_i |z_i(t)| + n\epsilon \sum_{i=1}^{n} |z_i(t)| \leq -\sum_{i=1}^{n} \xi_m |z_i(t)| + n\epsilon \sum_{i=1}^{n} |z_i(t)| \\ & = -\xi_m ||z(t)||_1 + n\epsilon ||z(t)||_1 \\ & = -(\xi_m - n\epsilon)||z(t)||_1 \end{aligned} \tag{15}$$

where $\xi_m = min\{\xi_i\} > 0,\ i = 1, 2, \cdots, n$. Clearly, the choice $0 < \epsilon < \frac{\xi_m}{n}$ directly implies from (15) that

$$\dot{V}(t) < 0, \forall z(t) \neq 0$$

Now, we consider the case where $z(t) = 0$. In this case, (14) satisfies:

$$\dot{V}(t) \leq -\sum_{i=1}^{n}\sum_{j=1}^{n} \eta_{ji} |\dot{z}_i(t-\zeta_{ji})| \tag{16}$$

Clearly, since $\eta_{ji} > 0$, if $\dot{z}_i(t-\zeta_{ji}) \neq 0$ for any pairs of i and j, then, from (16) we get that $\dot{V}(t) < 0$.

Now, we consider the case where $z(t) = 0$ and $z_i(t-\zeta_{ji}) = 0$ In this case, (12) satisfies:

$$\dot{V}(t) \leq -\epsilon \sum_{i=1}^{n}\sum_{j=1}^{n} |z_j(t-\tau_{ij})|$$

Clearly, since $\epsilon > 0$, if $z_j(t-\tau_{ij}) \neq 0$ for any pairs of i and j, then, $\dot{V}(t) < 0$. Let $z(t) = 0$, (for $z(t) = 0$, we have $g(z(t)) = 0$), $\dot{z}_i(t-\zeta_{ji}) = 0$, $\forall i, j$, and $z_j(t-\tau_{ij}) = 0$, ($z_j(t-\tau_{ij}) = 0$ implies that $g_j(z_j(t-\tau_{ij})) = 0$). In this case, $\dot{z}_i(t) = 0$, $\forall i$ and $\dot{V}(t) = 0$. Hence, $\dot{V}(t) = 0$ holds iff $z(t) = 0$, $g(z(t)) = 0)$,

$\dot{z}_i(t-\zeta_{ji}) = 0$, $\forall i, j$, $z_j(t-\tau_{ij}) = 0$, $g_j(z_j(t-\tau_{ij})) = 0$) and $\dot{z}_i(t) = 0$, $\forall i$. Clearly, $\dot{V}(t) < 0$ except for the origin. Hence, origin $z(t) = 0$ of (3) is asymptotically stable. It is easy to observe that the Lyapunov function employed to carry out the stability analysis is radially unbounded, ($V(t) \to \infty$ as $||z(t)|| \to \infty$), and therefore, $z(t) = 0$ is globally asymptotically stable. Q.E. D.

3 Comparisons

In this section, we will compare our results with the previous key stability results obtained in the literature. In order to make a precise comparison, we need to express these previously derived results for the stability of neutral-type Hopfield neural network model (1):

Theorem 2 [31]**:** For the neutral-type neural network model (3), assume that the activation functions satisfy (4). Let α be a positive constant with $0 < \alpha < 1$. Then, the origin of neutral-type Hopfield neural network model (3) is globally asymptotically stable if there exist positive constants $p_1, p_2, ..., p_n$ such that

$$\omega_i = p_i \frac{c_i}{\ell_i} - \frac{1+\alpha}{1-\alpha} \sum_{j=1}^{n} p_j(|a_{ji}| + |b_{ji}|) > 0,\ \forall i$$

and

$$\varepsilon_{ji} = \frac{\alpha}{n} p_i - (1+\alpha) p_j |e_{ji}| > 0,\ i, j = 1, 2, ..., n.$$

Theorem 3 [32]**:** For the neutral-type neural network model (3), assume that the activation functions satisfy (4) and $\zeta_{ij} = \zeta_j, \forall i, j$. Then, the origin of neutral-type Hopfield neural network model (3) is globally asymptotically stable if there exist positive constants $p_1, p_2, ..., p_n$ such that

$$\rho_i = p_i \frac{c_i}{\ell_i} - \sum_{j=1}^{n} p_j(|a_{ji}| + |b_{ji}|) > 0,\ \forall i$$

and

$$\mu_i = p_i \alpha - \sum_{j=1}^{n} p_j |e_{ji}| > 0,\ \forall i$$

In Theorem 2, since $0 < \alpha < 1$, the term $\frac{1+\alpha}{1-\alpha} > 1$, the conditions given by ξ_i in Theorem 1 improves the conditions given by ω_i in Theorem 2. It should also be noted that, if we choose $\kappa = \alpha$, then the conditions given by ε_{ji} in Theorem 2 are always less than the conditions given by η_{ji} in Theorem 1 since $0 < \alpha < 1$. Therefore, the results of Theorem 1 generalize the results of Theorem 2.

When the results of Theorems 1 and 3 are examined, it can be seen that the results of these two theorems are very similar. However, Theorem 1 considers the multiple neutral delays and Theorem 3 considers the discrete neutral delays in the neural network model (1). Therefore, the results of Theorem 1 can be considered as the generalizations of the results of Theorem 3 as Theorem 1 involves the stability results for a more general class of neutral-type neural network model.

4 Conclusions

The main aim of this study was to carry out an investigation into stability problem for the class of neutral-type Hopfield neural networks involving multiple time delays in states and multiple neutral delays in time derivative of states. By using a suitable Lyapunov functional, a new sufficient condition has been proposed for global asymptotic stability of neutral-type neural network of this class. The proposed stability condition is independently of time delay and neutral delay parameters, and it is totally stated in terms of the system matrices and network parameters. Thus, this new stability condition can be validated by only examining the some algebraic equations that are related to the system parameters and matrices of this neutral-type neural network. We have also compared the result of this paper with the previously reported key stability results for the neutral-type neural network with multiple delays. This comparison has demonstrated the main advantages of our results over the past literature results. Since stability analysis of the class of neutral-type neural networks considered in this paper has not been studied because of the difficulty of employing the proper and efficient mathematical techniques and methods to investigate the stability analysis of such neutral-type neural systems, the stability criterion obtained in this paper can be considered as one of important stability results for neutral-type Hopfield neural networks with multiple time and multiple neutral delays.

References

1. Chua, L.O., Yang, L.: Cellular neural networks: applications. IEEE Trans. Circ. Syst. Part-I **35**, 1273–1290 (1988)
2. Cohen, M., Grossberg, S.: Absolute stability of global pattern formation and parallel memory storage by competitive neural networks. IEEE Trans. Syst. Man Cybern. **13**(5), 815–826 (1983)
3. Hopfield, J.: Neural networks and physical systems with emergent collective computational abilities. Proc. Nat. Acad. Sci. **79**, 2554–2558 (1982)
4. Tong, S.C., Li, Y.M., Zhang, H.G.: Adaptive neural network decentralized backstepping output-feedback control for nonlinear large-scale systems with time delays. IEEE Trans. Neural Netw. **22**(7), 1073–1086 (2011)
5. Galicki, M., Witte, H., Dorschel, J., Eiselt, M., Griessbach, G.: Common optimization of adaptive preprocessing units and a neural network during the learning period. Application in EEG pattern recognition. Neural Netw. **10**, 1153–1163 (1997)
6. Kosko, B.: Bi-directional associative memories. IEEE Trans. Syst. Man Cybern. **18**, 49–60 (1988)
7. Niculescu, S.I.: Delay Effects on Stability: A Robust Control Approach. Springer, Berlin (2001)
8. Kolmanovskii, V.B., Nosov, V.R.: Stability of Functional Differential Equations. Academic Press, London (1986)
9. Kuang, Y.: Delay Differential Equations with Applications in Population Dynamics. Academic Press, Boston (1993)

10. Samidurai, S., Marshal, A., Balachandran, R.K.: Global exponential stability of neutral-type impulsive neural networks with discrete and distributed delays. Nonlinear Anal. Hybrid Syst. **4**(1), 103–112 (2010)
11. Shi, K., Zhu, H., Zhong, S., Zeng, Y., Zhang, Y.: New stability analysis for neutral type neural networks with discrete and distributed delays using a multiple integral approac. J. Franklin Inst. **352**(1), 155–176 (2015)
12. Liu, P.L.: Further improvement on delay-dependent robust stability criteria for neutral-type recurrent neural networks with time-varying delays. ISA Trans. **55**, 92–99 (2015)
13. Lee, S.M., Kwon, O.M., Park, J.H.: A novel delay-dependent criterion for delayed neural networks of neutral type. Phys. Lett. A **374**(17–18), 1843–1848 (2010)
14. Chen, H., Zhang, Y., Hu, P.: Novel delay-dependent robust stability criteria for neutral stochastic delayed neural networks. Neurocomputing **73**(13–15), 2554–25561 (2010)
15. Zhang, Z., Liu, K., Yang, Y.: New LMI-based condition on global asymptotic stability concerning BAM neural networks of neutral type. Neurocomputing **81**(1), 24–32 (2012)
16. Lakshmanan, S., Park, J.H., Jung, H.Y., Kwon, O.M., Rakkiyappan, R.: A delay partitioning approach to delay-dependent stability analysis for neutral type neural networks with discrete and distributed delays. Neurocomputing **111**, 81–89 (2013)
17. Dharani, S., Rakkiyappan, R., Cao, J.: New delay-dependent stability criteria for switched Hopfield neural networks of neutral type with additive time-varying delay components. Neurocomputing **151**, 827–834 (2015)
18. Shi, K., Zhong, S., Zhu, H., Liu, X., Zeng, Y.: New delay-dependent stability criteria for neutral-type neural networks with mixed random time-varying delays. Neurocomputing **168**, 896–907 (2015)
19. Zhang, G., Wang, T., Li, T., Fei, S.: Multiple integral Lyapunov approach to mixed-delay-dependent stability of neutral neural networks. Neurocomputing **275**, 1782–1792 (2018)
20. Liu, P.L.: Improved delay-dependent stability of neutral type neural networks with distributed delays. ISA Trans. **52**(6), 717–724 (2013)
21. Liao, X., Liu, Y., Wang, H., Huang, T.: Exponential estimates and exponential stability for neutral-type neural networks with multiple delays. Neurocomputing **149**(3), 868–883 (2015)
22. Jian, J., Wang, B.: Stability analysis in Lagrange sense for a class of BAM neural networks of neutral type with multiple time-varying delays. Neurocomputing **149**, 930–939 (2015)
23. Arik, S.: An analysis of stability of neutral-type neural systems with constant time delays. J. Franklin Inst. **351**(11), 4949–4959 (2014)
24. Lien, C.H., Yu, K.W., Lin, Y.F., Chung, Y.J., Chung, L.Y.: Global exponential stability for uncertain delayed neural networks of neutral type with mixed time delays. IEEE Trans. Syst. Man Cybern. Part B Cybern. **38**(3), 709–720 (2008)
25. Yang, Y., Liang, T., Xu, X.: Almost sure exponential stability of stochastic Cohen-Grossberg neural networks with continuous distributed delays of neutral type. Optik Int. J. Light Electron. Opt. **126**(23), 4628–4635 (2015)
26. Samli, R., Arik, S.: New results for global stability of a class of neutral-type neural systems with time delays. Appl. Math. Comput. **210**(2), 564–570 (2009)
27. Orman, Z.: New sufficient conditions for global stability of neutral-type neural networks with time delays. Neurocomputing **97**, 141–148 (2012)

28. Cheng, C.J., Liao, T.L., Yan, J.J., Hwang, C.C.: Globally asymptotic stability of a class of neutral-type neural networks with delays. IEEE Trans. Syst. Man Cybern. Part B Cybern. **36**(5), 1191–1195 (2008)
29. Akca, H., Covachev, V., Covacheva, Z.: Global asymptotic stability of Cohen-Grossberg neural networks of neutral type. J. Math. Sci. **205**(6), 719–732 (2015)
30. Ozcan, N.: New conditions for global stability of neutral-type delayed Cohen-Grossberg neural networks. Neural Netw. **106**, 1–7 (2018)
31. Arik, S.: New criteria for stability of neutral-type neural networks with multiple time delays. IEEE Trans. Neural Netw. Learn. Syst. (2019). https://doi.org/10.1109/TNNLS.2019.2920672
32. Arik, S.: A modified Lyapunov functional with application to stability of neutral-type neural networks with time delays. J. Franklin Inst. **356**, 276–291 (2019)

Reduction of Variables and Generation of Functions Through Nearest Neighbor Relations in Threshold Networks

Naohiro Ishii[1(✉)], Kazunori Iwata[2], Kazuya Odagiri[3], Toyoshiro Nakashima[3], and Tokuro Matsuo[1]

[1] Advanced Institute of Industrial Technology, Tokyo, Japan
nishii@acm.org, tokuro@aiit.ac.jp
[2] Aichi University, Nagoya, Japan
kazunori@vega.aichi-u.ac.jp
[3] Sugiyama Jyogakuen University, Nagoya, Japan
{kodagiri,nakasima}@sugiyama-u.ac.jp

Abstract. Reduction of data variables is an important issue and it is needed for the processing of higher dimensional data in the application domains and AI, in which threshold neural networks are extensively used. We develop a reduction of data variables and classification method based on the nearest neighbor relations for threshold networks. First, the nearest neighbor relations are shown to be useful for the generation of threshold functions and Chow parameters. Second, the extended application of the nearest neighbor relations is developed for the reduction of variables based on convex cones. The edges of convex cones are compared for the reduction of variables. Further, hyperplanes with reduced variables are obtained on the convex cones for data classification.

Keywords: Nearest neighbor relation · Generation of Chow parameters · Reduction of variables · Degenerate convex cones

1 Introduction

By Pawlak's rough set theory [1], a reduct is a minimal subset of features, which has the discernibility power as using the entire features, which shows the dimensionality reduction of features. Skowlon [2, 3] developed the reduct derivation by using the Boolean reasoning for the discernibility of data, which is a computationally complex task using all the data. A new consistent method for the generation of reduced variables and their classification in threshold networks is expected from the point of the efficient processing of data. In this paper, we have developed a method of reduction of data variables and it's classification based on the nearest neighbor relations [8]. First, it is shown that the nearest neighbor relations are useful for the generation of threshold functions and Chow parameters [5, 6]. Next, the extended application of the nearest neighbor relations is developed for the reduction of variables [9–11]. Then, the degenerate convex cones and their operations using nearest neighbor relation, are developed. The dependent relations and algebraic operations of the edges on the

L. Iliadis et al. (Eds.): EANN 2020, INNS 2, pp. 569–578, 2020.
https://doi.org/10.1007/978-3-030-48791-1_45

degenerate convex cones in the linear subspaces are derived for the reduction of variables. Finally, the hyperplanes using the reduced variables is derived based on the convex cones of nearest neighbor relations.

2 Nearest Neighbor Relations in Threshold Function

The nearest neighbor relation is also applicable to the generation of threshold functions. The function f is characterized by the hyperplane $WX - \theta$ with the weight vector $W(= (w_1, w_2, \ldots, w_n))$ and threshold θ. The X is a vertex of the cube 2^n. In the following, the threshold function is assumed to be positive and canonical threshold function, in which the Boolean variables hold the partial order [5].

Definition 1. The nearest neighbor relation (X_i, X_j) on the threshold function f is defined to be vertices satisfying the following equation,

$$\{(X_i, X_j) : f(X_i) \neq f(X_j) \wedge |X_i - X_j| \leq \delta(= 1)\}, \tag{1}$$

where $\delta = 1$ shows one bit difference between X_i and X_j in the Hamming distance (also in the Euclidean distance).

Definition 2. The boundary vertex X is defined to be the vertex which satisfies

$$|WX - \theta| \leq |WY - \theta| \quad \text{for the} \quad X(\neq Y \in 2^n) \tag{2}$$

Theorem 3. The boundary vertex X becomes an element of nearest neighbor relation in the threshold function.

Corollary 4. The boundary vertex X generates a pair of nearest neighbor relation in the threshold function.

2.1 Logical Operation for Nearest Neighbor Relation

Generation of threshold function is performed as follows. As an example, the three dimensional vertices are shown in the cube in Fig. 1. As true valued vertices, (101), (110) and (111) are given in the black circle, ●, which belongs to +1 class. As false valued vertices, (000), (010), (100), (001), and (011) are given in the circle, ○, which belongs to 0 class. In Fig. 1, the true vertex (101) has nearest neighbor relations as {(101), (001)} and {(101), (100)}. Then, the directed arrow vector indicates the nearest neighbor relation as $\overrightarrow{\{(101),(001)\}}$ Two directed arrow vectors, $\overrightarrow{\{(101),(001)\}}$ and $\overrightarrow{\{(101),(100)\}}$ generate one plane in the Boolean AND operation in Fig. 2. The $\overrightarrow{\{(101),(100)\}}$ has x_3 variable, while, $\overrightarrow{\{(101),(001)\}}$ has x_1 variable. By the AND operation x_1 and x_3, the Boolean product $x_1 \cdot x_3$ is generated. Similarly, the Boolean product $x_1 \cdot x_2$ is generated. Since these two planes are orthogonal, the threshold function $x_1 \cdot x_3 + x_1 \cdot x_2$ is obtained by OR connecting two perpendicular planes.

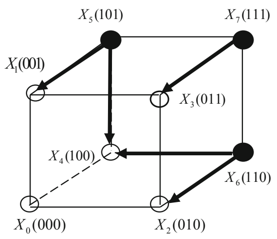

Fig. 1. Directed arrows for nearest neighbor relations

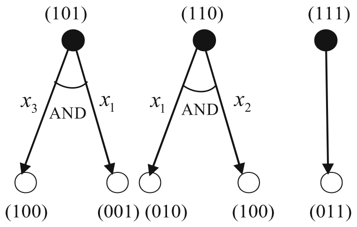

Fig. 2. Boolean AND operations for nearest neighbor relations

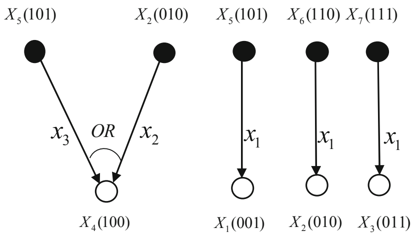

Fig. 3. Boolean OR operation for nearest neighbor relations

Similarly, another logical operation OR is developed as shown in Fig. 3, which also realizes the threshold function $x_1 \cdot x_2 + x_1 \cdot x_3$.

Theorem 5. Nearest neighbor relations in the threshold function are minimal information for generating the given threshold function in the Boolean logical form.

2.2 Iterative Generation of Chow Parameters of Threshold Functions Activated Through Nearest Neighbor Relations

The hyperplane is based on the independent true and false vertices, which are derived from the linear inequality equations of inputs [4, 5]. These independent true and false inputs become boundary vertices, which also make respective nearest neighbor relations in Theorem 5.

In Fig. 4, the iterative generation of Chow parameters with 5 variables [6] is performed based on the nearest neighbor relations of threshold functions. The Chow parameter shows 6 tuples $[m : s_1, s_2, s_3, s_4, s_5]$, in which m shows the summed number of true vertices, while s_1, s_2, s_3, s_4, s_5 indicate the summed number of the first component, that of the second component, …, that of the fifth component of the true vertices [6]. From the Chow parameter $[m : s_1, s_2, s_3, s_4, s_5] = [6 : 11111]$, the new Chow parameter $[7 : 22111]$ is generated changing the false boundary vertex (11000) to the true vertex in the nearest neighbor relation $\{(10000), (11000)\}$. The iterative generation of Chow parameters is performed through the small change of weights of the boundary vertex.

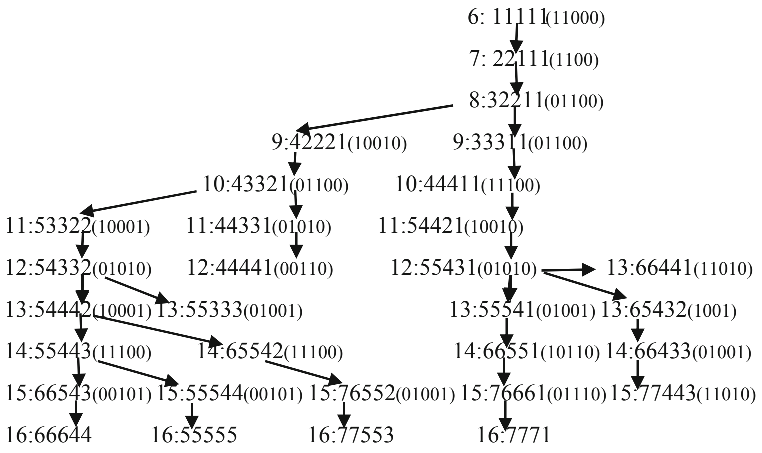

Fig. 4. Generation of Chow parameters with 5 variables of threshold functions through nearest neighbor relations. Parenthesis shows false vertex to generate next Chow parameter.

3 Extension to Threshold Networks Based on Nearest Neighbor Relations

A nearest neighbor relation with minimal distance is introduced here for the extension to threshold networks.

Definition 6. A nearest neighbor relation with minimal distance is a set of pair of instances, which are described in

$$\{(x_i, x_j) : d(x_i) \neq d(x_j) \wedge |x_i - x_j| \leq \delta\}, \tag{3}$$

where $|x_i - x_j|$ shows the distance between x_i and x_j. Further, $d(x_i)$ is a decision function and δ is the minimal distance. Then, x_i and x_j in the Eq. (3) are called to be in the x_j nearest neighbor relation with minimal distance δ.

3.1 Reduction of Variables Based on Convex Cones

An example of the decision table is shown in Table 1. The left side data in the column in Table 1 as shown in, $\{x_1, x_2, x_3, \ldots, x_7\}$ is a set of instances, while the data $\{a, b, c, d\}$ on the upper row, shows the set of attributes of the instance.

Table 1. Decision table of data example (instances)

Attribute	a	b	c	d	Class
x_1	1	0	2	1	+1
x_2	1	0	2	0	+1
x_3	2	2	0	0	−1
x_4	1	2	2	1	−1
x_5	2	1	0	1	−1
x_6	2	1	1	0	+1
x_7	2	1	2	1	−1

In Fig. 5, linearly separated classifications are shown for the data in Table 1. As the first step, one hyperplane A_1 divides the instances of data $\{x_3, x_5, x_7, x_4\}$ shown with $\times$ from those of $\{x_2, x_6\}$ shown with •. But, it misclassifies the instance $\{x_1\}$ with • from $\{x_3, x_5, x_7, x_4, x_1\}$ with $\times$. As the second step, another hyperplane A_2 divides the instance $\{x_1\}$ with • from $\{x_3, x_5, x_7, x_4\}$ with $\times$. In the linearly separated sub spaces, the divided instances are represented by the system of the linear inequality equations. Processing steps for the reduction of variables are classified to the following two steps, which are shown in circles ① and ② in Fig. 6.

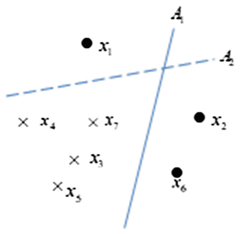

Fig. 5. Piecewise linear separated classification for data in Table 1

Step ① Variables of Nearest Neighbor Relations

Each approximated reduct based on the convex cone is generated based on the nearest neighbor relation, in the step, ① in Fig. 6. The obtained convex cone plays for the reduction of variables in steps ②.

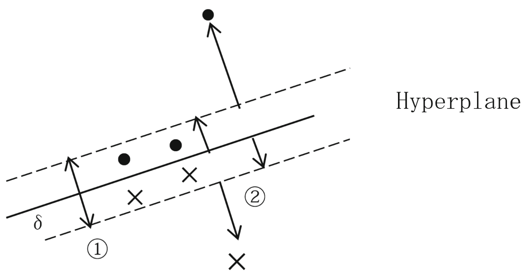

Fig. 6. Processing steps based on hyperplane derived from nearest neighbor relation

Step ② Removal of Variables Using Nearest Neighbor Relations
The convex cones based on the nearest neighbor relations are transformed to the reduced ones for the reduction of variables. Dependent relations and edge processing between the convex cones are applied for the complete reducts, which show the reduction of variables in the step ② in Fig. 6. In the next section, the reduction of variables on the convex cones is shown in the next Sect. 3.2, step (3.2.1) and step (3.2.2).

3.2 Dependent Relations on Degenerate Convex Cones, Step (3.2.1)

Independent vectors of nearest neighbor relations, which consist of the degenerate convex in the affine subspaces, are useful for the operations of dimensional reduction. Independent vectors are derived in the subspaces [4, 7] as follows.

$$\vec{X}'_3 = X'_3 - X'_6,\ \vec{X}'_5 = X'_5 - X'_6 \text{ and } \vec{X}'_7 = X'_7 - X'_6 \tag{4}$$

In the Eq. (4) vectors $\vec{X}'_3$, $\vec{X}'_5$ and $\vec{X}'_7$ are independent. The set of reduced variables $\{b, c\}$ is preserved from $\vec{X}'_3$ of the nearest neighbor relation $\{X_3, X_6\}$. Similarly, the set of reduced variables $\{c, d\}$ is preserved from $\vec{X}'_5$ or $\vec{X}'_7$ of the nearest neighbor relation $\{X_5, X_6\}$ or $\{X_7, X_6\}$, respectively. Thus, the reduced variables $\{b, c, d\}$ are preserved as shown in Fig. 7.

Theorem 7. If a linear dependent equation of the vector value holds on the degenerate convex of the nearest neighbor relations, the corresponding Boolean term to the vector value is removed by the absorption of Boolean terms of the nearest neighbor relations.

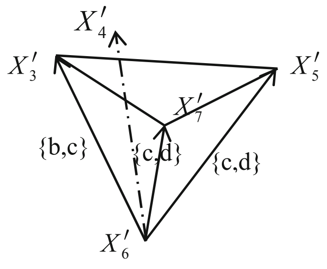

Fig. 7. Degenerate convex cone generated by X'_3, X'_5, X'_7 and X'_6

3.3 Chaining of Edges Between Degenerate Convex Cones, Step (3.2.2)

We can construct two degenerate convex cones as shown in Fig. 8. The upper de degenerate convex cone (solid line) is made of the nearest neighbor relations which is from different classes data, while the lower one (dotted line) is made of the same class data.

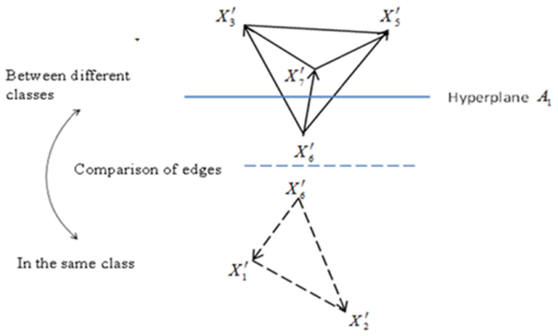

Fig. 8. Comparison of edges on degenerate convex cones in the subspaces

The data difference equations except the nearest neighbor relations are shown in (5)

$$(X_i' - X_j')_k \neq 0 \text{ for } i = 3,\ 4,\ 5,\ j = 1,\ 2 \text{ and } k = b,\ c,\ d \tag{5}$$

If the Eq. (5) hold for both $k = b$ and $k = c$, the element (x_i, x_j), is removed by the equality equation of $(X_i = X_j)_{k=b,k=c}$, since it is absorbed from the nearest neighbor relation $\{b, c\}$. Similarly, if the Eqs. (5) holds for both $k = c$ and $k = d$, the element (x_i, x_j) is removed, since it is absorbed from the nearest neighbor relation $\{c, d\}$. The left side of the Eqs. (5) is replaced to the following equation using the nearest neighbor relation in Fig. 8.

$$(X_i' - X_j')_k = (X_i' - X_6')_k - (X_j' - X_6')_k \tag{6}$$

From the Eq. (5), the Eq. (6) becomes

$$(X_i' - X_6')_k \neq (X_j' - X_6')_k \tag{7}$$

Theorem 8. The element (x_i, x_j) with Boolean variables are removed by the nearest relations with reference data X_ξ', where X_ξ' is in the class $\{j\}(\neq \{i\})$, if the following equations hold

$$(X_i' - X_\xi')_k \neq (X_j' - X_\xi')_k \tag{8}$$

for $i \in \{i\}, j \in \{j\}$, i and j are in the different class and k is components in X_l'.

By Theorem 8, an example of $X'_\xi = X'_6$ and $(X'_3 - X'_2)$, which are in the case of $i = 3$, $j = 2$, is developed as follows,

$$(X'_3 - X'_2) = (X'_3 - X'_6) - (X'_2 - X'_6) \tag{9}$$

As the final results in this section, by Theorem 8, all the elements (x_i, x_j) are removed by the nearest neighbor relations (X_3, X_6) , (X_5, X_6) and (X_7, X_6) using the hyperplane A_1. Thus, the reduced variables by the hyperplane A_1, become $\{b, c\}$ and $\{c, d\}$, which derive the Boolean sum terms $(b + c)$ and $(c + d)$. Similarly, by the hyperplane A_2, reduced variable (b) is obtained. By the Boolean product of terms of A_1 and A_2, $b \cdot (b + c) \cdot (c + d) = bc + bd$ is obtained. Then, complete reducts of reduced variables become $\{bc,\ bd\}$.

Corollary 9. The element (x_i, x_j) with Boolean variables is not removed, if the Eq. (8) holds. Then, the Boolean sum of the variables in the (x_i, x_j) is multiplied to other Boolean sum of variables of the nearest neighbor relations.

Theorem 10. Dimensionality reduction of variables for reducts is realized by convex cones on the nearest neighbor relations, which are generated by the linear subspaces.

4 Hyperplanes of Reduced Variables for Threshold Network

By using this reduct $\{bc\}$, a classification of the reduced variables is performed as shown in Fig. 9. In Fig. 9, three hyperplanes, $H_{1\{bc\}}, H_{2\{bc\}}, H_{3\{bc\}}$ are shown. The hyperplane A_1 in Fig. 5 is shown, which is also in the degenerated convex in Fig. 8.

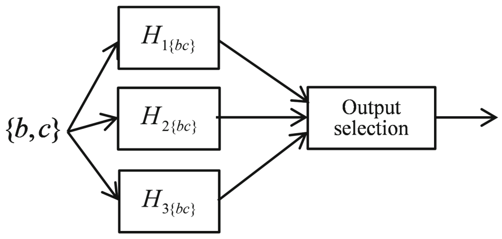

Fig. 9. Hyperplanes generated on convex cones with nearest neighbor relations

All the correct classifications of the classes are carried out by majority voting using these three hyperplanes with reduced variables, $H_{1\{bc\}}$, $H_{2\{bc\}}$, $H_{3\{bc\}}$ in Fig. 9. Then, all the instances are classified, correctly. Combining these three hyperplanes with reduced variables, correct classification is performed using the majority selection. The comparison of the classification accuracy is shown in Fig. 10.

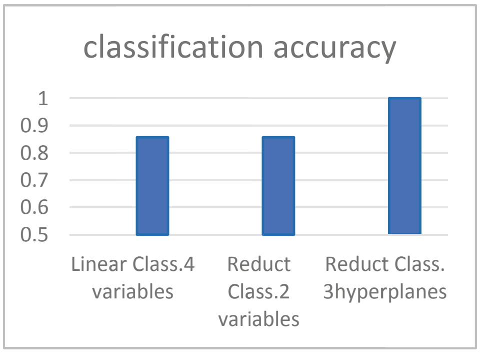

Fig. 10. Comparison of classification accuracy of reduced variables

5 Conclusion

In this paper, the reduction of data variables and it's classification through the nearest neighbor relations are proposed. First, it is shown that the nearest neighbor relations are useful for the generation of threshold functions and the Chow parameters. Next, the extended application of the nearest neighbor relations is proposed for the reduction of variables based on convex cones. Then, the dependent relations and the algebraic operations of edges on the degenerate convex cones are carried out in the linear subspaces. Further, hyperplanes with reduced variables are obtained on the same degenerate convex cones for data classification.

References

1. Pawlak, Z.: Rough sets. Int. J. Comput. Inf. Sci. **11**, 341–356 (1982)
2. Skowron, A., Polkowski, L.: The discernibility matrices and functions in information systems. In: Intelligent Decision Support-Handbook of Application and Advances of Rough Sets Systems, vol. 11, pp. 331–362. Kluwer Academic Publisher, Dordrech (1992)
3. Skowron, A., Polkowski, L.: Decision algorithms, a survey of rough set theoretic methods. Fundam. Inform. **30**(3-4), 345–358 (1997)
4. Fan, K.: On systems of linear inequalities. In: Kuhn, H.W., Tucker, A.W. (eds.) Linear Inequalities and Related Systems, pp. 99–156. Princeton University Press, Princeton (1966)
5. Hu, S.T.: Threshold Logic. University of California Press, California (1965)
6. Chow, C.K.: On the characterization of threshold functions. In: Switching Circuit Theory and Logical Design, vol. S-134, pp. 34–38. IEEE Special Publication (1961)
7. Prenowitz, W., Jantosciak, J.: Join Geometries - A Theory of Convex Sets and Linear Geometry. Springer, Cham (2013)
8. Ishii, N., Torii, I., Iwata, K., Odagiri, K., Nakashima, T.: Generation and nonlinear mapping of reducts-nearest neighbor classification. In: Advances in Combining Intelligent Methods, pp. 93–108. Springer (2017)
9. Ishii, N., Torii, I., Iwata, K., Odagiri, K., Nakashima, T.: Generation of reducts based on nearest neighbor relations and boolean reasoning. In: HAIS 2017, LNCS, vol. 10334, pp. 391–401. Springer (2017)

10. Ishii, N., Torii, I., Iwata, K., Odagiri, K., Nakashima, T.: Generation of reducts and thresh old function using discernibility and indiscernibility matrices. In: Proceedings ACIS-SERA, pp. 55–61. IEEE Computer Society (2017)
11. Ishii, N., Torii, I., Iwata, K., Nakashima, T.: Incremental reducts based on nearest neighbor relations and linear classification. In: Proceedings IIAI-SCAI, pp. 528–533. IEEE Computer Society (2019)

Optimization/Machine Learning

A Comparative Study on Bayesian Optimization

Lam Gia Thuan[1] and Doina Logofatu[2](✉)

[1] Vietnamese-German University, Le Lai Street,
Binh Duong New City, Binh Duong Province, Vietnam
`cs2014_thuan.lg@student.vgu.edu.vn`

[2] Nibelungenplatz 1, 60318 Frankfurt am Main, Hessen, Germany

Abstract. Well-known as an effective algorithm for optimizing expensive black-box functions, the popularity of Bayesian Optimization has surged in recent years alongside with the rise of machine learning thanks to its role as the most important algorithm for hyperparameter optimization. Many have used it, few would comprehend, since behind this powerful technique is a plethora of complex mathematical concepts most computer scientists and machine learning practitioners could barely familiarize themselves with. Even its simplest and most traditional building block - Gaussian Process - alone would involve enough advanced multivariate probability that can fill hundreds of pages. This work reviews this powerful algorithm and its traditional components such as Gaussian Process and Upper Confidence Bound in an alternative way by presenting a fresh intuition and filtering the complications of mathematics. Our paper will serve well as a functional reference for applied computer scientists who seek for a quick understanding of the subject to apply the tool more effectively.

Keywords: Bayesian Optimization · Gaussian Process · Upper Confidence Bound · Hyperparameter optimization · Expensive black-box functions

1 Introduction

1.1 What Is Bayesian Optimization?

Life always involves choices, each may bring forth certain up- and downsides. A normal person would be fine with making a random decision, but for big companies, especially those specialized in mass manufacturing, a slightly better or worse decision could generate an additional revenue or loss in millions. That inspired the birth of optimization algorithms that could optimize the decision-making process and search for a choice that maximizes the overall beneficial gain

Supported by the Frankfurt University of Applied Sciences.

as much as possible. Bayesian Optimization [12] is one such algorithm with certain characteristics that distinguish itself from the vast majority of alternatives such as quick convergence, no derivative required and combinable with other well-studied techniques. In its most generic form, the goal of this technique can be represented as in (1).

$$x^* = \underset{x \in X}{\operatorname{argmax}}(f(x)), \tag{1}$$

where f can be not only a non-differentiable function but also an extremely costly one implying that it may take a significant amount of resources such as time or money to evaluate.

1.2 Why Bayesian Optimization?

Optimization is an old and on-going research topic for decades with countless known solutions, many of which have demonstrated state-of-the-art performance in numerous scenarios such as genetic algorithm [9], ant colony optimization [6], particle swarm optimization [19], gradient descent [23] or Newton-Quasi method [13], L-BFGS-B [8] and much more. That leads to the question as for why Bayesian Optimization should be given special attention. The answer lies in its role as the most effective method for optimizing hyperparameters of machine learning algorithms.

The past decade has witnessed an incredible growth of machine learning and data science. Their influence on human lives has been pervasive more than never before and every bit of improvement on machine learning may have an enormous impact on every part of our society since they are everywhere. Machine learning algorithms can, however, rarely work out-of-the-box, but they must undergo a sequence of steps as illustrated in Fig. 1 to fully unleash their ability and hyperparameter optimization is one indispensable part.

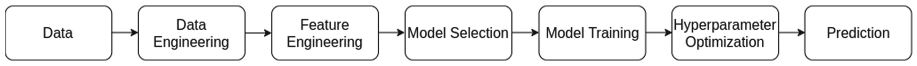

Fig. 1. A simplified workflow for machine learning

This step is, nonetheless, not something just any optimization algorithm can apply for the following reasons:

1. **Expensive.** Machine learning tasks are closely coupled with data. In this era of big data, machine learning rarely involves small number of training examples, which makes the process extremely costly. Population-based optimization techniques such as evolutionary algorithms, ant colony optimization or particle swarm optimization usually require a huge number of computations and hence are unsuitable for this task.

2. **Derivative-free.** A training algorithm is usually perceived as derivative-free and even if a derivative exists, formulating its analytic form is a demanding task. That disqualifies various gradient-based techniques such as Newton-Quasi method, L-BFGS-B or Gradient Descent. Albeit numerical methods [4] provide a painless alternative to compute the derivative (if exists), it is again too costly to be practical.

These problems, however, align perfectly with Bayesian Optimization's advantages. First, it is known for quick convergence in a small number of evaluations and hence reducing the need to evaluate the costly objective function too often. Secondly, it is known to work for any black-box derivative-free function. Optimization algorithms are numerous, but those with such properties are few, and Bayesian Optimization algorithm is the most important solution out of these few especially in hyperparameter optimization as it is the foundation of many techniques such as the recent Bayesian Optimization and Hyperband (BOHB) [7] which is just another variant. In addition, it is also the chosen technique utilized by various machine learning platforms such as Google Cloud, Amazon Web Services and Microsoft Azure [16]. That is why such an important algorithm deserves special attention.

1.3 Why This Review?

This powerful technique has been embedded in a variety of machine learning framework, and using them requires no knowledge of how Bayesian Optimization works. That is, nevertheless, not favorable against the research and development of optimization algorithms for machine learning. Furthermore, behind this powerful technique are complex mathematical concepts that are beyond the reach of the majority of applied computer and data scientists. Understanding this fact led us to the creation of this work to provide a more comprehensible and insightful guide to researchers who wish to learn more about this method, either for future research or just to apply it more effectively. After finishing this paper, researchers should have a vivid picture of how this algorithm works without worrying much of its internal implementation, which is impossible to achieve with the current publications in this area.

1.4 Organization

This work would begin by introducing the simplest-by-nature algorithm for optimization: Random Search. After that is a connection to the target Bayesian Optimization by minimal improvements. To aid the readers in acquiring the general idea easier, we also provide an example of *The Girlfriend and Flowers* to support our explanation. Last, but not least, will come a brief intuitive explanation for its most important building blocks: Gaussian Process as a probabilistic model and Upper Confidence Bound as an acquisition function. These concepts will, unfortunately, require a general understanding of basic probability including Gaussian (normal) distribution. Nonetheless, readers are only required to know the surface of these concepts like what it is about and need not to worry about its advanced properties, which is insignificant compared to the required knowledge in all classical literature in existence about this topic.

2 Bayesian Optimization - An Insightful Intuition

2.1 Random Search

In search of the best decision, the best method would be to try all possibilities and decide on the best after gathering all results. That method is, unfortunately, impractical for problems with infinite solution space. For example when searching for a flower a girl likes most, it is infeasible to buy all flowers in the world and ask for her opinion for all of them. Assuming that the budget is sufficient, it may still take her a lifetime just to analyze each and every kind of flower in existence. Alternatively, picking a few random types of flower and offer the one she likes most would be a more reasonable approach. That is the idea behind random search. In the view of a computer scientist, a random search algorithm would look like Algorithm 1.

Algorithm 1. Random Search

```
1: $x^* \in \emptyset, y^* \leftarrow -\infty$
2: for $i \in \{1, 2 \ldots N\}$ do
3:     Generate a random $x$
4:     $y \leftarrow f(x)$
5:     if $y^* < y$ then
6:         $x^* \leftarrow x$
7:         $y^* \leftarrow y$
8:     end if
9: end for
10: Output $(x^*, y^*)$
```

Algorithm 1 illustrates how a random search algorithm can be implemented where N in line 2 represents our budget such as the number of flowers that can be bought for testing. Line 3 says that we just consider a random solution such as picking a random flower. Line 4 indicates that we are testing the current solution by, for example, asking the girl how much she likes it. It is worth noting that process f is treated as an expensive black-box function in this paper. For example, it will take time to invite the girl on a date, a sufficient amount of money to book a place in a 5-star restaurant and a great amount of effort asking for her opinion. The whole procedure is, as described, extremely costly and non-differentiable. Steps 5−7 compare and optimize the current solution x^* - the currently best flower - and y^* - her opinion on it, which is a common block in all optimization algorithms. After repeating it as much as our budget N is allowed, step 10 concludes our algorithm. How can this simple, popular and intuitive algorithm be related to the advanced and efficient Bayesian Optimization?

2.2 Improved Random Search and Bayesian Optimization

As mentioned, since our objective function f is very costly, its evaluation should be prioritized for *special candidates* instead of random solutions. The question is how these special candidates can be found? What will happen if your obedient sister is already the best friend of the girl you like and they have shared a good amount of time together shopping and going out?

If that is the case, they may share the same hobbies, hence a flower your sister loves may also be your girlfriend's favorite, and asking your sister is much easier or you may already know it yourself as a good brother. So the process is as follows: 1) Ask for the best flower your sister likes, 2) show it to your girlfriend and ask for her opinion, and 3) tell your sister the new information to help her improve her knowledge. In the language of a computer scientist, the process is as the one described in Algorithm 2.

Algorithm 2. Bayesian Optimization

```
1: Make $g$ from initial $(x, y)$
2: $x^* \in \emptyset, y^* \leftarrow -\infty$
3: for $i \in \{1, 2 \ldots N\}$ do
4:     $x' \leftarrow \underset{x \in \mathcal{X}}{\operatorname{argmax}}(g(x))$
5:     $y \leftarrow f(x')$
6:     if $y^* < y$ then
7:         $x^* \leftarrow x'$
8:         $y^* \leftarrow y$
9:     end if
10:    Update $g$ with $(x', y)$
11: end for
12: Output $(x^*, y^*)$
```

As can be seen in Algorithm 2, from a random search algorithm that can be written from scratch by any computer science student in a couple of minutes to the advanced and extremely hard to understand, let alone implementing, Bayesian Optimization, the outlines differ by only 3 minor modifications in line 1, line 4 and line 10.

Line 1 means that we should not immediately focus on our expensive-to-handle target, and should search for a third-party helper which is inexpensive, such as asking the sister instead of the girlfriend. Line 4 says that instead of trying a random solution, asking the third-party helper for the best is more reasonable. For example, it is easier to ask your sister what her best flower is. Last, but not least, line 10 indicates that after the new information is acquired, it should be transferred to the third-party helper to improve its own reliability and performance. For instance, if the sister knows that the girlfriend does not like her choice, she may come up with a better plan next time. Those simple steps are the essence of Bayesian Optimization. After this section, readers should have the general idea of how Bayesian Optimization works. All classical publications in existence would start off differently by jumping right into the concept of Gaussian Process which may require hundreds of pages of literature to explain [17].

Further subsections will give an intuitive description of Gaussian Process which is known as a *surrogate* or *probabilistic model*, and Upper Confidence Bound - another building block of Bayesian Optimization named *acquisition function*. These concepts are important to implement the function g mentioned in Algorithm 2. Functionally, g is expected to possess the following qualities: a) cheap to evaluate, b) suitable for derivative-free black-box function, and c) commensurate to f, implying that if $g(x)$ is high, $f(x)$ is likely to be high and vice versa. After countless studies, it has been discovered that such a g function could be realized by composing 2 different function as shown in (2) where $\mathcal{A}$ is called an acquisition function such as Upper Confidence Bound and $\mathcal{S}$ is a surrogate or probabilistic model such as Gaussian Process. After such a function g is acquired, all known optimization techniques can be applied with no restrictions as it has been free of all special characteristics of a machine learning problem (Bayesian Optimization's most popular application).

$$g(x) = \mathcal{A} \circ \mathcal{S}(x) = \mathcal{A}(\mathcal{S}(x)) \tag{2}$$

2.3 Extending Bayesian Optimization

The simple design of Bayesian Optimization gives it the flexibility to evolve. By mutating $\mathcal{A}$ and $\mathcal{S}$ with appropriate acquisition functions and surrogate models, respectively, a variety of new algorithms could be born with their own interesting properties. Hence Bayesian Optimization acts more like a framework rather than an individual algorithm. Studies on this topic has existed since the last century with various results on what could integrate well with the Bayesian Optimization framework.

For surrogate models, the traditional and probably the first candidate is Gaussian Process [17] which implies that its resulting distributions will be Gaussian (normal distributions) [20]. This method has demonstrated state-of-the-art performance in various machine learning applications where the input vector is consisted of only real numeric features $x = (x_1, x_2 \cdots x_n)$ where $x_i \in \mathbb{R}$, which is in most of the cases, and hence still enjoys high popularity even after decades of presence. Recently, research on this topic has involved other types of distributions including the inverse Wishart [15] and Student-t distribution [11], and gave birth to a promising alternative called Student-t Process [18], but they are not yet as popular as the traditional model. Last, but not least, another lesser known model worth mentioning is Random Forests [1] - a well-known machine learning model which has also proven to work well as a surrogate for data with categorical features.

In the area of acquisition functions, the traditional methods still remain relevant. They include, but not restrict to, Upper Confidence Bound (UCB) [5], Expected Improvement (EI) [2], Knowledge Gradient (KG) [22], Entropy Search (ES) [10] and Probability of Improvement (PI) [21]. Nevertheless, most applications would employ EI and UCB by default for their superior performance.

In this paper, only Gaussian Process and UCB will be considered. The former has been known as the de facto standard for Bayesian Optimization, whilst for the latter, it is the simplest of all, which works well and is free from the burden of probability (at least for using it).

3 Gaussian Process

3.1 An Intuitive Explanation

Probably the best-known companion to Bayesian Optimization, a Gaussian Process (GP) is mathematically defined as a *probability distribution over all possible functions*. This popular definition of Gaussian Process is, however, far beyond the comprehensible realm of most applied engineers with a novice understanding of probability. Alternatively, a Gaussian Process could be regarded as *a collection of points* (x, y) and *all the functions (lines) going through ALL these points*. An intuitive example of a Gaussian Process in the 2-dimensional space could be visualized in Fig. 2. As can be seen in Fig. 2a, all functions - just lines in space - controlled by a Gaussian Process intersect at a certain number of points. There may be infinitely many such functions, but most of them are contained in the shaded area in Fig. 2b.

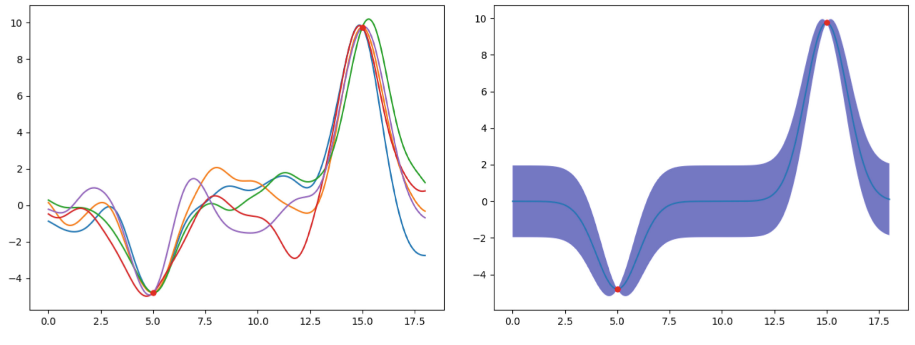

(a) Sample Draws of 5 (b) Mean and Variance

Fig. 2. A sample Gaussian Process of 2 points

What exactly are these lines? It is known that each function may be represented by a line. Our target function f is also a line in the multi-dimensional space. A Gaussian process is a tool that allows governance over an infinite number of lines with some common properties, one of which is to go through a fixed set of points. These points are the real observations we acquired from lines 4–5 in Algorithm 2. Since all the lines controlled by our Gaussian process going through the same points of our target function, they are believed to behave similarly to f. By updating the Gaussian process with new information as said in line 10 of

Algorithm 2, it means adding a newly found observation (point) to our Gaussian process as visualized in Fig. 3. As can be seen, the shaded area has become thinner, implying that the number of possible target functions has been reduced significantly and they have all been closer to our target, implying that even if our choice is wrong, it is still acceptable as it is close enough.

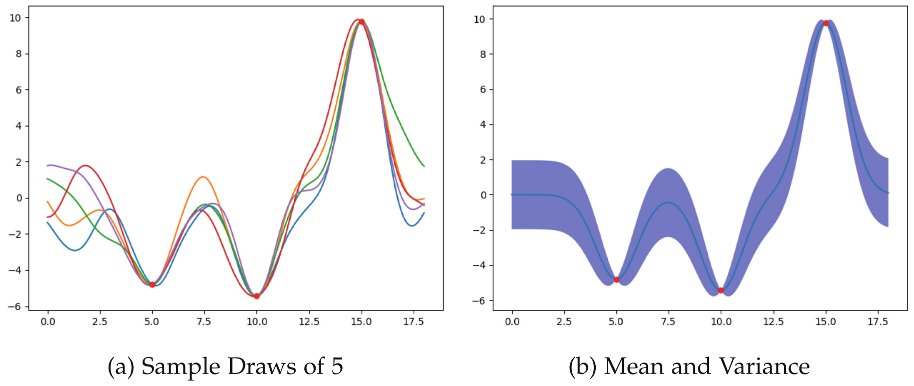

Fig. 3. A sample Gaussian Process of 3 points

As shown in (2), a Gaussian process acts like a normal mathematical function as shown in (3) known as a probabilistic model.

$$y = f(x) \tag{3}$$

In essence, compared to a normal function, a probabilistic model $\mathcal{S}$ differ by returning a probabilistic object called distribution, or more precisely a normal distribution defined by its mean μ and variance σ^2 in the case of a Gaussian process as illustrated in (4).

$$\mathcal{N}(\mu, \sigma^2) = \mathcal{S}(x) \tag{4}$$

Why is $\mathcal{S}(x)$ a distribution? Figure 4 explains why evaluating a function at a candidate solution x can return a distribution by drawing a vertical line at that location. As already known, a Gaussian process is a collection of lines, and all the lines belonging to our Gaussian process will intersect with the vertical line at an infinite number of locations. Their intersection values will form a distribution, which is assumed to be normal.

To summarize, a Gaussian distribution is a powerful mathematical tool that allows us to govern over an infinite number of possible candidate target functions which are expected to be similar to our original target function. A Gaussian process can be treated as a mathematical function which can be evaluated for a given solution x and can return some output which is, unfortunately, a distribution defined by its mean and variance. However, the pair (μ, σ^2) is like quality

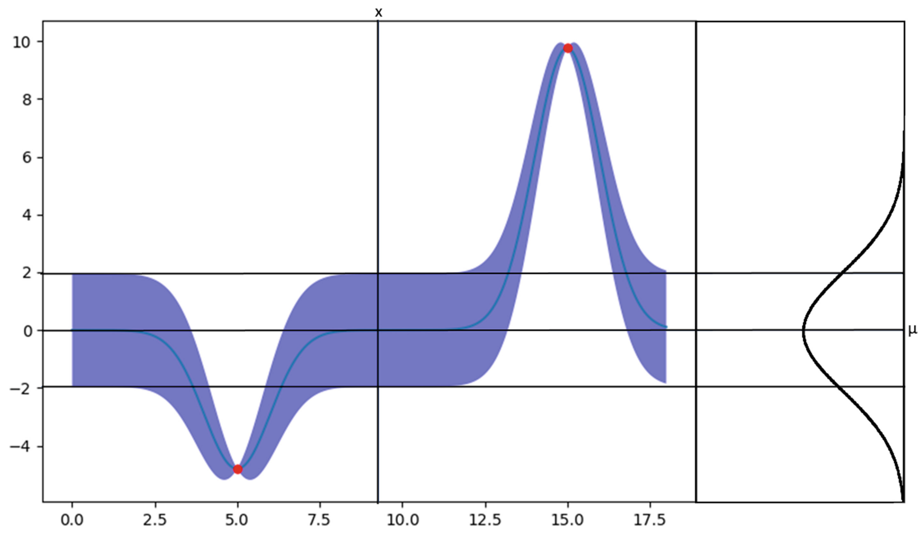

Fig. 4. Gaussian Process - evaluation as a normal distribution

and quantity which cannot be optimized simultaneously, and hence it requires another so-called acquisition function to summarize into a single numeric value that can be used for optimization problem.

3.2 Kernel for Gaussian Process

The previous subsection has provided sufficient information on what a Gaussian process is, but for those who wish to further explore it, it is insufficient. A Gaussian process could also be treated as a machine learning model, implying that it also needs training before being usable with the data being the observation points which we have known. What exactly needs to be trained? As previously know, a Gaussian process contains an infinite number of lines, but as shown in Fig. 2 and 3, it is far from enough to cover all possible lines in space, which implied that only some specific type of line can be considered for a Gaussian process. The one controlling that is called a *kernel* which is at the same time the component that needs to be trained. Exactly how the selection of lines is conducted is beyond the scope of this review. Alternatively, an insightful example can be given. As can be seen in Fig. 3a, all the line functions are very *smooth*. In case the term 'smooth' is confusing, let's take a look at a few *rough* (not so smooth) functions in Fig. 5 for comparison.

At this point, readers should have acquired a feeling of smoothness for a function, but mathematically, smoothness is measured by to what extent a function can be differentiated. The reason why functions in Fig. 3a are so smooth is because its kernel uses the radial basis function (RBF) whose analytic form is represented in (5) where x and x' are some multidimensional vectors of the same number of dimensions.

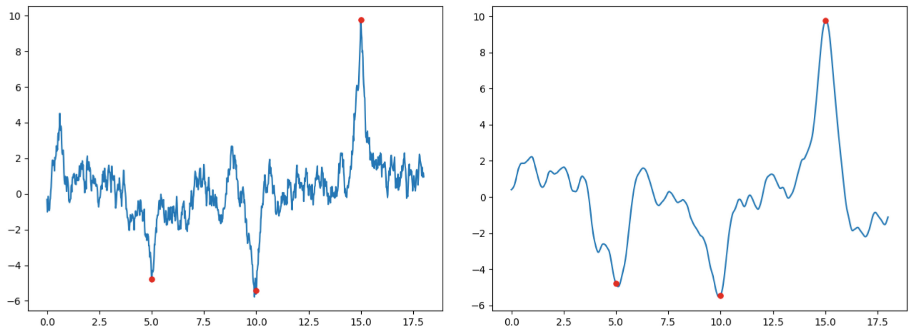

(a) A rough function (b) A smoother function

Fig. 5. Examples of function smoothness

$$k(x, x') = -\exp \frac{\|x - x'\|^2}{2\sigma^2} \tag{5}$$

As you may know, a function of type e^x is infinitely differentiable and hence its representative lines are extremely smooth. By mutating the kernel function with others, such as the Matern covariance function [14], the lines can be very rough as in Fig. 5a. This is but one example to show a criterion for filtering the target functions. The most important gain after reading this subsection is to understand what a kernel does for a Gaussian process.

3.3 Upper Confidence Bound

As known from the previous subsection, a probabilistic model such as Gaussian process will evaluate to a pair (μ, σ^2) defining a normal distribution which can not be directly used in an optimization problem. That is why an acquisition function comes in handy as it can summarize the information from the given distribution into a single numeric value suitable for maximizing or minimizing. One popular method for this task is Upper Confidence Bound, which works by balancing the trade-off between exploitation and exploration.

The pair (μ, σ^2) could be viewed as quality and quantity. If the mean is high, that means the overall fitness of all lines contained by the Gaussian process is high. As for the variance, high variance means that the shaded area is wider and that there are more possible functions implying that the probability that one of them is our target function is also higher. The Upper Confidence Bound theorem says that the best choice is one with high mean (exploitation) and high variance (exploration) and the 2 terms must be balanced by a third parameter called the confidence band β. The full form of the Upper Confidence Bound function is presented in (6). As can be deduced, the result will be just a single numeric value.

$$\mathcal{A}(\mu, \sigma^2) = \mu + \beta^{1/2}\sigma \tag{6}$$

How can it work? The answer to this question may require unnecessary mathematical knowledge which is against the purpose of this article, which is why to assure the readers that this formula works, it is worth pointing out that the same strategy has been applied in various applications, especially games and artificial intelligence, and has gained state-of-the-art performance in many of them. Most recent was the birth of the AlphaGo program by Google which was famous for defeating the human champion in Go [3] by employing a similar strategy in a slightly different form. In fact, this method is known to provide top performance for Bayesian Optimization, on par with Expected Improvement - the most popular technique in use - but much simpler to implement.

4 Conclusion and Future Work

This paper reviews the popular Bayesian Optimization algorithm and its popular building blocks from a fresh perspective of an applied computer or data scientist without the hassles of advanced mathematics such as multivariate probability. Beginning with the story of *The Girlfriend and Flowers* and the basic Random Search algorithm, we have presented the general idea of Bayesian Optimization in the most comprehensible way without analyzing the complex concept of Gaussian Process as in all articles in existence. After that comes intuitive explanations for Gaussian Process and Upper Confidence Bound with most focus on what they are. Our paper aims to provide researchers in this area a quick and functional reference to gain a general understanding of the subject without the need to read hundreds of pages in classical publications.

Albeit our paper emphasizes the importance of intuition, the value of mathematics is undeniable, especially for those who wish to completely explore the depth of this algorithm. To promote further research and development for this technique rather than its use only as a black box optimization method, we are working towards a short but comprehensible mathematics manual for all mentioned concepts which will complement, but not replace, this work.

References

1. Bajer, L., Pitra, Z., Holeňa, M.: Benchmarking Gaussian processes and random forests surrogate models on the BBOB noiseless testbed. In: Proceedings of the Companion Publication of the 2015 Annual Conference Genetic Evolutionary Computation, pp. 1143–1150 (2015)
2. Benassi, R., Bect, J., Vazquez, E.: Robust Gaussian process-based global optimization using a fully Bayesian expected improvement criterion. In: International Conference on Learning and Intelligent Optimization, pp. 176–190. Springer (2011)
3. Chang, H.S., Fu, M.C., Hu, J., Marcus, S.I.: Google deep mind's AlphaGo. OR/MS Today **43**(5), 24–29 (2016)

4. Chapra, S.C., Canale, R.P., et al.: Numerical Methods for Engineers. McGraw-Hill Higher Education, Boston (2010)
5. Contal, E., Buffoni, D., Robicquet, A., Vayatis, N.: Parallel Gaussian process optimization with upper confidence bound and pure exploration. In: Joint European Conference on Machine Learning and Knowledge Discovery in Databases, pp. 225–240. Springer (2013)
6. Dorigo, M., Blum, C.: Ant colony optimization theory: a survey. Theor. Comput. Sci. **344**(2–3), 243–278 (2005)
7. Falkner, S., Klein, A., Hutter, F.: BOHB: robust and efficient hyperparameter optimization at scale. arXiv preprint arXiv:1807.01774 (2018)
8. Fei, Y., Rong, G., Wang, B., Wang, W.: Parallel L-BFGS-B algorithm on GPU. Comput. Graph. **40**, 1–9 (2014)
9. Harik, G.R., Lobo, F.G., Goldberg, D.E.: The compact genetic algorithm. IEEE Trans. Evol. Comput. **3**(4), 287–297 (1999)
10. Hernández-Lobato, D., Hernandez-Lobato, J., Shah, A., Adams, R.: Predictive entropy search for multi-objective Bayesian optimization. In: International Conference on Machine Learning, pp. 1492–1501 (2016)
11. Ismail, M.E., et al.: Bessel functions and the infinite divisibility of the student t-distribution. Ann. Probab. **5**(4), 582–585 (1977)
12. Lizotte, D.J.: Practical Bayesian optimization. University of Alberta (2008)
13. Martınez, J.M.: Practical quasi-Newton methods for solving nonlinear systems. J. Comput. Appl. Math. **124**(1–2), 97–121 (2000)
14. Minasny, B., McBratney, A.B.: The Matérn function as a general model for soil variograms. Geoderma **128**(3–4), 192–207 (2005)
15. Nydick, S.W.: The Wishart and inverse Wishart distributions. J. Stat. **6**, 1–19 (2012)
16. Ranjit, M.P., Ganapathy, G., Sridhar, K., Arumugham, V.: Efficient deep learning hyperparameter tuning using cloud infrastructure: intelligent distributed hyperparameter tuning with Bayesian optimization in the cloud. In: 2019 IEEE 12th International Conference on Cloud Computing (CLOUD), pp. 520–522. IEEE (2019)
17. Rasmussen, C.E.: Gaussian processes in machine learning. In: Summer School on Machine Learning, pp. 63–71. Springer (2003)
18. Shah, A., Wilson, A., Ghahramani, Z.: Student-t processes as alternatives to Gaussian processes. In: Artificial Intelligence and Statistics, pp. 877–885 (2014)
19. Shi, Y., Eberhart, R.C.: Empirical study of particle swarm optimization. In: Proceedings of the 1999 Congress on Evolutionary Computation-CEC 1999 (Cat. No. 99TH8406), vol. 3, pp. 1945–1950. IEEE (1999)
20. Tong, Y.L.: The Multivariate Normal Distribution. Springer Science & Business Media, New York (2012)
21. Viana, F., Haftka, R.: Surrogate-based optimization with parallel simulations using the probability of improvement. In: 13th AIAA/ISSMO Multidisciplinary Analysis Optimization Conference, p. 9392 (2010)
22. Wu, J., Poloczek, M., Wilson, A.G., Frazier, P.: Bayesian optimization with gradients. In: Advances in Neural Information Processing Systems, pp. 5267–5278 (2017)
23. Zinkevich, M., Weimer, M., Li, L., Smola, A.J.: Parallelized stochastic gradient descent. In: Advances in Neural Information Processing Systems, pp. 2595–2603 (2010)

A Genetic Programming Method for Scale-Invariant Texture Classification

Haythem Ghazouani[1,2], Walid Barhoumi[1,2](✉), and Yosra Antit[1]

[1] Institut Supérieur d'Informatique, Research Team on Intelligent Systems in Imaging and Artificial Vision (SIIVA), LR16ES06 Laboratoire de recherche en Informatique, Modélisation et Traitement de l'Information et de la Connaissance (LIMTIC), Université de Tunis El Manar, Ariana, Tunisia
haythem.ghazouani@enicar.u-carthage.tn, yosra.antit@gmail.com

[2] Ecole Nationale d'Ingénieurs de Carthage, Université de Carthage, Tunis-Carthage, Tunisia
walid.barhoumi@enicarthage.rnu.tn

Abstract. Texture offers an effective characterization of image shape and orientation. Thus, a predominant task is to detect and extract texture features that discriminate accurately images within different semantic classes. The challenge resides in making these features invariant to several changes, such as affine transformation and viewpoint change, in order to ensure their robustness. Besides, the training phase requires a large number of images. To deal with these issues, Genetic Programming (GP) is adopted in this work with the intention of classifying precisely texture images using some training images per class. In fact, in order to automatically generate a descriptor that is invariant to illumination, rotation and scale; the proposed method combines GP with the scale extraction technique involved by SIFT. The performance of the proposed method is validated on five challenging datasets of non-scaled as well as scaled texture images. Results show that the method is robust not only to scale but also to rotation, while achieving significant performance compared to the state of the art methods.

Keywords: Texture · Genetic programming · Scale invariance · SIFT · Image classification

1 Introduction

Texture is an important characteristic in the field of image analysis compared to both shape and color primitives. It has been used in different areas of research in computer vision, pattern recognition and content-based image retrieval. Texture can be recognized either by touch or by vision. Indeed, the toughness level and the impression can give an important information about the texture type and this is known as "tactile texture". Nevertheless, human can distinguish between textures not only by the touch, but it exists another form which is the "visual texture". It is a variation of the intensity of a surface that affects human vision.

The visual texture can be noticeable without the need of the tactile texture. In order to represent the perception of the texture and to promote an automatic processing of the information that represents the texture, the analysis process aims to produce numerical features that represents the texture. To deal with this issue, three steps are commonly involved: (1) keypoint detection (2) feature detection and (3) feature extraction. The first step runs through the whole image and decides whether the current pixel is a keypoint or not. Various methods have been used to achieve this task, such as Hessian and Harris corner detection, Sobel Operator, Laplacian of Gaussian (LoG) for corner detection, Canny and Harris for edge detection, grey-level blobs and Principal Curvature-Based Region detector (PCBR) for blobs detection [12,16]. The second step consists to extract informative features, what means going from raw pixel values to another set of values in a lower dimension using mainly statistical measures (*e.g.* mean, variance, histogram...). This step aims to extract the important information while reducing the irrelevant ones. The last step is the feature extraction. It is the same process as the previous one with some changes in the input data, which are the extracted features from the previous step. The main goal is to reproduce a better set of features in order to improve the performance of the model. The difficulty resides in using an important number of images for training the model due to the increase in the complexity while detecting a reliable set of features. Indeed, training a model to perform the classification task is highly relying on the number of the training images and the quality of the extracted features. In this work, we propose to adopt the Genetic Programming (GP) within the task of supervised image classification, using a relatively small training set of textured images, while being invariant to illumination, rotation and scale. The main contribution of this work resides in constructing an efficient descriptor that preserves the rotation change while being invariant to several scale and illumination changes. Besides, the proposed method allows to reduce remarkably the computational cost of the training process.

The rest of this paper is structured as follows. A brief review about the related work is presented in Sect. 2. The proposed method is discussed in Sect. 3. The experimental design and the obtained results are described in Sect. 4. A conclusion and some ideas for future work are discussed in Sect. 5.

2 Related Work

In this section, classical texture classification methods are briefly discussed, before detailing a very well-known GP-based method that we adopted. Most research on texture classification focuses on feature extraction, since more powerful and highly discriminative features generally yield higher classification accuracies regardless the used classifier [14]. Indeed, descriptors must be invariant to many classes of transformations in order to ensure that changes in lighting conditions and camera parameters, notably scale change, do not induce large changes in feature description [2,6]. Classical descriptors can be divided into two groups: “dense” descriptors and “sparse” ones. Dense descriptors (*e.g.* Local

Binary Patterns (LBP)...) discriminate between the model and the background. However, sparse descriptors (*e.g.* Scale Invariant Feature Transform (SIFT) [9], Speeded-up Robust Filter (SURF) [4]...) are known by their robustness to variations in viewpoints and scales. In order to deal with invariance against the scale change, many methods are based on extracting a scale invariant feature from a selection of interest area in the image [7, 11]. Differently, some methods are based on logpolar transforms [15]. Furthermore, the fractal dimension and the Gabor filters proved to be scale invariant feature descriptors. To overcome scale variation, other methods generate a set of multi-scale representations from training images. Nevertheless, existing texture descriptors have multiple limitations. First, they require a domain expert to identify specific keypoints in an image. Second, the difficulty to find such a descriptor increases while the number of classes increases, and the final results rely on the preselected keypoints. Third, these descriptors are convoluted and some of them rely only on detecting a specific type of keypoints. Generally, the choice of keypoints is crucial for the quality of the descriptor and automating their detection would be much better than extracting them in a way that can be subjective. In addition, automation can be configured to reduce the search in a specific set of keypoints to ensure robustness to rotation and scale changes. An effective tool for the automation of keypoint extraction is Genetic Programming (GP), which has been evolving rapidly, and new techniques have been constantly proposed in order to tackle image changes within the texture classification framework. For instance, GP-criptor has been proposed [3] for the attention of manipulating an illumination-invariant descriptor. Al-Sahaf [1] extended this work and designed the GP-criptor^{ri} to handle image with rotation changes. The method incorporates automatically the illumination and rotation invariant descriptors while using only two instances, and it operates on raw pixel values like the previous method. Therefore, there is no human intervention to determine a set of predefined features. It is inspired by the LBP descriptor and uses specific operators in order to handle rotation changes. In the proposed method, we adapt the GP technique for the automatic extraction of keypoints. However, instead of making random sampling of the image, we select a specific set of keypoints. We use the first step of the SIFT algorithm to select only scale invariant keypoints. The reduction of the search space leads automatically to a reduction of the training computational cost without decreasing the classification accuracy, as will be shown in the results.

3 Proposed Method

The proposed Evolutionary Texture Classification Algorithm (ETCA) is an extension of the GP-criptor^{ri} technique, what guarantees the invariance against rotation and illumination changes. Besides, since features are defined according to only some SIFT-based keypoints, ETCA is also invariant against scale change, while being computationally efficient. In fact, in order to generate the descriptor, two main processes have to be performed (Fig. 1). First, the generation of SIFT features is performed on the input image in order to detect keypoints that form the GP process input. Then, the GP-based texture descriptor is generated.

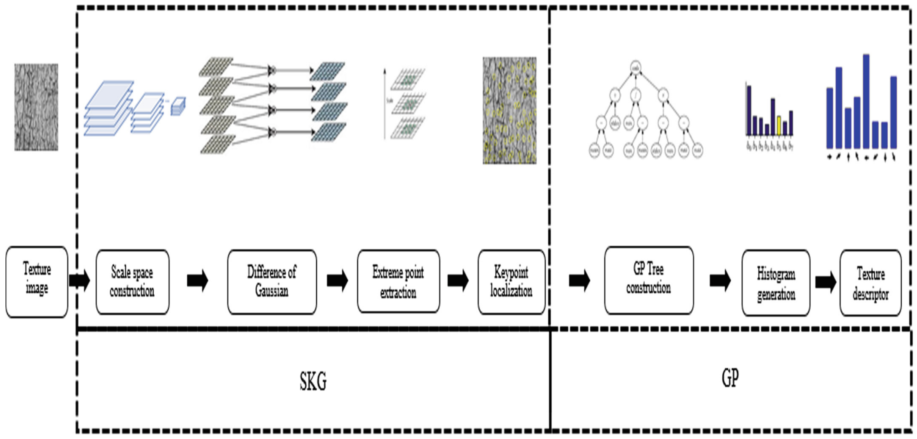

Fig. 1. Flowchart of the proposed method for scale-invariant texture classification.

3.1 First Step: SIFT Keypoint Generation (SKG)

Gaussian pyramids are firstly created from the input images by smoothing and subsampling them in various repetitions. Each image is processed with multiple Gaussian filters to generate a scale for each filter. Each set of scales is called octave, and the algorithm moves to the next octave by down-scaling the image of a factor 2 while generating another set of Gaussian blurred images. The algorithm continues until reaching a predefined threshold. From the set of octaves we can build the scale-space S which applies a smooth filter on the octave with multiple Gaussian filters of different values in order to create various scale of the image. Secondly, in order to detect stable keypoints locations in each scale-space, the difference of Gaussian is used to locate scale-space extrema. Then, keypoints are selected from local minima or maxima. In fact, each pixel $(x,\ y)$ is compared with its $3 \times 3 \times 3$ neighborhood σ; eight neighbor in the same scale and nine neighbors up and down scale. If the selected pixel represents an extremum, then it is a potential SIFT interest point. Finally, the keypoint localization step aims to localize for each interest point what is the best scale location (x, y, σ). Having a large number of keypoints, the goal is to eliminate those that cause noise due to low contrast or poor localized pixel on an edge. The edge should not be detected as a keypoint because it has a high maximal curvature and low minimal curvature. In contrast, a corner represents a keypoint since it has a high maximal and minimal curvature. This work relies not only on detecting those potential SIFT keypoints but also their neighborhoods, which offer a rich additional information. Hence, the $LBP_{8,1}$ is used to deal with invariance against rotation change and illumination variation. It detects image keypoints and generates a histogram that corresponds to the distribution of these keypoints.

3.2 Second Step: GP-Criptor^{ri} Loop

The input of the second step is the set of scale-invariant keypoints for each image. This allows to minimize the computation cost by using only potential keypoints instead of running through all the image pixel by pixel. Thus, a small number of input images is sufficient for the training, without needing human intervention. In the following paragraphs, we detail the representation of individuals as well as the fitness function. Then, we show the step of building histograms from the individual programs. Finally, we describe how the elected individuals generate the descriptors to be fed to the classifier. It is very important to begin by explaining the structure of the individuals (also referred to as "programs") of our GP process. In fact, each program corresponds to a tree of functions (Fig. 2), such that a quality fitness measure is assigned to it. These fitness values are then used to select the best parents for reproduction using crossover and mutation operators. Once the offspring programs are generated, children and parents compete for survival based on an environmental selection mechanism. Thus, the GP parent population is updated with the best programs. By running the GP for a certain number of generations, GP programs are optimized automatically thanks to the intelligent sampling of the search space. At the end of the run, the parent population programs define the descriptors for texture classification.

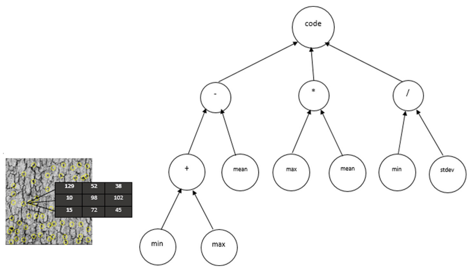

Fig. 2. Tree representation of an evolved program.

More specifically, a program is a tree made up by a root node, some internal nodes, and some leaf nodes (Fig. 2). The leaf nodes are scalar values, and the others are functions that could be arithmetic operators or complex loop structures. The terminal set can be categorized into four nodes of different type: min($\vec{x}$), max($\vec{x}$), mean($\vec{x}$) and stdev($\vec{x}$) which return minimum, maximum, mean and standard deviation values of a given vector $\vec{x}$, respectively. These four functions give always the same value even if the vector elements change orders, what is useful when dealing with rotation changes. The function set is composed by the code node and four arithmetic operators (+, −, *, /). The whole program is constructed to automatically detect the main keypoints in an image and extract a feature vector from it. To do so, we pursue five steps. Firstly, the system examines the leaf nodes and calculates its corresponding arithmetic function.

Secondly, the resulting values are communicated to the parent node. Thirdly, the parent node, which is the internal node, evaluates and returns the corresponding results to the parent node until it is the code node. Fourthly, the code node returns a binary code. Finally, the generated binary code is converted into decimal and fed into its position in a histogram which is incremented by 1. As in the GP-criptor^{ri}, we use a knowledge base D, which contains a set of feature vectors. D is a set that is thereafter used to train the classifier. Indeed, the two instances that are used during the mutative process are fed to the evolved descriptor to generate the knowledge base. To measure the performance of each program, accuracy cannot be used in this case. In fact, the number of instances is very low (only two instances), what can increase the probability of over-fitting. Instead of this, we adopt the fitness presented in [3] and described by (1):

$$fitness = 1 - (\frac{1}{1 + \exp^{-5(D_b - D_w)}}), \tag{1}$$

where, D_b is the average distance of between-class instances (2) and D_w is the average distance of within-class instances (3).

$$D_b = \frac{1}{z(z-m)} \sum_{\substack{u^\alpha, v^\beta \in S_{tr} \\ \forall \vec{u} \in u^\alpha \\ \forall \vec{v} \in v^\beta}} X^2(\vec{u}, \vec{v}), \qquad \alpha, \beta \in \{1, 2, \dots, C\}, \alpha \neq \beta \tag{2}$$

$$D_w = \frac{1}{z(m-1)} \sum_{\substack{u^\alpha, v^\alpha \in S_{tr} \\ \forall \vec{u} \in u^\alpha \\ \forall \vec{v} \in v^\alpha}} X^2(\vec{u}, \vec{v}), \qquad \alpha \in \{1, 2, \dots, C\} \tag{3}$$

$S_{tr} = \{(\vec{x_i}, y_i),\ i \in \{1, \dots, z\}\}$ is the training set, where $\vec{x_i}$ ($\in \mathbb{R}+$) is the feature vector and y_i is the class label. C and m are the total number of classes and the number of instances per class, respectively, and z is the total number of instances in the training set ($=C.m$), and x^α is the set of all instances of the α^{th} class in S_{tr}. The widely used $X^2(\cdot, \cdot)$ function measures the distance between two normalized vectors of the same length as follows:

$$X^2(\vec{u}, \vec{v}) = \frac{1}{2} \sum_i \frac{(u_i - v_i)^2}{(u_i + v_i)}, \tag{4}$$

where, u_i and v_i are the i^{th} element in the $\vec{u}$ and $\vec{v}$ vectors, respectively. Since X^2 returns values in [0, 1] and the fitness function returns values in [0.27, 0.73], the factor 5 is used in order to scale the output interval to be in [0, 1]. If the denominator of Eq. 4 is equal to 0, the function returns 0 in order to prevent the division per zero. Thus, the fitness measure (Eq. 1) returns 0 in the best scenario and 1 in the worst scenario. After the computation of the best fitness function of each keypoint, the best keypoints are fed into the knowledge base. The main difference between the GP-criptor^{ri} and ETCA is the input of the terminal set. The leaf nodes of an individual, in GP-criptor^{ri}, compute statistics of the pixel values of the sliding window, whereas ETCA takes statistics of the coordinates values of the sliding window of the generated keypoints from the scale space analysis process. The idea behind this is to enhance the program to take a set of pre-generated keypoints that are invariant to scale and fed them to the GP-criptor^{ri} program at the leaves' nodes. This permits particularly to reduce the computational time, since that instead of using a sliding window of a generated image that is invariant to scale, we use only the significant keypoints processed from the previous step. In fact, the sliding window is represented by only the selected keypoints. Furthermore, in order to understand how the descriptor is designed, it is very important to show how the program constructs the histogram from the selected keypoints. Indeed, each tree constructs a feature vector which is the binary code developed from the root node. The set of the feature vectors defines the histogram of the input instance. Indeed, the proposed method treats only the keypoints extracted by SIFT while using a sliding window. Then, for each keypoint, the ETCA performs six main steps: (1) the values of the current pixel are fed into the leaf nodes of the program tree, (2) minimum, maximum, mean and standard deviation values of the current window are computed, (3) resulting values are fed into the terminal nodes of the individual, (4) internal (non-terminal) nodes, apart from the root node, are evaluated starting from those near the leaves by applying the corresponding operator to the list of arguments, (5) the root node returns a binary code by converting each of its arguments to 0 if it is negative and to 1 otherwise, and here comes the role of the $LBP_{8,1}$ that works as a thresholding parameter (the central pixel represents the threshold), (6) the generated binary code is converted to decimal, and the corresponding bin of the feature vector (histogram) is incremented by 1. It is worth noting that the length of the generated code depends on the number of the children of the code node, which is equal to 2^n, where n is the number of the code node children.

To summarize briefly, the proposed method offers a descriptor that is invariant to scale, rotation and illumination using small number of instances. In fact, ETCA combines arithmetic operators and first-order statistics in order to form a model that takes an image as input and generates a feature vector in various steps as previously mentioned. The generated codes (histograms) are thereafter fed into a classifier to predict the class label. An important task is how to select and discriminate between the training instances in order to classify them regarding to the small number of images used in the training phase. Instead of using the accuracy to measure the fitness function that will be used to detect as much representative keypoints as possible, it reliably separates the distances of different classes further apart and keeps the distances between instances of the same class as close to each other as possible.

4 Experimental Study

Realized experiments are highlighted and discussed in this section. The discussion includes datasets, performance metrics, parameter settings and the results. The experiments have been executed on a PC with Windows 10 with

Table 1. A summary of the benchmark image classification datasets.

Dataset	Classes	Instances	Changes			Dimensions	
			Illum.	Rotation	Scale	Width	Height
KTH-TIPS [10]	10	810	✓	x	✓	200	200
UIUC [8]	25	1000	✓	✓	✓	640	480
MINC [5]	23	2500	✓	✓	✓	192	192
OUTEXTC10 [13]	24	4320	✓	✓	x	128	128
OUTEXTC00 [13]	24	4800	✓	x	x	128	128

Intel®$Core^{TM}$ i7-7500U CPU @ 2.70 GHz and 8G of memory. It is worth noting that the measured time in our experiments is the CPU time and not the wall-clock time.

4.1 Datasets and Evaluation Protocol

ETCA is evaluated on five challenging datasets widely used for texture classification assessment. The total number of instances in each dataset is equally divided between the training set and the test set. The instances of all texture datasets are grey-scale images. These five image datasets vary in number of classes (binary and multi-class), size of instances (from 128×128 to 640×480 pixels) and various texture applications (foliage classification, hair classification, brick, wall...). Thus, since the methods investigated in this work are evaluated using a set of carefully chosen benchmarks for image classification of varying difficulty, these methods can be used not only in the domain of image classification but also to perform other tasks such as image segmentation and content-based image retrieval. The datasets vary in domain (texture and object classification), illumination, scale, point of view, rotation, size of instances (images), number of classes and number of instances per class (Table 1). The datasets mentioned in Table 1 are primarily sorted in ascending order based on the total number of classes and then sorted by the total number of instances. As performance metrics, the classification accuracy is used as a fitness measure to indicate the performance of each individual to differentiate between instances of various classes. It is defined as the ratio between the number of correctly classified instances and the total number of instances. In the case of small number of instances (less than 10 instances), the use of accuracy is insufficient because the system can easily capture features that are good enough to discriminate between the training instances, but not sufficient to classify the unseen data. Thus, we rely also on the fitness function as defined in Eq. 1. Furthermore, in order to compute the required time to evolve a descriptor by the proposed method, the CPU time is measured for each evolutionary run from the beginning of generating the initial population until it reaches the stopping criterion.

Table 2. Parameter settings of the genetic process.

Parameter	Value	Parameter	Value
Crossover rate	*0.80*	Generations	*50*
Mutation rate	*0.20*	Population size	*200*
Elitism	*Keep the best*	Initial population	*Ramped half-and-half*
Tree min depth	*2*	Selection type	*Tournament*
Tree max depth	*10*	Tournament size	*7*

Table 3. The average time required to evolve a descriptor by ETCA.

Dataset	KTH-TIPS	MINC	UIUC	OutexTC00	OutexTC10
Time (hour)	4	4.9	4.8	1.4	1.1

4.2 Experimental Setup and Results

The parameter settings of ETCA are summarized in Table 2. The ramped half-and-half method is used to generate the initial GP population. Since we use a small number of instances, the task of dealing with the input images is an expensive task, so the population size is set to 200 individuals. A tournament of a size 7 is used to maintain the population diversity. The crossover probability is set to 0.80 and the mutation probability is set to 0.20. We notice that only the best mechanism in kept to prevent the evolutionary process from degrading. The tree depth of an evolved program is between 2 and 10 levels in order to avoid code bloating. To end with, the evolving process stops when the fitness value is very close to 0 ($<10^{-6}$), or the maximum number of generations is attempt (=50). It is known that the multi-scale space should cover a sufficient range of scales. It is worth noting that the size of the images is small (=128×128 in OutexTC00 and OutexTC10) and with the down-sampling process the image size will be much smaller, so we suppose that the down-sampling rate is greater than 1/10, what results to sub-images of a size larger than 20×20. Furthermore, we recorded the average time required to evolve an image descriptor on the different datasets (Table 3). It is clear that ETCA needs shorter time to evolve a descriptor on the OutexTC10 dataset compared to the time needed for the other datasets. This is expected mainly because this dataset has minimum size and number of instances. It has also cropped texture with different scales unlike the MINC dataset which has background with the texture. The UIUC dataset requires more time than the other datasets, given that it has bigger size instances.

Table 4 shows the results of applying seven relevant classification techniques using the generated features by ETCA as well as the ones of the baseline methods. Using the studied classification techniques, ETCA achieves comparable or better performance in most of the cases. This is the case with OutexTC00 and OutexTC10 datasets. However, the accuracy level degrades for MINC and UIUC datasets, as compared with the other datasets. Overall, ETCA has achieved

Table 4. The average accuracy (%) of seven classifiers using five image descriptors on five challenging standard datasets (best values are in bold).

	SIFT		SURF		DIF		$GPcript^{ri}$		ETCA	
	Training	Test	Training	Test	Training	Test	Training	Test	Training	Test
KTH-TIPS										
1-NN	100	52.4	100	64.8	22.5	17.4	95.1	40.9	100	**93.6**
Adaboost	100	78.4	93.05	45.2	11.1	9.0	52.1	48.9	100	**92.9**
SVM	96.4	90.4	98.1	53.9	15.3	14.7	100	31.0	100	**93.4**
NB	81.8	56.1	76.9	54.9	12.1	11.1	98.3	39.3	100	**91.3**
NB-Tree	93.8	50	93.8	53.0	12.2	12.3	100	34.5	100	**90.8**
NNge	92.4	90.1	93.1	53.0	15.9	15.7	97.8	45.1	100	**90.9**
K*	100	32.7	100	43.2	14.0	14.0	97.8	35.1	100	**93.1**
OutexTC00										
1-NN	100	65.1	100	73.2	25.2	17.4	100	87.7	100	**95.0**
Adaboost	100	72.4	70.1	45.1	11.6	9.0	60.2	57.1	100	**94.0**
SVM	93.1	70.7	65.7	35.2	16.2	14.7	85.1	73.9	100	**95.0**
NB	78.9	44.1	43.6	61.1	13.2	11.1	80.0	72.0	100	**93.2**
NB-Tree	89.3	64.1	88.2	44.7	15.1	12.3	95.0	79.9	100	**94.0**
NNge	70.4	33.1	100	77.9	16.2	15.7	100	85.4	100	**90.1**
K*	60.1	45.5	100	45.1	14.0	14.0	100	87.6	100	**95.2**
OutexTC10										
1-NN	90.5	45.1	80.0	33.1	15.1	8.2	100	86.8	100	**87.5**
Adaboost	80.8	32.1	60.4	22.1	10.2	6.6	70.0	51.2	100	**82.2**
SVM	70.1	15.0	55.5	15.2	10.5	7.4	90.0	72.2	100	**80.5**
NB	33.6	22.3	60.1	50.9	12.0	7.5	80.5	70.5	97.3	**81.5**
NB-Tree	20.1	9.5	20.0	10.1	12.0	7.7	100	**87.1**	100	**87.1**
NNge	20.0	11.2	15.2	7.6	12.0	9.4	100	85.6	100	**88.1**
K*	50.0	44.1	12.3	6.9	10.0	7.4	100	86.2	100	**87.1**
UIUC										
1-NN	100	**93.7**	100	72.1	54.1	32.5	85.0	33.1	100	85.8
Adaboost	80.1	54.4	75.0	66.1	33.2	8.9	77.1	25.9	100	**74.0**
SVM	93.2	65.4	83.4	71.8	12.1	7.9	56.2	23.3	100	**72.0**
NB	92.9	84.3	89.4	**72.5**	10.9	6.8	40.5	12.7	100	70.1
NB-Tree	96.4	70.9	53.3	48.4	33.5	10.9	36.7	15.1	100	**75.0**
NNge	71.1	66.3	93.4	**77.9**	12.1	7.4	28.5	18.1	98.3	70.0
K*	100	89.8	100	72.1	45.8	22.9	46.1	21.6	100	**75.0**
MINC										
1-NN	100	52.4	100	64.8	55.4	25.2	21.1	10.1	100	**72.0**
Adaboost	95.0	66.0	80.4	44.1	75.8	66.1	33.1	12.5	100	**74.0**
SVM	85.1	45.2	50.2	21.3	44.8	20.0	35.6	12.1	100	**75.0**
NB	81.8	56.1	76.9	54.9	25.1	9.4	40.1	25.3	100	**73.0**
NB-Tree	93.8	50.0	93.8	53.0	10.1	5.4	20.5	11.1	100	**77.0**
NNge	71.1	66.3	93.4	**77.9**	12.1	7.4	19.2	11.0	96.9	70.0
K*	100	32.7	100	43.2	33.1	10.1	23.4	10.1	100	**75.0**

the best performance among all the baseline methods with almost all the classifiers. Indeed, for the KTH-TIPS dataset the proposed method has achieved 93.6% as accuracy using 1-NN. KTH-TIPS provides images with variations in scale as well as variations in pose and illumination. In particular, ETCA shows better performance regarding SIFT and GP-criptor^{ri}. The latter one achieves only 41% average accuracy, since it does not handle scale change. Likewise, ETCA has achieved the overall best performance, which is 95.0%, on the OutexTC00 dataset, using the classifiers 1-NN, SVM and K*. This dataset is characterized by its extensive viewpoint and illumination changes, but it does not have scale and rotation changes. ETCA shows better performance to handle these changes in comparison to the GP-criptor^{ri}. Furthermore, in order to validate invariance against rotation change without considering scale change, the studied methods have been validated on the OutexTC10 dataset. The results show that the proposed method achieves the best performance accuracy, which is 88.1% using the NNge classifier. This confirms that our method is able to handle rotated and non rotated images with and without scale changes. Similarly, results on the UIUCTex dataset show that the proposed method records 95.00% accuracy using the 1-NN classifier and has the overall best performance among the compared methods (*e.g.* best SIFT accuracy is 89.8% using the K* classifier). This dataset is very challenging due to its high intra-class variation and to the presence of many deformations (illumination, viewpoint, rotation and scale). For the MINC-2500 dataset, SURF achieves the best accuracy which is 77.9% using the NNge classifier. Proposed method has achieved comparable performance accuracy which is 77.00% using the NB-Tree classifier. This confirms that ETCA can handle all kind of deformation at once. The overall (for all the classifiers) average accuracy for this dataset is about 77% for ETCA and about 50% for SURF.

5 Conclusion

This work is devoted to introducing a genetic programming method to elaborate optimal texture image descriptor for scale-invariant texture classification. Features are extracted using the SIFT technique in order to have potential keypoints with a significant neighborhood distance that captures keypoints at different levels (zoom) and fed them to a tree representation. Proposed method has the potential of classifying not only texture images but also real-world images. Moreover, ETCA does not require domain expert to detect a set of keypoints, since it detects these keypoints automatically and it does not require any domain knowledge. The main contribution of this work is to automatically evolve a descriptor generated from genetic programming based on a scale invariant set of keypoints extracted in a pretreatment step. The evaluation shows that the method is effective to evolve a descriptor that is invariant against illumination, rotation and scale changes, with no need to human intervention. Indeed, the application area and the obtained results demonstrate that using ETCA may result in data-driven elaboration of an optimal filter image descriptor for subsequent solution of the image classification task. As future work, genetic programming could be also adapted to generate a combination of textural and edge description of the texture, while preserving rotation and scale invariance.

References

1. Al-Sahaf, H., Al-Sahaf, A., Xue, B., Johnston, M., Zhang, M.: Automatically evolving rotationinvariant texture image descriptors by genetic programming. IEEE Trans. Evol. Comput. **21**(1), 83–101 (2017)
2. Al-Sahaf, H., Zhang, M., Johnston, M.: Genetic programming for multiclass texture classification using a small number of instances. In: Proceedings of the 10th International Conference on Simulated Evolution and Learning, pp. 335–346 (2014)
3. Al-Sahaf, H., Zhang, M., Johnston, M., Verma, B.: Image descriptor: a genetic programming approach to multiclass texture classification. In: Evolutionary Computation (CEC), pp. 2460–2467 (2015)
4. Bay, H., Tuytelaars, T., Gool, L.V.: SURF: speeded up robust features. In: Computer Vision-ECCV 2006, vol. 3951, no. 1, pp. 404–417 (2006)
5. Bell, S., Upchurch, P., Snavely, N., Bala, K.: Material recognition in the wild with the materials in context database. In: Computer Vision and Pattern Recognition (CVPR) (2015)
6. Giveki, D., Karami, M.: Scene classification using a new radial basis function classifier and integrated SIFT–LBP features. Pattern Anal. Appl. 1–14 (2020). https://doi.org/10.1007/s10044-020-00868-7
7. Kokkinos, I., Yuille, A.: Scale invariance without scale selection. In: IEEE Conference on Computer Vision and Pattern Recognition, pp. 1–8 (2008)
8. Lazebnik, S., Schmid, C., Ponce, J.: A sparse texture representation using local affine region. IEEE Trans. Pattern Anal. Mach. Intell. **27**, 1265–1278 (2005)
9. Lowe, D.: Distinctive image features from scale-invariant keypoints. Comput. Vision **60**(2), 91–110 (2004)
10. Mallikarjuna, P., Targhi, A., Fritz, M., Hayman, E., Caputo, B., Eklundh, J.O.: The KTH-TIPS database, July 2004
11. Mellor, M., Hong, M., Brady, M.: Locally rotation contrast and scale invariant descriptors for texture analysis. Trans. Pattern Anal. Mach. Intell. **30**(1), 52–61 (2008)
12. Mikolajczyk, K., Schmid, C.: A performance evaluation of local descriptors. IEEE Trans. Pattern Anal. Mach. Intell. **27**(10), 1615–1630 (2005)
13. Ojala, T., Maenpaa, T., Pietikainen, M., Viertola, J., Kyllonen, J., Huovinen, S.: Outex - new framework for empirical evaluation of texture analysis algorithms. In: Object Recognition Supported by user Interaction for Service Robots, vol. 1, pp. 701–706 (2002)
14. Roy, S.K., Ghosh, D.K., Dubey, S.R., Bhattacharyya, S., Chaudhuri, B.B.: Unconstrained texture classification using efficient jet texton learning. Appl. Soft Comput. **86**, 105910 (2020)
15. Sun, X., Wang, J., Kong, F.M.L.: Scale invariant texture classification via sparse representation. Neurocomputing **112**(1), 338–348 (2013)
16. Venkataramana, M., Sreenivasa, E., Satyanarayana, C., Anuradha, A.: A review of recent texture classification: methods. IOSR J. Comput. Eng. (IOSR-JCE) **14**(1), 54–60 (2013)

A Monetary Policy Strategy Based on Genetic Algorithms and Neural Networks

Talitha F. Speranza[1(✉)], Ricardo Tanscheit[2], and Marley M. B. R. Vellasco[2]

[1] Barcelona Graduate School of Economics, 08005 Barcelona, Spain
talitha.speranza@barcelonagse.eu

[2] Pontifical Catholic University of Rio de Janeiro, Rio de Janeiro 22451-900, Brazil
{ricardo,marley}@ele.puc-rio.br

Abstract. We propose a novel monetary policy strategy in an attempt to provide an auxiliary tool to central banks, whose main predictive models are still from the Dynamic Stochastic General Equilibrium (DSGE) family, which has some flaws. We derive an objective function from three empirical relationships that have long been established in the economic literature and we seek to minimise the value of this function by choosing the interest rate via a genetic algorithm. Since the function is forward looking, we use a neural network to predict values of unemployment and inflation. Using data from Brazil, simulation results suggest that had the Brazilian central bank applied our strategy, and all other economic conditions remained equal, inflation could have been lower for 62.48% of the time. Predicted unemployment, however, was lower only for 39.69% of covered periods, as it faces a trade-off with inflation.

Keywords: Neural networks · Monetary policy · Genetic algorithms

1 Introduction

Monetary authorities around the world conduct policy in order to stabilise inflation and mitigate its deleterious effects. Some of them also take unemployment explicitly into account, trying to minimise the trade-off between this variable and inflation. Whether this is the case or not, the policy instrument is the short-term interest rate almost everywhere and Dynamic Stochastic General Equilibrium (DSGE) models are the favourite choice of central bankers to help them setting the interest rate, despite these models' flaws. Efforts to subdue the shortcomings have been insufficient: to this date, there is an ongoing demand for building a new framework to support monetary policy.

We aim at filling this gap and apply our strategy to the case of Brazil. In contrast with the traditional approach, we do not build a model affected by *ad hoc* assumptions, identification issues, and questionable policy prescriptions. Rather,

Supported by Pontifical Catholic University of Rio de Janeiro.

L. Iliadis et al. (Eds.): EANN 2020, INNS 2, pp. 605–616, 2020.
https://doi.org/10.1007/978-3-030-48791-1_48

in a novel approach, we use a genetic algorithm and a neural network, seeking to minimise an objective function that depends on the interest rate through future inflation and future unemployment. We derive this objective function from three empirical relationships observed in a wide range of countries and periods.

Since the objective function is prospective, it is necessary to estimate future unemployment and inflation for every potential solution (i.e. series of interest rates) generated by the genetic algorithm. Predictions are computed by a multilayer perceptron, whose inputs are the attempted series of interest rates and a large set of covariates. Our results suggest that had the Brazilian central bank applied our strategy, and all other economic conditions remained equal, inflation could have been lower for 62.48% of the time. Predicted unemployment, however, was lower only for 39.69% of covered periods, as it faces a trade-off with inflation.

Given the importance of inflation and unemployment for any given country, and in particular for Brazil, where inflation has been historically high and unemployment is currently a major concern, this work's contribution intends to be of a practical nature above all. Nonetheless, it also adds to the literature on machine learning applied to monetary policy. There are few papers relating both subjects and, to the best of our knowledge, this is only the second study trying to create a novel interest rate rule based on machine learning. Unlike this previous study, which automatises a central bank's behaviour, ours suggests that our framework could be of help in lowering inflation.

The remainder of this article is organised as follows. The Sect. 2 is devoted to a very brief literature review. Section 3 describes our proposed model and lists the time series we used. Section 4 discusses the results and shows how the model can be used in practice. Section 5 concludes the article.

2 Background

2.1 Failure of DSGE Models

Before the 2008 financial crisis, the DSGE framework was standard, but the crisis was a disruption in the financial sector only comparable to that of 1929 and no economist could see it coming. Their models were evidently flawed. Problems have been recognised by several researchers: (i) assumptions are unrealistic and most conclusions were not empirically confirmed [1], (ii) policy implications are unconvincing [4], and (iii) there are more parameters to estimate than equations and all estimation methods are prone to cherry-picking [10]. The most promising proposed alternative to DSGEs, agent-based models, are also subjected to this last issue.

2.2 Macroeconomic Relationships

Our model stems from economic relationships that are observed across almost all countries and at most periods for which historical data is available. In the next subsections, we briefly discuss the literature on these relationships and their empirical validity, besides describing the correlations themselves.

Okun's Law: This law implies an empirical and negative relationship between the unemployment rate and the gross domestic product (GDP)[1] growth rate. Evidence that it holds for most countries is available [2]. Its general form is:

$$u - \bar{u} = F(y - \bar{y}) + \kappa \tag{1}$$

where u is the unemployment rate, $\bar{u}$ is the natural[2] unemployment rate, y is the GDP growth rate, κ is a random shock, $\bar{y}$ is the natural GDP growth rate and F is a function such that $\frac{\partial F(y-\bar{y})}{\partial (y-\bar{y})} < 0$.

Phillips Curve: The Phillips Curve, in its modern form, is an inverse relationship between expected inflation and unemployment. Strong empirical evidence across countries can be easily found [8]. The curve is stated as follows:

$$\pi = E_t[\pi] + H(u - \bar{u}) \tag{2}$$

where π is the inflation rate and ϵ is a stochastic variable. H is assumed to be a function such that $\frac{\partial H((u-\bar{u})}{\partial (u-\bar{u})} < 0$.

Liquidity Effects: Interest rates established by central banks impact a country's total production, albeit not immediately, but over time. Higher interest rates gradually decrease GDP growth, as empirically demonstrated by [6]. This relationship, the so-called liquidity effects, is shown below:

$$y_t = G^L(i) \equiv G(i_{t-d}, i_{t-d-1}, ..., i_L) \tag{3}$$

where i is the interest rate, d is an integer representing the distance of the first lag, L is the number of lags on i, and G is a function such that $\frac{\partial G(i)}{\partial i} < 0$.

2.3 Machine Learning Applied to Monetary Policy

Literature relating machine learning to monetary economics is rather scarce. Some recent applications can be found in [5,11]. The only study that is closely related to ours is [9], in which the authors proposed a new model for inflation targeting based on fuzzy control techniques. However, the fuzzy rules merely automate the Czech Central Bank's actual strategy, instead of pursuing a method for improving its performance.

[1] A country's total production of final goods and services.

[2] The word *natural* refers to the value of a given country's economic variable when production of goods and services is operating at full capacity, i.e. production would not increase with more resources.

3 Developing the Framework

The method we propose to minimise future inflation and unemployment consists of three steps. First, from three empirical relationships, we derive an objective function that depends on current and past interest rates (in Brazil, the SELIC rate[3]) through future inflation and future unemployment rates. Then the genetic algorithm generates potential solutions to the central bank's problem. Finally, using these potential solutions, a neural network predicts future inflation and unemployment rates. These two are necessary to evaluate the objective function for each potential solution and then pick the best among them. If the number of generations has reached a maximum, the procedure stops and the solution is considered to be the one for which the objective function value is the lowest. Otherwise, the genetic algorithm generates new potential solutions from the ones that were previously picked.

3.1 Overview

We now detail the procedure a little longer. For clarity, the whole process is illustrated in Fig. 1. The starting box (the upper pink one) states that there is an objective function $O(.)$ that we need to minimise by choosing an interest rate series $\{i_t\}_{t=1}^{T}$. We derived $O(.)$ from the three empirical relationships that were explained and justified in Sect. 2.2, and it has the following form:

$$O(.) = \sum_{t=1}^{T} R^t \cdot E_t[\pi_{t+17}] \cdot E_t[u_{t+17}] \cdot E_t[\pi_{t+34}] \cdot E_t[u_{t+34}] \tag{4}$$

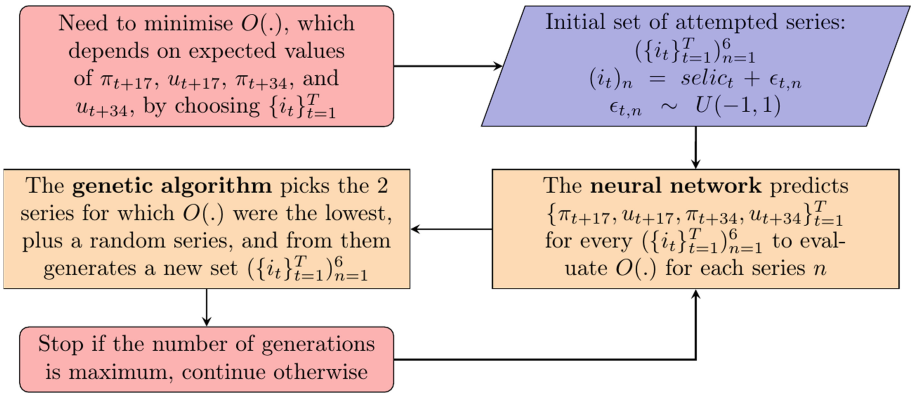
Need to minimise $O(.)$, which depends on expected values of π_{t+17}, u_{t+17}, π_{t+34}, and u_{t+34}, by choosing $\{i_t\}_{t=1}^{T}$
Initial set of attempted series: $(\{i_t\}_{t=1}^{T})_{n=1}^{6}$ $(i_t)_n = selic_t + \epsilon_{t,n}$ $\epsilon_{t,n} \sim U(-1,1)$
The **neural network** predicts $\{\pi_{t+17}, u_{t+17}, \pi_{t+34}, u_{t+34}\}_{t=1}^{T}$ for every $(\{i_t\}_{t=1}^{T})_{n=1}^{6}$ to evaluate $O(.)$ for each series n
The **genetic algorithm** picks the 2 series for which $O(.)$ were the lowest, plus a random series, and from them generates a new set $(\{i_t\}_{t=1}^{T})_{n=1}^{6}$
Stop if the number of generations is maximum, continue otherwise

Fig. 1. Detailed overview of the framework

[3] From portuguese, *Sistema Especial de Liquidação e Custódia*, which stands for Special Clearance and Escrow System. It is the base interest rate in Brazil.

Hence our objective function is a discounted sum of Cobb-Douglas value functions[4] $V(.) = E_t[\pi_{t+17}] \cdot E_t[u_{t+17}] \cdot E_t[\pi_{t+34}] \cdot E_t[u_{t+34}]$ where the discount factor is $R \in [0, 1]$, i.e. inflation and unemployment have more weight in periods that are closer to the current one (since the central bank is more concerned about recent periods). The arguments of $V(.)$ are the expected inflation and unemployment seventeen weeks (four months) ahead, as well as inflation and unemployment thirty four weeks (eight months) ahead, and these four variables are actually functions of the interest rate at time t. This means that we need to minimise $O(.)$ by choosing a whole series $\{i_t\}_{t=1}^{T}$.

Any choice of how far is the future (in our notation, it means how big is d) is good as any other, so here we defined that $\pi = \pi_{t+17}$ and $u = u_{t+17}$[5], i.e. both inflation and unemployment four months ahead. Moreover, we add π_{t+34} and u_{t+34} to the value function with two purposes: (i) increase the precision of the estimates, and (ii) account for mid-term inflation and unemployment.

Since $O(.)$ is forward looking, we need to calculate expected values for future inflation and unemployment. We do so by using a neural network, specified in Sect. 3.4. As depicted in the blue box in Fig. 1, the neural network initially predicts values for six series: the original SELIC series and five other series generated from this series by adding a draw from a random uniform distribution to each of its elements, five different times. Afterwards, as shown by the loop in Fig. 1, the network is fed by the genetic algorithm, which generates a new set of six series in its attempt to minimise $O(.)$.

3.2 Data

Time series were all extracted from the Central Bank of Brazil (CBB) website, with the exception of unemployment. In this case, the National Continuous Household Sample Survey (PNADC[6]) was used. A complete list of these series, their frequencies and precise sources is shown in Table 1. Note that most series are originally monthly ones, but if we had kept this frequency, there would have been too few data points to train the neural network. Since there are also daily series, we decided to work with weekly data[7]. Values for monthly data were repeated for all weeks of a given month, while data for daily series were collapsed in weekly averages. As a result, we obtained 728 observations ($T \equiv 728$) per series, stretching from the 48th week of year 2001 to the 34th week of 2016.

[4] This family of functions, i.e. $z = x_1^{a_1} \cdot x_2^{a_2} \cdot ... \cdot x_n^{a_n}$, possesses a number of important properties which have made it widely useful in the analysis of economic theories.

[5] We tried several other horizons, but this one delivered the best results.

[6] From portuguese, *Pesquisa Nacional por Amostra de Domicílios Contínua*, which translates into Continuous National Household Sample Survey.

[7] Although real world unemployment and inflation vary weekly, for these variables we dispose only of aggregate data from the end of each month. Therefore, the best approximation for a week of a given month is the value reported for the end of that same month. Some available data is daily and can be used to enhance this approximation through a forecasting model, which is part of what we are doing here.

Table 1. Time series used in this study

Description	Frequency	Source
International reserves (US$ millions)	Daily	CBB
Net public sector debt (%GDP)	Monthly	CBB
Public sector borrowing requirements (%GDP)	Monthly	CBB
United States official interest rates (%p.y.)	Monthly	FED[a]
Net current account (US$ millions)	Monthly	CBB
Net capital account (US$ millions)	Monthly	CBB
Exchange rate US$	Daily	CBB
National consumer price index (in 12 months)	Monthly	IBGE[b]
SELIC target (%p.y.)	Daily	CBB
SELIC in annual terms (basis 252, %p.y.)	Daily	CBB
GDP accumulated in the last 12 months (current R$ millions)	Monthly	CBB
Unemployment rate (PNADC, chained backwards)	Monthly	IBGE/FGV[c]

[a] Federal Reserve System
[b] Brazilian Institute of Geography and Statistics
[c] Fundação Getulio Vargas

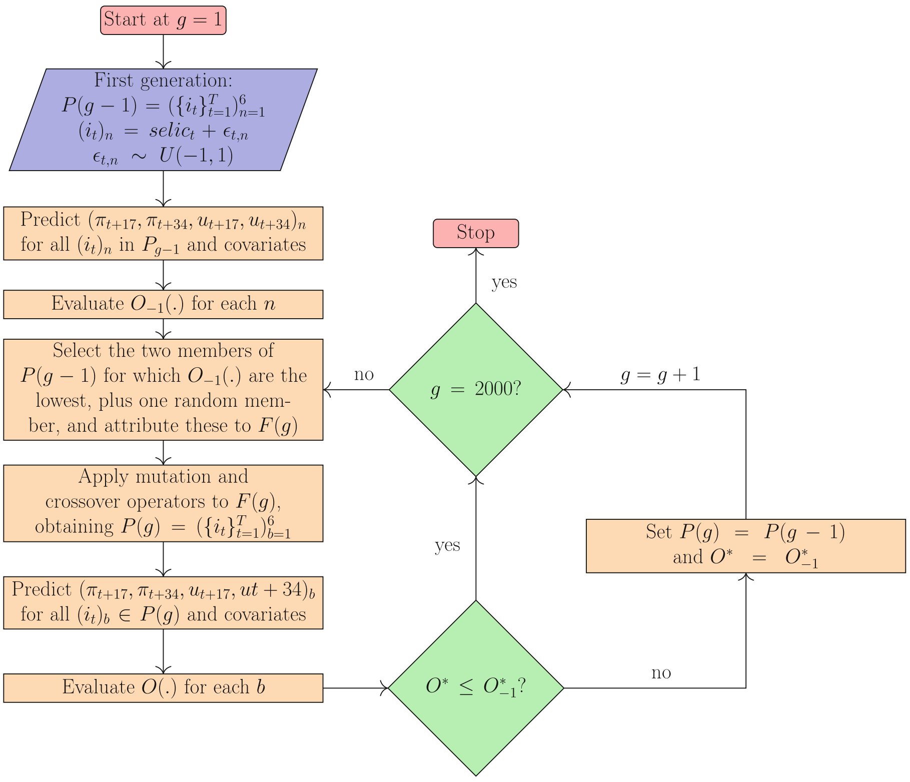
Start at $g = 1$
First generation:
$P(g-1) = (\{i_t\}_{t=1}^{T})_{n=1}^{6}$
$(i_t)_n = selic_t + \epsilon_{t,n}$
$\epsilon_{t,n} \sim U(-1,1)$
Predict $(\pi_{t+17}, \pi_{t+34}, u_{t+17}, u_{t+34})_n$ for all $(i_t)_n$ in P_{g-1} and covariates
Evaluate $O_{-1}(.)$ for each n
Select the two members of $P(g-1)$ for which $O_{-1}(.)$ are the lowest, plus one random member, and attribute these to $F(g)$
Apply mutation and crossover operators to $F(g)$, obtaining $P(g) = (\{i_t\}_{t=1}^{T})_{b=1}^{6}$
Predict $(\pi_{t+17}, \pi_{t+34}, u_{t+17}, ut+34)_b$ for all $(i_t)_b \in P(g)$ and covariates
Evaluate $O(.)$ for each b
$O^* \leq O^*_{-1}$?
yes
no
Set $P(g) = P(g-1)$ and $O^* = O^*_{-1}$
$g = g+1$
$g = 2000$?
no
yes
Stop

Fig. 2. Genetic algorithm flowchart

3.3 Genetic Algorithm

The algorithm we use to minimise Eq. 4 by choosing the whole SELIC time series is illustrated in Fig. 2 and works as follows. An individual (chromosome) is denoted by $\{i_t\}_{t=1}^{T}$. Naturally, a gene is considered to be an observation of the series. There are 728 observations for each series, but there is no need to find 728 values. In fact, the CBB chooses the SELIC every seven weeks so, since our data is weekly, an individual actually has $N \equiv T/7 = 728/7 = 104$ genes.

The first generation population, $P(g = 0)$, is composed of six individuals: the actual (original) SELIC rate and five other individuals generated from the actual SELIC series by adding an stochastic component, namely, a uniform random variable. We denote this set by $P(g = 0) = (\{i_t\}_{t=1}^{T})_{n=1}^{6}$, where $n \in [1, 6]$ indexes the individuals, so $(i_t)_n$ represents a gene t from individual n.

We then are able to evaluate the objective function $O(.)$ for each one of the six initial individuals. The weekly discount rate (parameter R in $O(.)$) we use is 0.0012. Thus, $(1 + R)^{52} \approx 6.5$, which is the mean annual SELIC interest rate over the period covered by the data. Using the base interest rate as a discount rate is standard in economic literature.

Next, we pick the two individuals for which $O(.)$ are the lowest and a random individual, the three survivors of the current generation. We apply crossover and mutation operations to these survivors to obtain six new individuals (by combining all possible pairs of survivors when crossing over), the candidate members of the new generation. If the lowest value $O^*(.)$ of the objective function among all members of the new generation is lower than the lowest value for the previous generation, $O^*_{-1}(.)$, we substitute the new generation for the old one. If not, we discard the new generation and apply the operators to the old one again, restarting the cycle. The algorithm stops after two thousand generations, the reason being explained in Sect. 4.2.

Crossover operation is standard: new individuals are generated from $N/2$ random genes from two parents, using a one-point cut in each chromosome (individual). As for mutation, a percentage of the total number of genes is randomly picked to be replaced by a random value. The percentage of mutated genes decays with generations: it starts at 7% and is reduced by a factor of 1.001 until it reaches the lower bound of 3%.

3.4 Neural Network Regression

Every week, the central bank will estimate future unemployment and inflation for each $i_t \in \{i_t\}_{t=1}^{T}$ for all attempted solutions, in order to evaluate the objective function 4, as part of the algorithm defined in Sect. 3.3. We use a multilayer perceptron (MLP) for this purpose.

The inputs of the MLP are seven lags of the following variables: unemployment rate, inflation rate, base interest rate (SELIC), effective interest rate[8], net government debt, government deficit, net current account, net capital account,

[8] This rate is slightly different from the SELIC, since it is determined by the market.

GDP, exchange rate with respect to US dollars, and United States official interest rate. Additionally, there are four outputs: unemployment in seventeen weeks (four months ahead), inflation in seventeen weeks, unemployment in thirty four weeks (eight months ahead), and inflation in thirty four weeks. All values are normalised to increase convergence speed.

The reason why we chose a window of size eight is that the CBB makes its decision about the base interest rate every seven weeks. Therefore, we assume it considers current variables as well as their values on each of the seven previous weeks. As for the variables themselves, they have long been established in economic literature to have predictive power over inflation and unemployment. We use a subset of variables that figure in the classical paper by James Stock and Mark Watson [12], which focus on forecasting inflation, and in a more recent work by Regis Barnichon and Paula Garda [3], about predicting unemployment.

4 Simulations

4.1 Neural Network's Predictions

We have tested a large range of parameters using a grid search to find the most appropriate configuration for the MLP. Choice was based on a 10-fold nested cross-validation procedure (also known as double cross validation), performed over 80% of randomly picked observations in our total sample, further split into random training (70% of the sub-sample) and validation (remaining 30% of the sub-sample) sets, both in external and internal loops. The other 20% of total observations have been used as a final testing set, again to avoid training bias.

The mean root mean square error (RMSE) over the 10 outer folds was of 0.104 and the best configuration turned out to be the following: (i) the activation function is the hyperbolic tangent (HTAN); (ii) there are four hidden layers with five neurons each; (iii) the solving method is the limited-memory Broyden–Fletcher–Goldfarb–Shanno (BFGS) algorithm. The RMSE of this network is of 0.095 for the training set and of 0.149 for the testing set, so the fact that the preferred configuration for the MLP does not suffer from overfitting seems warranted.

The other options for the activation function were the rectified linear unit function (RELU) and the logistic sigmoid function (LSIG), while the other possibilities for the solving method were the standard stochastic gradient descent (SGD) and the adaptive moment estimator (ADAM). The whole set of parameters used in the grid search are shown in Table 2.

4.2 Genetic Algorithm Evolution

Testing a range of parameters for the genetic algorithm was a challenge, since each battery of 1000 generations took approximately five hours[9] to run when the

[9] The machine in which we ran the algorithm has the following specifications: processor Intel(R) Core(TM) i7-4700MQ, CPU 2.40 GHz; memory 16 gb; operating system Ubuntu 18.04.2 LTS.

Table 2. Set of parameters used in the grid search

Parameter	Values
Number of neurons per hidden layer	3 to 5
Number of hidden layers	2 or 4
Solving algorithm	ADAM, SGD, or BFGS
Activation function	RELU, HTAN, or LSIG

least number of survivors per generation (2) was set. When we added one more survivor, the running time almost doubled: eight hours per 1000 generations. With four survivors per generation the running time got prohibitive and we simply interrupted the algorithm. A similar running time hike happened when we increased the initial population from six to greater numbers. The full set of tested values for parameters are presented in Table 3.

Table 3. Set of parameter values that were tested for the genetic algorithm. Preferred values are highlighted in blue.

Operator/Property	Parameter	Values
Mutation	Rate	0.03, 0.04, 0.06, 0.07, or $[0.03, 0.07]$
	Decay	1.001 or 1.0005
	Type	Random choice or random sum
Crossover	Type	One point
Survivors	Number	2, 3, or 4
Initial population	Number	6, 12, or 18

Other values were rejected on the basis of convergence speed. Fixed mutation rates reduced convergence speed, and the same was observed if the mutation rate was allowed to decrease from 7% to 3% at a rate of 1.0005, or if the mutation operator was adding to the chosen genes a random draw from a standard normal distribution (random sum) and not substituting random draws from a set of predetermined values for these genes (random choice).

Most of the evolution happened before 250 generations and convergence seems to have been achieved around the 1600^{th} generation. We tested for 4000 generations and there were no significant changes, i.e. the best individual improved only by a few hundreds, but these 2000 extra generations had a large cost in terms of time (10 h, due to nested loops inside the crossover operator).

4.3 Results

We now evaluate our strategy's performance. First, we compare the original SELIC series with the one generated by the genetic algorithm (the best individual after 2000 generations). Both are depicted in Fig. 3. We can see that, according to the strategy, the SELIC rate should in general have been lower. This is specially true in the two extremes of the period covered by our model.

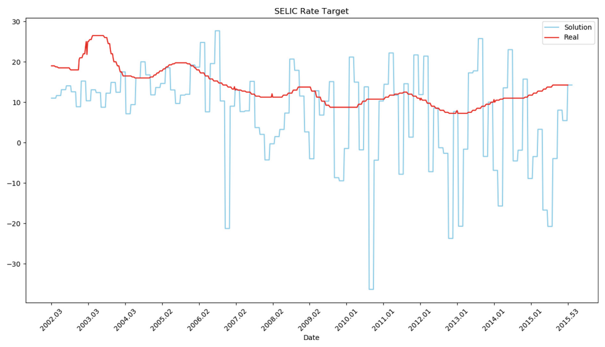

Fig. 3. SELIC target: actual series versus solution generated by the genetic algorithm

Moreover, it is clear that the generated SELIC series is significantly less persistent than the original series, albeit remaining in a shorter interval. Low persistence might pose a problem. According to several authors, for monetary policy to work, agents must be able to understand the central bank behaviour in order to adjust their expectations and make the decisions that, ultimately, policy-makers expect them to [7].

In agreement with this view, the central bank must have credibility and be able to commit to a certain smooth path for the target interest rate. If the SELIC frequently suffers large shocks, agents may not be able to believe in central bank's commitment, even if the institution anticipates these changes to the public. The policy would possibly be seen as discretionary, leading to negative effects on the economy. To avoid these possible deleterious effects, we smoothed the SELIC series, calculating its 12-month moving average (MA). As we note in Fig. 4, results now seem much less likely to cause the problems discussed above.

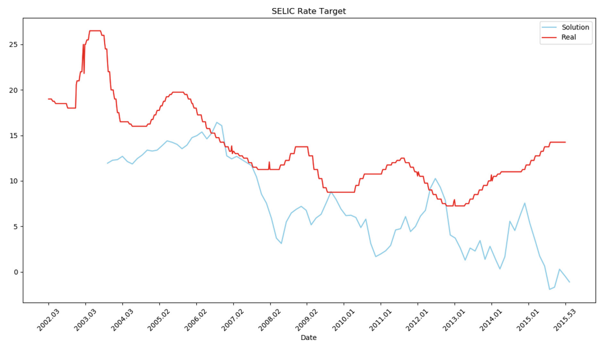

Fig. 4. SELIC target: actual series versus 12-month MA solution. First values were lost when calculating the MA.

We use the neural network to predict the values of unemployment and inflation for the MA version of our solution and compare it to actual inflation and unemployment. Inflation, for both horizons, was quite frequently lower when predicted by our solution as compared to what was observed under CBB actual policy decisions, while the same cannot be said about the unemployment rate. Table 4 summarises these results. On average, predicted inflation was lower than actual inflation for 62.48% of the time. Predicted unemployment, however, was lower only for 39.69% of weeks. This result might seem undesirable, but we need to stress, as we did in Sect. 2.2, that there is a trade-off between the expected inflation and the unemployment rate, so in fact we have achieved a reasonable outcome. It is possible, then, that the objective function has another minimum, where the predicted unemployment rate would be lower for most of the periods, as opposed to the predicted inflation.

Table 4. Descriptive statistics of genetic algorithm solution as compared to actual CBB solution

	Lower (%)	Relative volatility	Relative persistence
Inflation 4 mo	58.6	−0.07	−0.059
Unemployment 4 mo	45.27	−0.24	0.005
Inflation 8 mo	66.36	−0.08	−0.063
Unemployment 8 mo	34.11	−0.45	−0.009
SELIC	94.88	0.11	0.001

As a rule, predicted inflation and unemployment rate were less volatile than actual inflation and unemployment. This means that both variables remained bounded in a smaller interval, i.e. our strategy reduced the variance of both variables for the two horizons. This, of course, is a desirable feature of prospective inflation and unemployment, as it implies less uncertainty in the economy.

In spite of that, jumps were more frequent, with persistence, as estimated by AR(1) coefficient, being lower in all cases but the 4-months ahead unemployment and the SELIC. The MA version of the SELIC series generated by our strategy is, in its turn, lower than the actual SELIC for 94.88% of the time, which is a positive outcome in general, since lower interest rates is commonly associated with higher economic growth. In addition, using the same criteria as before, the MA of the SELIC series found by our algorithm is relatively more volatile, albeit almost as persistent as the CBB SELIC, meaning that we achieved our goal overall.

5 Conclusion

This paper presented in detail a novel tool to back the decision-making process of central banks. Our framework was based on well-established empirical evidence.

The first step was to obtain an objective function for the central bank, which we derived from three empirical relationships: Okun's Law, the Phillips Curve, and liquidity effects. Then we designed a genetic algorithm to minimise this objective function by choosing a time series of interest rates. Since the function is forward looking, we used a tuned multilayer perceptron to predict future values of unemployment and inflation.

The best individual was less persistent than the actual series set by the CBB. Thus we smoothed the series to avoid unfavourable economic results that could stem from low persistence. Compared to the original SELIC rate series, our solution was shown to be less volatile and lower 94.88% of the time, which is most likely positive from an economic standpoint. Besides, it implied lower values for inflation 62.48% of covered periods. Predicted unemployment, however, was lower only at 39.69% of the time, as it faces a trade-off with inflation.

References

1. Akerlof, G.A.: The missing motivation in macroeconomics. Am. Econ. Rev. **97**(1), 5–36 (2007)
2. Ball, L. et al.: Does one law fit all? Cross-country evidence on Okun's Law. In: documento presentado en el IMF-OCP Workshop on Global Labour Markets, Paris, vol. 1 (2016)
3. Barnichon, R., Garda, P.: Forecasting unemployment across countries: the ins and outs. Eur. Econ. Rev. **84**, 165–183 (2016)
4. Blanchard, O.: On the future of macroeconomic models. Oxford Rev. Econ. Policy **34**(1–2), 43–54 (2018)
5. Chakraborty, C., Joseph, A.: Machine learning at central banks. Bank of England working papers 674. Bank of England, September 2017
6. Christiano, L.J., Eichenbaum, M.: Liquidity effects, monetary policy, and the business cycle. J. Money Credit Bank. **27**(4), 1113–1136 (1995)
7. Clarida, R., Gali, J., Gertler, M.: The science of monetary policy: a new Keynesian perspective. J. Econ. Lit. **37**(4), 1661–1707 (1999)
8. Coibion, O., Gorodnichenko, Y., Ulate, M.: Is Inflation just around the corner? The Phillips curve and global inflationary pressures. In: AEA Papers and Proceedings, vol. 109, pp. 465–469 (2019)
9. Kukal, J., Van Quang, T.: A monetary policy rule based on fuzzy control in an inflation targeting framework. Prague Econ. Pap. **23**, 290–314 (2014)
10. Romer, P.: The trouble with macroeconomics. New York University, Technical report, Stern School of Business (2016)
11. Röonnqvist, S., Sarlin, P.: Bank distress in the news: describing events through deep learning. Neurocomputing **264**, 57–70 (2017)
12. Stock, J.H., Watson, M.W.: Forecasting inflation. J. Monet. Econ. **44**(2), 293–335 (1999)

Author Index

L. Iliadis et al. (Eds.): EANN 2020, INNS 2, pp. 617–619, 2020.
https://doi.org/10.1007/978-3-030-48791-1